MEASUREMENT 2015

10th International Conference on Measurement

Smolenice, Slovakia
May 25 - 28, 2015

Proceedings

MEASUREMENT 2015

ISBN 978-80-969672-9-2

Institute of Measurement Science
Slovak Academy of Sciences
Dúbravská cesta 9
841 04 Bratislava, Slovakia

The 10th International Conference MEASUREMENT 2015 was organized by the Institute of Measurement Science, Slovak Academy of Sciences, Bratislava, Slovakia.

MEASUREMENT 2015

Proceedings of the
10th International Conference on Measurement

Congress Center of the Slovak Academy of Sciences
Smolenice castle, Slovakia
May 25-28, 2015

MEASUREMENT 2015

Editors: Ján Maňka, Milan Tyšler, Viktor Witkovský, Ivan Frollo
Corrector: Andrej Dvurečenskij
Publisher: Institute of Measurement Science
Slovak Academy of Sciences
Dúbravská cesta 9, 841 04 Bratislava
Slovakia

ISBN 978-80-969672-9-2

Printed in Slovakia
by VEDA, Publishing House of the Slovak Academy of Sciences

ORGANIZATION OF THE CONFERENCE

Organizer
Institute of Measurement Science, Slovak Academy of Sciences, Bratislava, Slovakia

Co-organizer
Faculty of Electrical Engineering and Information Technology,
Slovak University of Technology, Bratislava, Slovakia

Technical sponsorship
IEEE Czechoslovakia Section
Slovak National Committee IMEKO, TC7 and TC13 committees,
Slovak Metrological Society
Slovak National Committee U.R.S.I.
Slovak Society of Biomedical Engineering and Medical Informatics

Conference Chairman

M. Tyšler, Slovakia

International Program Committee

J. Maňka, Slovakia, Chairman
B. Antić, Serbia
B. Arendacka, Germany
I. Bajla, Slovakia
G. Barbato, Italy
V. Boháč, Slovakia
E. Cocherová, Slovakia
K. De Buysser, Belgium
M.N. Durakbasa, Austria
I. Frollo, Slovakia
R. Harťanský, Slovakia
J. Havelka, Croatia
V. Havlíček, Czech Republic
Y.V. Chugui, Russia
A. Chunovkina, Russia
E. Kawate, Japan
R. Köning, Germany
G. Kozmann, Hungary
H. Kumar, India
F. Lehocki, Slovakia
L. Lhotská, Czech Republic
A. Liebert, Poland
K. Meigas, Estonia
V. Novickij, Lithuania
M. Potse, Switzerland
P.P.L. Regtien, The Netherlands
A. Rouane, France
K. Roubík, Czech Republic
V. Smieško, Slovakia
M. Štork, Czech Republic
T. Švantner, Slovakia
S. Takayama, Japan
M. Tarata, Romania
S. Trattnig, Austria
G. Wimmer, Slovakia
V. Witkovský, Slovakia
A. Woźniak, Poland

Local Organizing Committee

V. Witkovský
E. Bukovenová
P. Andris
M. Hain
J. Švehlíková
A. Dvurečenskij
D. Gogola
V. Juráš
M. Škrátek
M. Teplan

Reviewers
The submitted papers were evaluated by 62 reviewers, members of the International Program Committee and experts in the field. Each paper was scored by two or three reviewers.

This publication was supported by the Agency of the Ministry of Education of the Slovak Republic for the Structural Funds of the EU, Project Code 26240220073.

Preface

Measurement is only a limited special case
within the larger world and practice of assessment.

Prof. Lorrie A. Shepard, (2000), University of Colorado at Boulder

The MEASUREMENT conference organized by the Institute of Measurement Science, Slovak Academy of Sciences and focused on “Measurement Science” enters this year into its jubilee – the 10th repetition.

The first MEASUREMENT conference was held in 1997; however, already a long time before this date the Institute actively participated in organization of international workshops and EMISCON conferences focused on electronic measuring and information systems. Some of these events were held also on the beautiful premises of the Smolenice castle.

The initial intention of the workshops was to create a space for confrontation of results achieved by researchers of the Institute with the current outcome of foreign research institutions, usually presented by invited foreign experts. Traditional main topics of the workshops were - measurement theory, - design of experiments, - systems for measurement of selected physical quantities, - mathematical and computer modeling of bionic structures, - processing of biosignals, and, finally, - development of measuring systems for biomedicine.

Significant international success of these workshops has naturally led to the idea that the Institute of Measurement Science - in cooperation with other domestic and foreign institutions (Slovak University of Technology in Bratislava, Technical University in Kielce, Poland, Technical University Vienna, Austria, and University of West Bohemia, Czech Republic) - could organize a series of international conferences with the aim to create an international forum that could oversee the discipline of measurement science in Central Europe. The MEASUREMENT conference has been organized in a regular two-year cycle since 1997 and under the auspices of IMEKO technical committees TC7 and TC13 and with technical sponsorship of the IEEE organization since 2001.

At the initiative of the MEASUREMENT 2001 conference, the Institute of Measurement Science began publishing of the international scientific journal MEASUREMENT SCIENCE REVIEW in 2001. The magazine has become a major international scientific medium and its current publisher is De Gruyter Open. The journal is indexed in several databases and has a good Impact Factor. The mission of the journal is to publish papers on Measurement Science with orientation toward the theory of measurement, measurement of physical quantities and measurement in biomedicine.

Dear participants, it is our great honor to welcome you at the jubilee 10th international conference on measurement - MEASUREMENT 2015. We hope that the rewarding scientific program, together with the pleasant environment of the castle and offered social events, will attract your professional interest, create a working atmosphere and promote fruitful professional discussions.

Ivan Frollo
Conference Founder and Past Chairman

Milan Tyšler
Conference Chairman

CONTENTS

Invited Paper

The Envisaged New SI: Challenges for Precision Engineering

H. Bosse

Physikalisch-Technische Bundesanstalt (PTB), 38116 Braunschweig,
Bundesallee 100, Germany
Email: harald.bosse@ptb.de

Abstract. *In 1983 the definition of the SI unit of length, the metre, was defined by fixing the numerical value of a natural constant, namely the speed of light in vacuum c_0, without any uncertainty. The numerical value was derived from the most precise measurement values for c_0, known at the time of the definition. For the envisaged New SI, a similar approach is proposed for the re-definition of the SI units of mass, amount of substance, temperature and electrical current. For the definition of these SI units, the numerical values of the following natural constants are proposed to be fixed: Planck constant h, Avogadro constant N_A, Boltzmann constant k and elementary charge e. In this contribution it will be described how progress in precision engineering is needed to further reduce the uncertainties of experiments for the determination of h, N_A and k as a necessary prerequisite for the New SI to become effective in 2018 as proposed by the General Conference for Weights and Measures.*

Keywords: New SI, Defining constants, Precision engineering, XRCD method, Watt balance

1. Introduction

The system of Weights and Measures was recognized as a necessary basis for science, agriculture, construction and trade from the very beginning of ancient civilization. The importance of a reliable system of Weights and Measures or generally speaking of a reliable System of Units is documented by the fact that it has always been regarded as a governmental task of high priority until today. Throughout history the definitions of the units for Weights and Measures usually also differed from state to state until at the end of the 18^{th} century the idea was followed in France to base the definition of the unit of length on a stable natural reference, which was chosen to be the circumference of the earth. The metre standard (*mètre des Archives*) was thus defined as one ten-millionth of the distance from the North Pole to the Equator [1]. Finally, in 1875 the metre convention was signed by 17 national states and at the first General Conference on Weights and Measures in 1889 copies of the international protoypes of the kilogram and the metre made from Pt-Ir were distributed among the member states of the metre convention. All length measurements had to be referred to the international metre prototype (Pt-Ir bar with x-shaped cross-section and engraved lines). Starting with Michelson already in 1889 the development and application of interferometry allowed to decrease the uncertainty of length measurements. This was the reason that in 1960 the prototype-based definition was replaced by a wavelength-based definition of the metre using the orange spectral line of the ^{86}Kr spectral lamp.

This development shows that the definition of units should be flexible enough to make benefit of technological developments and to circumvent possible limitations of material standards or material effects. The envisaged New SI will be a big step in this direction. In particular, it will allow to replace the remaining prototype-based definition of the unit of mass, the kilogram, by a definition which fixes the numerical value of a natural constant, namely the Planck constant.

2. International System of Units (SI)

In 1960 the 11th General Conference on Weights and Measures (CGPM) adopted the name *Système International d'Unités* (International System of Units, international abbreviation SI), for the recommended practical system of units of measurement. The SI base units are a choice of seven well-defined units which by convention are regarded as dimensionally independent: the metre, the kilogram, the second, the ampere, the kelvin, the mole, and the candela. Derived units are those formed by combining base units according to the algebraic relations linking the corresponding quantities [2]. Taking into account the historical development of the system of units, also the SI was thought not to be static but to evolve to match the world's increasingly demanding requirements for precise measurements.

One important change to the SI was made in 1983 when the unit of length, the metre was defined by fixing the - at this time - best known numerical value of a natural constant, the speed of light in vacuum c_0, namely, 299 792 458 metre per second exactly, i.e. without attributing an uncertainty for c_0.

Envisaged "New SI"

This concept of defining an SI base unit by fixing the numerical value of a properly chosen natural constant or at least a so-called defining constant also inspired the envisaged "New SI" or the possible future revision of the SI.

In the "New SI" four of the SI base units, namely the kilogram, the ampere, the kelvin and the mole, will be redefined in terms of invariants of nature; the new definitions are proposed to be based on fixed numerical values of the Planck constant (h), the elementary charge (e), the Boltzmann constant (k), and the Avogadro constant (N_A), respectively, see figure 1.

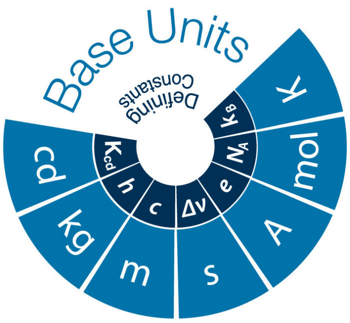

Fig. 1. Scheme of the base units and the defining constants in the New SI.

Different highly sophisticated experiments have been performed to realize precise measurements of the above mentioned natural constants. However, "while remarkable progress has been made over the last few years, the conditions for adopting the redefinitions, as set by the CGPM at its 23rd meeting (2007), have not yet been fully met" [3].

It is important to note, that *progress in precision manufacturing and precision engineering* is necessary to enable the envisaged New SI. In this contribution some examples of precision machining tasks and achievements in precision dimensional metrology will be discussed.

The most demanding conditions are set for the determination of the Planck constant h, which in the New SI will be used to define the unit of mass, the kg. The Consultative Committee for Mass (CCM) has formulated different prerequisites [4] before the new definition of the unit of mass could be put into place as well as a roadmap of different necessary steps to be achieved to reach the target until 2018. The updated CCM roadmap activity has been endorsed by the the CIPM at its 102nd meeting in 2013 and the CGPM at its 25th meeting in 2014 [5].

One of the conditions defined by the CCM is that at least three independent experiments, including work from watt balance and XRCD experiments, yield consistent values of the

Planck constant with relative standard uncertainties not larger than $5 \cdot 10^{-8}$ and that at least one of these results should have a relative standard uncertainty not larger than $2 \cdot 10^{-8}$.

3. Precision experiments for *h*

To determine the value of the Planck constant with the above mentioned uncertainties two different approaches are followed in metrology institutes worldwide, namely the watt balance experiments and the x-ray crystal density (XRCD) experiments [6].

In the watt balance experiments the gravitational force of a mass standard is compared with compensating electromagnetic forces generated by a coil in a static homogenous magnetic field in two different configurations, namely with a stationary coil carrying a defined current (weighing phase) and with the same coil moving at constant speed, thus inducing a constant voltage over the coil (moving phase), see figure 2 [7].

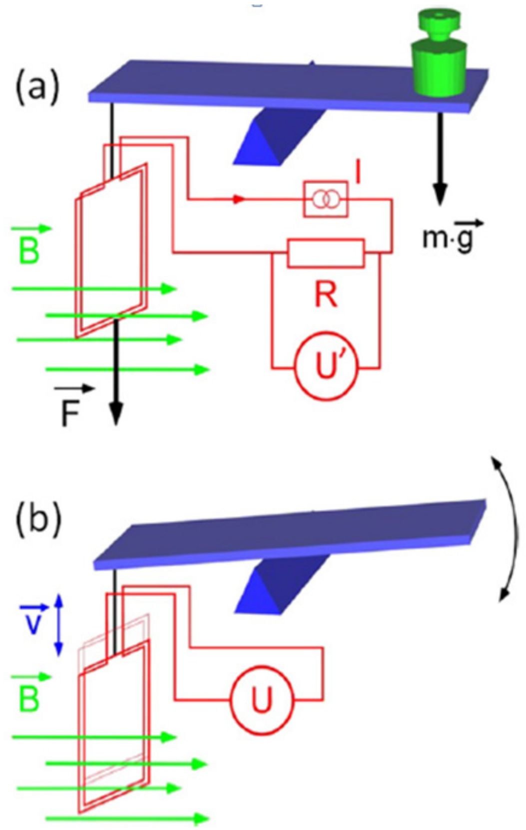

Fig. 2. a) static mode: the electromagnetic force acting on the current-carrying coil is balanced against the weight of the test mass m; b) dynamic mode: the coil is moved in the vertical direction through the magnetic field and the induced voltage U is measured. [7]

The precise alignment of the components of the watt balance as well as the control and interferometric measurement of the linear movement of the coil in the dynamic phase of the experiment are very demanding precision engineering challenges related to the watt balance experiments. In [8] an analysis on the alignment requirements was given for the watt balance operated at NRC. Different influences were analyzed, such as alignment of the laser beam, residual torques about horizontal axes and horizontal forces, alignment of the mass pan of the balance, determination of the Abbe offset, measurement and adjustment of the horizontal velocities, measurement of the angular velocities and changes in the coil position between phases. The resulting combined relative alignment uncertainty was estimated to be $5.5 \cdot 10^{-9}$. Recently, a new measurement value for the Planck constant *h* using the NRC watt balance has been reported with a relative uncertainty of $1.8 \cdot 10^{-8}$ [9], which would satisfy the condition set by CCM with respect to the smallest uncertainty of one from at least three independent experiments to be not larger than $2 \cdot 10^{-8}$.

In the XRCD method one uses a high purity, highly enriched ^{28}Si sphere (diameter of 93 mm and mass of about 1 kg) to precisely determine the Avogadro constant (N_A). The Avogadro constant links the atomic to the macroscopic world and is determined by the ratio of the density of an atomic unit cell of the ^{28}Si sphere and the density of the macroscopic sphere.

The measurement of the Avogadro constant is based on $N_A = n \cdot M / (\rho \cdot a^3)$, where $n = 8$ is the number of atoms per unit cell of a silicon crystal and ρ, M and a are the density, molar mass and lattice parameter, respectively. Precise measurements of the molar mass, the Si lattice parameter as well as the mass and the volume of the Si sphere are thus required to determine N_A. Because the molar Planck constant $h \cdot N_A$ is known from γ-spectroscopy experiments with an uncertainty of $7 \cdot 10^{-10}$ [10], a precise measurement of N_A also provides a precise value of h. A value for N_A using the XRCD method with a standard uncertainty of $3 \cdot 10^{-8}$ was published by the International Avogadro Consortium (IAC) in 2011 [11]. A new result of the IAC for N_A was recently measured with an improved standard uncertainty of $2 \cdot 10^{-8}$ [12].

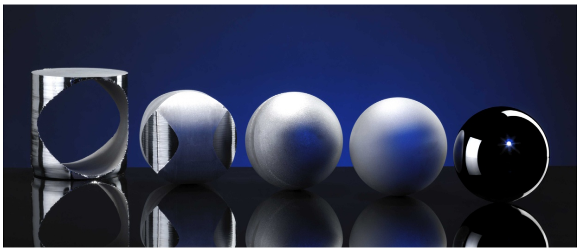

Fig. 3. Overview of different sphere manufacturing steps (hollowed ingot, cut form, turned, coarsely lapped and polished sphere).

In addition to the production requirements for the pure isotope enriched silicon single crystal material, also the manufacturing specifications for surface quality (average roughness values below 0.3 nm) and spherical form (roundness deviation below 30 nm in amplitude) of the macroscopic silicon spheres are very demanding, see figure 3 [13]. The biggest uncertainty contribution - about 2/3 of the total budget - so far is due to the volume determination of the silicon spheres. A special spherical Fizeau interferometer has been developed for this purpose, see figure 4 for a schematic drawing [14] as well as techniques to characterize the influence of different surface layers on the determination of N_A [15].

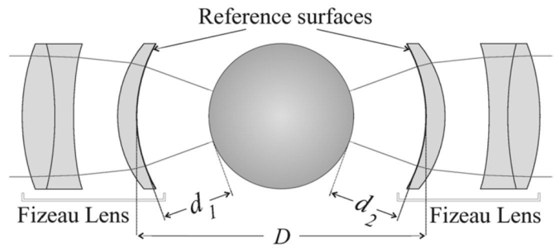

Fig. 4. Schematic drawing of the central part of the interferometer. The measured quantities are the distances between the sphere surface and the reference surfaces, d_1 and d_2, and the length of the empty etalon D.

Figure 5 shows a graphical representation of the resulting radius topography from all measurements performed on one of the silicon spheres manufactured along the process chain referred to in figure 2. One can clearly recognize the high symmetry with the characteristic of a rhombic dodecahedron – in the magnitude of several nanometers. This typical appearance of a cubic crystal is worked out in a unique and clear form (see figures 5, 6) and could also be repeated on other spheres.

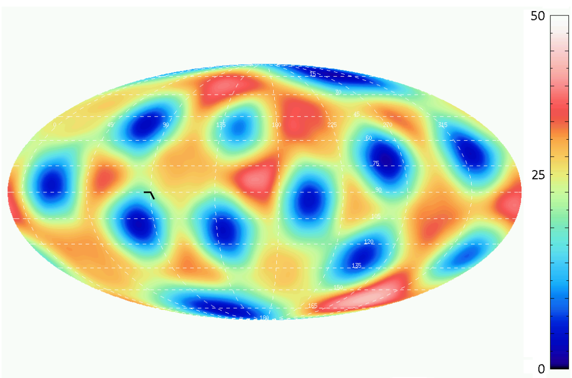

Fig. 5. Radius topography of silicon sphere PTB_11-01.

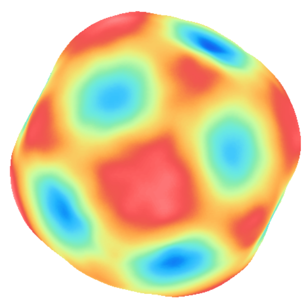

Fig. 6. Deviations from roundness of sphere PTB_11-01, 10^6-fold enhanced.

Although today three independent experiments for *h* have been published with uncertainties below $5{\cdot}10^{-8}$ and one experiment with an uncertainty below $2{\cdot}10^{-8}$ which also seem to be fairly consistent, one should not forget, that the CCM also requires procedures for the future realization and dissemination of the kilogram, as described in the *mise en pratique*, have been validated in accordance with the principles of the CIPM – MRA. This validation process of the procedures will need additional time as foreseen in the CCM roadmap.

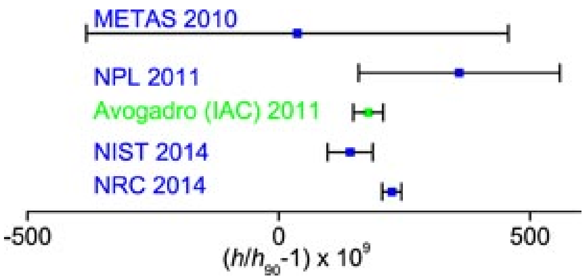

Fig. 7. Measurement results for Planck's constant *h*.

Figure 7 shows results and standard uncertainties of different experiments (watt balances and Avogadro (IAC)) for determination of *h*, as published in [16].

For an updated analysis of the measurement results on the NIST-3 watt balance over the last decade see [17].

4. Precision experiments for *k*

For precise determination of the Boltzmann constant *k*, different approaches are followed at NMI's worldwide. The most promising method with smallest achievable relative standard uncertainties below 10^{-6} is called acoustic gas thermometry (AGT). One experiment uses acoustic waves in a noble gas inside a precisely manufactured slightly ellipsoidal resonator to determine *k* [17], see figure 8. The small uncertainty obtained with this experiment was reported to be $u_R = 0.71 \cdot 10^{-6}$. In addition to other AGT experiments using spherical or slightly ellipsoidal resonators, there is another experiment which uses precisely manufactured cylindrical resonators for the AGT experiment [18].

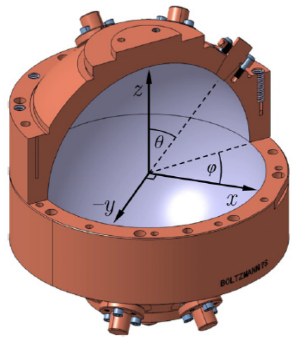

Fig. 8. Manufactured resonator for the NPL Boltzmann experiment [17].

One of the other independently developed methods for determination of *k* is based on dielectric-constant gas thermometry DCGT [19]. Here, the dielectric constant of a noble gas is measured under different pressures using a precise pressure balance. The calibration of the pressure balance is traceable to dimensional characterizations (diameter and form) of the effective area of cylindrical piston-cylinder pressure gauges, as shown in figure 9. Standard uncertainties of three-dimensional data of 8 nm for pistons and 16 nm for cylinders were obtained by a combination of high precision form and diameter measurements [21].

Fig. 9. Piston cylinder pressure gauge used for the determination of the Boltzmann constant *k* by means of the DCGT method.

5. Discussion

Some of the contributions from precision manufacturing and precision engineering for the progress of experiments in fundamental metrology aiming at the envisaged New SI were addressed. It has been shown how progress in manufacturing chains as well as in alignment and characterization of critical components of experiments contribute to the required further reduction of uncertainty of different experiments for determination of more precise numerical values of natural constants needed for the proposed definitions of the New SI.

Although today the formal requirements of the CCM with respect to the uncertainty and consistency of at least three independent experiments for determination of the Planck's constant *h* seem to be fulfilled, it will be of importance to follow the results of other watt balance experiments as well as repeated Avogadro experiments with a second lot of ^{28}Si material, which are under preparation. It is also of importance to maintain the established manufacturing chains and the described precision experiments for future use.

Acknowledgements

The author gratefully acknowledges the support of colleagues from PTB as well as external partners involved in the activities for the redefinition of the SI.

References

[1] Alder, Ken (2002). The Measure of all Things - The Seven-Year-Odyssey that Transformed the World. London: Abacus. ISBN 0-349-11507-9.

[2] The International System of Units (SI), http://www.bipm.org/en/measurement-units/, accessed March 30, 2015

[3] On the possible future revision of the SI, http://www.bipm.org/en/measurement-units/new-si/, accessed March 30, 2015

[4] Recommendation G1 (2013) of the Consultative Committee for Mass and Related Quantities, http://www.bipm.org/cc/CCM/Allowed/14/31a_Recommendation_CCM_G1%282013%29.pdf, accessed March 30, 2015.

[5] Resolution 1 of the 25th CGPM (2014), http://www.bipm.org/en/CGPM/db/25/1/, accessed March 30, 2015.

[6] Steiner R. History and progress on accurate measurements of the Planck constant. *Rep. Prog. Phys.* 76 016101 (46pp), 2013.

[7] Eichenberger A et al. Determination of the Planck constant with the METAS watt balance. *Metrologia,* 48: 133–141, 2011.

[8] Sanchez CA, Wood BM. Alignment of the NRC watt balance: considerations, uncertainties and techniques. *Metrologia,* 51: S42–S53, 2014.

[9] Sanchez CA, Wood BM, Green RG, Liard JO, Inglis D. A determination of Planck's constant using the NRC watt balance. *Metrologia,* 51: S5–S14, 2014.

[10] Mohr PJ, Taylor BN, Newell DB. CODATA recommended values of the fundamental physical constants: 2010. *Reviews of modern physics*, 84: 1527-1605, 2012.

[11] Andreas B et al. Counting the atoms in a ^{28}Si crystal for a new kilogram definition. *Metrologia,* 48: S1, 2011.

[12] Azuma Y et al. An improved result on the measurement of the Avogadro constant from a ^{28}Si crystal, accepted for publication in *Metrologia.*

[13] Nicolaus A, Meeß R, Bartl G. New Avogadro spheres for the redefinition of the kilogram. *Key Engineering Materials*, 613: 17-25, 2014.

[14] Bartl G. et al. Volume determination of the Avogadro spheres of highly enriched ^{28}Si with a spherical Fizeau interferometer. *Metrologia,* 48: S96, 2011.

[15] Busch I et al. Surface layer determination for the Si spheres of the Avogadro project. *Metrologia,* 48: S62, 2011.

[16] Robinson IA. Watt and joule balances. *Metrologia,* 51: S1, 2014.

[17] Schlamminger S et al. A summary of the Planck constant measurements using a watt balance with a superconducting solenoid at NIST, *Metrologia,* 52: L5–L8, 2015.

[18] de Podesta M et al. A low-uncertainty measurement of the Boltzmann constant. *Metrologia,* 50, 354, 2013.

[19] Zhang JT, Lin H, Sun JP, Feng XJ, Gillis KA, Moldover MR. Cylindrical Acoustic Resonator for the Redetermination of the Boltzmann Constant. *International Journal of Thermophysics*, 31(7): 1273-1293, 2010.

[20] Fellmuth B et al. Determination of the Boltzmann constant by dielectric-constant gas thermometry. *Metrologia,* 48, 382, 2011.

[21] Jusko O et al. Final results of the geometrical calibration of the pressure balances to be used for the new determination of the Boltzmann constant. *Key Engineering Materials*, 437: 150 – 154, 2010.

Theoretical Problems of Measurement

A Numerical Model of the Concept of a Graphene Polymer-Based Sensor

[2]M. Cap, [1]P. Fiala, [2]D. Nešpor, [1]P. Drexler

[1]SIX VUT v Brně, Technická 12, 616 00 Brno, Czech Republic,
[2]Department of Theoretical and Experimental Electrical Engineering, Technicka 12, 616 00 Brno, Czech Republic,
Email: capm@feec.vutbr.cz

Abstract. *The paper discusses the design and analysis of a graphene coaxial line suitable for sub-micron sensors of magnetic fields. The proposed numerical model is based on an analysis of a periodic structure with high repeatability, and it is built upon a graphene polymer having a basic dimension in nanometers. The model simulates the actual random motion in the structure as the source of spurious signals and considers the pulse propagation along the structure; furthermore, the model also examines whether and how the pulse will be distorted at the beginning of the electric line. The results of the analysis are necessary for further use of the designed sensing devices based on graphene structures.*

Keywords: Nanomaterials, Graphene, Signal sensing, Signal/Noise, Large periodic structure

1. Introduction

It is obvious from the research presented in papers [1] and [2] that the periodic structure of graphene should exhibit certain interesting electrical and electromagnetic properties regarding the propagation of an electromagnetic wave. The referenced articles nevertheless do not provide a clear conclusion that would facilitate prospective application of periodic structures with extreme properties in the field of EMG wave propagation. The authors have developed the idea to set up a simple numerical model and to propose an experiment suitable for the related verification. The numerical model enables us to evaluate the propagation of an electromagnetic wave along the surface consisting of a periodic structure (such as graphene or metamaterials) and the surrounding dielectric environment. Generally, the aim of the model is to evaluate the components of both the EMG wave and the power flux density in the time domain; thus, based on our knowledge of today’s manufacturing technologies, it would be easily possible to define the applicability of the periodic structure for specific purposes in electrical engineering and electronics. The model embodies an application of the quantum-mechanical model of matter and stochastic distribution of electric charge in individual elements of the structure. Although the structure is large, it exhibits a significant degree of periodicity; thus, it is possible to utilize, up to a certain level of complexity, the known finite methods (the finite and boundary element techniques or the finite volume method combined with a deterministic stochastic model, extreme modelling [3], [4]). An example is provided in Fig. 1a via the design of a single conductor with non-conductive surface, which represents the periodic structure of a graphene-based polymer or, by extension, a more complex application of such structure; to be more concrete, we can refer to Fig 1b and the model of a coaxial, symmetric electric line comprising two polymer systems formed on graphene basis.

2. Model of a Periodic Structure

The geometrical model designed to provide a simple comparison between classic materials and those based on a periodic structure with a large number of repeated elements is suitably expressed by the body shown in Fig. 1a, b. The presented drawing shows the concept of a macroscopic approach to the model combined with a quantum-mechanical model, both of which are characterised by concentric particles. In a radial coordinate, the model will assume dimensions in the order of nanometers, and in the longitudinal axis the dimensions will be more than several tens of millimeters.

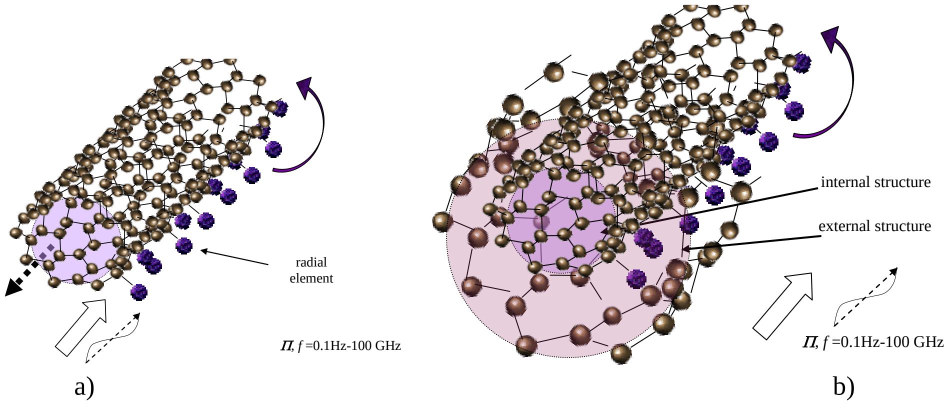

Fig. 1 Geometrical structure of the numerical analysis of surface wave propagation: a) single wire; b) coaxial line.

The proposed numerical model is based on the formulation of partial differential equations for the electromagnetic field (known as reduced Maxwell's equations); according to Heaviside's notation, we have the following formula for the magnetic field intensities and flux densities:

$$rot\,\boldsymbol{E} = -\frac{\partial \boldsymbol{B}}{\partial t} + rot\left(\boldsymbol{v}\times\boldsymbol{B}\right),\ \ rot\,\boldsymbol{H} = \boldsymbol{J}_T + \frac{\partial \boldsymbol{D}}{\partial t} + rot\left(\boldsymbol{v}\times\boldsymbol{D}\right),\ \ div\,\boldsymbol{B} = \boldsymbol{0},\ div\,\boldsymbol{D} = \rho, \tag{1}$$

where $\boldsymbol{H}$ is the magnetic field intensity, $\boldsymbol{B}$ is the magnetic flux density, $\boldsymbol{J}_T$ is the total current density, $\boldsymbol{D}$ is the electric flux density, $\boldsymbol{v}$ is the instantaneous velocity of the moving elements, and ρ is the electric charge volume density. Respecting the continuity equation

$$div\,\boldsymbol{J}_T = -\frac{\partial \rho}{\partial t}, \tag{2}$$

the vector functions are expressed by means of the scalar electric potential ϕ_e and the vector magnetic potential $\boldsymbol{A}$, and, after Coulomb calibration, the final relationship between the quantities is expressed as

$$rot\,\boldsymbol{H} = \gamma\left(\boldsymbol{E}+\boldsymbol{v}\times\boldsymbol{B}\right) - \frac{\partial\left(\varepsilon\,\boldsymbol{E}\right)}{\partial t} + \frac{\gamma}{q}\left(\frac{m_0\left(1-\frac{v^2}{c^2}\right)^{-\frac{1}{2}}\mathrm{d}\boldsymbol{v}}{\mathrm{d}t} + l\,\boldsymbol{v} + k\int_t \boldsymbol{v}\,\mathrm{d}t\right) + \frac{\partial \boldsymbol{D}}{\partial t} + rot\left(\boldsymbol{v}\times\boldsymbol{D}\right) \tag{3}$$

$$m\frac{\mathrm{d}\boldsymbol{v}}{\mathrm{d}t} + l\,\boldsymbol{v} + k\int_t \boldsymbol{v}\,\mathrm{d}t = q\left(\boldsymbol{E}+\boldsymbol{v}\times\boldsymbol{B}\right) - \frac{q}{\gamma}\frac{\partial\left(\varepsilon\,\boldsymbol{E}\right)}{\partial t}, \tag{4}$$

where m_0 is the quiescent mass of the particle, q is the electric charge of the moving particle, γ is the specific conductivity of the environment from the macroscopic perspective, l is the damping coefficient, k is the stiffness coefficient of the surrounding environment, the quantity indexes of the permeabilities μ and permittivities ε r denote the relative quantity value, and 0 denotes the value of the quantity for a vacuum.

Detailed Geometry of the Model of a Periodic Structure

The design of the geometrical model can now be characterized in greater detail. The fundamental element of a graphene-based periodic structure is a benzene core [5]; from the perspective of the stochastic distribution of the instantaneous position and arrangement of C valence electrons, the fundamental element can be schematically described as shown in Fig. 2, [6], Fig. 3.

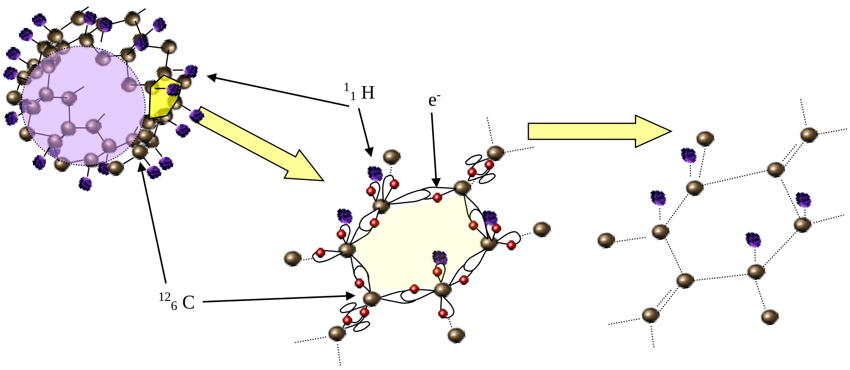

Fig. 2 Geometrical model of the basic structure element with probabilistic distribution of the valence electrons.

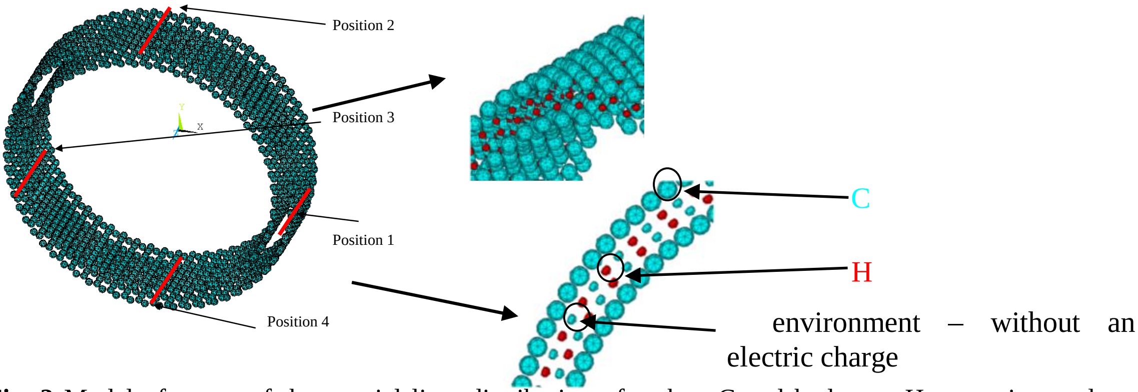

Fig. 3 Model of a part of the coaxial line: distribution of carbon C and hydrogen H atoms in a polymer structrure with a high degree of periodicity.

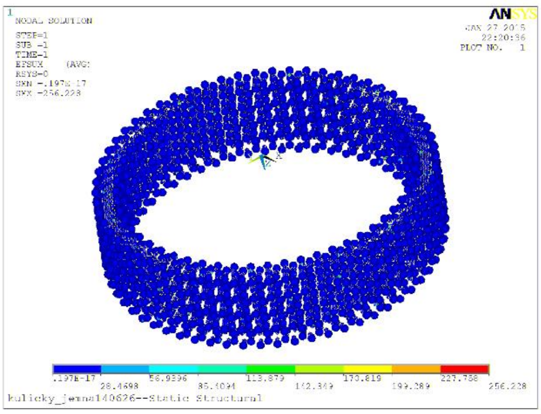

Fig. 4a Distribution of the electric field intensity module: E(t) [V/μm], t_1= 1 ps.

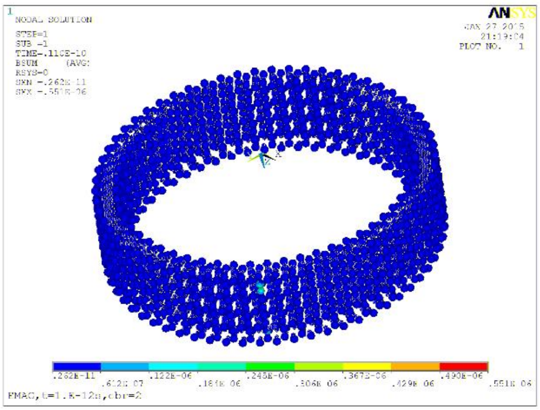

Fig. 4b Distribution of the magnetic flux density module: B(t) [pT], t_1= 1 ps.

Sensor design

The design that includes a coaxial conductor (Fig. 6) exhibiting the diameter of 7nm and external dimensions of less than 1μm must be loaded with suitable impedance at one of its ends, and the entire sensor comprising N threads is to be conceived as a Rogowski sensor.

3. Conclusion

We designed a geometrical model of a high periodicity nanostructure, and we also completed a numerical model for the solution and analysis of effects occurring in the propagation of an

EMG wave along the nanostructure. Within the procedure, initial numerical experiments targeting the propagation of an EMG wave in the given nanostructure were carried out too.

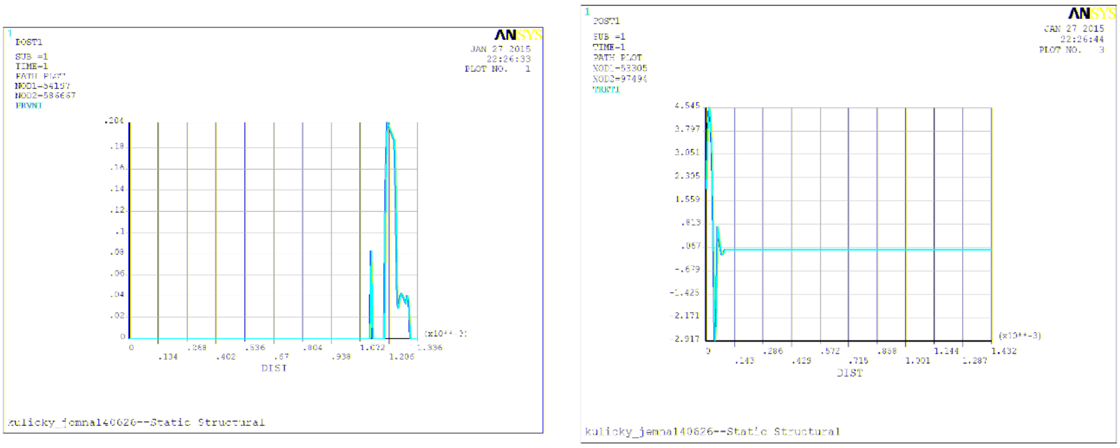

Fig.5 Behaviour of the distribution of the power specific density module $\Pi(t)$ [pW/μm^2], t_1= 1 ps along curve 1, (3).

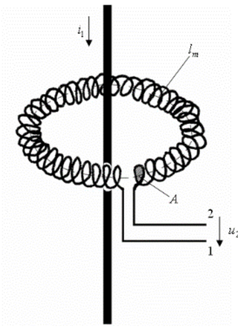

Fig. 6 Design and external dimensions (7nm) of the sensor conceived as a Rogowski sensor.

Acknowledgement

The research described in this paper was supported by the National Sustainability Program under grant No. LO1401. For the actual analyses and experiments, infrastructure of the SIX Center was used.

References

[1] van Vlaenderen KJ, and Waser A. Electrodynamics with the scalar field, *Physics*, 2: 1-13, 2001.

[2] van Vlaenderen KJ. A charge space as the orogin of sources, fields and potentials, *Physics*, arXiv:physics/9910022, v1 16 Oct 1999, 1-13, 1999.

[3] Fiala P, Macháč J., and Polívka J. Microwave noise field behaves like white light. *Progress in Electromagnetics*, 111, 311-329, 2011.

[4] Steinbauer M, Fiala P, Szabó Z, and Bartušek K. Experiments with accuracy of the air ion field measurement. *Advances in Electrical and Electronic Engineering*, 8(7): 276-279, 2008.

[5] Valentová E, Helánová V. Názvosloví a reakce organických sloučenin. Zemědělská 1, 613 00 Brno: Mendelova univerzita v Brně, 2012. 157 pp. ISBN 978-80-7375-602-4.

[6] http://www.computescotland.com/graphane-first-chemical-modification-of-graphene-2603.php, http://michaelgr.com/2009/01/31/is-graphenegraphane-the-future-of-cpus/.

An Algorithm for Demodulation of Correlated Quadrature Interferometer Signals

[1,2]G. Wimmer, [3]V. Witkovský, [4]R. Köning

[1]Mathematical Institute, Slovak Academy of Sciences, Bratislava, Slovakia
[2]Faculty of Natural Sciences, Matej Bel University, Banská Bystrica, Slovakia
[3]Institute of Measurement Science, Slovak Academy of Sciences, Bratislava, Slovakia
[3]Physikalisch-Technische Bundesanstalt, Braunschweig, Germany
Email: wimmer@mat.savba.sk

Abstract. *The measurement signals of the quadrature homodyne interferometers (say x and y, usually called Sine/Cosine signals and/or quadrature signals) typically exhibit offsets, unequal amplitudes and a phase difference that is not exactly* 90 *degree as would be expected in the ideal/theoretical case. Moreover, frequently there is a significant component of the measurement noise which is common to both signals (caused, e.g., by the amplitude noise of the laser), and as such, it results in a non vanishing correlation of the measured signals. Here we present a method for estimation of the unknown correlation coefficient from the observed data and suggest its implementation into the algorithm for demodulation and evaluation of the amplitude noise related uncertainty contribution of correlated quadrature interferometer signals, originally proposed by Köning, Wimmer and Witkovský in [2] for uncorrelated interferometer signals.*

Keywords: Quadrature homodyne interferometers, Heydemann correction, Ellipse fitting, Correlated interferometer signals, MINQUE

1. Introduction

In order to demodulate the observed homodyne interference signals an ellipse is fitted to both signals, x and y, simultaneously. This procedure was originally proposed by Heydeman [1] and is therefore known as Heydeman Correction (HC). The estimated ellipse parameters are used for demodulation of the quadrature interferometer signals and also for derivation of the associated uncertainties of the interferometric phase values and/or displacements (the parameters of primary interest in dimensional metrology), for more details see e.g. [1, 7]. In [2], we have suggested an iterative algorithm based on linearization of the originally nonlinear model (in fact the linear regression model with *nonlinear* constraints on its parameters). The nonlinear model is approximated locally by a linear regression model with *linear* constraints of type II, as suggested by Kubáček in [5], pp. 146 and 152. This allows to derive the *locally* best linear unbiased estimators (BLUEs) of the model (ellipse) parameters, as well as derivation of the (approximate) covariance matrix of the estimators. Using this solution the required interferometric phase values follow from (2), and their uncertainties can be obtained in a straightforward way by the law of propagation of uncertainty. The process of linearization/estimation can be iterated, until an adequately chosen convergence criterion is reached.

Originally, this method was suggested and derived for uncorrelated interferometer signals. However, as it was already mentioned, a component of the measurement noise common to both signals leads to (sometimes strongly) correlated measurement signals. So, in [3] we have modified the algorithm and presented a MATLAB implementation (`ellipseFit4HC`) which allows fitting also correlated interferometer signals, assuming that the correlation parameter is known in advance.

In situations when the number of measurements is sufficiently large, a simple analytic expression for the statistical uncertainty of the phase was derived in [4]. This allows to identify a practical limit of optical quadrature displacement interferometry, which already has been reached experimentally.

Mathematically, the (noiseless) output signals can be described as

$$\begin{aligned} x(\varphi) &= \alpha_0 + \alpha_1 \cos\varphi \\ y(\varphi) &= \beta_0 + \beta_1 \sin(\varphi + \varphi_0), \end{aligned} \tag{1}$$

where φ is the phase (the parameter of a primary interest), α_0 and β_0 denote the coordinates of the ellipse center (the offsets), α_1 and β_1 are the signal amplitudes, and $-\pi/2 < \varphi_0 < \pi/2$ is the phase offset. Under these circumstances, given the true values of the ellipse parameters, $\alpha_0, \beta_0, \alpha_1, \beta_1, \varphi_0$, and the particular signal values x and y (lying on this specific ellipse), the required interferometric phase φ is determined by using the relation

$$\varphi = \arctan\left[\frac{\alpha_1(y-\beta_0) - \beta_1(x-\alpha_0)\sin\varphi_0}{\beta_1(x-\alpha_0)\cos\varphi_0}\right]. \tag{2}$$

However, real applications have to use noisy experimental data (x_i, y_i), $i = 1, \ldots, n$. So it is a problem of fitting an ellipse to data by minimizing $SS(\vartheta) = \sum_{i=1}^{n} [x_i - (\alpha_0 + \alpha_1 \cos\varphi_i)]^2 + [y_i - (\beta_0 + \beta_1 \sin(\varphi_i + \varphi_0))]^2$. The procedure requires a minimization in the $(n+5)$-dimensional parameter space, with the parameters $\vartheta = (\alpha_0, \beta_0, \alpha_1, \beta_1, \varphi_0, \varphi_1, \ldots, \varphi_n)$. This is predictably cumbersome for relatively large n (a typical case for the interferometric measurements), so we shall rely on our approximation method. Here we focus mainly on the problem how to estimate the unknown correlation coefficient from the observed data.

2. Subject and Methods

We consider the following measurement model for the correlated quadrature output signals (x_i, y_i), $i = 1, \ldots, n$,

$$\begin{aligned} x_i &= \mu_i + \varepsilon_{x,i}, \\ y_i &= \nu_i + \varepsilon_{y,i}, \end{aligned} \tag{3}$$

with the following set of nonlinear restrictions on the model parameters,

$$\mu_i^2 + B\nu_i^2 + C\mu_i\nu_i + D\mu_i + F\nu_i + G = 0, \quad i = 1, \ldots, n, \tag{4}$$

where B, C, D, F, G represent the algebraic ellipse parameters. Notice that the ellipse parameters B, C, D, F, G only appear in the restrictions. They are uniquely related to the geometric ellipse parameters $\alpha_0, \beta_0, \alpha_1, \beta_1, \varphi_0$, for more details see [2]. In a matrix notation we get

$$\begin{pmatrix} \boldsymbol{x} \\ \boldsymbol{y} \end{pmatrix} = \begin{pmatrix} \mu \\ \nu \end{pmatrix} + \begin{pmatrix} \varepsilon_x \\ \varepsilon_y \end{pmatrix}, \quad \begin{pmatrix} \varepsilon_x \\ \varepsilon_y \end{pmatrix} \sim N\left(\begin{pmatrix} \mathbf{o} \\ \mathbf{o} \end{pmatrix}, \sigma^2 \begin{pmatrix} \boldsymbol{I} & \rho\boldsymbol{I} \\ \rho\boldsymbol{I} & \boldsymbol{I} \end{pmatrix}\right) \tag{5}$$

with $\boldsymbol{x} = (x_1, \ldots, x_n)'$, $\boldsymbol{y} = (y_1, \ldots, y_n)'$, $\mu = (\mu_1, \ldots, \mu_n)'$, $\nu = (\nu_1, \ldots, \nu_n)'$, $\varepsilon_x = (\varepsilon_{x,1}, \ldots, \varepsilon_{x,n})'$, $\varepsilon_y = (\varepsilon_{y,1}, \ldots, \varepsilon_{y,n})'$, such that $\varepsilon_x \sim N(\mathbf{o}, \sigma^2\boldsymbol{I})$ and $\varepsilon_y \sim N(\mathbf{o}, \sigma^2\boldsymbol{I})$ (possibly correlated, with $corr(\varepsilon_{x,i}, \varepsilon_{y,i}) = \rho$, $i = 1, \ldots, n$), and with nonlinear restriction on the model parameters of the form $\boldsymbol{B}\theta + \boldsymbol{b} = \mathbf{o}$, where $\boldsymbol{B} = [\nu^2 \vdots \mu\nu \vdots \mu \vdots \nu \vdots \mathbf{1}]$, $\theta = (B, C, D, F, G)'$, $\boldsymbol{b} = \mu^2$, $\mu^2 = (\mu_1^2, \ldots, \mu_n^2)'$, $\nu^2 = (\nu_1^2, \ldots, \nu_n^2)'$, $\mu\nu = (\mu_1\nu_1, \ldots, \mu_n\nu_n)'$, and $\mathbf{1} = (1, \ldots, 1)'$, $\mathbf{o} = (0, \ldots, 0)'$. Here, $[\boldsymbol{u} \vdots \boldsymbol{v}]$ denotes the concatenation of the vectors $\boldsymbol{u}$ and $\boldsymbol{v}$ to a matrix.

We shall linearize the nonlinear system of restrictions, $\boldsymbol{B}\theta + \boldsymbol{b} = \mathbf{o}$, by the first-order Taylor expansion about μ_0, ν_0, and θ_0,

$$\boldsymbol{B}\theta + \boldsymbol{b} \approx \boldsymbol{A}_0 \begin{pmatrix} \mu_\Delta \\ \nu_\Delta \end{pmatrix} + \boldsymbol{B}_0\theta_\Delta + \boldsymbol{c}_0, \tag{6}$$

where

$$\begin{aligned} \boldsymbol{A}_0 &= \left[\mathrm{Diag}\left(\left[\mathbf{o} \vdots \nu_0 \vdots \mathbf{1} \vdots \mathbf{o} \vdots \mathbf{o}\right] \theta_0 + 2\mu_0\right) \vdots \mathrm{Diag}\left(\left[2\nu_0 \vdots \mu_0 \vdots \mathbf{o} \vdots \mathbf{1} \vdots \mathbf{o}\right] \theta_0\right)\right], \\ \mu_\Delta &= \mu - \mu_0, \; \nu_\Delta = \nu - \nu_0, \\ \boldsymbol{B}_0 &= \left[\nu_0^2 \vdots \mu_0\nu_0 \vdots \mu_0 \vdots \nu_0 \vdots \mathbf{1}\right], \\ \theta_\Delta &= \theta - \theta_0, \; \boldsymbol{b}_0 = \mu_0^2, \; \boldsymbol{c}_0 = \boldsymbol{B}_0\theta_0 + \boldsymbol{b}_0 \text{ and } \theta_0 = (B_0, C_0, D_0, F_0, G_0)'. \end{aligned} \tag{7}$$

Thus, we get the (approximate) linear regression model with linear constraints,

$$\begin{pmatrix} \boldsymbol{x}_\Delta \\ \boldsymbol{y}_\Delta \end{pmatrix} \overset{approx}{\sim} N\left(\begin{pmatrix} \mu_\Delta \\ \nu_\Delta \end{pmatrix}, \boldsymbol{H}\right) \wedge \boldsymbol{A}_0 \begin{pmatrix} \mu_\Delta \\ \nu_\Delta \end{pmatrix} + \boldsymbol{B}_0\theta_\Delta + \boldsymbol{c}_0 = \mathbf{o}, \tag{8}$$

where $\boldsymbol{x}_\Delta = \boldsymbol{x} - \mu_0$, $\boldsymbol{y}_\Delta = \boldsymbol{y} - \nu_0$, $\boldsymbol{A}_0$, $\boldsymbol{B}_0$, and $\boldsymbol{c}_0$ are given by (7), and $\boldsymbol{H}$ is the correlation matrix of the measurement errors $(\varepsilon_x', \varepsilon_y')'$, here

$$\boldsymbol{H} = \sigma^2 \boldsymbol{I}_{2n,2n} + \delta \begin{pmatrix} \mathbf{o}_{n,n} & \boldsymbol{I}_{n,n} \\ \boldsymbol{I}_{n,n} & \mathbf{o}_{n,n} \end{pmatrix} = \sigma^2 \boldsymbol{V}_1 + \delta \boldsymbol{V}_2 \tag{9}$$

with $\delta = \sigma^2\rho$. This model serves as a first-order approximation to the nonlinear model (3)–(4). Hence, the (locally) best linear unbiased estimators (BLUEs) of the model parameters and their covariance matrix can be estimated by a method suggested in [5], for more details see also [2]:

$$\begin{pmatrix} \begin{pmatrix} \hat{\mu}_\Delta \\ \hat{\nu}_\Delta \end{pmatrix} \\ \hat{\theta}_\Delta \end{pmatrix} = -\begin{pmatrix} \boldsymbol{H}\boldsymbol{A}_0'\boldsymbol{Q}_{11,0} \\ \boldsymbol{Q}_{21,0} \end{pmatrix} \boldsymbol{c}_0 + \begin{pmatrix} \boldsymbol{I} - \boldsymbol{H}\boldsymbol{A}_0'\boldsymbol{Q}_{11,0}\boldsymbol{A}_0 \\ -\boldsymbol{Q}_{21,0}\boldsymbol{A}_0 \end{pmatrix} \begin{pmatrix} \boldsymbol{x}_\Delta \\ \boldsymbol{y}_\Delta \end{pmatrix}, \tag{10}$$

where $\boldsymbol{Q}_{11,0}$ and $\boldsymbol{Q}_{21,0}$ are blocks of the matrix $\boldsymbol{Q}_0$ defined by

$$\boldsymbol{Q}_0 = \begin{pmatrix} \boldsymbol{Q}_{11,0} & \boldsymbol{Q}_{12,0} \\ \boldsymbol{Q}_{21,0} & \boldsymbol{Q}_{22,0} \end{pmatrix} = \begin{pmatrix} \boldsymbol{A}_0\boldsymbol{H}\boldsymbol{A}_0' & \boldsymbol{B}_0 \\ \boldsymbol{B}_0' & \mathbf{0} \end{pmatrix}^{-1}, \tag{11}$$

together with its covariance matrix

$$Cov\begin{pmatrix} \begin{pmatrix} \hat{\mu}_\Delta \\ \hat{\nu}_\Delta \end{pmatrix} \\ \hat{\theta}_\Delta \end{pmatrix} = \begin{pmatrix} \boldsymbol{H} - \boldsymbol{H}\boldsymbol{A}_0'\boldsymbol{Q}_{11,0}\boldsymbol{A}_0\boldsymbol{H} & -\boldsymbol{H}\boldsymbol{A}_0'\boldsymbol{Q}_{12,0} \\ -\boldsymbol{Q}_{21,0}\boldsymbol{A}_0\boldsymbol{H} & -\boldsymbol{Q}_{22,0} \end{pmatrix}. \tag{12}$$

Then, the estimators of the original parameters μ, ν, and θ are given by $\hat{\mu} = \hat{\mu}_\Delta + \mu_0$, $\hat{\nu} = \hat{\nu}_\Delta + \nu_0$, $\hat{\theta} = \hat{\theta}_\Delta + \theta_0$.

Let σ_0^2, δ_0 be selected appropriate initial values of σ^2 and δ. Now, we shall derive the estimator (σ_0^2, δ_0)-MINQUE, i.e. the (σ_0^2, δ_0)-locally minimum norm quadratic unbiased estimator of σ^2, δ, which is optimum in the class of quadratic estimators of variance components. For more details see [6], Chapter 5.2, pp. 93-99.

For his purpose, first we shall create the 2×2 matrix $\boldsymbol{S}$, where

$$\{\boldsymbol{S}\}_{i,j} = \mathit{Trace}\left[\boldsymbol{A}_0'\boldsymbol{Q}_{11,0}\boldsymbol{A}_0\boldsymbol{V}_i\boldsymbol{A}_0'\boldsymbol{Q}_{11,0}\boldsymbol{A}_0\boldsymbol{V}_j\right], \quad i,j \in \{1,2\}, \tag{13}$$

and $Q_{11,0}$ is a block of matrix $\boldsymbol{Q}_0$ defined by (11) with using $\boldsymbol{H} \equiv \boldsymbol{H}_0 = \sigma_0^2\boldsymbol{V}_1 + \delta_0\boldsymbol{V}_2$. Then, the (σ_0^2, δ_0)-MINQUE of the variance components σ^2 and δ is given by

$$\begin{pmatrix}\hat{\sigma}^2\\ \hat{\delta}\end{pmatrix} = \boldsymbol{S}^{-1}\begin{pmatrix}\left(\begin{pmatrix}\boldsymbol{x}_\Delta\\ \boldsymbol{y}_\Delta\end{pmatrix} - \hat{\gamma}\right)'\boldsymbol{H}_0^{-1}\boldsymbol{V}_1\boldsymbol{H}_0^{-1}\left(\begin{pmatrix}\boldsymbol{x}_\Delta\\ \boldsymbol{y}_\Delta\end{pmatrix} - \hat{\gamma}\right)\\ \left(\begin{pmatrix}\boldsymbol{x}_\Delta\\ \boldsymbol{y}_\Delta\end{pmatrix} - \hat{\gamma}\right)'\boldsymbol{H}_0^{-1}\boldsymbol{V}_2\boldsymbol{H}_0^{-1}\left(\begin{pmatrix}\boldsymbol{x}_\Delta\\ \boldsymbol{y}_\Delta\end{pmatrix} - \hat{\gamma}\right)\end{pmatrix}, \tag{14}$$

where

$$\hat{\gamma} = \left(\boldsymbol{I}_{2n,2n} - \boldsymbol{H}_0\boldsymbol{A}_0'\boldsymbol{Q}_{11,0}\boldsymbol{A}_0\right)\begin{pmatrix}\boldsymbol{x}_\Delta\\ \boldsymbol{y}_\Delta\end{pmatrix} - \boldsymbol{H}_0\boldsymbol{A}_0'\boldsymbol{Q}_{11,0}\boldsymbol{c}_0. \tag{15}$$

The process can be iterated until convergence is reached. We should start with appropriate values $\mu_0^{(0)}$, $\nu_0^{(0)}$, $\theta_0^{(0)}$, σ_0^2, $\delta_{(0)}$. Such we obtain the (locally) BLUEs of the parameters μ, ν, θ and the (iterated) MINQUEs with their estimated covariance matrices.

3. Discussion

In this paper we have derived (and suggested to use) the explicit form of the (iterated) MINQUE estimator for estimation of the unknown correlation coefficient of the interferometer signals x and y. This helps to improve the previously suggested algorithm for demodulation and uncertainty evaluation of correlated quadrature interferometer signals.

Acknowledgements

This work was supported by the research projects VEGA 2/0047/15 and VEGA 2/0043/13.

References

[1] Heydemann PLM. Determination and correction of quadrature fringe measurement errors in interferometers. *Applied Optics* 20, 3382–3384, 1981.

[2] Köning R, Wimmer G, Witkovský V. Ellipse fitting by nonlinear constraints to demodulate quadrature homodyne interferometer signals and to determine the statistical uncertainty of the interferometric phase. *Measurement Science and Technology* 25, 115001 (11pp), 2014.

[3] Köning R, Wimmer G, Witkovský V. EllipseFit4HC: A Matlab algorithm for demodulation and uncertainty evaluation of the quadrature interferometer signals. In: Pavese, F. *et al* (eds.) *Advances in Mathematical and Computational Tools in Metrology and Testing X*, vol 86. World Scientific, Singapore, pp. 211–218, 2015.

[4] Köning R, Wimmer G, Witkovský V. The statistical uncertainty of the Heydemann correction – A practical limit of optical quadrature homodyne interferometry. *Measurement Science and Technology* 26. To appear, 2015.

[5] Kubáček, L. *Foundations of Estimation Theory*. Amsterdam: Elsevier, 1988.

[6] Rao CR, Kleffe J. *Estimation of Variance Components and Applications*. Amsterdam - New York - Oxford - Tokyo: North-Holland, 1988.

[7] Wu C-M, Su C-S, Peng G-S. Correction of nonlinearity in one-frequency optical interferometry. *Measurement Science and Technology* 7(4): 520–524, 1996.

Improved Cost Computation with Local Binary Features in a Multi-View Block Matching Framework

K. Valentín, S. Štolc, R. Huber-Mörk

AIT Austrian Institute of Technology GmbH, Intelligent Vision Systems
2444 Seibersdorf, Austria
Email: kristian.valentin.fl@ait.ac.at

Abstract. *We propose a methodological improvement to multi-view stereo / light-field block matching algorithms based on local binary features such as Census Transform (CT), Local Binary Pattern (LBP), etc. Instead of interpolating individual binary descriptors before matching, we propose to carry out the necessary interpolations involved in cost estimation, only after matching in the cost domain. This methodological twist offers a substantial performance increase for both CPU as well as GPU architectures, while delivering the same output quality. The proposed algorithm is analyzed from theoretical as well as practical viewpoints and its performance is compared to a naïve approach with binary interpolations.*

Keywords: Multi-view stereo matching, 3-D reconstruction, Light fields, Computational imaging

1. Introduction

Various methods to measure depth information by computer vision systems exist, e.g., conventional stereo vision, light-field/multi-view stereo, laser triangulations, time-of-flight sensors, etc. In this paper, we focus on 3-D sensing using a multi-view imaging system realized by a *multi-line scan light-field camera* [1].

In general, a *light field* is defined as a 4-D radiance function that describes the intensity of light passing through every point in space (free from occluders) in every direction [2]. Among other things, such light fields can be exploited for computational imaging, such as refocusing, changing depth of field, correcting optical aberrations, all-in-focus imaging, noise reduction, as well as 3-D reconstruction. Without loss of generality, in this paper we restrict ourselves to 3-D light fields, however, our proposed method can be used equally well in algorithms dealing with complete 4-D light fields.

As for the 3-D reconstruction approach, we consider a multi-view stereo matching algorithm described in [1] that operates in the EPI domain [3]. This algorithm requires a number of interpolation steps between image pixels in order to obtain cost values for tested disparity hypotheses. Due to involvement of multiple views, interpolations become necessary even when the disparity steps between the two extreme views are restricted to integer values.

In order to make stereo matching robust against local instabilities in the image intensity domain, many methods make use of *local binary features* (LBFs) which are afterwards compared by means of the *Hamming distance* [4]. LBFs are a class of texture operators used in computer vision that describe local image neighborhoods by means of binary vectors comprised of bits obtained by individual pixel comparisons within that neighborhood.

Well-known examples of LBFs are *Census Transform* [5] and *Local Binary Pattern* [6] operators. There are many applications of these descriptors in computer vision as they have certain computational and performance advantages over other matching approaches. On one hand they represent very compact and efficient approach to describing local image neighborhoods, and on the other hand they are exceptionally robust against many common image perturbations (e.g., locally non-constant illumination).

Nevertheless, the stated computational advantage of LBFs becomes less prominent when used in a multi-view stereo setup, where sub-hypothesis matching is an inevitable step requiring interpolation between descriptors.

In this paper, we propose a methodological improvement for efficient interpolation in the aforementioned domain. Considering a large number of interpolations that have to be performed in the course of 3-D reconstruction, we show that the proposed improvement has a significant impact on the overall performance of the matching algorithm.

2. Subject and Methods

When an object is acquired by the multi-line scan light-field camera, it is transported in front of the camera at a constant speed and direction. In each time instance, multiple lines are rapidly extracted from a CMOS area-scan sensor, which are then used to construct different views of the acquired object. Throughout this process a 3-D light field is being constructed.

The acquired 3-D light field is used to derive the depth information using a multi-view block matching algorithm [1] that makes use of LBFs. A very important part of this matching algorithm is the computation of cost estimates for each pixel of the reference view w.r.t. tested disparity hypotheses. Let d be the number of tested hypotheses, v the number of light-field views and w and h width and height of each light-field view, respectively, then in the course of all cost computations the upper bound N for the number of operations that require interpolations between descriptors is given as:

$$N = d\,(v-1)\,wh. \tag{1}$$

In practice, N can be lower because there are cases where the interpolation is in fact not necessary (e.g., when testing the zero disparity or when the tested disparity slope produces an integer shift in a certain view). Despite there is only a linear relationship between N and the other variables, the dependence on the number of pixels causes N to rise quickly (e.g., for 9 views of 512×512 px and 20 tested disparity hypotheses, N is already as high as 41.9 million). Thus, an effective cost computation may significantly improve the performance of the whole matching algorithm.

3. Proposed Method

The main operation in the cost computation is to evaluate the dissimilarity between a reference binary descriptor $\mathbf{r} \in \{0,1\}^n$ extracted from the reference view and an interpolated real-valued descriptor calculated from two binary descriptors $\mathbf{x}, \mathbf{y} \in \{0,1\}^n$ corresponding to two neighboring descriptors extracted from some other view. A conventional approach to computing this quantity would be to interpolate between $\mathbf{x}$ and $\mathbf{y}$ followed by computation of the distance between $\mathbf{r}$ and the interpolated descriptor.

We propose an alternative approach to this task, that is computationally much less expensive and, furthermore, leads to the same numerical results. The main idea behind is to compute distances between $\mathbf{r}$ and both $\mathbf{x}$ and $\mathbf{y}$ separately, followed by interpolation between the two computed distances. In this way, one avoids the explicit computation of the interpolated descriptor which is the most complex task in the entire cost calculation.

Stereo matching algorithms based on LBFs typically evaluate the dissimilarity between binary descriptors by means of the Hamming distance. The Hamming distance between two binary vectors $\mathbf{x}$ and $\mathbf{y}$ is defined as follows:

$$H(\mathbf{x},\mathbf{y}) = \sum_{i=1}^{n} x_i \oplus y_i, \tag{2}$$

where $\oplus$ is the XOR operator. Allowing for the interpolation between binary vectors, the resulting vector is no longer binary but rather real-valued with elements $\in [0,1]$. In order to measure distances between interpolated vectors, a generalized Hamming distance is used:

$$\widehat{H}(\mathbf{x},\mathbf{y}) = \sum_{i=1}^{n} |x_i - y_i|, \tag{3}$$

where $\mathbf{x},\mathbf{y} \in [0,1]^n$. Note that for strictly binary vectors $H(\cdot)$ and $\widehat{H}(\cdot)$ are equal.

The main idea of the proposed improvement to LBF-based block matching algorithms is to perform a computationally cheap interpolation between two ordinary Hamming distances, instead of costly interpolating between binary vectors and calculating generalized Hamming distance afterwards. Formally this can be expressed as follows:

$$\widehat{H}(\mathbf{r},\ w\,\mathbf{x} + (1-w)\,\mathbf{y}) = w\,H(\mathbf{r},\mathbf{x}) + (1-w)\,H(\mathbf{r},\mathbf{y}), \tag{4}$$

where $\mathbf{r}$ is a reference binary vector and $\mathbf{x}$ and $\mathbf{y}$ are binary vectors to be interpolated by a weight $w \in [0,1]$. For the sake of simplicity, we restrict ourselves to linear interpolation in this paper. However, a similar approach should be applicable to other interpolation schemes as well. To show the equivalence of Eq. (4), we conduct the following reasoning:

$$\begin{aligned}
\widehat{H}(\mathbf{r},\ w\,\mathbf{x} + (1-w)\,\mathbf{y}) &= \sum_{i=1}^{n} |r_i - [w\,x_i + (1-w)\,y_i]| \\
&= \sum_{i=1}^{n} |w\,(r_i - x_i) + (1-w)\,(r_i - y_i)| \\
&= \sum_{i=1}^{n} \begin{cases} w\,(r_i - x_i) + (1-w)\,(r_i - y_i) & \text{if } r_i = 1 \\ w\,(x_i - r_i) + (1-w)\,(y_i - r_i) & \text{if } r_i = 0 \end{cases} \\
&= \sum_{i=1}^{n} \left[w\,|r_i - x_i| + (1-w)\,|r_i - y_i| \right] \\
&= w \sum_{i=1}^{n} |r_i - x_i| + (1-w) \sum_{i=1}^{n} |r_i - y_i| \\
&= w\,\widehat{H}(\mathbf{r},\mathbf{x}) + (1-w)\,\widehat{H}(\mathbf{r},\mathbf{y}) = w\,H(\mathbf{r},\mathbf{x}) + (1-w)\,H(\mathbf{r},\mathbf{y}). \quad \square
\end{aligned} \tag{5}$$

Advantages of the Proposed Approach

There are three main advantages of the proposed approach over the naïve method: (i) distance is computed between two binary vectors, which can be done more efficiently than between a binary and a real-valued vector, (ii) compared to n interpolations in the naïve approach, there is only one scalar interpolation required, (iii) there is no need to unpack the individual bits from the descriptors to compute either interpolation or distance as it is in the naïve approach.

Implementation of the Proposed Approach

The ordinary Hamming distance between two binary vectors can be efficiently computed as a combination of a vector XOR operation followed by a set-bit-count function (also called *popcount* or *sideways sum*). Both these operation are usually available on most common CPU and GPU architectures. In the naïve approach, there is no such architectural support for binary vector interpolation and so each bit has to be algorithmically unpacked using a combination of bit-wise shift and AND operations. On physical platforms, some of the operations listed in Tab. 1 can be implemented using vector instructions, usually as multiples of 32/64-bit variants. Thus, the performance does not scale proportionally to the descriptor length in practice.

Table 1: Number of operations by type in tested implementations of the cost computation for one pixel and one disparity, where n is the length of the descriptor. These numbers hold for cases where $n \leq$ size of processor vector operations (typically 32 or 64 bits).

	Add	Sub	Mul	Abs	Bitshift	AND	XOR	Popcount
Naïve approach	$2n$	$2n$	$2n$	n	$3n$	$3n$	–	–
Proposed approach	1	1	2	–	–	–	2	2

4. Results and Conclusions

In this study, we proposed a methodological improvement to the light-field / multi-view stereo block matching algorithms based on local binary features. The proposed as well as the naïve cost computation methods were implemented on CPU and GPU architectures. For the Hamming distance computation, we exploited intrinsic `XOR` and set-bit-count operations. An overview of the executed operations are listed in Tab. 1. In the case of naïve method, the interpolated descriptors were computed at the same time with the distance computation in order to save memory. In both cases, we considered 32-bit descriptors.

The implementation for CPU architecture was done in C++, compiled using Microsoft Visual Studio 2013 and ran on a single core of a quad-core Intel Xeon E5 processor. We used the `std::bitset` class to represent LBF descriptors. As a result for we obtained a speedup factor as high as 20 between the proposed and the naïve methods. On the other hand, the GPU implementation was done in CUDA C and compiled using the CUDA 6.5 compiler. In this case, 32-bit unsigned integers were used to represent LBF descriptors. On a GeForce GTX TITAN graphics card we achieved a speedup factor of 13. Although these numbers do not scale as much as might have been expected from Tab. 1, they still represent a very high performance improvement for both tested architectures and therefore have great potential for practical applications.

As for the future research, we plan to investigate into LBF descriptors whose length is not strictly dependent on the size of the matching window. Such descriptors might prove useful for better conformity with the specifics of particular hardware architectures (i.e., vector operations, memory alignment, etc.), which is essential for further performance improvements as well as for enabling this type of algorithms on more limited embedded platforms.

References

[1] Štolc S, Soukup D, Holländer B, Huber-Mörk R. Depth and all-in-focus imaging by a multi-line-scan light-field camera. *Journal of Electronic Imaging* 23(5):053020, 2014.

[2] Levoy M., Hanrahan P. Light field rendering. In: *Proc. of Conference on Computer Graphics and Interactive Techniques*. New York, NY, USA, pp. 31–42, 1996.

[3] Bolles RC, Baker HH., David, Marimont H. Epipolarplane image analysis: an approach to determining structure from motion. *International Journal of Computer Vision* 1(1): 7–55, 1987.

[4] Hamming R. Error detecting and error correcting codes. *The Bell System Technical Journal* 29(2): 147–160, 1950.

[5] Zabih R, Woodfill J. Non-parametric local transforms for computing visual correspondence. In: Eklundh, J.-O. (ed.) *Computer Vision – ECCV 94*, Vol. 801 of *Lecture Notes in Computer Science*. Springer Berlin Heidelberg, pp. 151–158, 1994.

[6] Pietikäinen M, Ojala T. Texture analysis in industrial applications, 1996.

Comparison of Subpixel Corner Detection Based on Reprojection Error Criterion

L. Šroba, R. Ravas, J. Grman

Slovak University of Technology in Bratislava, Faculty of Electrical Engineering and Information Technology, Institute of Electrical Engineering, Bratislava, Slovakia
Email: lukas.sroba@stuba.sk

Abstract. *This paper deals with conception of subpixel detection where the focus on accuracy of corner points detection is a goal. Specifically there is traditional Harris corner detector together with two subpixel approaches compared. The first approach is based on the orthogonal vector theory while the other one is refining coordinates by fitting quadratic curves over usual cornerness map. As the procedure for the results evaluation there was reprojection error criterion chosen. This task requires employing several problems from image processing and computer vision area which are also briefly mentioned in presented paper. Also the statistical analysis was performed and obtained results were shown in corresponding graphs and tables. This paper may contribute to the answer if subpixel detection paradigm could be useful in such applications as 3D reconstruction, robot navigation or many others.*

Keywords: Corner detection, Subpixel detectors, Reprojection error, Epipolar geometry

1. Introduction

The area and theory behind corner detection in usual is very well known and often used as one of the first steps in many practical tasks, e.g. object detection and recognition, motion tracking , robot navigation, 3D modelling, stereo matching and many others.
It is generally known that the smallest part of an image is a pixel. To access information between pixels there can be some mathematical techniques to interpolate or approximate the brightness intensity among pixels employed and used to find the chosen features in subpixel accuracy [1] [2].
One of the applications where the accuracy of corner points is crucial in 3D scene investigation using image stereo pair. The theory behind this is quite complex and consists of several particular tasks. All these procedure steps together with the discussed corner detection algorithms are briefly described in the following sections. This paper also slightly follows our previous paper dealing with camera displacement stating using image stereo pair and subpixel corner detection [3], where the more details about experiments is explained.

2. Subpixel Corner Detection

The corner point itself can be understood as a point around which is high change of brightness intensity in all directions, point where at least two edges are intersected or a point having the smallest radius of curvature for example.
One of the most famous corner detection algorithms is Harris detector [4]. The basic idea is to find the minimum of intensity difference between the chosen part of an image and shifted image part in all directions. Traditional corner detection in pixel accuracy is usually the first step to localize the corner position in subpixel accuracy. Next step is to apply the specific algorithm to the chosen area surrounding previously found corner point and specify the point coordinates in higher accuracy.
The first compared algorithm [5] was designed only for *x*-corner points detection, working directly with image brightness intensities and is based on the fact, that vector from the corner

(marked *q*) to its adjacent area (marked *p*) should be perpendicular to the gradient of point *p* as it is shown in the following formula:

$$I(p_i)^T \cdot (q - p_i) = 0 \tag{1}$$

The position of point *q* is then solved through the iterations.
The second method [6] primarily used for any kind of corners is refining the position of initially found corner point by fitting the quadratic curve to the corner strength function (cornerness map) in *x* and *y* direction separately. The approximation function is following:

$$h(x) = ax^2 + bx + c \tag{2}$$

Maximum of this function corresponds to subpixel corner coordinate in particular direction.

3. Image Stereo Pairs

As it was already mentioned, the investigation of the relation between images in stereo pair consists of several steps.
First of them is the use of camera calibration [7] process to get camera intrinsic matrix and camera distortion coefficients. Once the image pair containing the same scene is given, the corresponding points in both images have to be found. For that purpose is the SIFT [8] algorithm used for example. Then the set of found corresponding coordinates has to be undistorted [9] due to the lens manufacturing errors. The theory behind epipolar geometry [10] allows us to get essential matrix which can be decomposed into their mutual rotation matrix and relative translation vector [11]. When these parameters are known, using the linear triangulation algorithm [12] gives us coordinates of considered point in 3D camera space. As the evaluation criterion of 3D projection precision can be used the reprojection error [13]. It quantifies the position difference between projection of triangulated point and the original one in 2D image space. The formula to calculate reprojection error could be like this:

$$d(p,q) = \sqrt{\sum_{i=1}^{n} (q_i - p_i)^2} \tag{3}$$

where the p_i and q_i are representing corresponding coordinates of compared points.

4. Experimental Tests

For the purpose to demonstrate the advantage the subpixel detection unlike the usual pixel one, the practical test comparison consisting of steps describing in previous chapter were performed. There is an example of scene structure and matched points correspondences between two images shown in Fig. 1.

Fig. 1. Corresponding points between both images.

Specifically the Harris corner detector (marked as *P*) and both described subpixel detection approaches were compared (marked as *A* and *B* in order of referring in text). There were different image resolution chosen and to make the analysis more robust and accurate, multiple mutual camera distances were used, while each was containing multiple tested image pairs. For these configurations the reprojection errors were stated as the aim of comparison. The found results were statistically analyzed and are described in following section.

5. Experimental Results

Because the whole process is relatively complex, the results are based mostly on the precision of corner point localization. There are the averaged values of reprojection errors for specific detection algorithm displayed in Fig. 2. The exact values are also stated in Table 1.

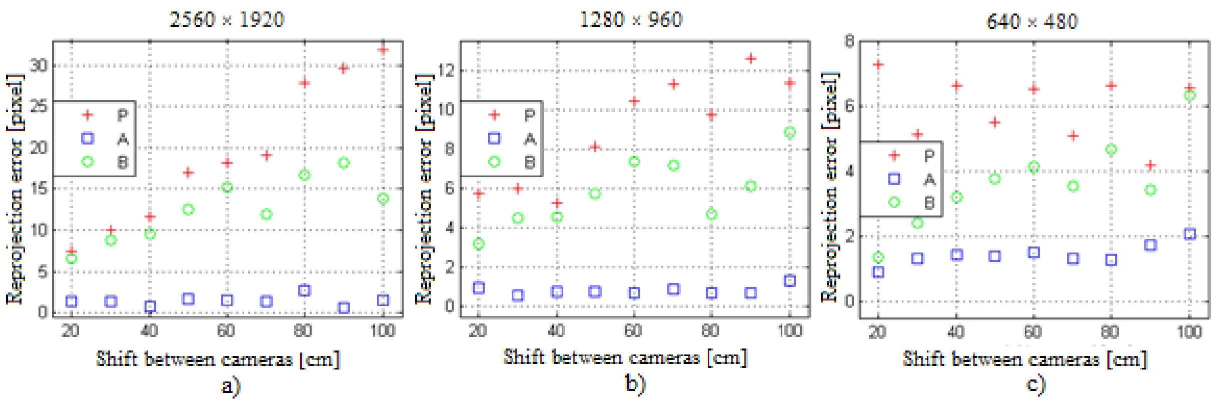

Fig. 2. The results of compared algorithms reprojection errors

As it is possible to see, the reprojection error for every parameters configuration in the case of subpixel approaches gives us better results than traditional pixel method. Moreover, the algorithm *A* produces significantly better results unlike the other two detectors.

Table 1. The reprojection error of compared algorithm based on tested configuration parameters

		Reprojection error [pixel]								
Resolution		*2560 × 1920*			*1280 × 960*			*640 × 480*		
Algorithm		*P*	*A*	*B*	*P*	*A*	*B*	*P*	*A*	*B*
Shift between cameras [cm]	*20*	7.54	1.43	6.62	5.75	0.98	3.18	7.29	0.92	1.37
	30	9.95	1.42	8.79	6.02	0.59	4.52	5.16	1.32	2.43
	40	11.65	0.80	9.49	5.28	0.80	4.60	6.66	1.44	3.22
	50	16.95	1.66	12.59	8.13	0.79	5.76	5.51	1.42	3.80
	60	18.23	1.47	15.25	10.39	0.71	7.39	6.56	1.54	4.15
	70	19.11	1.30	11.97	11.27	0.89	7.21	5.12	1.33	3.58
	80	27.90	2.77	16.71	9.72	0.69	4.67	6.66	1.29	4.68
	90	29.59	0.61	18.16	12.61	0.73	6.10	4.19	1.76	3.44
	100	31.83	1.45	13.80	11.37	1.32	8.88	6.58	2.10	6.34
$\bar{x}$		**19.19**	**1.43**	**12.60**	**8.95**	**0.83**	**5.81**	**5.97**	**1.46**	**3.67**

The explanation could be the fact, that this algorithm is suitable only for *x*-corners detection. The direct comparison between algorithm *B* and Harris detector looks also interesting, the reason being both of them are working with the same cornerness map. Follow the expectations, the reprojection errors are decreasing with the image resolution.

6. Conclusions

This paper has dealt with comparison of usual pixel and two subpixel corner detection algorithms. As the subject of this study the reprojection errors computed using chosen experiment related to image stereo pair area were compared.

In the first two sections the theory behind considered corner detectors and relation between two cameras investigating using image stereo pairs were introduced.

The experiment and the results were presented in next sections. It was shown, that subpixel detection can significantly decrease the reprojection error of triangulated points using image stereo pairs, what makes it suitable and convenient in many practical applications from computer vision area.

Acknowledgements

This work was supported by the Slovak Research and Development Agency under the contract No. APVV-0469-12.

References

[1] Qiao Y, Tang Y, Li J. Improved Harris sub-pixel corner detection algorithm for chessboard image. Conference on Measurement, Information and Control (ICMIC), Volume 02, 1408-1411, 2013.

[2] Chen N, Wang J, Yu L, Su Ch. Sub-pixel Edge Detection of LED Probes Based on Canny Edge Detection and Iterative Curve Fitting. International Symposium on Computer, Consumer and Control (IS3C), 131-134, 2014.

[3] Sroba L, Ravas R, Grman J. The Influence of Supixel Corner Detection to Determine the Camera Displacement. 25th DAAAM International Symposium, Proceedia Engineering, Volume 100, 834-840, 2015.

[4] Harris Ch, Stephens M. A combined corner and edge detector. In Alvey Vision conference, 147-152, 1988.

[5] Weixing Z, Changhua M, Libing X, Xincheng L. A fast and accurate algorithm for chessboard corner detection. CISP 2nd International Congress on, Image and Signal Processing, 1-5, 2009.

[6] Rea M, McRobbea D, Elhawary D, Tse Z, Lamperth M, Young I. Sub-pixel localization of passive micro-coil fiducial markers in interventional MRI. MAGMA, 2009.

[7] Brown D. Close-Range Camera Calibration. Photogrammetric Eng. Vol. 37, 855-866, 1971.

[8] Lowe D. Distinctive Image Features from Scale-Invariant Keypoints. International Journal of Computer Vision, Volume 60, Issue 2, 91-110, 2004.

[9] Brown D. Decentering distortion of lenses. Photogrammetric Eng. Vol. 32, 444-462, 1966.

[10] Hartley R, Zisserman A. *Multiple View Geometry in Computer Vision.* Cambridge

[11] University Press, 239-259, 2003.

[12] Wang W, Tsui H. A SVD decomposition of essential matrix with eight solutions for the relative positions of two perspective cameras. 15th International Conference on Pattern Recognition, 362-365, 2000.

[13] Hartley R, Zisserman A. *Multiple View Geometry in Computer Vision*. Cambridge University Press, 312-313, 2003.

[14] Hartley R, Zisserman A. *Multiple View Geometry in Computer Vision*. Cambridge University Press, 94-96, 2003.

Integral Nonlinearity Correction of Multi-Range ADC by Iterative Applying of Multi-Resistors Divider

[1]H. Zhengbing, [2]R. Kochan, [2]O. Kochan, [2]H. Klym, [3]S. Jun

[1] School of Educational Information Technology, Central China Normal University, No. 152 Louyu Road, 430079, Wuhan, China

[2] Lviv National Polytechnic University, 12 Bandery str., Lviv, 79013 Ukraine

[3] School of Computer Science, Hubei University of Technology, Hubei, China

Email: kochan.roman@gmail.com

Abstract. *The method of testing points generation for identification and correction of integral nonlinearity of high performance ADC is developed. The proposed method is based on averaging all voltages of multi-resistors voltage divider. The main idea of proposed method is in comparison results of analog to digital conversion obtained on different ranges of tested ADC for the same input signals. It is investigated influence of resistors' error and random error of ADC on residual error of integral nonlinearity correction for proposed method.*

Keywords: Integral nonlinearity, Multi-resistor voltage divider, Residual error

1. Introduction

Implementation of digital signal processing algorithms and computer systems in all fields of our life results in implementation of analogue-to-digital converters (ADC) as necessary a component of modern measurement systems. In some cases the ADC's metrology parameters determine the characteristics of whole measurement system. Particularly, this point is actual for measurement systems of electrical quantities. Therefore improving the ADC is actual task for accuracy increasing.

The market of DC precision ADC is covered by converters based on sigma-delta modulators SDM [1, 2]. High accuracy of these components is provided by implementation of null setting and calibration methods. These methods provide decreasing of additive and multiplicative components of conversion error. Therefore, the error of conversion results in determination of the following errors: calibration signal source, multiplexer and residual ADC's error. The main significant component of this residual ADC's error is their integral nonlinearity. For example, the maximum allowable integral nonlinearity of 24-bit ADC AD7714 [3] is 15 ppm. This nonlinearity corresponds to 16-th bit, therefore approximately 8 least significant bits (LSB) are priory inaccurate and excessive. Therefore, for this ADC integral nonlinearity should be corrected when we need accurate result than 15 ppm. In the same case, the noise level of this ADC does not exceed of 2,5 LSB. Therefore, we have approximately 5,5 stable bits, which cannot to be used because their inaccuracy. Also there is such precise measurement method as substitution measurement method [4]. The accuracy of measurement results for this method implemented on ADC is defined by ADC's integral nonlinearity [5]. So correction of ADC's integral nonlinearity brings accuracy improvement of measurement results.

In [6] the method of ADC's integral nonlinearity identification in the set of testing points conventionally called as basic method was proposed. This method provides generation the set of testing points, which corresponds to the number sequence $\frac{1}{N}U_R$ (U_R – range of connected ADC) with integer N. This implies that all generated testing points are grouped in the lower half of the ADC's range. Investigation of nonlinearity correction methods show that residual error is proportional to the density of testing points [7, 8]. It brings inefficiency of this method for signals, which corresponds to the top half of the ADC's range. Finally, basic method implementation for ADC's nonlinearity correction brinks that residual error for signals from top half of the ADC's range is more than 10 times greater than this error for signals from lower half of the range [6].

Proposed in [9, 10] method of testing points generation by direct measurement of the voltages on serially connected resistors of multi-resistors divider. This method implements basic method for nonlinearity of lower half of the ADC's range. Than it is measured voltages on serially connected resistors: R_1; R_1 and R_2; … $R_1 ... R_{N/2}$ (totally $N/2$ voltages, where N - total number of resistors in multi-resistors divider). The error of measurement results of all these voltages is small because they are in lower half of the ADC's range, where basic method is effective. Mainly error of these voltages is defined by ADC's random error. Measured voltages are used as testing points for all lower ranges of ADC. This method provides approximately uniform distribution of testing points for all lower ranges of ADC but its accuracy is significantly lower in comparison with basic method because of error accumulation.

The main goal of this work is development and investigation of method of ADC's integral nonlinearity identification and correction for multi range ADC which provides iterative implementation multi-resistors divider on different ranges of tested ADC.

2. Approach of Testing Points Generation

The basic of proposed method of testing points generation is based on analog to digital conversion of output signals of voltage divider consisting of N serially combined resistors $R_1, R_2, ..., R_N$, connected to reference power source U_{REF}. The measurement circuit is shown in Fig. 1. According to Kirchhoff voltage law, we have the following equation

$$U_{REF} = \sum_{i=1}^{N} U_{R\,i} \quad , \tag{1}$$

where $U_{R\,i}$, $i = \overline{1, N}$ is voltage of appropriate resistors of the divider.

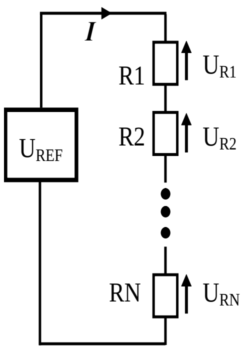

Fig. 1. Circuit of N-resistors voltage divider.

The average voltage of all resistors of the divider $\overline{U}$ could be computed as:

$$\overline{U} = \frac{1}{N} \sum_{i=1}^{N} U_{R\,i} \quad . \tag{2}$$

Taking into account eq. (1), the eq. (2) can be presented as

$$\overline{U} = \frac{U_{REF}}{N} \quad . \tag{3}$$

It means that average voltage of all resistors of the divider $\overline{U}$ does not depends of voltages of separate resistors. In addition, according to Ohm's law, the resistances of these resistors does not influence on average voltage.

Equivalently, we have indirect measurement describing by function $y = h(x)$, where $y \equiv \overline{U},\ x \equiv U_{REF}\ \ h(x) \equiv \frac{x}{N}$. Therefore, absolute error of measurement result is Δy [11]:

$$\Delta y = h^{/}(x) \cdot \Delta x \ , \tag{4}$$

where $h^{/}(x)$ – derivative of function $h(x)$; Δx – absolute error of argument.

Taking into account, that N is natural number, the eq. (4) could be convert to

$$\Delta_{\overline{U}} = \frac{\Delta_{U_{REF}}}{N} \quad , \tag{5}$$

where $\Delta_{\overline{U}}$ - absolute error of average voltage $\overline{U}$; $\Delta_{U_{REF}}$ - absolute error of power source U_{REF}.

The relative error of average voltage $\overline{U}$ – $\delta_{\overline{U}}$ is

$$\delta_{\overline{U}} = \frac{\Delta_{\overline{U}}}{\overline{U}} 100\% = \frac{\frac{\Delta_{U_{REF}}}{N}}{\frac{U_{REF}}{N}} 100\% = \frac{\Delta_{U_{REF}}}{U_{REF}} 100\% = \delta_{U_{REF}} \quad , \tag{6}$$

where $\delta_{U_{REF}}$ - relative error of power source U_{REF}.

Taking into account (6), the next intermediate conclusion should be made: the error caused by measurement converter based on multi-resistors voltage divider with averaging voltages of all resistors is trend to zero. It is provide the opportunity of generation the set of testing signals for ADC with exactly predefined ratio.

In the case of ADC calibration by power source of the divider U_{REF} ., the average voltage $\overline{U}$ as testing point for identification ADC's integral nonlinearity can be used.

So, as it is shown, that the multi-resistors voltage divider provides precision identification of ADC's integral nonlinearity in one testing point without using of precision components. Proposed method is called as basic method [6] and they provides increasing of number of generated testing points by choosing N. Since N has the set of natural divisors $\{m_1, \dots, m_t\}$, it is the set of natural numbers $\{k_1, \dots, k_t\}$, which satisfy of a claim $N = m_i \times k_i;\ i = \overline{1,t}$. It is allowed to conversion of voltages on the cascades of serially connected resistors $k_i,\ i = \overline{1,t}$ corresponding to eq. (1). Therefore, the integral nonlinearity of ADC can be computed in accordance to the set of t voltages:

$$\overline{U}_i = \frac{U_{REF}}{N} k_i = \frac{U_{REF}}{m_i}; \quad i = \overline{1,t} \quad . \tag{7}$$

The error of all these voltages is corresponded to eq. (6), and only one reference voltage source can be used.

3. Proposed Method of Generation Testing Points

According to the methodology, which was proposed in [6] it is proposed to generate testing points for nonlinearity identification of lower ranges of multi range ADC (in the simplest case for double range ADC) as average voltage for the same combinations of serially connected resistors, which implements basic method for highest range of ADC. It provides getting the set of testing points, which are proportional to calibration voltage of highest range of ADC with coefficient predefined as the deviation of integer numbers. In this case the relative error of all generated testing points is equal to relative error of reference voltage source. The calibration of all lower ranges is held by the voltage of serially connected resistors directly measured on the highest range. Taking into consideration that lover ranges are at least two times less than highest range the distribution of generated testing points for lover ranges will be evenly then it is provided by basic method for higher range. Besides the most generated testing points (besides calibration points) are more accurate than testing points generated by direct measurement the voltages on serially connected resistors of multi-resistors divider [9, 10]. So this method provides generation the same set of testing points as it is generated by basic method [6] but these points are situated higher in the range than it is for basic method. The total number of generated testing points is defined by the number of integer dividers of N. For example if $N = 12$ then this method provides generation five testing points using single channel DC voltage source and error of resistors should not influence on these points.

4. Investigation of the Residual Error

Investigation of the residual nonlinear error by experimental way demands extremely precision equipment with error of 3…5 times less then expected residual nonlinearity and it corresponds to 0,5 ppm. Besides, it is necessary to have the opportunity to set the level and view of ADC's nonlinearity with the same error level. So, it is proposed to make investigation of the proposed method by simulation and evaluate influence of resistors' error and ADC's noise on residual nonlinear error for different nonlinearity functions. Generally, the methodology of investigation results in emulation of integral nonlinearity by the set of curves and it's computing according the proposed method. The difference between emulated and computed curves is the error for analysis. Generally the algorithm of investigation is similar to the same in [6, …, 10]. Its implementation for the set of different curves, which describes nonlinearity of ADC, shows that maximal residual error of nonlinearity correction is on the largest segment between generated testing points. The value of this maximal residual error is proportional to noise level of tested ADC.

5. Conclusions

Investigation of the proposed method of integral nonlinearity identification and correction for lower range of ADC gives us the following conclusions:

- influence of resistors' error of the voltage divider on residual error is commensurable with ADC's resolution and it is neglecting small in comparison with other errors;
- the influence of ADC's random error on residual error is dominating and proportional to its noise level with proportionality factor three for 12-resistors voltage divider;
- it is rational to provide even distribution of testing points via the range of tested ADC for residual error minimization.

The weak sensitivity of proposed method to resistors' error and ADC's noise provides the opportunity of its implementation for metrology verification subsystem [12] of ADC using single channel reference voltage source. The error of such metrology verification is mainly defined by error of implemented reference voltage source, therefore, metrology support of such metrology verification subsystem is reduces to metrology verification of reference voltage source. It provides the opportunity to embed this metrology verification subsystem with reference voltage source into ADC.

Acknowledgment

This work was supported by China International Science and Technology Cooperation Project (CU01-11) and Ukrainian Ministry of Education and Science grant 0115U000446.

References

[1] Fowler K. Part 7: Analog-to-digital conversion in real-time systems. *IEEE Instrumentation & Measurement Magazine*, 6(3): 58-64, 2003.

[2] Kester W. Which ADC Architecture Is Right for Your Application? *Analog Dialogue*, 39(2):11-19. http://www.analog.com/library/analogdialogue/archives/3906/architecture. pdf .

[3] *24-Bit Sigma-Delta, Signal Conditioning ADC with 2 Analog Input Channels* - AD7714 Data Sheets.http://www.analog.com/en/analog-to-digital-converters/adconverters/ad7714/products/product.html.

[4] *Substitution Method For Measurement Of Medium Resistance*. http://www.myclassbook.org/substitution-method-for-measurement-of-medium-resistance/.

[5] Kochan RV. ADC implementation for measurement using substitution method. *Ukrainian Metrology Journal*, 3, 11-16, 2010.

[6] Kochan R, Kochan O, Chyrka M, Jun S, Bykovyy P. Approaches of voltage divider development for metrology verification of ADC. *Proc. of 7-th IEEE International Conference on Intelligent Data Acquisition and Advanced Computing Systems: Technology and Applications (IDAACS'2013)*. 12-14 September 2013, Berlin, Germany. pp. 70 – 75.

[7] Kochan RV. *Precision Analog-To-Digital Converters with Build-In Self Verification:* Monograph – Lviv: Publishing house of Lviv Nat. Polytechnic University, 2012.

[8] Kochan R. Methodology of multi-resistors voltafe divider implementation in metrology verification system of ADC. *Ukrainian Metrology Journal*, 1, 13-18, 2013.

[9] Zhengbing H., Kochan R., Kochan O., Jun S., Klym H. Method of Integral Nonlinearity Testing and Correction of Multi-Range ADC by Direct Measurement of Output Voltages of Multi-Resistors Divider. *Proc. of 13th IMEKO TC10 Workshop on Technical Diagnostics Advanced measurement tools in technical diagnostics for systems' reliability and safety.* June 26-27, 2014, Warsaw, Poland, pp. 76 – 80.

[10] Zhengbing H., Kochan R., Kochan O., Jun S., Klym H. Method of Integral Nonlinearity Testing and Correction of Multi-Range ADC by Direct Measurement of Output Voltages of Multi-Resistors Divider. *ACTA IMEKO*. (In press)

[11] Wang Z, Yi D, Duan X, Yao J, Gu D. *Measurement Data Modeling and Parameter Estimation*. – CRC Press, 2011.

[12] Sobolev V, Sachenko A, Daponte P., Aumala O. Metrological automatic support in intelligent measurement systems, *Computer Standards & Interfaces*, 24(2): 123-131, 2002.

Experimental Verification of Metrological Properties of Power Quality Analyser

[1]P. Otomański, [2]P. Zazula

[1]Poznan University of Technology Institute of Electrical Engineering and Electronics, Piotrowo street 3a, 60-965 Poznań, Poland

[2]Regional Verification Office in Poznań, Krakowska street 19, 61-893 Poznań, Poland

Email: przemyslaw.otomanski@put.poznan.pl

Abstract. *Electrical power quality assessment is a complex measurement task, requiring the usage of a system with suitable metrological properties. The parameters dedicated to assess the power quality are measured and registered with the use of measurement devices called power quality analysers. Examples of the results of testing a selected power quality analyser in a designed measuring system are presented in the paper. The measurement results were completed with a presentation of the uncertainty budget.*

Keywords: Power quality analyser, Harmonics, Fourier series, Uncertainty budget

1. Introduction

To assess the power quality, we use a set of standard and complementary quantities contained in documents [1] and [2]. Among them, there are two measures of harmonic content: amplitude spectrum, i.e. a set of values of particular harmonics as well as Total Harmonic Distortion (THD). These values, as well as other quantities used in power quality assessment, are measured with power quality analysers. The measurement results, registered with those devices, make it possible to diagnose the state of power network, e.g., through detecting disturbing loads. The discussion of these topics can be found, among others, in scientific papers [3] and [4]. Currently, there are a number of various power quality analysers on the market. The estimation of the uncertainty of measurement results obtained with the use of the investigated analyser is a very important issue. This paper presents the research results on a selected power quality analyser PQ-Box 100.

2. Measuring System for Testing Power Quality Analyser

The selected analyser PQ-Box 100 was tested in a measuring system presented in Fig. 1.

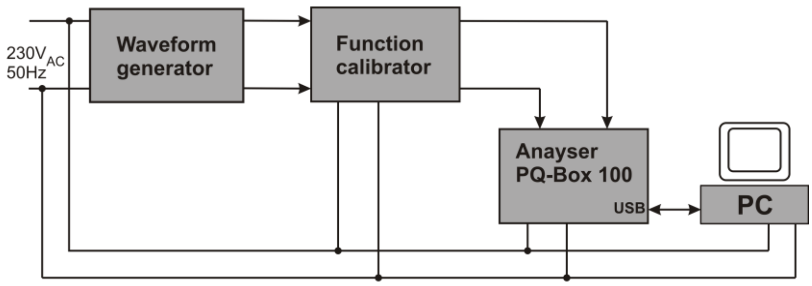

Fig. 1. Diagram of the measuring system for testing the power quality analyser PQ-Box 100

In the measuring system presented in Fig.1, waveform generator is designed to generate a given waveform and controls the operation of function calibrator. The calibrator generates a signal formed by the generator, with given rms values. The waveform generator was calibrated in the Central Office of Measures, where its accuracy was verified. The value of the limiting error of frequency reproduction, given in the calibration certificate, together with the uncertainty of its determination, for triangular wave is equal to $(198 \pm 68) \cdot 10^{-6}$ Hz. The

function calibrator generated a voltage signal with a form generated by the function generator. The value of limiting error for the considered signal values is equal to $\Delta = (0.042\%\, W_w + 0.005\%\, W_z)$, where W_w denotes the indicated value, and W_z denotes the value of measurement range. The signal generated in that way is then given to the tested analyser. Because the testing process is time-consuming, only selected values were verified: the voltage rms value and the distribution of harmonic components.
One of the test functions was a periodic signal that can be presented as a Fourier series. Such signal $u(t)$ can be shown in the form of trigonometric Fourier series, according to generally known dependencies. The representation of signal $u(t)$ in the form of a Fourier series refers to an infinitely great number of components. In practice, it is impossible. Therefore, a finite number of components are used. In practical measurement of power systems the first dozens of components are usually used. In the case considered, the measurements were limited to a harmonic of the 50th order. All the measurements were carried out in laboratory conditions, for the values of ambient temperature in a range of (22.5 ÷ 23.8) °C, and relative humidity in a range of (37.3 ÷ 46.7) %. Voltages were measured in all three phases, but given the result repeatability, the results were presented for a selected phase L_1. In all the measurements, measurement errors were determined as a difference between the measurement result and the value of reference quantity.

3. Experimental Research

Different test signals were used to verify the accuracy of measuring the rms value of voltage and harmonic content with selected power quality analysers. The investigated power quality analysers are calibrated in a two-phase process. The first phase consists in calibrating a meter with a distorted signal with a given rms value. The other phase consists in calibrating a meter with a sinusoidal signal with the same rms value as the distorted signal. During the tests two types of distorted waveforms were used:

a) Triangle wave – its expansion into Fourier series was presented with dependence (1):

$$u(t) = \frac{8U_m}{\pi^2}\left(\sin\omega_0 t - \frac{1}{3^2}\sin 3\omega_0 t + \frac{1}{5^2}\sin 5\omega_0 t - \cdots\right) \quad (1)$$

where: U_m denotes signal amplitude, $\omega_0 = \frac{2\pi}{T}$, T – test signal period

b) Waveform composed of a sum of two signals: fundamental harmonic and selected higher harmonic.

Calibration of the meter with the sinusoidal signal with the expected value of harmonic content equal to zero was aimed to testing the so-called "zero" of the analyser. For a distorted waveform composed of a sum of two signals, fundamental harmonic and selected higher harmonic, the basic harmonic had rms value equal to 230 V, and higher harmonics – value of 18.4 V, which constitutes 8 % of the value of fundamental harmonic. The rms value of such test signal was equal to 230.7 V. Table 1 presents examples of the results of verifying the test signal distorted with one harmonic component. Similarly as for other input signals, due to their repeatability, the results presented correspond to L_1 phase of the analyser. Because the publication size is limited, the results of experimental research concerning other test signals, triangle and sinusoidal signals, will be presented during the conference. All the measurements were repeated many times, at least 10 times, in order to determine the dispersion of measurement results and to eliminate possible gross error.

In order to determine the uncertainty value of a measurement result, it is necessary to correctly determine the measurement equation, which would take into consideration all the results affecting the final measurement result. In case of calibrating the analyser with distorted signal, with a given rms value, the equation for measurement error $\Delta_{THD\,dst}$ was presented with dependence (2):

$$\Delta_{THD\ dst} = W_{zmTHD\ dst} - W_{odnTHD\ dst} + \delta\Delta_{r\ dst} - \delta D_{dst} \tag{2}$$

where: $W_{zmTHD\ dst}$ – the value of quantity measured by the tested analyser, $W_{odnTHD\ dst}$ – reference value for a distorted signal, $\delta\Delta_{r\ dst}$ – value connected with the resolution of measuring device indications during the distorted signal measurement, δD_{dst} – value connected with limiting error of the reference standard during the distorted signal measurement.

Table 1. Summary of measurement results for signal with one harmonic component

Harmonic order	Measurement of THD Distorted signal with one harmonic component			
	Measurement result	Reference quantity value	Measurement error	Measurement uncertainty
	%	%	%	%
2	7.99	8.00	-0.01	0.19
3	7.99	8.00	-0.01	
4	7.99	8.00	-0.01	
5	7.99	8.00	-0.01	

To calibrate the analyser with sinusoidal signal with the same rms value as the distorted signal, the equation for measurement error $\Delta_{THD\ sin}$ is given with dependence (3):

$$\Delta_{THD\ sin} = W_{zmTHD\ sin} - W_{odnTHD\ sin} + \delta\Delta_{r\ sin} - \delta D_{sin} \tag{3}$$

where: $W_{zmTHD\ sin}$ – quantity value measured by the investigated analyser, $W_{odnTHD\ sin} = 0$ – reference value, $\delta\Delta_{r\ sin}$ – value connected with the resolution of measuring device indications during the sinusoidal signal measurement, δD_{sin} – value connected with limiting error of the reference standard during the sinusoidal signal measurement.

Combined standard measurement uncertainty $u_c(\Delta_{THD\ odk})$ of determining the analyser measurement error for distorted signals is given with dependence (4):

$$\begin{aligned} u_c^2(\Delta_{THD\ dst}) = {} & c_1^2 \cdot u^2(W_{zmTHD\ dst} - W_{odnTHD\ dst}) + c_2^2 u^2(\delta\Delta_{r\ dst}) \\ & + c_3^2 u^2(W_{zmTHD\ sin} - W_{odnTHD\ sin}) + c_4^2 u^2(\delta\Delta_{r\ sin}) \\ & + c_5^2 u^2(\delta D) \end{aligned} \tag{4}$$

where: c_1 – c_5 denote sensitivity coefficient, and δD denotes a value connected with limiting error of reference standard, which is determined as a geometric sum of values δD_{dst} and δD_{sin}.

When estimating the measurement uncertainty of the tested analyser, it is necessary to consider the following factors:

a) Standard uncertainty of measuring the difference of measurement results and reference value for distorted signal $W_{zmTHD\ dst} - W_{odnTHD\ dst}$,
b) Standard measurement uncertainty connected with the resolution of analyser indications during the measurement of distorted signal $\delta\Delta_{r\ dst}$,
c) Standard uncertainty of measuring the difference of the measurement result and reference value for sinusoidal signal $W_{zmTHD\ sin} - W_{odnTHD\ sin} = W_{zmTHD\ sin}$,

Because the expected value $W_{odnTHD\ sin}$ is equal to zero, randomization is done for random variable e_{THD} from measurement uncertainty $u(e_{THD})$. Standard measurement uncertainty, with normal distribution assumed, according to the uncertainty propagation law, is given with dependence (5):

$$u(e_{THD}) = \sqrt{\overline{(W_{zmTHD\ sin})}^2 + u^2(W_{zmTHD\ sin})}. \tag{5}$$

The uncertainty determined in that way is connected with the instability of indications of the tested analyser for sinusoidal signal. The complex standard uncertainty of measurement Δ_{THD} of distorted signal is expressed with dependence (6):

$$u_c^2(\Delta_{THD\ dst}) = u^2(W_{zmTHD\ dst} - W_{odnTHD\ dst}) + u^2(\delta\Delta_{r\ dst}) + u^2(e_{THD}) + u^2(\delta\Delta_{r\ sin}) + u^2(\delta D) \tag{6}$$

d) Standard measurement uncertainty connected with resolution of analyser indications during the measurement of sinusoidal signal $\delta\Delta_{r\ sin}$,
e) Standard uncertainty connected with limiting error of reference standard δD.

Standard uncertainties connected with the resolution of analyser indications, with rectangular distribution assumed, can be determined from formula (7):

$$u(\delta\Delta_r) = \frac{\Delta_r}{2\sqrt{3}} \tag{7}$$

where Δ_r denotes a value corresponding to the last indicated digit of the investigated analyser. All the components of expanded uncertainty mentioned above were determined and taken into consideration in the final uncertainty budget. Table 2 presents an example of uncertainty budget for the measurements contained in Table 1.

Table 2. Uncertainty budget for signal with a selected higher harmonic

Quantity symbol	Quantity estimate	Standard uncertainty $u(x_i)$		Probability distribution	Sensitivity coefficient c_i		Part of combined uncertainty	
W_{zm} - W_{odn}	-0.01	0.00019	V	Normal	1	V	0.00019	V
e_{THD}	0	0.08960	V	Normal	1	V	0.08960	V
$\delta\Delta_{r\ odk}$	0	0.00029	V	Rectangular	1	V	0.00029	V
$\delta\Delta_r sin$	0	0.00029	V	Rectangular	1	V	0.00029	V
δD	0	0.06731	V	Rectangular	-1	V	-0.06731	V
Δ_{THD}	-0.01	-		-	-		0.11207	V

4. Conclusions

A measuring system to assess the metrological properties of power quality analysers was presented in the paper. A number of tests on the voltage rms value and the Total Harmonic Distortion THD were carried out in this measuring system, with the use of selected test signals. The metrological analysis of the obtained measurement results let to final conclusions indicating that the determined values of uncertainty measurements of selected analyser are smaller than the uncertainty values declared by the manufacturer and defined in document [2].

References

[1] Decree of Ministry of Economy, dated 04.05.2007, on detailed conditions of power system operation.

[2] PN-EN 61000-4-30 Testing and measurement techniques – Power quality measurement methods.

[3] Otomański P. The applications of the Power Quality Analyser to determine of parameters describing electric power quality. In proceedings of the 6th International Conference on Measurement – MEASUREMENT 2007, 2007, 288-291.

[4] Otomański P., Wiczyński G. The usage of voltage and current fluctuation for localization of disturbing loads supplied from power grid. *Electrical Review,* 1: 107-111, 2011.

A New Method for Dielectric Parameters Testing and Model Identification Based on Differential Evolution

L. Michaeli, J. Šaliga, J. Lipták

Faculty of Electrical Engineering and Informatics, Technical University of Košice, Košice, Slovakia

Emails: {linus.michaeli, jan.saliga, jozef.liptak}@email.com

Abstract. *The paper describes a new method for direct estimation of dielectric material relaxation properties expressed by values of R and C in equivalent electric circuit. The unknown R,C values are calculated by the minimization of the cost function represented by the least square difference between measured charging current from the Isothermal Relaxation Current (IRC)-analysis of insulating materials and analytical description of the equivalent circuit. Proposed optimization by the differential evolution allows to determine R,C parameters in one step. It avoids uncertainty in R,C parameter calculus from time constants and peak values of single exponential components for finite resistance of the voltage source, switch and data acquisition board. The proposed method was verified by using PSpice model and optimization of analytical model in LabVIEW.*

Keywords: Dielectric IRC analysis, Signal decomposition, Differential evolution optimization

1. Introduction

Dielectric absorption of capacitors and charging process of insulating materials like HV cables is determined by the polarisation of dipoles in dielectrics and the latency in their polarization ([1], [2], [3], [4]). The charging/discharging relaxation process of dielectric dipole components in their final position is particularly delayed ([5], [6]). Relaxation processes cause memory effects in capacitors which limits precision of sample and hold circuits or linearity in of the conversion in integrating Analog to Digital Converters. Generally the polarisation effect can be modelled by electric Maxwell-Wagner circuit model, which consists of N parallel R_iC_i branches shown in Fig. 1.

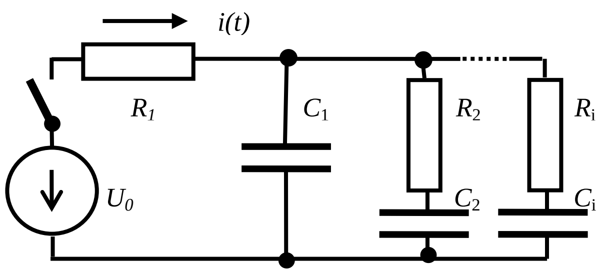

Fig. 1. Electrical model of the relaxation process in the dielectrics.

Each RC branch corresponds to the dipole moment of a chemical component in the mixture of dielectric materials used in the capacitor or cable isolation. After switching on the voltage source U_0, the R_iC_i circuits cause that the charging current $i(t)$ is in form of superposition of N exponential functions:

$$i(t) = A_1 e^{-B_1 t} + \sum_{i=2}^{N} A_i e^{-B_i t}, A_1 = \frac{U_0}{R_1} \tag{1}$$

where A_i are the peak values and B_i are the inverse values of the time constants of the current components (1). The currently used IRC test method assumes the ideal voltage source U_o ($R_1 \rightarrow 0$) and the ideal switch. Moreover, the data acquisition board (DAQ) measuring current is considered with internal resistance equal to zero. This assumption leads to the idealised simplified result that the first component in (1) is represented by the Dirac pulse ($A_1 = U_0/R_1$, $B_1 \rightarrow \infty$.). Parameters A_i, and B_i of other components are estimated by least square (LS) fit of successively added of the exponential components in (1) and acquired current $i(t)$ ([4] - [6]). The achieved fit for *i-th* exponential component is used as initial value for estimation of successive (i+1)-*th* exponential in (1). The fitting process is finished when all A_i, and B_i constants are achieved.

Because of the fact that signal components (1) are not the orthogonal under the influence of the real additive noise the successive identification of particular components leads into accumulation of errors transferred from previous fitting step. Real value of serial resistance R_1 represents mutual effect of real voltage source and input resistance of DAQ whose transverse voltage is used for measurement of the current $i(t)$. The estimation accuracy of R_i and C_i considering independent dipoles is highly sensitive on the distances among the exponential components A_i and B_i [4], [7].

2. New Proposed Method

Authors proposed the method of direct optimization of R_i,C_i components in circuit Fig. 1 with the aim to minimize difference between analytically expressed current $i(t)$ and its measured values $i_m(t_l)$in sampling instants t_l.

The charging process can be described by N linear differential equations for steady state circuit in Fig.1.:

$$\frac{d\boldsymbol{u}}{dt} = \boldsymbol{A}.\boldsymbol{u} + \boldsymbol{b}, \quad \text{where}$$

$$\boldsymbol{u} = \begin{bmatrix} u_1(t) \\ u_2(t) \\ \vdots \\ u_N(t) \end{bmatrix}, \quad \boldsymbol{A} = \begin{bmatrix} -\frac{G_T}{C_1} & \frac{G_2}{C_1} & \frac{G_3}{C_1} & \cdots & \frac{G_N}{C_1} \\ \frac{G_2}{C_2} & -\frac{G_2}{C_2} & 0 & \cdots & 0 \\ \frac{G_3}{C_3} & 0 & -\frac{G_3}{C_3} & \cdots & 0 \\ \vdots & \vdots & \vdots & \ddots & \vdots \\ \frac{G_N}{C_N} & 0 & 0 & \cdots & -\frac{G_N}{CN} \end{bmatrix}, \quad \boldsymbol{b} = \begin{bmatrix} U_0 / R_1 C_1 \\ 0 \\ \vdots \\ 0 \end{bmatrix}, \tag{2}$$

$$G_T = \sum_{i=1}^{N} \frac{1}{R_i}, \quad \text{and} \quad G_i = \frac{1}{R_i}$$

Theoretical analysis of the differential equation system (2) for the matrix **A** shows the exact values A_i and B_i are determined by the system of equations:

$$\left. \begin{array}{l} A_i = f_i(R_j, C_j,) \\ B_i = g_i(R_j, C_j,) \end{array} \right\} \quad \text{for } i = 1,\dots, N, \quad j = 1,\dots, N \tag{3}$$

Analytical solution of N ordinary differential equations of the first order is being programmed in the LabVIEW subroutine. It is obtained as solution of homogenous system (2) with the superposed particular integral. Analytical calculated steady state voltage $u_1(t)$ determines the charging current $i(t)$.

$$i(t)=\frac{U_0-u_1(t)}{R_1}=\frac{U_0-\sum_{i=1}^{N}\alpha_i e^{-\beta_i t}}{R_1}; \tag{4}$$

Where the constants β_i are the eigenvalues of matrix **A** for the voltages $u_1(t)$ and the peak values α_i are complex functions of eigenvector and initial conditions.

Optimization procedure estimates the parameters R_i and C_i with the scope to minimize cost function CF_{LS} represented by least squared difference between analytically expressed current $i(t)$ (4) and measured one $i_m(t)$ in the same time instants t_l.

$$\min(\mathrm{CF}_{\mathrm{LS}}(\mathbf{a}))=\min\left(\sum_{l=1}^{L}\left(i_{\mathrm{m}}(t_l)-i(t_l,\mathbf{a})\right)^2\right) \tag{5}$$

Here t_l are sampling instances and analytically expressed current $i(t,\mathbf{a})$ is a function of the circuit parameters $\mathbf{a}$ = [C_1, R_1, C_2, R_2, C_n, R_n] (Fig.1). Different strategies can be used to minimize (5). The authors utilized optimization method based on differential evolution which is metaheuristic method. Its main advantage is searching the possible solutions in very large space with higher resistance on convergence into local minima.

3. Experimental Results

The proposed method was tested in simulation. The model in Fig. 1 was first implemented in PSpice including model of real switch and source of voltage. Result from the Result from the PSpice TRANS analysis was recorded in a file and consequently circuit parameters **a** were optimized by the differential evolution optimization. Circuit parameters were input into program calculating analytically current $i(t,\mathbf{a})$ for (5). The results achieved by the simulated test using different number of samples L are listed in Table 1.

Table 1. The values of the matrix **a** with estimations of circuit parameters for different L using both algorithms.

L	C1	R1	C2	R2	C3	R3	C4	R4	ε(*L*)
	10u	20k	398n	8M	324n	40M	1n	1G	
10.	10.09u	20.00k	498.5n	7.693M	492.6n	123.6M	19.09n	1.499G	7.0 E-16
20.	9.993u	20.00k	370.8n	7.916M	375.3n	44.31M	135.1n	156.2M	4.9 E-16
50	9.996u	19.99k	484.5n	7.397M	486.7n	77.41M	2.748n	275.9M	3.7 E-16
100	10.00u	19.99k	377.3n	7.533M	408.7n	37.65M	178.6n	582.3M	3.6 E-16

Estimation precision was assessed by the averaged error $\varepsilon(L)=\frac{1}{L}\sum_{l=1}^{L}\left(i_m(t_l)-i(t_l,\mathbf{a})\right)^2$ between measured and estimated current for L samples in the time window (0, t_L)

The efficiency of the circuit parameters R_i,C_i direct estimation in comparison with methods based on the exponential signal decomposition and successive circuit parameters estimation was studied under two scenarios. The estimation of the circuit parameters for real insulation material represents first scenario. Measured material sample consists of calcined mica paper with glass cloth and polyethylenetereflat's foil. Everything is bind together by epoxy Remikaflex 45.004. The measured data representing second scenario were acquired from PSpice model. Here the inherent circuit parameters R_i,C_i are known and compared with parameters estimated by the proposed method and by exponential signal decomposition. Table.2 shows real and estimated parameters with relative error of their estimation.

Table 2. Estimation of the Maxwell-Wagner circuit model of polarisation effects

Maxwell-Wagner circuit model of dielectric relaxation		Estimated by proposed method	relative error	Two step estimation [3]	relative error
1st scenario	5μF	4.97 μF	- 1%	4.55 μF	- 9%
	500MΩ	498 MΩ	- 0%	523 MΩ	+ 5%
	150nF	152 nF	+ 2%	154 nF	+ 3%
	6MΩ	5.97 MΩ	- 0%	5.93 MΩ	- 1%
	5nF	5.15 nF	+ 3%	1.257 μF	+N/A
	300MΩ	510.6 MΩ	+70%	10.7 GΩ	+N/A
2nd scenario	10μF	10.13 μF	+ 1%	9.722 μF	- 3%
	1MΩ	0.978 MΩ	- 2%	1.034 MΩ	+ 3%
	500nF	357.4 nF	-29%	569.3 nF	+14%
	10MΩ	12.2 MΩ	+23%	12.08 MΩ	+21%
	25nF	39.0 nF	+56%	234.4 nF	+838%
	100MΩ	147 MΩ	+47%	166.1 MΩ	-83%

4. Conclusions

Paper deals with new method for measurement of the hidden parameters of the dielectric materials, mainly insulants using standardized IRC diagnostics. The method estimates all parameters contemporary which suppress transfer of estimation error from one approximation of exponential function to another caused by the additional noise. Another advantage of the proposed method is the consideration of the real resistance R_1 of the voltage source and the switch.

Acknowledgements

The work is a part of the project supported by the Science Grant Agency of the Slovak Republic (No. 1/0281/14).

References

[1] Kuenen JC, Meijer GCM. Measurement of dielectric absorption of capacitors and analysis of its effects on VCOs. *IEEE Transactions on Instrumentation and Measurement*, 45(1): 89-97, 1996.

[2] Menendez E. Dielectric Absorption of Multilayer Organic (MLO™) Capacitors.*Technical papers*. http://www.avx.com/docs/techinfo/MLO/Dielectric/ Absorption.pdf

[3] Kovaľ F, Cimbala R. IRC Analysis of insulation systems. Acta Electrotechnica et Informatica, 7(4): 1-7, 2007.

[4] Hofmann R, Kranz HG, Steinbrink D. IRC-Analysis: Destruction free dielectric diagnosis of mechanical and service aged polymeric insulation. *ISH 1999, Conference Publication* No 467, 1999.

[5] Hoff G, Kranz HG. Correlation Between Return Voltage and Relaxation Current Measurements on XLPE Medium VoltageCables, *11th ISH 1999*, London.

[6] Beigert M, Kranz HG. Destruction Free Ageing Diagnosis of Power Cable Insulation Using the Thermal relaxation Current. *IEEE Symposium on Electrical Insulation*, Pittsburgh, PA USA, June 5-8, 1994, pp. 17-21.

[7] Michaeli L, Šaliga J, Godla M, Lipták J. Measurement of Dielectric Absorption of Capacitors by Signal Decomposition. *Proc. of IMEKO TC-4 Symposium*, Benevento 2014, pp. 107-111.

Variable Frequency Pulse Width Modulation

[1]M. Stork, [2]J. Hammerbauer

University of West Bohemia/RICE, Plzen, Czech Republic
Email: stork@kae.zcu.cz, hammer@kae.zcu.cz

Abstract. *Pulse width modulation (PWM) is widely used in different applications. PWM transform the information in the amplitude of a bounded input signal into the pulse width output signal, without suffering from quantization noise. The frequency of the output signal is usually constant. In this paper the new PWM system with frequency changing (PWMF) is described. In PWMF the pulse width and also frequency is changed, therefore 2 independents information are simultaneously transmitted-PWM and frequency modulation (FM) are simultaneously used. Such system needs fast demodulator separately for PWM and FM. The circuit for fast demodulation of PWMF signal is also described and measuring results are presented. All described circuits were constructed and measured.*

Keywords: Pulse width modulation, Frequency modulation, Demodulation, frequency to voltage converter

1. Introduction

PWM, or pulse-duration modulation (PDM), is a technique used to encode a message into a pulsing signal. It is a type of modulation and therefore this modulation technique can be used to encode information for transmission. Pulse-width modulation uses a rectangular pulse wave whose pulse width is modulated resulting in the variation of the average value of the waveform. In this paper is described new approach for fast demodulation of PWM signal and also for FM signal. The new system therefore allows transmit simultaneously PWM an FM signals as 2 independents information in one PWMF signal and also fast demodulation.

2. Principle of Variable Frequency Pulse Width Modulation

Signals with PWM are very easy to demodulate. In addition to a number of other components, their spectrum contains also the baseband spectrum of the original modulating signal. A low-pass filter is therefore sufficient to separate the useful signal. This method, however, has a drawback in slow low-pass analog filter and needs of output buffer amplifier. It is important to note that PWMF signal change booth – pulse width and also frequency. In this paper the new approach is used for demodulation of PWM in every period (every rising edge). The principle of 2 independent information transmissions by means of PWMF signal and demodulation is shown in Fig. 1. On the top two period of modulated signal are shown, where first period is T_1=50 and width w_1=30 and second period is T_2=30 and width w_2=10. In the middle, the demodulation of PWM signal is displayed. The new values v_{1PWM} and v_{2PWM} are updated on every rising edge of PWMF signal. On the bottom, the demodulation of frequency modulated signal is shown. The new values, corresponding frequency of PWMF signal are also updated on every rising edge of PWMF signal. The value of demodulated PWM signal of period T_1 with width w_1 is v_{1PWM} (updated on the end of period T_1) and similarly for v_{2PWM}

$$v_{1PWM} = w_1 / T_1 = 30/50 = 0.6 \qquad v_{2PWM} = w_2 / T = 10/30 = 0.333 \qquad [\text{-, s, s}] \qquad (1)$$

The value of demodulated FM signal of period T_1 (for gain coefficient k_f=5) v_{1f} is (updated on the end of period T_1) and for T_2 is v_{2f} (updated on the end of period T_2)

$$v_{1f} = k_f / T_1 = 5/50 = 0.1 \qquad v_{2f} = k_f / T_2 = 5/30 = 0.166 \qquad [-, s, s] \qquad (2)$$

The circuit and measuring results for conversion of PVM signal to voltage and FM signal to voltage in one period (updated on every rising edge) is described in next part.

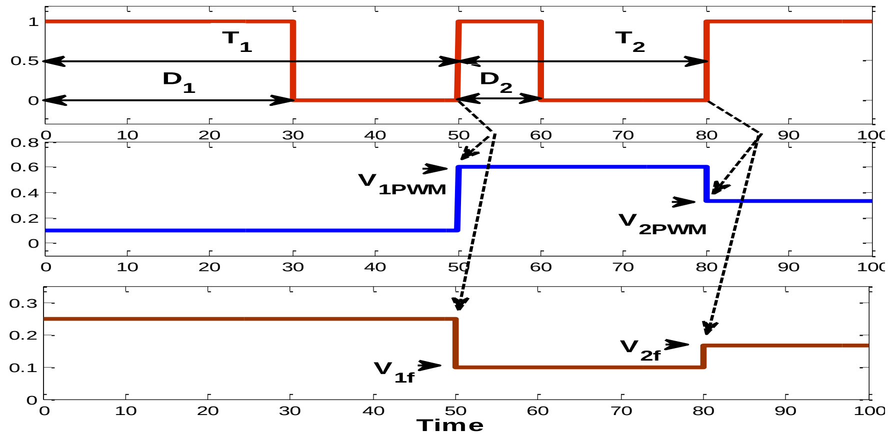

Fig. 1. The principle of PWMF modulation and fast demodulation (in every cycle – on rising edge of PWMF). Top - PWMF modulated signal, middle - PWM signal demodulation, bottom - demodulation of frequency modulation.

3. Circuit for Fast PWM Demodulation

For fast demodulator of PWM the IC's LTC2644 was used [1]. The simplified block diagram of LTC2644 is shown in Fig. 2 (left). The LTC2644 measures the period and pulse width of the PWM input signals and updates the voltage output DACs after each corresponding PWM input rising edge The input frequency is between 30 Hz and 6.25 kHz (12-bit), 25 kHz (10-bit) or 100 kHz (8-bit). The DAC outputs update and settle to 12-bit accuracy within 8µs typically. The most important is that slow analog filter was eliminated. The LTC2644 has a full-scale output of 2.5V using the 10ppm/°C internal reference. The circuit operates from a single 2.7V to 5.5V supply and supports PWM input voltages from 1.71V to 5.5V [2-3]. The demodulated output voltage V_{DEM} can be calculated by the following equation

$$V_{DEM} = V_{REF} \cdot t_1 / T \qquad [V, s] \qquad (3)$$

where V_{REF} is 2.5 V internal reference voltage (or external reference voltage) and t_1 is width of PWM signal and T is period of PWM signal. The measured example of PWM demodulation on every rising edge of input signal is shown in Fig. 2 (right).

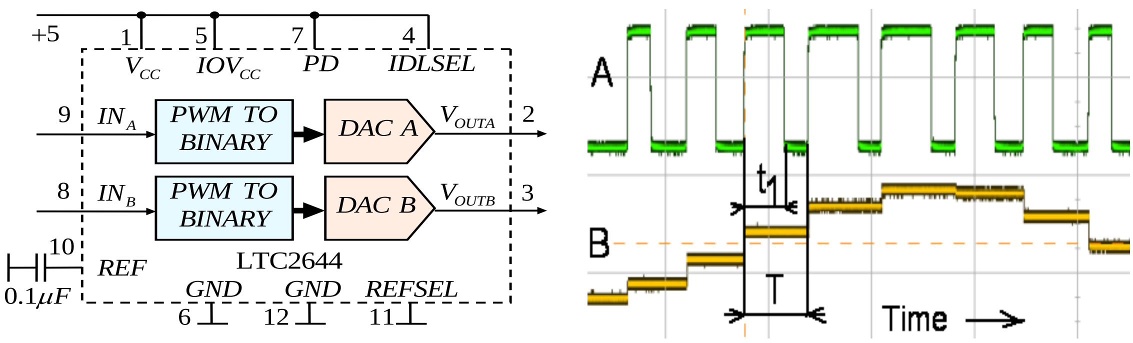

Fig. 2. The circuit diagram of 2 channel PWM/V converter LTC2644 (left). PWM inputs are 8 and 9, voltage outputs are 2 and 3. The scope of measured the PWM demodulation in every cycle of PWM signal - time evoluation of signals (right). The PWM signal (top), demodulated voltage output (bottom). The output of the demodulator is updated every rising edge of input signal.

4. Circuits and Measuring Results

In this part the circuits and measuring results are presented. The PWMF modulator based on LTC6992 is displayed in Fig. 3 [4]. V_{PWM} is analog input voltage for PWM modulation and V_{FM} is analog input voltage for FM modulation. Applying a voltage between 0V and 1V on the MOD pin sets the duty cycle. The frequency range is from 3.81 Hz to 1 MHz. For fixed PWM frequency (without FM modulation) a single resistor, R_{SET}, programs the LTC6992's internal master oscillator frequency. The output frequency is determined by this master oscillator and an internal frequency divider, divide by N_{DIV}, which is programmable to eight settings from 1 to 16384 (by means of R_1 and R_2) [4]. For $R_{FM}\to\infty$ (fixed PWM frequency) the output PWM frequency is given

$$f_{out} = \frac{5\cdot 10^{10}}{N_{DIV}}\cdot\frac{1}{R_{SET}};\quad N_{DIV} = 1, 4 \ldots 16384 \qquad [\mathrm{Hz}, \Omega] \qquad (4)$$

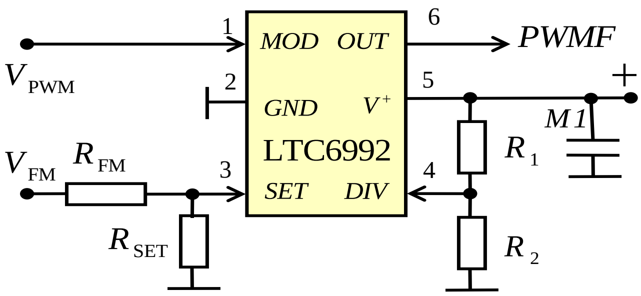

Fig. 3. The circuit diagram of PWMF modulator with LTC6992 IC's. V_{PWM} is analog input voltage for PWM modulation and V_{FM} is analog input voltage for FM modulation.

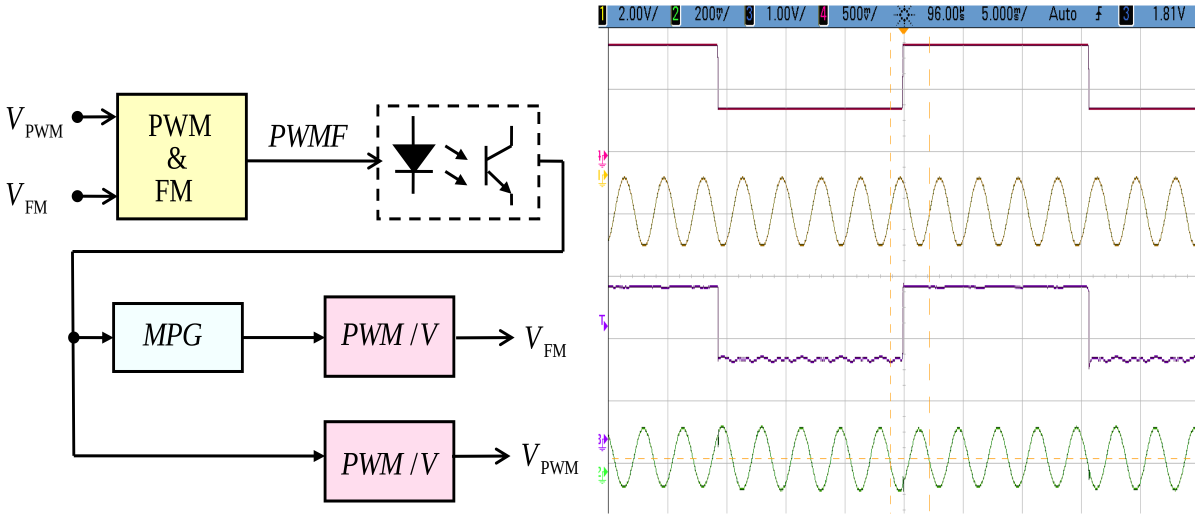

Fig. 4. The circuit diagram of PWMF modulator/demodulator with galvanic separation (left) and scope - time diagram of 2 independent signal transmission (right). PWM & FM – modulator (LTC6992), MPG – monostable pulse generator on every rising edge of PWMF, PWM/V – demodulator (LTC2644). The example of transmission 2 signals by means of PWMF. First (Top) – PWM modulator input signal, second – FM modulator input signal, third - demodulated PWMF signal, PWM output, bottom – demodulated PWMFsignal, FM output.

When the FM is also used, the output frequency is

$$f_{out} = \frac{5\cdot 10^{10}}{N_{DIV}}\cdot\frac{I_T}{V_{SET}} = \frac{5\cdot 10^{10}}{N_{DIV}V_{SET}}\cdot\left[V_{SET}\left(\frac{1}{R_{SET}}+\frac{1}{R_{FM}}\right)-\frac{V_{FM}}{R_{FM}}\right];\; N_{DIV} = 1, 4, \ldots 16384 \qquad [\mathrm{Hz, V, A}] \quad (5)$$

The block diagram of circuit for PWMF modulation/demodulation (with isolation barrier) of 2 separate signals is presented in Fig. 4 (left). For FM demodulation, on the first, monostable pulse generator (MPG) is used and output of MPG is connected to one of PWM/V demodulator. The MPG converts FM to PWM. For PWM to voltage the LTC2644 (according Fig. 2 (left)) is used. Result is shown in the Fig. 4 (right). The scope of modulation and demodulation of the PWMF signals are shown. The input (square wave, frequency=35 Hz) analog signal is on the top is connected on PWM input of PWM & FM circuit, the second (sine wave, frequency = 300 Hz) signal is connected on FM modulation input of PWM & FM circuit, the third, is demodulated output V_{PWM} of PWMF signal and bottom is demodulated output of V_{FM} signal.

5. Conclusion

In this paper was described new approach for fast demodulation of PWM signal and also for FM signal demodulation. The new system therefore allows transmit simultaneously PWM an FM signals as 2 independents information in one - PWMF signal. The demodulator measures the period and pulse width of the PWM input signals and updates the voltage output DACs after each corresponding PWM input rising edge. The basic PWM demodulator is not sensitive for input frequency changes. The DAC outputs update and settle to 12-bit accuracy within 8μs typically. The most important is that slow low-pass analog filter was eliminated. The fast demodulator can be also separately used as PWM demodulator, FM demodulator (the MPG circuit must be added, see Fig. 4) and demodulator for asynchronous sigma-delta modulator. The presented systems were described, simulated, constructed and measured.

Acknowledgements

This research has been supported by the European Regional Development Fund and the Ministry of Education, Youth and Sports of the Czech Republic under the Regional Innovation Centre for Electrical Engineering (RICE), project No. CZ.1.05/2.1.00/03.0094 and by the Internal Grant Agency of University of West Bohemia in Pilsen, the project SGS-2015-002.

References

[1] PWM to DC in One Cycle.http://cds.linear.com/docs/en/product-selectorcard/2PB_2645f.pdf, 2015.

[2] Convert PWM Inputs to 12-Bit Accurate Voltage Outputs with No Software, No Ripple & No Delay, http://cds.linear.com/docs/en/press-release/LTC2645.pdf, 2015

[3] LTC2644 - Dual 12-/10-/8-Bit PWM to VOUT DACs with 10ppm/°C Reference, http://www.linear.com/product/LTC2644, 2015.

[4] LTC6992-1/LTC6992-2/,LTC6992-3/LTC6992-4, Voltage-Controlled Pulse Width Modulator, http://cds.linear.com/docs/en/press-release/LT6992.pdf, 2015.

Fast Demodulator for Asynchronous Sigma-Delta Modulator Signals

[1]M. Stork, [2]P. Weissar, [3]K. Kosturik

University of West Bohemia/RICE, Plzen, Czech Republic
Email: stork@kae.zcu.cz, weissar@kae.zcu.cz, kosturik@kae.zcu.cz

Abstract. *Asynchronous sigma-delta modulator (ASDM) is closed-loop nonlinear system that transform the information in the amplitude of a bounded input signal into time information in the output signal, without suffering from quantization noise such as in synchronous sigma-delta modulators. This is an important advantage with many interesting applications. This paper investigates the commonly used asynchronous sigma–delta modulator, which consists of a Schmitt trigger and a continuous-time loop filter. Analysis is presented to accurately describe the properties of such modulator. The new circuit for fast demodulation of modulated signal is also described. The theoretical derivations were compared with simulation and measuring results. The presented circuits were analyzed, simulated, constructed and measured.*

Keywords: Asynchronous sigma-delta modulator, Pulse-width modulator, Demodulator, Digital-analog converter, Signal transmission

1. Introduction

Power requirement and dissipation due to analog to digital conversion as well as to wireless transmission are major limitations in the implementation of e.g. human implants or wireless EEG (Electro Encephalographic) signal measuring. Uniform sampling in the analog to digital converters (ADCs) requires synchronous implementation with a common clock shared with the digital signal processor. The need for a clock is a source of power consumption. In contrast, asynchronous circuits are not governed by a clock and consume low power. The elimination of clocks in these circuits also reduces device sizes and cuts electromagnetic interference (EMI) significantly. Due to these desirable properties, ASDMs have been proposed for data acquisition in bio-monitoring systems [1, 2]. An ASDM block diagram (Fig. 1) includes several functional blocks: an summation block, integrator, hysteretic comparator and a switch. The integrator output and switch output are shown in Fig. 2. It is a pulse width modulated (PWM) square wave of period T with a pulse-width t_1. The duty cycle *Duty* is proportional to the value of the input signal. Moreover, also the period T of the asynchronous modulator output depends on the input voltage.

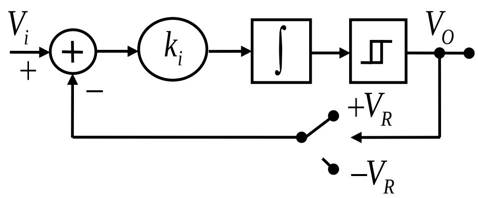

Fig. 1. The block diagram of the first order asynchronous sigma-delta modulator

Assume the band limited input voltage V_i ($|V_i|<V_R$). The output of the integrator V_{int} is (slope S_1, start from t_k to t_{k+1})

$$V_{int}(t_{k+1}) = k_i \int_{t_k}^{t_{k+1}} \left(V_i(t) + V_R\right) dt + V_{int}(t_k) \tag{1}$$

for $V_i(t)=V_i$ (constant input voltage) the time t_1 for $V_{int}(t_k)=-h$ and $V_{int}(t_{k+1})=h$ and time t_2 is

$$t_1 = t_{k+1} - t_k = \frac{Hys}{k_i\left(V_i + V_R\right)}; \quad t_2 = t_{k+2} - t_{k+1} = \frac{Hys}{k_i\left(V_R - V_i\right)} \tag{2}$$

and combining (2) and (3) output period T, frequency f and duty cycle D is

$$T = t_1 + t_2 = \frac{Hys}{k_i}\left(\frac{2V_R}{V_R^2 - V_i^2}\right); \quad f = \frac{1}{T} = \frac{k_i}{Hys}\left(\frac{V_R^2 - V_i^2}{2V_R}\right); \quad D = 100\frac{t_1}{t_1 + t_2} = 100\frac{t_1}{T} = 100\frac{V_R - V_i}{2V_R} \tag{3}$$

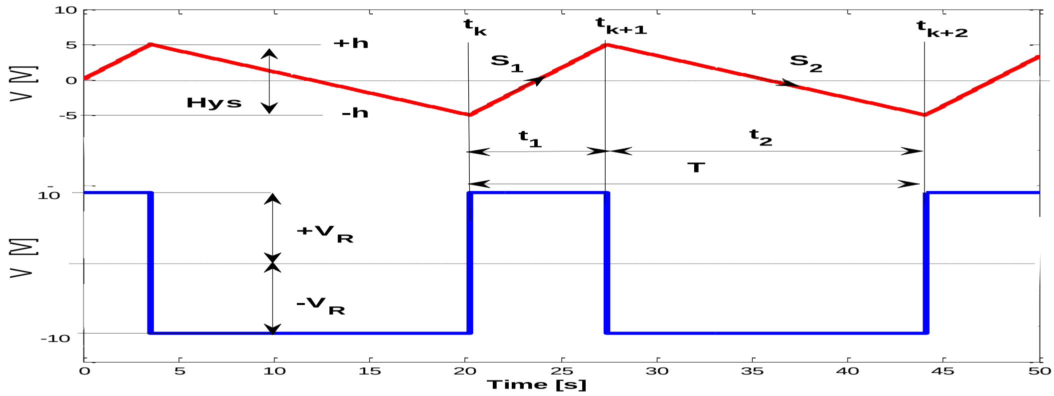

Fig. 2. The signals of the ASDM for $V_i = 4$ V, $V_R = \pm 10$ V, $h = 5$ V, $Hys = 10$ V and $k_i = 0.1$. Integrator output $y(t)$ (top), switch output (bottom) versus time. S_1 and S_2 slopes on the integrator output signal

2. Modulator

The circuit diagram of the simple, first order ASDM (based on operational amplifiers) and demodulator with voltage output is shown in Fig. 3.

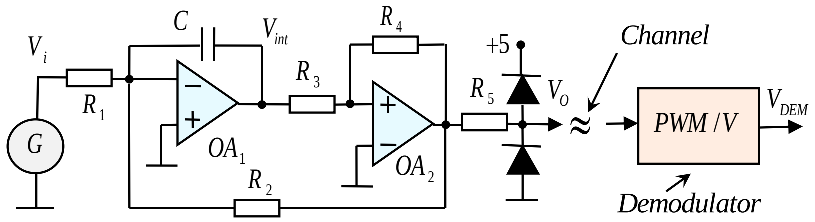

Fig. 3. The circuit diagram of the simple, first order ASDM (R1=R2=R3=R5=10 kΩ, R4=100 kΩ, C=100 nF, VR= 10.5 V, Hys=2.3 V, OA=TL072) signal transmission by different type of channel and demodulation by PWM/V block. V_i analog input voltage (from generator), V_{int} integrator output, V_0 output of modulator and V_{DEM} demodulated output voltage.

Instead k_i in eq. (1)-(4), for ASDM with operational amplifiers, k_i is substituted by *1/RC*, therefore

$$t_1 = RC\frac{Hys}{V_i + V_R}; \quad t_2 = RC\frac{Hys}{V_R - V_i}; \quad f = \frac{1}{t_1 + t_2} = \frac{1}{T} = \frac{V_R^2 - V_i^2}{2 \cdot RC \cdot Hys \cdot V_R} \quad [\text{s}, \Omega, \text{F}, \text{V}] \tag{4}$$

The calculated and measured results of ADSM for $R_1=R_2=R_3=R_5=10$ kΩ, $R_4=100$ kΩ, C=100 nF, $V_R= 10.5$ V, Hys = 2.3 V are shown in Fig. 4. From this figure can be seen almost the same calculated (dash lines) and measured (solid lines) duty and frequency dependencies versus input voltage. The measured (and calculated) duty cycle D_{CALC} versus V_i (for $V_i \in \langle -9 \div 9 \rangle$ [V]) can be approximated as

$$D_{CALC} = 50 - 4.83 \cdot V_i \quad [\%, \text{V}] \tag{5}$$

and measured (and calculated) output frequency f_{CALC} versus V_i are

$$f_{CALC} = 2.4 - 0.0216 \cdot V_i^2 \qquad \text{[kHz, V]} \qquad (6)$$

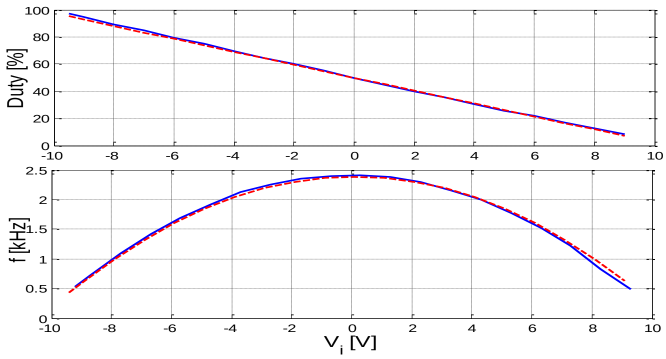

Fig. 4. The calculated (dash line) and measured (solid line) duty (top) and frequency (bottom) versus V_i for simple ASDM according Fig. 3, (for $V_i \in \langle -9 \div 9 \rangle$ [V])

3. Fast Demodulator

Signals with pulse-width modulation (or ASDM signals) are very easy to demodulate by lowpass filter but with slow response. This approach can be modified by using counters and digital-analog (D/A) converter. This principle of the PWM demodulation is used for fast demodulation of ASDM signal. It is important to note that PWM signal generated by ASDM change booth – pulse width and also frequency. Output of the fast demodulator is updated every rising edge of input signal. The LTC2644 IC’s (PWM/V converter, see Fig. 5) is used for fast demodulation [3, 4]. This IC’s is not sensitive for frequency changing. After each rising edge of input signal, the IC’s calculates the duty cycle based upon the pulse width and period and updates D/A output (within 8 μs for 12-bit). The demodulated output voltage V_{DEM} can be calculated by the following equation

$$V_{DEM} = V_{REF} \cdot t_1 / T \qquad \text{[V, s]} \qquad (7)$$

where V_{REF} is 2.5 V internal reference voltage (or external reference voltage) and t_1 is width of PWM signal and T is period of PWM signal.

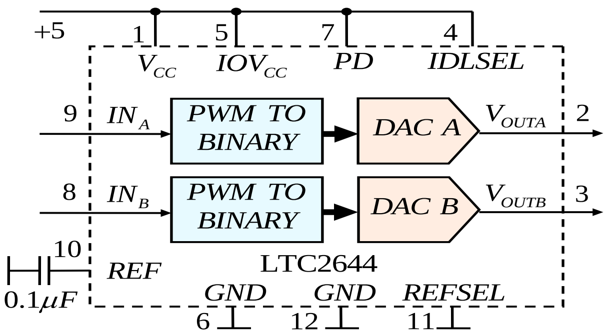

Fig. 5. The circuit diagram of 2 channel fast PWM/V demodulator - LTC2644. PWM input pins 8 and 9 are inputs, pins 2 and 3 are voltage outputs.

4. Measuring Results

The fast demodulator for ASDM signal was tested for analog signal transmission and demodulation. The time evolutions of the signals are shown in Fig. 6. In this figure are shown signals on input, integrator output, ASDM output and demodulated output. The frequency of input signal: 200 Hz. The maximal frequency of the ASDM: approx. 2.5 kHz (for $V_i = 0$) and minimal approx. 1.7 kHz (for $V_i \approx \pm 5$ V).

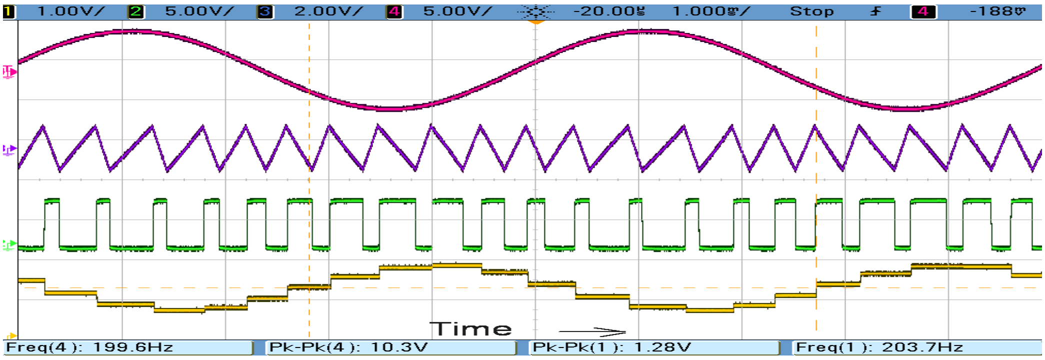

Fig. 6. The example of analog signal transmission by means of ASDM. From top to bottom (time signals): Input signal V_i from generator; output of the integrator V_{int}; output of the modulator V_0; demodulator output V_{DEM}

5. Conclusion

In this paper the fast demodulator for ASDM was described. This circuit can be used in different applications e.g. in biomedical engineering, optically coupled systems, sensors and other industry applications. Very important is fast demodulation of ASDM (demodulation in one period of ASDM signal) without using low-pass filter. The presented systems were described, simulated, constructed and measured. The paper illustrates a good match between theory and measuring results.

Acknowledgements

This research has been supported by the European Regional Development Fund and the Ministry of Education, Youth and Sports of the Czech Republic under the Regional Innovation Centre for Electrical Engineering (RICE), project No. CZ.1.05/2.1.00/03.0094 and by the Internal Grant Agency of University of West Bohemia in Pilsen, the project SGS-2015-002.

References

[1] Daniels J, Dehaene W, Steyaert M, Wiesbauer A. A/D Conversion using an Asynchronous Delta-Sigma Modulator and a Time-to-Digital Converter. *IEEE International Symposium on Circuits and Systems*, May, 2008.

[2] Senay S, Chaparro LF, Sclabassi RJ, Sun M, Mancini R, Palmer R. Time Encoding and Reconstruction of Multichannel Data by Brain Implants Using Asynchronous Sigma Delta Modulators. *31st Annual International Conference of the IEEE EMBS*, Minneapolis, Minnesota, USA, September 2-6, 2009.

[3] PWM to DC in One Cycle. http://cds.linear.com/docs/en/product-selector-card/2PB_2645f.pdf, 2015.

[4] LTC2644 - Dual 12-/10-/8-Bit PWM to VOUT DACs with 10ppm/°C Reference, http://www.linear.com/product/LTC2644, 2015.

Stochastic and Deterministic Dithering in Slow Measurements

M. Kamenský, K. Kováč, L. Makyta

Slovak University of Technology in Bratislava, Faculty of Electrical Engineering and Information Technology, Institute of Electrical Engineering, Bratislava, Slovakia
Email: miroslav.kamensky@stuba.sk

Abstract. *Unified concept for theoretical analysis of dithering techniques is presented. Slow measurements are considered where the dither frequency and the sampling frequency are much higher than the signal frequency. Averaging of samples is engaged in the process of sampled signal filtering. The Widrow's statistical model is directly applied for stochastic dithering (SD) and characteristic functions are used for evaluation of error moments. Both nonsubtractive and subtractive form of SD is covered by the developed methodology. Simulation results are confronted with theoretical analysis. The performance of SD is also compared with the performance of deterministic dithering (DD).*

Keywords: Quantization, Widrow's model, Dithering, ADC errors

1. Introduction

Dither is usually a random noise added to a signal prior to it (re)quantization in order to control the statistical properties of the quantization error. In measurement applications the dithering process yields to suppression of quantization error by mean value filtering of the quantizer output. Two types of such stochastic dithering are distinguished. A term subtractive (stochastic) dithering (SD) is used for the case, when the dither is subsequently subtracted from the sampled signal after quantization. In the process of nonstubtractive (stochastic) dithering (ND) the dither is not subtracted from processed quantized signal. Both alternatives are commonly used and further developed e.g. for microcomputer based measurements [1]. The SD offers better performance especially for audio/video applications, while the implementation of ND is easier. Moreover special deterministic dithering technique exists based on deterministic signal added to the system input.

Several theoretical concepts were presented for analysis of dither influence on quantization process. Generally statistical methods are useful for investigation of stochastic dithering while Fourier analysis could be demanded for application of DD. The paper presents unified concept for analysis of dithering techniques based on Widrow's statistical theory of qunatization. The total root mean squared error is confronted for both alternatives – SD and ND. Furthermore, we will show that the statistical concept could be helpful in analysis of DD too. The impact of sampling non-coherency is investigated using Fourier analysis. The analysis should explain trends in error behavior related to the non-coherency.

2. Statistical Theory of Stochastic Dithering

In the system with nonsubtractive dithering the quantizer input is u=s+d, where s is measured value and d is the added noise. The transfer function $Q(s)$ of an ideal quantizer without dither comprises quantization error, which characteristic Q_e(s) exhibits known saw-tooth shape with zero mean and peak-to-peak value of one quantization step q. In the system with ND the quantizer output is v=$Q(u)$=$Q(s+d)$. It is difficult to see positive contribution of the dither from the direct expression of the corresponding error ε=$Q_e(s+d)+d$. For measurement application statistical moments of error should be of interest. Reasonable approach for evaluation of error moments from characteristics functions (CF) was suggested by Widrow

[2]. From Widrow's concept of mathematic modeling of quantization (similar to standard modeling of signal sampling) it is possible to obtain CF of ε in the form

$$CF_{\varepsilon}(w,s)=\sum_{k=-\infty}^{\infty}\operatorname{sinc}\left(\frac{q(w+k\Psi)}{2}\right)CF_{\mathrm{d}}(w+k\Psi)e^{jk\Psi s} \tag{1}$$

where CF_{d} is CF of dither and $\Psi=2\pi/q$ is a constant. If CF of stochastic variable is known its moments could be evaluated by derivatives of the CF (σ_{d} is standard deviation of dither)

$$E[\varepsilon|s]=\frac{1}{j}\left.\frac{dCF_{\varepsilon}(w)}{dw}\right|_{w=0}=\sum_{k=1}^{\infty}\frac{q(-1)^{k}}{\pi k}CF_{\mathrm{d}}\left(k\frac{2\pi}{q}\right)\sin\left(k\frac{2\pi}{q}s\right) \tag{2}$$

$$E[\varepsilon^{2}|s]=\frac{1}{j^{2}}\left.\frac{d^{2}CF_{\varepsilon}(w)}{dw^{2}}\right|_{w=0}=\frac{q^{2}}{12}+\sigma_{\mathrm{d}}^{2}+\frac{q^{2}}{\pi^{2}}\sum_{k=1}^{\infty}\frac{(-1)^{k}}{k^{2}}\left(CF_{\mathrm{d}}(k\Psi)-k\Psi\, CF_{\mathrm{d}}^{\mathrm{d1}}(k\Psi)\right)\cos(k\Psi s) \tag{3}$$

The first moment (2) means the mean error $E[\varepsilon|s]$ and the second (3) is a mean squared error $E[\varepsilon^2|s]$. Also the variance is determined by (2) and (3) as it holds $Var[\varepsilon|s] = E[\varepsilon^2|s] - E^2[\varepsilon|s]$. Moments are dependent on the actual s. The overall measure of the error is obtained by integration of mean squared error within one quantization step [3]. From (2) one gets

$$\mu_{\varepsilon}^{2}=\frac{1}{q}\int_{-q/2}^{q/2}\left(E[\varepsilon|s]\right)^{2}ds=\sum_{k=1}^{\infty}\frac{q^{2}}{2\pi^{2}k^{2}}CF_{d}^{2}\left(k\frac{2\pi}{q}\right) \tag{4}$$

Similarly the mean value within one quantization step could be used for evaluation of overall root mean squared error (squaring is already included in $E[\varepsilon^2|s]$)

$$RMS_{\varepsilon}^{2}=\frac{1}{q}\int_{-\frac{q}{2}}^{\frac{q}{2}}E[\varepsilon^{2}|s]ds=\frac{q^{2}}{12}+\sigma_{d}^{2} \tag{5}$$

and of overall variance

$$\sigma_{\varepsilon}^{2}=\frac{1}{q}\int_{-q/2}^{q/2}Var[\varepsilon|s]ds=RMS_{\varepsilon}^{2}-\mu_{\varepsilon}^{2}=\frac{q^{2}}{12}+\sigma_{d}^{2}-\sum_{k=1}^{\infty}\frac{q^{2}}{2\pi^{2}k^{2}}CF_{d}^{2}\left(k\frac{2\pi}{q}\right) \tag{6}$$

Theoretical overall mean value (4), root mean squared value (5) and variance (6) of error ε are simply estimations of error moments of repeated measurements, if the probability of every position of s relative to boundaries of a quantization bin is the same.

If the mean error $E[\varepsilon|s]$ is evaluated for dithering systems and further investigated, it reveals that this mean has lower peak-to-peak value compared to original error characteristic $Q_{\mathrm{e}}(s)$ of the quantizer. This is the usual principle of dithering usage for suppression of quantization error for measurement applications. To achieve the error suppression the mean value has to be estimated from the samples employing low pass filter assuming constant measured value s during one measurement with the mean estimation. Unfortunately the filter output includes a random part for finite number of samples. Averaging is usual type of filter for dithering applications. The variance of the error after averaging $\xi = o\text{-}s$ is suppressed to $\sigma_{\varepsilon}^2=\sigma_{\varepsilon}^2/N$. Therefore also RMS of the final error ξ of system with ND is smaller compared to error (5) without dithering. It could be evaluated from (4) and (6) as

$$RMS_{\xi}^{2}(N)=\mu_{\varepsilon}^{2}+\frac{\sigma_{\varepsilon}^{2}}{N}=\frac{\frac{q^{2}}{12}+\sigma_{\mathrm{d}}^{2}}{N}+\left(1-\frac{1}{N}\right)\sum_{k=1}^{\infty}\frac{q^{2}}{2\pi^{2}k^{2}}CF_{\mathrm{d}}^{2}\left(k\frac{2\pi}{q}\right) \tag{7}$$

Evidently, for $N = 1$ the error expression simplifies to equation (5) and for $N\to\infty$ to (4). For some dither types and sufficiently large variance σ_d^2 considering only the first term of the sum in (7) could still lead to precise estimation of error [4].

Subtractive Dithering
Results of previous ND analysis could be easily adopted for system with SD and to its error ξ_{SD}. Mean error (4) remains the same (for symmetrical dither PDF with zero mean). The RMS error does not contain dither itself, as it was subtracted after quantization. Finally we can write

$$RMS^2_{\xi SD}(N) = \frac{q^2}{12N} + \left(1 - \frac{1}{N}\right)\sum_{k=1}^{\infty} \frac{q^2}{2\pi^2 k^2} CF_d^2\left(k\frac{2\pi}{q}\right) \tag{8}$$

For properly chosen dither distribution and variance the sum in (8) is zero, when the theoretical improvement of quantizer resolution is simply $\log_2(\sqrt{N})$ bits.

3. Deterministic Dithering with Non-Coherent Sampling

Deterministic signal could be used similarly as stochastic one for improvement of quantizer resolution. However the determinism of dither requires special access to certain features and regularities. For slowly changing measured value the achieved precision then could be estimated by formulas obtained for stochastic ND as DD is commonly implemented as nonsubtractive. The correlation between sampling and dither combined with averaging allows suppression of dither from samples in the extent that it reproduces subtractive stochastic dithering [5].

For correlated sampling of dither the best case is to achieve coherent sampling, when the samples correspond to integer multiples of dither periods. For non-coherent sampling the mean value estimated from samples, like any spectral component, is loaded by residual error. For its investigation Fourier analyses can be employed. Generally n-th spectral component of error is

$$FR_{DDE,n} = \frac{1}{T_w}\sum_{k=-\infty}^{\infty} FS_{d,k} FT_w\left(n\omega_w - k\omega_d\right) \tag{9}$$

where $FS_{d,k}$ is the k-th coefficient of Fourier series of deterministic dither and FT is Fourier transform of considered rectangular window.

4. Results and Discussion

Results of theoretical analyses were confronted with simulations and all discussed types of dither were compared together. In Fig.1 errors ξ for ND, ξ_{SD} for SD and $FR_{DDE,0}$ for DD are depicted in dependence on standard deviation σ_d of dither. Uniform and sinusoidal distributions of stochastic dithers are considered. For every simulated level of σ_d the RMS of error was evaluated from 20 repeated measurements of s uniformly distributed within one quantization step. For stochastic dithering theoretical error values are close to simulation results (except the area of very small σ_d) therefor only theoretical curves are plotted. However for sinusoidal distribution simplification of sums in (7) and (8) to only one member would cause significant deviation of theoretical estimations especially near the minimums and therefore 10 members where used. From presented graphs one can observe better performance of uniform dither against sinusoidal for both ND and SD and evidently better accuracy of SD for optimal or large σ_d. However DD still offers higher accuracy for coherent sampling (sampled exactly 3 periods here) of triangular waveform. Note that the shape of the error curve for DD is similar to theoretical curve of SD with uniform distribution but the error is lower for DD.

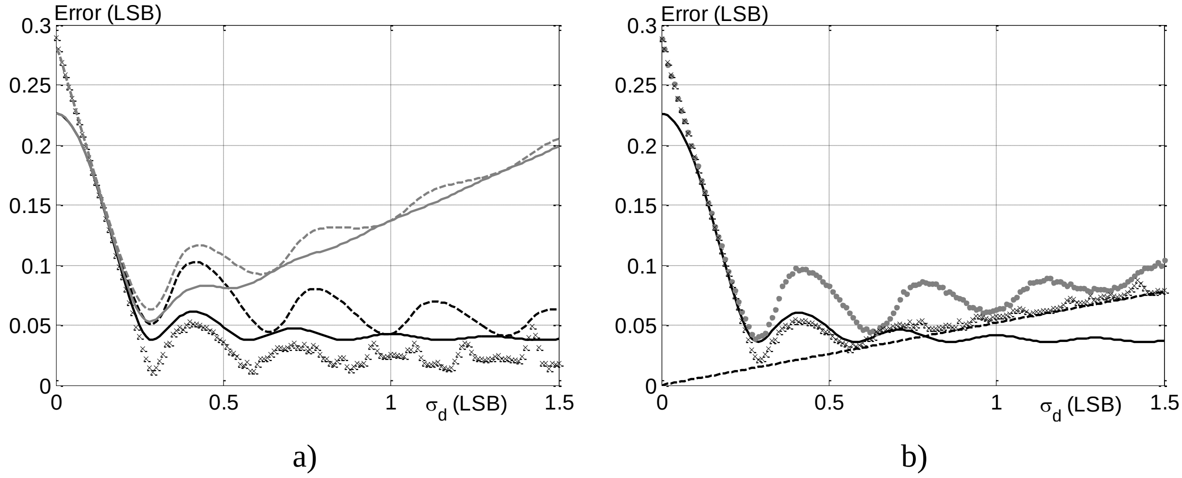

Fig. 1. Error dependence on dither standard deviation: a) ND (black) and SD (grey) with uniform (solid) and sinusoidal (dashed) distribution of dither compared with DD ("x") witch triangular waveform; b) DD with triangular (black "x") and cosine (grey "•") waveform confronted with theory of SD (for uniform dither - solid curve) and with theory of non-coherent sampling (for triangular waveform - dashed line).

The results of the DD behavior analysis by non-coherent sampling is shown in Fig.1b. We can see that despite higher number of samples the accuracy is worse than in the previous case. While there are still fluctuations correlated with the shape of theoretical curve of SD with rising σ_d the error dependency tends to theoretical error of non-coherent sampling (9). The results were plotted also for cosine waveform. Again the shape is similar to curve of SD with sinusoidal distribution (see Fig.1a) while the trend is rising because of non-coherent sampling.

Finally we can claim that for measurement of slow varying signals deterministic dithering leads to better accuracy compared to even subtractive stochastic dithering if conditions close to coherent sampling of dither are achieved. For the estimation of the shape of the RMS error curves the presented theory of stochastic dithering offers precise tool for both subtractive and non-subtractive form of stochastic dithering and approximate tool for deterministic dithering.

Acknowledgements

The work presented in this paper has been supported by the project KEGA-016STU-4/2014 and by Slovak Ministry of Education under grant No. 2003SP200280802.

References

[1] Bengtsson LE. Interpolation of Microcontroler ADC by Self-Induced Dithering. *International Journal on Smart Sensing and Inteligent Systems*, 6 (4): 1366-1382, 2013.

[2] Widrow B, Kollár I. Quantization Noise: Roundoff Error in Digital Computation, Signal Processing, Control, and Communications. Cambridge University Press, UK, 2008.

[3] Skartlien R, Oyehaug L. Quantization error and Resolution in Ensemble Averaged Data With Noise. *IEEE Trans. on Instrumentation and Measurement*, 54 (3): 1303-1312, 2005.

[4] Kamenský M, Kováč K. Analysis of Dithered Masurement Based on Widrow´s Quantization Theory. In Annals of DAAAM for 2010 & Proceedings : 21st International DAAAM Symposium Intelligent Manufacturing & Automation, 2010, 0855-0856

[5] Carbone P, Petri D. Performance of Stochastic and Deterministic Dithered Quantizers. *IEEE Transactions on Instrumentation and Measurement*, 49 (2): 337-340, 2000.

Comparison of Methods for Variable Selection in High-Dimensional Linear Mixed Models

J. Jakubík

Institute of Measurement Science, Slovak Academy of Sciences, Bratislava, Slovakia,
Email: jozef.jakubik.jefo@gmail.com

Abstract. *Currently is the analysis of high-dimensional data a popular field of research, thanks to many applications e.g. in genetics. At the same time, the type of problems that tend to arise in genetics, can often be modeled using LMMs in conjunction with high-dimensional data. In this paper we introduce two new methods and briefly compare them to existing methods, which can be used for variable selection in high-dimensional linear mixed models. As we will show in a small simulation study, both methods perform well compared to existing methods.*

Keywords: Linear mixed model, Variable selection, High-dimensional data

1. Introduction

Linear mixed model (LMM) allow us to specify the covariance structure of the model, which enables us to capture relationships in data, for example population structure, family relatedness etc. Therefore, LMMs are often preferred to linear regression models. Consider a LMM of the form

$$Y = X\beta + Zu + \varepsilon,$$

where

- Y is $n \times 1$ vector of observations,
- X is $n \times p$ matrix of regressors,
- β is $p \times 1$ vector of unknown fixed effects,
- Z is $n \times q$ matrix of predictors,
- u is $q \times 1$ vector of random effects with the distribution $\mathcal{N}(0, \sigma_D^2 I)$,
- ε is $n \times 1$ error vector with the distribution $\mathcal{N}(0, \sigma^2 I)$ and independent from u.

In genome-wide association studies in genetics, one studies the dependence of phenotype on the genotype. Genetic information can consist of 10^6 variables, but only information about the genotype of a small group of subjects is available. Variable selection in high-dimensional data refers to the selection of a small group of variables (denote it S^0, and $s^0 = |S^0|$ the number of relevant variables) which influence observations. In our case LMM we assume, that matrix X is high-dimensional and we select only variables from matrix X.

More information about the model can be found in Section 3.

2. Methods

In this paper we compare four methods for variable selection in high-dimensional LMMs.
All of the mentioned methods are primarily β estimation methods, not selection methods. However they can be thought of as selection methods if we define selected variables to be those for which $\beta_i \neq 0$ for $i = 1, \dots, p$.

LASSO

Least absolute shrinkage and selection operator [1, 2] is an established method for selecting variables in linear regression models. LASSO corresponds to the ℓ_1-penalized ordinary least squares estimate:

$$\hat{\beta} = \arg\min_{\beta} \left[\|Y - X\beta\|_2^2 + \lambda \|\beta\|_1 \right],$$

where λ is a fixed parameter.
In this study we use the LASSO as the reference, as it ignores LMM data structure.

LMM-LASSO

In [3], authors propose a data transformation, which eliminates correlation between observations. We first estimate σ_D^2, σ^2 by Maximum Likelihood under the null model, ignoring the effect of variables in matrix X. Let $K = 1/q \cdot ZZ^\top$. Having fixed $\hat{\gamma} = \hat{\sigma_D^2}/\hat{\sigma^2}$, we use the spectral decomposition of $K = U\Lambda U^\top$ to rotate our data, so that the covariance matrix becomes isotropic:

$$\tilde{X} = (\hat{\gamma}\Lambda + I)^{-\frac{1}{2}} U^\top X$$
$$\tilde{Y} = (\hat{\gamma}\Lambda + I)^{-\frac{1}{2}} U^\top Y.$$

After transforming the data we use the LASSO method

$$\hat{\beta} = \arg\min_{\beta} \left[\frac{1}{\hat{\sigma^2}} \|\tilde{Y} - \tilde{X}\beta\|_2^2 + \lambda \|\beta\|_1 \right].$$

New Approach One

The first approach consists in a transformation that removes group effects from data. The principle of this transformation is widely used in data analysis, for example in restricted/residual maximum likelihood (REML). In our case we transform the data as follows

$$\tilde{X} = (I - ZZ^+)X,$$
$$\tilde{Y} = (I - ZZ^+)Y,$$

where Z^+ is the pseudoinverse matrix. The transformation eliminates random segments of the problem (associated with matrix Z) and which allows us to use LASSO method for linear regression model.

New Approach Two

Recently, a publication [4, 5] in the field of variable selection for high-dimensional LMM data, presents methods based on non-convex optimization problem with one penalty parameter. For problems of dimension higher than 10^4 are methods based on non-convex optimization problem almost unusable, because their computational complexity is beyond the capabilities of current computers. One of the possible solutions to this problem is the simplification of the optimized function to convex function. Therefore, we have proposed a method based on the solution to the following convex problem

$$(\hat{\beta}, \hat{u}) = \arg\min_{\beta, u} \left[\|Y - X\beta - Zu\|_2^2 - \lambda \|\beta\|_1 - \Lambda \|u\|_2^2 \right],$$

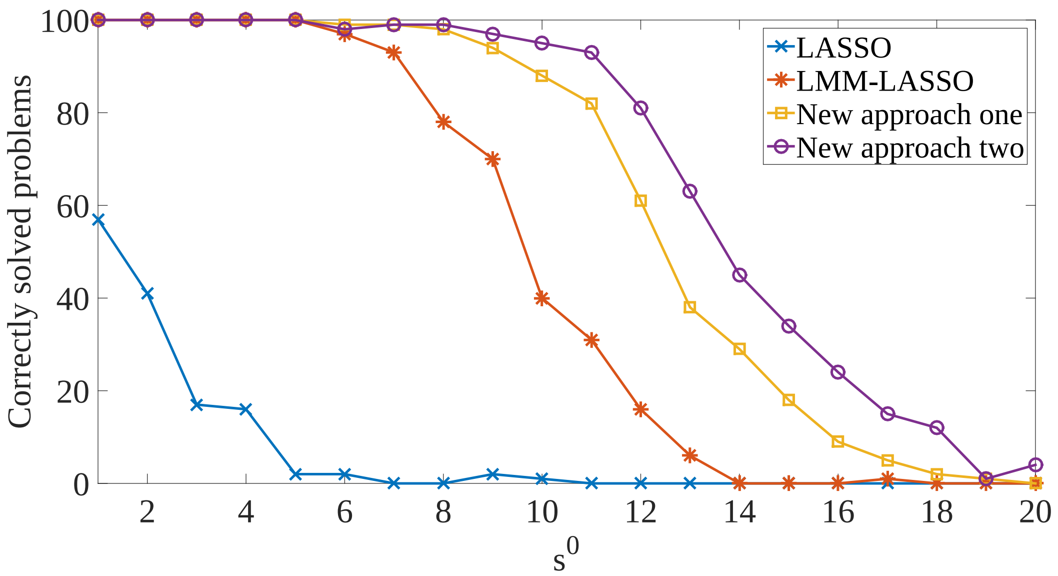

Fig. 1: Comparison of the number of correctly solved problems for different s^0 with four different methods.

where λ and Λ are fixed parameters.
Basically we are exchanging computational complexity for the need to inspect a two-dimensional parameter space.

3. Simulation Study

Data in our simulation study are divided into twenty groups of ten observations. Together we have $n = 200$ observations. For each observation we observe $p = 5000$ variables, but only $s^0 = \{1,\ldots,20\}$ variables influence observations. Relevant variables are randomly selected from all variables and effect of relevant variables is one. The effect of other variables is zero. Matrix Z captures group structure of the data. $Z_{i,j} = 1$ if the i-th observation belongs to the j-th group, 0 otherwise. Random effects u are randomly selected from $\mathscr{N}(0,I)$. Errors are from $\mathscr{N}(0,0.2\cdot I)$.
For all mentioned methods we get different sets of selected variables for different parameters λ or Λ. We generate a hundred problems as described in previous paragraph. As a correctly solved problem we consider only a problem for which the method gives for at least one parameter or parameter combination as the selected variable set exactly set S^0. Figure 1 shows the number of correctly solved problems for all four methods for different numbers of relevant variables (from 1 to 20). The methods from [4, 5] were not compared because they were not able to solve problems of dimension $p = 5000$.

4. Conclusion

In Figure 1 we can see that the LASSO method is not suitable if the problem has the structure of a LMM.
For small numbers of relevant variables the remaining methods are almost infallible. With the increasing number of relevant variables, the accuracy of methods decreases to almost zero. This is understandable, because with more relevant variables the correlation of each relevant variable with vector of observations decreases. Therefore, it is more difficult to identify correctly the exact set of variables.

This simple study hints at the potential of the newly proposed methods to significantly outperform both the LASSO and the LMM-Lasso.
However, this is only a preliminary study and one of the first addressing the question. A more extensive analysis can be expected in the future.

Acknowledgements

The work was supported by the Scientific Grant Agency VEGA of the Ministry of Education of the Slovak Republic and the Slovak Academy of Sciences, by the projects VEGA 2/0047/15 and VEGA 2/0043/13.

References

[1] Tibshirani R. Regression shrinkage and selection via the lasso. *Journal of the Royal Statistical Society. Series B (Methodological)*, 267–288, 1996.

[2] Bühlmann, P, Van De Geer S. *Statistics for High-Dimensional Data: Methods, Theory and Applications*. Springer Science & Business Media. 2011.

[3] Lippert C. Linear mixed models for genome-wide association studies. `https://publikationen.uni-tuebingen.de/xmlui/handle/10900/50003`, 2013.

[4] Schelldorfer J, Bühlmann P, van De Geer S. Estimation for high-dimensional linear mixed-effects models using ℓ_1-penalization. *Scandinavian Journal of Statistics* 38(2): 197–214, 2011.

[5] Rohart F, San Cristobal M, Laurent B. Selection of fixed effects in high dimensional linear mixed models using a multicycle ECM algorithm. *Computational Statistics & Data Analysis* 80, 209–222, 2014.

Prediction of Intracranial Pressure Values of Traumatic Brain Injured Patients Using Hierarchical Temporal Memory Network

[1]K. Valentín, [2]I. Bajla, [2]M. Teplan

[1]AIT-Austrian Institute of Technology GmbH, Seibersdorf, Austria,
[2]Institute of Measurement Science, Department of Theoretical Methods,
Slovak Academy of Sciences, Bratislava, Slovakia
Email: kristian.valentin.fl@ait.ac.at

Abstract. *The goal of this pilot study is to analyze intracranial pressure (ICP) data from a group of 42 patients and to build a Hierarchical temporal memory (HTM) model that will try to predict future ICP values. As a references, Support Vector Regression (SVR) with RBF kernel was used. To better compare the practical performance of the models, a binary alarm with threshold set to a value when a medical intervention is needed was used. The results show better recall and MSE for HTM while better false omission rate for SVR.*

Keywords: Intracranial pressure, Time series prediction, HTM – Cortical learning algorithms, Support vector regression

1. Introduction

Patients with severe traumatic brain injury (TBI) have a significant risk of hypotension, hypoxaemia, and brain swelling. Neurological damage invoked by these dangerous conditions may not occur immediately at the moment of primary injury at an accident scene, but evolves over time as a secondary injury. The secondary brain injury is the leading cause of in-hospital deaths after brain trauma and it is directly associated with the increase of intracranial pressure (ICP) and subsequent decrease in cerebral perfusion that brings about brain tissue ischaemia. As described in [1], organized emergency services can improve outcome for patients with severe TBI, provided the patients are immediately transported to an Intensive Care Unit (ICU) which has possibilities to monitor the ICP values permanently.

ICP is measured in millimeters of mercury (mm Hg) and, at rest, normally varies between 7–15 mm Hg for adults [2]. 30–40 mm Hg is the upper limit of ICP normality, and the values above this limit serve as an alarm for the initiation of special treatment [1]. Although, several neurological indicators are useful for the decision to trigger additional life-saving interventions in TBI cases, periodical (or continuous) measuring the ICP values represents the crucial indicator. Several papers were published ([3, 4]) in which attempts to analyze/evaluate inner structure of the ICP waveforms as functions of time have been described.

In our paper we treat the discretized (with the one-hour time step) ICP records as time series and investigate whether predicted ICP values can provide additional information important for making medical decisions on special TBI treatment initiation. Assuming similar causes of changes in ICP for various patients we propose to use a predictive model capable of learning from multiple independent time series. In order to allow for using the model for online analysis of the live ICP measurements at ICU we furthermore propose to use a model that provides online learning and inference. Currently, to our knowledge such criteria meet only Hierarchical Temporal Memory (HTM) with its up-to-date learning algorithms called *Cortical Learning Algorithms* (CLA) [5]. As a reference we used Support Vector Regression (SVR) model in a simulated online mode.

2. Subjects and Methods

Dataset

For our pilot study a set of clinical records of ICP for 42 TBI patients in the period of maximally 10 days were available. Within these data 30 records belonged to those patients who had survived and had been discharged from ICU in a stabilized state. 12 patients have deceased. Due to the various clinical limitations, the ICP recording was performed as non-overlapping one-hour intervals characterized by maximum values within those intervals. These maxima represented a discretized version of an ICP record (sequence). The starting time of the ICP records varied for individual patients, and for the survived patients the maximal duration of the ICP measurement was set to 10 days (240 time instants). The clinical protocol also lead to occasional discontinuity in the ICP recording caused by necessity to disconnect a patient for the time of examination at another clinical department. The remedy for all of such missing values has been made by linear interpolation of data. For each patient, there is a label of his/her state (lethal or vital) assessed at the time he/she left the ICU, however, this information was not used during learning.

Hierarchical Temporal Memory

Hierarchical temporal memory (HTM) is a large-scale computational model of the algorithmic and structural properties of the neocortex developed by Hawkins, George, and their colleagues at Numenta Inc. [6]. The reference implementation is distributed in the NuPIC[1] package.

Recently, the initial HTM learning algorithms (Zeta1), have been replaced by a new generation, called Cortical Learning Algorithms (CLAs) [5]. The main change is that CLAs work with data encoded in binary representations where only small percentage of the bits are "on" at one time and each bit only partly captures the original data. This is called a *sparse distributed representations* (SDRs). SDRs enables HTM to become an online learning system that models complex time-varying data and makes continuous predictions about future inputs. The proper function of HTM required that input data are first encoded into SDRs in such a way that similar inputs map into similar representations, i.e., a small change in the SDR should not greatly change the semantics of the data after decoding. In terms of structure, HTM is a hierarchical memory model comprised of neurons, called *cells*, organized into a grid of columns which form an HTM region. Multiple regions may be connected to form a more complex hierarchy. Each column in a region is connected to a unique subset of the input bits. Due to local inhibition among columns, the activations of the columns in a region form a SDR as well. A very important feature is that activation of a column is context-dependent, thus HTM can learn to represent the same pattern in different temporal contexts. In a column, one or multi-step prediction is implemented by creating lateral connections between an active cell with a subset of previously active nearby cells. The formation speed of these connections can by adjusted by a learning rate parameter.

3. Prediction of ICP

The basic idea of how to utilize these data for making reliable clinical decisions in every moment of the development of patients' health conditions is to explore a possibility of ICP values prediction, which can be used, together with apriori setting of a critical ICP threshold, for alarm triggering. We argue that a prediction of future ICP values could help to indicate future states of a patient, and thereby to make the earlier decision on initiation of the special treatment protocol. Thus we propose a binary alarm indicator implemented as a threshold set to 35 mm Hg. The alarm indicator from the predicted ICP sequences should match the alarm indicator from

[1] Numenta Platform for Intelligent Computing

original ICP sequences. There are 18 original ICP records (no. 2, 6, 7, 9, 11, 14, 15, 19, 20, 26, 27, 28, 33, 34, 35, 37, 38, and 39) for which all the ICP values are below the given threshold.

We have accomplished the "leave-one-out" cross-validation scheme, namely, for 42 sequences, one sequence was always selected as a test sample, while all 41 remaining sequences entered the learning procedure of the HTM network. These contain patterns common for both classes which can be helpful for the ICP values prediction. For the current ICP dataset we used one-step prediction. For a dataset or live measurements with shorter time scale (e.g., in order of minutes), a multi-step prediction might be necessary to better account of future trend. After the training phase, ICP data of the testing patient were put into the HTM network one by one, while a one-step prediction value was read out. With this procedure, HTM can calculate informative prediction immediately after seeing the first ICP value measured, and simultaneously it continues learning from incoming actual data.

As a prediction method for reference we selected the well-known SVR model with RBF kernel applied to the same one-step prediction task. SVR was trained to predict next value from k previous values, i.e., ICP at time $t+1$ was predicted based on values at times $t-k+1,...,t$. For each test sequence, a training dataset from all other sequences was generated at first. Then, as the prediction for the test sequence progressed starting from the $(k+1)$-th value, this dataset was augmented with new training data from the test sequence and SVR was retrained, i.e., simulating online learning.

4. Results

We used a public NuPIC implementation of HTM in the version 0.2.1. The HTM network consisted of one region with 2048 columns and 32 cells per column. The learning rate parameter was set to 0.036. These and other learning and inference hyperparameters (described in [5]) were optimized using a cross-validation procedure with Mean Absolute Percent Error metric, which is a part of NuPIC. SVR used RBF kernel with parameter C set to 1000 and parameter γ set to 0.003. The window size k was set to 8. These parameters were found using a leave-one-out cross-validation scheme.

For the evaluation of the model predictions for each patient we used the mean square error (MSE) metric. Predicted binary alarms were evaluated using the recall and false omission rate (FOR) characteristics. Recall is defined as the proportion of number of true positives to the number of all ground-truth positives (all original alarms). FOR is defined as the proportion of the number of false negatives w.r.t. number of all predicted negatives. The rationale is that false negatives should be treated with more care due to higher associated health risk compared to false positives. Results for each patient and prediction method are shown in Fig. 1. In overall, averaged over all patients, the SVR model yields lower FOR (0.038 vs 0.031), however, the HTM model yields lower MSE (53.474 vs 62.522) and higher recall (0.265 vs 0.211).

5. Conclusions

The goal of this pilot study was to explore the usefulness of prediction of ICP for making earlier decisions on triggering a special treatment protocol. We considered the set of acquired ICP sequences as retrospective time series for which a task of prediction can be of value. We proposed to apply an HTM intelligent network, that can learn from all ICP sequences and generate one-step prediction. The prediction results achieved have been compared to the prediction results generated by a reference method of Support Vector Regression model with RBF kernel on the basis of recall, FOR, and MSE statistics. We can conclude that the HTM network manifested encouraging results that deserve to be extended further in the ongoing research. Future research

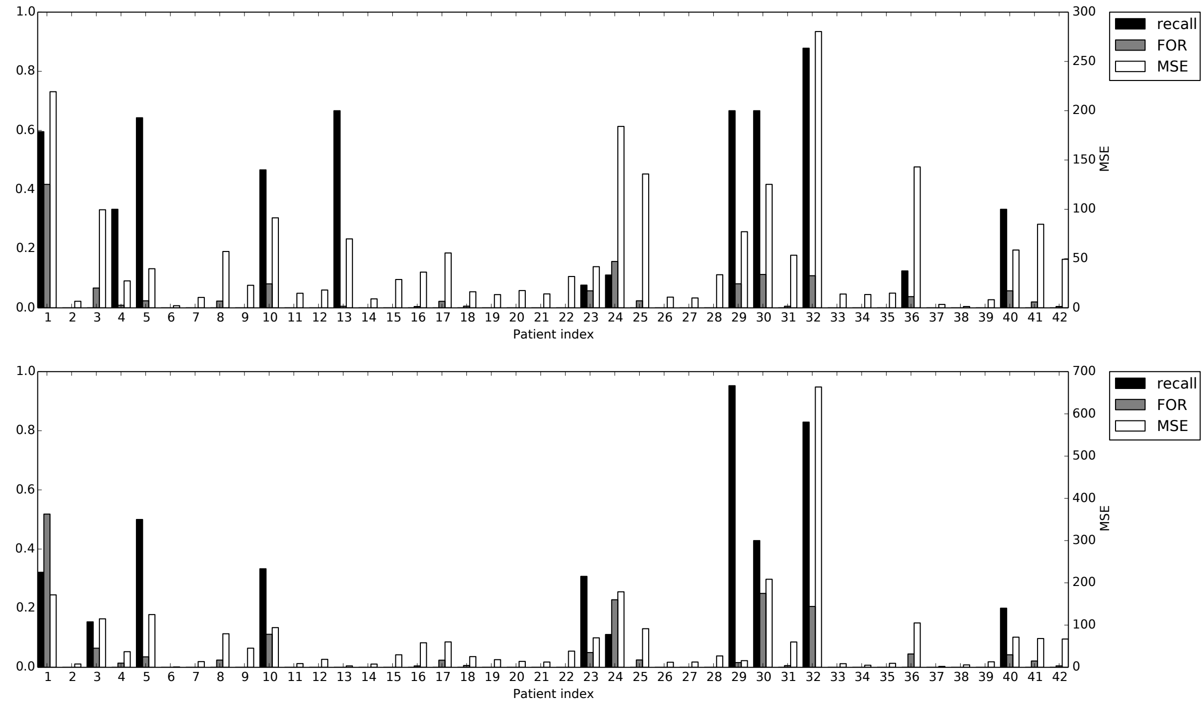

Fig. 1: Recall, false omission rate (FOR), and mean square error (MSE) for all patients for HTM (top) and SVR (bottom) predictors. Note that MSE has different scale, located on the right.

could also include combining these or similar models that have complementary performance.

Due to a lack of detailed information on medical conditions of patients with TBI at the time ICP starts, the analysis we proposed could not be complete. For more comprehensive exploration of retrospective data mining form ICP records complementary medical information will be needed.

ACKNOWLEDGEMENTS

This work has been supported by the Slovak Grant Agency for Science (project No. 2/0043/13) and by the MZ 2013/56-SAV-6 and APVV-0668-12 grants.

References

[1] Ghajar J. Traumatic brain injury. *The Lancet* 356(9233): 923–929, 2000.

[2] Steiner L, Andrews P. Monitoring the injured brain: Icp and cbf. *British Journal of Anaesthesia* 97(1): 26–38, 2006.

[3] Contant C, Robertson C, Crouch J, Gopinath S, Narayan R, Grossman R. Intracranial pressure waveform indices in transient and refractory intracranial hypertension. *Journal of Neuroscience Methods* 57(1): 15–25, 1995.

[4] Aries M, Czosnyka M, Budohoski K, Kolias A, Radolovich D, Lavinio A, Pickard J, Smielewski P. Continuous monitoring of cerebrovascular reactivity using pulse waveform of intracranial pressure. *Neurocritical Care Journal* 17(1): 67–76, 2012.

[5] Numenta (2011). Hierarchical Temporal Memory including HTM Cortical Learning Algorithms. Document version 0.2.1.

[6] George D, Hawkins J. Towards a mathematical theory of cortical micro-circuits. *PLoS Computational Biology* 5(10). DOI 10.1371/journal.pcbi.1000532, 2009.

Detailed Uncertainty Analysis of the Tricept Kinematic Structure

[1]M. Omachelová, E. Kureková, [2]M. Halaj, [3]I. Martišovitš

[1] Faculty of Mechanical Engineering, Slovak University of Technology,
812 31 Bratislava, Slovak Republic
[2] Bratislava, Slovak Republic
[3] Microstep spol. s.r.o, Čavojského 1, 841 04 Bratislava, Slovak Republic
Email: milada.omachelova@stuba.sk

Abstract. *The article investigates the theoretical aspects of the positioning accuracy of parallel kinematic structures (PKS), especially the accuracy of the Tricept type PKS. Unlike serially configured structures utilizing translating and rotating movement, parallel kinematic structures consist of telescopic drives that are joined by a solid platform. The functional relationship between the actuators and the resulting position coordinates is rather complex, because of the configuration of the kinematic system. The article provides a framework to analyze the influence of geometrical imperfections in the system using the law of uncertainties propagation, in order to determine the accuracy of the end effector. The approach may aid the design process of parallel kinematic structures by providing information on the theoretically achievable effector positioning accuracy.*

Keywords: Parallel kinematic structures, Tricept, positioning accuracy, Coordinates uncertainty

1. Introduction

Parallel kinematic structures (PKS) represent a non-conventional way for arrangement of movement elements, comparing to the widely used serial kinematic structures. They employ parallel arranged movement elements (telescopic rods, arms) that have one end located at a base frame and the second end is connected to a movable platform. Tricept belongs among the most known PKS [1]. It is a fixed platform connected with a movable platform via three driving telescopic rods and a not-driven central rod (see Fig. 1). Central rod is connected to a movable platform by a solid linkage; while it can move axially against the fixed platform (rotation of the central rod is prevented). Effector is usually connected to a movable platform, carrying the tools or technological heads.

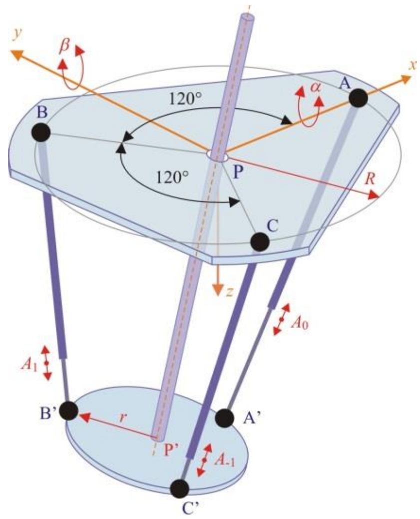

Fig. 1. Schematic representation of telescopic rods, joints and platforms

Servomotor located at the end of each telescopic rod enables extension of the rod by a ball screw and nuts. The skeleton together with a primary platform create a single kinematic element [1 to 3].

2. Influences that Affect Reaching of the Desired Position

Positioning accuracy of any manufacturing device represents the closeness between the actual reached position of the end effector and a programmed position, specified by the control system. For PKS, effector's endpoint is the point at the end of the central rod, respectively it is precisely defined point on the tool or technology head. In our case, the point P' is considered.

Based on theoretical analysis, one can summarize three types of errors affecting reaching of the desired position by PKS effector. The *geometrical errors* arise due to inaccuracies in manufacturing, inaccurate relative position of individual elements or due to wear of joints. The *stiffness errors* originate from elasticity of joints among individual elements as well as from flexures caused by own weights of individual elements or by an external load. Their magnitudes depend on the actual position of the effector. The *thermal errors* arise from thermal stress and dilatation of elements due to heat generated by internal or external sources, e.g. motors, bearings, etc. [2, 3].

3. Methodology for Determination of the Desired Position

If the device designer knows the theoretically achievable positioning accuracy, he has an important opportunity to influence critical pieces of equipment in the process of construction work. Uncertainties balance will help to identify the most significant influences on theoretically achievable positioning accuracy of the effector, which opens up the possibility of corrective interventions into the structure. Only geometrical influences on the overall uncertainty are considered in the paper.

Cartesian positions Q **=[**Q_x, Q_y, Q_z**]** of point Q_q (relative to "static" coordinate system bound with static platform (relative to point P), when (in general) angles α, β and shift z are nonzero) we obtain by applying transformations.

Matrix notation of transformation is q+ze3$Q = \boldsymbol{O}_y(\beta) \cdot \boldsymbol{O}_x(\alpha) \cdot (\boldsymbol{q} + z\boldsymbol{e}_3)$ that can be itemized as

$$\begin{pmatrix} Q_x \\ Q_y \\ Q_z \end{pmatrix} = \begin{pmatrix} \cos\beta & 0 & \sin\beta \\ 0 & 1 & 0 \\ -\sin\beta & 0 & \cos\beta \end{pmatrix} . \begin{pmatrix} 1 & 0 & 0 \\ 0 & \cos\alpha & \sin\alpha \\ 0 & -\sin\alpha & \cos\alpha \end{pmatrix} . \begin{pmatrix} q_x \\ q_y \\ q_z + z \end{pmatrix} \tag{1}$$

We can find their appropriate linear combinations to get the simplest relations equivalent to the relations of telescopic rods lengths. Three equations can be obtained in this way

$$\frac{-A_0^2 - A_1^2 - A_{-1}^2}{3} + r^2 + R^2 + z^2 - r.R.\cos\alpha - r.R.\cos\beta = 0 \tag{2}$$

$$-\frac{A_{-1}^2 - A_1^2}{\sqrt{3}} + 2R.z.\sin\alpha + r.R.\sin\alpha.\sin\beta = 0 \tag{3}$$

$$\frac{2A_0^2 - A_1^2 - A_{-1}^2}{3} + 2R.z.\cos\alpha.\sin\beta + r.R.\cos\beta - r.R.\cos\alpha = 0 \tag{4}$$

Let us denote the left sides of equations (2) to (4) as functions L_1, L_2, L_3 that depend on parameters A_0, A_1, A_{-1}, α, β, z, r, R. We will consider the movement of the point Q in time t that will be limitedly close to 0 and parameters A_0, A_1, A_{-1}, α, β, z, r, R will depend on time t as well. If partial derivation of left sides of equations (2) to (4) following equation is obtained

$$\boldsymbol{W}_{3\times3} \quad \boldsymbol{M}_{3\times5}\boldsymbol{W}_{5\times1} + \boldsymbol{W}_{3\times5}\boldsymbol{W}_{5\times1} = \boldsymbol{0} \tag{5}$$

where

$$\boldsymbol{W}_{3\times3} = \begin{pmatrix} \frac{\partial L_1}{\partial\alpha} & \frac{\partial L_1}{\partial\beta} & \frac{\partial L_1}{\partial z} \\ \frac{\partial L_2}{\partial\alpha} & \frac{\partial L_2}{\partial\beta} & \frac{\partial L_2}{\partial z} \\ \frac{\partial L_3}{\partial\alpha} & \frac{\partial L_3}{\partial\beta} & \frac{\partial L_3}{\partial z} \end{pmatrix}; \quad \boldsymbol{W}_{3\times5} = \begin{pmatrix} \frac{\partial L_1}{\partial A_0} & \frac{\partial L_1}{\partial A_1} & \frac{\partial L_1}{\partial A_{-1}} & \frac{\partial L_1}{\partial r} & \frac{\partial L_1}{\partial R} \\ \frac{\partial L_2}{\partial A_0} & \frac{\partial L_2}{\partial A_1} & \frac{\partial L_2}{\partial A_{-1}} & \frac{\partial L_2}{\partial r} & \frac{\partial L_2}{\partial R} \\ \frac{\partial L_3}{\partial A_0} & \frac{\partial L_3}{\partial A_1} & \frac{\partial L_3}{\partial A_{-1}} & \frac{\partial L_3}{\partial r} & \frac{\partial L_3}{\partial R} \end{pmatrix}; \quad \boldsymbol{W}_{5\times1} = \begin{pmatrix} \dot{A}_0(0) \\ \dot{A}_1(0) \\ \dot{A}_{-1}(0) \\ \dot{r}(0) \\ \dot{R}(0) \end{pmatrix}.$$

Matrix $\boldsymbol{M}_{3\times5}$ we express by the relation (5):

$$\boldsymbol{M}_{3\times5} = -\boldsymbol{W}_{3\times3}^{-1} \times \boldsymbol{W}_{3\times5} \tag{6}$$

When multiplying the equation (1) from left by matrix $\boldsymbol{O}_y^T(\beta)$ and adjustment we get

$$-O_y^T(\beta).Q + O_x(\alpha).(q + ze_3) = 0 \tag{7}$$

Left sides (7) is matrix $\boldsymbol{H}$. Let

$$\boldsymbol{F}_{3\times3} = \left(\frac{\partial H}{\partial Q_x}, \frac{\partial H}{\partial Q_y}, \frac{\partial H}{\partial Q_z} \right); \ \boldsymbol{G}_{3\times3} = \left(\frac{\partial H}{\partial \alpha}, \frac{\partial H}{\partial \beta}; \frac{\partial H}{\partial z} \right), \text{ then } \boldsymbol{M}_{3\times3} = \boldsymbol{F}_{3x3}^{-1}.(-\boldsymbol{G}_{3x3})$$

$$\boldsymbol{A}_{3\times5} = \boldsymbol{F}_{3x3}^{-1}.(-\boldsymbol{G}_{3x3}).\boldsymbol{W}_{3x3}^{-1}.(-\boldsymbol{W}_{3x5}) = \boldsymbol{M}_{3x3}.\boldsymbol{M}_{3x5} \tag{8}$$

Matrix $\boldsymbol{A}_{3\times5}$ from (8) is used for calculation of estimates of uncertainties of indirectly measured. Covariance matrix of those estimates is

$$\boldsymbol{U}_y = \boldsymbol{A}\boldsymbol{U}_x\boldsymbol{A}^{\mathrm{T}} \tag{9}$$

where matrix $\boldsymbol{U}_x$ is diagonal a known covariance matrix of the random vector $\boldsymbol{x} = (x_1, x_2, x_3, x_4, x_5) = (A_0, A_1, A_{-1}, r, R)$, where u_{x_i} is standard uncertainty of the estimate x_i of quantity X_i, $i = 1, 2, \dots 5$, $u_{x_{i,j}}$ is covariance among estimates x_i and x_j, $i = 1, 2, .., 5$, $j = 1, 2, .., 5$. Uncertainty of position of any point Q in the workspace can be calculated, if the matrix $\boldsymbol{U}_x$ is known.

Let $\boldsymbol{U}_x$ be a known constant symmetric matrix of 5×5 type, and $\boldsymbol{U}_y$ be an unknown symmetric matrix of 3×3 type that we want to determine and is given by (9). It is clear that the matrix $\boldsymbol{U}_y$ is correlated to the position of the point $Q[Q_x, Q_y, Q_z]$. We want to find the intervals for values of the matrix $\boldsymbol{U}_y$, when considering that Q_x, Q_y, Q_z may take any value, depending on how the reference point Q moves in some regular subspace (let it be a cube for purposes of this estimate, see Fig. 7) of the overall workspace.

If we fix the angles α and β, the virtual *beam* arises in cube, along which the reference point will move. It is sufficient to evaluate the expression for a particular beam only in the roots of this polynomial (if they overlap with workspace) and also in the endpoints of the beam, defined by the workspace borders. Among them we find the minimum and maximum, which will form the search interval for the selected element of matrix $\boldsymbol{U}_y$, for fixed angles α and β and a base matrix $\boldsymbol{U}_x$.

Impact of each element of the matrix $\boldsymbol{U}_x$ can be displayed using a three-dimensional function (see Fig. 2 until Fig. 6). Search estimate of the matrix $\boldsymbol{U}_y$ is obtained as a matrix of ordered pairs (minimum and maximum impacts of components of the matrix $\boldsymbol{U}_x$).

Using the software system MATHEMATICA, we created a program to search the entire work-space (or its subset thereof) and to estimate the matrix $\boldsymbol{U}_y$. To do so, the matrix $\boldsymbol{U}_x$ must be specified and the required division of the workspace must be selected.

For example, for matrix

$$\boldsymbol{U}_x = \left(\left(0{,}005/\sqrt{2}\right)^2, \left(0{,}005/\sqrt{2}\right)^2, \left(0{,}005/\sqrt{2}\right)^2, \left(0{,}01/\sqrt{2}\right)^2, \left(0{,}01/\sqrt{2}\right)^2 \right) \tag{10}$$

we found the estimate of $\boldsymbol{U}_y$

$$\begin{pmatrix} 0.0000185 & -7.0896\times10^{-6} & -7.3262\times10^{-6} \\ -7.0896\times10^{-6} & 0.0000185 & -7.3394\times10^{-6} \\ -7.3262\times10^{-6} & -7.3394\times10^{-6} & 0.0000038 \end{pmatrix} \le \boldsymbol{U}_y \le \begin{pmatrix} 0.0000368 & 7.0896\times10^{-6} & 7.2188\times10^{-6} \\ 7.0896\times10^{-6} & 0.0000370 & 7.3394\times10^{-6} \\ 7.2188\times10^{-6} & 7.3394\times10^{-6} & 0.0000138 \end{pmatrix} \tag{11}$$

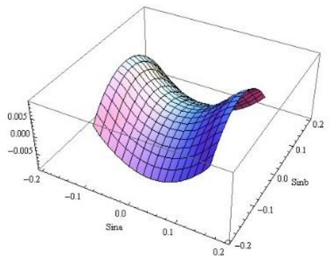

Fig. 2. Influence of element $\boldsymbol{U}_x$[1,4] on maximum value of the matrix $\boldsymbol{U}_y$[1,1]

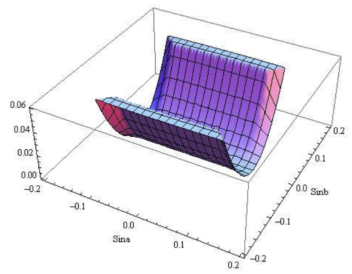

Fig. 3. Influence of element ***U****x*[5,5] on maximum value of the matrix ***U****y*[1,1]

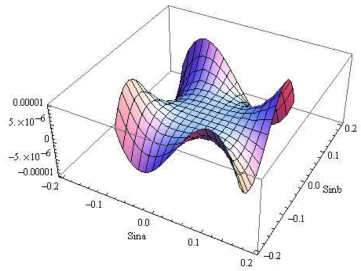

Fig. 4. Influence of element ***U****x*[4,4] on minimum value of the matrix ***U****y*[1,2]

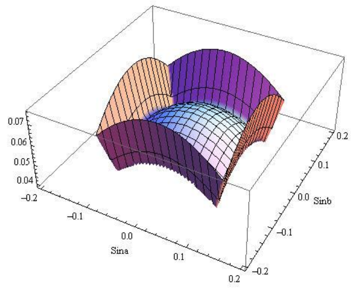

Fig. 5. Influence of element ***U****x*[5,5] on minimum value of the matrix ***U****y*[3,3]

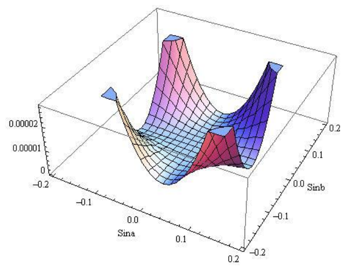

Fig. 6. Influence of element ***U****x*[4,4] on minimum value of the matrix ***U****y*[2,2]

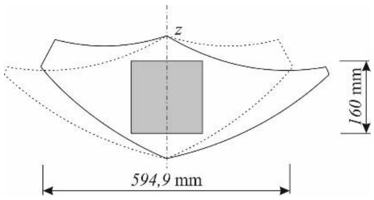

Fig. 7. Scheme of the cube that represents the biggest regular object in the workspace

4. Conclusions

This paper analyzed various issues related to the control of structures with parallel kinematics, especially that relating to the accuracy of positioning. The function describing the lengthening and shortening of the individual telescopic drives and the desired setpoint is non-linear. Because of this, the equations cannot be partially derived, making the uncertainty analysis unfeasible. In order to overcome this difficulty, the employment of an approach using infinite geometrical changes in the parameters is suggested. The limit variables for uncertainties were calculated here, suggesting that the achievable positioning accuracy is not constant for all setpoints within the workspace of the Tricept device.

Acknowledgment

This paper was created within the research grant supported by the Scientific grant agency of the Ministry for Education, grant number VEGA 1/0604/15.

References

[1] PKM Tricept, http://www.pkmtricept.com.

[2] Kureková E, Halaj M, Omachelová M, Martišovitš I. Theoretical positioning accuracy for serial and parallel kinemtatic structure. *Measurement Science Review*, 14 (5): 243-251, 2014.

[3] Onderová I, Kolláth L. Testing and verification of selected technological parameters of the PKS. In *Proceedins of the 15th International Carpathian Control Conference of the IEEE International Conference on Robotics and Automation*, 2014, 398-402.

Utilizing of Control Chart in the Management of the Measurement Process

[1]D. Jenčuráková, [2]R. Palenčár, [3]M. Kubiš

[1,2,3]Faculty of Mechanical Engineering, Institute of Automation, Measurement and Applied Informatics, Mýtna 36, 812 31 Bratislava 1, Slovak Republic,
Email: dana.jencurakova@stuba.sk

Abstract. *A broad range of methods for measurement control from the simplest comparative methods to the most sophisticated statistical based methods exist. A statistical based approaches play a big role in the measurement quality control. The goal of the statistical measurement control is to increase the probability to detect a measurement error and decrease a false rejections. Moreover, these methods can make an immediate decision whether a requirements on the measurement are fulfilled or not. Control charts of sample average and sample variation range are appropriate. These diagrams are one of the most effective combinations of control means of the measuring process. Using of diagrams the cumulative sums is sometimes more preferred.*

Keywords: Measurement, Measurement process, Control, Control charts

1. Introduction

Requirements on the metrological security of the main activities of organizations are increasing continuously. It is associated with high requirements on quality of services and products. Despite the fact that a large amount of the data comes from measurements, it is common that sufficient effort is not present in metrological security. The system of metrological security is an important part of an overall system of quality control. Hence, the control of measurement with the respect to achieving of the highest possible quality is needed.

2. Subject and Methods

The subject of the research was the process of measurement and its implementation. The current state in the management of measurements was analyzed. In particular, use the methods of statistical process control.

3. Statistical Methods in the Management of Measurement

A few of papers published at home and abroad, are dedicated to the use of statistical methods in the management of measurement. The most of them is devoted to the use of control charts in the management of measurement processes [1], [2], [3].

The present knowledge about control charts can be summarized in nine basic steps which are needed to be implemented regardless of the method of statistical process control [2], [3].

Cumulative sum (CUSUM) control chart is increasingly used in the management of measurement. CUSUM control charts are more sensitive to changes in the process (as opposed to Shewhart charts). These charts are used in the cases when the fast and cheap detection of the relatively short time period acting disturbances must be ensured [2], [3].

Shewhart control charts work with the data obtained from measurements of the gauge. Specific characteristics are calculated for each subgroup of the measured data. The most often these characteristics are sample average and sample variation range. These characteristics are recorded in the control charts [1].

Advantages of CUSUM charts against the traditional Shewhart control charts can be formulated as follows [2]:

- CUSUM charts are more sensitive to small and medium-sized (*0,5σ – 2,0σ*) changes in the process.

  The σ value represents standard deviation which expresses the variability of a measured parameter of a product or service.
- CUSUM charts are more economical for the risk of unnecessary signal $\alpha \leq 0,1$ and the effectiveness is higher as α is going to be smaller.

  The α symbol denotes a risk of false indication of limits violation and represents the probability of an unnecessary seeking of an definable influence based on the information from the control chart that the process is not statistically stable (e. g. a point is out of limits), even if no significant change of the process occurred.
- CUSUM charts indicates mentioned small and medium-sized changes in process 2-4 times faster with the same number of samples n.
- CUSUM charts are associated with a lower cost of control (with the smaller number of samples n) with the same risk α.
- CUSUM charts allows to determine more precisely the instant of change of the distribution of a controlled variable, to estimate the size of this change and the direction of action.

CUSUM control chart can be used in two ways. One of them is to determine the changes in historical values (measurement of planned or unexpected changes). The second way of use is intended to determine the period since the last change occurred [2], [3].

4. A Case Study

The task was using a control chart to manage the measurement process to meet the requirements of the specification. These specifications were based on measurements of the length of the component with a nominal value of 15 mm and the manufacturing tolerance ±60 μm. The measurement method was to measure the length of the component with a micrometer of the range 0 - 25 mm with a permissible error of ±1,0 μm. For monitoring of the measurement process measurements on the gauge block with the nominal size 20 mm and permissible error 0,6 μm under normal workshop conditions were utilized. Overall was chosen $N = 25$ subgroups, each of them with range of five: $m = 5$. The five trained employees conducted measurements five times a day in exactly scheduled time periods. The real situations in the measurement were characterized and the homogeneity of measurement was secured so that variability did not significantly affect the differences between subgroups within measurements.

The basic control chart involves [1], [2]: **Center Line (*CL*)** – represents expected value of the controlled variable, when the process is stable; **Upper Control Limit (*UCL*)** and **Lower Control Limit (*LCL)*** – bounds inherent variability of the process and are computed based on data gained in the time when the process was stable; points of observation, two neighboring points are connected with a line. **The mean value in the subgroup:** x_j and **variance range in the subgroup:** R_j were computed from measured data. Computed sample characteristics were drawn into the appropriate charts. Then **the mean value of the average values of subgroups** were computed: ***CL* for** x_j and **the mean value of the variance ranges of soubgroups: *CL* for** R_j were computed. These values represent **Central Lines** in charts. **Control limits *UCL*** and ***LCL*** were computed based on formulas presented in STN ISO 8258 [1], [2].

For type 1 error α = *5 %* Shewhart control charts $\overline{X}$ (Fig. 1) and *R* (Fig. 2) were constructed.

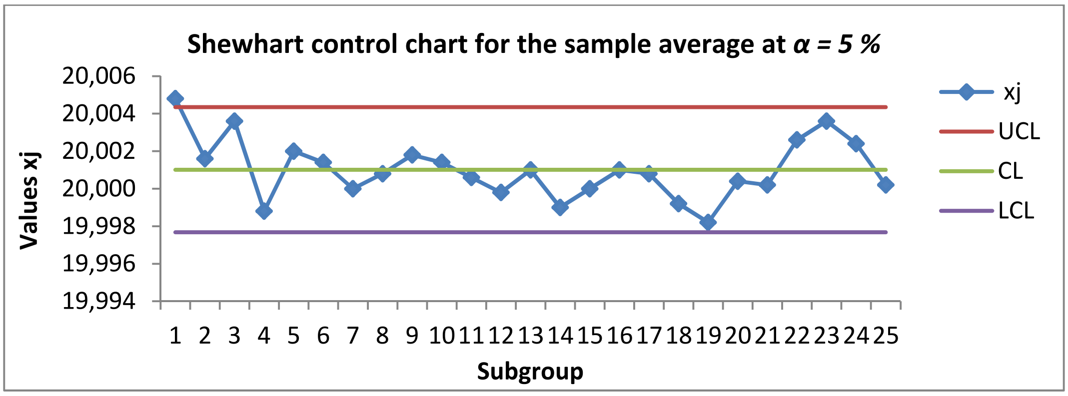

Fig. 1 Shewhart control chart for the sample average at α = *5 %* - the 1st analysis

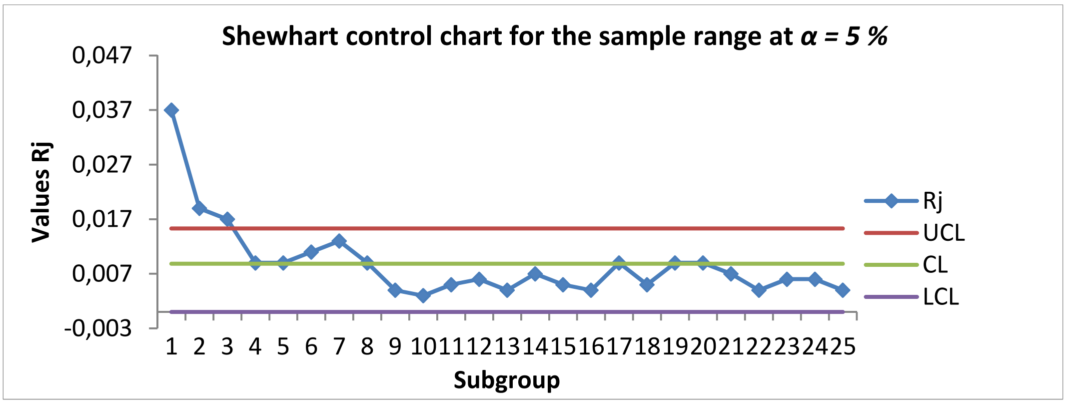

Fig. 2 Shewhart control chart for the sample range at α = *5 %* - the 1st analysis

Points of subgroups outside the regulatory boundaries were found. After the sources of errors were found points of subgroups were excluded. Subsequently new boundaries were calculated. Statistically mastered state of the measurement process of the case study was found only after the fourth analysis of Shewhart control charts for the sample average and the sample range.

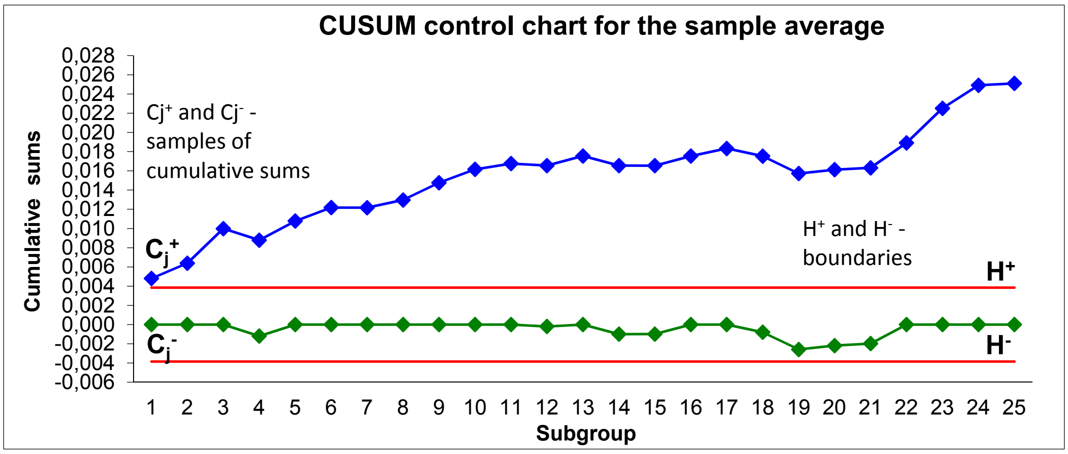

Fig. 3 Cumulative sum control chart for the sample average - the 1st analysis

CUSUM chart after the first utilization showed out that the metering process is not statistically controlled. In the process was a critical shift of the mean value of the measured quantity upward. Fig. 3 it is obvious that in the first subgroup is indicated a statistically uncontrolled state of the measurement process. The recommendation was in the next step to find determining cause, to take corrective action and restart the CUSUM chart from zero. If the setup process will be carried out, it may be useful to estimate the mean of the process caused by sliding.

5. Results

The solution of the case studies showed the ineffectiveness of use Shewhart control charts. Therefore it has acceded to the use of control chart of cumulative sums of sample averages. The following advantages have been confirmed:

- higher efficiency compared with Shewhart diagram,
- easy visual detection of shift of the mean value size,
- simple determination of the place where there was a shift of the mean value,
- suitable for cases where the cost of obtaining experimental data are high,
- efficiency was significant for lower values of α,
- four times faster indication of changes of process was observed by equal number of sample n,
- lower cost of process control,
- more precise detection of start of the change in parameters of the distributions of controlled value, direction of influence and its value.

6. Conclusions

The methodology of the utilization control charts introduces the specific rules with individual measurement results, which are outside the specified limits. In terms of the metrological assurance of product quality it is important to follow all measurement processes that are used in the development, manufacture, implementation into the operation and service of products. The aim is to ensure the confidence in the decisions or actions that are based on measured data. Building on the findings from the analysis of the use of statistical methods in the management measurement is suggested to focus on the method of cumulative sums (CUSUM chart). The use of this method in practice management of measurement is so far rare.

Acknowledgements

Authors wish to thank the Faculty of Mechanical Engineering of Slovak Technical University in Bratislava, grant agency VEGA project no. 1/0604/15 and no. 1/0748/15 for their support in writing this article.

References

[1] Terek M, Hrnčiarová, Ľ: *Štatistické riadenie kvality*. Bratislava: Iura Edition, 2004.

[2] Michálek J, Poskočilová A. Metoda kumulovaných součtů. In: *Národní informační středisko pro podporu jakosti, prezentácia,* 2007.

[3] Biaos S, Luh PB, Qing-Shan J, O'neill Z, Fangting S. Building Energy Doctors: An SPC and Kalman Filter-Based Method for System-Level Fault Detection in HVAC Systems. In: *IEEE Transactions on Automation Science and Engineering,* 11(1): 215-229.

[4] Arpaia, P, Betta G, Langella A., Sacco E. Measurement process control by means of algorithms based on digital image processing. In: *Science, Measurement and Technology, IEE Proceedings,* 146(1): 27 – 34, 1999.

Digital Transformation of Education & Training for Mobile Photonic Sensors 4.0 & Digital Image Processing with Smartpads

[1]D. Hofmann, [1]P.-G. Dittrich

[1]SpectroNet c/o Technologie- und Innovationspark Jena GmbH, Jena, Germany,
Email: d.hofmann@spectronet.de

Abstract. *Aim of the paper is a demonstration of the paradigm change in education and training with mobile smart digital computers, photonic micro sensors (sensors 4.0) and software apps for mobile smart photonic shape, color, spectral and hyperspectral measurement engineering and quality assurance. Due to the irreversible transformations in computational devices by their transitions from stationary desktop computers to consumerized mobile smartphones and smartpads new possibilities in education and training in photonic shape, color, spectral and hyperspectral measurement engineering and quality assurance are given. Manufacturers and system integrators of hardware modules for photonic imaging sensors (hardware apps) and software packages for digital image processing (software apps) are trying to reduce the significant qualification deficits of potential users for modern equipment by special activities in education and training.*

Keywords: Education, Training, Mobile, Smart, Micro sensors

1. Role of Subjects in the Added Value Generation Cycle

Fundamental aim of production processes is **first** to meet the customer's needs and **second** to generate sustainable added values for the manufacturers. With other words:

- The practical applications **PA** of products and/or services are key!
- The generation of added values is **not** accomplished in value chains, but in added value **cycles** (Fig. 1).
- The positive feedback of users is essential for sustainable demands of products and/or services by the users.

Due to the fantastic new possibilities in processing of big data the role of knowledge in the reproduction processes is currently overestimated. The reproduction pyramid has much more levels than knowledge. The source of economical most valuable knowledge are applications (Fig. 2). Main topic of the paper is directly aligned with the qualification of human resources **HR** for successful applications in measurement engineering and quality assurance.

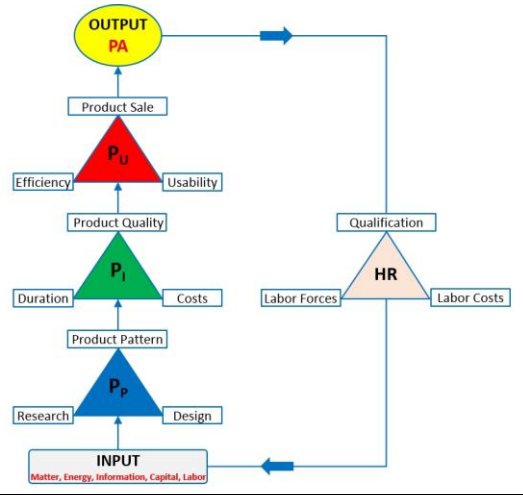

Notes:
HR Human Resources,
P_P Product Preparation,
P_I Product Implementation,
P_U Product Utilization,
Efficiency = Output/Mass {OP/kg},
Products = items and/or services [DIN EN ISO 9000],
Qualification = Education + Training + Experience,
Sale = Promotion + Distribution,
Usability = Convenience + Reliability + Affordability,
PA Practical Applications of Products and Services

Figure 1: The 3+1 Triangle rule of added value generation cycles [Hofmann 2014]

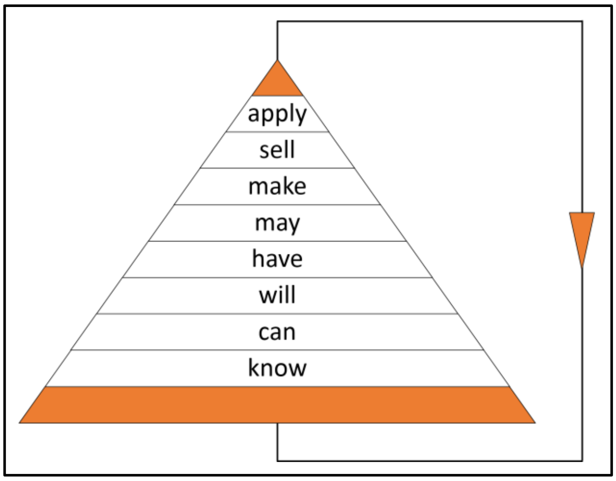

Figure 2: Reproduction pyramid and cycle

Enormous developments currently can be observed at mobile photonic shape, color, spectral and hyperspectral sensors as well as mobile digital image processing within the total added value generation cycle. For easier understanding of time dependent practical situations in different fields of interest some selected buzzwords can be mentioned (Fig. 3).

	P_P	P_Q	P_A	HR	Computer
2000	Holistic Approach	Supply Chain Management	Internet Bubble	cb-training	Desktop
2005	Heuristic Approach	Lean Management	Web 2.0	b-learning	Laptop
2010	Software-as-a-Service	Enterprise Resource Management	Executable Internet	e-learning	Smartpad
2015	Big Data	Cluster Management	Internet of Things	m-learning	Smartphone

Figure 3: Buzzwords in industry

Notes: **cb** computer-based, **b** blended, **e** electronic, **m** mobile

To increase the capabilities of operators for modern measuring equipment with software apps and smartpads the operating equipment can also be used for education and training. Some selected examples will be given in the next chapter.

2. Mobile Digital Learning Apps for Smart Photonic Shape, Color, Spectral and Hyperspectral Measurements

Mobile image processing specific paper apps and video apps on smartpads for end users

Highly recognized contributions to current education and training in image processing are provided by professional institutions (in alphabetical order) like AIA (visiononline.org), AMA (ama-sensorik.de), EMVA (emva.org), Fraunhofer-Allianz Vision (vision.fraunhofer.de), SpectroNet (spectronet.de), SPIE (spie.org), VDMA-Industrielle Bildverarbeitung (vdma.org) and by industry (Fig. 4).

analytikjena	AMA Verband für Sensorik + Messtechnik	Baumer	inspect	KONICA MINOLTA
analytik-jena.de	ama-weiterbildung.de	baumer.com	inspect-online.com	konicaminolta.eu
Mahr	MAZeT ELECTRONIC ENGINEERING & MANUFACTURING SERVICES	Ocean Optics	OMRON	Pool-i.d.
mahr.com	mazet.de	oceanoptics.com	industrial.omron.us	pool-id.com
pyramid building IT	STEMMER® IMAGING	Vision Components	ximea	ZEISS
polytouch.de	stemmer-imaging.de	vision-components.com	ximea.com	zeiss-campus.magnet.fsu.edu

Figure 4: Imaging specific ebooks for mobile smart photonic shape, color and spectral measurements

The transformations of analogue paper books, paper pictures and video tapes into their digital versions like ebooks and digital videos for smartpads are **irreversible**. The reasons are their convenience, reliability and affordability. They are efficient and flexible for individual use at work and at home. Clusterpartners of SpectroNet are elaborating valuable educational materials since years (see Fig. 4). A convenient, reliable and affordable conversion of .pdf papers into e-books is done for example by the digital publishing platform Yumpu (yumpu.com/de/browse/user/spectronet.de). To increase the efficiency of individual education and training processes, more than 2000 paper apps and more than 1000 digital videos apps for mobile smart photonic shape, color, spectral and hyperspectral measurements are **open** accessible at the cluster-platform www.spectronet.de (Fig. 5).

Figure 5: Educational material at www.spectronet.de

The digitized open platform contains paper apps, video apps, addresses of experts, institutions and enterprises dealing with mobile smart photonic shape, color, spectral and hyperspectral instrumentations, inspections, measurement engineering and quality assurance. The search and keyword functions in www.spectronet.de are enablers for end users to identify experts, institutions, enterprises and professional contents - convenient, reliable and affordable. Due to its longstanding existence and recognized expertise the www.spectronet.de platform can be recommended for trend scanning and trend watching also. Digitized paper books are **one side** of the educational coin only. The **other side** of the coin is the organization and realization of practical hands-on trainings.

Mobile image processing specific hands-on trainings either in industry and/or shared between industry and universities

Due to the miniaturization of the equipment the hands-on-training courses might be also organized as mobile courses. To cover a multilingual educational support for digital image processing a complete basic knowledge course – elaborated by STEMMER IMAGING GmbH (www.stemmer-imaging.de) is **online free** available in English and German languages:

- English: http://spectronet.de/de/vortraege_bilder/vortraege_2014/machine-vision-technology-forum-silverstone_hw69sjxz.html
- German: http://spectronet.de/de/vortraege_bilder/vortraege_2013/stemmer-imaging---technologieforum-bildverarbeitun_hoaj4wug.html

The multilingual knowledge courses cover planning, illumination, optics, cameras and so on. To keep alive personal contacts for mobile smart image processing specific communication and collaboration services new technological boundary conditions can be used - anytime, anywhere and on demand.

Image processing specific communication and collaboration services with smartphones and smartpads

The transition from stationary communication (phone) to mobile communication (smartphone) is increasing. Typical tools for efficient digital communication and collaboration are Skype and Teamviewer supplemented by content-delivering platforms. An open platform for mobile communication and collaboration in the field of mobile smart photonic shape, color, spectral and hyperspectral measurement engineering and quality assurance is www.spectronet.de.

3. Conclusions

Aim of the paper was the demonstration of the paradigm change in education and training with digital equipment for mobile smart photonic shape, color, spectral and hyperspectral measurement engineering and quality assurance. The transition from stationary analogue methods to mobile digital methods is up to date.

The added values for the users of www.spectronet.de are:

1. **convenient** open sources with more than 2000 digital paper apps, more than 1000 digital video apps and about 1000 addresses of experts, institutions and enterprises dealing with photonic shape, color, spectral and hyperspectral measurement engineering and quality assurance.

2. **reliable** trendscanner and trendwatcher for the development of mobile smart photonic shape, color, spectral and hyperspectral measurement methods and devices for the recent 10 years and as an enabler for sound predictions concerning future developments also.

3. **affordable** sources with open digital .pdf-papers, ebooks, videos and experimental structures for learning - anytime, anywhere at work and at home with efficient modules for mobile smart photonic shape, color, spectral and hyperspectral measurement engineering and quality assurance, independent of the individual conditions concerning time and space and financial resources of the users and learners.

Please feel free to use the search box of www.spectronet.de to get support for your tasks and visions.

Acknowledgements

Many thanks to our Clusterpartners and to BMWi Berlin for their long standing financial support in the frames of ZIM and go-cluster.

Recommendable Sources

[1] International Year of Light 2015. *Celebrating Light. 50 Ways Light-based Technologies Enrich Our World*. SPIE Press 2015.
[2] Trends 2015: *Sustainability, Miniaturization, Materials, Modularity, Economy.* PHOTONICS Spectra, January 2015
[3] 2015 Education Directory: *Global Directory of Programs in Optics and Photonics.* www.opticseducation.org

Measurement in Biomedicine

Does the Complexity of Sleep EEG Increase or Decrease with Age?

[1]A. Krakovská, [1]R. Škoviera, [2]G. Dorffner, [1]R. Rosipal

[1] Institute of Measurement Science, Slovak Academy of Sciences, Bratislava, Slovakia
[2]Section for Artificial Intelligence, Center for Medical Statistics, Informatics and Intelligent Systems, Medical University of Vienna, Vienna, Austria
Email: krakovska@savba.sk

Abstract. *The goal of this study is to contribute to discussions about age-related changes in electroencephalogram (EEG) complexity. Eight characteristics of complexity were evaluated for sleep EEG of 175 healthy subjects. The complexity of the sleep EEG significantly increased up to the age of about 60 years. Over 60 years, the complexity stagnated or slightly decreased. The same tendencies were manifested during all sleep stages and also during the episodes of wakefulness.*

Keywords: Sleep EEG, Complexity, Spectral measures, Fractal exponent

1. Introduction

Although there is no unique definition of complexity, a number of methods have been proposed that allow to measure the complexity of physiologic signals. Traditionally, the loss of complexity is characterized by relative reduction in the high-frequency components and increase in the low-frequency components. Furthermore, other measures of complexity, based on concepts from the modern field of nonlinear dynamics and chaos theory, can be used.

In 1992 Lipsitz and Goldberger [1] proposed that the aging process may be characterized by a loss of complexity in multiple physiologic processes including functioning of the brain. Since then, a number of studies hypothesized that aging or mental illness is accompanied by decline in the brain's adaptive capacity, demonstrated by changed patterns in brain signals.

An investigation of resting EEGs of 54 healthy children (new-borns to 14 years old) has shown that brain maturation is reflected in a highly significant increase in complexity with age [2]. The authors in [3] concluded that after a jump in the brain dynamics complexity during maturation (7–25 years) a linear increase, albeit more moderate, continues. Their oldest subject was 60 years old. In contrast, Takahashi claims that after reaching adulthood the complexity decreases with age [4].

In this study, to assess the complexity of young healthy subjects in comparison to the elderly, we have analysed EEG both by traditional spectral methods and by recently developed methods of complexity estimation.

The paper is organized as follows. Firstly, the data and the methods are described. Then eight characteristics of EEG complexity are introduced and estimated across the subjects and their individual sleep stages. Finally, the age-related changes of the measures are evaluated.

2. Subject and Methods

In total, 175 all-night sleep EEG recordings were analysed. They were taken from the SIESTA database of polysomnography recordings of healthy adults [5]. The average age of subjects was 51.2 year, the youngest subject was 20-year-old man, and the oldest was a 95-year-old woman. Subjects slept at their usual sleeping time, typically from 11 pm, the average recording time was about 8 hours. All subjects in the control group had a Pittsburgh Sleep Quality Index [6] of at most 5. Signals from electrodes C3-M2 and C4-M1 were used, where M1, M2 are the left and the right mastoids, following the 10-20 international electrode placement system. The data, originating from several departments, were resampled to 100 Hz.

We have used hypnograms (graphs that discriminate the sleep stages) based on the rules of Rechtschaffen and Kales (RKS) [7], obtained via the automatic RKS classifier Somnolyzer 24x7 [8]. Scoring consists in classifying all 30 s epochs of an all-night recording into one of the following five stages: wakefulness (W), rapid eye movement sleep (REM), the lightest sleep Stage 1 (S1), sleep Stage 2 (S2), and the deepest sleep stage referred to as slow wave sleep (SWS).

In the following, our eight characteristics of complexity are briefly introduced (more detailed descriptions can be found in [9]). All measures were computed for the EEG signals, step by step for the same 30 s long intervals, which were examined by the automatic sleep classifier.

The fractal dimension (*FD*), computed here by Higuchi algorithm [10], falls within an interval (1, 2) and reflects the property of a curve of filling more space than a line segment (*FD=1*) but less than an area (*FD=2*).

The fractal exponent (β), sometimes referred to as a spectral decay, or power-law exponent, is defined for signals with a power spectrum P(f), which is power-law dependent on the frequency f: $P(f) \sim f^{-\beta}$. This phenomenon is also known as 1/f-like behaviour. Power-law power spectra have also been validated in the case of EEG, especially when the slope of the spectral decay is calculated over the whole spectrum of EEG instead of considering narrow frequency ranges [11]. The power-law decay of the EEG spectrum is interpreted as an indication of non-trivial long-range correlations that are typical for scale-invariant or self-affine processes [12]. In our study, the fractal exponent was derived from the slope of the linear fit of spectral density in the double logarithmic graph over the frequency range of 0.5 - 40 Hz.

The Hurst exponent (*H*), defined and estimated as in [13], is another measure of long-term memory of time series. The closer the exponent value is to 0, the rougher are the traces. On the other end, as H approaches 1, the traces become more and more smooth. For traditional Brownian motion, $H=0.5$. Depending on whether H is larger than, or smaller than 0.5, the signal is persistent (with long-range correlations) or anti-persistent (anti-correlated).

The Hurst exponent estimated by a second method called *detrended fluctuation analysis* (H_{DFA}) is usually considered as more suitable for real data. Unlike some other methods designed for determining the statistical self-affinity DFA may also be applied to non-stationary signals [14].

With the Hurst exponent of EEG between 0 and 1 and fractal exponent β between 1 and 3, which are ranges characteristic for the fractional Brownian motion (fBm) of Mandelbrot and Van Ness [15], fBm begins to be considered as a suitable model for EEG. Recall that, for the fBm process, the following relationships between β, H and FD applies: $FD = \frac{5-\beta}{2} = 2 - H$.

The prediction error was evaluated for the evolution of an EEG trajectory reconstructed in a 3-dimensional space. Firstly, based on Takens' theorem [16], a state portrait was reconstructed from time delays of a one-dimensional observable: $\vec{x}_n = \left(X_{n-(m-1)\tau}, X_{n-(m-2)\tau}, \dots, X_n\right)$, where $\vec{x}_n$ is a vector in the reconstructed space, X is the one-dimensional variable, m is an embedding dimension and τ is the time delay. Next, from the trajectory, the nearest neighbours of the relevant point were found and the predicted value was assessed as their averaged image [17]. After search for optimal parameters for prediction, they were set as follows - embedding dimension 3, time delay 2, and number of nearest neighbours 20. As a prediction error, the root-mean-square error normalized by the standard deviation of the signal sample was taken.

The spectral entropy (spE) was calculated as $\mathrm{spE} = -\sum_{0.5\,Hz}^{40\,Hz} P(f)\ln P(f)$, where P(f) is a normalized power spectral density which can be treated as a probability density function.

The spectral mean is an example of a simple traditional estimate of the complexity using frequency properties of the signal.

The relative delta to relative beta power ratio (*delta/beta*) is the last of our measures of complexity, wherein relative power means an absolute spectral power in a specific band divided by the total spectral power. The power spectral density was estimated according to Welch's method of averaged modified periodograms. Spectral powers were computed in the frequency bands delta (0.5 - 4 Hz) and beta (16 - 30 Hz). The total power was computed from the frequency band 0.5 - 40 Hz.

The age-related trends in the computed characteristics were visualized with regression lines. How well the regression fits the data, is expressed as a correlation coefficient R^2. The closer R^2 to 1.00, the better the fit. Significance of parameters in the regression model was also tested, namely the relevant t-statistic and the p-values for the coefficients of the model were evaluated.

3. Results

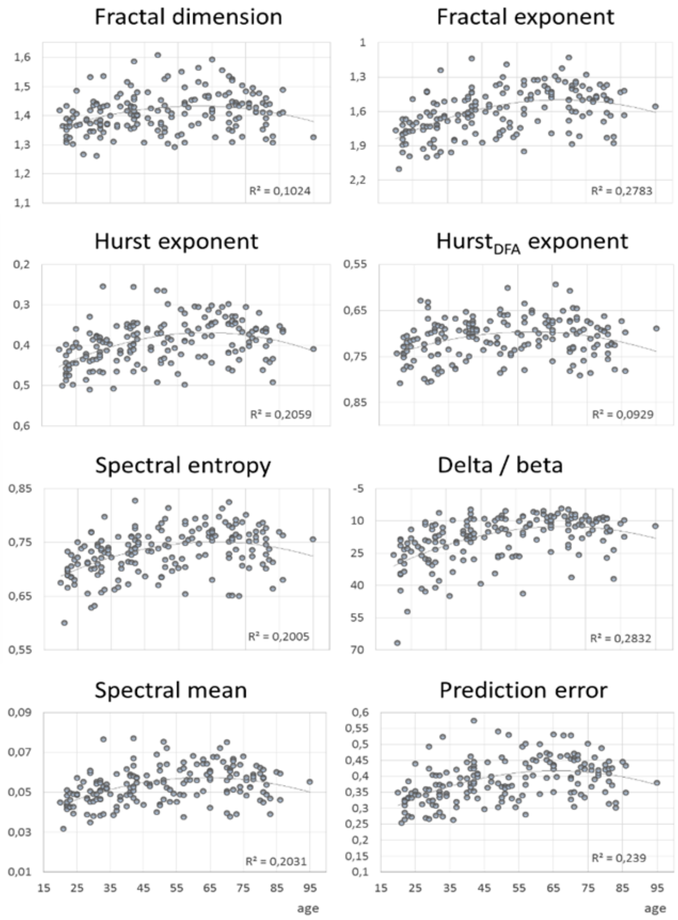

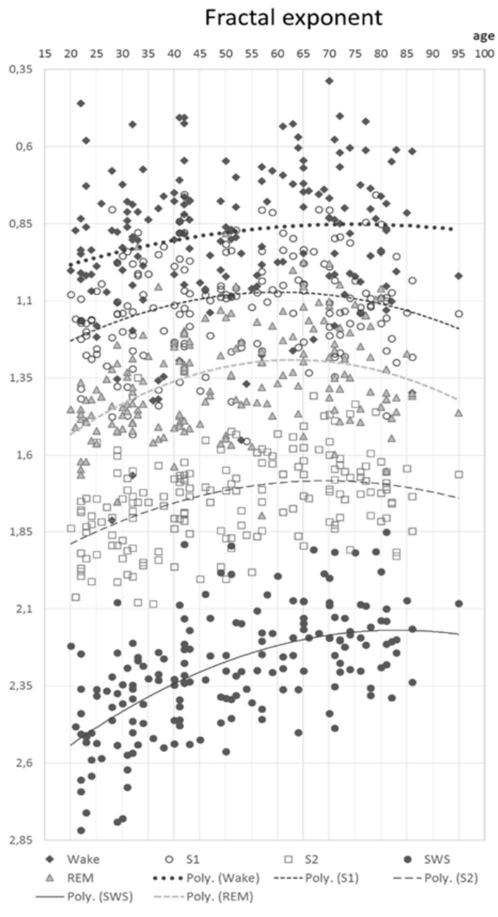

Fig. 1. Relation between the complexity measures and age presented through scatter plots and order 2 polynomial trend-lines. Each circle represents an all-night mean value of the respective measure for one of the subjects.

Fig. 2. Relationship between the fractal exponent and age presented through scatter plots and an order 2 polynomial. Mean values of the fractal exponent are presented for waking and the sleep stages separately.

The relative changes of the characteristics indicate that, in general, EEG complexity of healthy subjects increases with age. For interval 20-60 years, this was confirmed statistically (through the t-statistic and the p-values<0.05) if using simple linear regression for modelling the relationship between the individual complexity measures and age. In the scatter plots of Fig. 1, however, polynomial trend-lines of order 2 are shown, suggesting that over the age of 60 years, the EEG complexity could be stagnant or slightly declining.

We also evaluated the complexity for each sleep stage separately. The results for a selected measure (fractal exponent) are presented in Fig. 2. First of all, we see the highest EEG complexity during wakefulness and its decrease with the deepening of sleep. Secondly, looking at episodes of waking and each sleep stage separately does not reveal significant differences between the individual stages. In any case, the age-related complexity evolution shows the same course. The most pronounced increase of the complexity is observable in the SWS. In terms of spectral properties, considerably fewer delta waves and more faster beta waves were observed in elderly as compared to younger subjects.

4. Discussion and conclusions

Our results contradict the hypothesis of a loss of complexity of EEG in the healthy brain after reaching adulthood. In fact, we observed an increase in EEG complexity from age 20 to 60 years. After the age limit of about 60 years our findings do not exclude the possibility of a moderate age-related decrease of EEG complexity.

Recall that both the modern complexity measures (entropies, fractal exponent, fractal dimension, Hurst exponent, and prediction error) and the more traditional measures (spectral mean and the delta to beta ratio) led to the same conclusion. Higher complexity, simultaneously with considerably fewer delta waves and more faster beta waves were observed in elderly as compared to younger subjects.

Acknowledgements

This work was supported by the MZ 2013/56-SAV-6 and VEGA2/0043/13 research grants.

References

[1] Lipsitz LA, Goldberger AL. Loss of 'complexity' and aging: potential applications of fractals and chaos theory to senescence. *Jama*, 267 (13): 1806-1809, 1992.

[2] Meyer-Lindenberg A. The evolution of complexity in human brain development: an EEG study. *Electroencephalography and clinical neurophysiology*, 99 (5): 405-411, 1996.

[3] Anokhin AP, Birbaumer N, Lutzenberger W, Nikolaev A, Vogel F. Age increases brain complexity. *Electroencephalography and clinical neurophysiology*, 99 (1): 63-68, 1996.

[4] Takahashi T. Complexity of spontaneous brain activity in mental disorders. *Progress in Neuro-Psychopharmacology and Biological Psychiatry,* 45: 258-266, 2013.

[5] Klösch G, et al. The SIESTA project polygraphic and clinical database. *Engineering in Medicine and Biology Magazine, IEEE,* 20 (3): 51-57, 2001.

[6] Buysse DJ, Reynolds CF, Monk TH, Berman SR, Kupfer DJ. The Pittsburgh Sleep Quality Index: a new instrument for psychiatric practice and research. *Psychiatry research,* 28 (2): 193-213, 1989.

[7] Rechtschaffen A, Kales A, editors. A Manual of Standardized Terminology, Techniques and Scoring System for Sleep Stages of Human Subject. US Government Printing Office, National Institute of Health Publication, Washington DC, 1968.

[8] Anderer P, et al. An E-health solution for automatic sleep classification according to Rechtschaffen and Kales: validation study of the Somnolyzer 24 x 7 utilizing the Siesta database. *Neuropsychobiology*. 51 (3): 115-133, 2004.

[9] Šušmáková K, Krakovská A. Discrimination ability of individual measures used in sleep stages classification. *Artificial Intelligence in Medicine,* 44 (3): 261-277, 2008.

[10] Higuchi T. Approach to an irregular time series on the basis of the fractal theory. *Physica D: Nonlinear Phenomena,* 31 (2): 277-283, 1988.

[11] Krakovská A, Štolc S Jr. Spectral decay vs. correlation dimension of EEG. *Neurocomputing,* 71 (13): 2978-2985, 2008.

[12] Linkenkaer-Hansen K, Nikouline VV, Palva JM, Ilmoniemi RJ. Long-range temporal correlations and scaling behavior in human brain oscillations. *The Journal of neuroscience,* 21 (4): 1370-1377, 2001.

[13] Hurst HE, Black P, Simaika YM. Long-term storage: an experimental study. Constable. 1965.

[14] Peng CK, Buldyrev SV, Havlin S, Simons M, Stanley HE, Goldberger AL. Mosaic organization of DNA nucleotides. *Physical Review E,* 49 (2): 1685-1689, 1994.

[15] Mandelbrot BB, Van Ness JW. Fractional Brownian motions, fractional noises and applications. *SIAM review*, 10 (4): 422-437, 1968.

[16] Takens F. Detecting strange attractors in turbulence. In Dynamical systems and turbulence, Warwick, Springer Berlin Heidelberg, 366-381, 1981.

[17] Hegger R, Kantz H, Schreiber T. Practical implementation of nonlinear time series methods: The TISEAN package. *Chaos: An Interdisciplinary Journal of Nonlinear Science,* 9 (2): 413-435, 1999.

Using ASL Method for Monitoring of Brain Perfusion Changes in a Rat Model of Schizophrenia and After Chronic Administration of Aripiprazole

[1,2]E. Dražanová, [2,3]L. Grossová, [1]J. Pistovčáková, A. Khainar[5], [1]R. Demlová, [4]T. Kašpárek, [2] Z. Starčuk jr.

[1] Department of Pharmacology, Faculty of Medicine, Masaryk University, Brno, CZ.,
[2] Institute of Scientific Instruments, ASCR, Brno, CZ.,
[3] Dept. of Biomedical Engineering, Brno Univ. of Technology, Brno, Czech Republic
[4] Dept. of Psychiatry, Faculty of Medicine, Masaryk University, Brno, CZ.
[5] Applied Neuroscience Research Group, CEITEC, Masaryk University, Brno, CZ.
Email: edrazan@isibrno.cz

Abstract. *Animals prenatally exposed to polyriboinosinic–polyribocytidilic acid (poly I:C) can be used to parallel neuropathological abnormalities seen in schizophrenia patients. The aim of this study was to test the utility of Arterial Spin Labeling (ASL) MRI method for the evaluation of perfusion in different brain regions in the developmental poly I:C model of schizophrenia in rats. In these animals we further investigated the effect of chronic administration of the antipsychotic aripiprazole on brain perfusion. In the circle of Willis region, we observed significant (p<0,05) increase of blood perfusion in the poly I:C model of schizophrenia in both males and females, and significantly higher perfusion in males than in females in vehicle-treated controls. Perfusion in hippocampus (in both hemispheres) was found significantly higher in males than in females in both vehicle-treated controls and poly I:C prenatally exposed animals. The significantly increased blood perfusion in the circle of Willis in poly I:C prenatally exposed males was found to persist even after chronic administration of aripiprazole. These results add new data to understanding of antipsychotic effects and demonstrate the viability of the proposed approach of combination of the ASL MRI method and the selected rat model of schizophrenia.*

Keywords: ASL, schizophrenia, poly I:C animal model, rats, aripiprazole

1. Introduction

Several animal models simulate schizophrenia pathologies. These models fit into four basic categories: pharmacological models, lesion-induced models, genetic models and developmental models. The poly I:C developmental model was used in this study. Poly I:C is used to mimic neonatal exposure to viral pathogens that can lead to alterations resembling brain changes in schizophrenic patients. Using the ASL MRI method we examined the perfusion changes in poly I:C model in rats. According to the finding of Nordquist et al. (2007) that acute administration of aripiprazole dose-dependently decreased brain activity in several brain regions, we also measured brain perfusion after chronic administration of aripiprazole.

2. Subject and Methods

Animal model

The developmental poly I:C model in rats was induced by acute subcutaneous dose of poly I:C (8 mg/kg) to 10 pregnant Wistar rat dams in the 15th day of their pregnancy. Vehicle was administered to 10 controls in the same time period. The adult offspring, both males (n = 6-11) and females (n = 5-10), were used for MRI measurements.

Chronic administration of aripiprazole
Adult rat males were divided into two groups. For one month, aripiprazole (5 mg/kg/day, orally) was administered to one group (n = 7-8), and vehicle (1ml/kg/day, orally) to the other (n = 8-9). All adult males underwent MRI measurements.

MRI acquisition
The rats were kept in general anesthesia using 2.0% isoflurane. Their respiration and ECG were controlled by the anesthesia level (to maintain 60 breaths per minute, 350±10 BMP) and the body temperature was stabilized to 37.7±0.1°C. Animals were monitored during the whole measurement.

MR imaging was performed in an experimental 9.4T MR scanner (Bruker Biospin 94/30 USR by Bruker, Ettlingen, Germany) using a receive-only 2×2 array surface coil (400 ARR R.BR) and a volume transmitter coil.

A RARE sequence was used to obtain anatomical images with the following acquisition parameters: TR/TE 3500/36.0 ms, image matrix 256×256, slice thickness 1.25 mm, 2D FOV 50.0×20.4 mm and RARE factor 2. An ASL sequence FAIR-RARE was used with the following parameters: TR/TE 10000/37.78 ms, image matrix 128×96, slice thickness 1.25 mm, 2D FOV 50.0×20.4 mm; from one axial slice through the brain a set of 15 magnitude images with TI of 30, 50, 100, 200, 300, 500, 700, 900, 1000, 1100, 1500, 1800, 2200, 2800, 3200 ms was used to calculate the tissue blood flow map.

Data analysis
All ASL data were analysed in ParaVision 5.1 (Bruker) , ASL blood flow maps were analyzed in manually drawn brain ROIs by own Matlab R2010a code. MRI data were analysed in STATISTICA (StatSoft. Inc.) software by the Mann-Whitney U nonparametric test ($p<0.05$).

3. Results

Ventricular enlargement was seen in poly I:C exposed rats as compared to vehicle-exposed rats (Fig. 1). Brain blood-flow maps were created from ASL images (Fig. 2). Brain perfusion maps analysed by Mann-Whitney U test; the resulting box plots are shown in Fig. 3-6.

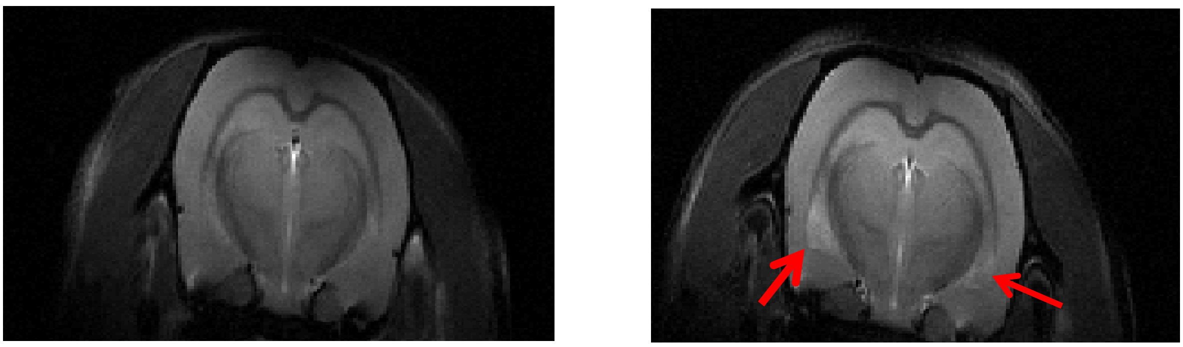

Fig. 1. Ventricular enlargement in a female rat prenatally exposed to poly I:C (right) versus a control, prenatally exposed to vehicle (left image).

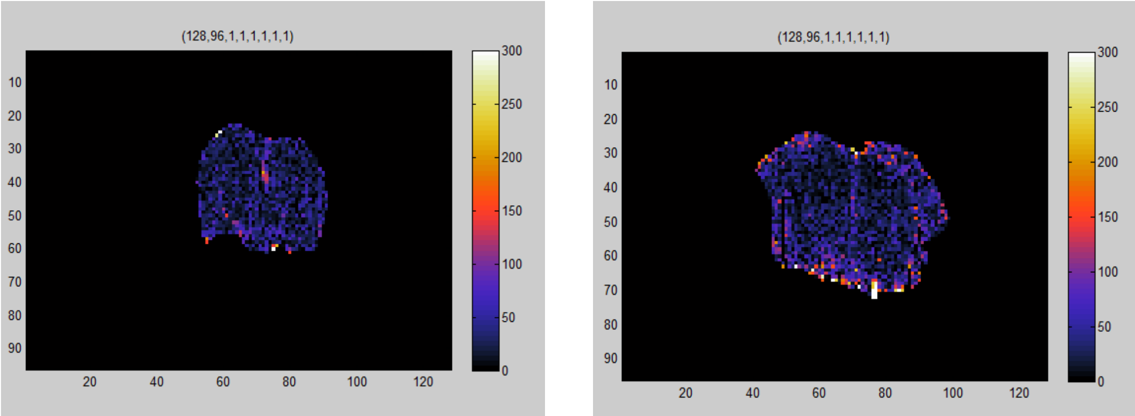

Fig. 2. Brain blood-flow maps created from ASL. A female rat prenatally exposed to vehicle (left image). A female rat prenatally exposed to poly I:C (right image).

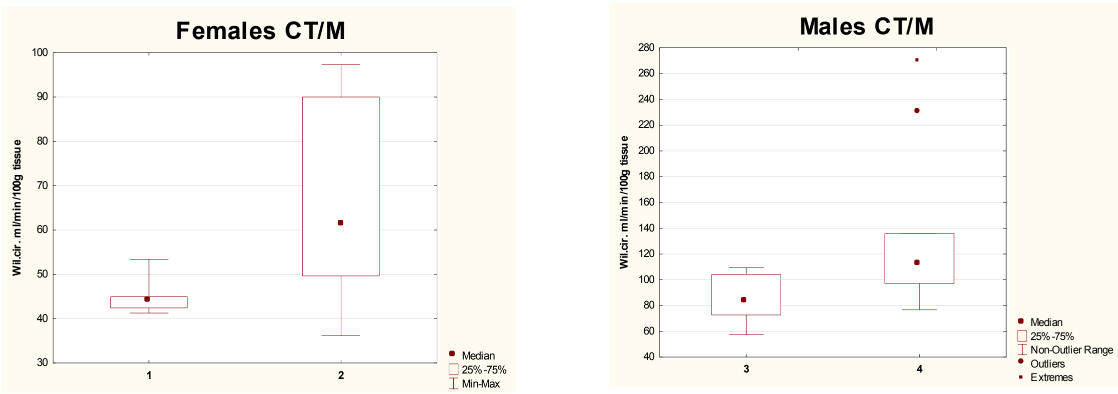

Fig. 3. Increased perfusion in the circle of Willis in rats prenatally exposed to vehicle (left column) / poly I:C (right column); females (left figure), males (right figure).

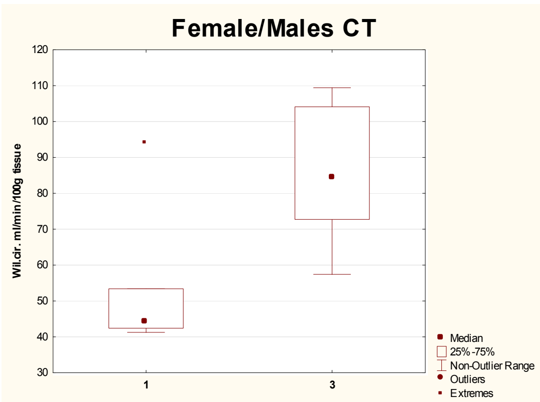

Fig. 4. Increased perfusion in the circle of Willis in vehicle-exposed male rats (right column) versus vehicle-exposed female rats (left column).

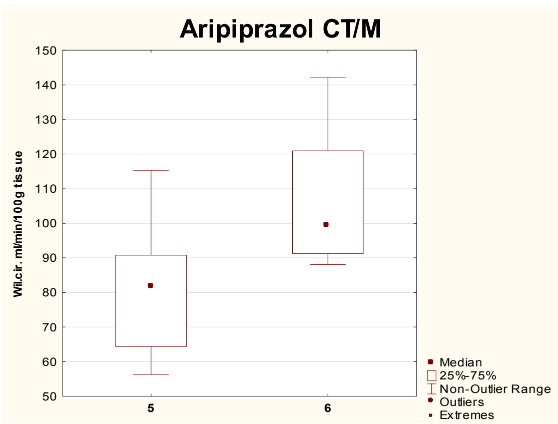

Fig. 5. Increased perfusion in the circle of Willis in male rats prenatally exposed to poly I:C (right column) versus vehicle (left column) in groups with chronic aripiprazole treatment.

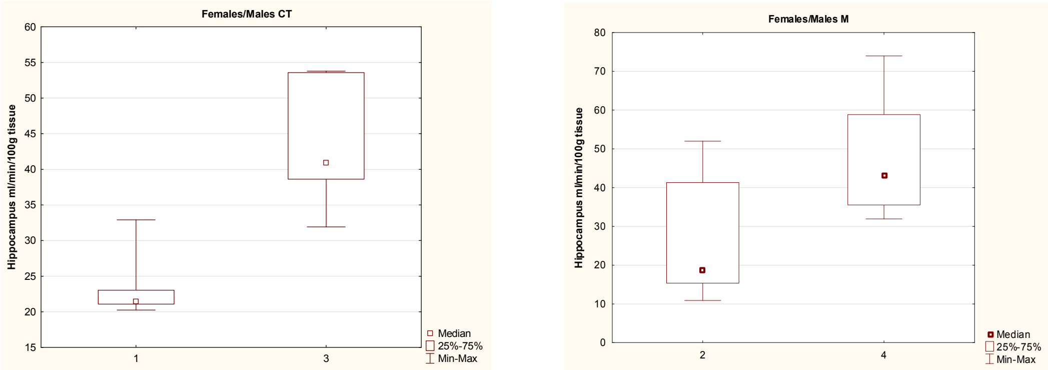

Fig. 6. Increased perfusion of hippocampus in rats prenatally exposed to vehicle (left figure) and poly I:C (right figure); females (left column) versus males (right column).

4. Discussion and Conclusion

We observed higher perfusion in the circle of Willis and hippocampus in male than in female rats. Futhermore, we found significantly increased perfusion in rats prenatally exposed to poly I:C in the circle of Willis region, which could explain the enlargement of lateral ventricles. These findings could be interpreted by an alteration of the dopaminergic system. Iadecola (1998) reported that dopamine profoundly influences all segments of cerebral circulation, and dopamine dysregulation is a hallmark of schizophrenia. *In situ* administration of dopamine produces vasoconstriction, but binding on D1 and D2 dopaminergic receptors induces vasodilation, hence increased perfusion. There was no evidence of aripiprazole effect on brain perfusion in male rats prenatally exposed to poly I:C. This can be explained by the fact that in humans, aripiprazole and its metabolite are partial agonists at D2 receptors, but its metabolite in rodents displays antagonist properties after a chronic administration [2]. Our results can further help in understanding of the mechanisms of antipsychotic effects. The combination of the ASL MRI method and the selected rat model of schizophrenia demonstrate a promising approach.

Acknowledgements

This work was partially supported by ACIU LM2011017, MŠMT (projekt. č. CZ.1.05/2.1.00/01.0017), MUNI/A/1116/2014

References

[1] Nordquist RE, Risterucci C, Moreau JL, von Kienlin M, Künnecke B, Maco M, Freichel C, Spooren W. Effect of aripiprazole/OPC-14597 on motor activity pharmacological models of psychosis, and brain activity in rats. *Neuropharmacology*, 2007, 54, 405-416.

[2] Wood MD, Scott C, Clarke K, Westaway J, Davies CH, Reavill Ch, Hill M, Rourke C, Newson M, Jones DNC, Forbes IT, Gribble A. Aripiprazole and its human metabolite are partial agonists at the human dopamine D2 receptors, but he rodent metabolite displays antagonist properties. *European Journal of Pharmacology*, 2006, 546, 88-94.

[3] Iadecola C. Neurogenic control of the cerebral microcirculation: is dopamine minding the store? *Nature Neuroscience*, 1998, 4, 263-265.

Neurochemical Changes Observed by ^{1}H MRS in Rats with Induced Age-related Early-stage Dementia

[1,2]R.Tušková, [3]B. Lipták, [3]M. Dubovický, [1]T.Liptaj, [1]S.Kašparová

[1]Slovak University of Technology in Bratislava, Faculty of Chemical and Food Technology, Institute of Analytical Chemistry, Bratislava, Slovak Republic
[2]High-Field MR Center, Department of Biomedical Imaging and Image-guided Therapy, Medical University Vienna, Vienna, Austria
[3]Slovak Academy of Sciences, Institute of Experimental Pharmacology & Toxicology, Bratislava, Slovak Republic
Email: raduss.tuskova@gmail.com

Abstract. *The aim of this study was to induce a sporadic form of age-related early-stage dementia, such as that in Alzheimer's disease (AD) by chronic injection of D-galactose and* $NaNO_2$ *to rats and investigate changes in brain metabolites levels using in vivo proton magnetic resonance spectroscopy. As reference methods behavioral tests were used. Localized proton magnetic resonance spectroscopy measurements in a brain showed a significant decrease in the concentration of N-acetylaspartate + N-acetylaspartylglutamate, glutamine + glutamate, and myo-inositol in the D-gal/*$NaNO_2$ *group compared to the control group. The dynamics of the learning process represented by the learning index in modified Morris water maze test revealed a reduction in learning in the D-gal/*$NaNO_2$*. The total motor activity in the Open-field test was also reduced compared to the control. We propose, that our results support the use of D-galactose in combination with* $NaNO_2$ *to rats to induce early-stage of dementia and could be a relevant model for the study of underlying mechanisms of sporadic forms of dementia in rats.*

Keywords: early-stage dementia, rat model, in vivo proton magnetic resonance spectroscopy, behavioral tests, D-galactose, $NaNO_2$

1. Introduction

Dementia is a broad category of brain diseases characterized by deterioration in memory, thinking, behavior and the ability to perform everyday activities. The most common type of dementia is Alzheimer's disease (AD). Two forms of AD are recognized, that are familial, which is very rare and sporadic form, where the cause is presently unknown. Several risk factors, such as lifestyle, excessive stress and excessive ingestion of sugar have been described, but the most important factor is considered to be the aging [1]. Medical treatment can be effective only for patients with early-stages, but the diagnosis is problematic. Therefore, it is very important to identify disease-specific biomarkers for early diagnosis.

D-galactose (D-gal) and $NaNO_2$ treatment is currently used in mice to induce dementia-like signs[2]. In order to understand the changes in the brain, *in vivo* proton magnetic spectroscopy (^{1}H MRS) can be used. We used single-voxel ^{1}H MRS on a 4.7 T magnet, and observed these six metabolites: N-acetylaspartate and N-acetylaspartylglutamate (*NAA+NAAG)*, creatine and phosphate creatine (*Cr+PCr*), glycerophosphocholine and phosphocholine (*GPC+PCh*), myo-inositol (*mIns*), glutamate and glutamine (*Glu+Gln*), and taurine (*Tau*). All of these metabolites are of particular interest, since they belong to specific neuronal and glial metabolic pathways, membrane constituents, and energy metabolism.

There are several experimental approaches to investigate cognitive processes in laboratory rats. Modified Morris water maze (MWM) is presently the most widely used method for the evaluation of visual-spatial learning and memory skills [3]. Open-field (OF) test is a relevant experimental tool to analyse locomotion and habituation in a new environment [4].

The purpose of this study was to characterize in details changes in the brain metabolite levels using *in vivo* ^{1}H MRS after chronic injection of D-gal and $NaNO_2$ to adult male rats. Moreover, relevant behavioral variables with a focus on spatial learning, exploratory and anxiety-like behaviours were evaluated as well.

2. Subject and Methods

Animals
Male Wistar rats (6 months old, weight 250-320g, n = 16) were used in the study. Rats were kept under standard laboratory conditions with food and water ad libitum, and housed four in each cage on a regular light/dark cycle. Animal housing, care, and experimental procedures were conducted under the guidelines of the Animal Ethics Committee and were approved by the State Veterinary and Food Administration of the Slovak Republic. Animals were treated intraperitoneally with D-gal at a dose of 120 mg/kg and $NaNO_2$ at a dose of 20 mg/kg, dissolved in redistilled water (D-gal/$NaNO_2$ group, n = 8). The drugs were administered to animals daily for 30 days simultaneously.

In vivo ^{1}H MRS
During all MRS measurements, animals were anaesthetized by inhaling 2% isoflurane. Body temperature was maintained at 37.5°C by warm air circulating the body, and respiration was monitored during the whole experiment (SA Instruments, Inc. Stony Brook, NJ, USA). In vivo ^{1}H MRS measurements were performed on a 4.7 T horizontal bore (diameter of 12.5 cm) magnet, equipped with 400 mT/m gradients (Agilent, USA) with a transmit-volume/receive-surface combination of coils (Rapid Biomedical, Germany) intended for animals. A fast spin echo multislice sequence (FSEMS) was used for voxel localization, with the following parameters: repetition time TR= 3000 ms; echo time TE= 74.24 ms; number of acquisitions NA= 8; data matrix= 256x192; slices= 20; slice thickness= 1mm; gap= 0; field of view FOV= 40x40mm. The single-voxel localization was performed by the SPECIAL sequence, which enables the use of a short TE and preserves the full magnetization available from the selected volume of interest (VOI), with following parameters: TR = 2000 ms; TE = 4.45 ms; NA = 8x64 in combination with outer volume suppression and VAPOR water suppression. One scan without water suppression was acquired for quantification purposes. First- and second-order shim values were optimized using the FASTMAP method. Shimming resulted in an unsuppressed water spectral line width of ~10 Hz. Resulting proton spectra were analyzed using the LCModel [5]. Metabolite values that had Cramer-Rao lower bounds ≥20% were excluded from further analysis. *In vivo* ^{1}H MR spectra (Fig. 1) were obtained from an area of the hippocampus and cortex (voxel size of 4 x 4 x 4.5 mm^3).

Behavioral tests
The modified MWM was used to investigate spatial learning in experimental animals [3] and OF to analyse locomotion and habituation in a new environment.

Statistical analysis
The data are expressed as a mean ± standard deviation. Repeated measures ANOVA were used to evaluate significance between the groups. Behavioral data were statistically analyzed by STATISTICA software. Differences of $p<0.05$ were considered statistically significant in all analyses.

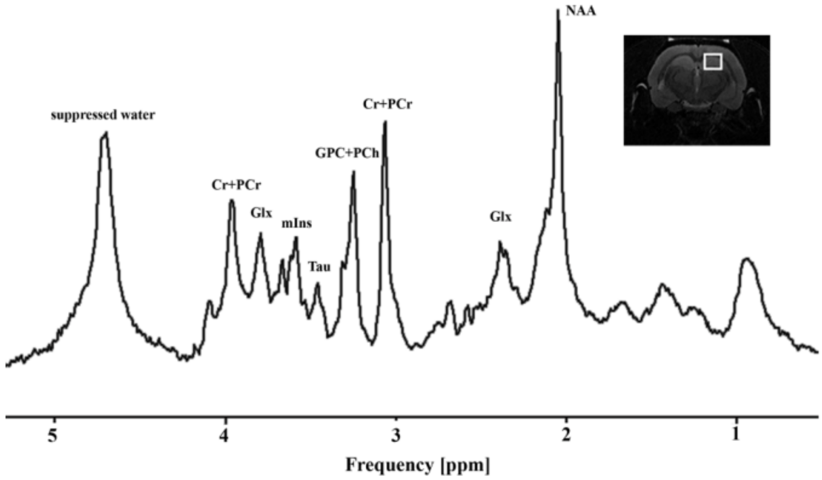

Fig. 1. A representative image and localized ^{1}H spectra from a rat brain (voxel 4x4x4.5mm^3) acquired on a 4.7T magnet.

3. Results

In vivo ^{1}H MRS

A quantification of absolute concentrations of metabolites from ^{1}H MRS in the D-gal/$NaNO_2$ versus the control group showed a significant decrease in the concentration of NAA+NAAG ($p<0.002$), as well as a significant decrease in the concentration of mIns ($p<0.008$) and Glu+Gln ($p<0.02$) (Fig. 2).

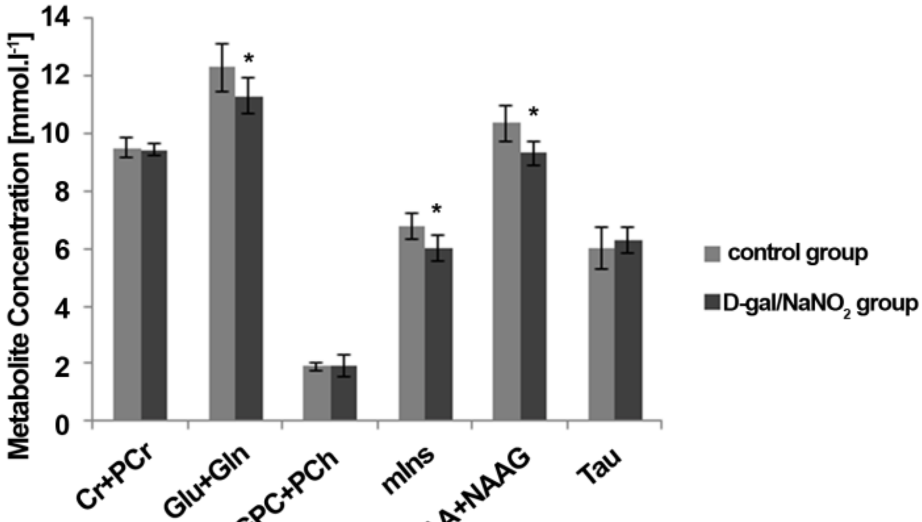

Fig. 2. A bar graph showing absolute concentrations of metabolites in the D-gal/$NaNO_2$ versus the control group.

Behavioral tests

The mean learning index (MWM) calculated for the D-gal/$NaNO_2$ group was lower compared to controls ($p<0.059$) and the rapidity of learning was significantly lower in the D-gal/$NaNO_2$ group compared to control group ($p<0.044$). The motor activity (OF) of animals did not continuously decrease (they did not habituate), as expected in the repeated open-field test exposures.

4. Discussion

It has recently been reported that the process in mice treated with D-gal and $NaNO_2$ resembles observations in humans with some age-related dementia. The doses of D-gal in combination with $NaNO_2$ for intraperitoneal injection in mice are well known. We had to test dose for rats. The dosage of D-gal in rats was determined from past experiments. We tested more doses of $NaNO_2$ and the most suitable dosage for long term and survival intraperitoneal administration was determined at 20mg/kg. Numerous *in vivo* and *in vitro* ^{1}H MRS studies of AD and transgenic animal models have been performed and have shown the typical neurochemical profile demonstrated by a decrease in brain NAA and Glu and an increase in mIns. We observed similar changes in our rat brain model for the metabolites NAA+NAAG and Glu+Gln. Decreased brain NAA concentration may reflect neuronal dysfunction and decreased Glu level can mirror disturbed learning and memory systems. A decrease of mIns concentration was observed, which is contrary to some *in vivo* and *in vitro* ^{1}H MRS studies that have found increased mIns. As was suggested by Mlynarik et al. (2012), an increase in mIns can be detected only when the pathology is severe. The results from the behavioral study reflect in some extent the results obtained by means of MRS approaches.

5. Conclusions

In good agreement with previous *in vivo* and *in vitro* ^{1}H MRS findings, our *in vivo* ^{1}H MRS at 4.7T observed decreased NAA and Glu in the hippocampus of rats, so we concluded that we induced age-related dementia (prodromal stage of dementia, such as AD) by mentioned substances. The results of the present work may at least partially provide some evidence for a possible role for MRS in early diagnosis and for surrogate biochemical markers to monitor disease progression and therapeutic response.

Acknowledgements

This work was supported by the grant agency VEGA, grant no.: 2/0084/11 and 2/0168/15, and by the Support for Young Researchers, Slovak University of Technology in Bratislava.

References

[1] Querfurth HW, Laferla FM. Alzheimer's Disease. *J. Med.*, pp. 329–344, 2011.

[2] Zhang D, Liu G, Shi J, Zhang J. Coeloglossum viride var. bracteatum extract attenuates D-galactose and NaNO2 induced memory impairment in mice. *J. Ethnopharmacol.*, vol. 104, no. 1–2, pp. 250–6, Mar. 2006.

[3] Vorhees CV, Williams MT. Morris water maze: procedures for assessing spatial and related forms of learning and memory. *Nat. Protoc.*, vol. 1, no. 2, pp. 848–58, Jan. 2006.

[4] Prut L., Belzung C. The open field as a paradigm to measure the effects of drugs on anxiety-like behaviors: A review. *Eur. J. Pharmacol.*, vol. 463, pp. 3–33, 2003.

[5] Provencher SW. Automatic quantitation of localized in vivo 1H spectra with LCModel. *NMR Biomed.*, vol. 14, no. 4, pp. 260–4, Jun. 2001.

Atrial Fibrillation Detection Based on Poincaré plot of RR Intervals

[1]G. Tuboly, [1]G. Kozmann

[1]Department of Electrical Engineering and Information Systems, Faculty of Information Technology, University of Pannonia, Veszprém, Hungary
Email: tuboly.gergely@virt.uni-pannon.hu

Abstract. *Atrial fibrillation (AF) is one of the most common types of arrhythmia which significantly increases the risk factor of stroke – especially in elderly population. In this paper an algorithm is presented which is suitable for the effective detection of AF, by using merely heart rate data as input. The method is based on the processing of Poincaré plots constructed from the set of 30 RR intervals. During the analysis of Poincaré plots the dispersion of points around the diagonal line is calculated and the number of clusters is determined by a self-developed cluster analyzer. The decision criterion of AF relies on these two parameters. On the one hand, the algorithm was tested on 10 AF and 10 normal rhythm ECG signals of the PhysioNet Database, achieving the average sensitivity (Se) of 98.69% and the average specificity (Sp) of 99.59%. On the other hand, 10 AF and 10 normal clinically confirmed records of a heart rate meter were also processed, resulting the average Se and Sp of 96.89% and 99.00%, respectively.*

Keywords: Atrial Fibrillation Detection, RR intervals, Poincaré plot, Cluster Analysis

1. Introduction

Atrial fibrillation (AF) is a supraventricular arrhythmia characterized by irregular atrial activation. Consequently, the performance of atrial myocardium decreases drastically [1]. Although this kind of arrhythmia is not directly life-threatening, its importance cannot be underestimated. In the 1980s the Framingham Study revealed that AF is a major risk factor of stroke [2]. Later on it was found that ischemic stroke associated with AF is approximately twice as likely to be fatal than without AF. The severe consequences of stroke among survivors are also claimed to be more frequent with the presence of this arrhythmia [3]. For the earliest start of AF treatment, it is essential to develop efficient detection algorithms that can identify this cardiac disorder as soon as possible, and can be made available for the vast majority of people – e.g. as part of smartphone applications [4].

There are two main ECG markers of AF. The first one is the replacement of P waves by high frequency low amplitude fibrillatory waves and the another one is the irregular heart rhythm [1]. The absence of P waves can be very difficult to investigate in ECG signals with significant level of noise, e.g. in telemedical circumstances. Thus it is practical to develop AF detection methods relying merely on the heart rate, which can be determined more easily and accurately than the presence of P wave. In the spirit of this approach, several algorithms have been proposed in the last decade based on Poincaré plots consisting of RR intervals [5-7]. Inspired by the work of Park et al. [7] we tried to develop an AF detector which surpasses the previously developed methods in terms of sensitivity (*Se*) and specificity (*Sp*).

2. Subject and Methods

The processing of ECG signals was designed according to the following two steps: preprocessing and AF detection.

Preprocessing

The filtering of ECG signals is performed by applying two Butterworth filters: a 4^{th} order highpass filter at 1 Hz to eliminate baseline wandering and a 8^{th} order lowpass filter at 40 Hz to remove power line interference and higher frequency noise components. After filtering, the cardiac cycles are identified by an adaptive QRS detection algorithm elaborated by Christov [8]. Finally, the fiducial point is determined for each cardiac cycle as the steepest point of the QRS complex.

Atrial fibrillation detection

The series of RR interval values is divided into sections containing 30 consecutive RR values. For each section, a "yes or no" type decision is made regarding AF according to the Poincaré plot related to the corresponding 30 RR intervals.

The Poincaré plot can be defined as follows. Let $I_1, I_2, I_3, I_4, ..., I_{n-1}, I_n$ denote the consecutive RR interval values in milliseconds. Then the coordinates of points in the Poincaré plot are given by the pairs of $(I_1, I_2), (I_2, I_3), ..., (I_{n-2}, I_{n-1}), (I_{n-1}, I_n)$. The dispersion of points around the diagonal line – which is an important factor in AF detection – is calculated as

$$d = \frac{\sqrt{\frac{1}{2(n-1)}\sum_{i=1}^{n-1}\left(I_i - I_{i+1}\right)^2 - \left(\frac{1}{(n-1)\sqrt{2}}\sum_{i=1}^{n-1}\left|I_i - I_{i+1}\right|\right)^2}}{\frac{1}{2(n-1)}\left(-I_1 - I_n + 2\sum_{i=1}^{n-1} I_i\right)} \tag{1}$$

where

I_i	i^{th} RR interval value [ms]
n	number of RR intervals (in our case: $n = 30$)
d	dispersion of points around the diagonal line [7].

If d is less than or equal to the empirical threshold of 0.06, then the algorithm does not detect significant level of heart rate irregularity, therefore it marks the section as non-AF. In the case of $d > 0.06$, an additional step is needed to check the distribution of points. If the high-dispersion set of points is systematically organized, the possibility of significant heart rate irregularity (therefore AF) can be ruled out. This can happen for example due to ectopic beats, that produce much more consequent rhythm changes than AF. However if d is high and no system can be found in the distribution of points, then a chaotic heart rhythm can be assumed. In this case, the algorithm marks the section as AF.

To decide whether the points in the high-dispersion Poincaré plot are systematically organized, we developed a clustering algorithm based on k-means [9], to determine the number of well-defined clusters. The principle of this method is to perform the k-means clustering with 9 different configurations: by setting the number of clusters from 2 to 10. After that the optimal clustering is chosen by the average silhouette values [9] corresponding to the results with different clustering configurations. If the maximum of the 9 average silhouette values (s_{max}) is below 0.85 then no optimal clustering is found and the number of detected clusters (k) is set to 1. Otherwise, k becomes the number of clusters corresponding to s_{max}.

Essentially, AF is detected if the high-dispersion ($d > 0.06$) Poincaré plot does not contain well-defined clusters (i.e. $k = 1$) or it has too many clusters (currently used threshold: $k = 10$). Four Poincaré plot examples can be seen in Fig. 1.

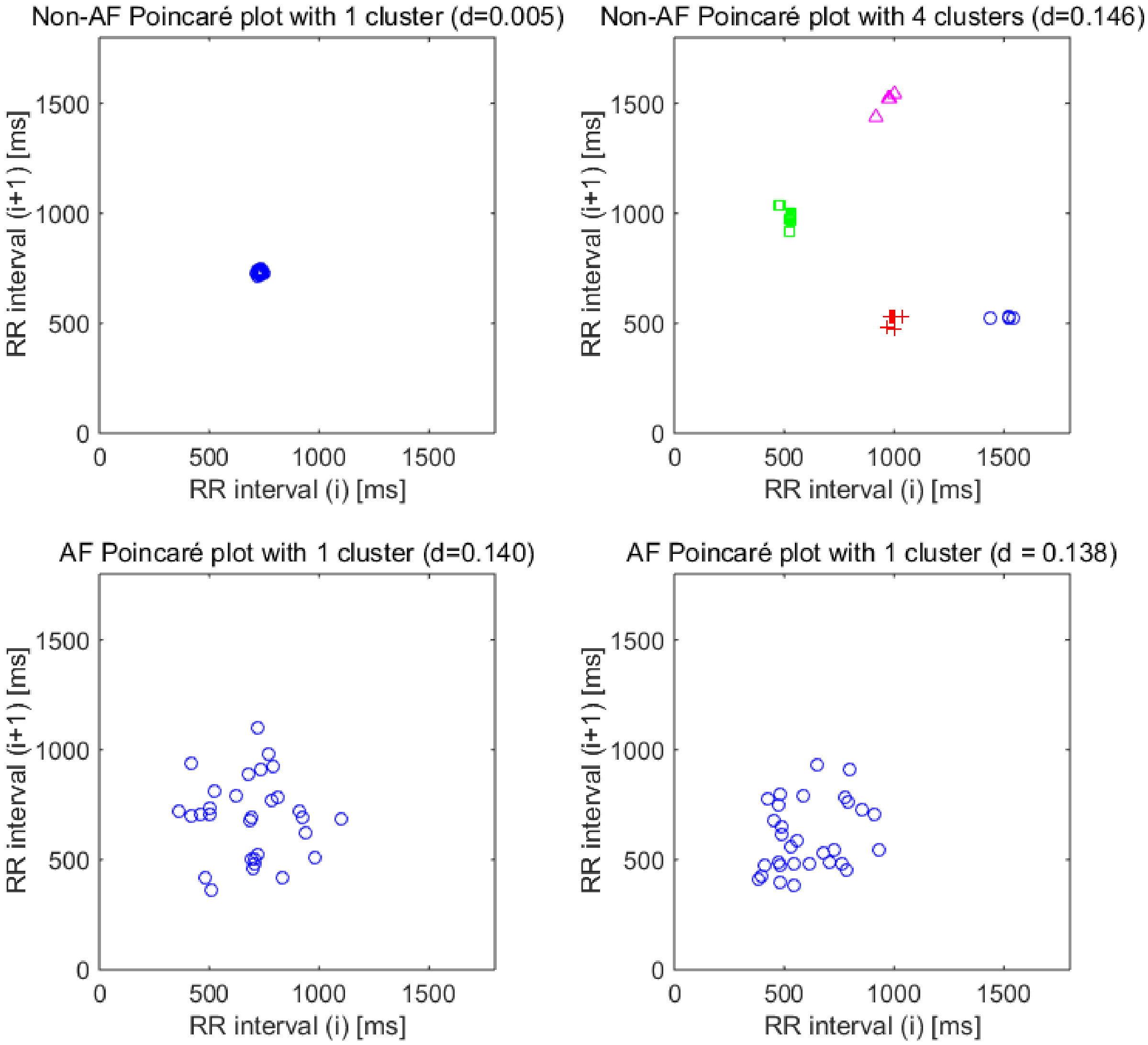

Fig. 1. Poincaré plots with the detected clusters. Upper left: non-AF case with 1 cluster and low dispersion. Upper right: non-AF case with 4 clusters and high dispersion. Lower left and right: AF cases with 1 cluster and high dispersion.

3. Results

The algorithm was tested on ECG signals of the PhysioNet Database. 10 AF records were selected from the Long-Term AF Database and 10 control signals were chosen from the MIT-BIH Normal Sinus Rhythm Database [10]. In each case, we processed around 500 consecutive RR sections (each section contained 30 RR intervals). In summary, 5263 AF and 5237 non-AF sections were analysed, resulting an average *Se* = 98.69% and an average *Sp* = 99.59%.

In addition, 10 AF and 10 normal clinically confirmed records of a heart rate meter (Cardiosport TP3, [11]) were also processed. These measurements were only few minutes long, producing 105 AF and 93 normal RR sections overall, resulting an average *Se* = 96.89% and an average *Sp* = 99.00%.

4. Discussion and Conclusions

Based on the results, the developed AF detection algorithm is very effective in terms of *Se* and *Sp*, considering both the ECG signals of PhysioNet and the records of a commercial heart rate meter. Since the similar previously published algorithms seem to be less efficient (e.g. *Se* = 91.4% and *Sp* = 92.9%, [7]), we claim that this is a significant progress in AF detection. By relying only on the heart rate, our method can be used in the processing of ECG signals even with relatively high level of noise, which makes it very suitable in telemedical or home care application.

Acknowledgements

This research has been supported by the European Union and co-funded by the European Social Fund. Project title: "Telemedicine-focused research activities in the field of Mathematics, Informatics and Medical sciences". Project number: TÁMOP-4.2.2.A-11/1/KONV-2012-0073.

References

[1] January CT, Wann LS, Alpert JS, Calkins H, Cigarroa JE, Conti JB, et al. 2014 AHA/ACC/HRS guideline for the management of patients with atrial fibrillation: a report of the American College of Cardiology/American Heart Association Task Force on Practice Guidelines and the Heart Rhythm Society. *Journal of the American College of Cardiology*, 64 (21): e1-e76, 2014.

[2] Wolf PA, Abbott RD, Kannel WB. Atrial Fibrillation: A Major Contributor to Stroke in the Elderly. The Framingham Study. *Archives of internal medicine*, 147 (9): 1561-1564, 1987.

[3] Lin HJ, Wolf PA, Kelly-Hayes M, Beiser AS, Kase CS, Benjamin EJ et al. Stroke severity in atrial fibrillation. The Framingham Study. *Stroke*, 27 (10): 1760-1764, 1996.

[4] Lindsberg PJ, Toivonen L, Diener HC. The atrial fibrillation epidemic is approaching the physician's door: will mobile technology improve detection? *BMC medicine*, 12 (1): 180, 2014.

[5] Thuraisingham RA. An electrocardiogram marker to detect paroxysmal atrial fibrillation. *Journal of Electrocardiology*, 40 (4): 344-347, 2007.

[6] Kikillus N, Hammer G, Wieland S, Bolz A. Algorithm for Identifying Patients with Paroxysmal Atrial Fibrillation without Appearance on the ECG. In proceedins of the 29th Annual International Conference of the IEEE/EMBS, 2007, 275-278.

[7] Park J, Lee S, Jeon M. Atrial fibrillation detection by heart rate variability in Poincare plot. *BioMedical Engineering OnLine*, 8 (38): 1-12, 2009.

[8] Christov II. Real time electrocardiogram QRS detection using combined adaptive threshold. *BioMedical Engineering OnLine*, 3 (28): 1-9, 2004.

[9] Kaufman L, Rousseeuw PJ. Finding Groups in Data: An Introduction to Cluster Analysis. John Wiley & Sons, Hoboken, 2009.

[10] Goldberger AL, Amaral LA, Glass L, Hausdorff JM, Ivanov PC, Mark RG et al. PhysioBank, PhysioToolkit, and PhysioNet. Components of a New Research Resource for Complex Physiologic Signals. *Circulation*, 101 (23): e215-e220, 2000.

[11] Welcome to Cardiosport, 2014.
Available from: "http://www.cardiosport.com/products.html". 28 March 2015.

Accuracy of the Body Surface Potential Approximation

E. Aidu, V. Trunov, A. Kalinin

Institute for Information Transmission Problems of the Russian Academy of Sciences (Kharkevich Institute), Moscow, Russia,
Email: aidu@iitp.ru

Abstract. *The problem of construction of body surface potential maps (BSPM) is important for many aspects of clinical practice. This study compares several methods of BSPM approximation, including three variants of spherical harmonics approximation and two variants of Laplacian interpolation. The methods were evaluated for their accuracy using tomographic and electrophysiological studies, as well as the results of computer modeling. The accuracy measures were locally estimated giving the distribution of these measures over the whole body and their variation during the cardiac cycle. Recommendations on the method implementation and proposals for further research are formulated.*

Keywords: Body Surface Potential; Noninvasive Electrocardiographic Imaging; Electrocardiotopography; Inverse ECG Problem.

1. Introduction

A comprehensive knowledge of the cardiac electric field is gained from electrophysiological studies using multiple electrodes (up to 400) evenly distributed over the whole body surface. Diagnostic analysis of synchronously recorded cardiac electrical signals may be conducted in two ways.

Historically the first approach is to construct and analyze electrocardiotopograms, i.e., body surface potential maps (BSPM) [1]. The position of electrodes on such maps is conditional, as it reflects their relative positioning on the chest with no allowance for individual inter-patient variability of their coordinates. For graphic BSPM presentation, local 2D approximation (interpolation) is conducted for continuous smooth filling of gaps between conditional points of measurement. BSPM approximation (interpolation) on detailed polygonal models of the body surface was intensively investigated as a tool for consolidation of the diagnostic experience with the data from different multi-electrode lead systems (e.g., [2 – 4]).

Another approach to diagnostic analysis implies the solution of inverse ECG problem and reconstruction of electrophysiological processes in the myocardium. BSPM approximation on the numerical model of the body surface is usually the preliminary step of the inverse ECG problem solution.

BSPM approximation is also necessary for the detection and spatial filtration of noise and various signal distortions.

2. Subject and Methods

Various methods of BSPM approximation were evaluated for their accuracy using tomographic and electrophysiological studies, as well as the results of computer modeling.

Data Preparation

Torso and heart models represented by triangular meshes and coordinates of 240 electrodes were obtained from electrophysiological studies using Amycard diagnostic complex [5].

Torso and heart tetrahedral finite element presentations and other necessary data, including sites and electrical parameters of stimulation, parameters of bidomain myocardial model, electric conductivity of the medium, were used as input data for the Cardiac Chaste software complex [6]. As a result, we obtained heart surface electrograms and potentials and electrocardiograms on the body surface during one cardiac cycle in each vertex of the corresponding triangular meshes.

Let us introduce the following notation: $\boldsymbol{r}_i = (x_i, y_i, z_i)$, Cartesian coordinates of the *i*-th vertex of the triangular mesh; t_j, time point of the *j*-th ECG. Then, $u(\boldsymbol{r}_i, t_j) = u_i(t_j) = u_{ij}$ are potentials in the *i*-th vertex of the torso triangular mesh in the *j*-th time point; $u_i(t)$, ECG in the *i*-th vertex; $\mathbf{u} = \{u_{ij}\}$.

'Measured' ECGs were defined as ECGs recorded at the electrode sites, and all of the rest records were classified as 'unknown'. Each of the below listed methods was used to approximate ECGs over the whole torso surface.

Approximation Methods

Multipole expansion or Spherical harmonics approximation. The general solution of the Laplace equation for a bounded domain that does not contain a neighborhood of the origin, can be presented as an expansion in terms of the singular and regular solid spherical harmonics [7]. Then ECG in any torso point can be presented in the form:

$$u(\boldsymbol{r}, t) = \sum_{n=0}^{\infty} \sum_{m=-n}^{n} \left(a_n^m(t)\, S_n^m(\boldsymbol{r}) + b_n^m(t)\, R_n^m(\boldsymbol{r}) \right), \quad (1)$$

where $S_n^m(\boldsymbol{r}) = r^{-(n+1)} Y_n^m(\theta, \varphi)$, $R_n^m(\boldsymbol{r}) = r^n Y_n^m(\theta, \varphi)$ are solid spherical functions; $Y_n^m(\theta, \varphi)$ are real spherical functions or harmonics; n and m are degree and order of the spherical function; (r, θ, φ) are spherical coordinates of the point $\boldsymbol{r}$; $a_n^m(t), b_n^m(t)$ are the time-dependent expansion coefficients.

The three variants of the spherical harmonics subset were used for approximation: singular solid functions with origin in the torso centre (SSF-S-Tc); singular solid functions with origin in the heart centre (SSF-S-Hc); singular and regular solid functions in the heart centre (SSF-SR).

Laplacian interpolation (LI) [8]. The Laplacian $\mathbf{L}$ for the torso surface triangle mesh is calculated and the ECGs $u_i(t)$ in all "unmeasured" vertices of the surface are adjusted to globally minimize the two-norm of the mesh potential Laplacian $\|\mathbf{Lu}\|$. There are several reasons that Biharmonic interpolation (BI) gives more smooth interpolation. To realize it, the double Laplacian two-norm $\|\mathbf{LLu}\|$ should be globally minimized.

Accuracy Measures

The differences between the potentials and their approximations were documented by several measures along only time, along only space and altogether.

The measures along time are integral measures of error during the whole cardiac cycle for every vertex. They are maps. The three such accuracy measures were used

$$\text{MaxErrMap}(\boldsymbol{r}_i) = \max_j \left| u_{ij} - \hat{u}_{ij} \right|, \text{ maximal error in vertex } i\,; \quad (2)$$

$$\mathrm{RMSErrMap}(\boldsymbol{r}_i) = \sqrt{\tfrac{1}{J}\sum_{j=1}^{J}(u_{ij} - \hat{u}_{ij})^2}\text{ , root mean square error in vertex } i; \qquad (3)$$

$$\mathrm{RelDifMap}(\boldsymbol{r}_i) = \sqrt{\sum_{j=1}^{J}(u_{ij} - \hat{u}_{ij})^2 \Big/ \sum_{j=1}^{J} u_{ij}^2}\text{ , relative mean square error in vertex } i\,. \quad (4)$$

The measures along space are integral measures of error over the whole torso surface. They are functions of time. The three such accuracy measures were used: MaxErrF(t_j), maximal error at instant *j*; RMSErrF(t_j), root mean square error; RelDifF(t_j), relative error. Their formulae are quite the same as (2)-(4), if in max and sum operators change *j* for *i*.

3. Results

The BSPMs were obtained for the two variants of the torso and heart triangular meshes and 7 variants of the cardiac pacing sites as described in the "Data preparation" section above. The approximation methods were applied, and the accuracy measures were locally estimated giving the distribution of these measures over the whole body and theirs variation during the cardiac cycle. The results for one typical case of accuracy variation during the cardiac cycle are shown in fig. 1, 2.

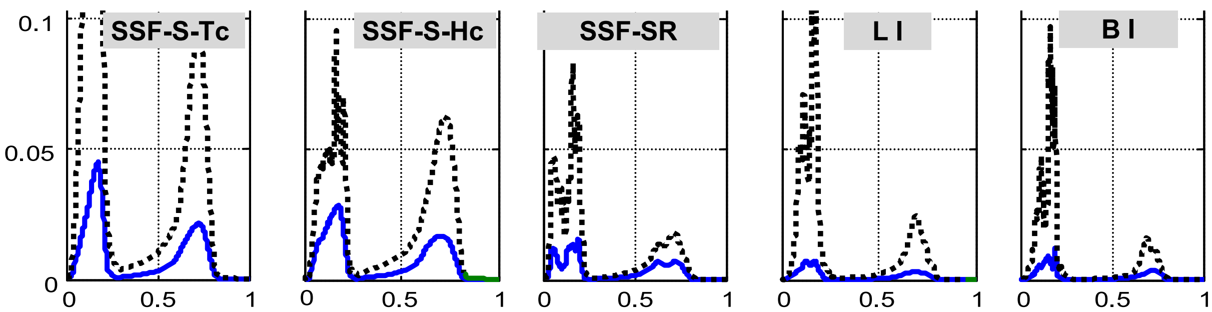

Fig. 1. Accuracy (RMSErrF, solid line; MaxErrF, dotted line) of the BSPM approximations during one cardiac cycle for different methods (designations of methods are introduced above).

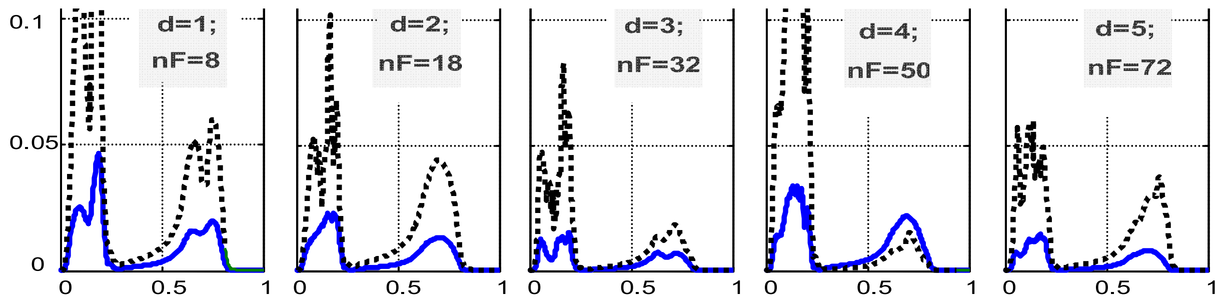

Fig. 2. Accuracy (RMSErrF, solid line; MaxErrF, dotted line) of the BSPM approximations during one cardiac cycle for the SSF-SR variant of the multipole expansion with different d, maximum degrees of spherical harmonics used for approximation (nF, total number of functions).

4. Discussion

No one methodology can be optimal in every context for every accuracy measure. Only three of the five methods tested may be advantageous in some cases or in terms of a certain accuracy measure. These include SSF-SR version of multipole expansion, Laplacian interpolation, and Biharmonic interpolation. It is more often that the latter turns out to be preferential. LI or BI always wins in terms of mean square metric, but SSF-SR or BI always superior in terms of uniform metric.

Multipole expansion with the origin in the torso center is always least accurate in terms of all measures. Multipole expansion should be as close as possible to the ‘center of gravity’ of the sources of the cardiac electric field.

Examining the maps of accuracy measures (2)-(4) reveals the regions with high errors. This is useful for the development of new and improved BSPM approximation methods.

It is noteworthy that accuracy of the BSPM approximation method was previously assessed using an *in vivo* model of the perfused canine heart placed into the electrolyte body model [4], whereas in the present study, we have conducted simulation experiments *in silico*.

The results obtained encourage a number of even more interesting studies, particularly, to evaluate the accuracy of the inverse ECG problem solution based on the potential reconstruction on the myocardial surface. It will be of interest to compare the results of such studies and to evaluate the effect of approximation accuracy on the accuracy of the inverse problem solution.

Acknowledgements

This work was partially supported by RFBR grant 13-01-00521A.

References

[1] Taccardi B. Distribution of Heart Potentials on the Thoracic Surface of Normal Human Subjects. *Circulation Research*, 12: 341-352, 1963.

[2] Hoekema R, Huiskamp GJ, Oostendorp TF, Uijen GJ, van Oosterom A. Lead system transformation for pooling of body surface map data: a surface Laplacian approach. *Journal of Electrocardiology*, 28(4): 344-5, 1995.

[3] Sándor G, Kozmann G, Cserjés Z, Farkas N, Préda I. Body surface potential field representation fidelity: analysis of map estimation procedures. *Journal of Electrocardiology*, 32(3): 253-61, 1999.

[4] MacLeod RS, Lux RL, Taccardi B., Translation of body surface maps between different electrode configurations using a three-dimensional interpolation scheme, in Proceedings of the International Congress on Electrocardiology, XXth Annual Meeting, 1993, 179–182.

[5] Bokeriya LA, Revishvili AS, Kalinin AV, Kalinin VV, Lyadzhina OA, and Fetisova EA. Hardware–Software System for Noninvasive Electrocardiographic Heart Examination Based on Inverse Problem of Electrocardiography. *Biomedical Engineering*, 42(6): 273-279, 2008.

[6] Pitt-Francis J, Pathmanathan P, Bernabeu MO, Bordas R, Cooper J, et al. Chaste: a test-driven approach to software development for biological modelling. *Computer Physics Communications*, 180: 2452-2471, 2009.

[7] Tikhonov AN, Samarskii AA. Equations of Mathematical Physics. Pergamon Press, London –New York, 1963.

[8] Oostendorp TF, van Oosterom A, and Huiskamp GJ. Interpolation on a triangulated 3D surface, *Journal of Computational Physics*, 80(2): 331–343, 1989.

Ventricular Repolarisation Analysed in Young Adult Men and Women Using Autocorrelation Maps

K. Kozlíková, M. Trnka, D. Kosnáč

Institute of Medical Physics, Biophysics, Informatics and Telemedicine,
Faculty of Medicine in Bratislava, Comenius University in Bratislava, Bratislava,
Slovak Republic
Email: katarina.kozlikova@fmed.uniba.sk

Abstract. *Electrocardiographic voltage distributions over the whole chest surface can be displayed in form of a set of isopotential maps (IPMs) that can be analysed quantitatively using the Pearson´s correlation coefficient allowing the construction of autocorrelation maps (ACMs). The aim of this retrospective study was to analyse the ACMs in young adults during the time standardised ST-T interval assuming slow changes of repolarisation. We constructed 21 IPMs at equidistant intervals for 89 young adult controls (41 men). For each ST-T interval, every IPM was compared with every IPM using Pearson's correlation coefficient r. These values were displayed in form of ACMs. The mean correlation coefficients of single ACMs were 0.838 ± 0.073. The high positive correlation r ≥ 0.900 covered in average (53 ± 13) % of the whole ACM area. Negative correlations occurred at the ACM borders with the mean value - 0.067 ± 0.062. We identified 4 basic types of ACMs according to the values of correlation coefficients. In the first 3 types, only positive correlation coefficients occurred. In the type I, the high positive correlation coefficients r ≥ 0.900 covered at least 75 % of each single ACM area (7 cases); in the type II, 50 % - 75 % (42 cases); in the type III, 25 % - 50 % (30 cases). In the type IV, negative correlation occurred (10 cases). This is in accordance with our hypotheses that the ST-T map pattern changes only slowly in healthy subjects.*

Keywords: Body surface potential mapping; Ventricular repolarisation; Autocorrelation maps; Time standardisation

1. Introduction

Voltage distributions over the whole chest surface can be displayed in form of a set of isopotential maps (IPMs) that can be analysed quantitatively using the Pearson´s correlation coefficient [1] allowing the construction of autocorrelation maps (ACMs). Autocorrelation maps concerning body surface potential mapping were first introduced in 1976 [2] to express the normal ventricular repolarization in the body surface distribution of T potentials. Until now, the autocorrelation maps were used to analyse the effect of intrathoracic heart position on electrocardiogram [3], and the atrial activation and ventricular depolarisation in healthy young adults [4, 5].

The aim of this retrospective study was to analyse the autocorrelation maps in young adults during the time normalised ST-T interval. We assumed that the ST-T map pattern changes only slowly in healthy subjects, therefore, the autocorrelation maps should present prevailingly positive values of correlation coefficients close to 1.

2. Subject and Methods

We studied 89 young adults, 48 women, 41 men, mean age (18.6 ± 0.4) years. None of the subjects had signs of cardiovascular diseases or cardiovascular risk. All subjects had normal

12-lead standard electrocardiographic and echocardiographic findings as well as blood pressure values.

Unipolar electrocardiograms for body surface potential mapping were registered using the limited 24-lead system after Barr based on a grid of 10 rows and 15 columns and processed using the mapping system ProCardio [6, 7]. All data were registered in supine position during normal expiration. Linear baselines were taken through two sequential TP segments in each electrocardiogram. The onset of the ST segment (equal to the QRS complex end) and the offset of the T wave were established manually from the root mean square signal. For time standardisation, the ST-T interval of each subject was divided into 20 equidistant parts. We constructed 21 isopotential maps for each subject [8]: the first map (map 1) corresponded to the ST segment beginning, the last map (map 21) to the T wave end (Fig. 1). For each subject, every isopotential map (let say map A) of a single beat was compared with every isopotential map (let say map B) of the same beat using the Pearson´s correlation coefficient r (r_{AB}) [1]

$$r_{AB} = \frac{\sum_{i=1}^{150}\left(U_{Ai} - \overline{U}_A\right)\cdot\left(U_{Bi} - \overline{U}_B\right)}{\sqrt{\sum_{i=1}^{150}\left(U_{Ai} - \overline{U}_A\right)^2}\cdot\sqrt{\sum_{i=1}^{150}\left(U_{Bi} - \overline{U}_B\right)^2}}, \tag{1}$$

where U_{Ai} (U_{Bi}) is the value of the electric potential in the i^{th} point of the map A (B),

$\overline{U}_A$ ($\overline{U}_B$) is the mean value of the electric potential of the whole map A (B).

Comparisons were presented in form of autocorrelation maps, i. e. squared graphs displaying the correlation coefficients of every possible pair of IPMs. The ACMs have the values $r = 1$ on the main diagonal and are symmetrical due to it (Fig. 2). We analyzed the regions with positive correlation $r \geq 0.500$ corresponding to slow potential distribution changes. Results are given in form of mean values ± standard deviations. Parameter comparisons between men and women were performed using unpaired t-test as all evaluated data were normally distributed.

3. Results

The isopotential maps of the ST-T interval revealed typical features (Fig. 1). Positive potentials appeared over the most of the anterior and the left lateral chest with the maximum located in the midprecordial region. Negative potentials occupied much smaller areas on the right upper anterior and posterior chest. The spatial distribution of positive potentials remained constant throughout the whole ST-T interval only changing the values of a single maximum. A single minimum moved between the upper anterior and posterior chest.

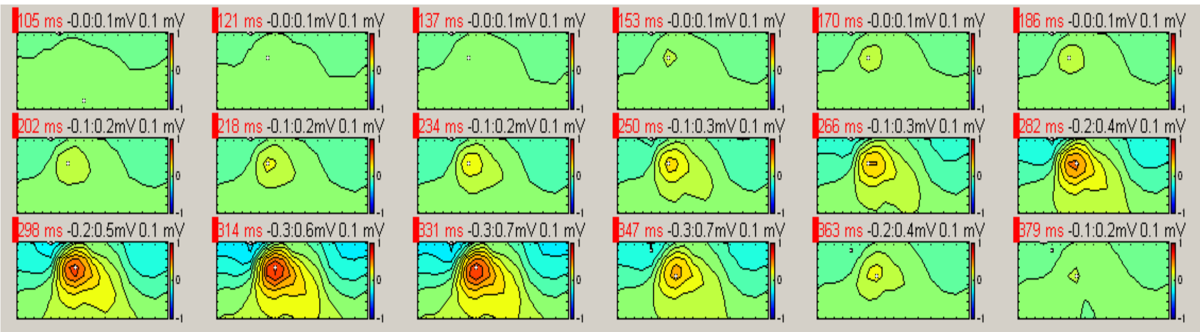

Fig. 1. The sequence of isopotential maps corresponding to the type II of ACM. The maps 2 to 19 are displayed. The left half of the rectangles corresponds to the anterior chest, the right half to the back.

The mean ST-T interval duration was (300 ± 31) ms. The potential values in single isopotential maps changed from - 0.55 mV to 1.51 mV in men, from - 0.54 mV to 0.93 mV in women. The mean correlation coefficients of single ACMs were 0.838 ± 0.073 (range $0.613 - 0.961$). The high positive correlation coefficients $r \geq 0.900$ covered in average (53 ± 13) % of the whole ACM area (mean r: 0.966 ± 0.004; 28 % – 88 %) while $r \geq 0.500$ covered in average (93 ± 7) % (mean: 0.875 ± 0.035; 71 % – 100 %). Negative correlations occurred at the borders of ACMs corresponding to the comparisons between the IPMs of the ST segment and the IPMs of the T wave. The mean value was -0.067 ± 0.062 (minimum $r = -0.164$). They were found in only 2 men (5 %), but in 8 women (17 %). Differences between men and women of selected analysed parameters are given in Table 1.

Table 1. Selected analysed parameters in men and women subgroups.

Parameter	Men	Women	Significance
ST-T interval duration [ms]	293 ± 31	306 ± 30	NS
T wave maximum [mV]	1.04 ± 0.25	0.57 ± 0.16	$p < 0.05$
T wave minimum [mV]	- 0.30 ± 0.10	- 0.28 ± 0.06	NS
Mean correlation coefficients of single ACMs	0.866 ± 0.048	0.815 ± 0.083	$p < 0.05$
Correlation coefficient $r \geq 0.900$ in ACMs [%]	57 ± 12	50 ± 14	$p < 0.05$
Mean of single ACMs for $r \geq 0.900$	0.968 ± 0.004	0.965 ± 0.003	$p < 0.05$
Correlation coefficient $r \geq 0.800$ in ACMs [%]	76 ± 12	67 ± 15	$p < 0.05$
Mean of single ACMs for $r \geq 0.800$	0.940 ± 0.011	0.935 ± 0.014	$p < 0.05$

We identified four basic types of ACMs according to the values of correlation coefficients. In the first three types, only positive correlation coefficients occurred. In the type I, the high positive correlation coefficients $r \geq 0.900$ occupied at least 75 % of each single ACM area (4 men, 3 women). In the type II, the high positive correlation coefficients occupied from 50 % to 75 % of each single ACM area (25 men, 17 women). In the type III, the high positive correlation coefficients occupied from 25 % to 50 % of each single ACM area (10 men, 20 women). In the type IV, negative correlation occurred (2 men, 8 women). According to the Pearson chi-square test, the frequency difference of ACM types between men and women is statistically significant ($p < 0.05$).

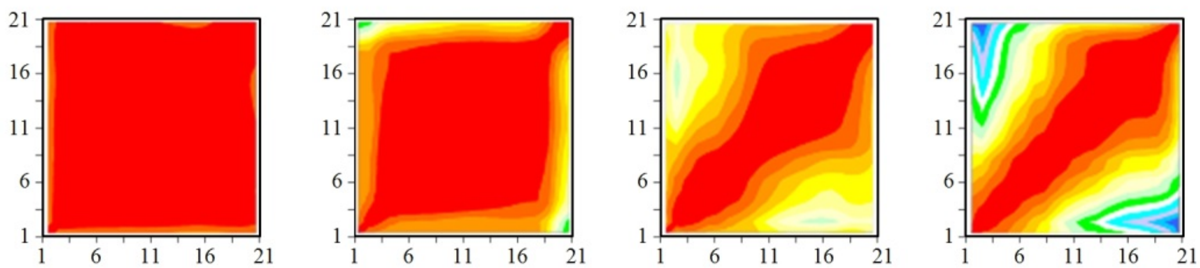

Fig. 2. Examples of 4 different types of autocorrelation maps for women (from left to right: I, II, III, and IV). The numbers on the axes correspond to the sequential map numbers. The red colour represents the correlation coefficients from 0.9 to 1.0; next colours represent lower values with the step 0.1. The autocorrelation map II corresponds to the isopotential maps in Fig. 1.

4. Discussion and Conclusions

According to the experimental study concerning the QT interval [3], the autocorrelation maps reflect only phenomena taking place in the electric source (myocardium). They are very little influenced by the geometry of the volume conductor (thorax) that connects it to the lead system, but very sensitive to variations in the activation sequence.

Although different shapes of autocorrelation maps occurred among the studied subjects, at least 28 % of the ACMs area revealed high correlation coefficient $r \geq 0.900$ in all subjects. This is in accordance with our hypothesis that the ST-T map pattern changes in healthy subjects only slowly, even very slowly.

We could identify 4 main types of autocorrelation maps. It is not clear yet, why they occurred with different frequency in men and in women, but it could be due to "flatter" isopotential maps in women than in men (such differences are known from previous studies, for example [9]). Very low potentials values (at noise level) lasting for longer time may occur at the beginning of the ST segment and at the end of the T wave and this also may influence the form of the autocorrelation maps in some cases.

Acknowledgements

This work was partially supported by the VEGA project 1/0727/14 from the Ministry of Education, Science, Research and Sport of the Slovak Republic.

References

[1] Kozlíková K, Martinka J. Základy spracovania biomedicínskych meraní II (Essentials of Biomedical Measurement Processing). Asklepios, Bratislava, 2009.

[2] Abildskov JA, Burgess MJ, Lux RL, Wyatt R, Vincent GM. The expression of normal ventricular repolarization in the body surface distribution of T potentials. *Circulation,* 54 (6): 901 – 906, 1976.

[3] Corlan AD, MacLeod RS, DeAmbroggi, L. The effect of intrathoracic heart position on electrocardiogram autocorrelation maps. *Journal of Electrocardiology,* 38 (2): 87 – 94, 2005.

[4] Kozlíková K. Atrial activation as displayed in autocorrelation maps of young adult controls – a preliminary study, in Electrocardiology 2013, Proceedings of the 40th International Congress on Electrocardiology. ÚM SAV, Bratislava, 2014, 165 – 167.

[5] Kozlíková K, Trnka M. Analysis of the ventricular depolarisation using autocorrelation maps in young adult men and women, in Electrocardiology 2014, Proceedings of the 41st International Congress on Electrocardiology. ÚM SAV, Bratislava, 2014, 229 – 232.

[6] Barr RC, Spach MS, Herman-Giddens GS. Selection of the number and positions of measuring locations for electrocardiography. *IEEE Transactions on Biomedical Engineering,* 18 (2): 125 – 138, 1971.

[7] Rosík V, Tyšler M, Turzová M. Portable device of for ECG mapping, in Proceedings of International Conference of Measurement. Frollo I and Plačková A, Editors. SAV, Bratislava, 1997, 367 – 370.

[8] Kozlíková K. Povrchové integrálové mapy, ich charakteristiky a metódy kvantitatívnej analýzy (Surface integral maps, their characteristics and methods of quantitative analysis). *Bratislavské lekárske Listy,* 91 (11): 815 – 823, 1990.

[9] Green LS, Lux RL, Haws CW, Williams RR, Hunt SC, Burgess MJ. Effects of age, sex, and body habitus on QRS and ST-T potential maps of 1100 normal subjects. *Circulation,* 71 (2): 244 – 253, 1985.

Modeling as a Tool for Understanding of Changes in ECG Signals

[1]J. Švehlíková, [1]J. Zelinka, [2]V. Szathmáry, [3]L. Bachárová, [1]M. Tyšler

[1]Institute of Measurement Science, Slovak Academy of Sciences, Bratislava, Slovakia
[2]Institute of Normal and Pathological Physiology, Slovak Academy of Sciences, Bratislava, Slovakia
[3]International Laser Centre, Bratislava, Slovakia
Email: jana.svehlikova@savba.sk

Abstract. *An updated program for modeling simplified heart geometry and simulation of action potentials propagation is presented. The implemented model allows simulation of geometry changes as well as changes in action potentials amplitude and duration. In propagation simulation real conduction velocities can be considered.*
Two different pathological situations were simulated using the model. First, only geometrical changes were applied simulating the left ventricular hypertrophy, second, only action potentials properties simulating activation propagation velocity were changed. The resulting ECG signals on the torso were very similar. It is shown that modeling and simulation is useful for explaining of discrepant observations in clinical diagnostics.

Keywords: Computational heart model, Simulation of activation propagation, Modeling of pathologies, ECG signals simulation

1. Introduction

Electrocardiography is considered a basic diagnostic method for different heart diseases providing essential information about the electrical properties of myocytes and activation wavefront propagation that results in systematic electro-mechanical work of the heart.

In this paper an updated programming tool for creation of simplified heart model and simulation of its normal and pathological activity is presented. The importance of using such model for interpretation of observed ECG signals is demonstrated on examples of two different pathologies.

2. Subject and Methods

Heart Model

A simplified geometry of ventricles consists of parts of eight ellipsoids as it is described in [1]. To model the physiological or pathological heterogeneity of action potentials durations, the walls of both ventricles are divided in five layers. For each layer an action potential amplitude and duration can be defined separately as well as the activation propagation velocity (Fig. 1). To mimic Purkynje fiber properties, the activation propagation velocity in the endocardial layer is defined three times higher than in other tissues. It is possible to change the properties of the model in a selected subvolume. The whole modeled volume is discretized using regular cubic grid. The properties of myocardial cells are assigned to each grid element.

The action potential propagation is started in selected starting points according Durrer's experimental findings [2] and later developes in spherical or ellipsoidal wavefronts using cellular automaton principle. The former algorithm computed the activation in discrete time steps, the new algorithm allows set real values of conduction velocity in simulation and maximal time step in propagation is chosen by the formula:

$$max\_time\_step = model\_grid\_resolution/max\_model\_conduction\_velocity \qquad (1)$$

A realistic action potential shape is predefined according the experiments on canine wedge preparations [3],[4]. The resulting equivalent electrical heart generator is computed in the form of a multiple-dipole. The number/density of dipoles can be chosen as multiple/fold of the basic volumetric element of the model.

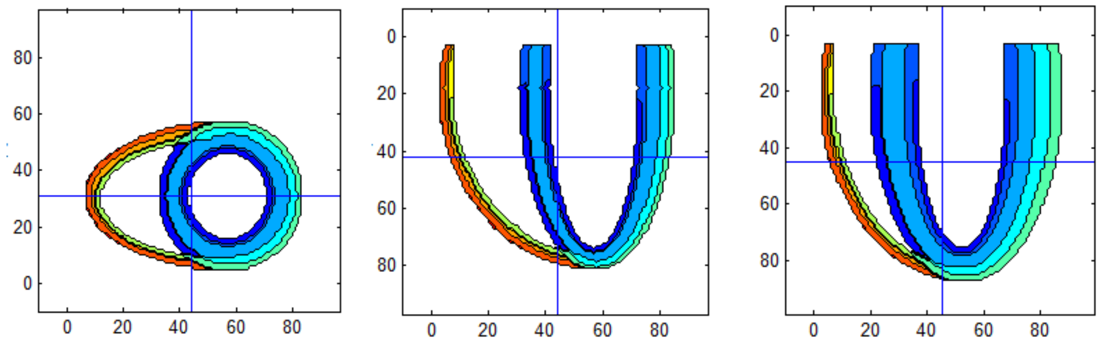

Fig. 1. From left to right: Horizontal and vertical crosssection of the normal heart model. Vertical crossection of the model of left ventricular hypertrophy. The axes mark dimensions of the model in mm.

Software Implementation of the Model

The program for modeling the heart as an equivalent electric generator is designed as a modular system with graphical user interface. Each program module is represented by separate worksheet (Fig. 2):

M module – creates the geometrical model, allows individual detailed definition of the model size, thickness of anterior, lateral and posterior walls of each ventricle as well as the thickness of ventricular septum and apex. The extent of Pukynje fibers area can also be defined.

P module – allows the definition of a pathological area in the modeled myocardium as the intersection of the modeled heart volume with additionally defined ellipsoid representing the pathological area. In the pathological area the properties of action potentials and conduction velocities can be predefined. This process can be applied multiple times to model complex pathologies.

S module – in this worksheet the activation propagation is simulated in the defined volume. The additional input data are the file with positions and timing of starting points of activation and the file with definitions of action potential properties and conduction velocity.

I module – serves for inspecting the simulation results in the form of 3D visualization of the resulting heart vector and imaging of the propagation wave in chosen time instants. Time series of the x,y,z components of the heart vector are also depicted.

Simulations

Two types of pathologies were simulated using the model. First, anatomical enlargement of the left ventricle called left ventricular hypertrophy (LVH). The thickness of the left ventricular wall was increased by 50% without any other changes of the modeled myocardium. Second, structural changes were modeled, when the conduction velocity in the midwall layers of the left ventricle was slowed down by 50% without any changes in size of the heart model.

The resulting equivalent electrical generator of the heart (multiple-dipole) was inserted to realistically shaped torso model assuming the presence of main inhomogeneities such as the ventricular cavities filled with blood with three times higher conductivity than the mean conductivity of the torso and lung lobes with a conductivity four times lower than the mean conductivity of the torso. The ECG signals s(t) on the torso surface were computed using boundary element method [5] by the formula:

$$s(t) = Ad(t) \qquad (2)$$

where A is the time-independent transfer matrix representing the geometrical properties of the torso as piece-wise homogeneous volume conductor and d(t) is the vector of dipole moments of equivalent heart generator in each time step.

The standard 12-leads ECG signals were computed on the surface of an inhomogeneous torso model for both simulated pathological situations and compared with normal reference simulation.

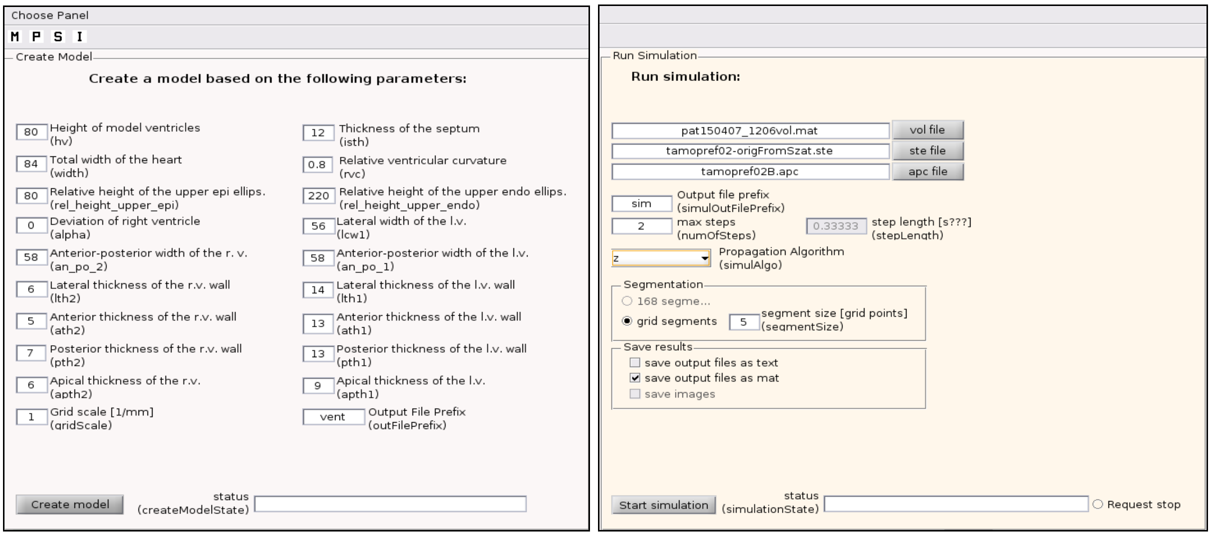

Fig. 2. Examples of worksheets for model creation (M module) and simulation (S module).

3. Results

The resulting ECG signals in precordial leads V1 – V6 computed from normal activation and two simulated pathologies are depicted in Fig 3.

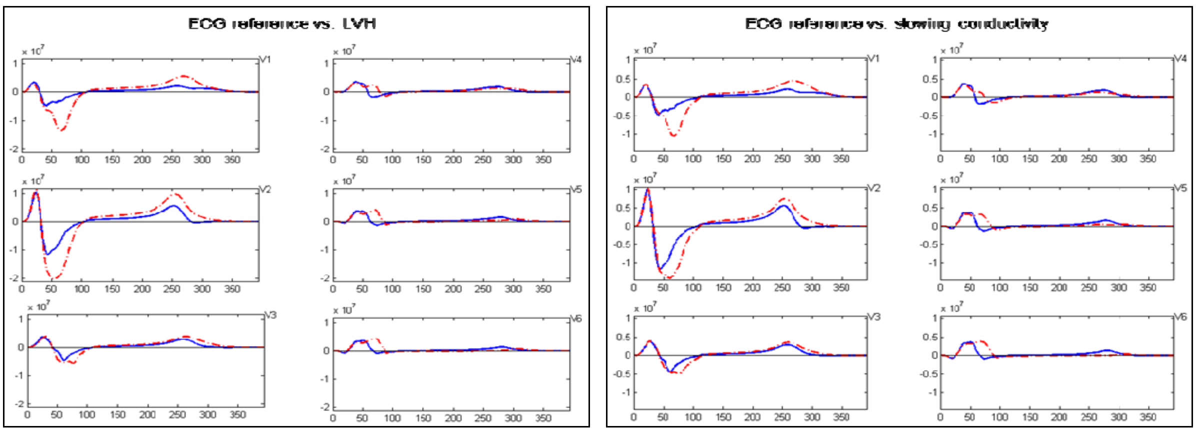

Fig. 3. Computed ECG signals in leads V1-V6. Full lines represent reference signals for normal activation. Dashed lines represent ECG signals for simulation of the left ventricular hypertrophy (left) and for the simulation of slowing down a conduction velocity in the mid-wall layers of the left ventricle (right).

4. Discussion and Conclusions

As it can be seen from the results, the both figures (Fig.3 left, right) are very similar. Dashed lines represent ECG signals of two different types of pathologies. The changes are apparent in the QRS complex as well as in the T wave. The increased signals amplitudes are one of the specific signs of the left ventricular hypertrophy and they were explained by the enlargement of the left ventricular mass [6]. However, in practice, using echocardiographic diagnostic methods in many cases the enlargement of left ventricular mass was not confirmed in spite of the presence of the ECG LVH markers [7]. Our second simulation in which only the conduction velocity was changed can provide an explanation for the contradiction mentioned above.

Although the presented heart model has numerous simplifications, it allows study of various factors influencing the resulting ECG signals, what is helpful in understanding ambiguous or questionable diagnostic results.

Acknowledgements

This work was supported by research grants No.2/0131/13 and No.2/0138/13 of the Vega Grant Agency in Slovakia.

References

[1] Szathmary V, Osvald R. An Interactive Computer-Model of Propagated Activation with Analytically Defined Geometry of Ventricles. *Computers and Biomedical Research,* 27: 27–38, 1994.

[2] Durrer D, van Dam RT, Freud GE, Janse MS, Meijler FL, Arzbaecher RC. Total Excitation of the Isolated Human Heart. *Circulation,* 41: 899–912, 1970.

[3] Tysler M, Turzova M, Svehlikova J. Modeling of heart repolarization using realistic action potentials. *Measurement Science Review,* 3: 37–40, 2003.

[4] Yan GX, Shimizu W, Antzelevitch C. Characteristics and distribution of M cells in arterially perfused canine left ventricular wedge preparations. *Circulation,* 98: 1921–7, 1998.

[5] Stenroos M, Haueisen J. Boundary element computations in the forward and inverse problems of electrocardiography: Comparison of collocation and Galerkin weightings. *IEEE Transactions on Biomedical Engineering,* 55: 2124–33, 2008.

[6] Bacharova L, Szathmary V, Kovalcik M, Mateasik A. Effect of changes in left ventricular anatomy and conduction velocity on the QRS voltage and morphology in left ventricular hypertrophy : a model study. *Journal of Electrocardiology,* 43: 200–8, 2010.

[7] Pewsner D, Jüni P, Egger M, Battaglia M, Sundström J, Bachmann LM. Accuracy of electrocardiography in diagnosis of left ventricular hypertrophy in arterial hypertension: systematic review. *British Medical Journal,* 335: 711-715, 2007.

Analysis of the Activation Propagation Velocity in the Slab Model of the Cardiac Tissue

E. Cocherová

Institute of Measurement Science, SAS, Bratislava, Slovakia
Email: elena.cocherova@stuba.sk

Abstract. *In the study, the activation propagation velocity in cardiac tissue was simulated in COMSOL Multiphysics environment using the modified FitzHugh-Nagumo model of the electrical excitation. The influence of different model parameters and stimulation conditions on the activation propagation velocity was evaluated. The homogeneous slab model was used as the model of the atrial wall. Results of simulations could help to explain the differences in activation propagation velocities in measured data.*

Keywords: Myocardium, Monodomain Model, Activation Propagation Velocity

1. Introduction

Electrophysiological activity of human cardiac cells may be modelled using local or space membrane models. The space models suitable for simulation of electrical activation propagation are based on reaction - diffusion equations in monodomain or bidomain models [1]. Electrical activation in the monodomain model of the cardiac tissue is described by the partial differential equation:

$$\frac{\partial V_m}{\partial t} = \frac{1}{\beta C_m} \nabla \cdot (\sigma \nabla V_m) - \frac{1}{C_m}(I_{ion} + I_s) \tag{1}$$

where V_m is the membrane potential
β is the membrane surface-to-volume ratio
C_m is the membrane capacitance per unit area
σ is the tissue conductivity
I_{ion} is the ionic transmembrane current density per unit area and
I_s is the stimulation current density per unit area.

Using substitutions

$$D = \frac{\sigma}{\beta C_m}, \qquad i_{ion} = \frac{I_{ion}}{C_m} \qquad \text{and} \qquad i_s = \frac{I_s}{C_m} \qquad (2), (3), (4)$$

the equation (1) describing the time change of the membrane potential V_m can be rewritten in the form:

$$\frac{\partial V_m}{\partial t} = \nabla \cdot (D \nabla V_m) - i_{ion} + i_s \tag{5}$$

The local membrane models could be obtained from (5) by omitting the space derivatives:

$$\frac{\partial V_m}{\partial t} = -i_{ion} + i_s \tag{6}$$

The local membrane properties of atrial cells may be modelled using various less or more complex models, e.g. the Courtemanche-Ramirez-Nattel (CRN) model [2] or the modified FitzHugh-Nagumo (FHN) model [3] - [6]. In the CRN model, the ionic current comprises different membrane currents, e. g. the fast sodium current, calcium, potassium and other membrane currents. Such physiological models could comprise tens of dependent variables and so tens of ordinary differential equations.

If using the less computationally demanding equations of the modified FHN model, the normalized ionic transmembrane current density i_{ion} from equation (6) is:

$$i_{ion} = k\,c_1(V_m - B)\left(-\frac{(V_m - B)}{A} + a\right)\left(-\frac{(V_m - B)}{A} + 1\right) + k\,c_2 R(V_m - B) \qquad (7)$$

and

$$\frac{dR}{dt} = k\,e\left(\frac{(V_m - B)}{A} - R\right) \qquad (8)$$

where R is the recovery variable,
a is relating to the excitation threshold,
e is relating to the excitability,
A is the action potential amplitude,
B is the resting membrane potential, and
c_1, c_2 and k are the other membrane-specific parameters.

2. Subject and Methods

In the article, the atrial wall was approximated by SLAB 1 or SLAB 2 model of size 50 x 50 x 2 mm or 5 x 50 x 2 mm (i. e., the thickness of the atrial wall was $w = 2$ mm). The 1D propagation in SLAB 2 represented a plane wave, while the 2D propagation in SLAB 1 represented a convex (circular) wave front.

If not mentioned otherwise, as the default model parameters were used modified FHN atrial membrane parameters from [5]: $a = 0.13$, $c_1 = 2.6$, $c_2 = 1$, $e = 0.0132$, $k = 1000\ \text{s}^{-1}$, $A = 0.120$ V, $B = -0.085$ V, $D = 0.0005\ \text{m}^2/\text{s}$ (relating to σ = 0.5 S/m) and $i_s = 40$ A/F (lasting 0.002 s). Stimulation current was applied in the centre of the SLAB 1 model in the cylindrical area, with base radius of 2 mm or at one side of the SLAB 2 model, in the area where $x <= 2$ mm (gray areas in Fig. 1). Initial values of the membrane potential and the recovery variable were -0.085 V and 0, respectively.

Models were numerically solved using the FGMRES iterative solver in COMSOL Multiphysics environment. The zero Neumann boundary condition was used, with exception of the two lateral boundaries in the SLAB 2 with periodic boundary conditions (Fig. 1).

Velocity of activation propagation was evaluated for default FHN model parameter values in both SLAB1 and SLAB 2 models, as well as for 20 % decrease and 20% increase of selected parameters in SLAB 2 model (Table 1).

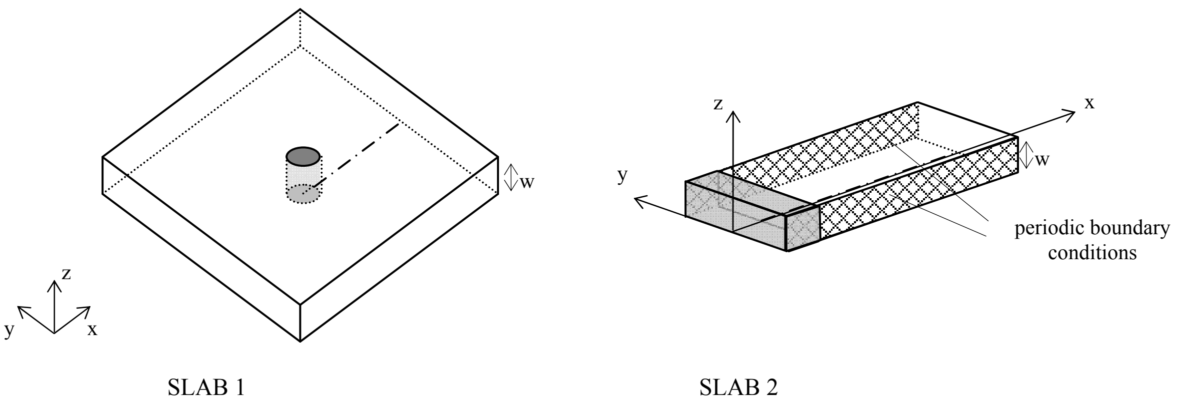

Fig. 1. The atrial wall models: SLAB 1 (left), with coordination system centered in the middle of the stimulated cylinder, and SLAB 2 (right).

3. Results

Examples of the membrane potential V_m distribution in the SLAB 1 and SLAB 2 models are shown in Fig. 2.

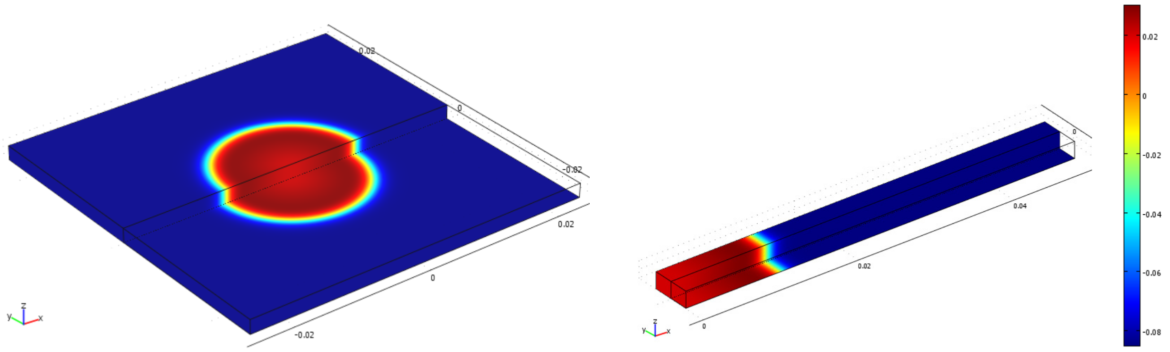

Fig. 2. Distribution of the membrane potential V_m [V] in the SLAB 1 (left), and SLAB 2 (right) in time 0.02 s after stimulation onset (activated areas are in the middle and on the left of the slabs).

Activation propagation velocity was determined from action potentials (APs) obtained in separate points along the positive x axis (shown as dot-and-dashed lines in Fig. 1) using time instants when AP crossed the -20 mV value (marked by circles in Fig. 3A). Activation propagation velocity v in SLAB 1 in the area near to stimulation area was smaller than in SLAB 2 (Fig. 3 B). The velocity of activation propagation in SLAB 1 increased with the distance from the stimulation area. This is in accordance with data measured in [7] and this phenomenon relates to the convex curvature of activation front.

For the default values of FHN model parameters, activation propagation velocity in SLAB 2 reached a constant value of 0.586 m/s within few millimetres away from the stimulation area (Fig. 3 B).

Further, in SLAB 2 the activation propagation velocity v was evaluated also for 20 % decrease and 20% increase of selected FHN model parameter values, results are shown in Table 1.

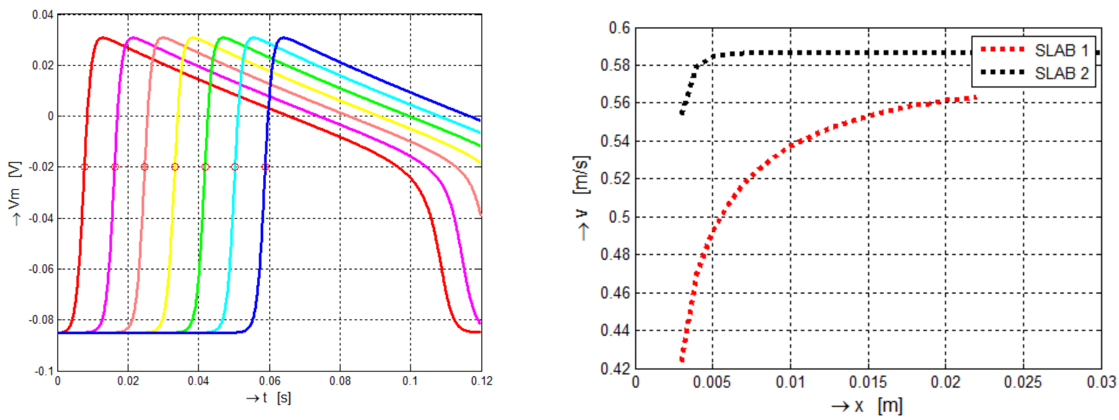

A B

Fig. 3. Time courses of the membrane potential V_m for default FHN model parameters at points $x = 0.005$ m, 0.010 m, ..., 0.035 m in the SLAB 2 (A), dependence of activation propagation velocity v on the distance from of the stimulated area in the SLAB 1 and SLAB 2 (B).

Table 1. Sensitivity of the propagation velocity *v* on the FHN model parameters in the SLAB 2 model.

	20% decrease of selected parameter		20% increase of selected parameter	
Parameter	v [m/s]	Δv [%]	v [m/s]	Δv [%]
c_1	0.519	-11.5	0.646	10.1
k [s^{-1}]	0.525	-10.6	0.642	9.6
D [m^2/s]	0.525	-10.5	0.642	9.5
a	0.630	7.4	0.543	-7.5

4. Conclusions

Sensitivity of the propagation velocity of the activation front was examined with respect to parameters of the modified FitzHugh-Nagumo atrial tissue model. The most pronounced effect on the propagation velocity was observed for parameters: c_1, that relates mainly to conductivity of sodium membrane channels and rate of their opening; *k*, that relates mainly to the speed of all reactions (depending e. g. on temperature); *a*, relating to the excitation threshold and *D*, determined mainly by the tissue conductivity. The effect of other examined parameters was less than 1 %. The differences in activation propagation velocities in SLAB 1 and SLAB 2 correspond to different shapes of activation fronts, wherein the plane activation front reached higher velocities than the convex activation front.

Acknowledgements

The work was supported by grant 2/0131/13 from the VEGA grant agency and by grant APVV-0513-10 from the Slovak Research and Development Agency.

References

[1] Potse M, Dubé B, Richer J, Vinet A, Gulrajani RMA. Comparison of Monodomain and Bidomain Reaction-Diffusion Models for Action Potential Propagation in the Human Heart. *IEEE Transactions on Biomedical Engineering*, 53 (12): 2425-2435, 2006.

[2] Courtemanche M, Ramirez RJ, Nattel S. Ionic mechanisms underlying human atrial action potential properties: insights from a mathematical model. *The American Journal of Physiology - Heart and Circulatory Physiology*, 275 (1): 301-321, 1998.

[3] FitzHugh R. Impulses and physiological states in theoretical models of nerve membrane. *Biophysical J.*, 1: 445-466, 1961.

[4] Nagumo J, Arimoto S, Yoshizawa S. An active pulse transmission line simulating nerve axon. *Proc. IRE.*, 50: 2061-2070, 1962.

[5] Sovilj S, Magjarević R, Lovell NH, Dokos S. A simplified 3D model of whole heart electrical activity and 12-lead ECG generation. *Computational and Mathematical Methods in Medicine*, 2013, doi:10.1155/2013/134208.

[6] Macfarlane PW, van Oosterom A, Pahlm O, Kligfield P, Janse M, Camm J. Comprehensive Electrocardiology. Springer-Verlag, London, 2011.

[7] Clayton RH, - Bernus O, Cherry EM, et al. Models of cardiac tissue electrophysiology: Progress, challenges and open questions. *Progress in Biophysics and Molecular Biology*, 104 (1-3): 22-48, 2011.

Influence of Modeled Heart Cavities on the Noninvasive Localization of Ectopic Ventricular Activity

[1,2]O. Punshchykova, [3]J. Švehlíková, [1]P. Kneppo, [1]R. Grünes, [1,4]K. Sedova, [1]B. Senysh, [5]P. Osmančík, [5]J. Žďárská, [5]D. Heřman, [1,3]M. Tyšler

[1]Czech Technical University in Prague, Kladno, Czech Republic,
[2]National Technical University of Ukraine "KPI", Kyiv, Ukraine,
[3]Institute of Measurement Science SAS, Bratislava, Slovakia,
[4]Institute of Physiology RAS, Syktyvkar, Russia,
[5]University Hospital Kralovske Vinohrady, Prague, Czech Republic
Email: olena.punshchykova@fbmi.cvut.cz

Abstract. *Noninvasive localization of premature ectopic ventricular activity was performed for four patients using integral body surface potential maps and inverse solution to one dipole. The influence of two different models of heart cavities on the accuracy of the inverse solution was studied. Despite improvement in some cases, better accuracy of the inverse solution for more detailed models of heart cavities was generally not achieved.*

Keywords: Body Surface Potential Mapping, Ectopic Ventricular Activation, Inhomogeneous Torso Model, Inverse Problem of Electrocardiography

1. Introduction

It is a common knowledge that premature ventricular contractions (PVC), or ventricular ectopic beats, in patients with local myocardial ischemia or infarction might cause ventricular fibrillation and even lead to death. It is possible to treat PVC with anti-arrhythmic drugs or by a catheter radiofrequency ablation. The ablation is an invasive procedure, performed during the electrophysiological study (EPS) in a catheter laboratory. The catheter is guided under X-ray control and/or by a 3D navigational system to localize the focus of the pathological PVC. The duration of such a procedure usually takes up to several hours. Therefore, it would be desirable to localize the PVC origin before the invasive EPS and significantly decrease the time of the ablation procedure. The identification of local changes in ventricles from body surface potential maps (BSPMs) was proposed in [1]. Body surface potential mapping is a noninvasive method and in comparison to invasive EPS it does not present additional risks as bleeding, infection, damage of the vessel, perforation of the heart, etc. The localization of the PVC from BSPMs by an inverse solution might be influenced by various factors, such as the number of measured leads for BSPM computation, the type of the used BSPMs, the model of the patient's geometry or the method of the inverse solution.

In this study noninvasive localization of the PVC origin in four patients was performed using an inverse solution to one dipole [2] computed from integral BSPMs. The influence of the extent of patient-specific heart cavities included in the torso model on the inverse solution fidelity was studied.

2. Material and Methods

Two male (Pat002-57Y, Pat004-77Y) and two female patients (Pat005-43Y, Pat007-54Y) with premature ventricular activity underwent a measurement of BSPM, computer tomography (CT) scanning and intracardiac EPS using the Carto 3 navigation system. All procedures were approved by Ethic Committee of the University Hospital Kralovske

Vinohrady where the data were collected after obtaining written informed consent from patients.

Multichannel ECG recording was performed using ProCardio-8 system [3] with 1 kHz sampling frequency with 96 (12 stripes with 8) evenly distributed Ag/AgCl electrodes on patient's thorax (Fig. 1A). For each patient five ectopic beats were selected from the ECG record and processed to compute integral BSPMs for initial 0-15 ms interval of the ventricular activation [4] (Fig. 1C). After multichannel ECG recording, the patients underwent CT scanning of the whole torso (slice thickness 0.3 mm) with fixed ECG electrodes (Fig. 1B).

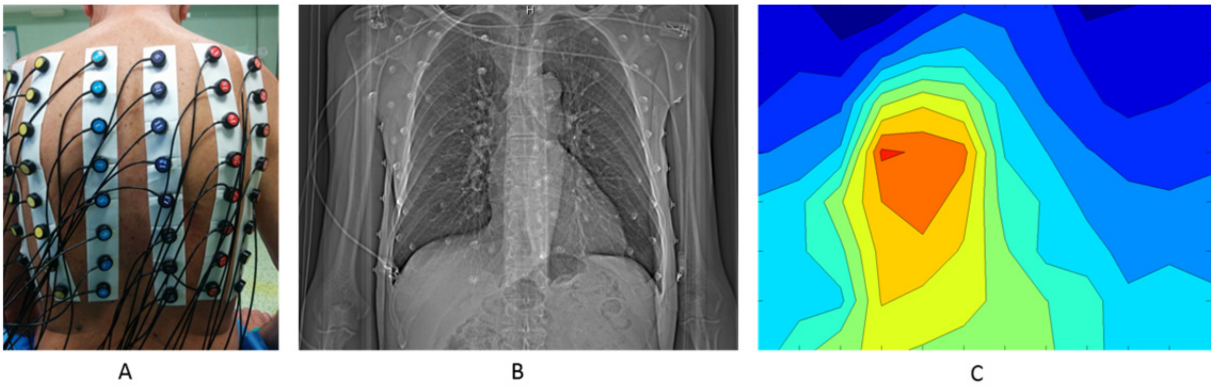

Fig. 1. Input data acquisition for inverse solution. A: Measurement of the multichannel ECG record using 96 electrodes. B: CT scan of torso with electrodes. C: Computed integral body surface potential map for the initial interval of premature ventricular activation.

From the obtained CT images patient-specific 3D geometries of torso, lungs, atria and ventricles (epi- and endocardial surfaces), aorta and pulmonary artery were created (Fig. 2) using TomoCon Workstation® software ver. 20.

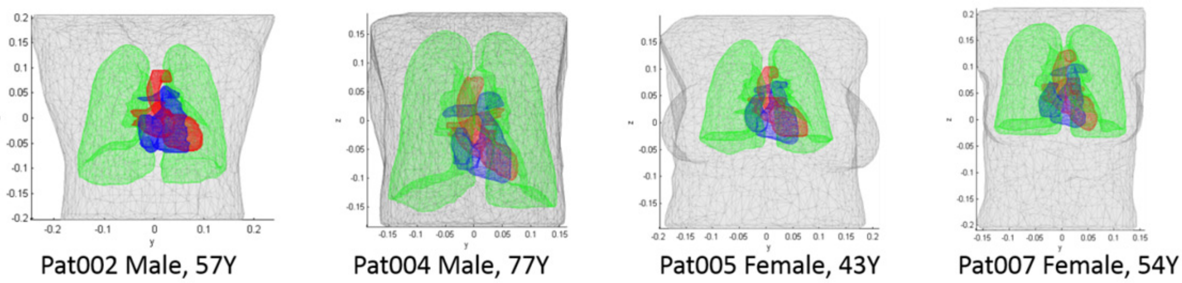

Fig. 2. CT-based 3D models of patient-specific geometries of the torso, lungs and heart cavities.

On the next day during intracardiac EPS the ablation of the PVC origin was performed in each patient. Location of the pathological arrhythmogenic tissue was defined using the electrophysiological navigation system. Results of the intracardiac intervention were compared with the results of the inverse solution computed from the measured BSPMs.

The inverse solution was based on dipole model of the cardiac electric generator computed from measured integral BSPMs representing the initial PVC activation. Integral BSPMs can be generally defined as

$$im = \int_I \phi(t)dt \qquad (1)$$

where im integral body surface potential map,
$\phi(t)$ body surface potential map in specific time instant,
I examined time interval of the initial activation.

Assuming that the area activated during the examined time interval can be represented by a single dipole, the inverse solution in predefined position in the ventricles can be computed using the equation:

$$G' = \mathbf{B}^{+} im \qquad (2)$$

where G' dipolar equivalent integral generator,
$\mathbf{B}^{+}$ the pseudo-inverse of the transfer matrix B representing relation between the equivalent heart generator and potentials on the torso representing an inhomogeneous volume conductor.

Equivalent generator G' was computed for all positions of a regular 5 mm grid in the modeled ventricular myocardium. The best position of the equivalent integral generator was selected according to the criterion of the minimal value of relative residual error RRE between the input integral BSPM (*im*) and BSPM computed from the equivalent integral generator G' (*Rm*) obtained by the formula:

$$RRE = \sqrt{\sum_{i=1}^{n}(im_i - Rm_i)^2 \Big/ \sum_{i=1}^{n} im_i^2} \qquad (3)$$

where n is the number of measured points in the BSPM.

Two torso models, reconstructed from the CT scan were studied: A - torso with lungs and ventricles; B - torso with lungs, atria, ventricles, aorta (AO) and pulmonary artery (PA). The conductivity of lungs was assumed four times lower than conductivity of the torso and conductivity of heart cavities, AO and PA was assumed three times higher than conductivity of the torso.

3. Results

Results of the intracardial EPS were compared with the inverse solution from 5 ectopic beats for both torso models in each patient. The number of "correct" resulting dipoles out of five possible results for both torso models in each patient is shown in Fig. 3. For Pat002 no correct inverse solution was obtained. In Fig. 4 all inverse solutions for Pat002 are localized in the anterior part of the left ventricle, while the successful ablation was performed in the posterior part of the left ventricle (see arrows in Fig. 4C). For three other patients the results were more promising, the best results were obtained for Pat005 where 4 inversely found dipoles corresponded with the position of the initial ectopic activity found during the EPS.

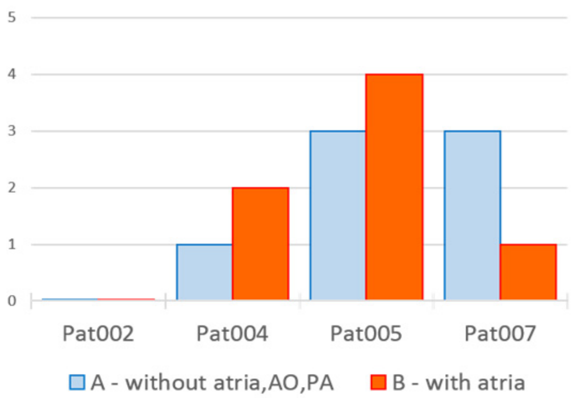

Fig. 3. Number of correct resulting dipoles for all 5 ectopic beats and for both types of the torso model (without and with atria, AO, PA).

4. Discussion and Conclusion

Preliminary results of the influence of the atria, aorta and pulmonary artery cavities models on inverse solution were obtained. For torso model A, the results in the female group were considerably better than in the male group. Comparison of the A and B models did not show whether the presence of atria, aorta and pulmonary artery in the models of cavities filled with blood can increase the accuracy of the inverse solution.

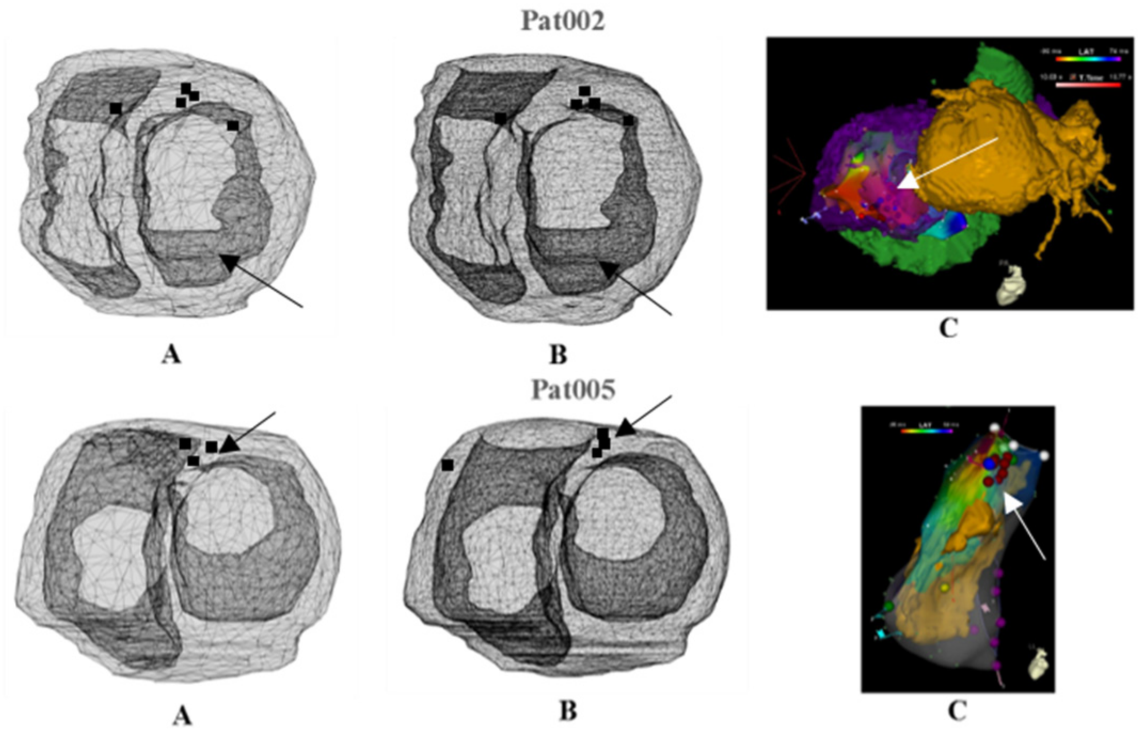

Fig. 4. Results of the inverse solution and ablation positions from the electrophysiological studies for Pat002 (the worst) and Pat005 (the best). A: heart model with only ventricular cavities; B: heart model with ventricular and atrial cavities, AO and PA (apex to base view); C: intracardial model from the Carto 3 navigation system with CT.

Obtained "incorrect" results can be caused by improper selection of the time instants for integral BSPMs, inaccuracy in the models from CT scans, improper signal processing, simplifications in the thorax model (conductivities of lungs and blood in heart cavities), grid size of the mesh for predefined dipole positions, etc. All above mentioned factors should be studied in more details. However, despite the noninvasive localization was not accurate enough in all patients, the presented method could be helpful for shortening the time needed for successful ablation procedure.

Acknowledgements

The present study was supported by research grants 3/229/OHK4/3T/17 from the SGS CVUT in the Czech Republic, APVV-0513-10 from the Research and Development Agency and 2/0131/13 from the VEGA Grant Agency in Slovakia and by the project Biomedicine University Research Park Bratislava, Slovakia (ITMS code 26240220087).

References

[1] Tysler M, Kneppo P, Turzova M, Svehlikova J, Karas S, Heblakova E et al. Noninvasive Assessment of Local Myocardium Repolarization Changes Using High Resolution Surface ECG Mapping. *Physiological Research*, 56(1): S133–S141, 2007.

[2] Tysler M., Tinova M. Representation of Myocardium Depolarization by Simple Models. In proceedings of the Computers in cardiology*,* 1993, 703-706.

[3] Rosík V, Karas S, Hebláková E, Tyšler M, Filipová S. Portable Device for High Resolution ECG Mapping. *Measurement Science Review,* 7(6): 57-61, 2007.

[4] Punshchykova O, Svehlikova J, Kneppo P, Maksymenko V, Tysler M. Noninvasive Localization of the Ectopic Focus Using Time Integral ECG Mapping. *Experimental and Clinical Cardiology*, 20(7): 1564-1570, 2014.

Magnetic Resonance Imaging of PEG Magnetite Nanoparticles with and without BSA Protein

[1]D. Gogola, [1]O. Štrbák, [1]A. Krafčík, [1]M. Masárová, [2]I. Antal, [2]M. Kubovcikova, [2]M. Koneracka, [2]V. Zavisova, [2]P. Kopcansky, [1]I. Frollo

[1]Institute of Measurement Science, SAS, Bratislava, Slovakia,
[2]Institute of Experimental Physics SAS, Kosice, Slovakia
Email: daniel.gogola@savba.sk

Abstract. *Aim of the study was to detect whether there is a observation change in MRI contras of magnetite nanoparticles stabilized with PEG, after BSA protein binding on the surface of particles. The reason is applicability of this feature in clinical practice, for molecular imaging of specific substances. Contrast agent can bind to this specific substance (e.g. marker of disease) and the change of MRI contrast will indicate the presence of marker.*

Keywords: MRI, Magnetic Nanoparticles, BSA Protein, Contrast Change

1. Introduction

Magnetic nanoparticles in combination with some proteins, like bovine serum albumin (BSA) or human serum albumin (HAS), have wide range of applications such as drug delivery systems, or as contrast agents for MRI [1-3]. Proteins play role also as biomarkers of various diseases (e.g. inflammation, cancer), and their changes in concentration levels are associated with various pathological processes. Magnetic nanoparticles, as a consequence of proton spins coupling with larger magnetic moments of nanoparticles, reduce the transversal relaxation (T2 relaxation time), increasing thus a relaxivity of water. This can be done also by some proteins. Therefore the goal of this study was determine the degree of influence of BSA protein to the T2 relaxation time, after binding to the magnetic nanoparticles. Such interaction could have an influence on the contrast properties of MRI contrast agents, disturbing such desired MRI information.

2. Subject and Methods

Magnetite nanoparticles with BSA protein and without BSA protein were diluted on 20 samples, so that the each of the samples had half concentration of previous one. The samples were measured at clinical MRI scanner ESAOTE 0.178 T, with Spin Echo T2 weight pulse

Table 1. The table of samples with concentrations.

No.	Concentration [mg/ml]	No.	Concentration [mg/ml]	No.	Concentration [mg/ml]	No.	Concentration [mg/ml]
0	reference	6	0.11875	12	9.277e-3	18	7.248e-5
1	3.8	7	0.029687	13	4.6387e-4	19	3.62e-6
2	1.9	8	0.0148	14	1.16e-4	20	1.81e-6
3	0.95	9	7.42e-3	15	5.798e-5	-	-
4	0.475	10	3.71e-3	16	2.899e-5	-	-
5	0.2375	11	1.855e-3	17	1.45e-5	-	-

sequence, with parameters TR = 1500 ms, TE = 50 ms, 2 acquisitions, 5 mm slice thickness, 0 mm gap, 5 slices, FOV = 256x256. The samples were made at first from magnetic liquid MKPEG-20.000-6C without BSA protein and with concentration of magnetite c_{mag} = 7.6 mg/ml and next from magnetic liquid MKPEG-20.000-BSA-6Cc with binding of protein BSA and concentration of magnetite c_{mag} = 3.8 mg/ml.

3. Results

The Fig.1 and Fig.2 shows relative change of signal/contrast intensity (due to reference) with increase of concentration of magnetic nanoparticles in the samples. Both liquids (with/without BSA protein) were diluted so that the same number of sample has the same concentration for comparison. Progress of curves of both liquids was very similar but not equal. The chart shows, that the biggest change of contrast was achieved with samples 7 to 11 for both liquids. Concentration of magnetit nanoparticles were between 3.71 to 59.375 µg/ml. Recommended concentration of clinical contrast agent - Resovist (on basis of iron oxide) in the bloodstream is approximately 97 µg/ml.

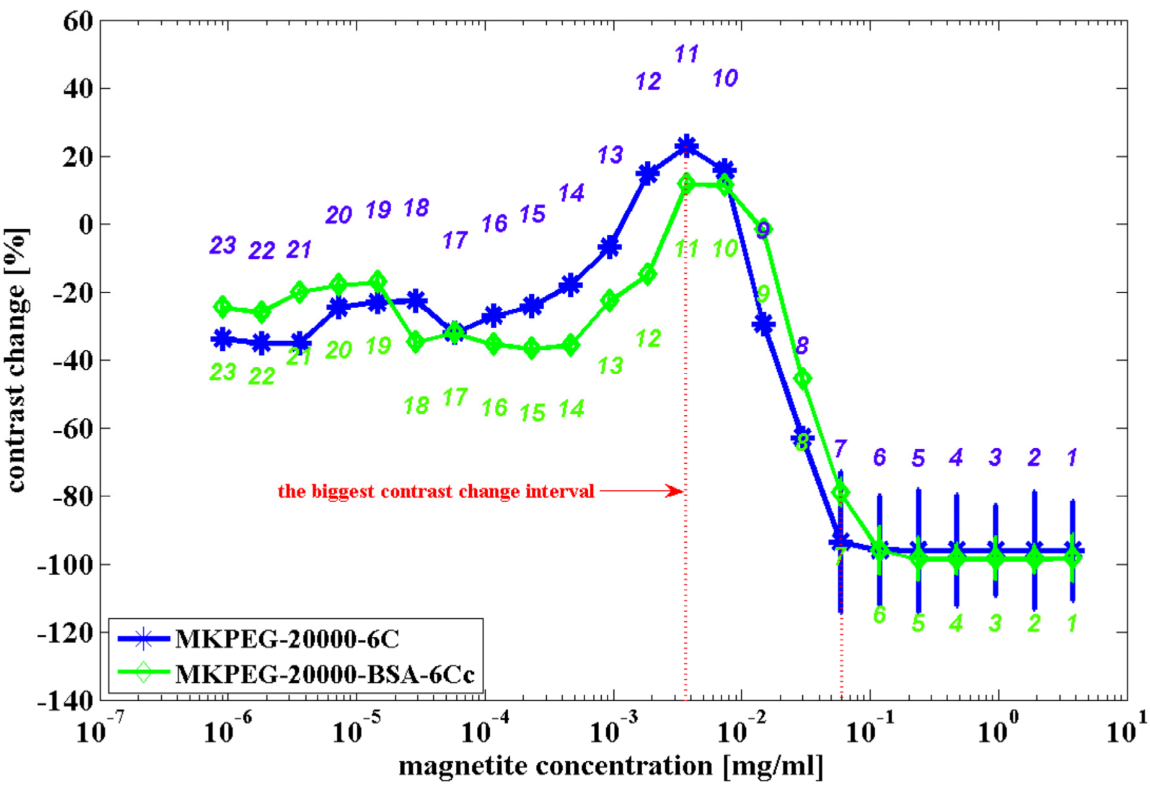

Fig. 1. Relative changes of signal intensity between each samples for both liquid (with/without protein).

The higher concentrations of the magnetite nanoparticles caused large artefacts and measurement error. In fact they have been virtually indistinguishable. The samples 11 to 14 was distinguishable at the border of visibility with the naked eye for our system (approximately 15 % of contrast change), but showed increase of signal intensity with increase of concentration, which not agree with theory, because the iron oxide particles should shorten T_2 relaxation time. The samples 14 to 23 were also hardly distinguishable for us. Therefore, for practical use, in terms of the changes in contrast, as the most appropriate appears the interval with concentration from 3.71 to 59.375 mg/ml for both fluids.

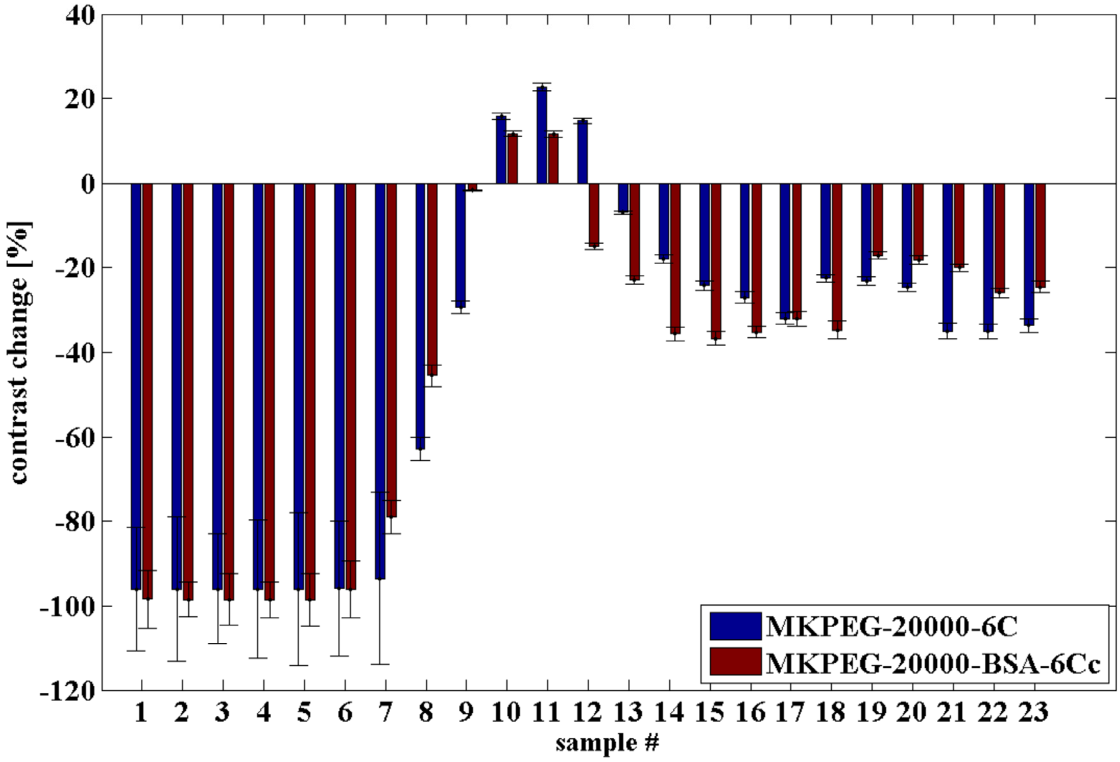

Fig. 2. The image show changes of contrast between each liquid and its concentration.

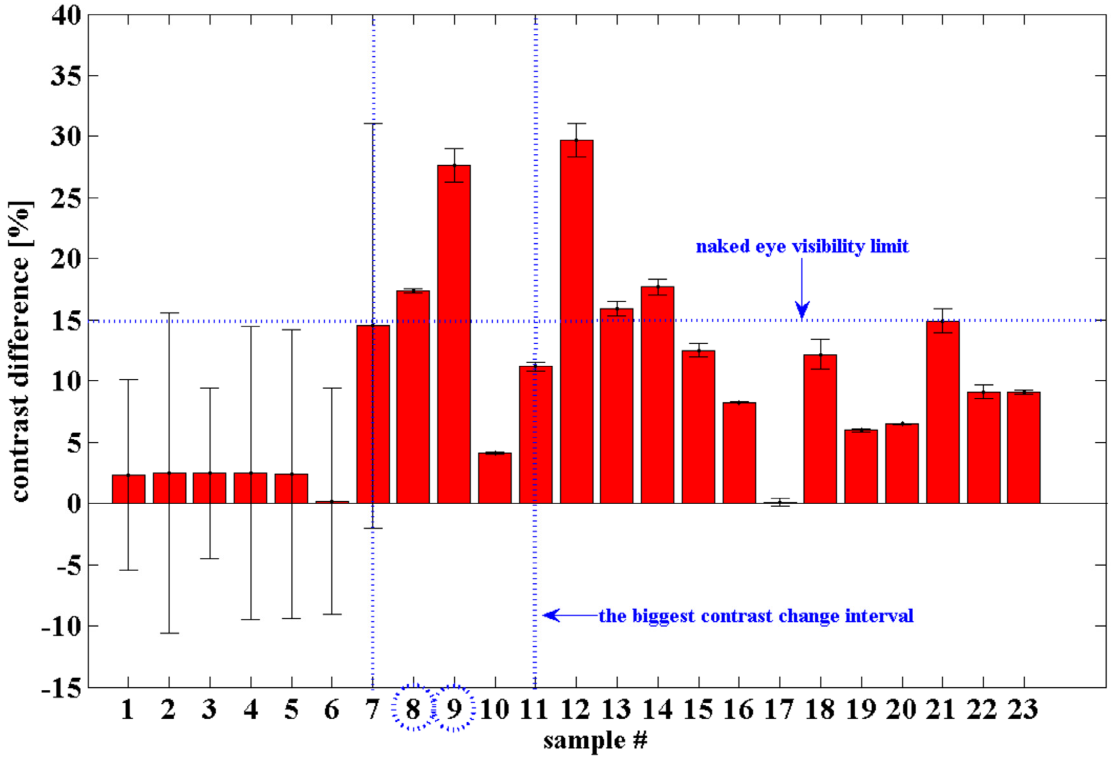

Fig. 3. The figure shows the difference in contrast between individual samples with and without binding of BSA protein.

The Fig. 3 shows, that the highest changes in the contrast between individual liquids is dissymmetrical for samples 7 to 9, 11 to 16, and 19 and 21. Above the border of visibility with naked eye are only 5 samples: 8, 9 12, 13 and 14. The sample number 12 achieved maximum change of contrast (almost 30 %). But this sample is out of interval in the fig.1 (samples number. 7 to 11). Therefore, for practical use of magnetite nanoparticles stabilized with PEG 20000 in clinical practice we recommend to use the concentration interval from 14.8 to 29.7 μg/ml.

4. Discussion and Conclusions

We have shown, that for the magnetite nanoparticles stabilized with PEG 20000 in specific concentration interval exist significant difference in contrast (visible with naked eye) after binding of protein BSA to the surface of particles. This effect can be use in clinical practice for molecular magnetic resonance imaging of specific proteins, as biomarkers of pathological processes.

Acknowledgements

This work was supported by the Slovak Scientific Grant Agency VEGA 2/0013/14 and within the project of the Slovak Research and Development Agency Nr. APVV-0431-12.

References

[1] Grinstaff MW, Suslick KS. Nanoqueous liquid filled microcapsules. *Polymer Preprints,* 1 (32): 255-256, 1991.

[2] Grinstaff MW, Kolbeck KA, Magin RL, Suslick KS, Webb A, Wilmes LJ, Wong M, Desai NP, Sandford PA, Soon-Shiong P. Fluorocarbon filled protein microspheres as contrast agents for MRI. *Proc. Soc. Biomater,* (20): 113-115, 1994.

[3] Suslick KS, Grinstaff MW. Protein microencapsulation of nonaqueous liquids. *J. Am. Chem. Soc.,* (112): 7807-7809,1990.

Measurement of the Magnetite Nanoparticles Relaxivity During Encapsulation into PLA Carriers

[1]O. Strbak, [1]D. Gogola, [2]L. Baciak, [1]A. Krafcik, [1]M. Masarova, [3]I. Antal, [3]M. Kubovcikova, [3]M. Koneracka, [3]V. Zavisova, [3]P. Kopcansky, [1]I. Frollo

[1]Institute of Measurement Science, Slovak Academy of Sciences, Bratislava, Slovakia
[2]Faculty of Chemical and Food Technology, Slovak Technical University, Bratislava, Slovakia
[3]Institute of Experimental Physics, Slovak Academy of Sciences, Kosice, Slovakia
Email: oliver.strbak@savba.sk

Abstract. *PLA are widely used in biomedical applications, where imaging modalities are very demanded. However, there is lack of information about contrast properties of the PLA-magnetite carriers in MRI. We measured the transversal relaxivity of the magnetite nanoparticles during the encapsulation into PLA spheres. The aim was to find a non-invasive method for particles tracking in different loading conditions. MRI measurements were performed on 4.7 T and 0.178 T systems, and the relative contrast,* T_2*, and* r_2 *of the PLA with encapsulated (interior) and non-encapsulated (exterior) particles were evaluated and compared. The results showed that these parameters can be used in determination of the magnetic nanoparticles encapsulation into PLA carriers, as well as in quantification of the particles loading rate.*

Keywords: Magnetite nanoparticles, encapsulation, PLA, MRI, relaxivity

1. Introduction

The polymer-based magnetic nanoparticles attract a big interest in biomedical applications, including MRI, hyperthermia, molecules separation, drug targeting, etc [1]. Many types of polymers have been used to synthesise these carriers, however only polylactide (PLA) based polymers are currently widely used in medical applications (tissue engineering). It is mainly because of their excellent biocompatible, biodegradable properties, and low toxicity [1]. Although the magnetic behaviour, as well as general properties of PLA-based magnetic carriers are quite well described [2], there is lack of information about contrast properties of such carriers in MRI applications, in regard to the encapsulation rate of magnetic nanoparticles. We studied the relative contrast, transverse relaxation time (T_2), and transverse relaxivity (r_2) changes induced by different loading factor of magnetite nanoparticles (MGNPs) into PLA carriers.

2. Material and Methods

PLA-magnetite carriers were prepared by a modified nanoprecipitation method as described in [3]. Briefly, 100 mg of PLA was dissolved in 10 ml of acetone to prepare the organic phase. An aqueous colloid was prepared by mixing a solution of Pluronic F68 as a stabilizing agent (25.6 mg in 5 ml) and 0.8 ml magnetic fluid (45 mg Fe_3O_4 / ml). Then, the organic phase was added drop-wise into the aqueous colloid and stirred vigorously for several hours to allow complete evaporation of the organic solvent at room temperature. A turbid nanoparticle suspension was formed. Not-loaded PLA nanospheres were prepared by the same way but without the magnetic nanoparticles. PLA samples were divided into three groups: (i) PLA without MGNPs, (ii) PLA with non-encapsulated MGNPs, and (iii) PLA with encapsulated MGNPs. Moreover, the last were prepared with different MGNPs input concentration (1, 2, 5, 7, 17, 30 mg/ml), resulting in diverse loading factor of MGNPs into

PLA. Relaxivity measurements were performed on 4.7 T system (VARIAN). Images were acquired with T_2-weighted Multi Echo Multi Slice (MEMS) sequence, TR = 81 ms, TE = 8 ms. Transverse relaxation time T_2 was obtained spectroscopically by CPMG-echo pulse sequence. For comparison, relative contrast measurements were performed also on 0.178 T system (ESAOTE), where images were acquired with standard T_2 weighted Gradient Echo protocol (TR = 3500 ms, TE = 22 ms). For all samples, relative contrast, transverse relaxation time T_2, and transverse relaxivity r_2 values were evaluated and compared.

Relative contrast is defined as follows:

$$RC= (I - I_0)/I_0 \quad (1)$$

where I_0 - signal intensity without magnetite nanoparticles (reference), and I - signal intensity with magnetite nanoparticles.

Transverse relaxivity r_2 is calculated as follows:

$$R_2 = r_2C + R_2^0 \quad (2)$$

where R_2^0 - transverse relaxation rate of in the absence of nanoparticles, R_2 - transverse relaxation rate in the presence of nanoparticles, C - nanoparticles concentration

Dynamic Light Scattering (DLS) method (Zetasizer, Malvern Instruments) was used to determine the hydrodynamic diameter (D_{hydro}) of loaded, as well as non-loaded PLA carriers.

3. Results and Discussion

We found that PLA itself have negligible influence to the relaxation properties of medium, as well as to the contrast properties of magnetite nanoparticles (Fig. 1). Relative contrast change for PLA carriers with non-loaded ("out"), and loaded ("in") magnetite nanoparticles with different input concentration is shown in Fig. 2. Although we are able to distinguish among loaded and non-loaded sample, and moreover among different input concentrations, there is no clear gradual pattern enable to determine the rate of nanoparticles encapsulation, based on the different input concentration.

Different situation is in Fig. 3 and Fig. 4, where we can see clearer gradual difference among loaded PLA carriers. Fig. 3 represents T_2 relaxation time decrease for both types of carriers. Different between 5 and 7 mg/ml for input concentration in loaded carriers is not so obvious, as for other concentrations (Fig. 4). For the highest input concentration (30 mg/ml) the encapsulation process probably starts to be saturated, and sample produce T_2 and r_2 values similar to sample with non-loaded particles (“out”). However, transverse relaxivity r_2 provides the best differentiation for the followed encapsulation process.

Hydrodynamic diameters of loaded, as well as non-loaded PLA carriers obtained by DLS method are shown in Table 1.

Table 1: Hydrodynamic diameters of MGNPs and PLA carriers.

	MGNPs	**out**	**in (1 mg/ml)**	**in (2 mg/ml)**	**in (5 mg/ml)**	**in (7 mg/ml)**	**in (17 mg/ml)**	**in (30 mg/ml)**
D_{hydro} (nm)	71.5	146.1	167.1	139.85	138.85	122.6	205.35	173.35
PDI	0.137	0.*11*	0.062	0.18	0.17	0.1	0.1	0.1

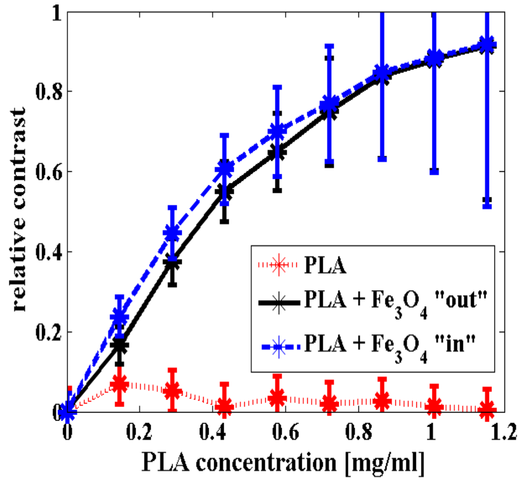

Fig. 1. Comparison of relative contrast values of blank PLA carriers and PLA carriers with loaded ("in") and non-loaded ("out") MGNPs in concentration range of 0.01 – 0.08 mg/ml.

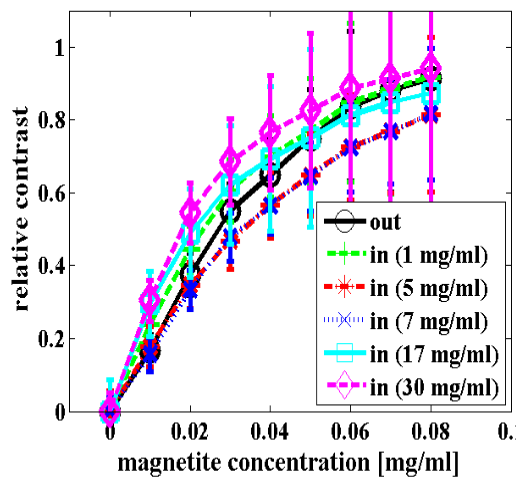

Fig. 2. Relative contrast values of PLA carriers with loaded ("in") and non-loaded ("out") MGNPs in concentration range of 0.01 – 0.08 mg/ml. Loaded samples are with different MGNPs input concentration (1, 5, 7, 17, 30 mg/ml).

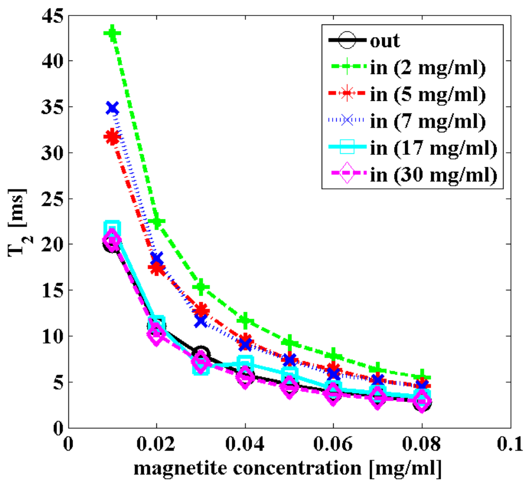

Fig. 3. T2 relaxation time values of MGNPs outside PLA ("out"), and encapsulated into PLA ("in") with different MGNPs input concentration (2, 5, 7, 17, 30 mg/ml).

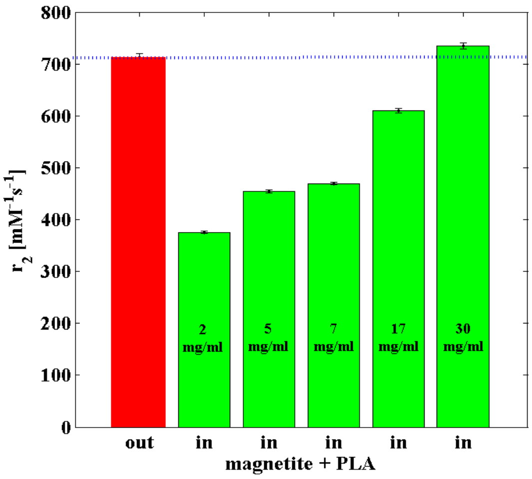

Fig. 4. Transverse relaxivity r2 values of MGNPs outside PLA (out), and encapsulated into PLA (in) with different MGNPs input concentration (2, 5, 7, 17, 30 mg/ml).

4. Conclusions

The studied MRI parameters (relative contrast, T2, r2) of the MGNPs encapsulated into PLA showed that we are able to distinguish between loaded and non-loaded particles, as well as to determine the rate of encapsulation from the relaxivity value. It can be used in biomedical applications to determine the rate of drugs encapsulation into carrier system, as well as for drug delivery, and drug release tracking.

Acknowledgements

This work was supported within the project of the Slovak Research and Development Agency Nr. APVV-0431-12, and Slovak Scientific Grant Agency VEGA 2/0013/14.

References

[1] Auras R, Lim LT, Selke SEM, Tsuji H (ed.). Poly(Lactic Acid): Synthesis, Structures, Properties, Processing, and Applications. Hohn Wiley & Sons, Inc., 2010. doi:10.1002/9780470649848.

[2] Hamoudeh M, Faraj AA, Canet-Soulas E, et al. Elaboration of PLLA-based superparamagnetic nanoparticles: Characterization, magnetic behaviour study and in vitro relaxivity evaluation. *International Journal of Pharmaceutics*, 338: 248-257, 2007.

[3] Fessi H, Puisieux F, Devissaguet JP, et al. Nanocapsule formation by interfacial polymer deposition following solvent displacement. International Journal of Pharmaceutics, 55(1): R1-R4, 1989.

Evaluation of a Novel Maghemite Hybrid Nanocarrier for MR Imaging (Pilot Study)

[1]A. Malá, [2]A. Bakandritsos, [1]O. Macíček, [2]E. Rousalis, [1]E. Dražanová, [1]R. Jiřík, [1]L. Dvořáková, [1]L. Grossová, [1]Z. Starčuk jr.

[1]ASCR, Institute of Scientific Instruments, Brno, Czech Republic
[2]Department of Materials Science, University of Patras, Rion, Greece
Email: malaa@isibrno.cz

Abstract. *The aim of this study was to investigate Mag 102-6, a maghemite hybrid drug nanocarrier, as a potential T_2 contrast agent (CA) for magnetic resonance imaging (MRI). Samples of agar gel mixed with different Fe concentrations of Mag 102-6 were measured at laboratory temperature for relaxivity r_2 determination in 9.4 T. The results were compared with commercial CA FeraSpin XXL measured in the same arrangement. In addition, the r_2 of Mag 102-6 in saline solution at physiological temperature 37.7°C was measured. MRI was performed with four mice using a 9.4T NMR scanner before, and up to 24 h post-injection (p.i.) of Mag 102-6 (dose 5 mg Fe kg^{-1}). Images of abdomen were continuously acquired by segmented Multi Gradient Echo (MGE) pulse sequence from 1 minute before the CA application to 20 minutes p.i. The T_1-weighted (T_1-w) and T_2-weighted (T_2-w) images were captured before the application and 25 minutes, 3.5, 7 and 24 hours after CA application. R_2* changes in time were estimated from MGE images for various anatomical regions (kidney, muscles, liver) by fitting of signal intensities. Mag 102-6 and FeraSpin XXL had comparable r_2 values. Mag 102-6 showed the potential to be monitored by MRI as a T_2 CA.*

Keywords: Nanocarrier, Maghemite, Contrast Agent, MRI, r_2

1. Introduction

The connection of therapeutics and diagnostics into one "theranostic" assembly enables monitoring of drug circulation. Controlling the drug distribution is important for appropriate disease treatment. The most important phenomenon that enables magnetic resonance imaging to provide high contrast of soft tissues, revealing anatomic and physiologic information, are the relaxation processes of hydrogen protons as they proceed at the magnetic field of the scanner. By shortening relaxation times (T_1, T_2), MRI contrast agent particles modify proton signal intensities around themselves. The ability of a CA to increase the longitudinal relaxation rate R_1 (=1/T_1) or the transverse relaxation rate R_2 (=1/T_2), which both depend linearly on the CA concentration, expressed per millimolar concentration of agent, is the longitudinal relaxivity r_1 or transverse relaxivity r_2 [s^{-1} mM^{-1}]. Maghemite nanoparticles act as a T_2 contrast agent – their presence decreases the MRI signal intensity. The first step for the evaluation of CA characteristics was in vitro measurement of r_2 (in conditions ideally close to physiologic) and comparison with a similar commercial CA. The second step was in vivo measurement involving monitoring of the changes in signal intensity for different tissues and checking the tolerance of the CA bolus by animals.

2. Subject and Methods

Mag 102-6 as Contrast Agent

Hybrid magnetic drug nanocarrier Mag 102-6 consisted of a graft-type copolymer, poly(methacrylic acid)-graft-poly(ethylenglycol methacrylate), (p(MAA-g-EGMA)), which acts as a corona for magnetic iron oxide nanocrystals. Mag 102-6 combines bio-repellent properties, high magnetic response and excellent loading capacity for anticancer drug doxorubicin [1]. Its mean hydrodynamic diameter (D_h) was 52 nm. Mag 102-6 without doxorubicin loading was used for whole study.

In Vitro Measurements

Six samples of saline (Isotonic Saline Solution 0.9%, Braun, Germany) mixed with Mag 102-6 with concentrations of 0, 0.02, 0.05, 0.10, 0.19 and 0.37 mM Fe were measured at laboratory temperature and at 37°C. Six samples of 1.5% agar gel mixed with 150 µL of Mag 102-6 with concentrations of 0, 0.02, 0.04, 0.09, 0.13 and 0.33 mM and, for comparison, a commercial contrast agent for preclinical applications, FeraSpin XXL (Miltenyi Biotec, Bergisch Gladbach, Germany), with D_h = 60-70 nm, in 1.5% agar gel at concentrations 0, 0.02, 0.04, 0.08, 0.13 and 0.33 mM Fe was measured at laboratory temperature. All samples were measured in 2-mL Eppendorf microtubes.

MRI measurements were performed with a 9.4 T (Bruker-BioSpec 94/30USR, Ettlingen, Germany) NMR system. Images for T_1 and T_2 quantification were acquired using a Rapid Acquisition with Refocused Echoes (RARE) pulse sequence. The parameters for T_1 quantification were: TR = 100-15 000 ms, TE = 10 ms; for T_2 quantification: TR = 15 000 ms, TE = 10-150 ms; where TR is the repetition time and TE the echo time. Slice thickness (SL) for all acquisitions was 1 mm, matrix 128×128, field of view (FOV) 6×4 cm, single slice, RARE factor = 2. The values of T_1 and T_2 were calculated for each sample in manually drawn regions of interest (ROIs) using the Image Sequence Analysis tool (ParaVision v.5.1, Bruker BioSpin, Ettlingen, Germany).

Finally, the r_1 and r_2 relaxivities were calculated as proportionality constants of the linear relation between the reciprocal relaxation time and the contrast-agent concentration.

In Vivo Measurements

All animal work was in accordance with national law. Four 4-6 week- old (33-35 g) wild type male mice (Laboratory Animal Breeding and Experimental Facility, Masaryk University, Brno, Czech Republic) underwent MR imaging under isoflurane anesthesia using the 9.4-T MR scanner. Each animal was positioned lateral with left kidney placed on the center of a 2×2 array of surface linear-polarized receive-only radiofrequency (RF) coils for the rat brain (Bruker, Ettlingen, Germany). Quadrature volume RF coil 112/86 mm (Bruker, Ettlingen, Germany) was used for excitation. Animal respiration was monitored by a respiration sensor (SA Instruments, Stony Brook, USA). Animals received intravenous dose of Mag 102-6 at 5 mg Fe kg^{-1} body weight (=0.09 mmol Fe kg^{-1}) through a catheter placed in the lateral tail veins. The catheter was immediately flushed with 0.1 mL saline. The CA and saline were administered by a syringe pump with infusion rate 1 $mL{\cdot}min^{-1}$ (PHD2000 Syringe Programmable, Harvard Apparatus, Massachusetts, U.S.A.).

T_1- and T_2*-weighted images of abdomen were continuously acquired from 1 minute before the administration of CA to 20 minutes p.i. by a segmented MGE pulse sequence (2 segments, one segment per respiration cycle, 10 dummy scans before each segment to establish steady-state magnetization): TR = 24 ms, TE = 2.5, 5.0, 7.5, 10.0, 12.5, 14.9 ms, SL 1.42 mm, flip angle 14°, matrix 128×64, FOV 32×20 mm, 700 frames, respiration gating. T_1-w and T_2-w images were acquired before the CA application and 25 min, 3.5, 7 and 24 h after it by RARE. The parameters were for T_1-w: TR = 666 ms, TE = 10.4 ms, 2 averages, RARE factor = 1; and for T_2-w: TR = 3 500 ms, TE = 36 ms, 3 averages, RARE factor = 8; SL 0.7 mm, 25 slices, no gating. Animals were observed for up to 4 weeks p.i.

Image Analysis of Dynamic MGE

The signal intensities of dynamic MGE images *SI*(TE,t) were converted to quantitative R_2*(t) images using signal model equation [2]:

$$SI(TE) = SI_{TE0} \cdot \exp\left(-\frac{TE}{T_2^*}\right) + C, \tag{1}$$

where *SI*(TE) are signal intensities within a pixel, measured with various echo times TE, SI_{TE0} is pixel signal intensity in the ideal case of TE = 0, T_2^* is the effective transversal echo time and C is an offset constant, which helps to approximate noisy magnitude MRI data especially in case of lower SNR. The vector of model parameters P = [SI_{TE0}, T_2^*, C] is estimated using constrained nonlinear optimization algorithm using MATLAB lsqnonlin function (MATLAB Optimization Toolbox, The MathWorks Inc., Natick, Massachusetts, U.S.A.). This process can be expressed as minimization of the criterial cost function in the sense of minimization of least squares error between the model and measured samples as

$$\arg\min_{P} \sum_{TE} \left\{ \left[SI_{TE0} \cdot \exp\left(-\frac{TE}{T_2^*}\right) + C \right] - SI(TE) \right\}^2 \tag{2}$$

Signals of R_2^* and SI_{TE0} for various anatomical regions (kidney cortex, kidney medulla, back muscles and liver) were derived by spatial averaging over manually drawn ROIs using our perfusion-analysis software.

3. Results

The relaxivities r_2 for Mag 102-6 in saline solution in 9.4 T were 184 $s^{-1}mM^{-1}$ at laboratory temperature and 126 $s^{-1}mM^{-1}$ at 37.7°C, with the ratio r_2/r_1 = 218. The relaxivity r_2 of agar gel with Mag 102-6 was 55 $s^{-1}mM^{-1}$ and with the commercial CA FeraSpin XXL 61 $s^{-1}mM^{-1}$, measured at laboratory temperature in 9.4 T.

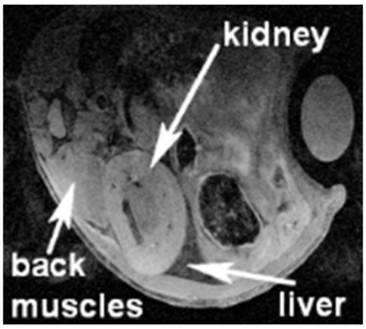

Fig. 1. T_1-weighted anatomical images of mouse abdomen 25 minute p.i.

In anatomical images (example in Fig. 1), liver signal intensity p.i. stayed low for a long period compared to the signal intensity before CA application. Other tissues showed no visible difference between T_1- and T_2-w images acquired before application and after 25 minute p.i.

Changes of R_2^* and SI_{TE0} in time after CA application were very similar for each mouse. For kidneys (medulla and cortex) there was fast increase of R_2^* and SI_{TE0} immediately after CA application, followed by a slow return to the default level. This evolution was the same also for SI_{TE0} of liver. R_2^* of liver did not decrease after the initial rise, instead it slowly increased with time. There was no noticeable change in muscles. Examples of R_2^* and SI_{TE0} in time of various anatomical regions are in Fig. 2.

There were no visible p.i. changes in mice conditions (weight and behavior) for 4 weeks.

4. Discussion

This new hybrid drug nanocarrier Mag 102-6 provides an adequate ratio r_2/r_1 at 37°C for T_2 CA according to information from literature [3]. The slightly lower r_2 of Mag 102-6 compared to FeraSpin XXL is supposed to be caused by the carrier size difference (increase of r_2 with higher D_h [3,4]).

We deduce that CA accumulates in liver based on the low signal intensity of T_1-w and T_2-w images of liver region for long period of time after CA application, which corresponds to literature (CA uptake by macrophages [3]). Changes of signal intensity were obvious in regions with numerous blood vessels after CA application – kidney and liver – but not in muscles. Muscles were farther away from the surface coil and thus the change due to the CA is supposed to have been too small to be detected in noise.

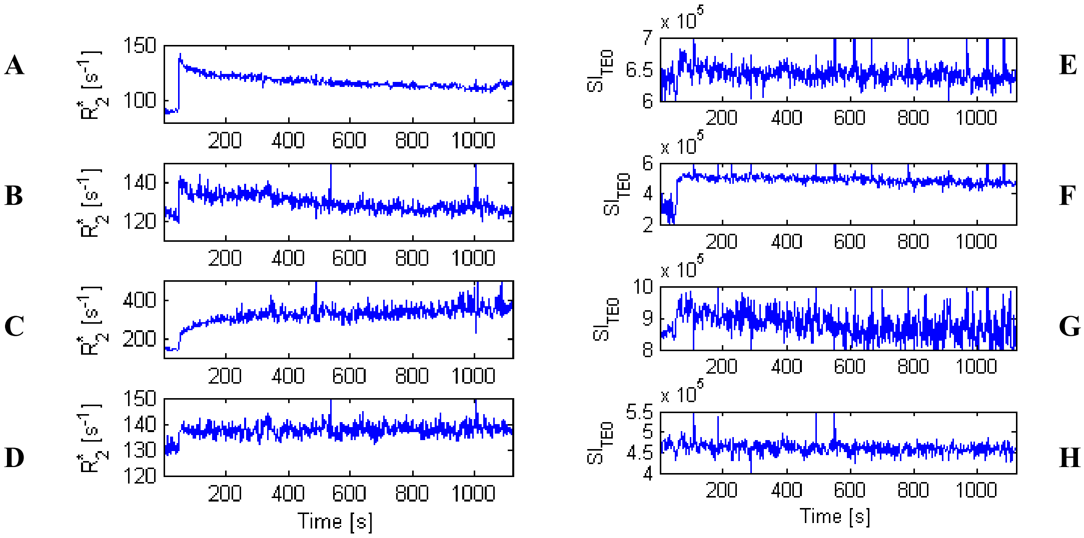

Fig. 2. R_2^* and SI_{TE0} time-development for chosen ROIs of kidney cortex (A,E) and medulla (B,F), liver (C,G), back muscles (D,H).

The time development of R_2^* and SI_{TE0} are estimates of the CA-concentration development. The SI_{TE0} signals are directly proportional to the CA concentration in the vascular and extravascular space (for low CA concentrations), but are more noisy (due to substantially lower r_1 compared to r_2). On the other hand, R_2^* signals are less noisy but are not directly proportional to the CA concentration because of the decreased CA compartmentalization due to the CA extravasation. For estimation of the CA concentrations in the intra- and extravascular spaces, pharmacokinetic modeling of the SI_{TE0} and R_2^* signals would have to be done [5]. In spite of measurement of only a small number of animals, the maghemite hybrid nanocarrier Mag 102-6 showed the potential to be monitored by MRI as a T_2 contrast agent.

Acknowledgements

The study was supported by Ministry of Education, Youth, and Sports of the Czech Republic (project No. LO1212).

References

[1] Bakandritsos A, Papagiannopoulos A, Anagnostou EN, Avgoustakis K, Zboril R, Pispas S, Tucek J, Ryukhtin V, Bouropoulos N, Kolokithas-Ntoukas A, Steriotis TA, Keiderling U, Winnefeld F. Merging high doxorubicin loading with pronounced magnetic response and bio-repellent properties in hybrid drug nanocarriers. *Small,* 8 (15): 2381-2393, 2012.

[2] Wood JC, Enriquez C, Ghugre N, Tyzka JM, Carson S, Nelson MD, Coates TD. MRI R_2 and R_2^* mapping accurately estimates hepatic iron concentration in transfusion-dependent thalassemia and sickle cell disease patients. *Blood*, *106* (4): 1460-1465, 2005.

[3] Weissleder R, Ross BD, Rehemtulla A, Gambhir SS. Magnetic Nanoparticles, in Molecular Imaging: Principles and Practice. Weissleder R, Editor. People`s Medical Publishing House-USA, 2010, 523-541.

[4] Shokrollahi H. Contrast agents for MRI. *Materials Science and Engineering C*, 33: 4485-4497, 2013.

[5] Sourbron S, Heilmann M, Walczak C, Vautier J, Schad LR, Volk A. T_2^*-relaxivity contrast imaging: first results. *Magnetic Resonance in Medicine*, 69 (5): 1430-1437, 2013.

Physical Model of Deposition of Magnetic Particles in Lung Alveolus

[1]A. Krafčík, [2]P. Babinec, [1]I. Frollo

[1]Institute of Measurement Science, SAS, Bratislava, Slovakia
[2]Faculty of Mathematics, Physics and Informatics, UK, Bratislava, Slovakia
Email: andrej.krafcik@savba.sk

Abstract. *Due to lung anatomy, ability to use safely bigger particles for targeting, and reduced viscosity of air in comparison to blood, lungs represent unique opportunity for magnetic drug targeting. The most important issue is to understand dynamics of magnetic particle motion on alveolar level. Therefore we have developed physical model describing magnetic particle dynamics in a rhythmically expanding and contracting distal and proximal alveolus subjected to high-gradient magnetic field generated by cylindrical Halbach array of permanent magnets. We concluded that magnetic deposition can overcome both, aerodynamic forces as well as gravitational sedimentation.*

Keywords: Alveolus, Magnetic Targeting and Deposition, SPIONs, FEM, Halbach Array

1. Introduction

For the prediction of particle transport and deposition, and for the development of effective drug delivery strategies for the lung, it is the most important to understand flow phenomena on the alveolar level [1, 2]. Recently, it was pointed to using magnetic particles and gradient magnetic fields for targeting drugs in lungs of mice [3]. To further improve drug efficacy in the lungs, it may be advantageous to control aerosol deposition and to target aerosols using magnetic gradient fields. Our aim was therefore to develop physical model describing magnetic deposition of particles in lung alveolus [4].

2. Physical Model

The differential equation governing the motion of a spherical particle with mass m_p and nonzero magnetic moment $\boldsymbol{\mu}_p$ subjected to gravity field $\mathbf{g}$ and external magnetic field $\mathbf{B}$ is

$$m_p \frac{\mathrm{d}^2\mathbf{r}_p}{\mathrm{d}t^2} = \mathbf{F}_D + m_p\mathbf{g} + (\boldsymbol{\mu}_p \cdot \nabla)\mathbf{B}\,, \tag{1}$$

where $\mathbf{r}_p$ is the instantaneous particle position, and $\mathbf{F}_D$ is the drag force exerted on the particle, with neglected stochastic Brownian forces. For details see our paper [4].

Drag Force and Alveolar Flow Model

The drag force exerted on a spherical particle with D_p in diameter (and with slip correction factor C) suspended in Stokesian flow field $\mathbf{v}_f$ of air with dynamic viscosity η_f is given as

$$\mathbf{F}_D = 3\pi\eta_f D_p (\mathbf{v}_f - \mathbf{v}_p)/C\,. \tag{2}$$

Alveolar Flow Model (AFM) [1]

AFM views single-alveolus configuration as a hemispherical cavity attached at a rim to a flat plane. The flow passing through the alveolar duct near the alveolus is approximated by a simple oscillatory shear flow over the flat plane, far upstream or downstream from the hemispherical cavity. The plane and the attached cavity perform an oscillatory, self-similar expansion and contraction movement. Assuming that the flow field is governed by the creeping flow equations, superposition of the following two flow fields is allowed: 1) *expansion flow* (alveolar flow)—the flow induced by the self-similar expansion and contraction of the alveolus with zero downstream flow inside the adjacent airways, and 2) *shear flow* (ductal flow)–the flow induced by shear flow over a hemispherical rigid cavity with vanishing velocity at the boundaries. Due to the quasi-steadiness of Stokes flows, the time variable can be viewed as a parameter that enters the problem via time dependent boundary conditions.

Expansion Flow

Expansion flow velocity vector field $\mathbf{v}^{\mathrm{H}}$ induced by a unit surface radial velocity for a unit radius hemisphere [1] in polar toroidal coordinate system (ξ,η,ϕ):

$$\begin{aligned}
v^{\mathrm{H}}{}_{\xi} =& -\frac{\sinh\xi\left(\cosh\xi\cos\eta-2\sin^2\eta-1\right)}{\left(\cosh\xi-\cos\eta\right)^2}-\frac{3}{2}\sin\eta\tanh\frac{\xi}{2}\left(\frac{1-\cos\eta}{\cosh\xi-\cos\eta}\right)^{1/2}\\
&+\frac{3}{2}\frac{\sin\eta\sinh\xi}{\left(\cosh\xi-\cos\eta\right)^{1/2}}\int_0^\infty F_h(\alpha,\eta)P'_{-1/2+\mathrm{i}\alpha}(\cosh\xi)\,\mathrm{d}\alpha\\
&-\sinh\xi\left(\cosh\xi-\cos\eta\right)^{1/2}\int_0^\infty\frac{\partial F_h(\alpha,\eta)}{\partial\eta}P'_{-1/2+\mathrm{i}\alpha}(\cosh\xi)\,\mathrm{d}\alpha,\\
v^{\mathrm{H}}{}_{\eta} =& +\frac{\sin\eta\left(-\cosh^2\xi-2\cos\eta\cosh\xi+3\right)}{\left(\cosh\xi-\cos\eta\right)^2}-\frac{3}{2}\frac{\left(1-\cos\eta\right)^{3/2}}{\left(\cosh\xi-\cos\eta\right)^{1/2}}\\
&+\frac{\left(\cosh^2\xi-\cosh\xi\cos\eta+3\right)}{2\left(\cosh\xi-\cos\eta\right)^{1/2}}\int_0^\infty F_h(\alpha,\eta)P'_{-1/2+\mathrm{i}\alpha}(\cosh\xi)\,\mathrm{d}\alpha\\
&+\sinh^2\xi\left(\cosh\xi-\cos\eta\right)^{1/2}\int_0^\infty F_h(\alpha,\eta)P''_{-1/2+\mathrm{i}\alpha}(\cosh\xi)\,\mathrm{d}\alpha,
\end{aligned} \tag{3}$$

where: $P'_{-1/2+\mathrm{i}\alpha}(s)$ and $P''_{-1/2+\mathrm{i}\alpha}(s)$ are the derivatives of the Legendre function of complex degree, and $F_h(\alpha,\eta)$ is the representation function for hemispherical alveolus [1, 4].

Shear Flow

Shear flow velocity vector field $\mathbf{v}^{\mathrm{P}}$ induced by a unit shear flow over a unit hemispherical cavity was studied in [2], employing a numerical boundary integral method. The velocity field depends on the three independent unknown functions of the coordinates (ρ,z) to be determined numerically. The solution possesses the general following form in Cartesian coordinates

$$\mathbf{v}^{\mathrm{P}}=\left[v^{\mathrm{P}}{}_1(\rho,z)\cos^2\phi+v^{\mathrm{P}}{}_2(\rho,z),\,v^{\mathrm{P}}{}_1(\rho,z)\cos\phi\sin\phi,\,v^{\mathrm{P}}{}_3(\rho,z)\cos\phi\right]^T. \tag{4}$$

The 3D solution for $\mathbf{v}^{\mathrm{H}}$ and $\mathbf{v}^{\mathrm{P}}$ obtained in [1] and [2], defined for unit depression radius and unit shear rate, can be utilize to solve the quasi-steady problem for alternating shear rates embedded in time protocols, and yields for drag force:

$$\mathbf{F}_D=-\frac{3\pi\eta_f D_p}{C}\left\{R_0\beta\omega\left[\sin(\omega t)\mathbf{v}^{\mathrm{H}}\left(\frac{\mathbf{r}_p}{R(t)}\right)+\gamma\sin(\omega t+\delta)\mathbf{v}^{\mathrm{P}}\left(\frac{\mathbf{r}_p}{R(t)}\right)\right]+\frac{\mathrm{d}\mathbf{r}_p}{\mathrm{d}t}\right\}, \tag{5}$$

where ω is the breathing frequency, R_0 is the mean radius of the alveolus, $R_0\beta$ is the alveolus expansion amplitude, δ is phase difference between expansion and shear flow, and γ is a ratio of their amplitudes ($\gamma > 1000$ at the first few generations (e.g. 16–19th), and remains $\gamma > 100$ for the most of the acinar generations).

Magnetic Force and FEM Model of Magnetic Field Source

Magnetic Force for fully magnetically saturated particle with magnetic moment $|\boldsymbol{\mu}_p|$ (for values of parameters see Table 1) in external magnetic field $\mathbf{B}$ is

$$\mathbf{F}_M = |\boldsymbol{\mu}_p|((\mathbf{B}/B)\cdot\nabla)\mathbf{B}\,. \tag{6}$$

As source has been used cylindrical Halbach array of permanent magnets (for finite element method (FEM) model see Fig. 1) [4]. Gradient of magnetic field, $\mathbf{G}_M = ((\mathbf{B}/B)\cdot\nabla)\mathbf{B}$, has reached value almost $G_M \approx 100\ \mathrm{T/m}$ at alveolus location.

Table 1. Parameters of particles used in simulations [4].

Quantity	Magnetite sphere	Droplet with SPIONs[a]
diameter, D_p (m)	1.0×10^{-6}	3.5×10^{-6}
mass, m_p (kg)	2.6×10^{-15}	22.9×10^{-15}
magnetic moment[b], $\lvert\boldsymbol{\mu}_p\rvert$ (A·m^2)	250×10^{-15}	26.4×10^{-15}

[a] Water aerosol droplet with content of 2930 superparamagnetic iron-oxid nanoparticles (SPIONs) [3].

[b] Magnetic moment of fully magnetically saturated particle.

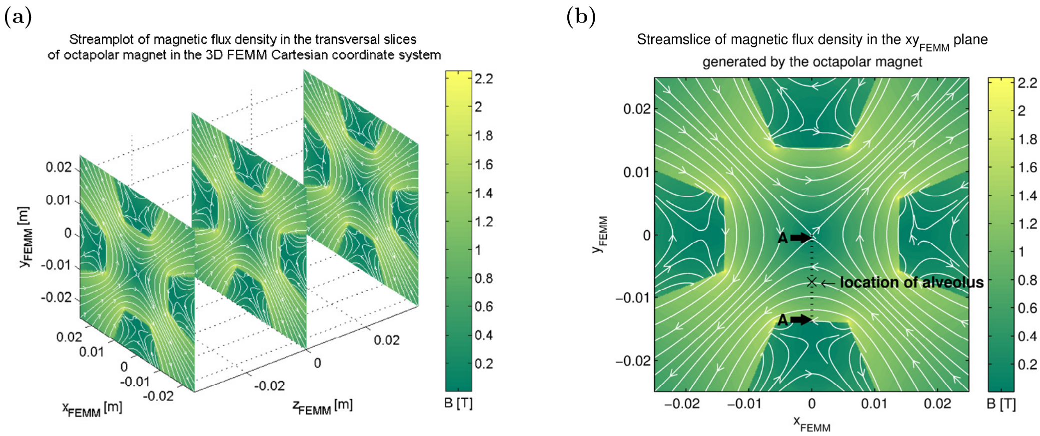

Fig. 1. FEM model of cylindrical Halbach array as a source of gradient magnetic field. Obtained using FEMM v.4.2 (D. Meeker). [4]

3. Results

Simulations have been performed using MATLAB built in ode15s ordinary differential equations solver for alveolus with the following geometrical and physiological properties: $R_0 = 150\ \mu\mathrm{m}$, $\beta = 0.1$, $\gamma = 300$ (distal airways generations), $\delta = 0°$, and $\omega = 12$ breaths-per-minute; see Fig. 2. Also, in similar way for $\gamma = 1000$ (proximal airways generations).

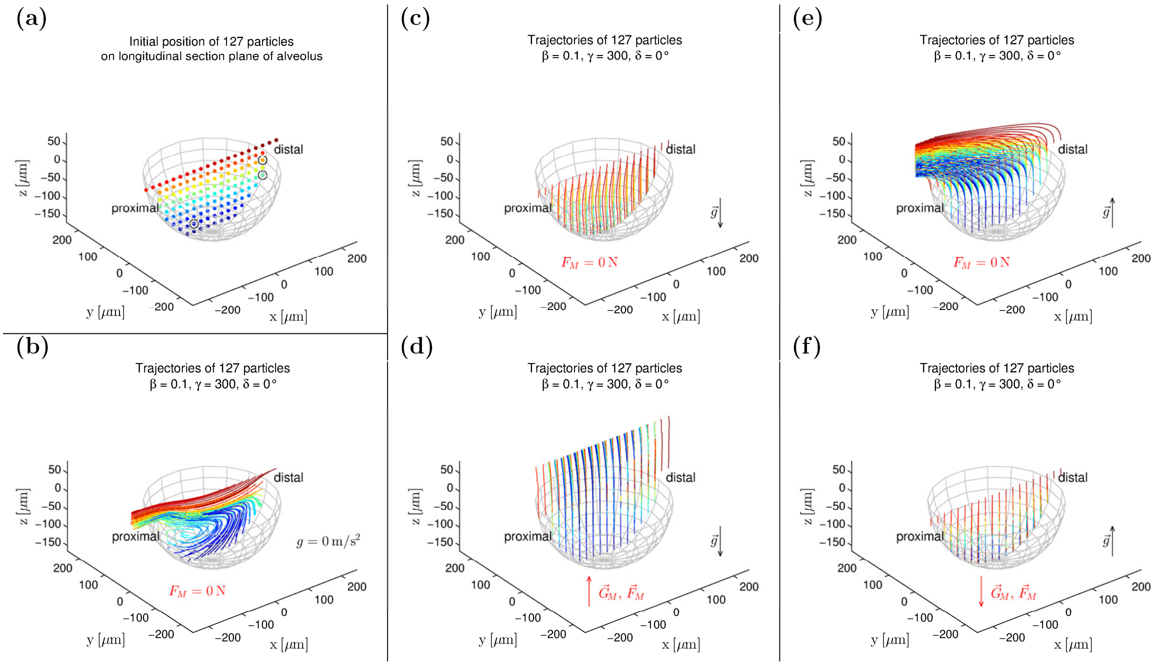

Fig. 2. Simulation results [4]: (a) initial positions; and trajectories of droplets with SPIONs in alveolus: (b) in gravity-free and magnetic-free conditions, (c, e) with presence of gravity and magnetic-free conditions, and (d, f) with presence of gravity and magnetic gradient.

4. Conclusions

Magnetic deposition of particles in alveolus can overcome both, aerodynamic forces and gravitational sedimentation, not only in the case of magnetite spheres with large magnetic moment, but also in the case of water aerosol droplets with content of SPIONs, whose magnetic moment is reduced in comparison with magnetite spheres. It was occurred not only in alveolus in distal airways generations with reduced ductal flows, but also in proximal ones.

Acknowledgements

This work was supported by Grant Agency of the Slovak Academy of Sciences (VEGA 2/0013/14 and VEGA 1/0871/14); and realized on MATLAB ISS CVTI SR.

References

[1] Haber S, Butler JP, Brenner H, Emanuel I, Tsuda A. Shear flow over a self-similar expanding pulmonary alveolus during rhythmical breathing. *Journal of Fluid Mechanics*, 405:243-268, 2000.

[2] Pozrikidis C. Shear flow over a plane wall with an axisymmetric cavity or a circular orifice of finite thickness. *Physics of Fluids*, 6(1):68-79, 1994.

[3] Dames P, Gleich B, Flemmer A, Hajek K, Seidl N, Wiekhorst F, Eberbeck D, Bittmann I, Bergemann C, Weyh T, Trahms L, Rosenecker J, Rudolph C. Targeted delivery of magnetic aerosol droplets to the lung. *Nature Nanotechnology*, 2(8):495-499, 2007.

[4] Krafcik A, Babinec P, Frollo I. Computational analysis of magnetic field induced deposition of magnetic particles in lung alveolus in comparison to deposition produced with viscous drag and gravitational force. *Journal of Magnetism and Magnetic Materials*, 380:46-53, 2015.

In Vivo Diffusion Tensor Imaging of the Rat Spinal Cord – Pilot Study

[1]L. Dvořáková, [1]R. Jiřík, [2]M. Burian, [3]A. Hejčl, [1]Z. Starčuk

[1]Institute of Scientific Instruments, CAS, Brno, Czech Republic,
[2] International Clinical Research Center – ICRC, Brno, Czech Republic,
[3] Institute of Experimental Medicine, CAS, Prague, Czech Republic
Email: lenkad@isibrno.cz

Abstract. *In vivo diffusion tensor imaging (DTI) of rat thoracic spinal cord was performed on five healthy rats. Axial diffusion images were obtained using a standard spin echo diffusion weighted sequence. The fractional anisotropy (FA), longitudinal (LD) and transverse (TD) diffusivities and the mean diffusivity were estimated. Differences in these parameters between white and grey matter were in accord with theory and in the range reported in literature.*

Keywords: spinal cord, magnetic resonance imaging, diffusion tensor imaging

1. Introduction

Diffusion tensor imaging (DTI) is a magnetic resonance (MR) technique capable of measuring the magnitude and direction of diffusion of water molecules in various tissues. DTI was developed from diffusion weighted (DW) imaging, which measures the attenuation of MR signals caused by diffusion of water molecules, and was initially used for brain imaging [1].

DTI studies of spinal cord and DTI tractography can be useful in probing the integrity of white matter fiber tracts in traumatic spinal cord injuries (SCI) [2]. In the published studies both spin-echo (SE) [3,4] and echo-planar imaging (EPI) pulse sequences [5] have been presented. To minimize possible geometry distortion related to EPI, SE sequence was preferred in our study. The purpose of this pilot study is to establish and optimize DTI acquisition in rat spinal cord at our institution using our equipment. Our motivation is to step forward to in vivo rat spinal cord tractography. To the authors' knowledge so far only one in-vivo tractography of the rat spinal cord was performed [6] and the reproduction of its results is hardly possible due to the incomplete description of its acquisition and post-processing methods and parameters.

2. Methods

Animal Preparation and MRI

For this pilot study, 5 female healthy rats (250-300 g) were used. A surface coil custom made in the Institute for Clinical and Experimental Medicine (IKEM, Prague, CZ) was used for both transmitting and receiving of the radiofrequency signal. Local excitation was used to eliminate the motion artefacts due to the beating heart by not exciting it. The rats were anesthetized with isoflurane and positioned supine over the surface coil. The center of the coil was placed in the thoracic area of the spine. The rat was maintained under anesthesia (2.5% isoflurane) for the duration of imaging. A respiratory sensor (SA Instruments, Stony Brook, NY, USA) was taped over the abdomen and a rectal temperature probe (SA Instruments, Stony Brook, NY, USA) was inserted for monitoring of the animal. All experiments were in accordance with national legislature.

All imaging was performed on a 9.4T NMR system (Bruker-Biospec 94/30 USR by Bruker, Ettlingen, Germany). Fast low-angle shot (FLASH) IntraGate was used for scout imaging to locate the spinal cord. Rapid Acquisition with Refocused Echoes (RARE) sequence was used for anatomical images of the spinal cord in the sagittal and coronal views. The parameters of the RARE sequence were as follows: TR/TE = 1300/46.6 ms, slice thickness = 0.5 mm, matrix = 256×256 and field of view = 4.98 cm × 4.98 cm, where TR and TE are the repetition and echo times, respectively. Then a standard multislice spin-echo DW sequence based on the Stejskal-Tanner diffusion preparation [7] was used. The parameters of the DTI sequence were as follows: TR/TE = 1000/28.7 ms, slice thickness = 2.0 mm, matrix = 128×128, field of view = 2.22 cm × 2.46 cm, diffusion gradient duration = 4 ms, number of b=0 images = 3, diffusion gradient separation 15 ms and b-value = 800 s/mm^2. For higher b-values, the signal to noise ratio in the acquired images was too low for a reliable DTI analysis. Images were acquired in six DW directions ([±0.33, 0.67, 0.67], [0.67, ±0.33, 0.67], [0.67, 0.67, ±0.33]). Adding directions to the DTI experiment would provide more accurate results. Nonetheless, in vivo measurements are time-limited and for the spinal cord six directions seemed to be sufficient, according to our results. The inter-slice thickness was not standardized in this pilot study. The sequence was respiration gated to avoid motion artefacts. The gating was set such that two excitations fit in one breathing cycle. The acquisition time of the DTI sequence was around 45 minutes, depending on the breathing frequency.

DTI Processing

DWI data were processed in the FSL software (Analysis group, FMRIB, Oxford, UK) to create fractional anisotropy (FA) map, eigenvalue (ε_1, ε_2, ε_3) maps and their eigenvector (v_1, v_2, v_3) maps. The longitudinal (LD) and transversal (TD) diffusivity (defined as the largest eigenvalue ε_1, and the average of the remaining two eigenvalues, $(\varepsilon_2 + \varepsilon_3)/2$, respectively) were calculated. Mean diffusivity (MD) was determined as the average of the eigenvalues, $(\varepsilon_2 + \varepsilon_3 + \varepsilon_3)/3$. [4] All maps were imported into the ImageJ software (National Institutes of Health, Bethesda, MD). For region of interest (ROI) analysis, two slices were selected for each animal. ROIs were drawn using ImageJ according to Fig. 1. An example of an eigenvector map is shown in Fig. 2.

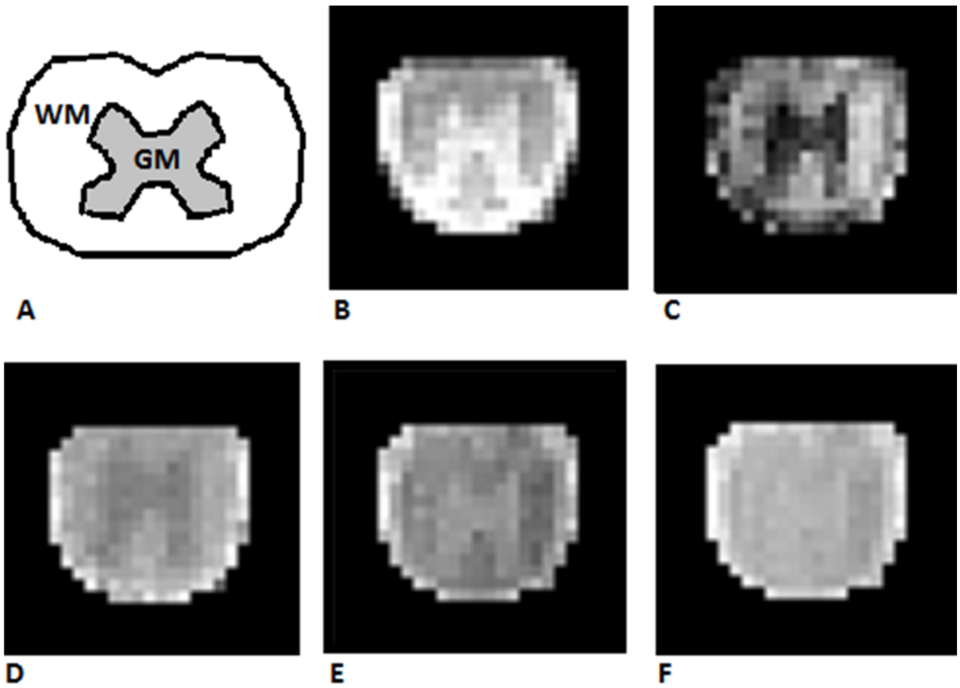

Fig 1. A: Schematic of the rat thoracic spinal cord section: WM – white matter, GM – grey matter. B: Anatomical image of the thoracic spinal cord. C-F: Maps of diffusion parameters. C: fractional anisotropy (FA) map. D: longitudinal diffusivity (LD) map. E: transverse diffusivity (TD) map. F: mean diffusivity (MD) map.

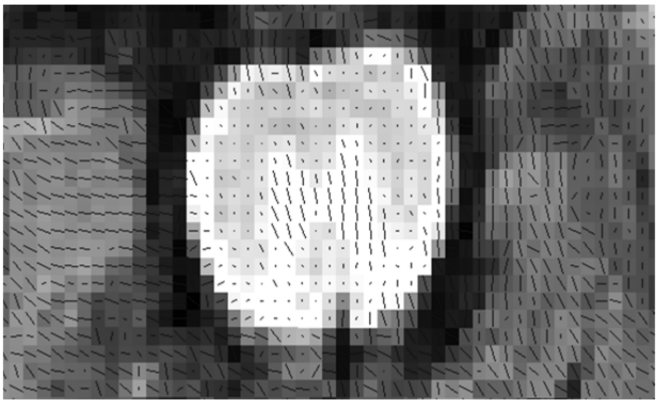

Fig 2. Map of eigenvectors of the highest eigenvalue (lines) with anatomical image of the rat thoracic spinal cord section in the background. If the vector is displayed as a dot, it indicates direction perpendicular to the imaging plane.

3. Results

The resulting diffusivity maps are shown in Fig. 1. The contrast between WM and GM was observed in the FA, LD, TD and partly in the MD maps. FA and LD are clearly higher in WM than in GM which corresponds to the rostral-caudal tracts in WM. This phenomenon can be also seen in Fig. 2 (eigenvector in WM mostly oriented along these tracts). The average DTI values for each rat are summarized in Table 1 and 2 for WM and GM, respectively.

Table 1. Values of diffusion parameters for WM. In the last four rows literature values are stated.

Rat no.	FA	LD [$\times10^{-3}$ mm^2/sec]	TD [$\times10^{-3}$ mm^2/sec]	MD [$\times10^{-3}$ mm^2/sec]
1	0.73±0.11	2.31±0.58	0.65±0.23	1.48±0.31
2	0.77±0.14	2.20±0.34	0.54±0.21	1.37±0.18
3	0.88±0.16	2.46±0.60	0.30±0.30	1.37±0.33
4	0.67±0.16	1.98±0.55	0.63±0.25	1.30±0.30
5	0.68±0.17	1.84±0.38	0.65±0.18	1.20±0.19
Gullapalli[3]	0.79±0.02	1.80±0.08	0.22±0.03	1.01±0.02
Ellingson[4]	0.696±0.005	0.851±0.008	0.230±0.003	0.437±0.004
Mogatadakala[5]	0.83±0.052	1.94±0.115	0.29±0.069	0.86±0.056

Table 2. Values of diffusion parameters for GM. In the last two rows literature values are stated.

Rat no.	FA	LD [$\times10^{-3}$ mm^2/sec]	TD [$\times10^{-3}$ mm^2/sec]	MD [$\times10^{-3}$ mm^2/sec]
1	0.56±0.11	1.90±0.27	0.82±0.17	1.36±0.10
2	0.48±0.13	1.63±0.20	0.80±0.14	1.21±0.08
3	0.63±0.15	1.77±0.38	0.62±0.18	1.18±0.18
4	0.40±0.12	1.36±0.16	0.77±0.10	1.06±0.08
5	0.48±0.14	1.53±0.27	0.78±0.09	1.15±0.13
Ellingson[4]	0.589±0.008	0.724±0.008	0.262±0.004	0.416±0.004
Mogatadakala[5]	0.38±0.039	1.49±0.106	0.77±0.116	1.04±0.071

4. Discussion

We have described a pilot DTI study of a rat spinal cord in the thoracic region. We have found expected differences in diffusion properties between the spinal cord WM and GM. WM showed higher FA and LD and lower TD, which corresponds to the rostral-caudal orientation of the fibre tracts in WM [2]. This was also in line with the main direction of the diffusion tensor (Fig. 2).

Our results both in WM and GM were close to literature values (Tables 1, 2). In particular, the FA values were fairly close to the listed published values. Other diffusion parameters show high variance between different authors and it can be seen that our values are consistent with the literature ranges. Overall the variability of the diffusion parameters within the ROIs and within the animal group shows fairly high reproducibility of our experiment.

In conclusion, the presented method seems to be eligible for SCI imagining. For this purpose, the measuring protocol has to be standardized, especially the positioning of the slices so that the DTI analysis is done in the same locations of the same vertebrae. For DTI tractography, more slices will be necessary. For in-vivo measurement, the acquisition time should not exceed 150 minutes. This means that with the present DTI parameters we would be able to scan at least 12 slices in one experiment. For the current slice thickness of 2.0 mm, the overall length of the imaged spinal cord would be 24 mm, which is sufficient to cover the whole lesion, which size is planned to be less than 20 mm [8]. The goal of our study is to use DTI for evaluating the integrity of white matter tracts after experimental SCI. For blunt injuries, DTI may represent a non-invasive method for longitudinal follow up after SCI.

Acknowledgements

The study was supported by Ministry of Education, Youth, and Sports of the Czech Republic (project No. LO1212) and by the European Regional Development Fund – Project FNUSA-ICRC (No. CZ.1.05/1.1.00/02.0123).

References

[1] Chiang CW, Yang Y, Sun P. Quantifying White Matter Tract Diffusion Parameters in the Presence of Increased Extra-Fiber Cellularity and Vasogenic Edema. *Neuroimage,* 2014, 310-319.

[2] Schwarz E, Cooper E, Chin CL. Ex vivo Evaluation of ADC Values within Spinal Cord White Matter Tracts. *Journal of Neuroradiology,* 2005, 390-397.

[3] Gullapalli J, Krejza J, Schwartz E. In Vivo Diffusion Tensor Imaging of the Rat Spinal Cord at 9.4T. *Journal of Magnetic Resonance Imaging*, 2008, 634-642.

[4] Ellingson B, Kurpad S, Li S. In Vivo DTI Evaluation of White Matter Tracts in Rat Spinal Cord. *Journal of Magnetic Resonance Imaging*, 2006, 231-234.

[5] Motagadakala K, Narayana P. In-vivo Diffusion Tensor Imaging of Thoracic and Cervical Rat Spinal Cord at 7T. *Journal of Magnetic Resonance Imaging*, 2009, 1236-1241.

[6] Wang F, Huang S, He X, Li X. Determination of the Ideal Rat Model for Spinal Cord Injury by Diffusion Tensor Imaging. *Clinical Neuroscience*, 2014, 1386-1392.

[7] Stejskal EO, Tanner JE. Spin echoes in the presence of a time-dependent field gradient. *Journal of Chemical Physics Spin diffusion measurement*, 1965, 288-292.

[8] Hejčl A, Urdzíková L, Šedý J, Lesný P, Pradný M, Michálek J, Burian M, Hájek M, Zámečník J, Jendelová P, Syková E. Acute and delayed implantation of positively charged 2-hydroxyethyl methacrylate scaffolds in spinal cord injury in the rat. *J Neurosurg Spine*. 2008, 67-73.

Water-Fat Separation in Rat by MRI at High Field (9.4T)

R. Korinek, K. Bartusek, Z. Starcuk

ASCR, Institute of Scientific Instruments, Královopolská 147
612 64 Brno, CZ
Email: radim.korinek@gmail.com

Abstract. *High fields yield benefits such as higher sensitivity along with specific problems - water-fat shift in the image or stronger susceptibility artifacts. Measurement in small animals is more problematic than in humans because the high field necessary to reach better sensitivity causes stronger susceptibility artifacts and requires shortening of specific time intervals used for encoding of the specific phase shift between water and fat. This article illustrates water and fat separation in rat at high fields. The data were acquired by a FSE-based 3-point Dixon technique employing iterative decomposition of water and fat with echo asymmetry and least-squares estimation (IDEAL) algorithm. The rat was measured in a standard volume coil. The fat/water fraction (FF, WF) map was calculated from the separated water and fat images. The results presented here show a FF map characterizing the fat distribution in a coronal slice of abdomen/pelvis region of a rat.*

Keywords: fat, rat, high field, IDEAL, Dixon

1. Introduction

One of the interesting domains in MRI is water and fat separation/suppression. The first articles describing various approaches for separation/suppression water and fat appeared almost 30 years ago. Methods for water and fat separation are based on either of two physical principles: difference in their longitudinal relaxation T_1 or chemical shift (CS). Methods for water and fat separation/suppression are very useful for diagnosis in liver diseases [1], [2], [3], cardiology [4], [5] [6] and other clinical applications. The methods can be divided into four main categories: Inversion recovery (IR), Fat-Sat, spectral-spatial excitation, and finally Dixon techniques. Besides the application in humans, these methods can be used in preclinical research involving small animals such as mice, rats, rabbits or others mammals. The fat in the tissue can be used as a biomarker in specific diseases of liver (e.g., NAFLD) or heart [7].

Of all the above mentioned categories of water-fat separation/suppression techniques, which are all used in clinical and pre-clinical imaging, the Dixon separation methods, utilizing the chemical shift difference between the water and the major lipid signal, have several advantages: the frequency difference is a well-defined, stable and known parameter (unlike T_1), and no narrow-bandwidth excitation is necessary, which makes these methods immune to static field inhomogeneity. The original method was introduced by Thomas Dixon [8] in 1984. Several modifications of this technique have been proposed; these derived techniques can be classified as one-, two-, three- or multi-point methods. The big challenge for Dixon techniques is the removal of phase errors for correct separation of water and fat signals. Removing the phase errors is crucial for the success of these techniques. Several methods have been proposed for the phase correction (post-processing algorithms, data acquisition or combination of both) [9], [10], [11], [12].

Subject and Methods

For the acquisition of experimental data by a 3-point Dixon (3PD) technique with water-fat phase shifts of (0, π, 2π), a modified FSE technique was used because FSE [13] is relatively insensitive to B_0 field inhomogeneities and provides useful T_2-weighted (T2W) images. The measurements were performed with a 9.4T MRI system (Bruker Biospec 94/30 USR) at Institute of Scientific Instruments of the ASCR, v. v. i. in Brno.

All measurements on animals were approved by the local ethics committee. The rat was anesthetized and placed into an 86-mm inner-diameter volume coil. All measurements were synchronized to breathing for reducing respiratory motion artifacts. The measured data were processed by iterative decomposition of water and fat with echo asymmetry and least-squares estimation (IDEAL) [12] algorithm. The algorithm was implemented in Matlab. The resulting water and fat images were used for the calculation of the FF map [14]

$$FF = \frac{|F|}{|F| + |W|} \cdot 100 , \tag{1}$$

where |F| is magnitude of fat image,
|W| is magnitude of water image,
FF is fat fraction [%].

The basic parameters of the measurement were: repetition time T_R = 3000 ms, echo time: T_E = 4.774 ms, effective echo time ETE = 9.548 ms, matrix = 192 × 192, field of view FOV = 70 × 70 mm and bandwidth BW = 150 kHz. The chemical shift between water and fat was 1400 Hz.

2. Results

The calculated water and fat coronal images of rat abdominal and pelvis region are shown in Fig. 1 (B, C) and the calculated FF maps in Fig. 2 B.

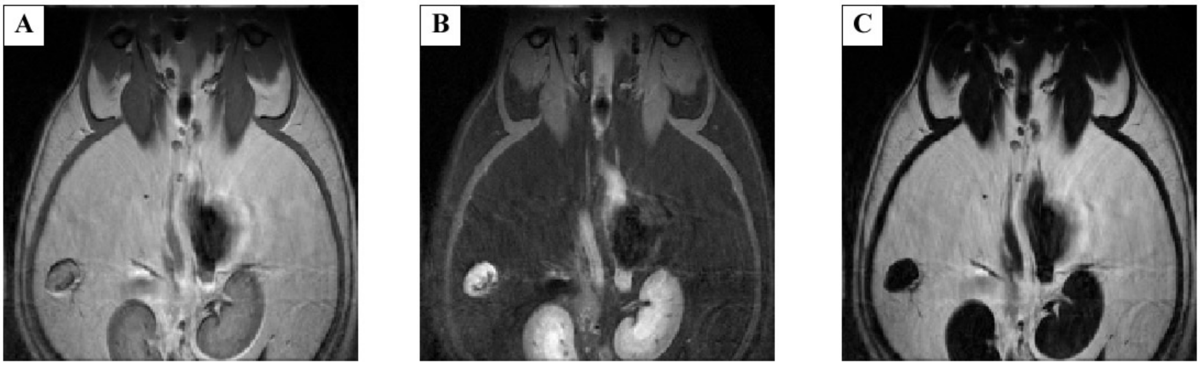

Fig. 1. A: water + fat image. B: calculated water image. C: calculated fat image.

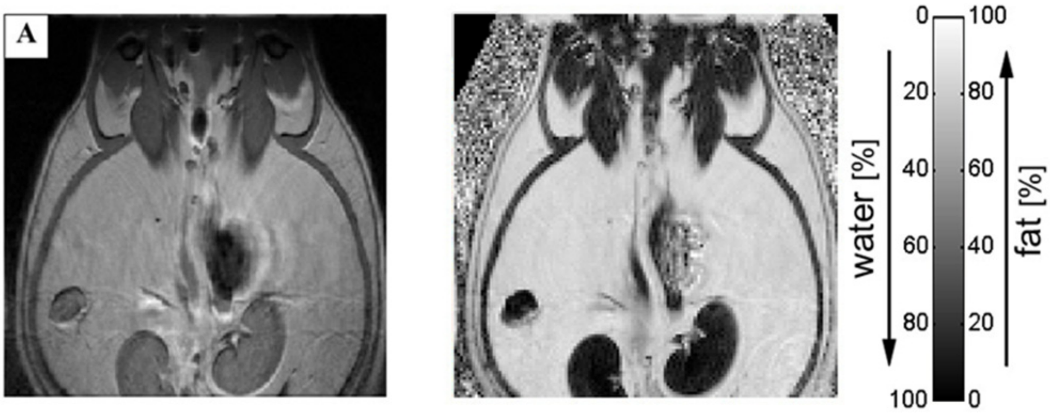

Fig. 2. A: T2W coronal image of rat abdomen and pelvis region (kidneys). B: calculated fat fraction map.

3. Discussion

The 3PD method based on modified FSE sequence with echo asymmetry was successfully implemented and tested in rat at 9.4 T MRI system. The measurement at such a high field is accompanied by specific problems. One of them are the consequences of inhomogeneity of magnetic susceptibility: considerable local static field inhomogeneity may lead, in some voxels, to considerable resonance line broadening, which may complicate the separation of water and fat components. The 3PD technique assumes a relatively simple signal model where water and fat have a single resonance frequency, in spite of the fact that fat has several spectral peaks. The inaccuracy of the simple signal model leads to incompletely separated water and fat images, as can be seen in Fig. 1B. Despite all this, we acquired water and fat images with good quality. For more accurate water-fat separation, multi-frequency fat spectrum modelling can be used. A more accurate signal model might yield better water and fat separation. However, in case of the FSE-based Dixon technique, the multi-point acquisition is more time consuming in comparison with the 3PD technique.

In high fields, the chemical shift between water and fat is increased, and to achieve small chemical shift displacement, strong gradients and large acquisition bandwidths must be used, with possible consequences such as non-negligible eddy currents or reduced SNR. In our case, gradients of 50 mT/m were sufficient to limit the chemical-shift displacement to 0.65 mm; with the pixel size of 0.365 mm, it still represents a 2-pixel displacement. If such a displacement was a problem for a specific application, increased gradients are technically feasible, but at the expense of lower SNR and hence increased risk of post-processing failure. Transfer of the implemented 3PD method to a lower magnetic field is possible.

Beside the abdominal application this method can be used elsewhere, e.g., in cardiac imaging.

Acknowledgements

This work was financially supported by the Ministry of Education, Youth and Sports, Czech Republic, in Program “National Programme of Sustainability I” (NPU I) (LO 1212) (Grant no. MSMT-34807/2013).

References

[1] Qayyum A, Goh JS, Kakar S, Yeh BM, Merriman RB, Coakley FV. Accuracy of liver fat quantification at MR imaging: comparison of out-of-phase gradient-echo and fat-saturated fast spin-echo techniques-initial experience. *Radiology,* 237 (2): 507-511, 2005.

[2] Kim H, Taksali SE, Dufour S, Befroy D, Goodman TR, Petersen KF, Shulman GI, Caprio S, Constable RT. Comparative MR study of hepatic fat quantification using single-voxel proton spectroscopy, two-point dixon and three-point IDEAL. *Magnetic Resonance in Medicine,* 59 (3): 521-527, 2008.

[3] Peng XG, Ju S, Qin Y, Fang F, Cui X, Liu G, Ni Y, Teng GJ. Quantification of liver fat in mice: comparing dual-echo Dixon imaging, chemical shift imaging, and 1H-MR spectroscopy. *The Journal of Lipid Research,* 52 (10): 1847-1855, 2011.

[4] Liu CY, Redheuil A, Ouwerkerk R, Lima JA, Bluemke DA. Myocardial fat quantification in humans: Evaluation by two-point water-fat imaging and localized proton spectroscopy. *Magnetic resonance in medicine,* 63 (4): 892-901, 2010.

[5] Kellman P, Hernando D, Shah S, Zuehlsdorff S, Jerecic R, Mancini C, Liang ZP, Arai AE. Multiecho dixon fat and water separation method for detecting fibrofatty infiltration in the myocardium. *Magnetic resonance in medicine,* 61 (1): 215-221, 2009.

[6] Farrelly C, Shah S, Davarpanah A, Keeling AN, Carr JC. ECG-gated multiecho Dixon fat-water separation in cardiac MRI: advantages over conventional fat-saturated imaging. *American Journal of Roentgenology,* 199 (1): 74-83, 2012.

[7] Lu M1, Zhao S, Jiang S, Yin G, Wang C, Zhang Y, Liu Q, Cheng H, Ma N, Zhao T, Chen X, Huang J, Zou Y, Song L, He Z, An J, Renate J, Xue H, Shah S. Fat deposition in dilated cardiomyopathy assessed by CMR. *JACC: Cardiovascular Imaging,* 6 (8): 889-898, 2013.

[8] Dixon WT. Simple proton spectroscopic imaging. *Radiology,* 153 (1): 189-194, 1984.

[9] Glover GH, Schneider E. Three-point Dixon technique for true water/fat decomposition with B0 inhomogeneity correction. *Magnetic resonance in medicine*, 18 (2): 371-383, 1991.

[10] Glover GH. Multipoint dixon technique for water and fat proton and susceptibility imaging. *Journal of Magnetic Resonance Imaging,* 1(5): 521-530, 1991.

[11] Yu H, Shimakawa A, McKenzie CA, Brodsky E, Brittain JH, Reeder SB. Multiecho water-fat separation and simultaneous R2* estimation with multifrequency fat spectrum modeling. *Magnetic resonance in medicine,* 60(5): 1122-1134, 2008.

[12] Reeder SB, Pineda AR, Wen Z, Shimakawa A, Yu H, Brittain JH, Gold GE, Beaulieu CH, Pelc NJ. Iterative decomposition of water and fat with echo asymmetry and least-squares estimation (IDEAL): application with fast spin-echo imaging. *Magnetic resonance in medicine,* 54 (3): 636-644, 2005.

[13] Hennig J, Nauerth A, Friedburg H. RARE imaging: a fast imaging method for clinical MR. *Magnetic resonance in medicine,* 3(6): 823-33, 1986.

[14] Buxton RB, Wismer GL, Brady TJ, Rosen BR. Quantitative proton chemical-shift imaging. *Magnetic resonance in medicine,* 3(6): 881-900, 1986.

Sodium MRI Predicts the Macromolecular Changes in Achilles tendon after Ciprofloxacin Administration

[1,3]V. Juras, [2]Y. Winhofer, [1,3]P. Szomolanyi, [1]J. Vosshenrich, [1]B. Hager, [2]P. Wolf, [1]M. Weber, [2]A. Luger, [1]S. Trattnig

[1]MR Centre of Excellence, Department of Biomedical Imaging and Image-Guided Therapy, Vienna, Austria

[2]Department of Internal Medicine III, Division of Endocrinology and Metabolism, Vienna, Austria

[3]Institute of Measurement Science, Slovak Academy of Sciences, Bratislava, Slovakia

Email: vladimir.juras@meduniwien.ac.at

Abstract. *The aim of this study was to determine if quantitative magnetic resonance (MR) imaging techniques (sodium MR imaging) could be used as potential markers for biochemical changes in the Achilles tendon induced by ciprofloxacin intake. The results demonstrated a ciprofloxacin-induced reversible reduction of the normalized sodium MR imaging signal in the Achilles tendon of healthy volunteers. Changes in sodium MR imaging in men may reflect a decrease of GAG content in the Achilles tendon after ciprofloxacin intake.*

Keywords: Sodium MRI, ciprofloxacin, MRI, glycosaminoglycan

1. Introduction

Fluoroquinolones (FQs) are frequently prescribed antibiotics and they are well established in both inpatient and outpatient settings for urinary and respiratory tract infections and skin, bone, joints, abdominal, and gastrointestinal infections [1]. In addition to gastrointestinal, central nervous system, and skin adverse effects, and prologantion of the QT interval prolongation, cumulative evidence suggests that FQ might be associated with Achilles tendinopathy [2, 3]. The occurrence of FQ-associated tendinopathy seems to be dose independent, and some risk factors were described in patients who develop FQ-related tendinopathy: age older than 60 years, (additional) glucocorticoid or immunosuppressive therapy, and renal failure [4]. However, cases of FQ-associated tendinopathy in the absence of these risk factors were described. Symptoms of tendinopathy include acute onset of tendon pain, tenderness, and swelling that affects the function of the tendon.

Because the biochemical composition of the Achilles tendon is closely related to its function, and biochemical alterations precede morphologic changes, the detection of biochemical changes can help elucidate the risk of developing tendinopathy. Pathologic alterations include an increase in the amount of glycosaminoglycans (GAGs), which is also accompanied by an increased sodium concentration. For proteoglycans, the sulfate and carboxyl groups associated with GAGs predominate, and they provide proteoglycans with a net negative charge. These negatively charged molecules preferentially attract positive counter ions. Recently, several MR imaging methods were introduced that are capable of noninvasive evaluation of the ultrastructural composition of the Achilles tendon. The similar principle of the direct proportion of the sodium ions and GAG content as known in cartilage was used to investigate the increase of GAG content in Achilles tendinopathy [5]. In addition, this method offers the opportunity to assess changes in the sodium concentration of the cartilage.

The aim of this study was to determine whether quantitative MR imaging technique (sodium MR imaging) could be used as potential markers for biochemical changes in the Achilles tendon induced by ciprofloxacin intake.

2. Subject and Methods

Patients

The ethics committee of the Medical University of Vienna approved the protocol (ethics committee number 1225/2012), and all subjects gave written, informed consent. Seven healthy men (mean age, 32 years ± 12 [standard deviation]) were recruited by advertisement in the public areas of the Medical University of Vienna between September 2012 and September 2013 and were included in our prospective study, and both ankles were measured. Exclusion criteria were as follows: known allergy against antibiotic agents; history of tendinopathy, tendon rupture, or joint diseases; and heavy exercise, which was defined as engaging in physical activity or sports for more than 3 hours per week. All patients underwent MR imaging at three time points: at baseline, at 10 days, and at 5 months after ciprofloxacin intake (1000 mg/day in two doses - 500 mg in the morning and 500 mg in the evening for 10 days). The first ciprofloxacin dose was taken after the baseline MR examination, and the last dose in the morning before the second MR examination.

MR Examination

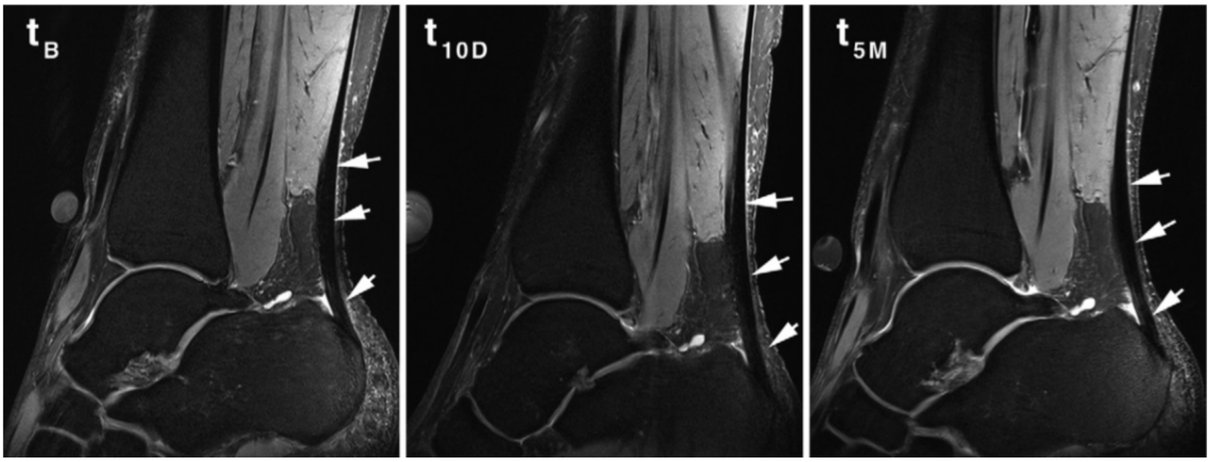

Fig. 1. Morphologic image of a patient at baseline before ciprofloxacin intake (t_B), 10 days after ciprofloxacin intake (t_{10D}), and at the 5-month follow-up examination (t_{5M}). There were no significant morphologic changes observed in any of the patients at 10 days and 3 months after ciprofloxacin intake (arrows show the top, middle, and bottom tendon parts, which are the insertion, mid portion, and musculotendinous junction, respectively).

All participants underwent MR examinations on a 7-T investigational MR unit (Siemens, Erlangen, Germany) with a 28-channel knee coil (Quality Electrodynamics, Mayfield Village, Ohio) for proton imaging and a 15-channel knee coil (Qed; Quality Electrodynamics) for sodium imaging. Morphologic imaging sequences and collagen- and GAGspecific MR imaging methods were used. Morphologic assessment was determined with a sagittal intermediateweighted turbo spin-echo sequence with fat saturation by using the Vienna Morphologic Achilles Tendon Score. This score is based on four characteristics of the Achilles tendon (thickness, continuity, signal intensity, and associated pathologies), and the scores from 0 to 100, with 0 being the worst and 100 being the best. For sodium imaging, the variable echo-time sequence adapted to x-nuclei capabilities was used. In the interest of time, the two-dimensional mode with three sections was used, and the echo time was 2.45 msec.

Data Processing

MR imaging parameters were calculated with a manually drawn region-ofinterest (ROI) analysis in the three regions of the Achilles tendon (insertion, middle, and muscle-tendon junction; Fig 1). ROIs were drawn on two and three consecutive sections for sodium images. The length of each of the parts was defined as a third of the total Achilles tendon length, measured from the most proximal to the most distal. Values were also recorded for the sum of all three regions, hereafter referred to as the whole tendon. The sodium signal was normalized by the signal from the reference tube measured along each ankle with a known sodium concentration.

Statistical Analysis

All statistical calculations were performed by using statistical software (SPSS version 21.0, SPSS, Chicago, Ill; pROC version 1.5.4 of R Statistical Package, R Foundation, Vienna, Austria). Descriptive statistics were performed to calculate the mean and standard deviation of age and normalized sodium signal in the Achilles tendon and cartilage separately for various time points. To compare average normalized sodium signal in different ankles (right and left), we used a repeat-measure analysis of variance. The longitudinal aspect was modelled by using time points as level 1 and laterality as level 2 nested within individuals (level 3) and by modelling covariance structures. We also applied a diagonal, unstructured first-order autoregressive covariance matrix but presented only the results from the unstructured covariance matrix as it provided the best model fit. The relationship among three variables (MR parameter, time points, and laterality) is referred to as interaction. A P value equal to or below .05 was considered to indicate statistically significant results.

3. Results

The mean Vienna Morphological Achilles Tendon Score was 89.6 ± 6.9 for the baseline, 93.75 ± 5.96 10 days after ciprofloxacin intake, and 93.75 ± 5.69 5 months thereafter. None of the volunteers experienced any clinical symptoms from the intake of ciprofloxacin. At the three time points for the whole tendon, the mean normalized sodium signal was 130 arbitrary units (au) ± 8, 98 au ± 5, and 116 au ± 10, respectively. Using the repeated measures analysis of variance, a statistically significant difference was found between imaging at baseline and 10 days after for both whole tendon and the insertion in normalized sodium signal. Five months after ciprofloxacin intake, there was no significant change compared with baseline.

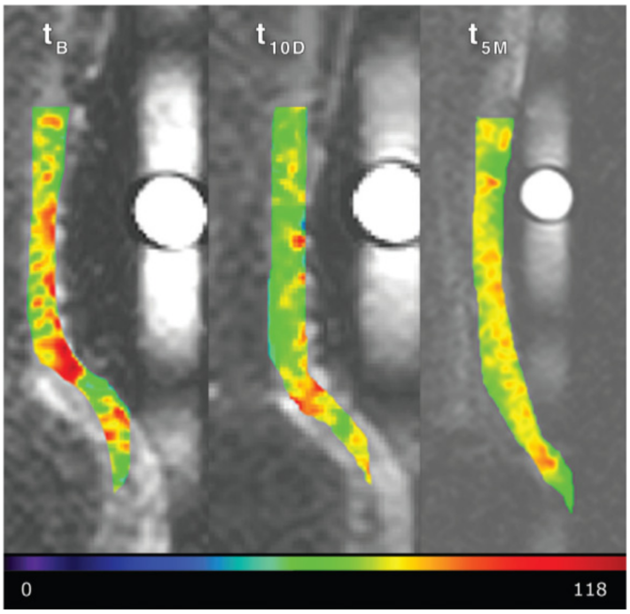

Fig. 2. The normalized sodium signal in the Achilles tendon at baseline before ciprofloxacin intake (t_B), 10 days after ciprofloxacin intake (t_{10D}), and at the 5-month follow-up examination (t_{5M}). Images were scaled equally. The decrease in the sodium signal in the tendon after intake is shown. The scale at the bottom of the image indicates the normalized sodium signal in arbitrary units.

4. Discussion

Our study demonstrates that sodium MR imaging is likely to detect changes in GAG content in the Achilles tendon after ciprofloxacin intake in healthy men. The changes were observed 10 days after ciprofloxacin intake, while the sodium signal returned to normal after 5 months. There were no visible morphologic changes in the Achilles tendon between the respective time points. Our study further links ciprofloxacin intake to Achilles tendinopathy. Of interest, while previous studies offered suspicions that FQ-associated Achilles tendinopathy is closely related to the age of the patient, cortisone treatment, and renal failure, our study demonstrates that changes in the Achilles tendon can also be observed in healthy young men. Although verified by MR imaging, the changes did not lead to clinical symptoms of tendinopathy or tendon injury; however, all subjects were asked to refrain from intense physical activity at least 14 days after ciprofloxacin initiation. Ciprofloxacin-associated tendinopathy and accompanying tendon rupture most commonly occur in the Achilles tendon, which is likely related to the weight-bearing role of the Achilles tendon [6]. Other tendons, including the supraspinatus, patellar, and quadriceps tendons, may also be occasionally affected by FQ drugs [7]. It is possible that the tendinitis observed in certain patients treated with FQs is secondary to an alteration in fibroblast cell homeostasis that results in the structural compromise of the tendon. The correlation coefficients of test-retest reliability showed high values for all three MR parameters, which suggests that there is no spontaneous change of the parameters over time. However, this is a confirmation rather than a proof of that expectation.

5. Conclusions

In conclusion, our study demonstrates the changes in sodium MR imaging in men after ciprofloxacin intake were very likely caused by a decrease of GAG content in the Achilles tendon. The observed changes in GAG content may contribute to the characterization of the pathomechanism of FQ-associated tendinopathy in the future.

Acknowledgements

Supported by the Austrian Science Fund (FWF) P 25246 B24, Vienna Advanced Imaging Center (VIACLIC) FA102A0017, and Slovak Scientific Grant Agency VEGA (grant 2/0013/14).

References

[1] Archer GL, Polk RE. Approach to Therapy for Bacterial Diseases, in Harrison's Principles of Internal Medicine, D. Longo, et al., Editors. 2012, McGraw-Hill.

[2] Zabraniecki, L, et al., Fluoroquinolone induced tendinopathy: report of 6 cases. *J Rheumatol,* 1996. 23(3): 516-20.

[3] Stephenson AL, et al. Tendon Injury and Fluoroquinolone Use: A Systematic Review. *Drug Safety*, 2013. 36(9): 709-721.

[4] Williams RJ, 3rd, et al. The effect of ciprofloxacin on tendon, paratenon, and capsular fibroblast metabolism. *Am J Sports Med*, 2000, 28(3): 364-9.

[5] Juras V. et al. Sodium MR imaging of Achilles tendinopathy at 7 T: preliminary results. *Radiology*, 2012. 262(1): 199-205.

[6] Huston KA. Achilles tendinitis and tendon rupture due to fluoroquinolone antibiotics. *N Engl J Med*, 1994. 331(11): p. 748.

[7] McGarvey WC, Singh D, Trevino SG. Partial Achilles tendon ruptures associated with fluoroquinolone antibiotics: A case report and literature review. *Foot & Ankle International*, 1996. 17(8): p. 496-498.

Simultaneous Dynamic PCr and Pi Imaging of the Calf Muscle During Exercise and Recovery Using ^{31}P Gradient-echo MRI at 7 T

[1,2]L.Valkovič, [3]M.Meyerspeer, [1]W.Bogner, [2]I.Frollo, [3]E.Moser, [1]S.Trattnig, [3]A.I.Schmid

[1]Department of Biomedical Imaging and Image-guided Therapy, Medical University of Vienna, Vienna, Austria
[2]Institute of Measurement Science, Slovak Academy of Sciences, Bratislava, Slovakia
[3]Center for Medical Physics and Biomedical Engineering, Medical University of Vienna, Vienna, Austria
Email: ladislav.valkovic@meduniwien.ac.at

Abstract. *Acquisition of dynamic changes in phosphocreatine (PCr) during exercise by ^{31}P-MRI has been recently show beneficial for evaluation of oxidative muscle metabolism in diverse muscle groups. In this study, a 3-D gradient-echo sequence for simultaneous dynamic ^{31}P-MRI of both PCr and inorganic phosphate (P_i) resonances was developed and tested at 7 T. The developed sequence allowed for multiple frequency-selective excitations of the PCr and P_i signals in an interleaved sampling scheme. The achieved spatial resolution was ~2 ml with an acquisition time of 5.8 s. Seven healthy subjects performed plantar flexions in an exercise-recovery experiment in between ^{31}P-MRI acquisitions. This allowed to observe differences in the mean PCr depletions during exercise between gastrocnemius (medialis: 44±14 %, lateralis: 40±11 %) and soleus (15±8 %). As expected from the low concentration of P_i, the P_i images had inherently low SNR at rest, but its signal was clearly detected in voxels of actively exercising muscles. In conclusion, simultaneous acquisition of PCr and P_i images with high temporal resolution, suitable for measuring PCr and P_i kinetics in exercise-recovery experiments, was demonstrated using a 3-D gradient-echo sequence at 7 T.*

Keywords: high energy phosphate, dynamic X-nuclei imaging, exercise, skeletal muscle

1. Introduction

Phosphorus magnetic resonance spectroscopy (^{31}P-MRS) is an established non-invasive method for studying muscle metabolism [1]. In particular, PCr and P_i kinetics in exercise-recovery experiments allow quantification of mitochondrial function or capacity, and provide insights into physiology, training status [2] and pathophysiology, e.g., in diabetes mellitus [3] or peripheral arterial disease [4]. Recently, the importance to spatially resolve differently exercising muscles (e.g., soleus and gastrocnemius) became more apparent [5].

In particular, ^{31}P-MRI with spectrally selective excitation has been proposed for spatially resolved detection of ^{31}P metabolites, e.g., PCr, at rest [6-8]. The 2-D spin-echo approach, originally proposed by Ernst et al. [6], was improved first by using TSE sequences and expanded to 3-D acquisition [8]. Techniques have been proposed even for simultaneous acquisition of multiple ^{31}P metabolites, e.g. interleaved excitation [7]. Recently, PCr imaging with temporal resolution in the order of seconds has been demonstrated by Greenman et al. [9] and Parasoglou et al. [10].

The aim of this study was to acquire both, PCr and P_i, images simultaneously with even higher temporal resolution. ^{31}P imaging experiment is used for simultaneous acquisition of both PCr and P_i time-courses during exercise-recovery experiments.

2. Subject and Methods

Seven healthy subjects (3f/4m, age 25.6±2.6 y, BMI=22.5±1.9 kg/m^2) participated in this study. All measurements were performed using a 7 T MR system (Siemens Healthcare, Erlangen, Germany) equipped with a ergometer, designed for plantar flexions [5]. An in-house built form-fitted 3-channel ^{31}P/ 2-cahnnel ^{1}H transceive coil was used.

For simultaneous acquisition of PCr and P_i data, a 3-D gradient-echo sequence was modified to perform multiple frequency-selective excitations in an interleaved scheme (Fig. 1). The excitation and readout frequency offsets were adjusted to the chemical shifts (PCr: 0 Hz, P_i: 570 Hz). The acquisition of a k-space line at the second frequency is shifted by $T_R/2$. This means that both images are shifted in time by only $T_R/2$. The excitation pulse was a 5 ms long sinc with truncated side lobes and with a bandwidth of 600 Hz.

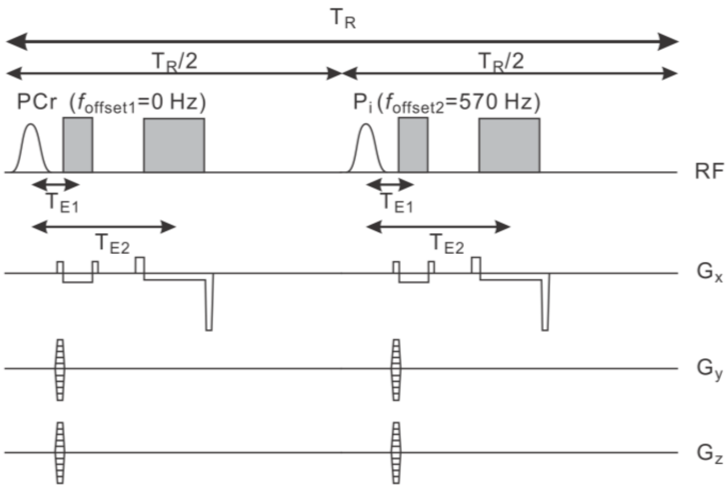

Fig. 1 Schematic of the interleaved, multi-frequency-selective 3-D gradient-echo sequence. $f_{offset1}$=0 Hz (PCr) and $f_{offset2}$=570 Hz (P_i). Corresponding sample images are shown in Fig. 2.

For dynamic ^{31}P imaging, the measurement parameters were as follows: T_R=60 ms; two echoes were acquired, to test the influences of the echo time and the receiver bandwidth on the temporal SNR of the PCr and Pi images, with T_E=3.8 ms and 14 ms; bandwidth 280 and 120 Hz/pixel, respectively. The matrix size was 16×16×6 with nominal spatial resolution of 9.4×9.4×20 mm^3. The resulting acquisition time for both PCr and P_i images was 5.8 s.

The maximum voluntary contraction (MVC) force of subjects was determined individually, before MR experiments, to set the workload to ~40% MVC. The dynamic ^{31}P-MRI protocol consisted of rest/exercise/recovery, lasting 1/3/4 minutes, respectively. The time between two complete sets of images was set to 10 s (5.8 s MRI + 4.2 s delay). During the exercise part of the protocol, subjects performed during the delay two plantar flexions.

Three ROIs were drawn, in the medial and lateral gastrocnemius and soleus, based on the anatomy images, resampled and applied to the ^{31}P images. The temporal SNR was calculated in the ROIs during the last two minutes of recovery. The temporal SNR of the P_i images was calculated during the second minute of exercise. The time-courses integrated over the ROIs were used to calculate PCr depletion and the time-constant of exponential recovery.

3. Results

Both PCr and P_i gradient-echo images with high temporal and spatial resolution were acquired with the proposed protocol. PCr was visible without averaging in as little as 5.8 s, in all three investigated muscles (Fig. 2a and 2b). The mean temporal SNR of PCr was 17.0±4.6 at T_E=3.8 ms and 18.6±3.2 at T_E=14 ms ($p<0.05$, paired t-test). P_i has an inherently low signal at rest since its concentration is much lower than that of PCr. It was therefore only visible in voxels from exercising muscles. The mean temporal SNR of P_i in gastrocnemius muscles was 3.5±1.6 at TE=3.8 ms, with no detectable signal at TE=14 ms. PCr and P_i images during exercise are displayed in Fig. 2c and 2d, respectively.

A decrease in PCr and an increase in P_i were observed in six volunteers during exercise. The mean PCr signal dropped by 44±14% and 40±11% in medial and lateral gastrocnemius muscles, respectively, while only by 15±8% ($p<0.01$, ANOVA, Tukey post hoc) in the soleus. One subject was excluded from further analysis due to poor compliance with the protocol and resulting low PCr depletion. The calculated τ_{PCr} values were 55.7±11.7 s and 57.1±14.1 s for gastrocnemius medialis and lateralis, respectively. Single subject data are given in Table 1. No assessment of recovery time-constant was performed in soleus due to low PCr depletion.

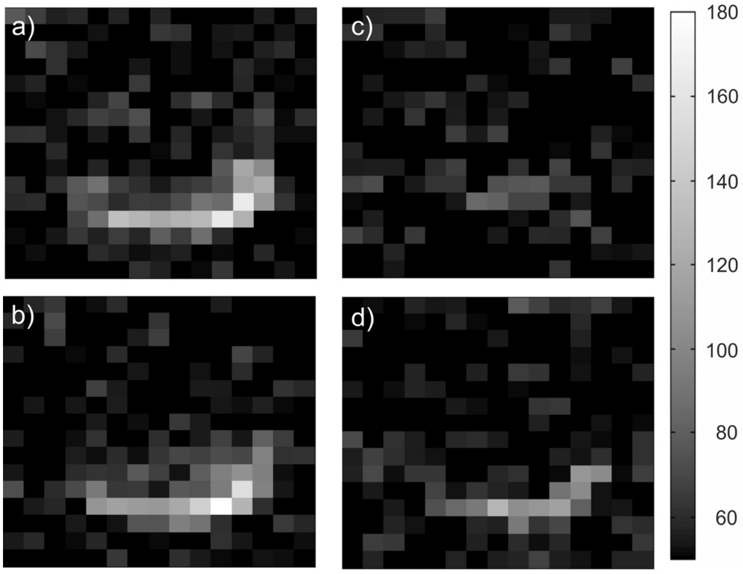

Fig. 2. ^{31}P MR images acquired during the exercise-recovery experiment (averaged over 3 acquisitions). (a) PCr at rest, and (b) at the end of recovery are similar. (c) Lower PCr signal during exercise is accompanied by (d) detectable P_i signal in gastrocnemius muscles. Note that no resting P_i image is provided due to low SNR, caused by its low concentration.

Table 1. Exercise intensities (%MVC), PCr depletion (ΔPCr) and recovery time-constants (τ_{PCr}) are shown for each analyzed subject. The bottom line shows the group average ± standard deviation (SD).

		gastrocnemius medialis		gastrocnemius lateralis		soleus
Subject	%MVC	ΔPCr [%]	τ_{PCr} [s]	ΔPCr [%]	τ_{PCr} [s]	ΔPCr [%]
1	42	31	39.1	37	33.9	3
2	38	66	57.2	40	48.0	20
3	43	42	46.3	19	63.1	11
4	39	56	71.9	46	58.3	17
5	35	38	56.4	48	73.0	16
6	41	30	63.2	47	66.4	25
Mean ± SD	40 ± 3	44 ± 14	55.7 ± 11.7	40 ± 11	57.1 ± 14.1	15 ± 8

4. Discussion

In our study, we present a frequency-selective 3-D gradient-echo sequence for simultaneous acquisition of PCr and P_i images. We have successfully used the designed sequence for dynamic localized measurements of oxidative muscle metabolism during and after exercise, providing time-courses of both PCr and P_i from the calf in a group of healthy volunteers.

The PCr depletion in the gastrocnemius, measured at 40% MVC, is in the range of literature values from localized MRS examinations [5]. The reported τ_{PCr} values are also in agreement with literature values from ^{31}P-MRI measurements [10]. The temporal resolution of 10 s, achieved in this study, is higher than previous reports of 24 s on fully sampled k-space, and still slightly better than 12 s using compressed sensing with TSE approach at 7 T [10]. The spatial resolution in this study (1.76 ml) was comparable to the spatial resolution of dynamic ^{31}P imaging (PCr only) using 3-D TSE imaging at 7 T (1.6 ml) by Parasoglou et al. [10].

The sequence described here has additionally the benefit of acquiring the PCr and P_i images simultaneously, thus providing more information on muscle metabolism at the same time.

Interleaved excitation of PCr and P_i was recently published using TSE sequence at 3 T, but low temporal resolution (4 minutes) rendered dynamic studies impossible [7].

5. Conclusions

The combined high temporal and spatial resolution achieved with the designed sequence at 7 T presents a valuable alternative to MRS for simultaneous PCr and P_i imaging during exercise-recovery experiments. Simultaneous and rapid measurements potentially allow for identifying local injuries, myopathies or functional deficits, in e.g., peripheral arterial disease.

Acknowledgements

This study was supported by the Christian Doppler Society – Clinical Molecular MR Imaging (MOLIMA to S.T.), by the Austrian BMWFJ FFG – Vienna Research Studio for Ultra-High Field MR Applications (grant #832107 to E.M.), by the OeNB Jubilaeumsfond (grant #15455 to L.V. and #16133 to W.B.), by the FWF Agency (grant #I1743-B13 to M.M.), and by the Slovak Grant Agency (VEGA grant #2/0013/14 to I.F. and APVV grant #0431-12).

References

[1] Bottomley PA, Charles HC, Roemer PB, Flamig D, Engeseth H, Edelstein WA, Mueller OM. Human in vivo phosphate metabolite imaging with 31P NMR. *Magnetic Resonance in Medicine,* 7(3): 319-36, 1988.

[2] Valkovič L, Ukropcová B, Chmelík M, Baláž M, Bogner W, Schmid AI, Frollo I, Zemková E, Klimeš I, Ukropec J, Trattnig S, Krššák M. Interrelation of 31P-MRS metabolism measurements in resting and exercised quadriceps muscle of overweight-to-obese sedentary individuals. *NMR in Biomedicine,* 26(12): 1714-22, 2013.

[3] Crowther GJ, Milstein JM, Jubrias SA, Kushmerick MJ, Gronka RK, Conley KE. Altered energetic properties in skeletal muscle of men with well-controlled insulin-dependent (type 1) diabetes. *American Journal of Physiology: Endocrinology and Metabolism,* 284(4): E655-62, 2003.

[4] Schocke M, Esterhammer R, Greiner A. High-energy phosphate metabolism in the exercising muscle of patients with peripheral arterial disease. *Vasa,* 37(3):199-210, 2008.

[5] Meyerspeer M, Robinson S, Nabuurs CI, Scheenen T, Schoisengeier A, Unger E, Kemp GJ, Moser E. Comparing localized and nonlocalized dynamic 31P magnetic resonance spectroscopy in exercising muscle at 7 T. *Magnetic Resonance in Medicine,* 68(6): 1713-23, 2012.

[6] Ernst T, Lee JH, Ross BD. Direct 31P imaging in human limb and brain. *Journal of Computer Assisted Tomography,* 17(5):673-80, 1993.

[7] Greenman RL, Wang X, Smithline HA. Simultaneous acquisition of phosphocreatine and inorganic phosphate images for Pi:PCr ratio mapping using a RARE sequence with chemically selective interleaving. *Magnetic Resonance Imaging,* 29(8): 1138-44, 2011.

[8] Parasoglou P, Xia D, Regatte RR. Spectrally selective 3D TSE imaging of phosphocreatine in the human calf muscle at 3 T. *Magnetic Resonance in Medicine,* 69(3): 812-7, 2013.

[9] Greenman RL, Smithline HA. The Feasibility of Measuring Phosphocreatine Recovery Kinetics in Muscle Using a Single-shot P-31 RARE MRI Sequence. *Academic Radiology,* 18(7): 917-23, 2011.

[10] Parasoglou P, Feng L, Xia D, Otazo R, Regatte RR. Rapid 3D-imaging of phosphocreatine recovery kinetics in the human lower leg muscles with compressed sensing. *Magnetic Resonance in Medicine,* 68(6): 1738-46, 2012.

Effect of Examined Persons Weight on the Acoustic Noise Produced by an Open-air NMR Imager

J. Přibil, T. Dermek, I. Frollo

Institute of Measurement Science, SAS, Dúbravská cesta 9, Bratislava, Slovakia
Email: Jiri.Pribil@savba.sk

Abstract. *The paper analyzes how influenced the weight of lying examined person in the scanning area of the open-air magnetic resonance imaging equipment on properties of an acoustic noise produced by mechanical vibration of the gradient coils system. This noise signal exhibits harmonic character, so it is suitable to analyze its properties in the spectral domain. Obtained results of will be used for precision of noise reduction of recorded speech signal during phonation for the human vocal tract modeling in an NMR imager.*

Keywords: Acoustic noise, Spectral analysis, NMR imaging.

1. Introduction

Magnetic resonance imaging (MRI) devices are also used for non-invasive MR scanning of vocal tract spaces of subjects for speech configuration or in phonation position of their resonant cavities for each vowel enables to develop the three-dimensional (3D) computer models of the human vocal tract [1]. To obtain the 3D vocal tract model with good quality the synchronicity between image and audio acquisition must be ensured as well as a good signal-to-noise ratio must be achieved [2]. The MRI device consists of a gradient coil system that produces three orthogonal linear fields for spatial encoding of a scanned object. The noise is produced by these gradient coils due to rapidly changing Lorentz forces during fast switching inside the weak static field B_0 environment [3]. This process subsequently propagates in the air a progressive sound wave received by the human auditory system as a noise [4]. Due to its harmonic nature and the audio frequency range, the produced acoustic noise of this device can generally be treated as a voiced speech signal. Therefore it can be recorded by a microphone and processed in the spectral domain using similar methods as for the speech signal analysis.

To investigate the transmission of noise signal originated of the plastic holder in the MRI device scanning area, as well as the magnetic filed homogeneity the measurement arrangement consisting of the testing phantom inserted in the scanning RF coil is usually used [2]. The situation changes when the testing person lies in the scanning area and the holder of the lower gradient coils is loaded with his/her weight. The motivation of this work was to analyze how influenced the weight of testing person on properties of the acoustic noise signal produced by mechanical vibrations of the gradient coils of the MRI equipment. Obtained results will be used to devise an improvement of the developed cepstral-based noise reduction method [5] in the speech recorded during 3D MR scan of the human vocal tract.

2. Spectral Properties of the Acoustic Noise Signal

The basic as well as the supplementary spectral properties are usually determined from the frames (after segmentation and widowing). To obtain the smoothed spectral envelope, the mean periodogram can be computed by the Welch method. For detailed analysis the nearest region of interest (ROI) is better to determine. In addition, the spectral distances D_{RMS} of analysed envelopes can be calculated and the position F_{max} of maximum difference ΔP_{max} can be determined for further comparison. Obtained values are subsequently analysed, the basic statistical parameters (minimum, maximum, mean, standard deviation) are calculated.

3. Subject and Experiments

The analyzed open-air MRI equipment E-scan OPERA contains also an adjustable bed which can be positioned in the range of 0 ÷ 180 degrees, where the 0 degree represents the left corner near the temperature stabilizer device [6] – see principal angle diagram of the MRI scanning area in Fig. 1a. This noise has almost constant sound pressure level (SPL) and consequently it can be easily subtracted as a background. Due to the low basic magnetic field B_0 (up to 0.2 T) in the scanning area of this MRI machine, any interaction with the recoding microphone must be eliminated. As the noise properties depend on the microphone position, the optimal recording parameters (the distance between the central point of the MRI scanning area and the microphone membrane, the direction angle, the working height, and the type of the microphone pickup pattern) must be found. The chosen type of the scan MR sequence together with the basic scan parameters – repetition time (TR) and echo time (TE) – have significant influence on spectral properties of the generated noise signal. The realization of the acoustic noise measurement experiments consists of two phases:

1. Mapping of the level of the SPL in the MRI neighbourhood by measurements of:
   - directional pattern per 12.5 degree of the acoustic noise on the MRI neighborhood in distances of {45, 60, and 75 cm} from the central point of scanning area with a testing phantom (see Fig. 1a),
   - noise SPL at directions {30, 90 and 150 degrees} in distance of 60 cm with different testing persons lying in the scanning area of the MRI device.
2. Recording of the noise signal during execution of a MR scan sequence using:
   - the test phantom only placed in the middle point of the scanning area (see Fig. 1b),
   - different testing persons lying in the scanning area of the MRI device (see Fig. 1c).

Measurement of the noise SPL was realized by the measuring device DT 8820, the resulting graph of the directional pattern for three measuring distances is presented in Fig. 2a. The mean SPL values obtained with the help of male/female examined persons and water phantom for three positions of DT 8820 device are shown in Fig. 2b. In the second part of our experiment, the noise signal was parallel recorded (at sampling frequency of 16 kHz) with the help of the Behringer PODCAST STUDIO equipment connected to a separate personal computer. The recording microphone was located in the distance of 60 cm, horizontally in the positions of 30, 90, and 150 degrees (the bed with the examined person at 180 degrees in all cases) and vertically in the middle between both gradient coils. By this way collected noise database consists of the records from six testing persons (3 male + 3 female) that were lying in the MRI scanning area (with the approximate weights as it is shown in Table 1), and using only the water phantom (WP) with a holder.

Table 1. The approximate weights of the testing persons/object used in our experiment.

Person/object	**JP** (Male1)	**TD** (Male2)	**LV** (Male3)	**AP** (Female1)	**BB** (Female2)	**ZS** (Female3)	**XX** (WP)
Weight [kg]	78	75	80	53	50	55	0.75

The measurement and recording was realized during execution of the MR sequence SSF-3D (with setting of TE=10 ms, TR=45 ms) that is often used for the 3D MR scans of the human vocal tract [5]. By this way obtained noise signals were subsequently processed as follows:

- visual comparison of determined spectral envelopes in the full frequency range of $0 \div f_s / 2$ (0-8k) and for the sub-ranges of 0 ÷ 2.5 kHz (0-2k), and of 2 ÷ 6 kHz (2-6k);
- determination of the spectral distances D_{RMS} between the envelopes calculated from acoustic noise obtained with using of an individual person and/or the testing phantom;

- localization of frequency position F_{max} of the maximum spectral difference ΔP_{max} within the low-frequency band of 0 ÷ 2.5 kHz – see an example in Fig. 3;
- basic statistical analysis of the achieved values – see the mean values in Table 2 and the box-plot of the basic statistical parameters in Fig. 4.

Fig. 1. An arrangement of noise SPL measurement (a) and noise recording in the MRI Opera using the testing water phantom (b), and a lying examined person (c).

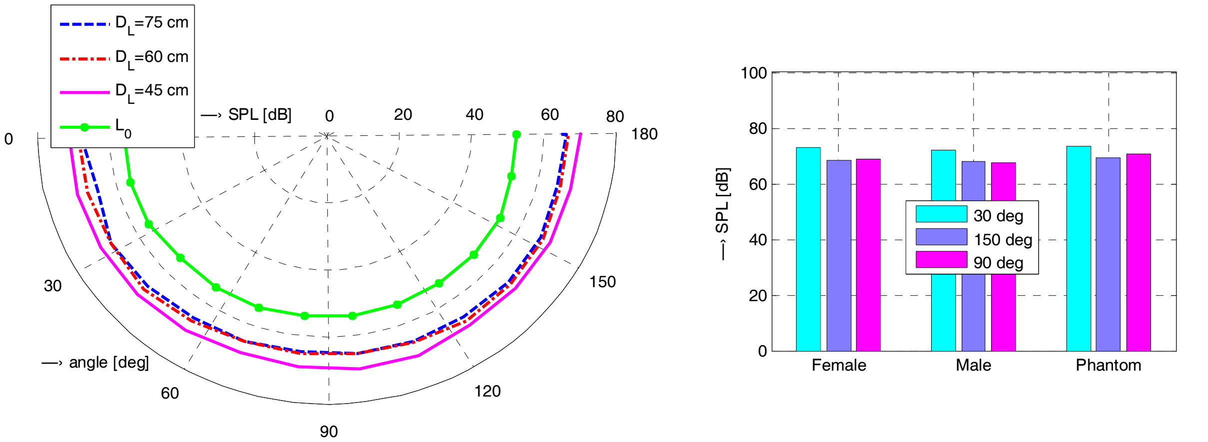

Fig. 2. Directional pattern of the noise source together with the background noise L_0 for three distances using a water phantom (left); the noise SPL values for selected three positions of DT 8820 device (right).

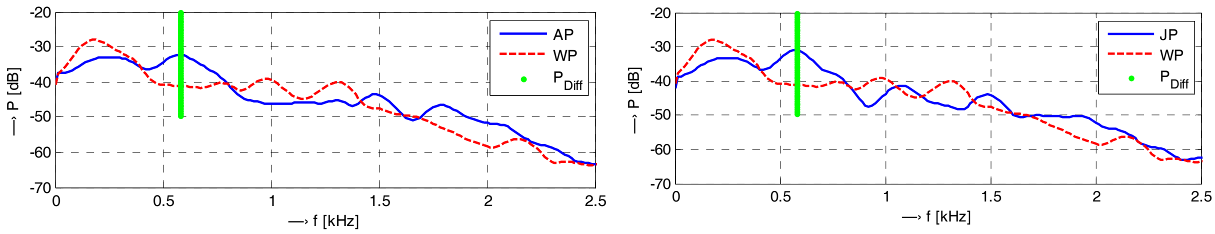

Fig. 3. Differences of spectral envelopes in the low frequency band up to 2.5 kHz for: female person (AP) to phantom (WP) ─ left, and male person (JP) to phantom (WP) ─ right; microphone at 90 degrees.

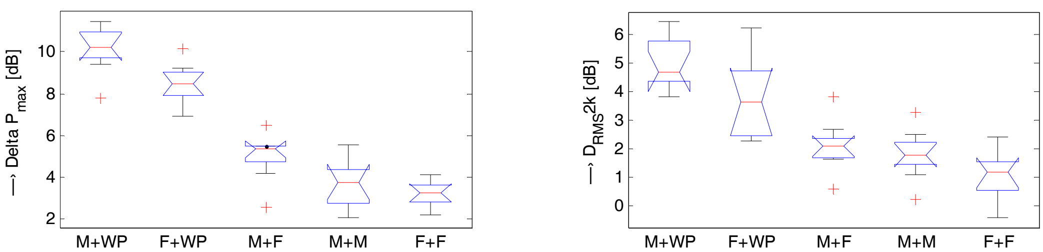

Fig. 4. Box-plot of basic statistical parameters of the spectral envelope differences within the low frequency band up to 2.5 kHz: ΔP_{max} at frequency F_{max}.= 576 Hz (left), spectral distances D_{RMS} 0-2k (right); tested pairs of: Male + WP, Female + WP, Male + Female, Male + Female, Female + Female; joined values for all there microphone positions at 30, 90, and 150 degrees.

Table 2. Comparison of mean values of the basic spectral properties of acoustic noises for the tested pairs of male/female persons and water phantom (WP) inserted in the scanning area of the MRI device.

Tested pairs [*)]	F_{max} **[Hz]**	ΔP_{max} **[dB]**	D_{RMS} **0-2k [dB]**	D_{RMS} **2-6k [dB]**	D_{RMS} **0-8k [dB]**
Female + WP	575	8.95	4.18	2.78	3.55
Male + WP	577	9.81	4.34	3.85	4.25

[*)] The noise signal recorded at 90 degree.

4. Discussion and Conclusion

Results of performed measurement of the noise SPL distribution in the MRI equipment neighbourhood help to find the sub(optimal) placement of the pick-up microphone for the next acoustic noise recording experiment. The mean values of the SPL obtained with the help of male/female lying person and water phantom for three tested locations show that no significant differences exist; however, the maxima were obtained for the microphone position at 90 degree – opposite to the face of the examined person. At the position of 0 degree the influence of the MRI temperature stabilizer can be superimposed as an additive noise with normal distribution, and finally the microphone position at 150 degree is unnatural from the point of the lying person. In all cases, the measurement confirms a principal influence of under load of the MRI plastic cover by a person lying on the produced acoustic noise. As documents achieved the mean values in Table 2 and the basic statistical parameters in Fig. 4, the weight of lying persons also effected on the spectral properties of the generated noise. From the spectral envelopes can be determined frequencies (positions), where is the noise spectrum supressed or increased in dependence on the acting weight of the examined person.

Obtained results will serve to create databases of initial parameters (such as the bank of noise signal pre-processing filters) very useful in an experimental practice – when it is often occurs, that the basic parameter setting of the used scanning sequence as well as the other scanning parameters must be changed depending on the currently tested person.

Acknowledgements

The work has been supported by the Grant Agency of the Slovak Academy of Sciences (VEGA 2/0013/14) and within the project of the Slovak Research and Development Agency Nr. APVV-0431-12.

References

[1] Vampola T, Horáček J, Švec JG. FE modeling of human vocal tract acoustic. Part I: Production of Czech vowels. *Acta Acustica United Acustica*, 94: 433-447, 2008.

[2] Aalto D. et al. Recording speech sound and articulation in MRI. International Conference on Biomedical Electronics and Devices Biodevices 2011, Rome, Italy, pp. 168-173.

[3] Tomasi D, Ernst T. A simple theory for vibration of MRI gradient coils. *Brazilian Journal of Physics*, 36: 34-39, 2006.

[4] Moelker A, Wielopolski PA, Pattynama MT. Relationship between magnetic field strength and magnetic-resonance-related acoustic noise levels. *Magnetic Resonance Materials in Physics, Biology and Medicine*, 16: 52–55, 2003.

[5] Přibil J, Horáček J, Horák P. Two methods of mechanical noise reduction of recorded speech during phonation in an MRI device. *Measurement Science Review,* 11: 92-98, 2011.

[6] E-scan Opera. Image Quality and Sequences manual. 830023522 Rev. A, Esaote S.p.A., Genoa, April 2008.

The Influence of Magnetic Field on Living Matter

[1]E. Vlachova Hutova, [2]R. Korinek, [3]L. Havel, [2]K. Bartusek

[1]Brno University of Technology, Faculty of Electrical Engineering and Comunication, Dept. of Theoretical and Experimental Electrical Engineering, Brno, CZ,
[2]ASCR, Institute of Scientific Instruments, Královopolská 147, 612 64 Brno, CZ,
[3]Faculty of Agronomy, Mendel University in Brno, Brno, CZ
Email: xhutov00@stud.feec.vutbr.cz

Abstract. *The objective of this study was the monitoring of the growth and development of early somatic embryos in a magnetic field strength of 4.7 T. The samples were exposed to radiofrequency (RF) field, gradient (G) field and combination of both fields. To measure longitudinal (T_1) and transverse relaxation times (T_2), the spin echo based techniques were used. The aspects of major interest for the investigation of the related biological processes are the various image contrasts and the change of the relaxation times T_1 and T_2 on the boundary between the embryo and the substrate. Control measurements of changes in the size of the investigated tissue of early somatic embryos was done using camera and subsequently evaluated in MATLAB. All measurements were realized at the Institute of Scientific Instruments in Brno.*

Keywords: MRI Contrast, Early Somatic Embryos, Plants, Relaxation T_1 and T_2.

1. Introduction

Magnetic resonance imaging (MRI) is a non-invasive tool applied by many researchers to study molecules. The MRI approach is frequently used not only in medicine, but also in biological, biochemical, and chemical research. In plant biology, MRI is utilized to support the research of water and mineral compounds transported within a plant, the determination of plant metabolites, the investigation of cellular processes, and the examination of the growth and development of plants. MRI is also instrumental towards monitoring water changes in early somatic embryos of spruce (ESEs) [1]. These embryos constitute a unique plant model system applicable for the study of various types of environmental stresses (including metal ions) under well-controlled experimental conditions [2 - 4]. Some other measurements for different settings of the external magnetic field can prove that the external magnetic field can change the dynamics of the model of matter [5].

2. Method

The general aim of the experiment was to perform in vivo measurement of the ESEs using MRI techniques, and the entire process comprised several stages. Within the first step, we compared the acquired T_1- and T_2-weighted MR images, the next stage of the experiment consisted in determining the changes of the size of ESEs. To measure the T_2 relaxation, we applied spin-echo (SE) technique (echo times (TEs): 18, 30, 50, 100 and 200 ms); the measurement of the T_1 relaxation was realized using inversion recovery spin echo (IRSE) technique (inversion times (TIs): 10, 100, 300, 1000 and 3000 ms). Other samples of ESEs were "measured" by the same techniques, but in the first case, the only gradients were switched off and in the second case, the only RF field was switched off. All the described experiments were performed on the 4.7 T (Magnex) MRI system at Institute of Scientific Instruments in Brno. The MAREVISI (8.2) and MATLAB (R2014b) programs were used for the processing. The progress of growth was evaluated from 2D images of clusters in the Petri dishes, and the area of the ESEs was calculated. The acquired images of the ESEs were processed to provide the required data. For that reason, we created an application in MATLAB, which allows for the recognition and subsequent calculation of the area occupied by the ESEs [6]. Table 1 shows the distribution of the Petri dishes during the experiment.

Table 1. Distribution of Measured Samples

Sample n.	1	2	3	4	5	6	7	8
Method	IRSE, SE	RF	G	Control / without external field	IRSE, SE	RF	G	Control / without external field
Date of measurement	2014/10/20 - 2014/11/06				2014/10/21 - 2014/11/07			

3. Plant Material and Cultivation Conditions

A clone of early somatic embryos of the Norway spruce (*Picea abies/L./ Karst.*) marked as 2/32 were used in our experiments. The cultures were maintained on a semisolid (Gelrite Gellan Gum, Merck, Germany) half-strength LP medium with modifications. The cultivation was carried out in Petri dishes (diameter 50 mm). The sub-cultivation of stock cultures was carried out in 2-weeks intervals; the stock and experimental cultures were maintained at the temperature of 23±2°C in a cultivation box kept in a dark place. The experiment started with colonies of early somatic embryos which weight was about 3 mg. Only one cluster per one Petri dish was cultivated.

4. Results

Fig. 1 shows the images of the pre-processed Petri dishes. From these images was evaluated increase tissue during the experiment.

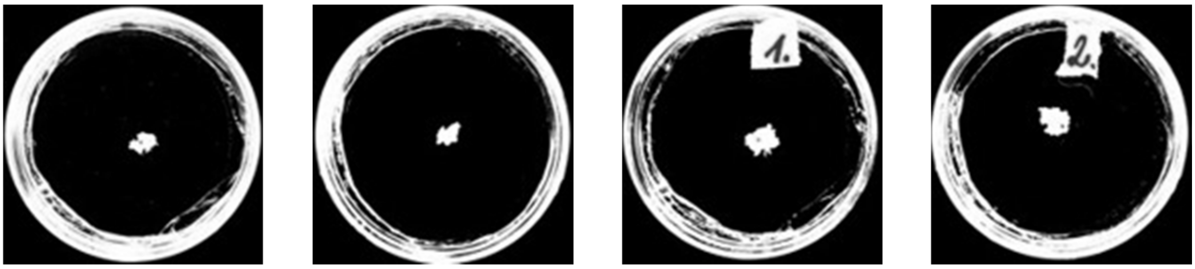

A. B. C. D.

Fig. 1. Petri dishes with ESEs prepared to evaluate the size of the tissue. A, B: images of sample 1 and 2 from the first day of experiment; C, D: corresponding images from the 13th day.

Fig. 2 shows the changes of the size of ESEs tissues. These results show that the most stable and suitable conditions for tissue growth were provided during the measurement of T_1 and T_2. If the increase in these two samples expressed as a percentage, these values are 189.7 % (sample 1) and 169.5 % (sample 5). On the other side was very different growth and development of control samples that were exposed only to the influence of the magnetic field of the earth. If the increase in these two samples expressed as a percentage, these values are 136.4 % (sample 4) and 250 % (sample 8). Values which reflect an increase in the area may be dependent on the error, which is caused for example by bad evaluating the size of the surface tissue.

The other aspects of interest for the investigation of the related biological processes is the various image contrasts and the change of the relaxation times T_1 and T_2 on the boundary between the embryo and the substrate. Fig. 3 shows the T_1 and T_2 maps and the changes in development of sample 1 at first and last day of experiment.

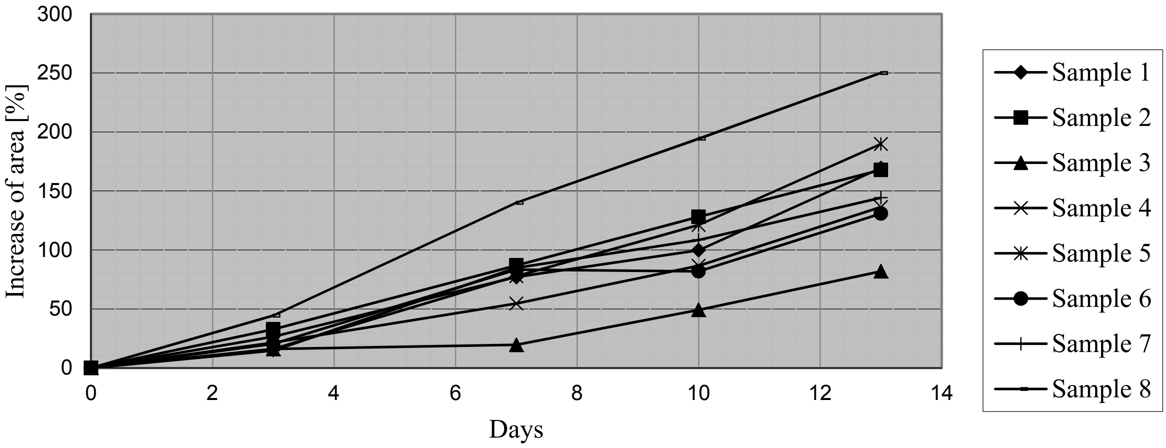

Fig. 2. The growth of individual samples during the experiment.

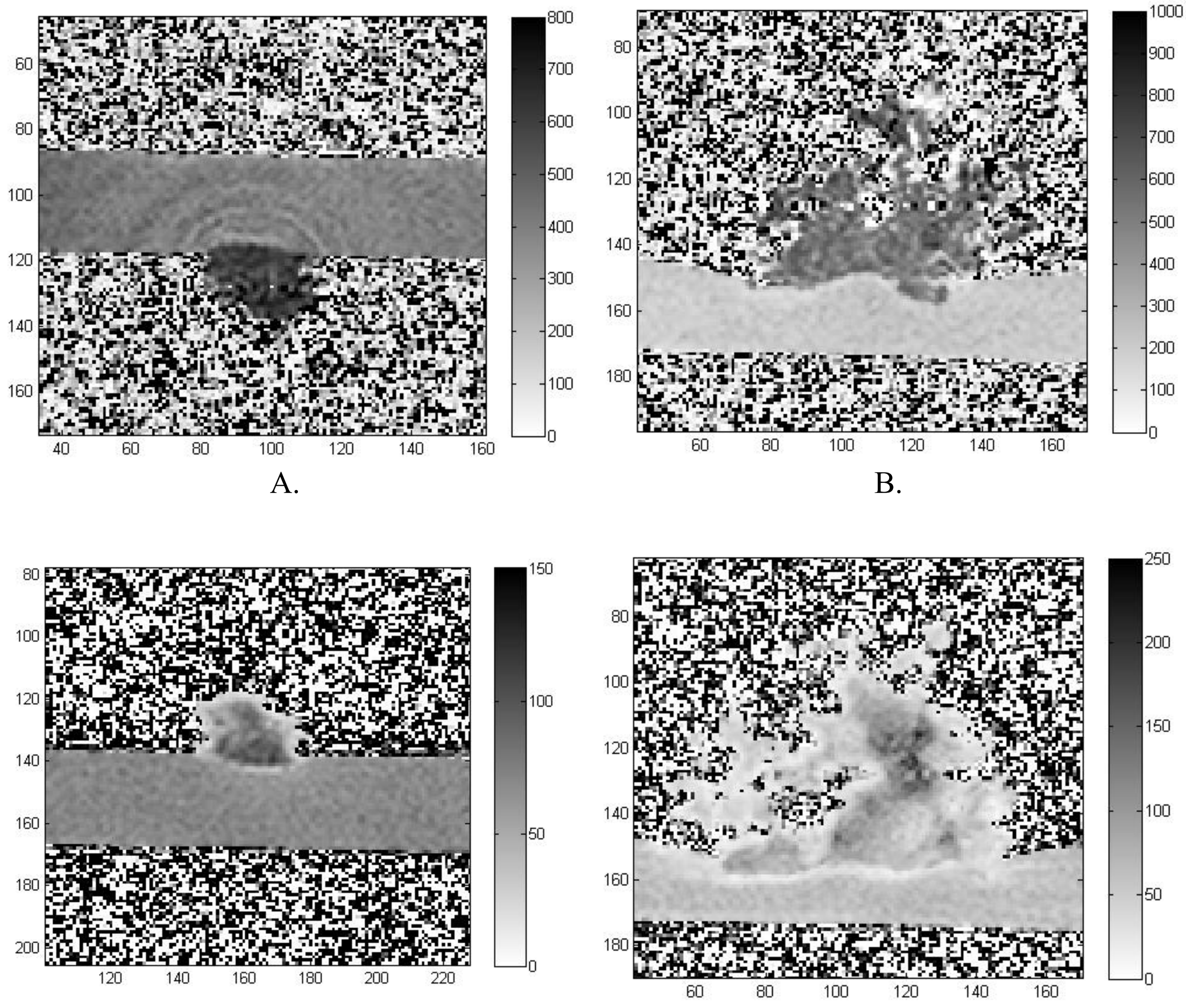

Fig. 3. The changes in development of sample 1 during the experiment: A, C: T_1 and T_2 maps (ms) in first day of the experiment (0 day); B, D: T_1 and T_2 maps (ms) in 13th day.

A comparison of the mean of the relaxation times T_1 and T_2 in the ESEs (sample 1) and the substrate can be seen in Table 2.

Table2. The relaxation times (mean value) T_1 and T_2 of the ESEs and the substrate.

B_0 field	T_1 [ms]	T_2 [ms]	Method
first day of experiment (0 day)			
ESEs	634	61	IRSE/SE
Substrate	398	36	
last day of experiment (13^{th} day)			
ESEs	761	86	IRSE/SE
Substrate	386	46	

5. Conclusion

The experimental results show that the effect of gradient magnetic fields on ESEs varies considerably (Table 1). We are still unable to assess whether the effect of stationary magnetic fields for plant organisms is positive or not but we now that the external magnetic field changes the dynamics of the model of matter and theoretically can change the growth of organisms. Table 2 shows the relaxation times T_1 and T_2 of the samples in different magnetic fields. The changes of the relaxation times T_1 and T_2 on the boundary between the embryo and the substrate are of interest for the investigation of biological processes.

Acknowledgements

The research described in the paper was financially supported by Czech Science Foundation (GA 13-09086S).

References

[1] Supalkova V, Petrek J, Baloun J, Adam V, Bartusek K, Trnkova L, Beklova M, Diopan V, Havel K, Kizek R. Multi-instrumental Investigation of Affecting of Early Somatic Embryos of Spruce by Cadmium(II) and Lead(II) Ions, *Sensors*, 7: 743, 2007.

[2] Mikelova R, Baloun J, Petrlova J, Adam V, Havel L, Petrek H, Horna A, Kizek R. *Bioelectrochemistry*, 70: 508, 2007.

[3] Petrek J, Vitecek J, Vlasinova H, Kizek R, Kramer KJ, Adam V, Klejdus B, Havel L. *Anal. Bioanal. Chem.*, 383: 576, 2005.

[4] Víteček J, Adam V, Petřek J, Vacek J, Kizek R, Havel L. Esterases as a marker for growth of BY-2 tobacco cells and early somatic embryos of the Norway spruce, Plant *Cell Tissue Organ Cult.* 79: 195-201, 2004.

[5] Vlachova Hutova E, Bartusek K, Fiala P. The Influence of a Magnetic Field on the Behaviour of the Quantum Mechanical Model of Matter. In PIERS 2014 Guangzhou Proceedings. Progress In Electromagnetics, 2014, 1847-1851.

[6] Vlachova Hutova E, Bartusek K, Mikulka J. Study of the Influence of Magnetic Fields on Plants Tissues. In Proceedings of PIERS 2013 in Taipei. Progress In Electromagnetics, 2013, 57-60.

[7] Bartusek K, Gescheidtova E, Mikulka J. Data processing in studying biological tissues, using MR imaging techniques. 33th International Conference on Telecommunications and Signal Processing, Asszisztenda Szervezo, Budapest, 2010, 171–175.

Comparison ASL and DCE-MRI Perfusion Map in Small Animal Model of Cancer

[1,2]L. Grossová, [1]R. Jiřík, [3,4]K. Souček, [1,5]E. Dražanová, [1]Z. Starčuk jr.

[1]Institute of Scientific Instruments, AS CR, Brno, Czech Republic,
[2]Dept. of Biomedical Engineering, Brno Univ. of Technology, Brno, Czech Republic
[3]Dept. of Cytokinetics, Institute of Biophysics, AS CR, Brno, Czech Republic
[4]Center of Biomolecular and Cellular Engineering, International Clinical Research Center, St. Anne's Univ. Hospital Brno, Brno, Czech Republic
5Dept. of Medical Pharmacology, Faculty of Medicine MU, Brno, Czech Republic
Email: grossoval@isibrno.cz

Abstract. *This paper is focused on quantitative perfusion analysis using pulsed ASL (FAIR-RARE) and DCE-MRI (using high- and low-molecular-weight contrast agents) in a mouse tumour model. Tumour blood-flow maps of both methods were compared using visual assessment, region analysis (median, percentiles), scatter plots and correlation coefficients. ASL blood-flow estimates matched the DCE-MRI blood-flow estimations in some cases. Possible reasons for poor match in the other cases were investigated. This study indicates that in tumour perfusion analysis, we might profit from the combination of ASL and DCE-MRI instead of using just one of them.*

Keywords: Blood Flow Quantification, ASL, DCE-MRI, Perfusion, Tumour

1. Introduction

Blood flow imaging is an important tool, especially in oncology, neurology and cardiology. Magnetic resonance imaging (MRI) provides three quantitative methods of blood flow imaging: Dynamic Susceptibility Contrast MRI (DSC-MRI, contrast-agent based, mostly for brain applications), Dynamic Contrast-enhanced MRI (DCE-MRI, contrast-agent based, mostly for tumour applications) and Arterial Spin Labeling (ASL, no contrast agent, mostly for brain applications). In studies focused on brain imaging, ASL was compared to DSC-MRI. In recent years, several studies comparing ASL vs. DCE-MRI appeared due to an expansion of ASL from brain applications also to other organs (kidneys [1], pulmonary parenchyma [2], tumour-treatment response [3]). These studies indirectly compared blood flow estimated with ASL to the perfusion parameters estimated by DCE-MRI (k_{ep}, K^{trans}, v_e) which are only related to blood flow but not equivalent. Our DCE-MRI method is based on advanced pharmacokinetic models providing estimates of blood flow. This provides a direct comparison of the same quantity, one estimated using ASL and one using DCE-MRI. Also, compared to the previous approaches, here we do not intend to replace one method by another but aim at their combination to provide more reliable estimation of perfusion parameters.

2. Subject and Methods

Subjects

This study was evaluated on preclinical data from five BALB/c mice (approved by the animal care committees required by law). Murine colon tumour cells CT26.WT (ATCC, CTL-2638) were subcutaneously implanted into the left flank (1×106 cells in HC Matrigel). Each mouse underwent one ASL examination, and two DCE-MRI examinations, one with a high-molecular-weight contrast agent (Gadospin P, MiltenyiBiotec, BergischGladbach, Germany) and one with a standard low-molecular-weight contrast agent (Magnevist, Bayer HealthCare Pharmaceuticals, Berlin, Germany).

MRI Acquisition

MR imaging was performed on mice using an experimental 9.4T Biospin (Bruker Biospin MRI, Ettlingen, Germany) scanner. A surface receiver coil and a volume transmitter coil were used. The mice were anesthetized with Isoflurane and O_2 mixture (2% of Isoflurane, 800ml/min of O_2). Their respiratory rate was monitored continuously during the whole measurement. The ASL sequence FAIR-RARE was used with the following acquisition parameters: 2D sequence with TR/TE 10 000/37.78 ms, image matrix 128×96 pixels, slice thickness 1 mm, FOV 23.2×35 mm, one axial slice through the tumour middle was imaged with 15 TI values (30, 50, 100, 200, 300, 500, 700, 900, 1000, 1100, 1500, 1800, 2200, 2800, 3200ms).

The acquisition parameters of DCE-MRI sequence were as follows: 2D FLASH sequence with TR/TE 14/2.5 ms, flip angle 25°, image matrix 128×96 pixels, slice thickness 1 mm, one axial slice (same as in ASL), sampling interval 1.05 s, acquisition time 13 min. Before the bolus administration, 15 pre-contrast images were recorded with 6 TRs (14, 30, 50, 100, 250, 500 ms) to convert the dynamic image sequence to the contrast-agent concentration. In addition, anatomical images were recorded using the RARE sequence (T_2-weighted and T_1-weighted pre- and post-contrast).

Data Analysis

All ASL data were analysed using the ParaVision software, version 5.1 (BrukerBrukerBiospin MRI, Ettlingen, Germany). ASL blood flow maps in manually drawn tumor ROIs were calculated with the following formula

$$F = \lambda \cdot \frac{T1_{nonsel}}{T1_{blood}} \left(\frac{1}{T1_{sel}} - \frac{1}{T1_{nonsel}} \right) \quad (1)$$

Where F is tissue blood flow [ml/min/g tissue], λ is the tissue-blood partition coefficient for water and T_{1sel} and $T_{1nonsel}$ are longitudinal relaxation times of blood estimated using the selective or nonselective images, respectively.

All DCE-MRI data were analysed in Matlab™ (MathWorks, Nattick, USA). Adiabatic-approximation of the tissue homogeneity (ATH) pharmacokinetic model was used to model the tissue contrast-agent concentration time curves. Blind deconvolution was used for estimation of the arterial input function (part of the pharmacokinetic model) [4].

3. Results

Blood-flow maps from ASL and DCE-MRI data were first compared visually (Figs. 1, 2).For two mice (M1, M2), the maps were in a good agreement while for three mice (M3-M5) the maps did not match. Region analysis was done for manually drawn tumour ROIs for pixels where $v_e < 1$(v_e – fractional interstitial volume estimated from DCE-MRI) to exclude necrotic regions where the pharmacokinetic model of DCE-MRI is not valid. The median and the 25th and 75th percentiles were calculated (Table 1). Scatter plots (Figs. 3) and the corresponding Pearson correlation coefficients were calculated to compare quantitatively the ASL and DCE-MRI results. To assess the validity of the DCE-MRI blood-flow estimates, an additional perfusion parameter estimated by DCE-MRI, *PS* (vessel permeability surface area product), was also reported (Table 1).

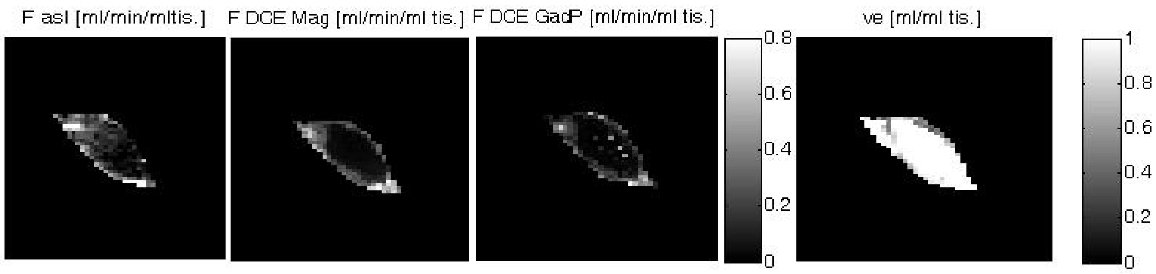

Fig. 1. Mouse M1 blood-flow maps, from the left ASL, DCE Magnevist, DCE GadospinP and ve.

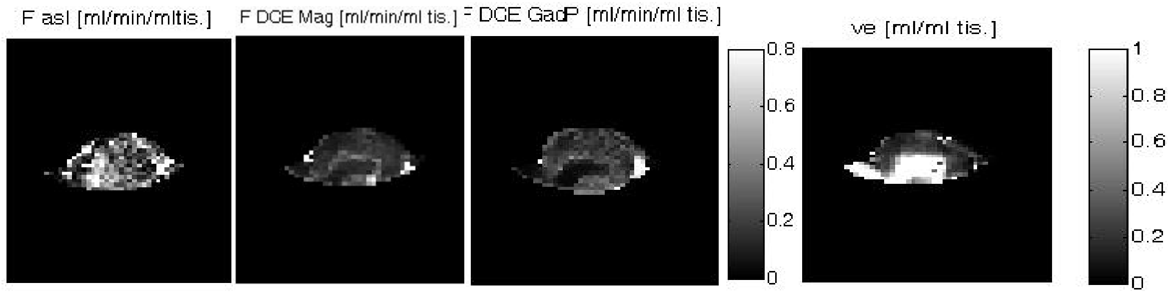

Fig. 2. Mouse M4 blood-flow maps, from the left ASL, DCE Magnevist, DCE GadospinP and v_e.

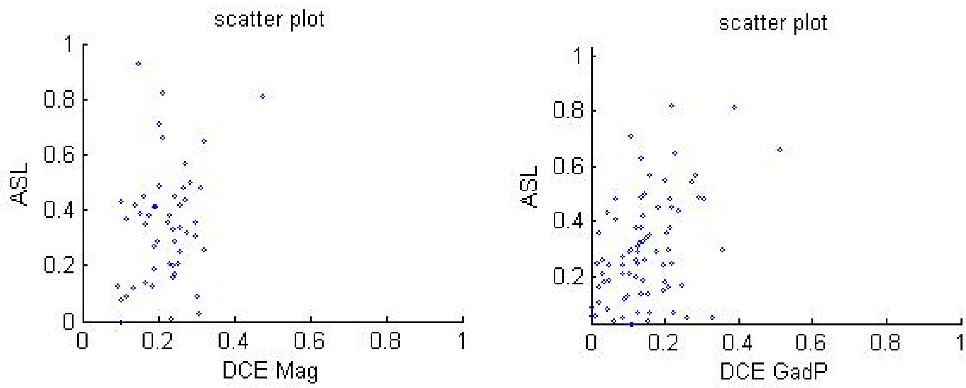

Fig. 3. Mouse M1 blood-flow scatter plots, left ASL vs. DCE (Magnevist), right ASL vs. DCE (GadospinP).

Table 1. Tables of blood-flow and PS median[25th; 75th percentiles], C - Pearson correlation coefficients, Mag - Magnevist, GadP - GadospinP, M - mouse.

M	F_{asl} [ml/min/g tis.]	F_{Mag} [ml/min/g tis.]	F_{GadP} [ml/min/g tis.]	PS_{Mag} [ml/min/g tis.]	PS_{GadP} [ml/min/g tis.]	$C_{asl\text{-}Mag}$	$C_{asl\text{-}GadP}$
1	0.25[0.1;0.6]	0.24[0.1;0.4]	0.13[0.1;0.2]	0.11[0.1;0.3]	0.03[0.01;0.07]	0.5	0.3
2	0.33[0.1;0.7]	0.31[0.1;0.5]	0.23[0.1;0.3]	0.15[0.1;0.2]	0.08[0.03;0.14]	0.4	0.3
3	0.34[0.1;1.0]	0.27[0.2;0.4]	0.21[0.1;0.3]	0.16[0.1;0.2]	0.10[0.07;0.15]	-0.02	0.1
4	0.36[0.1;0.7]	0.15[0.1;0.3]	0.16[0.1;0.2]	0.10[0.1;0.2]	0.06[0.04;0.09]	0.1	0.1
5	0.34[0.2;0.8]	0.26[0.2;0.4]	0.29[0.2;0.3]	0.11[0.1;0.2]	0.05[0.04;0.07]	-0.2	0.01

4. Discussion

The ASL and DCE blood-flow maps were consistent for mice M1 and M2, especially when comparing ASL to Magnevist DCE-MRI where the best match of blood flow medians and

Pearson correlation coefficients were obtained. This is in line with theoretical assumptions because GadoSpinP DCE-MRI data were noisier than Magnevist DCE-MRI data due to the limited extravasation of the high-molecular-weight contrast-agent. This was also shown by the approximately twofold decrease in the *PS* parameter. Furthermore, the low-flow areas corresponded well with the necrotic area indicated by high values in the v_e maps and bright areas in the post-contrast T_1- weighted images. For mice M3 – M5, the agreement of ASL and DCE-MRI was poor because of several factors. First, the tumours were necrotic to a large extent, so the agreement could be evaluated only in few pixels. Another source of error might be seen in movement artefacts due to breathing, which were not so pronounced for M1 and M2. For mouse M4, ASL clearly failed (the T_1 quantification algorithm in the ParaVision software got trapped in a wrong estimate, checked by using own implementation). The reason for poor match in M3 and M5 is not completely clear. The above mentioned indirect measures of the DCE-MRI accuracy (consistency of *PS* and consistency of the flow maps with the v_e maps and post-contrast T_1-weighted images) were similar as for mice M1, M2, suggesting that ASL failed also for these recordings.

5. Conclusions

The ASL perfusion analysis (using the ParaVision software, version5.1) gave blood-flow values consistent with DCE-MRI (analysed using ATH pharmacokinetic model and blind deconvolution according to [4]) for two mice, while poor match was obtained for three other mouse experiments. The reasons for this mismatch will be analysed on a larger set of recordings with possibly larger highly perfused regions and less necrotic tissue. Our results also indicate a suboptimal reliability of the ASL-analysis part of the ParaVision software. This will be studied thoroughly as a follow-up work. The results indicate that it makes sense to combine ASL and DCE-MRI methods instead of using just one of them.

Acknowledgements

The study was supported by Ministry of Education, Youth, and Sports of the Czech Republic (project No. LO1212) and by the project FNUSA-ICRC (CZ.1.05/1.1.00/02.0123).

References

[1] Cutajar M, Thomas D L, Hales P W, Banks T, Clarc Ch A,Gordon I. Comparison of ASL and DCE MRI for the non-invasive measurement of renal blood flow: quantification and reproducibility. *European Radiology*. 2014, vol. 24, issue 6, s. 1300-1308. DOI: 10.1007/s00330-014-3130-0.

[2] Li F, Liu S, Sun F, Xiao X, Clarc CH A, Gordon I. Assessment of pulmonary parenchyma perfusion with FAIR in comparison with DCE-MRI—Initial results: quantification and reproducibility. *European Journal of Radiology*. 2009, vol. 70, issue 1, s. 41-48. DOI: 10.1016/j.ejrad.2007.12.013.

[3] Wenchao C, Li F, Wang J, Huarui D, Wang X, Zhang J, Fang J,Jiang X. A comparison of arterial spin labeling perfusion MRI and DCE-MRI in human prostate cancer. *NMR in Biomedicine*. 2014, vol. 27, issue 7, s. 817-825. DOI: 10.1002/nbm.3124.

[4] Jiřík R,Souček K,Mézl M, Bartoš M, Dražanová E, Dráfi F, Grossová L,Kratochvíla, J,Macíček O,Nylund K,Hampl A,Gilja O,Taxt T,Starčuk Z. Blind Deconvolution in Dynamic Contrast-Enhanced MRI and Ultrasound. *In 36th Annual International Conference of the IEEE Engineering in Medicine and Biology Society*. 2014. p. 4276 - 4279. ISBN 978-1-4244-7929-0.

Comparison of Iron Accumulation in Clinical MRI Data

[1]M. Masárová, [1]A. Krafčík, [1]M. Teplan, [1]O. Štrbák, [1]D.Gogola, [2]P. Bořuta, [1]I. Frollo

[1]Institute of Measurement Science, SAS, Bratislava, Slovakia
[2]Slovak Medical University, Bratislava, Slovakia
Email: marta.masarova@savba.sk

Abstract. *The aim of this study is to clarify whether clinical MRI data can be used in evaluation of the pathological processes associated with disrupted iron homeostasis, such as neurodegenerative processes, or cirrhosis. MRI has potential to become a non-invasive biomarker of such pathology, however new quantification methods must be introduced. Our findings confirmed that it is possible to detect significant difference between healthy and pathological tissue from standard T2 weighted MRI protocols. Moreover, diagnostic tool might be developed from our approach, as discriminant analysis yielded 9.7 % overall error rate.*

Keywords: MRI, Iron, Contrast Change, Neuroinflammation Disease, Human Brain

1. Introduction

Iron is an essential nutrient, required by every human cell. Iron concentration is normally maintained in a narrow homeostatic range, in about 40 mg Fe/kg of body weight in women, and 50 mg Fe/kg in men. [1][2]

The iron in human body has two major forms. Heme and nonheme iron. About 80% of body iron is functional, located in red blood cells as hemoglobin, in muscles as myoglobin, and in muscle, and also as a part of iron-containing enzymes. Nonheme iron can be found in transporter molecules such as transferrin, as well as, in storage molecules such as ferritin and hemosiderin. Transferrin is an intravascular transport protein that delivers iron to the liver, bone marrow, and other tissues. Ferritin is a spherical protein shell, which is able to accumulate and store up to 4500 iron atoms. [1] [3]

Iron plays an important role in the central nervous system (CNS) where it is involved in oxygen transport, neurotransmitter synthesis and nerve myelination [2]. Abnormal accumulation of iron or disruption of iron metabolism has been detected in various liver disease and neurodegenerative diseases such as Parkinson disease (PD) and Sclerosis multiplex (SM). Highest concentrations of iron in neurodegenerative disease were found in basal ganglia and related structures (BGRS): Globus pallidus (21μg/100g fresh weight), Substantia nigra, red nucleus and putamen [1] [2].

Ferritin and hemosiderin are supposed to be the most important sources of iron related to signal changes in cerebral MRI. Presence of iron has influences on the final contrast of T2 weighted MR images. The loss of the signal in T2 weighted images is caused by a shortening of the transversal relaxation times of protons, especially in deep gray matter nuclei of the brain. Such iron caused hypointensive artifacts have a potential to become a new non-invasive tool of iron related disorders. [1]

The aim of this study is to find out, with the help of clinical MRI data, whether it is possible to distinguish between healthy and pathological tissue (with standard MRI protocols), enable such iron quantification and non-invasive diagnostics of iron-related disorders.

2. Subject and Methods

The aim of our research is comparison of healthy (control) and pathological clinical MRI data with respect to signal modification caused by biogenic iron accumulation. Clinical data were obtained from the Slovak Medical University Bratislava (ass. prof. P. Boruta), and were measured on 3T system Siemens Vario, by standard T2 weighted GE protocol. 31 persons with different sex and age were evaluated. 18 persons were identified as healthy, and 13 persons were diagnosed as Sclerosis Multiplex (SM) or Parkinson disease (PD) patients. For image data processing and basic analysis we used the following software tools: Marevisi (NRC - Institute for Biodiagnostic, Winipeg, Canada), and Matlab R2011b (Mathworks Inc., Natick, Massachusetts, USA).

The Regions of Interest (ROI), comprising of BGRS as well as reference sites, were identified by radiologist in every evaluated person, for both groups (control and pathological). Relative T2 contrast for every person, every slice, and every ROI was calculated as follows:

$$RC = \frac{(c - c_0)}{c_0} \qquad (1)$$

where RC relative contrast,
c mean intensity of each sample ROI in MRI image slice,
c_0 grand mean [4] intensity of all reference ROIs in same MRI image slice.

Standard statistical tools were applied to distinguish between pathology and control sample. Shapiro-Wilk test was used for normal distribution evaluation, and Kruskal-Wallis test to distinguish whether data originate from the same distribution. The control group (healthy subjects) comprises of 281 data samples (ROIs) from 18 subjects, and pathological group (PD or SM patients) includes 138 data samples (ROIs) from 13 subjects.

3. Results

Total relative contrast value for control and pathological group is shown in Fig. 1. The result indicates that we are able to clearly distinguish between healthy and diseased group. Statistical tests were applied to verify the significance of such findings. Shapiro-Wilk test has shown that both groups (control, and pathological) were not distributed normally (Fig. 2). Subsequent non-parametric Kruskal-Wallis test confirmed that both groups are very significantly different, with p-value smaller than 10^{-10}.

As the next step we focused on the approach valuable from the diagnostic point of view. Leave-one-out cross-validation was implemented in order to simulate new patient approaching for diagnostics. From 31 subjects each time one subject was omitted, while from the rest of 30 subjects RC distribution for pathological and control groups were separately formed. “New” patient was classified into one of the two groups based on the comparison of his or her distribution of RC with distributions belonging to pathological and control groups. Greater of the two p-values from Kruskal-Wallis test was interpreted in such a way that two distributions under comparison were closer to each other. Thus, the patient was classified just into this group. 11 out of 13 subjects from pathological group were discriminated correctly, which yields 84.6 % sensitivity, or complementarily 15.4 % false negative error rate. For control group, 17 out of 18 subjects were classified correctly, yielding 94.4 % specificity, or 5.6 % false positive error rate. The overall error rate was at the level of 9.7 %. By this procedure we were able to obtain relatively strong discriminating rates in spite of the fact that control and pathological distributions are apparently overlapping to greater extent.

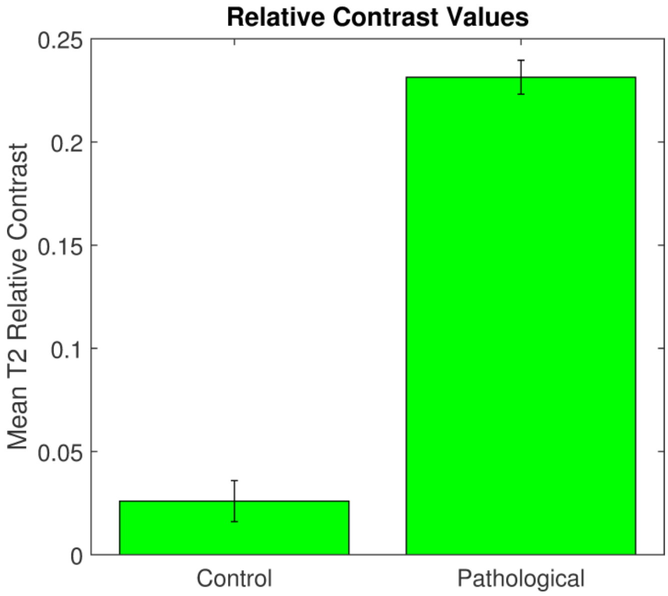

Fig. 1. Relative contrast value for control and pathological group

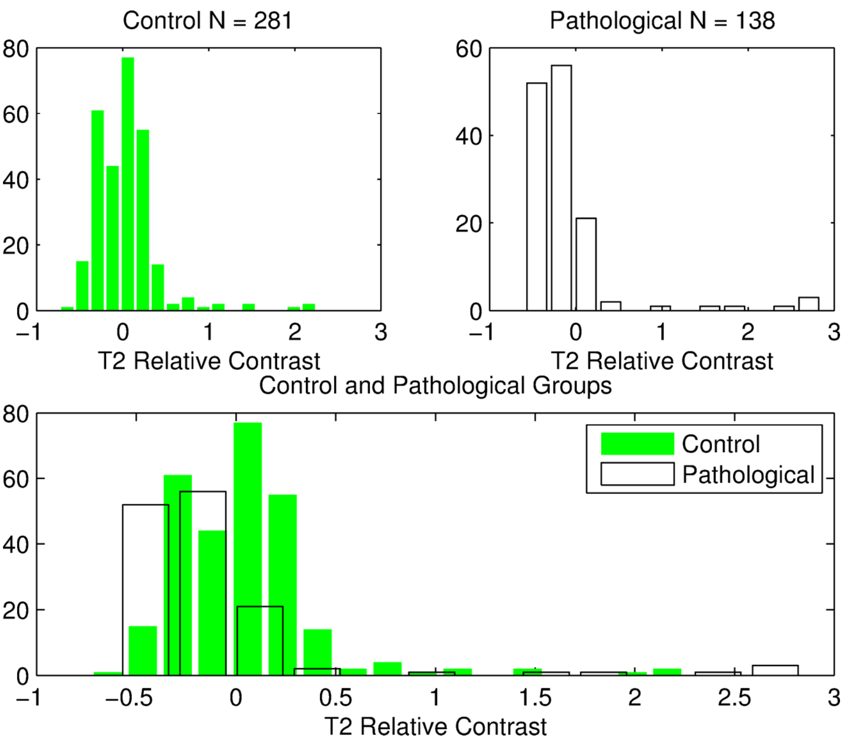

Fig. 2. T2 Relative contrast control and pathological group

4. Conclusions

Statistical evaluation of standard T2 weighted MR images of selected brain tissue objects has shown significant difference between control (without neuropathology) and pathological group, using non-parametric statistical method. Based on these limited data it seems feasible that diagnostic tool for several iron sensitive neurodegenerative conditions may be developed. Outcome of this study is our starting point for further research in the field of iron quantification and non-invasive diagnostics of neuropathological diseases associated with the accumulation of iron in brain tissue.

Acknowledgements

This work was supported by the Slovak Research and Development Agency APVV-0431-12, and by the Slovak Scientific Grant Agency VEGA 2/0013/14, and 2/0043/13.

References

[1] Dusek P, Dezortova M, Wuerfel J. Imaging of Iron. *International Review of Neurobiology,* 110 (2013), 195-239.

[2] Sirlin CB, Reeder S B. Magnetic Resonance Imaging Quantification of Liver Iron. *Magn Reson Imaging Clin N Am,* 18 (2010), 359–381.

[3] You LH, Li F, Wang L, Zhao SE, Wang SM, Zhang LL, Zhang LH, Duan XL, Yu P, Chang YZ. Brain Iron Accumulation Exacerbates the Patogenesis of MPTP-Induced Parkinson's Disease. *Neuroscience,* 284 (2015), 234-246.

[4] Burton DA. Composite Standard Deviations. available [online] (March 2015).<http://www.burtonsys.com/climate/composite_standard_deviations.html>.

Heat Transfer Modeling for Pulse Laser – Assisted Removal of Arrhytmogenic Sources

[1]J.Urzová, [1,2]M. Jelínek, [1,2]J. Remsa, [3]L.Vajner

[1]CTU in Prague, Faculty of Biomedical Engineering, Kladno, Czech Republic
[2]Institute of Physics of the Czech Academy of Sciences, Prague, Czech Republic
[3]2nd Faculty of Medicine, Charles University in Prague, Prague, Czech Republic
Email: rygadwyn@email.cz

Abstract. *One of the possible applications of medical lasers is in treatment of heart arrhythmia. Pulse lasers can become an alternative to conventional treatment or its supplement. Its precision and targeted removal of arrhythmogenic sources without damaging the surrounding tissue is a major advantage. Using nanosecond pulses with this technology achieves the necessary photoablation while preventing heat stress, commonly seen when using continuous-wave lasers. In the case of a pulse laser there is no heat stress in the surrounding healthy tissue because any surplus is transferred away by blood perfusion. A theoretical mathematical model has been created to describe heat transfer in tissues throughout the procedure. The model was created with the COMSOL Multiphysics software. All the necessary parameters were either calculated or experimentally determined in the laboratories of FBME CTU and it's where the model had been experimentally verified as well.*

Keywords: Heart Arrhythmia, Absorption Coefficient, Ablation Depth, Bioheat Transfer Modeling

1. Introduction

Catheter ablation aimed at removal of arrhythmogenic sources with a laser is one of the alternatives to pharmacological treatment of heart arrhythmia. Continuous-wave lasers are currently in use for that very purpose. Their advantage is in precise removal of the pathological tissue but their use can lead to overheating in the tissue. Rising temperatures in the tissue can cause irreversible damage, the scale of which depends on the temperatures reached and on the duration of exposure to these temperatures. Current research is looking into the possibility of using pulse lasers which, with appropriate repeating frequency, would prevent any undesirable overheating. A pulse laser with adequate energy density can effectively remove any pathological tissue by photoablation and any excess heat is transferred into its surroundings. The aim of our work is to create a functioning theoretical model to predict heat transfer in in tissues surrounding the laser-treated area.

2. Subject and Methods

The theoretical model was created using the COMSOL Multiphysics 4.4 software, with the pre-defined module „Bioheat Transfer“ (Fig. 1), with tissue parameters for optical and thermophysical quantities of heart muscle either calculated or predetermined experimentally. Laser beam parameters (pulse length, repetition frequency, energy density) can be adjusted for each specific application.

During our experiments the tissue (porcine heart) was exposed to laser beams with varying energy densities (700 – 2500 $mJ.cm^{-2}$) and varying repetition frequencies (5 – 25 Hz). For that a KrF excimer laser (248 nm) was used. The resulting ablation craters were examined with two goals in mind – to determine the ablation depth and to describe the crater‘s shape and development over time.

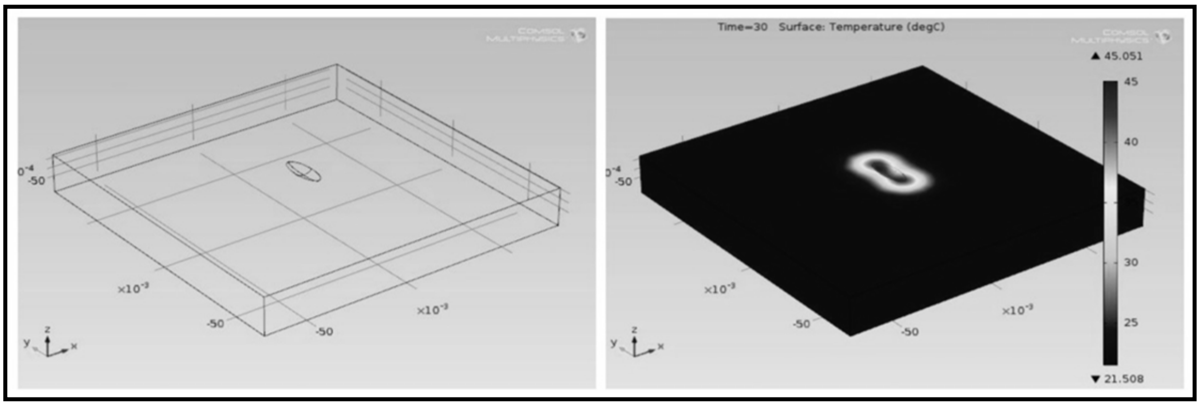

Fig. 1. Heat transfer model created in the COMSOL software. Geometry of the sample with an ablation crater on the left and graphical output with measured temperatures

Crater´s depths measured using various methods (direct measurement, focusing method, scanning). CT scan of its profile proved to be the most optimal and the results from other methods were used only as a reference. The scans were obtained using the XR 4.0, PHYWE RTG unit set at 35 kV and 1 mA on the anode with potassium iodide used as a contrast dye. Fig. 2 displays five craters with a pin of known length (27.05 mm) to help determine their depths. MATLAB was used to ascertain the precise crater depth. Experimentally established crater depths (14.0 ± 1.5) µm for heart muscle tissue were compared to published values [7], [8]. The value we established matches the published values.

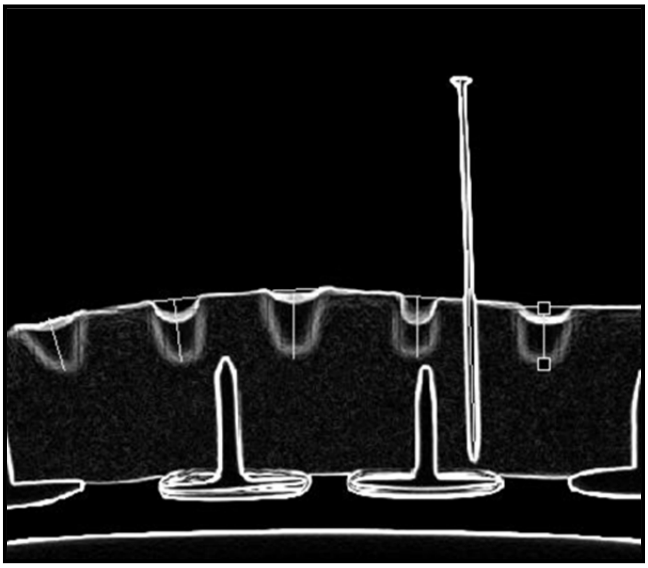

Fig. 2. A CT image of the craters' profile (500 pulses, 1240 mJ.cm^{-2})

Another one of the parameters necessary for the simulation model is the absorption coefficient of heart muscle tissue. Through spectrophotometric analysis, using the Shimadzu UV-VIS-NIR 3600, the transmittance values of bovine myocardium were measured in a wide wavelength range from 185 to 3300 nm. 50 µm thick samples were used, which is enough to neglect local non-homogeneous segments of the tissue, while maintaining precision of the measurement. The absorption coefficient was calculated from the obtained transmittance values for the wavelength range examined (Fig. 3).

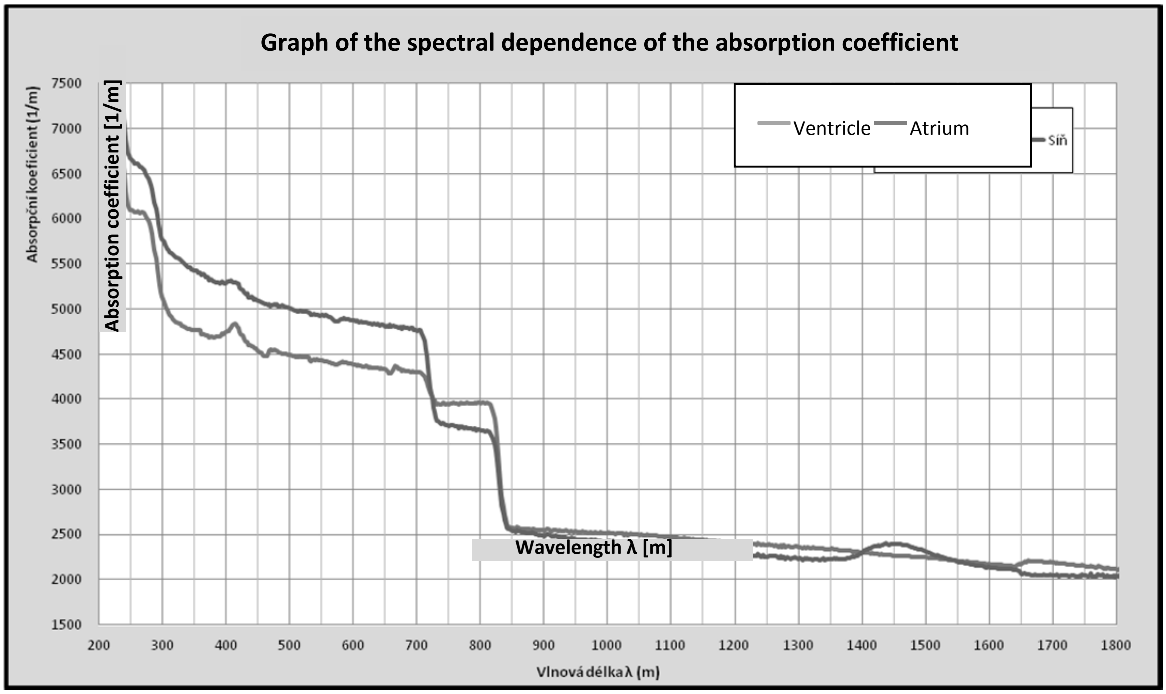

Fig. 3. Spectral dependence of the absorption coefficient for heart muscle in a selected range of wavelengths.

For validating the proposed model a theoretical calculation of the surface heat transfer was compared to an image captured by a thermal camera monitoring the sample surface throughout the exposure (fig. 3). FLUKE TI55/20FT is thermal imaging camera with 320 × 240 resolution, sensitivity of 0.05 ^{o}C and all data recorded at 60 Hz.

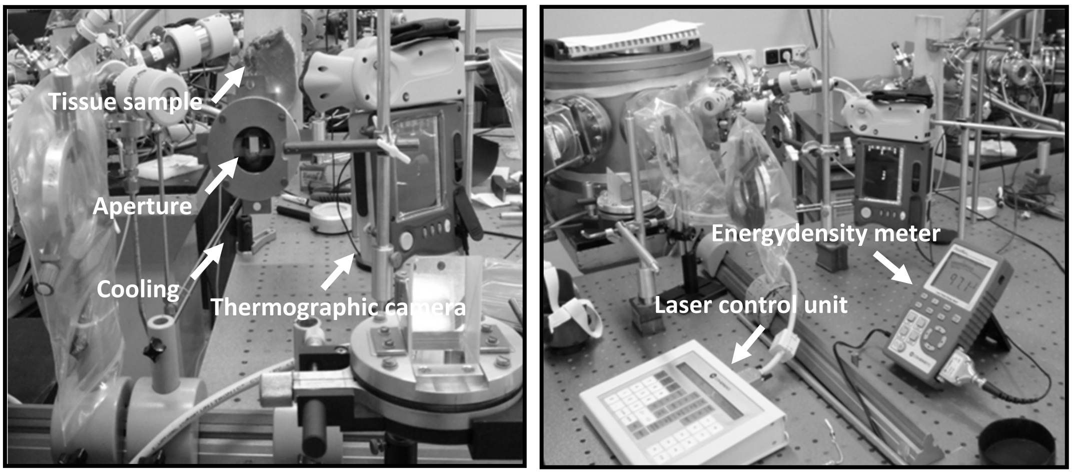

Fig. 4. Surface heat monitoring apparatus.

Neither blood perfusion nor metabolic heat was included in this experiment and for the default sample temperature the real value was used. Convective heat dissipation from the surface of the sample was included.

3. Results

A model of heat transfer in heart muscle tissue during removal of pathological nodes by photoablation was created. Parameters describing the laser-tissue interaction were determined experimentally or calculated from the chemical composition of the tissue. Spectral dependence of absorption coefficient for heart muscle tissue of the atrium as well as the ventricle was measured for wavelengths ranging from 200 nm to 3000 nm and as a result the model is applicable for lasers using various wavelengths when an appropriate absorption coefficient is used. The ablation depth and shape of the crater, created through photoablation, were detailed using CT images. The model was experimentally verified by monitoring the sample's surface heat transfer and its comparison to the calculated theoretical values. It is possible to determine the maximal temperature reached in the tissue and its duration to help assess the risk of irreversibly damaging the tissue. We have created a working model of heat transfer in heart muscle tissue following its exposure to a laser and subsequently verified it experimentally. The model allows us to predict changes in temperature during the process of removing arrhythmogenic sources using a pulse laser. With it, the type of laser and its parameters (energy density, frequency) can be tailored for each individual procedure.

4. Discussion

Using adequately set up pulse lasers is proving to be a perspective alternative method for use in heart arrhythmia treatment. The pulse mode allows for setting a repeating frequency that prevents any excessive heat from spreading into and damaging surrounding healthy tissue, because the heat is transferred from it by conduction and blood perfusion. If a thermal imaging camera monitors the tissue surface during the procedure, the heat transfer can be immediately compared to the theoretically predicted development and then, if necessary, the repetition frequency can be adjusted without terminating the procedure.

Acknowledgements

We thank doc. J. Hozman of FBME CTU for his help with capturing images of the ablation craters using the XR 4.0, PHYWE unit and the CUT Grant Commission for financial support under project No. SGS15/111/OHK4/1T/17 and No. SGS14/168/OHK4/2T/17.

References

[1] Carslaw HS, Jaeger JC. Conduction of Heat in Solids. Oxford University press, 2007.

[2] Niemz M. Laser-Tissue interactions. Berlin Springer-Verlag, 1996.

[3] Goldman L, Rockwell RJ. Lasers in medicine. Ronald Waynant. CRC press, 2002.

[4] Kanawade R, Mehari F, Knipfer Ch. Pilot study of laser induced breakdown spectroscopy for tissue differentiation by monitoring the plume created during laser surgery - An approach on a feedback laser control mechanism. *Spectrochimica Acta Part B: Atomic Spectroscopy*. 2013, 87: 175-181. DOI: 10.1016/j.sab.2013.05.012.

[6] Urzová J. Stanovení termofyzikálních parametrů tkání výpočtem ze znalosti jejich chemického složení: Determination of thermophysical parameters of tissues from their chemic composition. *Československý časopis pro fyziku*. 20130400, 63 (2): 112-122.

[7] Jansen E, Freny M, Kadipasaoglu K. Laser – Tissue Interaction During Trans-myocardial Laser Revascularization. *The Annals of ThoracicSurgery*. 1997, 63(3): 640-647. DOI: 10.1016/S0003-4975(96)01143-5

[8] Haffner C, Folwaczny M, Hickel R. Ablation of temporomandibular joint structures of a pig with a fibre-guided 308 nm excimer laser light - an in vitro investigation. *Journal of Cranio-Maxillofacial Surgery.* 2004, 32(6). DOI: 10.1016/j.jcms.2004.05.006.

Dimensional Stability of Addition Silicones - Influence of Setting Time on the Accuracy of Working Casts

[1]M. Potran, [2]B. Štrbac, [1]K. Vicko, [1]T. Puškar

[1] Department of Dentistry, Medical Faculty, University of Novi Sad, Novi Sad, Serbia
[2] Department of Production Engineering, Faculty of Technical Sciences, University of Novi Sad, Novi Sad, Serbia
Email: michalpotran@gmail.com

Abstract. *Addition silicones present contemporary dental impression materials with high dimensional stability. Major factor that influences the accuracy of dental impressions is setting time of the material, and as such it was adressed in this study. The master model presented a partially edentulous upper jaw with central incisors, canines and first molars. The master model was measured and corresponding data was used to create custom tray by rapid prototyping. Impressions were made with a monophasic technique, setting times were set at 3,3.5,4,4.5 and 5 minutes.Six working casts were made for each time period. Measurement of the working casts was performed 24 hours later on coordinate measuring machine. The dimensions of working casts abutments were different in comparison to the master model, especially in the interabutment regions. The precision of the working cast abutments increased in relation to prolonged setting time. In conclusion, prolonged setting time improves dimensional stability of the impression material because of the higher degree of polymerization.*

Keywords: Addition Silicones, Dimensional Stability, Setting Time, Master Model

1. Introduction

The manufacturing of indirect dental restorations includes a wide range of clinical and laboratory procedures, starting with tooth preparation and taking of dental impression. The dental impression presents a recording of intraoral tissues, and as such poses a link between the clinical and laboratory procedures. The accuracy of impression is of great importance for further compliance of these two distinct pathways.

Making of an successful dental impression depends on the properties of the material, the conditions of the oral environment and the skill of the therapist. The accuracy of dental impression is of vital importance for production of working casts, which present a reference model for manufacturing in dental laboratory. The basic requirement for impression material use is high dimensional stability. Dimensional stability is mesured through the ability of the material to withstand the biological and mechanical factors of oral surounding, maintaining its acquired dimensions. This ensures the accuracy of the recording, during and after the setting of the material. Fully set material should exhibit elastic properties, which is pronounced in presence of undercuts and in gingival sulcus [1]. Narrow areas are the source of high tensile stresses and can lead to plastic deformation and tear of the material. Larger defects are easily detected, and require repeating of impression procedure. Smaller defects, such as plastic deformation, are difficult to notice and can be easily overlooked. Dimensional stability depends on the degree of polymerization. Higher degree of polymerization improves elastic properties of the material and lowers the possibility of permanent deformation. This is called a setting time and is stated by the manufacturer. As the procedure of making of an impression is usually unpleasant to a patient, it is vital that this is conducted in the shortest time possible, while achieving the desired material's properties. In relation to this, the aim of this study was to assess the influence of setting time on the accuracy of working casts, by direct measurement of the working casts on coordinate masuring machine (CMM).

2. Subject and Methods

The master model consisted of six abutment teeth, replicating the shape of the upper incisors, canines and first molars after grinding. The dimensions and distances between abutment teeth were taken from the literature [2].

The master model was mesured five times on CMM (*Contura G2, Carl Zeiss, Germany*) with maximum permissible error with 1.9 + L/330 µm (L is length expressed in mm). The measurement results were used for construction of CAD model, a modified negativ of the master model. This was performed by enlarging the inner space around the abutments for 2 mm and contouring the outer shell of the tray to fit the dimensions of the master model (Fig. 1). The inner space enlargement of 2mm was ment to be used as reservoir for the impression material. The CAD model was transfered to a physical form by rapid prototyping (*Z310 plus, 3D Systems, USA),* thus creating the custom tray with 2 mm spacing.

The impressions were made with addition silicone, using a monophasic technique (*Elite Hd+ light body, Zhermack, Italy).* Before taking of the impressions, the master model was heated to a temperature of 37 ºC, using a waterbath. The impression material was inserted into the custom tray and the custom tray was seated on top of the master model. The working time was set to 60 sec, while setting time differed between the groups and was set to: 3, 3.30, 4, 4.30 and 5 minutes. After the immpression was taken, the working casts were poured in gypsum typ IV (*Elite rock, Zhermack, Italy*), with 30 minutes delay. Gypsum was allowed to set for 60 min, after which the custom tray and working cast were separated. Six models of working casts were made for each time interval, measurement was done 24 hours later on CMM.

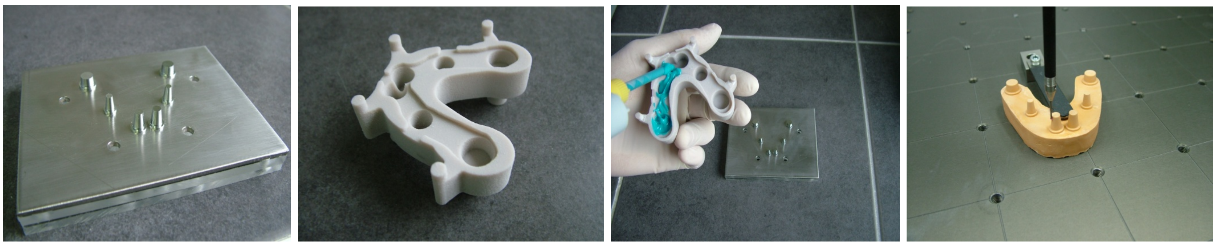

Fig. 1. The protocols of impression procedure and measurement of the working casts.

The measurement of working casts was performed using the same measurement strategy as for the master model. Inspection was conducted conformant to the new generation of product geometry specification (GPS) [3]. The measurement model consisted of geometrical features as cone, cylinder and plane. Each geometrical features was measured by discrete points, randomly distributed on the measurement surface. The measurement of abutments (cones) was made in 100 discrete points, while measurement of the chamfer (cylinder) was made in 50 discrete points. The output parameters of the measurement presented a coordinates that were mathematicaly processed to form a substitute geometry. The geometrical specifications (size, form, orientation, location) were determined by software processing. The abumtents were measured in three planes, transverzal (x1 - x3), sagittal (y1 - y6) and vertical (z1 - z6) (Fig. 2).

The comparison and analysis of the results was done by statistical analysis, with Student's T-test and One way ANOVA.

Table 1. The results of the measurement

Distance	Master [mm]	Mean [mm] 3min	3,5min	4min	4,5min	5min	Difference/Standard deviation [μm] 3min	3,5min	4min	4,5min	5min	t-test (p-value) 3min	3,5min	4min	4,5min	5min	ANOVA (p-value)
X_1	8.507	8.519	8.517	8.518	8.515	8.514	12 ±2	10 ±5.7	11 ±3.3	8 ±1.4	7 ±1.7	0.00	0.00	0.00	0.00	0.00	0.06
X_2	30.002	30.024	30.018	30.018	30.015	30.016	22 ±5.9	16 ±4.8	16 ±5.1	13 ±5	14 ±2.2	0.00	0.00	0.00	0.00	0.00	0.02
X_3	46.015	46.076	46.064	46.065	46.060	46.063	61 ±8.8	49 ±11	50 ±11	45 ±8.4	48 ±6	0.00	0.00	0.00	0.00	0.00	0.05
Y_1	18.144	18.162	18.157	18.154	18.154	18.153	18 ±2.5	13 ±3.9	10 ±3.7	10 ±4.9	9 ±2.6	0.00	0.00	0.00	0.00	0.00	0.00
Y_2	42.051	42.097	42.089	42.089	42.083	42.083	46 ±5	38 ±4.8	38 ±7.1	32 ±3	32 ±7.6	0.00	0.00	0.00	0.00	0.00	0.00
Y_3	24.364	24.392	24.390	24.391	24.387	24.384	28 ±3	26 ±2.1	27 ±3.4	23 ±4	20 ±2.3	0.00	0.00	0.00	0.00	0.00	0.00
Y_4	18.319	18.330	18.328	18.326	18.325	18.325	11 ±2.3	9 ±2.9	7 ±4	6 ±3.4	6 ±4	0.00	0.00	0.00	0.00	0.01	0.04
Y_5	42.149	42.196	42.193	42.189	42.186	42.184	47 ±9.7	44 ±9	40 ±10.9	37 ±9.3	35 ±9.9	0.00	0.00	0.00	0.00	0.00	0.24
Y_6	24.277	24.308	24.308	24.305	24.305	24.304	31 ±9.3	31 ±4.6	28 ±11	28 ±9.8	27 ±10	0.00	0.00	0.00	0.00	0.00	0.92
Z_1	7.506	7.514	7.515	7.511	7.514	7.508	8 ±40.7	9 ±13.2	5 ±13	8 ±8.6	2 ±8.3	0.65	0.13	0.32	0.05	0.47	0.93
Z_2	7.507	7.537	7.519	7.518	7.506	7.512	30 ±27	12 ±17	11 ±14.2	-1 ±21.4	5 ±7.5	0.04	0.14	0.11	0.95	0.13	0.09
Z_3	6.923	6.919	6.927	6.923	6.928	6.928	-4 ±22.7	4 ±18.9	0 ±6.8	5 ±13.1	5 ±7.8	0.78	0.61	0.83	0.32	0.12	0.59
Z_4	6.926	6.922	6.916	6.927	6.933	6.928	-4 ±22.6	-10 ±11.1	1 ±14.3	7 ±8	2 ±5.4	0.72	0.09	0.84	0.07	0.30	0.31
Z_5	4.5	4.506	4.499	4.493	4.497	4.499	6 ±17.2	-1 ±14.3	-7 ±6.4	-3 ±13.8	-1 ±6	0.43	0.87	0.05	0.61	0.98	0.69
Z_6	4.497	4.498	4.482	4.5	4.494	4.496	1 ±23.6	-15 ±17.2	3 ±20.4	-3 ±9.9	-1 ±12.7	0.95	0.08	0.72	0.41	0.83	0.38

3. Results

The results of the measurement are presented in Table 1. The accuracy of working casts increased with prolonged setting time.

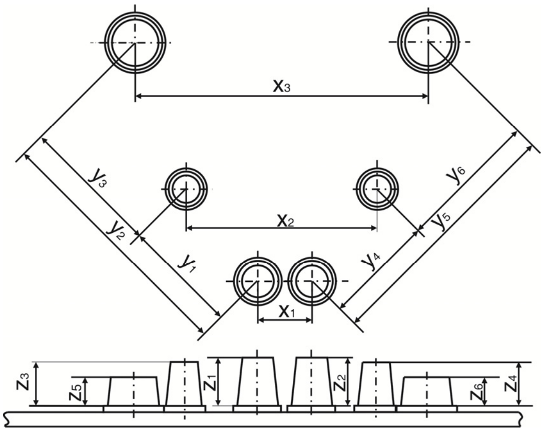

Fig. 2. The parameters of the measurement.

4. Discussion

The results presented show that extended polymerization time affects the accuracy of working casts. It can be seen that most pronounced difference is in the group with setting time of 3 minutes. The replica abutments were larger in all of the observed dimensions. The errors increased proportionally to the increase of distance between the abutments. From clinical point of view, this means that the replica abutments will be wider than that of the mouth. This is of special importance when constructing long span bridges. The future framework of dental bridges will be wider in transversal and sagittal plane, which will affect the accuracy of fit, especially in the marginal area. The marginal fit is most crucial part for longevity of dental restorations, considering the biological factors of oral environment and the increase of cement thickness, which can cause mechanical failure. While 3 minutes were considered a borderline setting time for completion of polymerization reaction, it was proven to be difficult to achieve successful impression in this time period. Some impressions made at this interval had to be discarded due to incomplete polymerization and plastic deformation of the material upon removal of the impression. This is of utmost importance for formation of elastic properties and prolonged setting time should be recommended, especially in the presence of undercuts or enclosed gingival sulcus. Within the limitations of this study, it can be concluded that prolonged setting time will increase the accuracy of working casts.

Acknowledgements

The results presented in this paper were obtained in the framework of the project entitled "Research and development of modelling methods and approaches in manufacturing of dental recoveries with the application of modern technologies and computer aided systems" – TR 35020, financed by the Ministry of Education, Science and Technological Development of the Republic of Serbia.

References

[1] Balkenhol M, Haunschild S, Erbe Ch, Wostmann B. Influence of prolonged setting time on permanent deformation of elastomeric impression materials. *J Prosthet Dent* 2010, (103): 288-294.

[2] Sched R.C, Weiss G. Woelfel's dental anatomy (8th ed.). Lippincott Williams&Wilkins, Wolters Kluwer business, Philadelphia, USA, 2012, p 41.

[3] ISO/TS 17450-1. Geometrical product specification (GPS) – General concept – Part 1: Model for geometric specification and verification. International Organization for Standardization 2002, Geneva.

What Are the Initial Measurement Skills of Medical Students?

V. Haverlíková

Faculty of Medicine Comenius University in Bratislava, Slovakia
Email: viera.haverlikova@fmed.uniba.sk

Abstract. *The background of measurement theory is provided to medical students at the Faculty of Medicine Comenius University in Bratislava (FMCU) within the biophysics course. The paper presents results of the research focused on collection of information about student's former physics education and characteristics of selected student's measurement skills (74 respondents). The research was realised using written questionnaire administered to 616 first-year-students and observation of 74 students during their practical training. In accordance to students' responses, totally 60% of them realized laboratory measurements as a part of their former physics education and more than three quarters of those students proceeded also measurement protocols (47% of all students). Short test and observation of students' practical skills showed that 35% of students did not discern the value of the smallest division while reading the measured value from a scale, 69% of students did not know to read the measured value while using the instrument with a band switch and multiple analogue scales. Research results show that students' initial knowledge and skills are not sufficient for effective study of biophysics. To facilitate understanding of evidence-based-medicine the even very essentials of measurement theory should be an integral part of medical-physics education.*

Keywords: education, measurement, skills, medicine

1. Introduction

There is no doubt about the crucial role of measurement in medicine and clinical decision-making. A medical doctor has to know to select the appropriate measurement method, proceed the measurement correctly, read the measured value, evaluate the measurement and interpret the result. Students learn most of specific measurement methods during their clinical training and newest methods also later in their praxis.

The background of measurement theory is provided to medical students at the Faculty of Medicine Comenius University in Bratislava (FMCU) already at the beginning of their study - within the biophysics course. Certainly, the biophysics course is built on the assumption that students acquired some basic physics knowledge and skills during their former education. For example, it is expected that students are able to perform elementary measurements of length, liquid volume, temperature, electric current and/or voltage and understand the term accuracy of measurement. Hence the explanation of general rules of measurement is not included in the training.

Does the assumption about student's initial knowledge and skills correspond to real circumstances? Are the first-year medical students prepared to study probability and theoretical distributions, numerical and statistical evaluation of measurements [1] that are essential for understanding medical research and evidence-based-medicine?

2. Subject and Methods

Two types of information were collected within the research - subjective characteristics of student's former physics education and objective characteristics of selected student's measurement skills.

Characteristics of student's former physics education were collected using the written questionnaire with short open questions and questions with simple choice of an answer (yes/no). The questionnaire was administered at the very beginning of the biophysics practical training in academic year 2014/15. Totally 616 first-year-students were involved in the survey (see Table 1): 362 students who finished their upper secondary study in Slovak schools studying General Medicine in Slovak language (GM_S) or Dentistry in Slovak language (D_S), and 254 students studying General Medicine in English language (GM_{En}) or Dentistry in English language (D_{En}). Students in English programmes finished their upper secondary study mainly in Germany 39%, Greece 21%, Italy 8%, Austria 7%, Poland 6% and Slovakia 6%.

Two questionnaire items were focused directly on measurement - we asked the students whether they performed laboratory measurements as a part of their former physics education and whether they elaborated measurement protocols as a part of their former physics education.

Table 1. The sample characteristics – Number of students answered the questionnaire focused on former physics education and number of students answered the short test

Study program	Number of students answered the questionnaire	Number of students answered the short test on measurement skills
GM_S	324	42
D_S	38	-
GM_{En}	220	32
D_{En}	34	-

Selected characteristics of student's measurement skills were collected using short test and observation of student's performance of simple measurement. Totally 74 students were involved in this part of the research: 42 general medicine students studying in Slovak language in the academic year 2013/14 and 32 general medicine students studying in English language in the academic year 2014/15.

The short test was administered at the beginning of the first biophysics practical training in order to identify student's actual skills and knowledge. One question was focused on reading the measured value from a scale. Next week students were observed when they read the measured value from a simple linear scale of the wet spirometer. One more week later students were observed when they measured illuminance using analogue luxmeter with a band switch.

3. Results

Measurement in Previous Physics Education

Summary of student's responses related to their experience with measurement during their former physics education can be seen in Table 2. Totally 60% of respondents realized laboratory measurements during their former physics education and more than three quarters of those students proceeded also measurement protocols (47% of all students).

Measurement Skills

Approximately one third of students did not discern the value of the smallest division (Fig. 1, Table 3). They assumed that it is 1/10 of centimetre. Nobody mentioned spontaneously the uncertainty of a single measurement. The item was discussed with students and explained.

Table 2: Summary of student's responses relating to measurement in their previous physics education.

	GM_S (N = 324)	D_S (N = 38)	GM_{En} (N = 220)	D_{En} (N = 34)	Totally (N = 616)
I performed laboratory measurements as a part of my former physics education	70%	75%	46%	27%	60%
I wrote/prepared measurement protocols as a part of my former physics education	55%	42%	41%	10%	47%

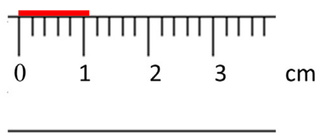

Fig. 1. Test question focused on measurement skills: What is the length of the line ?

One week later students measured vital capacity of their lungs using a mechanical spirometer, where the smallest division of the scale was "quite large" (note: the distance of two lines representing 0.5 litre was 1 cm). After the single intervention a week ago, still 27% of students were not able to understand that it is not allowed to divide the scale into smaller divisions (neither in their minds) to make the measurement more precise. One more intervention was given to these students about the uncertainty of single measurement and information given by the scale division.

Students faced a new challenge up when they used the analogue luxmeter with a band switch. Almost 69% of students were not able to choose the appropriate scale and read the correct value of illuminance. The item was explained to these students. Some of them needed repeated explanation with several different measurement instruments.

Table 3. Summary of student's measurement skills observation.

	GM_S (N = 42)	GM_{En} (N = 32)	Totally
Correct reading from a simple scale focused on smallest division of the scale. (1st training)	66.7%	62.5%	64.9%
Correct reading from a simple scale focused on uncertainty of simple measurement. (2nd training)	76.2%	68.8%	73.0%
Correct reading of the measured value with band switch and multiple analogue scales (3rd training)	35.7%	25.0%	31.1%

4. Discussion

Though students in general accept the importance of measurement in clinical decision making, the non-formal discussion with students showed that they do not feel the necessity to improve their knowledge and skills. Most students believe in their competency to realise simple measurements, but this believe arise form daily-life experience not from the scientific and/or technological expertise.

Our research showed that the initial measurement skills of medical students at FMCU are not sufficient for effective study of the biophysics course. However the upper secondary physics curricula declare measurement as inevitable part of physics education and basic principles of measurement are taught usually already in primary schools, a lot of students expressed that they did not provide measurement as a part of their former physics education. The situation was significantly better among students studying in Slovak language than among students studying in English language (chi-square test $p < 0.001$). Similar findings came also from the research of FMCU student's initial factual knowledge in physics [2]: the average score among students studying in Slovak language was significantly better than the average score of students studying in English language ($p < 0.005$). These findings do not necessarily mean that the upper secondary education is more effective in Slovakia (note: The OECD findings in research on scientific literacy [3] showed that Slovak students are below the average). The above mentioned difference can be a consequence of the admission criteria that does not require any level of knowledge in physics.

Though new tools are developed to assess children's experimental skills (including measurement), to our knowledge no such attempt was realized to assess university students.

If students are not able to read the measured value correctly, how can they evaluate and interpret it? Our goal is to teach students to understand different measurement methods, to be able to select the best one in specific situation and use it correctly. But: if our students do not understand the very essentials in measurement theory, can we assume "this is not our job"?

5. Conclusions

It is a nowadays inevitability to consider students' initial knowledge and skills in teaching biophysics at the university level. Otherwise students will achieve neither real understanding nor operational knowledge nor expert competencies necessary in their future praxis.

Research results show that even very essentials of measurement theory should be an integral part of medical-physics education. It is a great challenge to do this in limited time, with growing content and decreasing readiness and motivation of students to study biophysics. New teaching technologies like e-learning, can help only partially. A practical training and personal involvement of teachers are irreplaceable.

Acknowledgements

This work was supported by KEGA 020UK-4/2014 „Innovation in the content, forms and methods of practical exercises of Biophysics and Medical Biophysics to the study of Medicine and Biomedical Physics".

References

[1] Kozlíková K, Martinka J. Theory and tasks for practicals on Medical Biophysics. Tribun EU, Brno, 2010.

[2] Haverlíková V, Kozlíková K. Medical students readiness to study biophysics in the view of their initial physics knowledge. In: Medical physics and biophysics at the beginning of 21st century: Applications of physics in medicine, Comenius University, Bratislava, 2014, 38-41. ISBN 978-80-223-3761-8. *(in Slovak)*

[3] OECD: PISA 2012 Results, 2014, avaialable on internet: http://www.oecd.org/pisa/keyfindings/pisa-2012-results.htm (quoted on 2015-03-12)

Experiments with Sensing and Evaluation of Ionosphere Changes and Their Impact on the Human Organism

[1]M. Hanzelka, [2]J. Dan, [1]P. Fiala, [1]M. Steinbauer, [3]V. Holcner

[1]Department of Theoretical and Experimental Electrical Engineering, Brno University of Technology, Brno, Czech Republic
[2]Rector´s Office, Personnel Management Office, Masaryk University, Brno, Czech Republic
[3]Faculty of Economics and Management, University of Defence, Brno, Czech Republic
Email: fialap@feec.vutbr.cz

Abstract. *The impact of the environment upon living organisms constitutes a crucial problem examined by today's science. In this context, research institutes worldwide have analysed diverse positive and negative factors affecting the biological system of the human body. One such factor consists in the influence of the surrounding electromagnetic field. This paper presents the results of an investigation focused on ionosphere parameter changes and their impact on the basic function of the nervous system. It is a well-known fact that the frequency of the alpha waves of brain activity [1] ranges within 6 – 8 Hz. Changes in the electromagnetic and chemical structure of the Earth's surface may cause variation of signals in the above-defined frequency region of 6 – 8 Hz.*

Keywords: Ionosphere, Human Body, Brain Activity

1. Introduction

The low-level measurement of low frequencies (0.01-10 Hz) performed to evaluate the effect of magnetic fields on the human organism can be regarded as an interdisciplinary branch of science that embraces different types of research. By further extension, the low-level measurements are interesting from the perspectives of theoretical electrical engineering and research of magnetic fields. At this point, is important to consider applied research disciplines, for example the measurement and radar technology in the following ranges: the ULF (Ultra Low Frequency Band: 300 Hz - 3 KHz), SLF (Super Low Frequency Band: 30 Hz - 300 Hz, and ELF (Extreme Low Frequency Band: 0.1 Hz - 30 Hz). Scientists and researchers are currently preparing to solve special tasks related to the objectivisation of the impact of low-level magnetic fields upon the human organism; such impact will be examined from the perspective of physical harm to cells [2] and mental condition of humans [2], [3], Fig. 1.

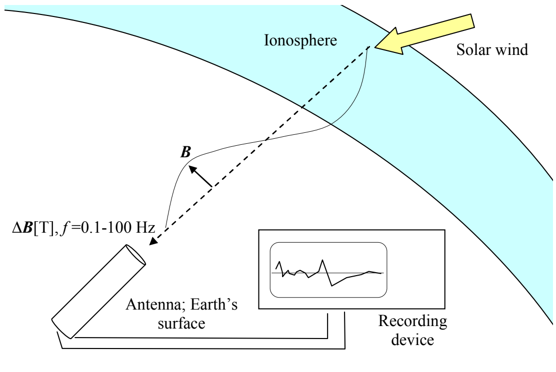

Fig. 1. Schematic arrangement of the problem of detecting the changes in the Earth's ionosphere.

2. Research of Geomagnetic Effects

Ionosphere changes can be objectively measured using already known methods [4]. Based on earlier observations, it is possible to demonstrate via secondary research that a connection exists between magnetic field changes and the social behaviour of groups of humans. According to Alexander Tchijevsky, 80% of the most significant events in human history occurred within the approximately five years of the maximum solar activity; this assumption is represented by the related diagram (1750-1922), [5] (Tchijevsky A, 1971), and later measurement Fig. 2.

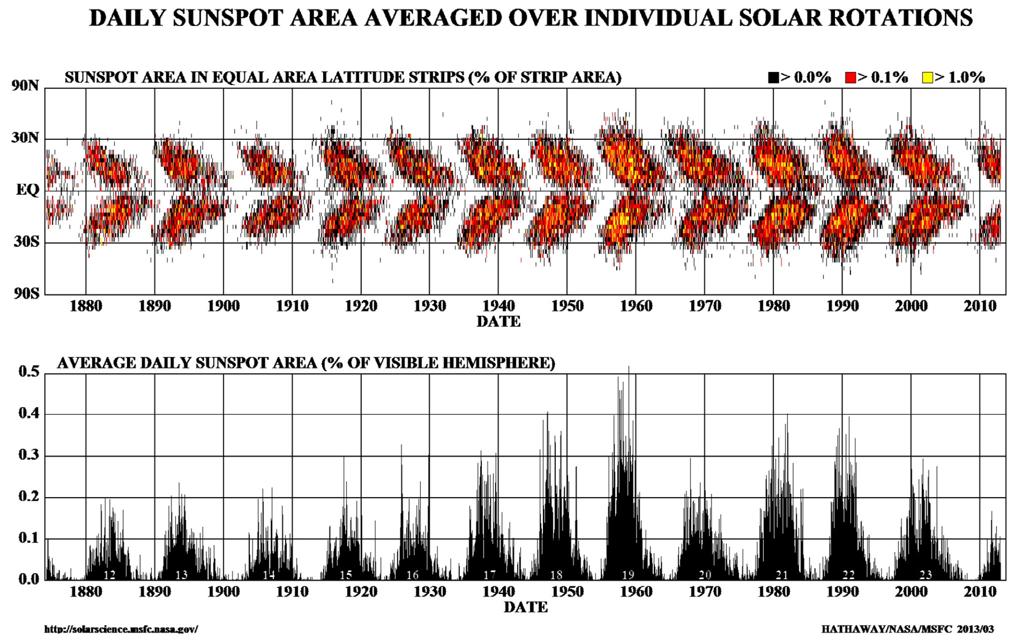

Fig. 2 The development of geomagnetic storms - Royal Observatory , Greenwich monitored from May 1874 in daily measurements and continuously since 1976 - Solar Optical Observing Network (SOON), supported by the US National Oceanic and Atmospheric Administration (NOAA).

3. Description of the Experimental Research

The laboratory research comprising a homogeneous sample of 49 subjects (men and women aged 19 to 25) was launched on April 22, 2014 and lasted until June 26, 2014. The total time required for the examination of psychophysiological parameters in a subject corresponded to 19 minutes. We used a Nickelodeons Infiniti (Thought Technology Ltd.) unit to perform the entire task, and the measurement proper involved four phases: Rest; Color; Rest; Math; and Rest. At the Color stage, a special (Stroop) test was utilized to acquire the psychophysiological responses of each subject to a load on their organism. Generally, this tool demonstrates that a person performing the given task can be easily distracted due to their automatic reactions and habits; the procedure is named after John Ridley Stroop (1897-1973), an American psychologist who first described the phenomenon in 1929. In the Math phase, then, the respondents were asked to progressively subtract the number 7 from the initial value of 1081, and we examined the psychophysiological stress generated during such quiet countdown. The total number of measurements was 210, with the average of 4.29 per respondent.

The relationship between the former indicator and the number of subjects who completed the task is shown in Tab. 1. The respondents were measured in special laboratories to ensure comparable parameters and constant temperature, noise, humidity, lighting, concentration of positive and negative ions, and a homogenized component of the geomagnetic field, Fig. 4b).

Tab. 1. The relation between the number of completed measurements and the number of respondents.

Number of respondents	Number of measurements
4	1
1	2
4	3
12	4
24	5
4	6
49	SUM

4. Description of the Measurement Procedures for the Given Sample of Respondents

To measure the psychophysiological characteristics of the human body on the respondents, we used the BioGraph Infiniti devices providing bio- and neurofeedback. The following variables were measured:

B: BVP amplitude mean (Rel), B: BVP HR mean (beats/min), B: BVP HR std. dev., B: BVP peak freq. mean (Hz), B: BVP IBI std. dev. (SDRR), B: BVP VLF % power mean, B: BVP LF % power mean, B: BVP HF % power mean ,B: BVP VLF total power mean, B: BVP LF Total power mean, B: BVP HF total power mean, B: BVP LF/HF (means), Total spectral power, C: EMG mean (uV), D: EMG mean (uV), E: Skin conductance mean (uS), E: SC as % of value mean (%),F: Temperature mean (Deg), F: Temp as % of value mean (%),G: Resp rate mean (br/min), B&G: (HR max-min) mean (b/min), G: Abd amplitude mean (rel), H: Thor amplitude mean (rel), G&H: Abd-tho ampl diff (means). The measurement comprised three relaxation and two stress phases, with an emphasis on intensive psychological stress in the respondents. The stress stages were laboratory-generated using a low-level electromagnetic field generator, an amplifier, and Helmholtz coils to interact with the EEG brain waves of the respondent. The resulting low-level field enabled us to simulate the effect of changes in solar activity as an additional offset to the related real intensity indicators prepared for each day by NASA.

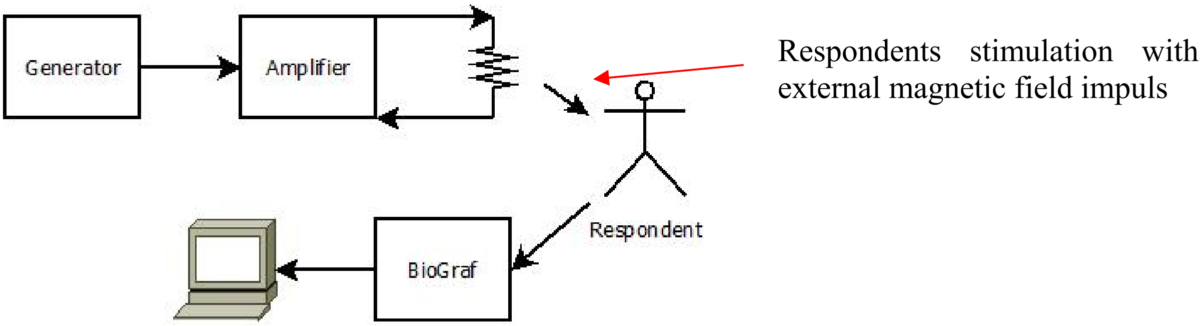

Fig. 3. Scheme of measurement and simulation apparatus.

a)

b)

Fig. 4. a) Documentation shots from measurements in laboratory conditions, b) Laboratory space of measurements with geomagnetically stable component of the magnetic field.

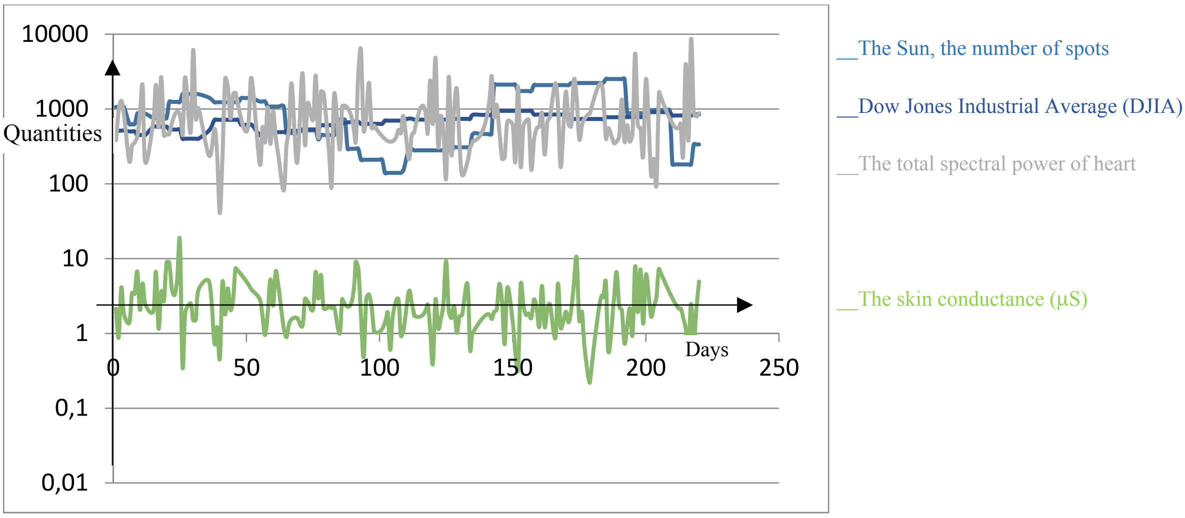

Fig. 5. Evaluation of measurement parameters of individual characteristics and Solar Activity (over 230 days).

The field strength in the Helmholtz coil was set to the level of terrestrial magnetic field, and the major parameters were as follows: impulse $f = 1$ kHz; start = 100 ns; $\lambda / 2 = 168$ µs. Fig. 3 shows a diagram of the stimulation and measurement apparatus. Fig. 4 then presents shots of the BioGraph Infiniti measurements.

5. Conclusion

The prepared experiments and its measurement can prove the influence of the above-mentioned aspects on the human emotional system, thus pointing to the hitherto applied boundary values of magnetic flux density B in relation to the alterations of the magnetic field for very slowly changing electric currents, Fig.5. The experiments also highlight the impact these currents might have on human beings permanently present in such environment.

Acknowledgement

The research described in this paper was financed by the National Sustainability Program under grant No. LO1401 and by Czech Science Foundation under grant No. 13-09086S. For the actual analyses and experiments, infrastructure of the SIX Center was used.

References

[1] Ferris J. The brain generates an electric field that influences its own activity Scientific American Mind 21, 10 (2010). Published online: 28 October 2010.

[2] Scorretti R, Burais N, Nicolas L, Nicolas A. Modeling of induced current into the human body by low-frequency magnetic field. *IEEE Trans Magnetics*, 41(5), 2005.

[3] Carrubba S, Marino AA. The effects of low-frequency environmental-strength electromagnetic fields on brain electrical activity: a critical review of the literature. *Electromagnetic Biology and Medicine*, 27 (2): 83-101, 2008.

[4] Hanzelka M, Dan J, Fiala P, Friedl M, Holcner V. Methods for the Sensing and Evaluation of Ionosphere Changes and Their Impact on the Human Organism. In: Proceedings of PIERS 2014 in Guangzhou. Guangzhou, 2014, 781-786.

[5] Tchijevsky A. Physical Factors of the Historical Process. 1971.

Measurement of Physical Quantities

The New Position Control and Data Acquisition Concept of the Nanometer Comparator

R. Köning, P. Köchert, J. Flügge

Physikalisch-Technische Bundesanstalt (PTB), Braunschweig, Germany,
Email: Rainer.Koening@ptb.de

Abstract. *The Nanometer Comparator, the PTB reference comparator for length graduations, was upgraded with a high precision positioning system using laser interferometric feedback signals acquired with a self-developed phase meter. The position feedback data is transferred by a high speed serial link from the phase meter to an FPGA controller. This upgrade of the Nanometer Comparator led to a 7-fold reduction of the position noise and a 100-fold reduction of the nonlinear motion deviations in the dynamic case.*

Keywords: Optical Interferometry, Position control, FPGA

1. Introduction

The Nanometer Comparator [1] provides traceable measurements of line scales, photomasks, incremental encoders and interferometers in the range up to 540 mm with expanded measurement uncertainties of a few nanometres only. This level of uncertainty can only be reached by operating the optical interferometers, which are well integrated into the mechanical setup, completely in vacuum. In recent years the Nanometer Comparator has been upgraded to provide straightness measurements using a mirror at one sidewall of a Zerodur sample carrier and an additional (y) interferometer system using three measurement beams [2,3]. This heterodyne interferometer system requires six additional input channels to eliminate the perturbation introduced by the use of optical fibers at the interferometer entrance [4]. Therefore, a newly developed phase meter [5] is employed, which also replaced the commercial one currently used for the main measurement (x) axis and the pitch interferometer as well. Consequently, the data acquisition software had to be extended.

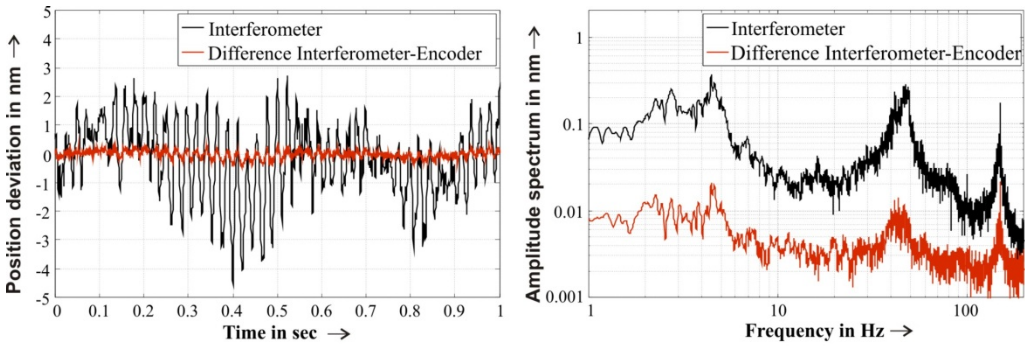

Fig. 1. Left diagram: position noise of the main interferometer (black curve) and differences of the measurement signals of the interferometer and the measurement object (incremental encoder). Right diagram: Related amplitude spectra

In addition, the position noise of the measurement slide disturbs the measurements, which is illustrated in Fig. 1. The black curve in the left diagram shows the position noise of the interferometer and the red one the difference between the interferometer and the measurement object, an incremental encoder in this case. The right diagram contains the related amplitude spectra. They reveal that, although the data acquisition of both displacement sensors has been synchronized by means of a common trigger signal, the position noise appears in reduced form in the position differences and therefore increases the related measurement uncertainty.

The influence will be larger if other sensors, which cannot be synchronized so well to the interferometer, have to be used. A CCD camera, which acquires the image of an optical microscope used in line scale measurements, may serve as an example.

Therefore, in order to reduce the achievable measurement uncertainty, the drive and the related position control system of the Nanometer Comparator needed to be improved.

2. A new position control and data acquisition concept

New drive concept

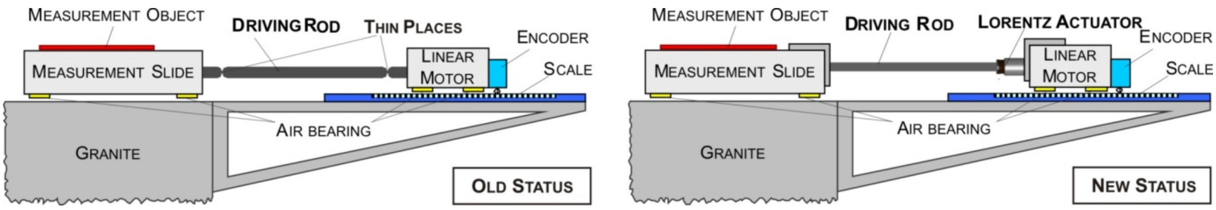

Fig. 2. Mechanical connection of linear drive and measurement slide. Left: Former solution using two thin places. Right: Integration of the Lorentz actuator in the setup. Note: Elements are not to scale.

Fig. 2 shows a schematic of the old and new connection of the linear drive to the measurement slide. The lateral air bearing guides of the motor and the slide have been omitted for the sake of simplicity. In order to minimize the influence of the heat generated by the linear drive on the measurements, the slide and the motor are separated by a carbon fiber driving rod of about 1 m in length. Both use different mechanical guides, which are not perfectly collinear. Therefore, two thin places were used in the former setup to accept the related guiding deviations so that neither the drive nor the slide gets seized in its guide. These thin places, however, reduce the stiffness of the position control loop and do limit the available control loop bandwidth to about 20 Hz. In the new setup, these thin places have been replaced by a Lorentz actuator. The gap between the coil and the magnet can accept the aforementioned guiding deviations. In addition, the Lorentz actuator is used as an additional fast and highly precise fine positioning drive. It uses the vacuum interferometer signals, which exhibit a resolution and nonlinearities of less than 10 pm, as feedback signal and operates at a control rate of 160 kHz. In the former setup, only the incremental encoders of the linear drive with a resolution of 1 nm were used at a control rate of 2.25 kHz.

New control and software concept

The new control concept is illustrated in Fig. 3. The old motion controller (delta tau, PMAC 2 VME) still controls the four coarse positioning drives of the x measurement axis. The Lorentz actuator is controlled by an FPGA board (NI PXI-7854R). It is located together with a second FPGA board (NI PXI-7852R) in a PXI chassis operated by a real-time controller (NI PXIe-8102). The second FPGA board implements the y, yaw, pitch and height control loops. A roll control loop may be added in the future if required. While the y, yaw, and pitch deviations of the measurement slide will also be acquired using interferometers, the height deviations will be sensed by a lateral encoder located at the measurement slide. All these signals are used to control piezoelectric actuators. The height actuators are also used to provide the motion required to focus the optical microscope in the case that line scale measurements are performed. The new phase meter also contains user programmable FPGA units. They are not only used to realize a fast lock-in based phase evaluation algorithm but also implement serial data links that provide position feedback data to the FPGA boards in the PXI chassis. The interferometer data used for the measurements is saved temporally in a ring buffer implemented in onboard memory of the phase meter and transferred over a VME bus to the

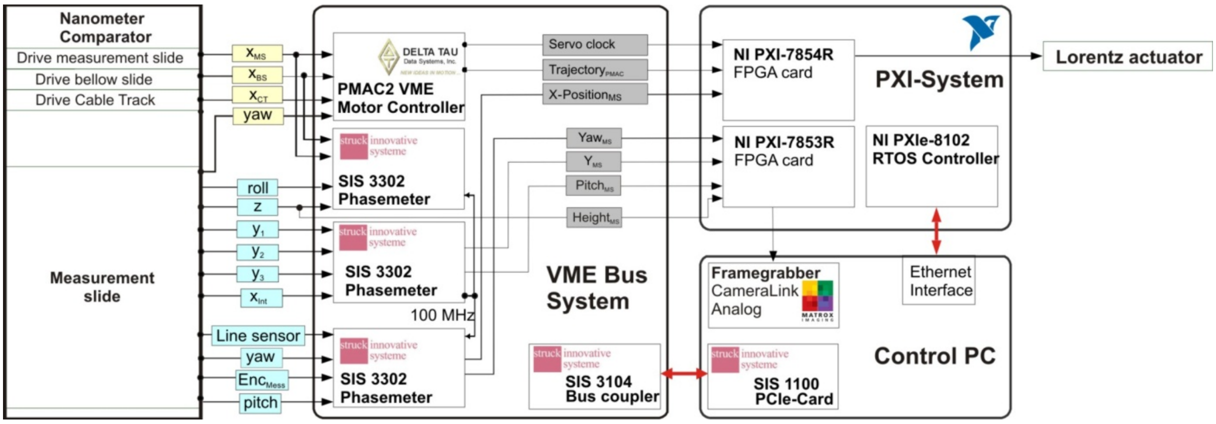

Fig. 3. Principle layout of the new data acquisition and control concept.

control PC and immediately saved to the disc. In this way sample rates of about 50 ksamples / sec can be maintained over hours. In addition, the control PC is used to issue fine motion commands performed with the Lorentz or the piezo actuators, to change the control settings of the FPGA controllers, and to collect and display the monitor data acquired by the FPGA controllers in the PXI system. Furthermore, the PC hosts the image acquisition hardware and acquires the CDD images. Finally, the control PC provides the user interface required to operate and perform measurements with the Nanometer Comparator. Not shown in Fig. 3 is the acquisition of the environmental data, like the sample and air temperature, the humidity or the air pressure, etc. required to evaluate the measurement data [6] which is performed autonomously by other PCs.

The software required to implement this concept consists of four categories. Firstly, the FPGA units on the new phase meter were programmed using VHDL. Secondly, the FPGAs in the PXI chassis and the FPGA controller were programmed in LabView. Thirdly, the image acquisition software and the control program were written in C. Here, LabWindows is used to implement the user interface but the whole program is compiled using Microsoft Visual Studio. Finally, Matlab is employed for an offline data evaluation.

3. Results

Static results

Fig. 4 shows a comparison of the position noise of the measurement slide obtained using the old and the new setup. The spectra shown in the right diagram indicate a significant reduction of the position noise in the frequency range below 50 Hz. In total, the integration of the Lorentz actuator led to a reduction of a factor close to 7.

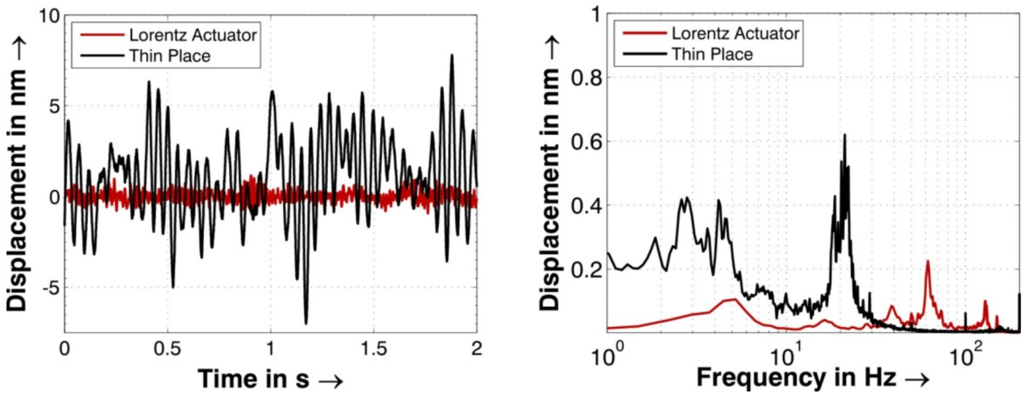

Fig. 4. Left diagram: Position noise of the measurement slide before (black) and after the integration of the Lorentz actuator (red). Right diagram: Amplitude spectra of both signals.

Dynamic results

Because incremental systems are measured dynamically, that is with a measurement speed of about 1 mm/sec, the improvement of the dynamic behaviour due to the use of the Lorentz actuator has been evaluated as well. The figure of merit is here the deviation from a linear motion performed with constant speed. These deviations could be reduced by more than two orders of magnitude, as shown in Fig. 5.

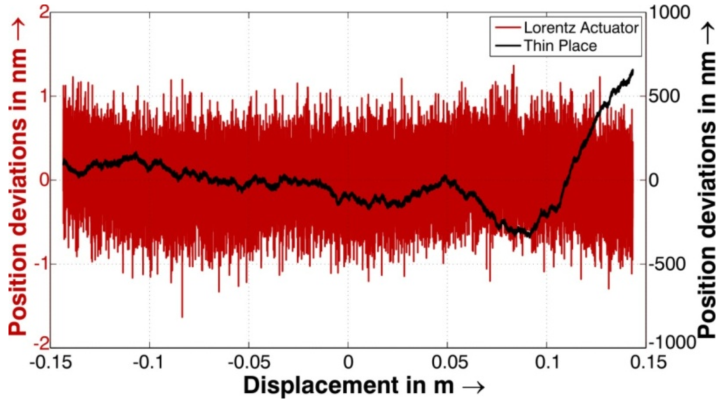

Fig. 5. Nonlinear motion deviations of the measurement slide while moving with constant speed of 1 mm/s before (black) and after the integration of the Lorentz actuator (red).

4. Conclusion

We successfully integrated a fine positioning control system based on a Lorentz actuator in the Nanometer Comparator. It uses vacuum interferometric feedback signals and an FPGA-based controller. It reduced the position noise and nonlinear deviations by a factor of 7 and 100, respectively.

References

[1] Flügge J, Köning R, Status of the nanometer comparator at PTB. In proceedings of the conference "Recent Developments in Traceable Dimensional Measurements" edited by Decker J E and Brown N; 2001, SPIE Vol. 4401, 275-283, and references there in.

[2] Flügge J, Köning R, Weichert C, Häßler-Grohne W, Geckeler R D, Wiegmann A, Schulz M, Elster C, Bosse H. Development of a 1.5D reference comparator for position and straightness metrology on photomasks. In proceedings of Photomask Technology, 2008, Proc. SPIE 7122, 71222Y

[3] Elster C, Weingrätner I and Schulz M. Coupled distance sensor systems for high-accuracy topography measurement: Accounting for scanning stage and systematic sensor errors, Precision Engineering 30 (2006) 32–38

[4] Weichert C, Flügge J, Köchert P, Köning R, Tutsch R. Stability of a fiber fed interferometer. In proccedings of 10th IMEKO Symposium Laser Metrology for Precision Measurement and Inspection in Industry, 2011, ISBN 978-3-18-092156-3, p.243 - 250

[5] Köchert P, Flügge J, Weichert C, Manske E. Phase measurement off various commercial heterodyne He-Ne-laser interferometers with stability in the picometer regime, Meas. Sci. Technol. 23 (2012) 074005 (6pp)

[6] Bönsch G, Schuster H J, Schödel R. Hochgenaue Temperaturmessung mit Thermoelementen, Technisches Messen, 68 (2001) 550 - 557

[7] The Network Variable Library is part of the LabView and LabWindows distributions of National Instruments. See the related user manuals for details.

Fusion of Microphone and Accelerometer Sensing for the Identification and Measurement of Inner Race Defect

R. Kumar, A. Kumar

Precision Metrology Laboratory, Department of Mechanical Engineering,
Sant Longowal Institute of Engineering and Technology, Longowal-148 106, India
Email: rajesh_krs@rediffmail.com, rajesh_krs@sliet.ac.in

Abstract. *Use of uni-axial accelerometer is simplest and cost effective way to monitor vibration in a single direction. Situation in which, fault is rotating/changing its direction extraction of defect frequency is difficult from it. However, some of the bursts can be properly analysed. The acoustic sensor is another cost effective device which is generally omnidirectional and can be used in identification of bearing defect. In this paper, data from both the acoustic sensor and accelerometer are utilised and fused to have complete information for identification of defect type and estimation of its width. The present work utilizes defect identification using envelope demodulation of acoustic signal. Subsequent measurement of defect width is carried out from accelerometer signal. Continuous wavelet transform (CWT) of vibration signal is carried out using adaptive wavelet to produce 2D scalogram. Finally, time marginal integration (TMI) of CWT coefficient is performed for the measurement of defect width.*

Keywords: Bearing, Inner Race Defect, Adaptive Wavelet, Time Marginal Integration.

Introduction

Components of rotating machine having relative motion are susceptible to failure due to dynamic stressing conditions. Rolling element bearing is one of such components. In recent past, development has been made in sensing technology as well as in digital signal processing [1-3]. Fusion of data to get the required information is also being attempted [4].

The uni-axial accelerometer is a cost effective vibration sensor but it captures burst with sufficient amplitude only in the direction of its sensitivity. This works well for stationary defect like outer race defect which generally remains fixed. However, in the more multifaceted case like inner race defect which rotates with the speed of the shaft, defect identification from frequency domain vibration signal using uni-axial accelerometer is difficult. On another hand acoustic sensor is generally omnidirectional and can overcome this problem but the data is contaminated by the noise from surrounding.

Utilising the advantage of both the acoustic and vibration sensing towards a low cost solution to complex problems, a signal processing scheme is proposed. The scheme is implemented for identification and measurement of inner race defect of a cylindrical roller bearing. The defect identification is carried out by envelope spectrum of Intrinsic Mode Function (IMF) generated by Ensemble Empirical Mode Decomposition (EEMD) of acoustic signal. After identification of defect, evaluation of its size is made by applying Continuous Wavelet Transform (CWT) using adaptive wavelet to the vibration signal to produce 2D map of CWT coefficient. CWT operation act as band pass filtering and produce high coefficient at scale analogous to frequency of burst. Finally Time Marginal Integration (TMI) of CWT coefficient is carried out for the measurement/evaluation of defect width.

Theory

Signals from both the microphone and accelerometer can be recorded simultaneously on different tracks using the same data acquisition system. For identification of type of defect and measurement of its size a processing scheme for microphone/acoustic signal and accelerometer/vibration signal respectively is proposed and given in Fig.1.

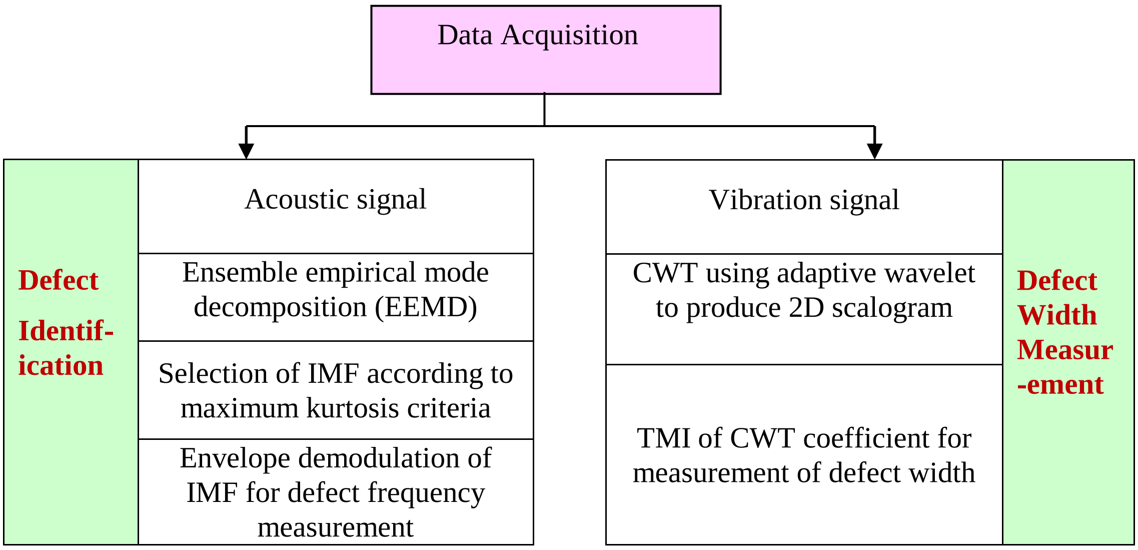

Fig. 1: Processing scheme for identification of bearing defect and measurement of its size

The EEMD is employed to decompose the nonlinear and non-stationary acoustic signal due to race defect into a number of intrinsic mode functions (IMFs) [5]. Out of which, IMF having maximum kurtosis is further processed by envelope demodulation for identification of defect frequency [6].

To enhance feature of defect in the vibration signal, CWT is carried out using adaptive wavelet [7]. TMI of CWT coefficient is carried out for evaluation of defect width. The TMI is analogous to the instantaneous power of the signal and reveals how the power of signal changes with time. TMI of CWT coefficient over scale a and time location b can be expressed as [8]:

$$TMI = \int_{-\infty}^{+\infty} CWT(a,b) da \qquad (1)$$

Experiment analysis

Experiment is performed on a bearing test rig. Seeded groove of width 0.94 mm in axial direction is introduced by electric discharge machining (EDM) process on the inner race of the cylindrical roller bearing (NBC NU205). The bearing has 13 rollers of diameter (d) as 7.50 mm. The microphone and accelerometer are used for acquisition of acoustic and vibration data using NI-USB-4431 DAQ system. Both the data are acquired simultaneously using two different ports of the DAQ system.

A typical acoustic signal of 0.1 sec for defective bearing is shown in Fig. 2(a). For identification of defect, EEMD of the signal is carried out. Application of EEMD produces several IMFs. Out of this, IMF1 has maximum kurtosis and is presented in Fig. 2(b) and is selected for further processing by envelope demodulation. Envelope spectrum of IMF1 is shown in Fig. 2(c). The spectrum has peak at shaft speed (F_d) and it's multiples which indicates presence of misalignment. The obtained defect frequency (F_d) is 258.5 Hz which is close to theoretical inner defect frequency (265 Hz) of the specified bearing at the specific speed. This indicates presence of inner race defect. Presence of inherent misalignment due to defect is observed at frequency $2F_s$. The interaction of defect frequency with the speed of shaft is also present in frequency spectrum in Fig. 2(c).

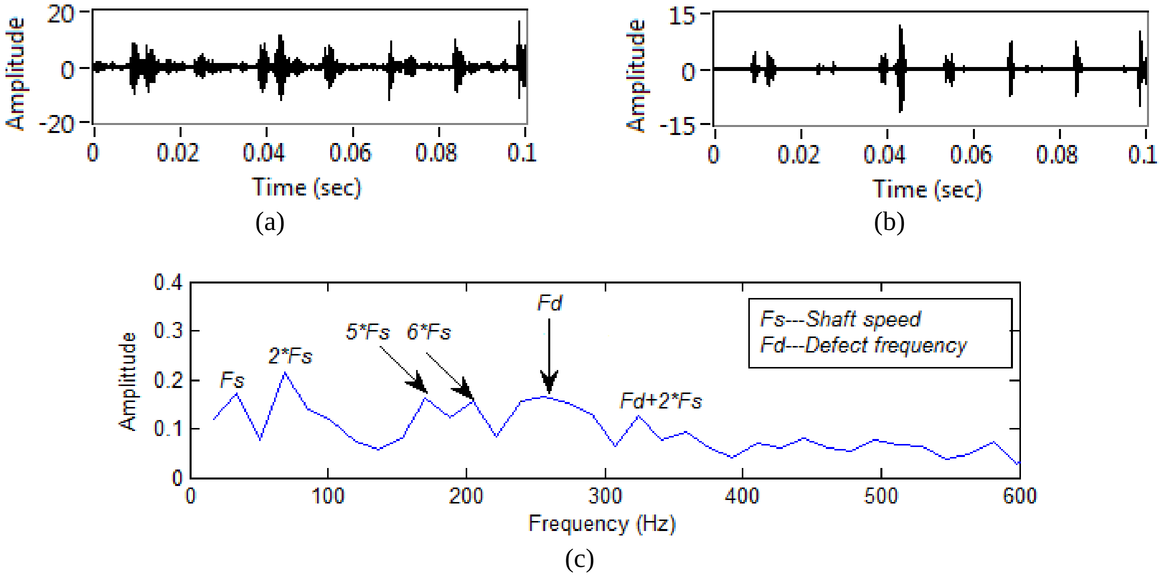

Fig. 2. A typical acoustic signal of bearing inner race defect (a) Raw signal (b) IMF1 using EEMD of signal in Fig. 2(a), and (c) Envelope spectrum of signal in Fig. 2(b)

A typical vibration signal for estimation of defect size is presented in Fig. 3(a). The magnified view of encircled burst in Fig. 3(a) is shown in Fig. 3(b). Although point of exit (GC2) of roller from the defect is easy to detect, spotting defect commencement point (GC1) from raw signal is difficult because of low energy of signal at that point of time. To minimize the ambiguity in spotting the GC1, a process stated in Fig.1 is implemented. Outcome of corresponding stages of processing is shown in Fig. 3(a), Fig. 3(b), Fig. 3(c) and Fig. 3(d). Defect commencement (GC1) and exit (GC2) can now be easily spotted from the TMI signal.

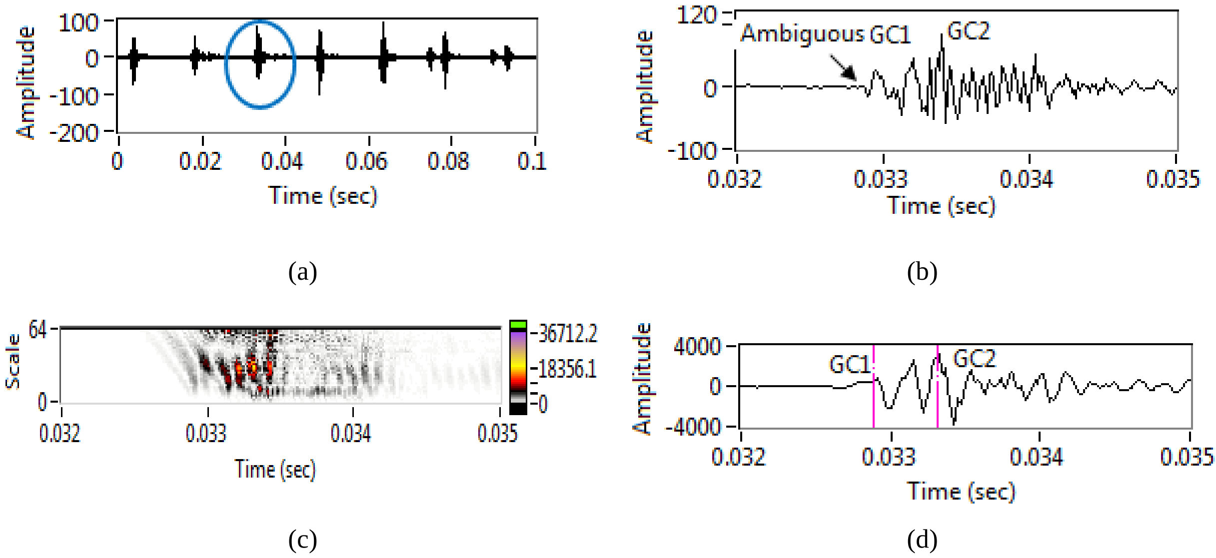

Fig. 3. A typical vibration signal for inner race defect (a) Raw signal (b) Magnified view of encircled burst in signal, (c) CWT scalogram of signal in Fig. 3(b) using adaptive wavelet, and (d) TMI of CWT coefficient

The inner race defect width (L_{IR}) can be calculated by making use of burst duration (Δt) determined from TMI graph, inner race diameter (D_I), shaft speed (F_S) and fundamental train frequency ($F.T.F$). The mathematical expression of inner race defect width is expressed as [9]:

$$L_{IR} = \pi \times \Delta t \times D_I \times (F_s - F.T.F) \quad (2)$$

The inner race diameter (D_I) of the specified bearing is 30.96 mm. The burst duration (Δt) is calculated by averaging taken from 10 bursts and is 0.0004432 sec. At shaft speed of 34.16 Hz and FTF of 13.75 Hz the defect width evaluated using the proposed scheme is 0.89 ± 0.07 mm.

Conclusions

A simple method to process the fused data of acoustic and vibration sensors has been proposed to resolve complicated issues such as identification of inner race defect as well as estimation of defect size. The processing scheme uses EEMD, envelope demodulation, CWT and TMI as applicable. Defect frequency has been identified with accuracy of 97.54% and the defect width has been evaluated with accuracy of 94.15%.

References

[1] McFadden P.D, Smith J.D. Vibration monitoring of rolling element bearings by the high-frequency resonance technique — a review. *Tribology International*, 17 (1): 3-10, 1984.

[2] Glowacz A. Diagnostics of DC and Induction Motors Based on the Analysis of Acoustic Signals. *Measurement Science Review*, 14 (5): 257–262, 2014.

[3] Hong H, Liang M, Fault severity assessment for rolling element bearings using the Lempel–Ziv complexity and continuous wavelet transform. *Journal of Sound and Vibration*, 320 (1–2): 452-468, 2009.

[4] Safizadeh M.S, Latifi S.K. Using multi-sensor data fusion for vibration fault diagnosis of rolling element bearings by accelerometer and load cell. *Information Fusion*, 18: 1-8, 2014.

[5] Wu Z.H, Huang N.E. Ensemble empirical mode decomposition: a noise assisted data analysis method. *Advances in Adaptive Data Analysis*, 1 (1): 1-41, 2009.

[6] Wang D, Miao Q, Fan X, Huang H.-Z. Rolling element bearing fault detection using an improved combination of Hilbert and Wavelet transforms. *Journal of Mechanical Science and Technology*, 23: 3292-3301, 2009.

[7] Kumar A, Kumar R. Adaptive Wavelet Based Signal Processing Scheme for Detecting Localized Defects in Rolling Element of Taper Roller Bearing. Proc. of Surveillance 7, Institute of Technology of Chartres, France, 2013.

[8] Addition, PS. The Illustrated wavelet transform handbook Introductory theory and application in science engineering medicine and finance. 1st ed. Institute of Physics Publishing, Bristol and Philadelphia, 2002.

[9] Singh M, Yadav R, Kumar R. Discrete Wavelet Trans-form Based Measurement of Inner Race Defect Width in Taper Roller Bearing. *MAPAN-Journal of Metrology Society of India*, 28 (1): 17–23, 2013.

Envelope Detection and Cepstrum Analysis for Gear Fault Diagnosis – A Comparative Study

[1, 2]M. El Morsy, [1]G. Achtenová

[1]Czech Technical University in Prague, Czech Republic
[2]Helwan University, Cairo, Egypt
Email: mohsabry@helwan.edu.eg, mohsabry1976@gmail.com

Abstract. *While operating a gear with local fault impulse is created, the high-frequency shock vibration is then generated and the vibration amplitude is modulated by the pulse force. Both the envelope and cepstrum analyses are useful tools to identify the fault frequencies and distinguish them from other frequency contents. Since the envelope analysis method provides an important and effective approach to analyse the fault signals of high-frequency impact vibration, it has been applied to the roller bearing fault diagnosis successfully. The intent of this article is to introduce these two tools and compare them between in a pragmatic way and to demonstrate their properties by using practical example of a gear fault. All the experimental data are acquired from vehicle gearbox which is tested on the laboratory stand equipped with three dynamometers; the input dynamometer serves as internal combustion engine, the output dynamometers introduce the load on the flanges of output joint shafts. The pitting defect is manufactured on one tooth of pinion gear on the output shaft. The results obtained from practical experiments prove that Cepstrum analysis provides a clear indication of fault for machine parts such as vehicle gearbox in addition to evaluate the efficiency of the common envelope analysis.*

Keywords: Cepstrum Analysis, Envelope Detection, Gear Fault Diagnosis

1. Introduction

The vibration signal obtained from operating machines contains information related to machine condition as well as noise. Further processing of the signal is necessary to elicit information particularly relevant to gear faults. Many techniques have been employed to process the vibration signals in gear faults detection and diagnosis. In the early stage of gear's faults, those periodic impulse components usually submerged in noises and the harmonic components such as gear meshing frequency components and rotating frequency components. Therefore, it is difficult to detect gear's local faults by using envelope analysis of the vibration signals of the gear effectively. Aiming at that problem, a method for fault diagnosis of gears based on resonance-based sparse signal decomposition and envelope spectrum was proposed [1]. From the previous work, the experimental results indicate that limited information can be found from the time-domain signals. The key features of those signals comprise of a large number of sinusoidal waveforms of overlapped dissimilar frequencies. Considerable interference between vibrations signals make it difficult to figure out useful information regarding to the gears conditions [2]. Since the cepstrum estimates the average sideband spacing over a wide frequency range, it is applicable to both detection and diagnosis of gear faults. In particular, Cepstral analysis has the advantage of identifying the fault period without regard to system characteristics, namely frequency (or impulse) response. The other methods that make use of the frequency spectrum usually depend on system resonance that provides a high signal-to-noise ratio. The cepstrum was used to separate and extract the periodic components of the dense modulated signals being difficult to identify, and based on that it also was recognized the rotating speed-frequency of fault positions, the type and location of faults were diagnosed using meshing frequency and rotating speed frequency obtained with these two kinds of spectral analysis methods. [3]. The challenge lies in coming up with a highly reliable and cost efficient monitoring system which though not necessarily comprehensive but should be capable of tracking down the major causes of gear failures and give an early indication thereby enabling effective preventive maintenance and eventually reduce costs per failure [4].

2. Signal Processing

Envelope Signal Processing

Envelope Signal Processing is a two-stage process. The first process involves band-pass filtering of the time domain signal using a band pass filter that center on the region of high frequency energy. The second stage of the process is to pass this filtered time signal through an envelope in order to extract the repetition rate of the spiky bursts of energy. The envelop analyzer is an electronic circuit that demodulates or rectifies the signal. The result of passing the signal through the envelop analyzer: The extracted signal is the repetition rate of the impacts [1].

Cepstrum Analysis

Cepstrum, which is an anagram of spectrum, is a nonlinear signal processing technique used to identify and separate harmonic families in the spectra of gearbox signals. Table 1 compares the terms used in the spectral and Cepstral analyses. Exact definitions vary across the literature. The different cepstrum forms can be found [3]:

$$C_{cplx} = \frac{1}{2\pi} \int_{-\pi}^{\pi} log\left[X(e^{j\omega})\right] e^{j\omega n} d\omega \tag{1}$$

$$C_{real} = \frac{1}{2\pi} \int_{-\pi}^{\pi} log\left|X(e^{j\omega})\right| e^{j\omega n} d\omega \tag{2}$$

The cepstrum is complex if the phase information of the original time waveform is preserved. The complex cepstrum has the corresponding inverse complex cepstrum. In this case the time waveform can be reconstructed from a modified cepstrum. On the other hand, if the input of the inverse Fourier transform is real (no phase information), for example, the magnitude of the Fourier transform of the signal, the cepstrum is real-valued.

Table 1. Comparison of terms used in spectral and cepstral analyses .

Spectral analysis	Cepstral analysis
spectrum	cepstrum
frequency (Hz)	quefrency (second)
harmonic	rahmonic
filter	lifter

3. Description of the test set-up

Experimental set-up

The measurements are conducted on an open loop test bed which consists of three dynamometric machines. Our purpose, we did the measurements in steady state regimes only. Fig. 1 shows the real photo of arrangement layout of test rig components with indication of the position of accelerometer and tachometer (left figure) and the internal arrangement of gears, shafts and bearings in the investigated gearbox (right figure).

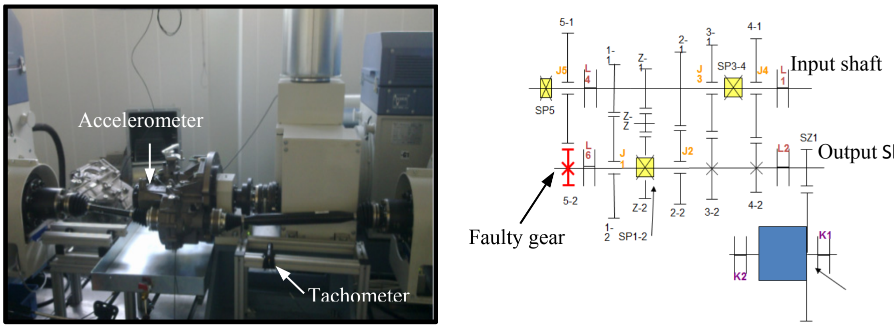

Fig. 1. Open loop test bed used for investigation of faults and internal arrangement of in the investigated gear.

The gearbox used for our measurements is the type most commonly used in small and mid-size passenger cars: a five-speed gearbox with final drive gear and front wheel differential.

Description of the Artificial Damage

The pinion for fifth speed has artificially fabricated fault on one tooth only. The total surface area of the pit is 4.58 mm^2. The gearwheel is treated as damaged if the surface of damage on one tooth is greater than 4% of the tooth surface. In our case the damage equals 3% of the tooth surface. This means there is a significant pit, but the pinion gear can't yet be treated as damaged.

4. Experimental procedures and results

A Brüel & Kjaer portable and front-end type 3050-B-040 4channel input Module 50 kHz analyzer is used. The speed is measured using a Tachometer Type MM360, and a tri-axial (Telta Tron type 4524B) accelerometer was used to record the vibration acceleration signals, both mounted upon the gearbox case as shown in Fig. 1. The vibration signal in vertical and radial terms is presented in this article. The sampling frequency used was 6.4 kHz and signals of 0.5 sec duration were recorded.

Fig.2 and Fig. 3 show the cepstrum analysis and envelope spectrum of original time signals in vertical direction for the faulty gear (37 teeth) on the output shaft in fifth speed, input shaft speeds 2000 rpm and 3000 rpm and constant input torque 130 Nm. Fig.2a and Fig. 3a illustrate, that the damage is the driven gear, by presentation the number of rahmonics of driven shaft rotation as the source of the problem. Cepstrum indicates periodicity at 22.2 ms (45 Hz, rotating frequency of output shaft) and 14.8 ms (67.56 Hz, rotation by the output shaft). On another hand as shown in Fig. 2b and Fig. 3b, the Envelope Detection for the gear fault has an amplitude modulating effect on its characteristic frequencies. The characteristic frequency of the faulty gear and its harmonics are presented at rotating frequency 45 Hz and 67.6 Hz at the two operating speeds respectively, and constant input torque 130 Nm. It is evident that both the methods were effective in identifying the gear defect.

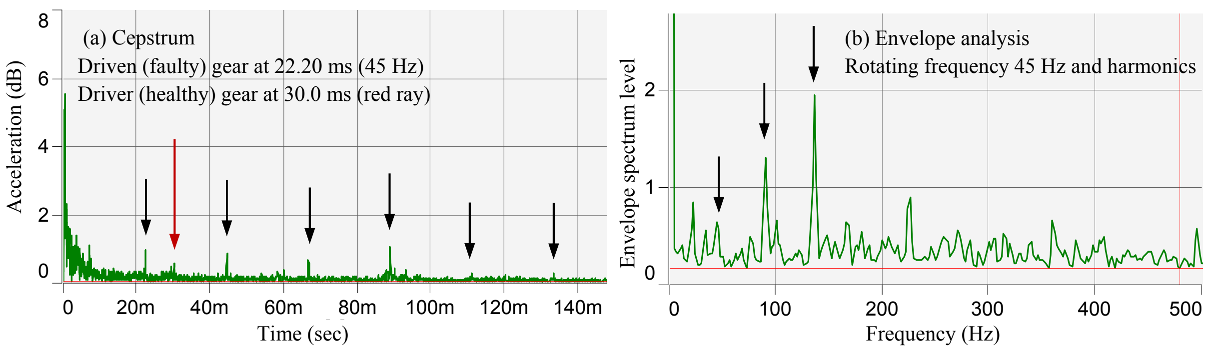

Fig. 2. Cepstrum and Envelope analyses for the faulty gear in fifth speed, at speed 2000 rpm and load 130 Nm.

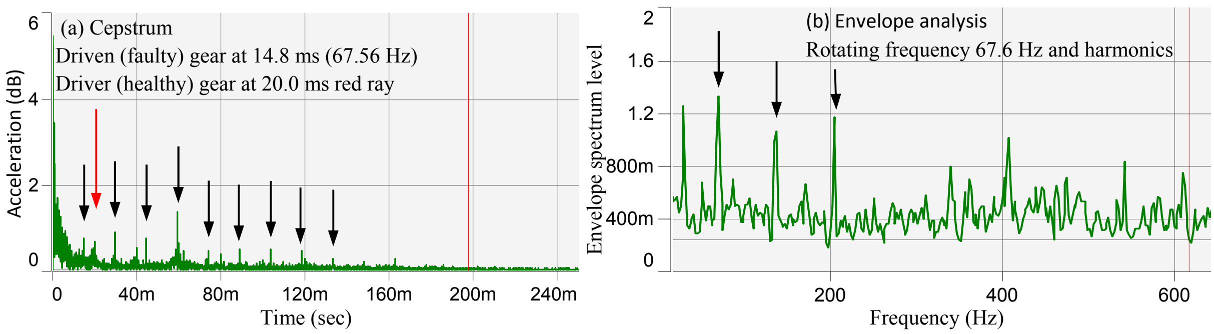

Fig. 3. Cepstrum and Envelope analyses for the faulty gear in fifth speed, at speed 3000 rpm and load 130 Nm.

5. Conclusion

In the present paper cepstrum and envelope analyses are used to a gear fault diagnosis in the early stage of gear's fault. Real comparative study was done; results show that the two methods are effective and reliable but the disadvantage of conventional envelope analysis is, that the central frequency of filter has to be chosen in advance, which demands some experience. Concerning the comparison, the squared envelope analysis was discussed in a separate publication [5]. Cepstrum technique appears to be efficient for detecting changes not easily notable in the spectrum. Major benefit of using cepstrum technique would be earlier damage identification because it is clear and easier to separate periodic events (fault) from random events (noise).

Acknowledgements

This publication was supported by the European Social Fund within the framework of realizing the project “Support of inter-sectoral mobility and quality enhancement of research teams at Czech Technical University in Prague”, Prague, Czech Republic, CZ.1.07/ 2.3.00/ 30.0034.

The support of the Ministry of Education, Youth and Sports program NPU I (LO), project LO1311Development of Vehicle Centre of Sustainable Mobility.

References

[1] Zhang, W., Yu, D., Chen, X., "Fault diagnosis of gears based on resonance-based sparse signal decomposition and envelope spectrum" China Mechanical Engineering, Vol. 24, Issue 24, 2013, pp 3349-3354, DOI: 10.3969/j.issn.1004-132X.2013.24.017

[2] McFadden. P, Smith. J, “A Signal Processing Technique for Detecting Local Defects in a Gear from the Signal Average of the Vibration”, Proc. European Conference, IMechE, Vol. 199, No. C4, pp. 287 – 292, 1985.

[3] Luo, Y., Zhen, L.-J. 2015, "Diagnosis method of turbine gearbox gear crack based on wavelet packet and cepstrum analysis" Journal of Vibration and Shock, 34 (3), pp. 210-214, DOI: 10.13465/j.cnki.jvs.2015.03.034

[4] Bardou. O, 1994 "Early Detection of Leakages in the Exhaust and Discharge Systems of Reciprocating Machines by Vibration Analysis", Mechanical Systems and Signal Processing, Vol. 8, No. 5, pp. 551– 570.

[5] M. El Morsy, G. Achtenova (2014). "Modern Vibration Signal Processing Techniques for Vehicle Gearbox Fault Diagnosis". International Science Index 94, International Journal of Mechanical, Aerospace, Industrial and Mechatronics Engineering, 8(10), 1594 - 1599.

Noncontact Vibrometer Based on the Fibre Optical Michelson Interferometer

[1,2]I. Glebus, [1]S. Makarov

[1]Technological Design Institute of Scientific Instrument Engineering,
Siberian Branch of the Russian Academy of Science (TDI SIE SB RAS)
Novosibirsk, Russia
[2]Novosibirsk State Technical University
Novosibirsk, Russia
Email: ilya-neo@ya.ru

Abstract. *Research results of designing a vibrometer based on the state-of-the-art circuitry are presented. An interferometric scheme sensitive to the distance to an object based on the Michelson interferometer is used. A quadrature interferometric signal is received by laser pumping current modulation and further signal filtering. Object surface displacement signals as a result of experimental measurements and processing of the data obtained signals of an object's surface displacement are recovered for the vibration mode with the preset frequency and amplitude. The surface vibration frequency corresponds to the generator signal frequency (30 Hz), with the amplitude of the investigated point being equal to 4 ± 0.05 µm. A random displacement amplitude equals 0.3 µm when signal is absent. It is revealed that the vibrometer setup can detect quadrature interferometric signals and recover surface displacements of vibration objects. Further research on the proposed setup as well as on improving its accuracy characteristics and bringing it to a prototype are planned.*

Keywords: Michelson Interferometer, Vibration, Quadrature Signal, Fibre Optics

1. Introduction

Measurement and inspection of vibrations are used in various fields such as microelectronics, mechanical engineering, railroad industry, aircraft construction, etc. [1]

The measuring devices must ensure noncontact method, high resolution (10…100 nm), long distance to the object (up to 10 m) and high frequency surface vibrations (1…10 kHz).

Potentially the optical methods meet all these requirements. Design of these devices is on the modern technologies edge. However, the leading experts don't publish the schemes, algorithms and methods details of their developments. Moreover, the foreign devices are enough expensive. But modern fiber optical components are of low cost and rather reliable. It allows us assembling the vibrometer optical scheme, for example, based on the structurally simple Michelson interferometer scheme by the unified blocks.

The aim of this work is to design amplitude vibrometer and its characteristic research.

2. Measuring Method and Vibrometer Scheme

This method is based on the Michelson interferometer scheme [2] which is sensitive to the distance between device and object. Resulting intensity on an interferometer photodetector is described by the equation:

$$I(L) = I_1 + I_2 + 2\sqrt{I_1 I_2}\cos(2kL), \tag{1}$$

where

I the signal intensity on a photodetector

I_1 the intensity signal of the first interferometer arm

I_2 the intensity signal of the second interferometer arm

k the wave number

L distance from vibrometer to the object.

Because the distance from the object surface to vibrometer can both increase and decrease the quadrature addition of interferometric signal is required [3], i.e. signals pair

$$x(L) \sim \cos(2kL), \tag{2}$$

$$y(L) \sim \sin(2kL), \tag{3}$$

where

x interferometric signal

y quadrature addition.

This problem can be solved using lasers with tunable wavelength (e.g. DFB Lasers [4]), frequency modulation and signal filtering [5].

The scheme presented in Fig. 1 is based on the fibre-optical Michelson interferometer.

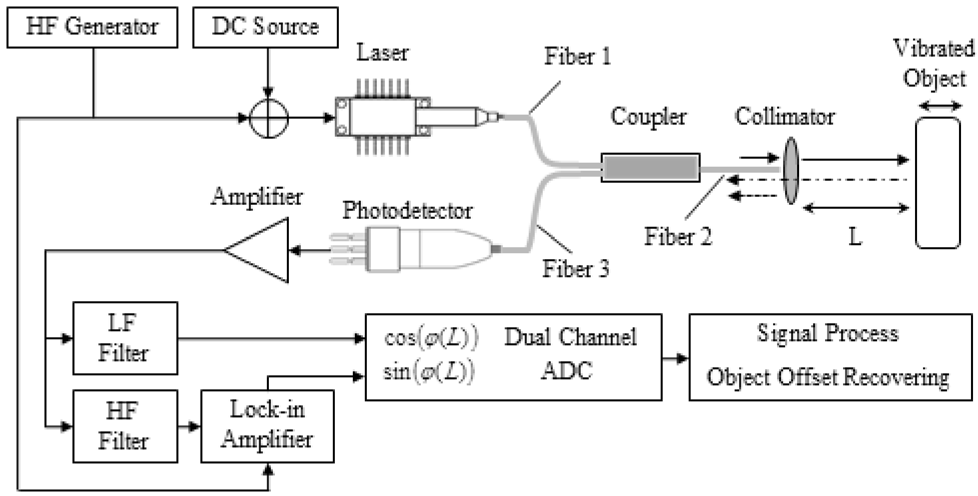

Fig. 1. The fibre-optical vibrometer general scheme.

Vibrometer operation is the following. Laser radiation propagates through Fiber 1, Coupler and Fiber 2 to butt of Fiber 2. After that the radiation is separated on 2 directions: part of it is collimated, followed to the object (solid line), reflected from this object (dash-dotted line) and entered to Fiber 2. Another part of radiation is reflected from butt (dotted line). Then these parts interfere on photodetector.

But as mentioned above quadrature signal should be received. Therefore the laser is supplied by summation of operation current from DC Source and a bit modulation current from HF generator. Due to modulation the laser generates the optical radiation with variable wavelength.

Thus the interferometric signal on a photodetector consists of a low-frequency part proportional to cosine of phase difference (2) and a high-frequency part proportional to sine of phase difference (3) after synchronous detection. Then LF and HF filters separate the original signal into two components [6]. After that the resulting signal are digitized for its further processing and analyzing to surface displacement recovering.

3. Experimental Research

Setup presented in Fig. 2 was assembled for carrying out the vibration measurement experiments. The setup consists of the fibre-optical interferometric scheme with fiber SMF-28e [7] and fibre-optical coupler Thorlabs 10202A-50-FC) [8], DFB Laser FITEL FRL15DCWD-A81 (wavelength 1550 nm) [9], collimator F810FC-1550 [10], photodetector with amplifier scheme, electronic scheme (including PC sound card with sampling frequency 44 kHz) and low-noise power supply (battery 12 V).

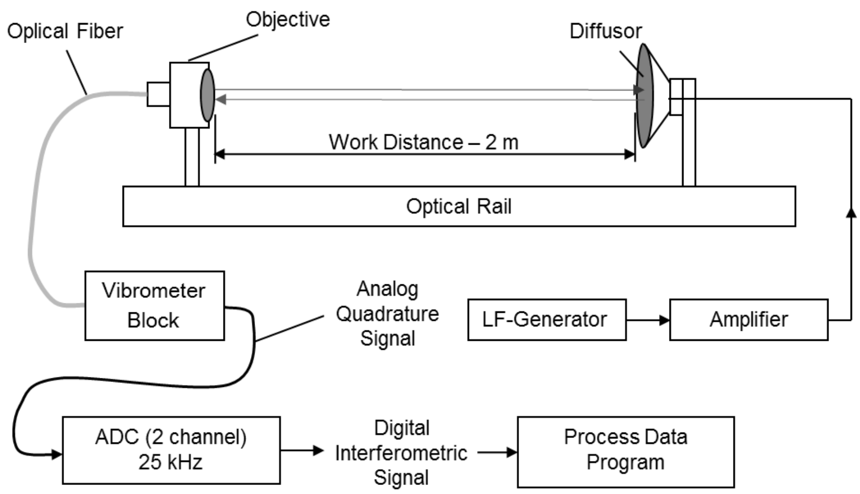

Fig. 2. Experimental setup of the vibrometer.

Two operating modes were used for carrying out experiments.

Object vibration mode with preset frequency and amplitude. The sine signal is supplied to the speaker coil with frequency equals to 30 Hz.

No signal mode of LF Generator. There isn't current to the speaker coil.

4. Results

Quadrature signal and the fragment of surface displacement recovered signal in the first mode are presented in Fig. 3 a, b.

As follows from the process physics the interferential picture is variable due to the distance changing. Surface vibration frequency corresponds to the generator signal frequency and amplitude in useful point equals to 4 ± 0.05 μm (confidence level equals to 0.95).

Quadrature signal and the fragment of surface displacement recovered signal in no signal mode are presented in Fig. 3 c, d. However, interferometric signal and its quadrature addition are variable. There is surface vibration due to diffusor own fluctuations and mechanical setup vibrations. Random displacements estimation is equal to 0.3 ± 0.05 μm.

Obviously that there is natural vibration in both modes but it is visible poorly due to high useful signal level in first mode.

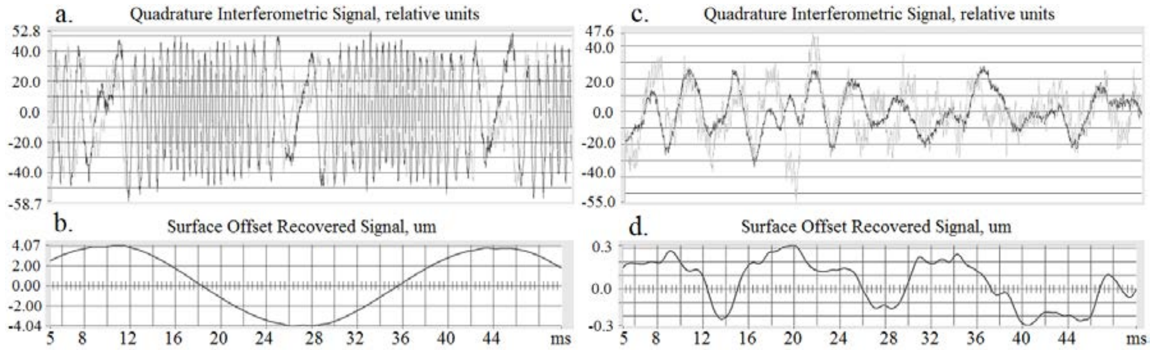

Fig. 3. Recovering signal of surface displacement (left graphs – vibrating with 30 Hz; right graphs – no generator signal mode).

5. Conclusions

The aim of this work was the vibrometer design based on modern fibre-optical components. Michelson interferometer scheme was chosen as the vibration measuring method. The vibrometer setup was assembled and experimental measurements of vibration amplitude were carried out for diffuse scattering surface. As a result the vibrometer based on the fibre-optical components can detect the quadrature signal with error of 0.05 µm and the frequency band equal to 20 kHz. It proves the ability of vibrometer realization using the fibre-optical components.

References

[1] Klyuev VV. Devices and systems for measuring noise and shock vibration. Handbook: in 2 vol. Mashinostroenie, Moscow, 1978 (in Russian).

[2] Fercher AF. Optical coherence tomography. *Journal of Biomedical Optics*, 1 (2): 157-173, 1995.

[3] Atavin VG, Mokhnatov AA, Khudyakov YuV. New possibilities for vibration-amplitude measurement by heterodyne laser vibrometer. *Measurement Techniques*, 2: 32-34, 2000.

[4] Svelto O. Principles of lasers. Springer, New York, 1989.

[5] Glebus I, Makarov S, Chugui Y. Noncontact interferometric fibre optics vibrometer. *Science Bulletin of the NSTU*, 4 (57): 49-58, 2014.

[6] Romanov I. Active RC-filters: schemes and calculations. *Radio*, 3: 45-48, 1995.

[7] CORNING. Available at: http://www.corning.com/uploadedFiles/Corporate/Russia/Products_+_Services/Telecommunications/Optical_Fiber/Pdfs/SMF_28eplus.pdf (accessed 20.01.2015).

[8] SM Coupler. Thorlabs, Inc. Available at: http://www.thorlabs.de/thorcat/1300/10202A-50-FC-AutoCADPDF.pdf (accessed 20.01.2015).

[9] Laser diode module FRL15DCWD-A81-W1550. The Furukawa Electric Co., Ltd. DataSheets.com: For electronic engineers & buyers. Available at: http://www.datasheets.com/search/partdetail/FRL15DCWDA81W1550/The+Furukawa+Electric+Co-dot-,+Ltd (accessed 20.01.2015).

[10] FC/APC collimation package F810FC-1550. Thorlabs, Inc. Available at: http://www.thorlabs.de/thorcat/13800/F810APC-1550-AutoCADPDF.pdf (accessed 02.02.2015).

Photonic Micro Sensors for Mobile Color and Spectral Characterization of Colored Liquids in Laboratories and in Field

P.-G. Dittrich, D. Hofmann

SpectroNet c/o Technologie- und Innovationspark Jena GmbH, Jena, Germany
Email: pg.dittrich@spectronet.de

Abstract. *Aim of the paper is to show possible applications for color inspections and measurements of liquids. The paper tackles different technologies of multi-spectral and spectral micro sensors which can be used in laboratories and in field - convenient, reliable and affordable. Multi-spectral and spectral micro sensors are differentiated by their spectral resolutions, measurement speeds, accuracies and costs. Multi-spectral micro sensors are less expensive. The paper describes how dielectric-interference multi-spectral micro sensors are calibrated. Practical applications for the colorimetric characterization of petroleum oils and fuels and their colorimetric characterization by liquid color scales are tackled.*

Keywords: Multi-Spectral Micro Sensors, Photonic Micro Sensors, Color, Spectral

1. Subjective Liquid Color Inspections

In chemical, pharmaceutical and cosmetic industries the quality expectations for colored liquids are growing. Typical colored liquids are solvents, oils, fatty acids and fuels. The qualities of optically clear liquids are characterized for example by their colors. For different liquids a bigger number of characterizing standards and scales in the past have been developed and applied (Fig. 01) [01].

Colored Liquids	Liquid and Application Specific Color Characterization
Chemicals & industrial oils	Pt-Co/Hazen/APHA, Garner, Iodine, CIE values, spectral data
Petroleum oils & fuels	Saybolt, ASTM Color, Pt-Co/Hazen/APHA, CIE values, spectral data
Dark oils & fats	FAC, Gardner, CIE values, spectral data
Beers, malts and caramel	EBC (CIE & 430 nm), ASBC (CIE & 430 nm), CIE values, spectral data
Pharmaceutical solutions	EUR, US & Chinese Pharmacopoeia Color, Pt-Co/Hazen/APHA, CIE values, spectral data
Industrial oils and surfactants	Klett Color (blue filter KS-42), Pt-Co/Hazen/APHA, CIE values, spectral data
Sugars, syrups and honeys	ICUMSA Color (420, 560, 710 nm), Honey Color, CIE values, spectral data
Water & wastewater	ADMI (spectral & tristimulus filter methods), Pt-Co/Hazen/APHA, CIE values, spectral data
Transparent liquids	CIE values, L*a*b* or L*C*h* color space, Hunter Lab color space, spectral data

Fig. 01. Liquid specific colorimetric characteristics

Nowadays the color analysis of liquids can be applied by so called:
- subjective visual color inspection methods, where qualified inspection persons compare **subjective** the investigated liquid probes with defined mechanical color standards or
- objective tristimulus multi-spectral and spectral measurement methods where measurement systems compare **objective** the investigated liquid probes with defined electrical color standards

A fundamental preposition for objective quality assurance are appropriate measurement systems. Innovative measurement systems are combinations of photonic micro sensor modules and digital image processing with smartpads. These systems are **mobile** applicable in laboratories and in field (Fig. 02) [02] [03].

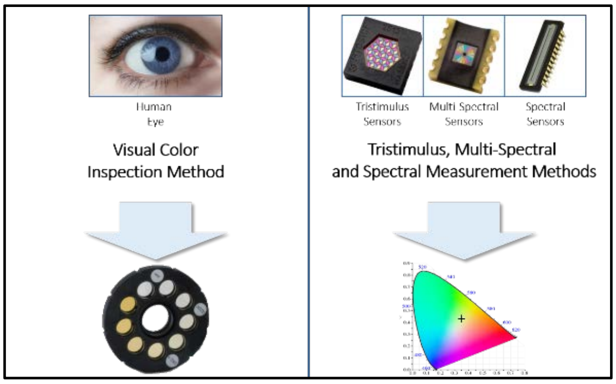

Fig. 02. From subjective inspections to objective measurements

In the International Vocabulary of Metrology calibration is defined (VIM 2.39): "**Calibration** is an operation that, under specified conditions, in a first step, establishes a relation between the quantity values with measurement uncertainties provided by measurement standards and corresponding indications with associated measurement uncertainties and, in a second step, uses this information to establish a relation for obtaining a measurement result from an indication." **Calibration standards** for color inspections and measurements are manifold. Calibration standards can be used to match the capabilities, performance and ease-of-use of smart mobile photonic micro measurement systems. Concerning the differences between laboratory and in-field measurements the environmental conditions for in-field measurements might be more complex than in laboratory. Nevertheless the resolutions, accuracies and reproducibilities of laboratory and in-field measurements should be more or less equal. Main problem is the task specific calibration of in-field measurement systems. The colorimetric characterization of optically clear colored liquids with calibrated multi-spectral micro sensor modules is documented in the DIN EN 1557, 1997 [04] and the ASTM E 308 – 99, 2013 [05]. The determination for example of Saybolt color numbers is documented in ASTM D 6045 – 96, 2013 [06]. Aim of the investigations was the color and spectral characterization of optically clear colored liquids which can be described by the Saybolt color scale. The Saybolt color scale is an empirical scale from −15 (darkest) to +30 (lightest) to express the colors of clear petroleum oils and fuels (Fig. 03) [06].

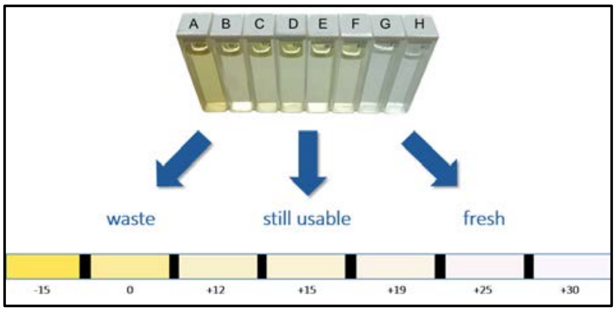

Fig. 03. Liquid probes (top), quality of liquid probes (center) and Saybolt color scale for liquids (down)

The Saybolt color scale is used not only for the colorimetric characterization of petroleum oils and fuels but also for a wide variety of petroleum products such as undyed motor and aviation gasoline, aviation turbine fuels, naphtha, kerosine, pharmaceutical white oils, diesel fuel oils, heating oils, and lubricating oils [06].

2. Objective Color and Spectral Measurements of Liquids

The paper tackles also technologies for so called multi- and hyper-spectral micro sensors which can be used for objective measurements in industry, biology/medicine, agriculture/

environment, administration and security. Four different multi- and hyper-spectral micro sensor technologies can be distinguished. **Spectral Sensors** with digital image processing show the intensity of light as a function of wavelength. The deflection is produced either by refraction with prism or by diffraction with a diffraction grating (Fig. 04) [03].

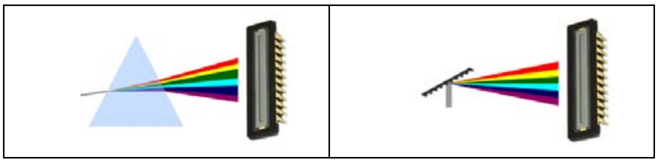

Fig. 04. Spectral sensor with prism (left) and grating (right)

Micro-patterned multi-spectral micro sensors have narrowband optical filters integrated on photodiodes. The patterning is a combination of dielectric, metal and conductive coatings. The micro-patterned technology enables a specific spectral selective sensor design. An example setup was realized with 8 spectral channels into a 9.0 mm square footprint (Fig. 05) [07]. The photodiodes are configured for common cathode operation, providing low noise and fast temporal response. Targeted spectral bands are located in VIS and NIR bands from 400 nm up to 1000 nm. **Nano-structured multi-spectral micro sensors** have sub-wavelength hole arrays as the spectral selective elements integrated on photodiodes. The used physical effect is called surface plasmon effect [08]. The nano-structured technology enables a specific spectral selective sensor design. An example setup was realized with 16 spectral channels into a 2.5 mm square footprint (Fig. 06) [09]. The integration of amplifiers and signal processors is possible within CMOS-processes. Targeted spectral bands are located in VIS and NIR bands from 400 nm up to 1000 nm. **Dielectric-interference multi-spectral micro sensors** have titanium dioxide and silicon dioxide filter stacks as the spectral selective elements integrated on photodiodes. The dielectric-interference technology enables a specific spectral selective sensor design. An example setup was realized with 6 spectral channels into a 2.4 mm square footprint and all in all in a SMD chip with 7.0 x 6.0 x 1.7 mm (Fig. 07) [10]. The dielectric-interference filters show no aging in comparison to absorption filters and have no thermal drifts. Targeted spectral bands are located in VIS and NIR bands from 400 nm up to 1000 nm.

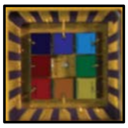

Fig. 05. Micro-patterned multi-spectral micro sensor

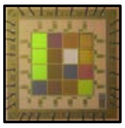

Fig. 06. Nano-structured multi-spectral micro sensor

Fig. 07. Dielectric-interference multi-spectral micro sensor

Fabry-Pérot interferometric hyper-spectral micro sensors have Fabry-Pérot interferometric filters on top of each pixel as the spectral selective elements. Fabry-Pérot interferometric hyper-spectral technology enables a spatial spectral selective sensor design. Example setups were realized as so called line-scan, snapshot-tiled and mosaic into ceramic 95 pin PGA and µPGA 18.6 mm x 18.6 mm packages (Fig. 08) [11].

		
LINE-SCAN	SNAPSHOT-TILED	MOSAIC
• 100+ spectral bands • 600-1000 nm, 4 nm incremental steps • FWHM 10-15 nm • Spatial resolution 2048 x (100+ each band x 8 pixels)	• 32 spectral bands • 600-1000 nm, 12nm incremental steps • FWHM 10 - 15 nm • Spatial resolution per band: 256 x 256	• 4x4 mosaic, 16 spectral bands • 470-630 nm, 11 nm incremental steps • FWHM 10 - 15 nm • Spatial resolution per band: 512 x 272

Fig. 08. Fabry-Pérot interferometric hyper-spectral micro sensors

The hyper-spectral filters are integrated monolithically on top of the sensor at wafer-level. That provides high-level performance with significant reduction in size and cost. Targeted spectral bands can be in VIS and NIR bands from 470nm up to 1000 nm.

3. Multi-Spectral Micro Sensor Value Interpretation

For the transfer of the specific multi-spectral micro sensor outputs into standardized, for example Saybolt color numbers, a calibration must be accomplished [12]. A common calibration method is the application of a so called target based **correction matrix**. The correction matrix is based on a general comparison of existing reference values (or measured values of a spectral sensor) with the actual values of a multi-spectral micro sensor. The measurements of the values are realized by parallelization of a spectral and a multi-spectral micro sensor. The relationship between the **spectral micro sensor values** ($\underline{T}$) and the **multi-spectral micro sensor values** ($\underline{S}$) are used for the target based correction matrix (01).

$$\underline{T} = \underline{K} \cdot \underline{S} \quad (01)$$

After transposition of equation (01) into the correction matrix $\underline{K}$ (02) the corrected measurement values can be calculated by:

$$\underline{K} = \left(\underline{T} \cdot \underline{S}^T\right) \cdot \left(\underline{S} \cdot \underline{S}^T\right)^{-1} \quad (02)$$

After a successful calibration colorimetric calculations according to standards can be applied. It is necessary to transfer the sensor outputs to the liquid specific color scales.

4. Summary and Conclusions

Aim of the paper was to show possible applications for color inspections and measurements of liquids with multi-spectral and spectral micro sensors. Different sensor technologies have been tackled. Subject matter of the investigations where optically transparent liquids like petroleum oils and fuels, which can be described as a result of the colorimetric characterization on the Saybolt color scale. In the presentation it will be shown that objectified mobile color measurements of petroleum oils and fuels can be realized by multi-spectral micro sensor modules in laboratories and in field.

Acknowledgements

Many thanks to our Clusterpartners and to BMWi Berlin for their long standing financial support in the frames of ZIM and go-cluster.

References

[01] Lovibond - The Tintometer Ltd., „Lovibond® PFXi-195 Series - Accurate, efficient spectrophotometric colorimeters“, Amesbury, UK, 2010

[02] Orbeco-Hellige Inc., “Color | Orbeco-Hellige - Laboratory and Field Instruments and Reagents for Water Analysis and Color Measurement”, [Online], Available: http://www.orbeco.com/color. [Zugriff am 15 Februar 2014].

[03] Hamamatsu Photonics K.K., “Back-thinned type CCD linear image sensor S11155-2048-01 | Hamamatsu Photonics”, [Online], Available: http://www.hamamatsu.com/jp/en/product/alpha/C/4206/4214/S11155-2048-01/index.html. [Zugriff am 15 Februar 2014].

[04] DIN - Deutsches Institut für Normung e.V., „DIN EN 1557 - Colorimetric characterization of optically clear colored liquids (products) as X, Y, Z tristimulus values in transmission“, Beuth Verlag GmbH, Berlin, 1997.

[05] ASTM International, „ASTM E 308 - 99 - Standard practice for computing the colors of objects by using CIE system“, ASTM International, ASTM D 6045 - 96, 2013.

[06] ASTM International, „ASTM D 6045 - 96 - Standard test method for color of petroleum products by the automatic tristimulus method“, ASTM International, West Conshohocken, 2013.

[07] PIXELTEQ, "Multispectral Imaging & Sensing Solutions for the UV to SWIR", Eric Chandler, [Online]. Available: http://spectronet.de/de/suche/multispectral-imaging-sensing-solutions-for-the-uv_hxf5m3sn.html. [Zugriff am 15 Februar 2014].

[08] T.W. Ebbesen, Extraordinary optical transmission through sub-wavelength hole arrays, Macmilian Publishers Ltd, 1998

[09] Fraunhofer IOSB, "Video: Optische Stoffcharakterisierung von Flüssigkeiten", Stephan Junger, [Online], Available: http://spectronet.de/de/suche/video-optische-stoffcharakterisierung-von-fl%C3%BCssigk_huv7aelt.html. [Zugriff am 15 Februar 2014].

[10] MAZeT GmbH, "Multiple Color Sensors - English", MAZeT GmbH, [Online], Available: http://www.mazet.de/en/products/jencolor/multiple-color-sensors?set_language=en. [Zugriff am 15 Februar 2014].

[11] Ximea GmbH, “Video: Miniature Hyperspectral Imaging Cameras”, Max Larin, [Online], Available: http://spectronet.de/de/videos_2014/video-miniature-hyperspectral-imaging-cameras_i3tabv8f.html. [Zugriff am 15 Februar 2014].

[12] K.-H. Franke und R. Nestler, Tagungsband der Beiträge zum 12. Workshop Farbbildverarbeitung, Ilmenau: ZBS e.V., 2006.

Selection of Antenna Factor for EMI Measurements

M. Bittera, M. Mician, V. Smiesko

Slovak University of Technology in Bratislava, Institute of Electrical Engineering, Bratislava, Slovakia,
Email: mikulas.bittera@stuba.sk

Abstract. *The general and also the standard recommendation in the scientific community is to use a free-space antenna factor for electromagnetic interference measurements. This paper deals with the proposal of a "site" antenna factor which also includes, besides the free-space antenna factor the contribution of the imperfections of used test site. The relation between the "site" antenna factor and the site imperfections is examined based on a number of antenna factor measurements by the standard site method to confirm this proposal.*

Keywords: Antenna Factor, EMI Measurement, Normalized Site Attenuation, Test Site

1. Introduction

In electromagnetic interference (EMI) measurements it is necessary to obtain electric field strength for determining the compliance with the EMI standard requirements [1], [2]. The electric field strength of radiated emission is measured by a suitable receiving antenna connected to a measuring receiver. An antenna factor, the most important parameter of an antenna for EMI measurements, is seldom included among the antenna basic characteristics. The antenna factor is defined as a quantity relating the strength of the field in which is the antenna immersed to the output voltage across the load connected to the antenna; the field strength is then equal to the output voltage multiplied by the antenna factor. EMI antennas have characteristics that may be affected by a ground plane, e.g. the antenna factor of a tuned dipole for 30 MHz varies by about 6 dB when the height of the antenna above the ground plane is adjusted from 1 m to 4 m [4]. As EMI measurements require a single value of the antenna factor, standard bodies have decided to use the free-space value of the antenna factor in EMI measurement.

The free-space antenna factor is an antenna factor which is not influenced by adjacent objects. Standard [3] has also introduced a new set of terms and concepts, inter alia, near-free-space antenna factor and geometry-specific antenna factor. The same standard also describes three main methods of antenna factor calibration: the standard site method (SSM), the reference antenna method and the equivalent capacitance substitution method. Additional methods are described in [5]. However, low uncertainty of the antenna factor measurement does not explicitly mean low uncertainty of the EMI measurement due to imperfections of the test site where the measurement is performed. Then, an antenna factor including these test site imperfections may be used to reduce the EMI measurement uncertainty.

2. Problem description

The quality of test sites may be deduced from the difference of the theoretical normalized site attenuation (NSA) in the ideal test site and the measured NSA in a particular test site. Theoretical values of NSA, expressed in dB, are defined as [6]:

$$NSA = 48.92 - 20\log f - E_{\mathrm{Dmax}} \quad (1)$$

where f is the frequency and E_{Dmax} is the theoretically obtained maximum value of the electromagnetic field strength, also in dB, at the given frequency, measuring distance and polarization of the antenna.

Imperfections in a test site will yield practical site attenuation values which are different from the theoretical values. Practical test site normalized attenuation can be measured using an antenna setup shown in Fig. 2. Thus:

$$NSA = SA - AF_{\mathrm{T}} - AF_{\mathrm{R}} = V_{\mathrm{Rdir}} - V_{\mathrm{Rsite}} - AF_{\mathrm{T}} - AF_{\mathrm{R}} \qquad (2)$$

where SA is the site attenuation, V_{Rdir} is the voltage measured with the two antenna cables connected directly to each other, V_{Rsite} is the voltage measured with the two antennas in their locations while the height of the receiving antenna is adjusted to obtain the maximum reading. AF_{T} and AF_{R} are the free-space antenna factors of the transmitting and receiving antennas. All standards recommend a limit of ±4 dB for the residual imperfections.

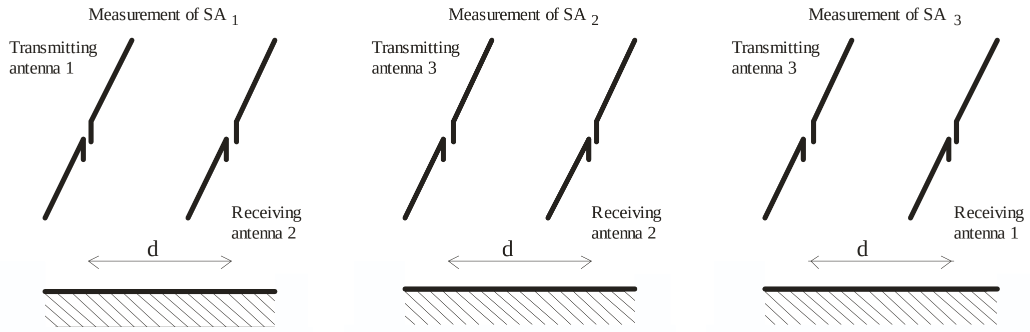

Fig. 1. Principle of measurement antenna factor [3]

For an antenna calibration over a conducting ground plane, the standard site method (SSM) is the most commonly used method. The standard site method requires three site attenuation measurements under the identical geometries, see Fig. 1, as well as using three different antennas taken in pairs. Three equations associated with these measurements of the site attenuation SA may then be obtained and from these equations the values of AF may be calculated:

$$\begin{aligned} AF_1 &= 0.5(SA_1 + SA_3 - SA_2) - 24.46 + 10\log f + 0.5E_{D\max} \\ AF_2 &= 0.5(SA_1 + SA_2 - SA_3) - 24.46 + 10\log f + 0.5E_{D\max} \\ AF_3 &= 0.5(SA_2 + SA_3 - SA_1) - 24.46 + 10\log f + 0.5E_{D\max} \end{aligned} \qquad (3)$$

In compliance with the geometry defined by [3], with the transmitting and receiving antennas 10 m apart the transmitting antenna in the horizontal polarization at the height of 2 m and the receiving antenna being adjusted in height from 1 m to 4 m, the resulting antenna factor, which is minimally affected by the test environment, is defined as the near-free-space antenna factor. The free-space antenna factor, necessary for EMI measurements, can be obtained in conjunction with the geometry-specific correction factors, known just for dipoles and biconical antennas [3].

Antenna characteristics are usually specified for far-field conditions. The far-field data is valid for arbitrary distances assuming that the measuring distance is very large compared to the antenna length. However, when the antenna length becomes comparable to the measuring distance, i.e. 3 m or shorter distances, additional correction factor should be added to the antenna factor value [3].

If such an antenna factor is used in EMI measurements, all these facts will lead to a higher uncertainty budget. Therefore, we propose the use of a “site” antenna factor instead of the free-space antenna factor. This antenna factor includes the test site imperfections, e.g. effect of the ground plane, and avoids, of course, the correction for near-field in which case two different antenna factors have to be obtained, i.e. for horizontal and vertical polarization.

3. Results

Since only one test site was at our disposal, twenty sets of antenna factor, as well as NSA, measurements were performed, for both polarizations, five distances from 2.25 m to 3.25 m with 0.25 m step and two heights of the transmitting antenna, 1 m and 2 m. The measurements were performed for 25 discrete frequencies logarithmically distributed in the range from 30 MHz to 1000 MHz. The measurement setup is given by standards [1], [3], see Fig. 2. The height of the receiving antenna was varied from 1 m to 4 m to get the maximum voltage V_{Rsite}. Three different antennas were used:

1) Bilog broadband antenna VULB 9161(transmitting & receiving);
2) Bilog broadband antenna VULB 9163 (receiving);
3) Set of biconical and log-periodical antenna VHBA 9123 & VPA 6108 (transmitting).

For these antennas, the free-space antenna factor is known. The correction factor C helps to reduce the uncertainty budget; its effect cannot be neglected, see Fig. 3. It is given as:

$$C = 20\log\left(\frac{d + P_f}{d}\right) \tag{3}$$

where d is the measuring distance from the source to a tip of the antenna and P_f is a phase-center position as a function of frequency. Also ideal values of NSA were calculated for every measurement geometry.

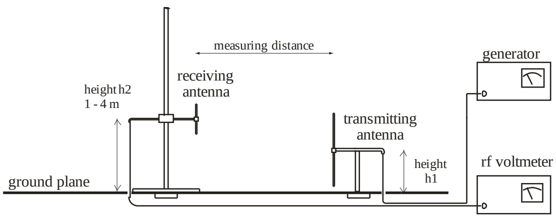

Fig. 2. Antenna factor and NSA measurement setup [2]

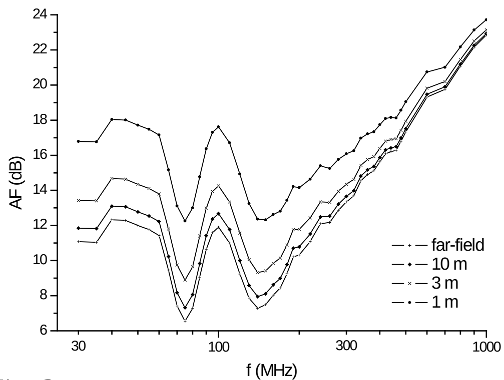

Fig. 3. Correction of antenna factor for Bilog broadband antenna VULB 9163

All the measured NSA values fulfill the ±4 dB criterion; in fact the maximal deviation does not exceed ±3.5 dB value, see Fig. 4. Better results were reached for horizontal polarization due to a negligible mutual coupling between the antennas and the orthogonal feeder, and the smaller ground screen edge reflections. Also the horizontally polarized ground reflections are less sensitive to differences in the ground plane material characteristics than the vertically polarized reflections [7].

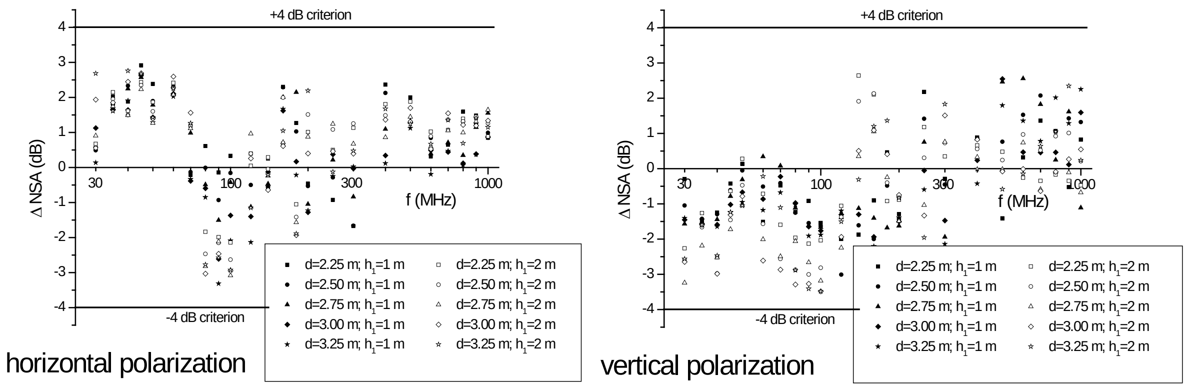

Fig. 4. NSA deviation data for various geometry using antennas “1” and “2”

Furthermore, “site” antenna factor values of used antennas were calculated, see Fig. 5. As it can be seen neither antenna factor deviation exceeds 1.6 dB. However, it is evident that the tendency of all the “site” antenna factor deviations copies the tendency of the NSA deviations. Correlations of these similarities were calculated as Pearson’s product moment coefficient. Values of correlation of 0.81 for horizontal polarization and 0.78 for vertical polarization indicate high dependency between these deviations.

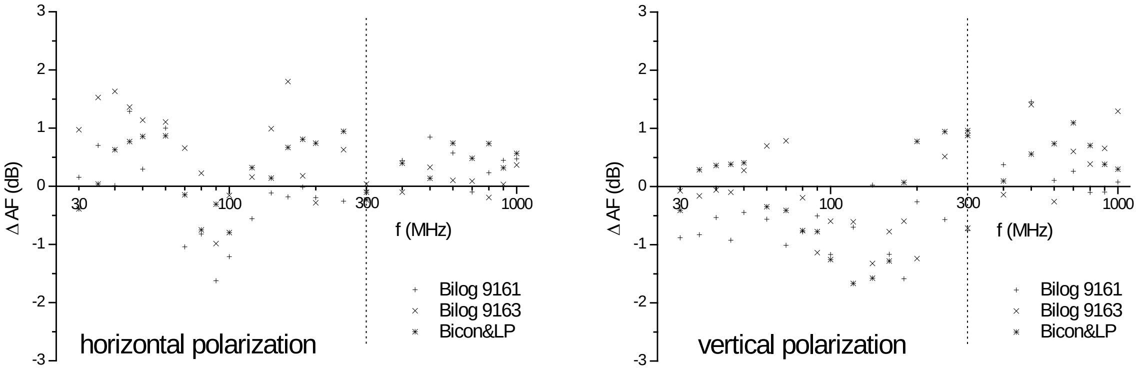

Fig. 5. AF deviation data of used antennas for 3 m distance and 1 m transmitting height

4. Discussion

The use of the “site” antenna factor for EMI measurements is proposed in this paper. Such an antenna factor measurement has to be performed in the same test site as is the EMI measurement itself. Then in contrast to the free-space antenna factor, the “site” antenna factor includes the test site imperfections, such as effects of the ground or any auxiliary devices. This antenna factor, when used for EMI measurements, leads to the measurement uncertainty reduction because there is no necessity to include the test site imperfections into EMI measurements uncertainty.

Acknowledgements

This work was supported by the Slovak Research and Development Agency under the contract No. APVV-0333-11.

References

[1] CISPR 16-2-3:2010 Specification for radio disturbance and immunity measuring apparatus and methods - Part 2-3: Methods of measurement of disturbances and immunity - Radiated disturbance measurements

[2] ANSI C63.4:2014 American national standard for methods of measurement of radio-noise emissions from low-voltage electrical and electronic equipment in the range of 9 kHz to 40 GHz

[3] ANSI C63.5:2006 American national standard for electromagnetic compatibility - radiated emission measurements in electromagnetic interference (EMI) control - calibration of antennas (9 kHz to 40 GHz)

[4] Umeda T, et al. EMI antenna calibration on an absorber-lined ground plane for measuring free-space antenna factor. In proc. of IEEE Symposium on EMC, 2002, 43-48

[5] Mescia L, et al. Antenna Calibration Methods for Antenna Factor Measurements. *Int. Journal of Measurement Technologies and Instrumentation Eng.*, 2(4): 43-59, 2012

[6] Bittera M, Smiesko V, Kovac K. Modified uncertainty estimation of antenna factor measurement by standard site method. *Measurement*, 45 (2): 190-198, 2012.

[7] Hartansky R, Slizik J, Marsalka L. Dipole near field analysis – A closed form calculation in Cartesian coordinates. *Journal of Electrical Engineering*, 64(5): 327-330, 2013.

Charge Pump Design for Use in NVM Device Test and Measurement

[1]D. Matoušek, [2, 1]O. Šubrt, [1]J. Hospodka,

[1] FEE CTU Prague, Prague, Czech Republic
[2] ASICentrum, a company of the Swatch Group, Prague, Czech Republic
Email: matoudav@fel.cvut.cz

Abstract. *Today, the emerging technology to fabricate deep-submicron Non-Volatile Memories (NVMs) requires extensive use of efficient methods for measurement and test. A high-voltage (HV) generator must be used to invoke NVM test modes, either placed on-chip or used from external. Our article focuses on the development of the Charge pump, being a core of such high-voltage generator. We consider an on-chip variant for the purpose of NVM measurement and test, the HV generator has to meet several criteria listed above. In our article we will particularly take into account the design criteria for the Charge pump to be used in such HV generator and the ways how to optimize its properties.*

Keywords: Charge Pump, Voltage Gain, Efficiency, NVM Test Modes.

1. Introduction

Test modes and methods are discussed e.g. in [1], above all we can give an example of Sector/Block/Mass modes, parallel programming, redundancy and reference matrix and internal nodes analysis.

Beside the necessary digital and control hardware (such as decoders, matrix drivers, etc.), there is also a need of powerful and efficient high-voltage generator.

The HV generator has to meet several criteria for the purpose of NVM measurement and test: adjustable output voltage possibly (to serve for Sector/Block/Mass Write or Erase modes), selectable current output drive capability, controlled slope of HV rise.

From design scope, efficiency plays main role. Charge Pump efficiency is reduced by many phenomena. Relatively strong effect has threshold voltage of used transistors or diodes. This paper is concentrated on optimizing of properties of proposed variant Charge Pump, as well.

Dickson Charge Pump (DCP)

Well known Charge Pump architecture is Dickson Charge Pump (DCP) [2]. Equations for description and design of DCP are summarized in [3]. The output voltage depends on input voltage, number of stages and voltage gain of one stage.

Optimal value of voltage gain is equal to amplitude of clocks. But the stray capacitance of nodes reduces the voltage gain. Main effect on resulted value of output voltage has usually threshold voltage of used transistors. Especially for supply voltage lower than 1 V the threshold voltage limits implementation of Dickson Charge Pump. So sub-volt applications use another architectures of Charge Pumps [4], [5].

Generally used principle for threshold effect suppression is a change of connection of transfer transistor from diode mode to switcher mode [6]. So voltage drop between two nodes does not equal to the threshold voltage but is equal to the saturation voltage of channel. Cross-coupled Charge Pump is well known architecture that uses this principle. Another variant is proposed and optimized.

Proposed variant of Charge Pump

Proposed variant of Charge Pump uses 2-phase clocks. One cell (stage) as a basic building block of this Charge Pump is shown on Fig. 1. The cell consists of two inverter totems (M_1, M_2 and M_3, M_4), bias transistor (M_5) and transfer capacitor (C_T).

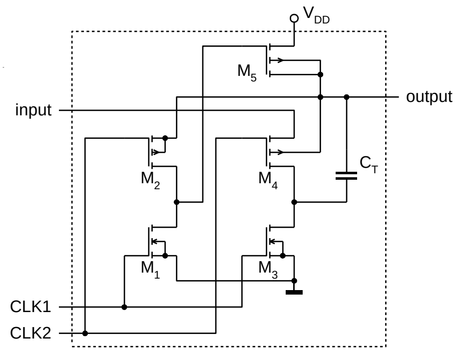

Fig. 1. One cell (stage) of proposed Charge Pump.

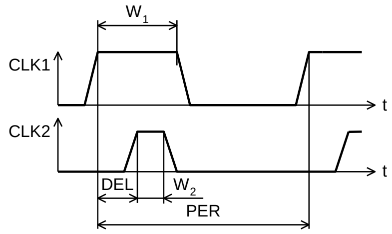

Fig. 2. Waveforms of 2-phase clocks.

The first inverter M_1, M_2 is driven by signal CLK2. This inverter controls gate voltage for bias transistor M_5. The second inverter M_3, M_4 is driven by signal CLK1. This inverter connects transfer capacitor C_T to ground or cell input. So transfer capacitor is pre-charged to V_{DD} in first clock phase and then transfer capacitor is connected between input and output nodes in second clock phase. Thus internode voltage (so called voltage gain) ideally equals to V_{DD}.

The clocks signals which are used for driving of both inverters have overlapped character as is drawn on Fig. 2. Symbols W_1 and W_2 mark widths of pulses of both clock signals. DEL marks the delay between rising edges of the CLK1 and CLK2 signals. PER is the period of both clock signals.

Setting of W_1, W_2 and DEL parameters is crucial for the best ratio between values of output voltage and resulting efficiency.

2. Simulations

6-stage Charge Pump according to Fig. 3 was used to simulate. Clocking signal is buffered by strong buffers (invertors). The last stage is connected to the detector based on transistor M_D. Resistor R_L a capacitor C_L model output load. Symbol I_S marks the consumed current. Output voltage at load is marked V_{OUT}.

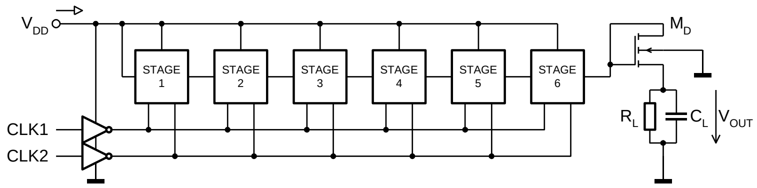

Fig. 3. Simplified schematic diagram of simulated Charge Pump.

Firstly, the optimal value of DEL value was found. CLK1 pulse width $W_1 = 24$ ns was selected as starting value according to the period of the clock signals.

Consequently DEL value was swept for various values of CLK2 pulse width W_2. See Fig. 4. The best value of efficiency $\eta = 12.2$ % was located for case DEL = 0, $W_2 = 10$ ns with output voltage $V_{OUT} = 4.036$ V. But the maximal value of output voltage $V_{OUT} = 4.107$ V with efficiency $\eta = 10.0$ % was located for case DEL = 0, $W_2 = 24$ ns.

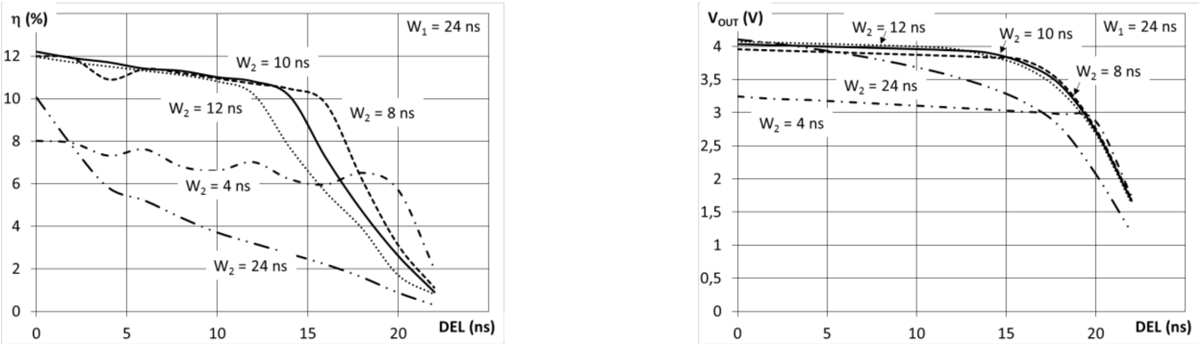

Fig. 4. a) Graph of efficiency, b) Graph of output voltage as functions of W_2 and DEL.

One important result was implied from the first simulation batch. Maximal value of efficiency was in case then DEL = 0 ns. So edges of both clocks must have started simultaneously.

Table 1. Parameters used for simulations (6-stage Charge Pump).

Parameter	Value
Clock frequency and temperature	f = 20 MHz (period PER = 50 ns), t = 27 °C.
Supply voltage, amplitude of clocks	$V_{DD} = 0.7$ V, $V_{CLK} = 0.7$ V.
Capacitance of transfer capacitors	$C_T = 5$ pF.
Load	$C_L = 300$ pF, $R_L = 2.8$ MΩ.
Buffers transistors (L = 0.1 μm)	NMOS_HVT: W = 5 μm, PMOS_HVT: W = 12.5 μm.
Cell transistors (L = 0.1 μm)	NMOS_HVT: W = 0.5 μm, PMOS_HVT: W = 1.25 μm.
Detector transistor	Native NMOS_NA18 (L = 0.8 μm, W = 20 μm).

Secondly, the simulations with variable W_1 (width of CLK1 pulse) were performed as is shown in Fig. 5. The best value of efficiency $\eta = 13.3$ % was for case $W_1 = 36$ ns, DEL = 0, and $W_2 = 10$ ns, but the output voltage had value $V_{OUT} = 3.907$ V only.

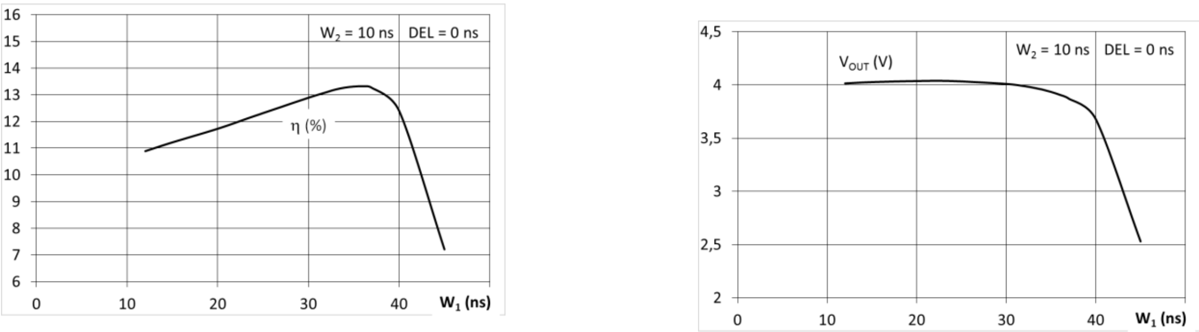

Fig. 5. a) Graph of efficiency b) Graph of efficiency and output voltage as functions of W_1.

The case $W_1 = 24$ ns, DEL = 0, $W_2 = 10$ ns was selected as a compromise between optimal values of the output voltage and efficiency. The ramp of the output voltage for this case is documented on Fig. 6. Rise time had value $t_R = 74.3$ μs.

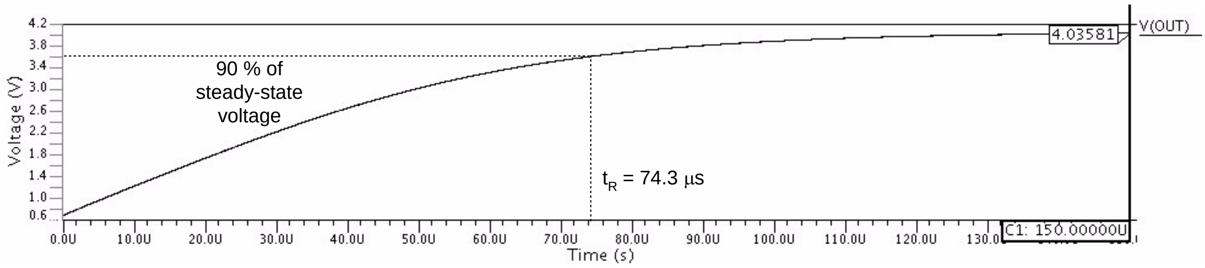

Fig. 6. Ramp of output voltage (W_1 = 24 ns, W_2 = 10 ns, DEL = 0).

3. Results

Maximal value of the output voltage V_{OUT} = 4.036 V with efficiency η = 12.2 % has been achieved. These results were obtained for CLK1 pulse width W_1 = 24 ns when CLK2 pulse width was W_2 = 10 ns and delay had value DEL = 0 ns. W_2 value may vary from 8 to 12 ns but value of efficiency varies very small.

4. Discussion

Optimizing of proposed Charge Pump was performed based on previously documented simulations.

Although maximal values of output voltage and efficiency are obtained for different values of timing parameters, these maxima are relatively close.

The important advantage of proposed variant of Charge Pump is in fact, that both clock signals are derived from same base clock. Both clock signals have simultaneous rising edges. The width of each clock signal may be simply tuned by a delay network.

Future work will be focused to the more complex circuit including clock generator to optimise. So we will find global efficiency of proposed Charge Pump.

References

[1] Campardo G, Micheloni R, Novosel D. VLSI-Design of Non-Volatile Memories. Springer-Verlag, 2005.

[2] Dickson JF. On-Chip high-voltage generation in NMOS integrated circuits using an improved voltage multiplier technique. *IEEE Journal of Solid-State Circuits, vol. 11, no. 3,* 374-378, 1976.

[3] Pan F, Samaddar T. Charge Pump Circuit Design. McGraw-Hill, New York, 2006.

[4] Palumbo G, Pappalardo D. Charge pump circuits: An overview on design strategies and topologies. *IEEE Circuits and Systems Magazine, First Quarter 2010,* 31-45, 2010.

[5] Matousek D. Comparison of selected architectures of negative Charge Pumps with new design. In: Proceedings of the 24th International Conference Radioelektronika, 2014, 1-4.

[6] Yamazoe T, Ishida H, Nihongi Y. A Charge Pump that generates positive and negative high voltages with low power-supply voltage and low power consumption for non-volatile memories. In: International Symposium ISCAS, 2009, 988-991.

The PH32 Readout Integrated Circuit

[1]Z. Janoska, [2]M. Carna, [2]M. Havranek, [2]M. Hejtmanek, [2]V. Kafka, [2]M. Marcisovsky, [2]G. Neue, [2]L. Tomasek, [2]V. Vrba

[1]Faculty of Electrical Engineering, Czech Technical University in Prague, Technicka 2, 166 27 Prague, Czech Republic,

[2]Faculty of Nuclear Sciences and Physical Engineering, Czech Technical University in Prague, Brehova 7, 115 19 Prague, Czech Republic

Email: zdenko.janoska@fjfi.cvut.cz

Abstract. *The PH32 readout chip has been developed for measurement of X-rays, beta radiation and charged ions including alpha particles. The chip has been manufactured in a commercial 180 nm CMOS technology and its applications include dosimetry, spectroscopy, medical diagnostics and radiotherapy. Its main capability with connected sensor are hit counting and measurement of the deposited charge in the range from 2.5 ke$^-$ to 10 Me$^-$ in two operational modes. The signal charge collected by silicon strips can be determined to an accuracy of about 1500 e$^-$ for a chip calibrated for the charge of 50 ke$^-$. This paper is focused on the measurement of the channel response to the injected charge. The measurements presented here include channel uniformity, gain, noise, linearity and dispersion during chip calibration.*

Keywords: Silicon radiation detector, Front-end chip, 180 nm, CMOS

1. Introduction

In recent years there is a steadily growing demand for more sophisticated, precise and at the same time flexible detection systems of diverse radiation fields used in numerous practical applications. The “distributed brain” of such systems constitute front-end chips. The variety of different applications and demands corresponds to the used technology and chip architecture. The readout chip is the most crucial part of every such detection system.

The driving force for the development are R&D projects of large high-energy physics experiments at CERN, e.g. ATLAS or CMS. The most common solution are hybrid pixel detectors consisting of readout chips and silicon sensors, connected together by bump-bonding. The technology used for readout chips FE-I3 [1], FE-I4 [2] or MediPix [3], [4] developed at CERN has a large application potential. However, those chips are too large in terms of relatively high amount of channels and they need expensive and complicated interconnection technology (bump-bonding). This is a limiting factor for many applications.

Chips of the PH32 series can serve as the readout of strip or pad sensor arrays. Such sensor granularity is still sufficient for numerous applications, allowing to replace the expensive bump-bonding by much cheaper wire bonding. The detection system with PH32 chip has substantially higher radiation tolerance than the common electronics for commercial applications, thus PH32 chips can be used in medical applications like diagnostics and radiotherapy, dosimetry or spectroscopy with the minimum amount of hardware and for an affordable price. This article summarizes the overall chip description and evaluation of the chip response to the charge injected during the chip calibration.

2. Chip Architecture

A block schematic of the chip is shown in Fig. 1. It contains 32 identical readout channels with analog inputs, which can be connected to 32 sensitive silicon strips. The chip is designed to

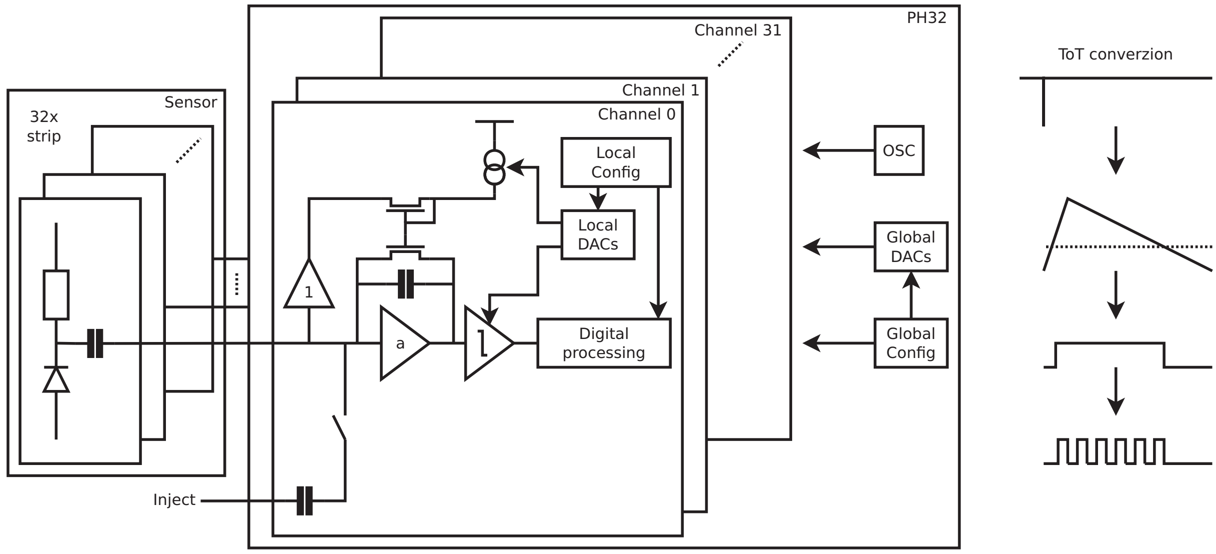

Fig. 1: Block schematic of the PH32 chip.

collect the negative charge. Signal from the sensor is led through an AC coupling capacitor to the input of the channel processed by the Charge Sensitive Amplifier (CSA).

In order to cover the dynamic range of the charge, we can adjust the CSA sensitivity in two modes: High Gain Mode (HGM) for soft X-rays and beta radiation and Low Gain Mode (LGM) for ions. Each channel includes Digital to Analog Converters (DAC) for tuning electrical properties of the CSA of each channel separately. Signal from the CSA is led to a discriminator with adjustable threshold and to a digital part. The chip can be configured to work in the hit counting mode or in the mode for particle energy measurement by the method known as the Time over Threshold (ToT) mode with sampling frequency in the range of tens to hundreds of MHz. The power supply voltage of the chip is 1.8 V. Static consumption is less than 150 µW for analog part and dynamic consumption is approximately 100 µW for digital part per channel. The total power consumption is less than 15 mW.

Threshold Tuning

Detection performance like gain, noise, linearity, dispersion between measurement channels, etc., is closely related to the analog part of the channel. In order to obtain relevant data from the sensor, the analog part has to be calibrated with the help of the charge injected from an external generator to the input. This substitutes the signal from the sensor and allows to perform calibration to obtain the minimal dispersion between individual channels. A specific charge in range from 2.5 ke$^-$ to 100 ke$^-$ for HGM and from 350 ke$^-$ to 10 Me$^-$ for LGM is used for calibration with respect to silicon sensor thickness (525 µm) and desirable sensitivity to X-rays but also to alpha particles. Calibration is performed simultaneously with the change of DAC values to adjust discriminator and CSA operation.

3. Results

Here we present the analysis of the PH32 chip response on the charge injection at the chip input. This process allows us to reveal the basic parameters of the chip. All measurements were done without sensor connected to the chip.

In order to determine the dispersion of ToT values between individual channels, various charge values have to be injected repeatedly to all channels during one measurement. The HGM

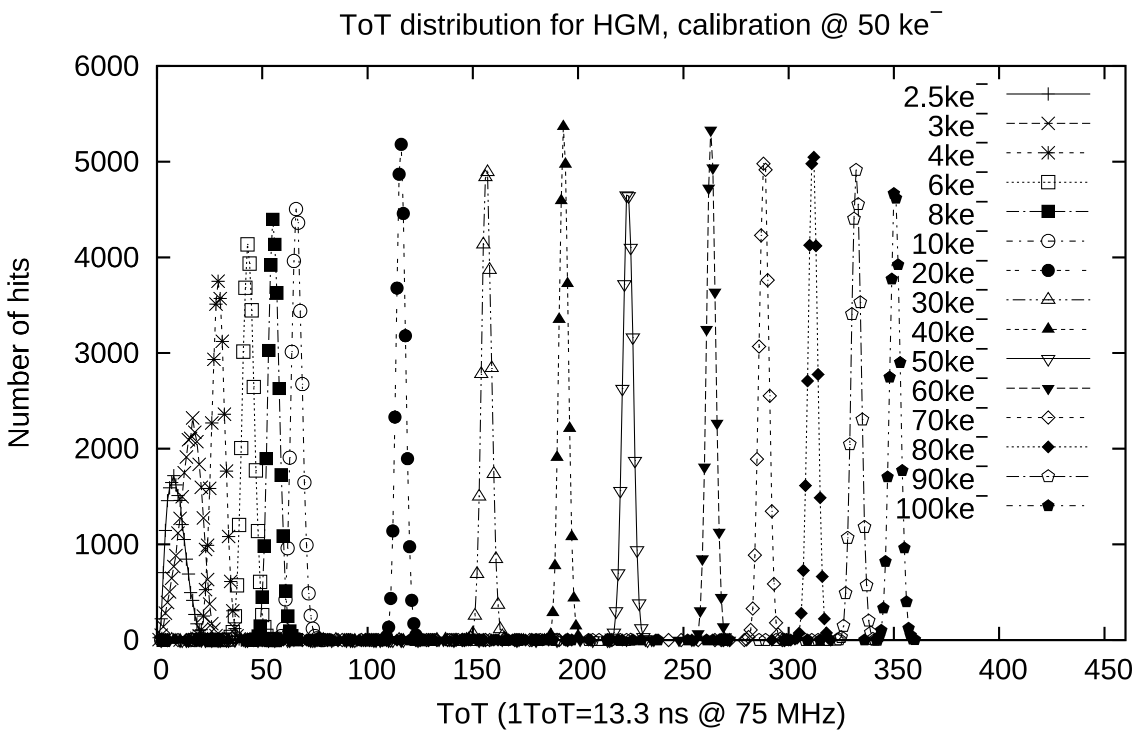

Fig. 2: Response to 1000 injections for injected charge varying from 2.5 ke^- to 100 ke^-. The chip was operated in HGM and calibrated for a charge of 50 ke^-. The curves represent the sum of signal from all channels.

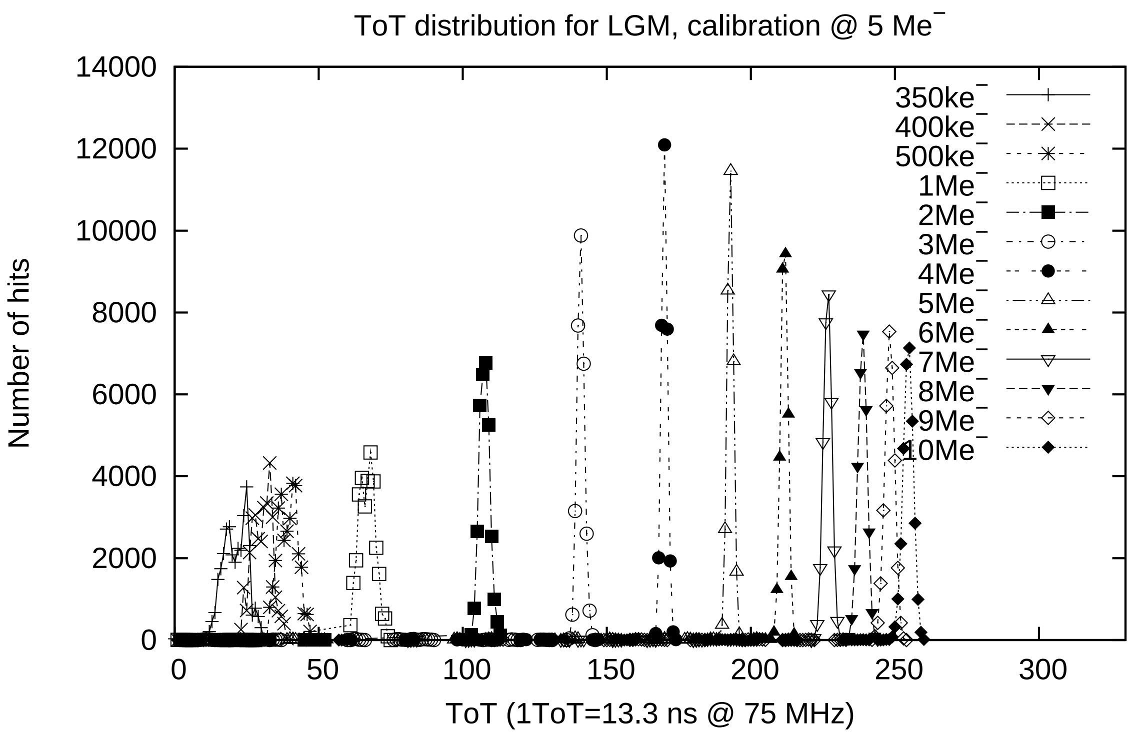

Fig. 3: Response to 1000 injections for injected charge varying from 350 ke^- to 10 Me^-. The chip was operated in LGM and calibrated for a charge of 5 Me^-. The curves represent the sum of signal from all channels.

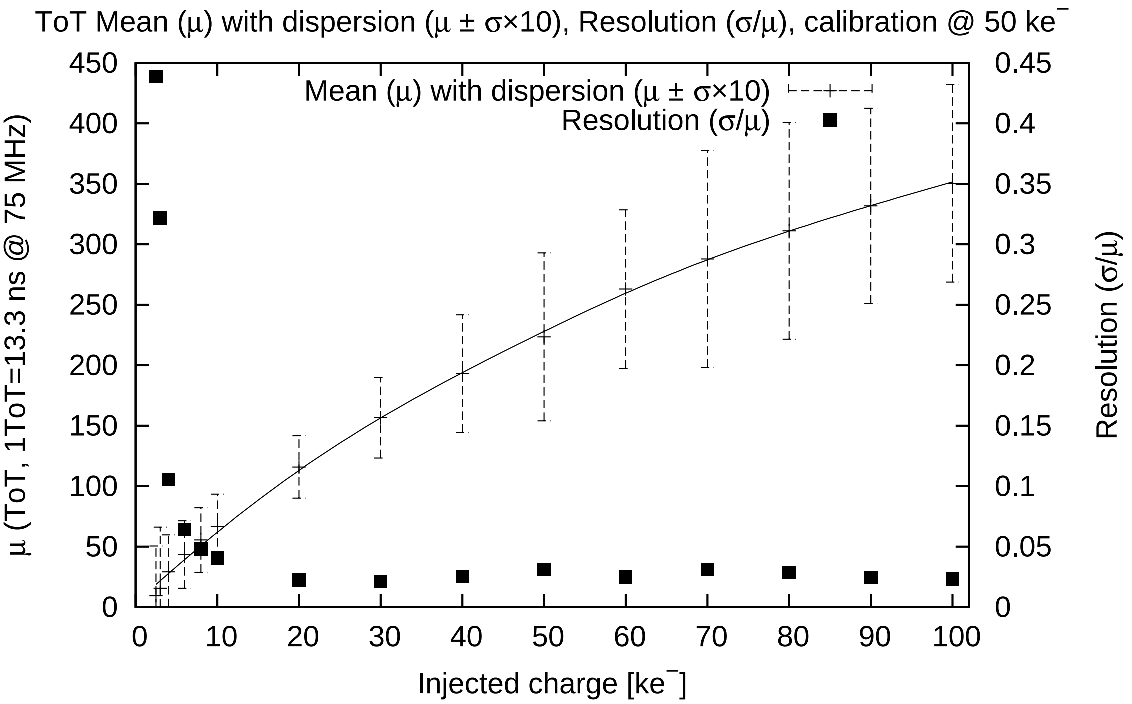

Fig. 4: Mean value of ToT $F(\mu)$ and resolution (σ/μ) as a function of the injected charge (1000 injections with various value of injected charge) in HGM, for a chip calibrated at 50 ke^-.

calibration has been done with the charge injection in the range from 2.5 ke^- to 100 ke^- for the chip calibrated for 50 ke^-charge (shown in Fig. 2). The LGM calibration has been done with the charge injection in the range from 350 ke^- to 10 Me^- for the chip calibrated for 5 Me^-charge (shown in Fig. 3). The results for both modes are qualitatively comparable. Each individual peak in Fig. 2 and Fig. 3 belongs to a specific charge and the width of the peak represents fluctuations of response between individual channels mainly due to the electronic noise, imperfect calibration method and quantization error. A significant indicator of the chip performance is the resolution. Fig. 4 represents mean and standard deviation of the measurement performed in HGM. The resolution depends directly on the sample frequency from internal oscillator operated at 300 MHz, which can be lowered by an implemented divider. However, noise contamination has been observed for higher frequencies due to the voltage drop on power rails inside the chip. The measurement was provided for a 75 MHz sample frequency.

4. Conclusions

The PH32 readout chip is suitable for measuring X-rays, beta radiation and alpha particles and can be used in dosimetry, spectroscopy, medical diagnostics and radiotherapy. The PH32 is able to measure the signal in a wide range in two separate operational modes. Both modes demonstrate very good performance. The signal charge collected by silicon strips can be determined to the accuracy of about 1500 e^- for a specific calibration charge of 50 ke^- in HGM and approximately 180 ke^- for a specific calibration charge of 5 Me^- in LGM (at 75 MHz sampling frequency). The noise is approximately 3 ke^- for specific calibration charge in HGM. The chip indicates some problems like voltage drop due to high sampling frequency and crosstalk between digital and analog parts. These will be solved in the next version of the chip along with the higher noise reduction.

References

[1] Perić I. et al. The FEI3 readout chip for the ATLAS pixel detector. *Nucl. Instr. and Meth.* A 565, 178–187, 2006.

[2] Garcia-Sciveres M. et al. The FE-I4 pixel readout integrated circuit. *Nucl. Instr. and Meth.* A 636, 155–159, 2011.

[3] Llopart X. et al. Medipix2, a 64k pixel read out chip with 55 μm square elements working in single photon counting mode. *IEEE Transaction on Nuclear Science* NS-49, 2279, 2003.

[4] Ballabriga R. et al. Characterization of the Medipix3 pixel readout chip. *Journal of Instrumentation* 6, C01052, 2011.

RF Resonator Array for MR Measurement System

D. Nespor, P. Drexler, P. Fiala, P. Marcoň

Department of Theoretical and Experimental Electrical Engineering,
Brno University of Technology, Brno, Czech Republic,
Email: drexler@feec.vutbr.cz

Abstract. *The contribution reports on the possibilities of the fabrication of resonator array structures for MR imaging purposes. Suitable array configuration may improve the RF field homogeneity. The key issues of resonators fabrication are introduced together with achieved results from the samples parameters measurement.*

Keywords: Planar Resonator, Periodical Structure, Magnetic Resonance, Metamaterial

1. Introduction

Magnetic resonance (MR) is continuously evolving measurement, spectroscopy and imaging technique for examination of specific samples and biological tissues. RF magnetic field distribution and its homogeneity in the MR system's resonator are crucial parameters. They can be influenced by proper resonator design. The attention of scientific community has been recently pointed at the new possibilities of manipulation of the RF magnetic field distribution. Certain effort in this field is directed to the possibilities of manipulation of RF magnetic field with the goal of improving the received signal, which leads to better MR image quality [1]. Such approaches exploit novel properties of composite metamaterial (MTM) structures, which found applications in various research directions [2], [3]. The components of MTM structure can be fabricated as they have insignificant response in the DC magnetic field. Simultaneously, they can exhibit strong effective susceptibility around a certain resonant frequency. The components of MTM structure are mutually coupled and magneto-inductive waves are formed in the structure [4].

2. Resonator Array fabrication and measurement

Examined MTM structure is based on array of electromagnetic (EM) resonators with RF response. The resonator exhibits an effective inductance and capacitance matched in such way that it resonates closely to Larmor’s frequency. The resonant frequency relates to its dimension, mainly due to its inductance. The resonator dimension has to be smaller than quarter of the operating wavelength. This sets the constraint on its maximal dimension. Another constraint is given by the dimension of the sample to be imaged. Since the RF field should be uniform in sample’s volume, the minimal dimension requirement on the MTM device is given. These constraints lead to design of a resonator array with the total number of components *i*. The simple resonator can be in form of a single split ring (SSR), which is a loop conductor with narrow slit. It can be deposited on printed circuit board (PCB) substrate (FR4). The resonant behavior of SSR (d = 5 mm, w = 0.2 mm) is shown in Figure 1a), which exhibits resonance around 6 GHz. If we take into account the operating frequency in RF domain (around 200 MHz for 4.7 T system) and given dimensions constraints, the form of the resonator would be a SRR tuned with lumped capacitance of tens of pF as shown in Figure 2b).

The capacitor loaded SSR array structure is shown in Figure 2a). Figure 2b) shows the rings dimensions and Figure 2c) the fabrication of the SSR) array.

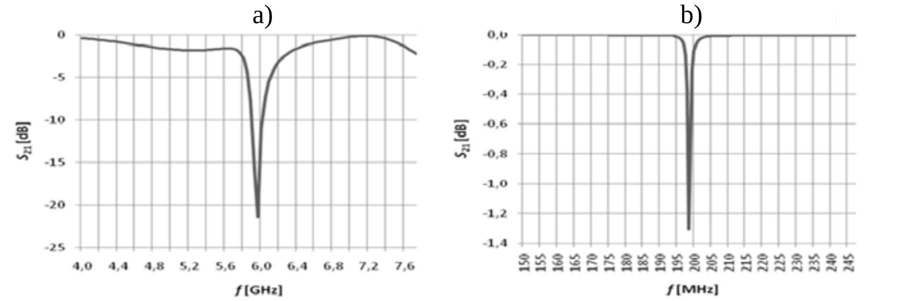

Fig. 1. SSR‘s scattering parameter s_{21} for transmitted wave; without a) and with b) capacitor.

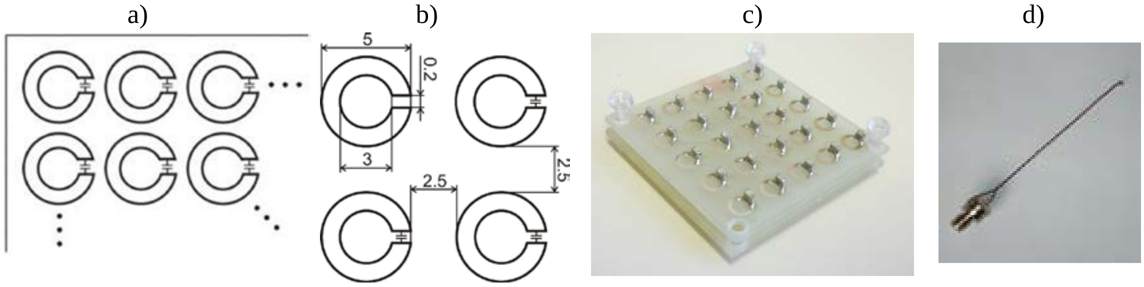

Fig. 2. Array of single split rings (SSR) a); ring dimension b); resonator array fabrication c); inductive probe for examination of SSR resonant frequencies d).

The alignment of resonant frequencies $f_{r,i}$ of all of the resonators is important and influences the quality of the modified RF field. Besides this, other parameters determine the overall structure properties (as the quality factor Q_i). Above all, the mutual coupling (capacitive and inductive) between resonators in the array has a great importance. The particular resonant frequencies of all of the resonators are strongly influenced by the coupling. The coupling magnitude is determined by resonators design and significantly by their spacing. The spacing influences also the uniformity of modified RF field. Since the resonators mutual coupling has complex influence on the overall array properties, it is most advantageous to design the array (consequently the resonators spacing) by means of numerical modeling and simulation.

Since the tuning of each resonator is a critical point determining the structure parameters, it deserves significant attention. There are three basic factors that influence the resultant resonance behavior of the array. Firstly, all resonators shall have exactly identical dimensions (inner and outer diameter, thickness, slit width). This depends on the PCB manufacturing technology and its precision. Classical approach is wet etching. The second factor is the value matching of all capacitors used. Common ceramic chip capacitors have the lowest production value tolerance ±1% for capacitances over 10 pF. At 200 MHz, the 1% capacitance variation causes the resonance frequency shift of 1 MHz, which is unacceptable for MR purposes. The third factor is the precision of chip capacitor assembly on the SSR. Variation of solder amount used and the quality of each soldered connection influences the inductance and capacitance of each resonator and also its Q-factor.

In case of perfect resonator matching, the mutual coupling comes into play. The coupling causes splitting of all of the particular resonant frequencies and the resultant structure’s resonant curve becomes broad.

In order to handle and evaluate the above mentioned issues, two experimental SSR arrays with 5×5 resonators have been designed and fabricated using 35 μm thick cooper on FR4 substrate. The first array dimensions are defined in Figure 2b). The modified Wheeler formula [5] was used for SSR inductance calculation. To achieve the desired resonant frequency of

200 MHz, a combination of three, precise selected capacitors was used (100 pF, 10 pF, 1.2 pF). The capacitors were manually soldered. The fabricated array (Figure 3a)) underwent the measurement of the resonant frequencies. Each frequency can be measured by positioning a loop probe in vicinity of each resonator [6]. In this measurement, an improved inductive loop probe (Fig. 2d) has been used together with network analyzer, which has measured a dip in s_{11}. The improved probe minimized the influence of the probe-SSR coupling on the measured resonant frequency value. The results of the measurement are shown in Figure 3c), which graphically shows the mutual differences in particular resonant frequencies by means of intensity scale. It is apparent that large differences occur, despite the careful selection of the capacitors. Obviously, the effect of non-uniform capacitor assembly and hand soldering came into play.

In the second attempt, a single capacitor with nominal value of 100 pF per resonator has been used. All the capacitors have been carefully selected in order to minimize the value tolerance. To achieve the same resonant frequency, dimensions of the SSR were recalculated according to [5]. The new ring diameter was 5.3 mm. In order to preserve similar mutual coupling, the resonator's spacing was increased in the ratio of the diameter change to 2.65 mm. Within the fabrication, the flux was deposited by the help of a precise mask; the capacitors were assembled by the manipulator and the reflow soldering was finally used. This resonator array (Figure 3b)) underwent measurement of the particular resonant frequencies as described above. The results of measurement are shown in Figure 3d). A significant reduction in the resonant frequencies differences is apparent from the intensity map.

The mutual coupling of the resonators leads to effect, when the total resonance curve of the structure is not identical with the curve of a single resonator. The array resonance curve will be broadened and its peak will be significantly reduced. In order to obtain the total resonance curve of the array, a measurement device has been designed and built, Figure 4a). The device comprises of cubic cavity equipped with two N-type connectors. Connector's middle conductors are connected through the cavity.

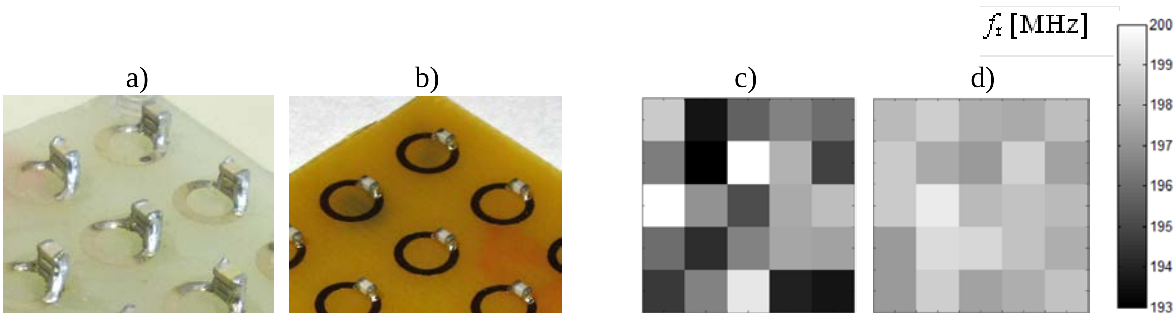

Fig. 3. Detail of the array with 3 capacitors combination a) and array with 1 capacitor b).

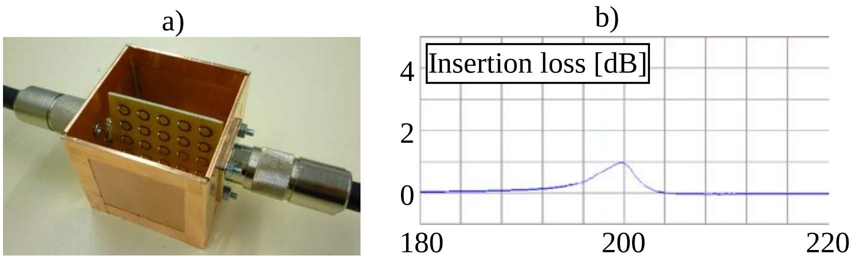

Fig. 4. Cavity for resonance measurement a); result for array-1 capacitor per resonator b).

The resonator array is placed inside the cavity and the insertion loss of the cavity is measured. Figure 4b) shows the resultant insertion loss of the array from Figure 3b). It is obvious that the resonance curve is broad with very low peaking, due to mutual coupling of the resonators. This effect is even raised by the non-ideal tuning of each resonator on the same desired frequency.

3. Conclusion

From the above described experiment can be concluded, that fabrication of the SSR resonator arrays is accompanied with severe issues. The key issues are selection of capacitors in view of the exact capacitance value and reproducible capacitor assembly. It has to be mentioned also, that capacitors with very low susceptibility has to be used in order to avoid MR image distortion. In order to overcome these limitations, the resonator design without lumped capacitors is proposed. Such resonators have only distributed capacitance, which leads to a more complicated layout design as shown in Figure 5. Numerical analyses of these resonant structures have been started and they give very promising results. Details on the new resonators structures, computed and measured parameters will be reported in the near future.

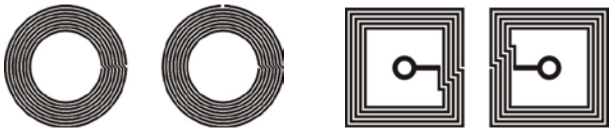

Fig. 5. Variations of the resonators with distributed capacitance.

Acknowledgements

The paper was supported by the project GA13-09086S.

References

[1] López M A, Freire M J, Algarín J M, Behr V C, Jakob P M, Marqués R. Nonlinear split-ring metamaterial slabs for magnetic resonance imaging. Applied Physics Letters, 98: 133508-1 - 133508-3, 2011.

[2] Faruque M R I, Islam M T, Ali M A M. A New Design of Metamaterials for SAR Reduction. Measurement Science Review, 13(2): 70-74, 2013

[3] Drexler P, Fiala P. Power supply sources based on resonant energy harvesting. Microsystem Technologies, 18(7-8): 1181-1192, 2012.

[4] Campione S, Mesa F, Capolino F. Magnetoinductive Waves and Complex Modes in Two-Dimensional Periodic Arrays of Split Ring Resonators. IEEE Transactions on Antennas and Propagation, 61(7), 2013.

[5] Bartusek K, Drexler P, Fiala P, Kadlec R, Kubasek R. Magnetoinductive lens for experimental mid-field MR tomograph. In proceedings of Progress In Electromagnetics Research Symposium PIERS, 2010, 1047-1050. ISBN: 978-1-934142-14-1. ISSN: 1559-9450.

[6] Bartusek K, Nespor D, Drexler P, Fiala, P. Properties of magnetoinductive resonator array for MRI application. In proceedings of Measurement 2011 International Conference, 2011, 217-220.

Application of Preisach Model to Low Loss Ferromagnetic Materials

J. Eichler, M. Košek, M. Novák,

Technical University in Liberec, Liberec, Czech Republic
Email: miroslav.novak@tul.cz

Abstract. *Exact and accurate description of ferromagnetic materials for purpose of their modelling, as an instance, is a very difficult task. A general approach is to use the Preisach model. Main problem in the model application is to find the weighting function that is done by material properties. Two methods are presented, how to get the weighting function. The results are similar and agree with experiment, as for technical accuracy.*

Keywords: Preisach Model, Ferromagnetic Materials, Rectangular Hysteresis Loops, Current Measurement of Ferromagnetic Loops, Modelling.

1. Introduction

Materials used in electronics and elements made from them are now modeled by sophisticated methods in order their outputs will be as close as possible to experiment. Since the ferromagnetic materials exhibit hysteresis, their modeling is extremely complicated, irrespective of work made in this area. The most universal model is the Preisach one [1]. The key part of the model is the weighting function that characterizes the magnetic properties of the material. It can be derived from the measurements. The basic theoretical procedure for experimental data processing is presented in literature [1]. However, due to the experimental errors some modifications are necessary. Different attempts are presented, for instance, in [2]. Another approach is to guess the weighting function [3].

A good model of ferromagnetics is not important only in technical praxis, but also in basic research or in the education. In technical praxis, for instance, the transition effects connected with power switching have more than 10 time higher currents than currents predicted from linear models. In material research the weighting function is a full characteristic of material. Other magnetic parameters can be, in principle, derived from it and different materials can be compared using this function. In education the perfect model can simulate all the magnetic effects more clearly and in higher quality than output of the apparatus, irrespective of high price of standard apparatus and necessary experience with its control.

In the paper we describe the Preisach model, we will present the experiment, and we mention the data processing and compare both the approaches for obtaining the weighting function.

2. Theory

According to physical structure the basic unit of the Preisach model is the ideal elementary dipole exhibiting rectangular hysteresis loop with parameters: dipole momentum m_o, low and up magnetic field strengths H_d and H_u, respectively. According to the position of external magnetic field H with respect to H_d and H_u and previous history, the dipole momentum is either $+m_o$ or $-m_o$. Schematic summary of elementary dipoles is in Fig 1a.

Several specific elementary hysteresis loops can be found in Fig. 1a. No hysteresis is on the major diagonal. Symmetric loops are in the minor diagonal. Therefore we can expect the maximum of weighting function on that minor diagonal. On the left hand vertical side the value H_d is fixed. On the contrary, on the upper horizontal side the upper field H_u is fixed.

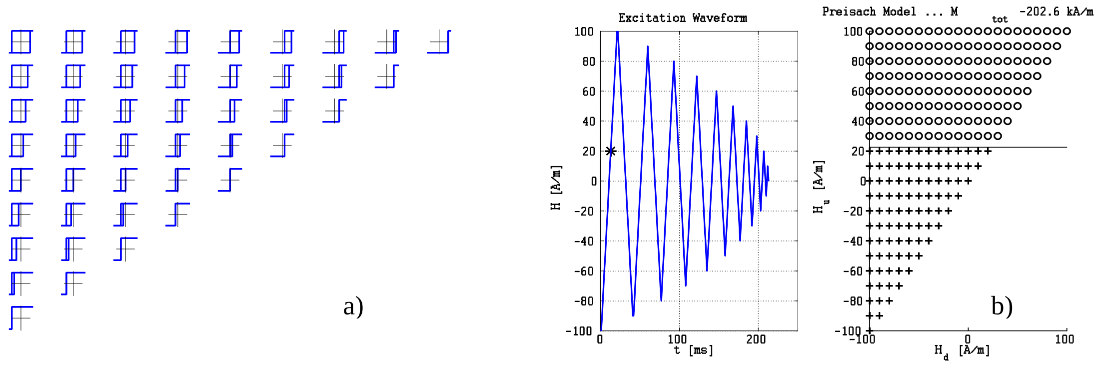

Fig. 1. a) Elementary dipoles as basic elements of Preisach model. b) Application of the model.

The work of Preisach model can be explained simply by geometrical means. The elementary dipoles in the net like that in Fig. 1a are oriented up (represented by plus sign) or down (circles) as in Fig. 1b. Suppose that the sample was polarized down and external field strength H increases from minimum value. For selected time instant its position on waveform and its level on Preisach diagram are shown in left and right hand part of Fig. 1b, respectively. The horizontal field level moves in up direction. All elementary dipoles with $H_u < H$ are polarized up. If the external field decreases, the vertical level that moves from right to left is used. The dipole switching is similar, all dipoles with $H_d > H$ are in the down orientation.

Mathematically, the Preisach model for the computation of material magnetic momentum M of the specimen (usually magnetization) at time t is given by the formula [1]

$$M(t) = \iint_{H_u \geq H_d} w(H_u, H_d) \hat{m}(H_u, H_d) H(t) \, \mathrm{d}H_u \mathrm{d}H_d \; . \qquad . \qquad (1)$$

The hysteresis operator $\hat{m}(H_u, H_d)$ forms the elementary magnetic momentum for given field strength $H(t)$ according to the explanation in Fig. 1, for instance. Therefore, $\hat{m}(H_u, H_d).H(t)$ means either $+m_o$ or $-m_o$. The weighting function $w(H_u, H_d)$ is determined by the material and it should be found.

It is proved in [1] that the weighting function is a partial derivative of momentum function $M(H_u, H_d)$ in (1) by both the field strengths H_u and H_d. Therefore, the momentum function should be known in Preisach triangle in Fig. 1.

In order to ensure simple and stable initial conditions in experiments, the external magnetic field should increase from minimum value to several one (local maximum, which is less than absolute maximum) and then should decrease again to absolute minimum. The curve from local maximum, H_u^*, to absolute minimum is termed the first order transition curve. Some of them are shown in Fig. 2a for the investigated material. The branch corresponding to field increase should be the same for all the transition curves bellow the maximum H_u^* and these curves should lay above it.

3. Experiment and Data Processing

The task of experiment is to get the first order transition curves like those in Fig. 2a. We have used standard full automated experimental apparatus with one modification. Since the current source is necessary we get it from the commercial universal voltage source Kikussui PCR

2000LA by suitable series resistance. More difficult solution was to program the voltage source by specific voltage waveform. However, the current source cannot operate at power net frequency of 50 Hz, since the coil impedance is high and voltage source does not produce required currents. Therefore we decreased operating frequency to 1 Hz, which has brought other problems due to the long time measurement, about 4 minutes,

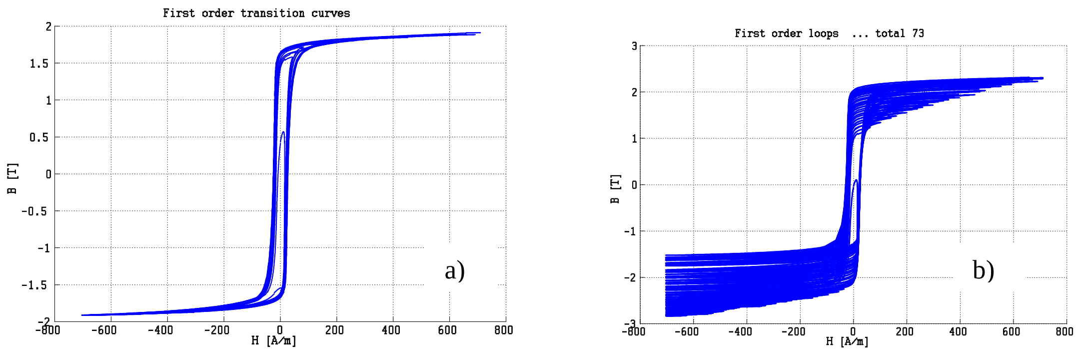

Fig. 2. a) First order transition curves after numeric processing, b) Original curves from experiment..

The induced secondary voltage is low and noise, especially at 50 Hz, distorts the outout waveform. Furthermore, the source produces field strength waveform with deviations near zero crossing. However the integration of the secondary voltage reduces both the effects. On the other hand the low frequency reduces eddy currents losses. Therefore the loops may be closer to ideal ones

Unfortunately, the most important second order effect was the zero drift of the secondary voltage that was due to the measuring chain offset. Although it was almost eliminated at the start of measurement, due to the measurement long time it led to the vertical shift of the transition curves. Typical results from expriment after standard integration are in Fig. 2b. The spread is very high, therefore the data preprocessing is necesssary.

The simple method of preprocessing uses data averaging at the curve start and the vertical shifting, in order to ensure the curve symmery. The effect of this simple data processing can be judged by comparing results in Fig. 2 for original (right) and improved data (left).

Opposite to the simple use of Preisach operator in (1), the determination of weighting function is very complicated. Because of high level noise, the numeric derivation is impossible. There are two basic ways for weighting function determination

1. Guess the weighting function [3].
2. Modify the systematic procedure on experimental data suggested in [1].

The estimation method uses the weighting function in the form of probability density. Three, relative similar distributions were considered: normal, Cauchy and lognormal. Because of symmetry, the centre of weighting function must be on the minor diagonal, where the elementary loops are symmetrical, see Fig. 1a. The loop width then determines the mean value. The only parameter to be found is the standard deviation. Since we considered product of two densities, two parameters are searched. The search is automated by nonlinear programming, by the fminsearch function in MATLAB.

The use of partial derivation needs to approximate the data momentum surface by analytical function of two variables H_u and H_d. We have used the simplest function arctan($k(H - H_o)$) that matches data well, if the range of independent variable contains both positive and negative values. It uses two selectable parameters coefficient k and shift H_o. The approximation is applied in both the directions, horizontal with variable H_d and vertical with variable H_u. The surface formed by magnetic momentum is approximated by a product of these arctan functions with different parameters. Its derivation is similar to Cauchy probability density

4. Results

In this section we present in Fig. 3 the comparison of two approximations: the result of estimation is in Fig. 3a and the systematic method output is presented in Fig. 3b. The agreement with experiment is better for simpler method. It can be explained by automated procedure, while the surface approximation by systematic method was handmade.

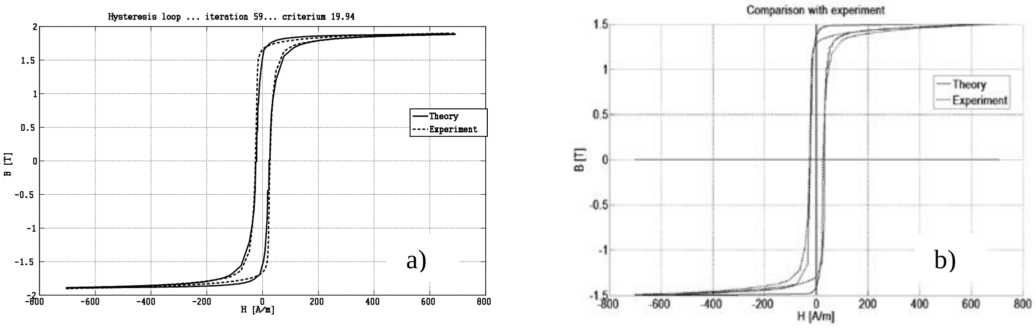

Fig. 3. Comparison with experiment: a) Estimation method, b) Systematic method.

5. Discussion and conclusions

Two methods were used for Preisach model identification with similar results. The estimation method is simpler, needs only one measurement near the saturation and surprisingly leads to better results. In general, the basic limitation of systematic method is a low experimental accuracy and the need to approximate the two-dimensional function (surface). On the other hand it can be successfully applied in all cases. The presented accuracy of modelling is acceptable from the technical point of view, since the difference of magnetic properties in samples from magnetic material can reach almost 10 %.

Future work should be focused both to the experiment and computations. In the experiment the accuracy can be improved by the use of higher frequency (3 or 10 Hz), for instance. In the computation area the automated approximation of the momentum surface should be made.

Acknowledgements

The work was supported by the Student Grant Competition of Technical University of Liberec

References

[1] G. Bertotti, I. Mayergoyz, The science of hysteresis. Vol. 1, 2 and 3. 1^{st} ed., Elsevier, 2006. ISBN 978-0--2-369431-7, Chapter 3.

[2] G. Consolo, G. Finocchio, M. Carpentieri, E. Cardelli, B. Azzerboni, “About Identification of Scalar Preisach Functions of Soft magnetic Materials,” IEEE trans. on Magnetics, vol. 42. no. 4, pp. 923-926, Apr. 2006.

[3] P. Pruksanubal, A. Binner, K. H. Gonschorek, “Determination of Distribution Functions and Parameters for the Preisach Hysteresis Model,” In. 17^{th} Int. Zurich Symp. on Electromagnetic Compatibility, 2006, pp. 258-261.

A Method for the Determination of Thermal Time Constant of Pyroelectric Sensor from Voltage Response to Step Optical Input Signal

A. Odon

Poznan University of Technology, Institute of Electrical Engineering and Electronics, Piotrowo 3A, 60-965 Poznan, Poland
Email: andrzej.odon@put.poznan.pl,

Abstract*. A method for measuring of the thermal time constant of pyroelectric sensor using the voltage response to a step optical input signal is proposed. An important advantage of this method over the traditional one is, that to get a correct result of the thermal time constant measurement it is no longer required that the thermal and electric time constants should be significantly different.*

Keywords*: Pyroelectric Sensor, Responsivity, Thermal Time Constant of Pyroelectric Sensor*

1. Introduction

The key parameters determining the performance of pyroelectric sensors are the thermal and electric time constants. The electric time constant can be relatively easily predicted already at the stage of design and later experimentally verified, but analytical determination of the thermal time constant is usually much more difficult. The problem is that the thermal energy absorbed by the sensor is passed to the environment simultaneously via three heat transporting processes: conduction, convection and radiation, which is rather difficult of exact modelling. Consequently, thermal time constant is usually determined in experiment.

In general, the problem of experiments performed to establish the thermal time constant of a pyroelectric sensor has been rarely presented in research reports and has been described in a brief manner. Usually, the thermal time constant, τ_{th} , is found on the basis of the Bode plot of voltage sensitivity of the sensor R_V as a function of frequency ω of the sinusoidal signal of radiation exciting the pyroelectric sensor. The thermal time constant is calculated from the relation $\tau_{th} = 1/\omega_{th}$ with ω_{th} obtained from the Bode plot as corresponding to 3 dB limit of the frequency band, [1, 2]. This method of measurement is illustrated in Fig. 1.

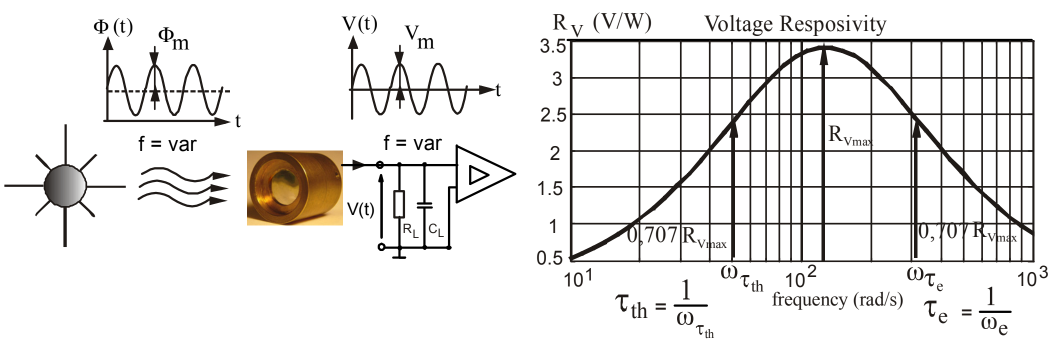

Fig. 1. The principle of thermal time constant determination with the use of Bode plot.

The above method has significant limitations as the relation $\tau_{th} = 1/\omega_{th}$ holds only when the thermal time constant τ_{th} and electric time constant τ_e take significantly different values. Moreover, this method is rather technically difficult as the majority of the commercially available electromechanical modulators of radiation are designed to produce rectangular or trapezium shape signals of radiation.

The paper presents a new method proposed for determination of the thermal time constant of a pyroelectric sensor based on the use of the peak voltage response of the sensor to the radiation signal which is of the unit step function. The proposed equation derived for calculation of the thermal time constant permits determination of this constant without the condition that the thermal and electric time constant must be significantly different. Another advantage of this method is the use in experiment of an easily generated step signal (e.g. rectangular) of optical radiation to excite the sensor.

2. Subject and Methods

In general, analytical considerations and implied the final form of the equation describing the voltage response $V(t)$ of the sensor to excitation by step optical signal of the amplitude of radiation power Φ_m are known and have been described in many papers, e.g. [3]. The equation of voltage response $V(t)$ can be derived in several different ways but the mathematical form of the final equation is similar in the most of articles. Therefore, in this paper only the main mathematical expressions and the most important explanation are given. Usually the starting point of such analyses is the equivalent circuit of the pyroelectric sensor[3, 4] and the corresponding mathematical description (Fig. 2).

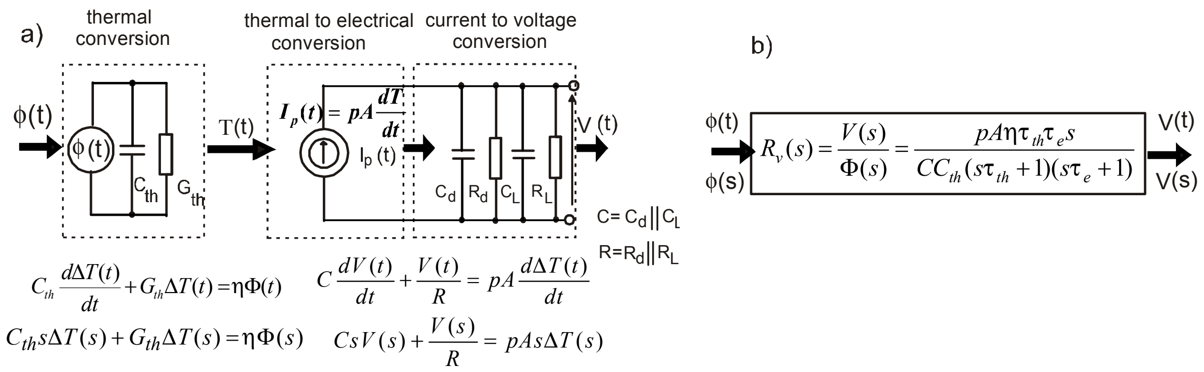

Fig. 2. a) Equivalent circuit of a pyroelectric sensor cooperating with voltage amplifier. b) Transfer function model of sensor[3,4]. Symbols in Fig.1: C_{th} – thermal capacity of pyroelectric sensor, G_{th} - thermal conductance of pyroelectric sensor, η – absorption coefficient of radiation, p – pyroelectric coefficient, $\Delta T(t)$ – temperature changes of pyroelectric material, C – equivalent capacitance for parallel connected pyroelectric capacitance C_d and input amplifier capacitance C_L: $C = C_d + C_L$, R - equivalent resistance for parallel connected leakage resistance R_d of pyroelectric sensor and input amplifier resistance: $R = R_d R_L/(R_d + R_L)$, τ_{th} – thermal time constant $\tau_{th} = C_{th} / G_{th}$, τ_e - electric thermal time constant $\tau_e = CR$, $R_v(s)$, A - active surface of the sensor, $R_v(s)$ – voltage responsivity of sensor in the Laplace domain.

The equivalent circuit of pyroelectric sensor presented in Fig.2 a permits modelling of the process of transformation of the radiation power signal $\Phi(t)$ absorbed by the pyroelectric into a voltage signal $V(t)$ passed to the input of the amplifier. This process is composed of the three stages of conversion: thermal, thermoelectric and electric. Each stage is described by appropriate differential equation and the corresponding equation in the Laplace domain, this problem is described in detail in [3,4]. After necessary mathematical transformations of the Laplace domain equations (Fig. 2) a mathematical model of the pyroelectric sensor can be obtained in the form of a Laplace transfer function $R_V(s)=V(s)/\Phi=p\eta\tau_{th}\tau_e s/CC_{th}(s\tau_{th}+1)(s\tau_e+1)$ (Fig 2b), which describes the relation between the output signal $V(s)$ and the input signal $\Phi(s)$ for the circuit presented in Fig. 2a. If the input signal is described by the relation of the unit step type, $\Phi(t) = \Phi_m \mathbf{1}(t)$, then as a result of the inverse Laplace transformation we get the equation describing the voltage response $V(t)$ of the pyroelectric sensor as

$$V(t) = £^{-1}[\Phi(s)R_v(s)] = \frac{pA\eta\Phi_m\tau_e\tau_{th}}{CC_{th}(\tau_e - \tau_{th})}(e^{-t/\tau_e} - e^{-t/\tau_{th}}), \ \ \tau_{th} \neq \tau_e \tag{1}$$

Similar results for the voltage response of a pyroelectric sensor to a step signal of optical radiation have been presented e.g. in [5].

Fig. 3 presents an exemplary plot of the pyroelectric sensor voltage response $V(t)$ to a step signal of optical radiation. Parameters of the sensor were specified in Fig. 3.

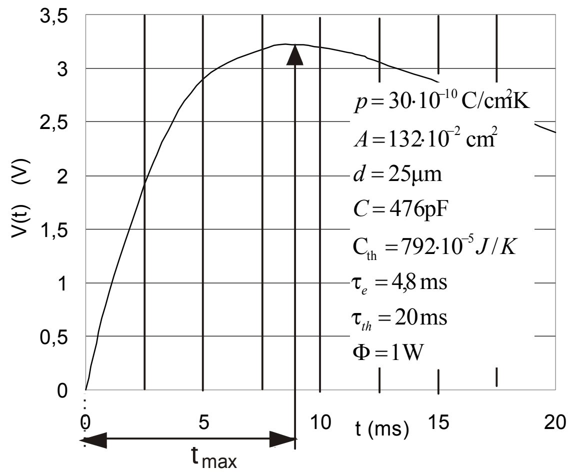

Fig. 3. Voltage response $V(t)$ of pyroelectric sensor to step signal of optical radiation.

time $t_{max} = [\tau_e\tau_{th}/(\tau_{th}-\tau_e)]ln(\tau_{th}/\tau_e)$ [5]. After transformation of this relation we get the following equation:

$$\ln\frac{\tau_{th}}{\tau_e} + \frac{t_{max}}{\tau_{th}} - \frac{t_{max}}{\tau_e} = 0. \tag{2}$$

Equation (2) is of key significance for determination of the thermal time constant of a pyroelectric sensor τ_{th} . If the value of t_{max} is known from the experimentally found voltage response to a single step signal of optical radiation, $V(t)$, and if the electric time constant τ_e is known from the parameters of the sensor and amplifier working with it, then by solving equation (2) we find τ_{th}. Equation (2) can be easily solved numerically using appropriate computer applications.

Results

Figs. 4a and 4b show the plots of two time dependencies of the sensor voltage response to the step signal of optical radiation. The plot in Fig. 4a was obtained experimentally on the basis of measurements for a specific sensor of known material and size parameters. The recorded signal of voltage response (Fig. 4a) with use of the digital oscilloscope permits determination of t_{max}. With the known $t_{max} = 9$ ms and $\tau_e = 4.7$ ms, the value of the thermal time constant can be calculated from eq. (2) as $\tau_{th} \approx 20$ ms . The second normalised plot, shown in Fig. 4b, is obtained on the basis of the theoretical relation (2) for the calculated thermal time constant τ_{th} = 20 ms and all other parameters whose values were determined from the known construction features of the sensor and catalogue data for the pyroelectric material applied. The plots presented in Figs. 4a and 4b show the acceptable similarity in shape, especially in the time range of the plot rising edge to the maximum value.

a)

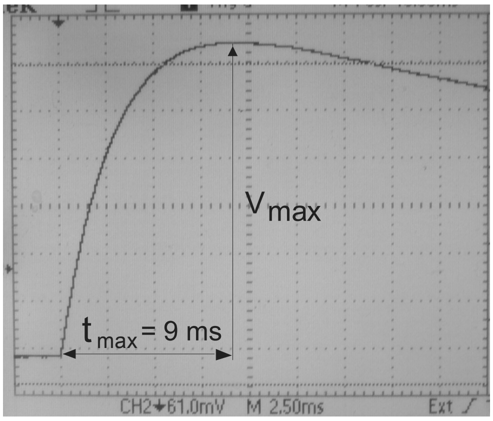

b)

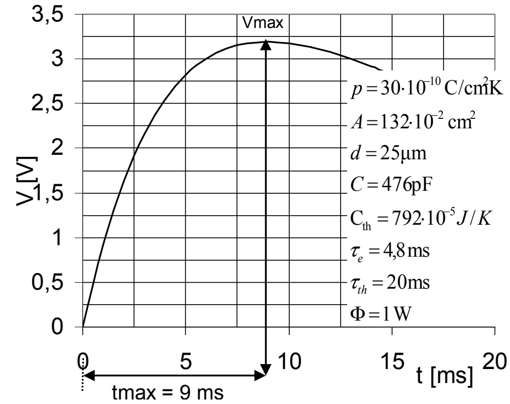

Fig. 4. Voltage response of the pyroelectric sensor to a single step signal of optical radiation a) obtained experimentally, b) theoretical.

3. Conclusions

The proposed method for the measurement of the thermal time constant of the pyroelectric sensor on the basis of its voltage response to single step optical radiation signal can be a competitive alternative to the usually applied methods employing the frequency dependencies obtained for a sinusoidal signal. The method proposed is easy to perform with the help of typical modulators. The subsequent operations include recording of the voltage response of the sensor, determination of the time at which the response reaches the maximum value and necessary calculations.

References

[1] Kao M. C., Chen H. Z., Yang S. L. , Chen Y. C., Hsieh P. T., Yu C. C., Pyroelectric Ta-modified LiNbO3 thin films and devices for thermal infrared detection, *Thin Solid Films*, 516, 16, 2008 p. 5518–5522.

[2] Peng Q. X., Wu C. G., Luo W. B., Chen C., Cai G.Q., Sun X.Y., Qian D. P., An infrared pyroelectric detector improved by cool isostatic pressing with cup-shaped PZT thick film on silicon substrate, *Infrared Physics & Technology*, 61, p. 313–318, 2013.

[3] Wheless W. P., Wurtz L. T., Wells J. A., An equivalent-circuit radiation sensor model, Southeastcon 94, Creative Technlogy Transfer: A Global Affair, Proc. of IEEE, 1994, 7-11.

[4] Odon A., Modelling and Simulation of the Pyroelectric Detector Using MATLAB/Simulink, *Measurement Science Review*, vol. 10, No 6, 2010, 195-199,

[5] Simhony M., Shaulov A., Pyroelectric Voltage Response to Step Signals of Infrared Radiation in Triglycine Sulphate and Strontium Barium Niobate*, J. Appl. Phys.*, 42, 1971, 3741-3744.

Absolute Flow Velocity Measurements by Means of the Thermal Waves

A. Rachalski, M. Bujalski, P. Ligęza, E. Poleszczyk

Strata Mechanics Research Institute, Polish Academy of Sciences, Krakow, Poland,
Email: rachalsk@img-pan.krakow.pl

Abstract. *The paper considers of applying the thermal wave method of absolute measurements of very low flow velocity. The method is based on approximate analytical solution of thermal wave propagation in flowing gas. Some results of air flow velocity measurements were presented.*

Keywords: Flow Velocity Measurement, Thermal Wave, Absolute Measurement.

1. Introduction

The idea of flow velocity measurement by means of thermal wave method is not new. The method consists of measuring the time of wave passage within the flow at known distance. Since early works of Kovasznay [1] and Walker and Westenberg [2] the method has been developed, and nowadays is used in flowmeters widely applied in manifold areas of experimental sciences and technology. The interesting application of the method, intensively progressing recently is measurements of micro and nanoflows [3],[4]. The theoretical analysis of the method is commonly restricted to particular solutions of measuring devices and circumstances of measurement. The thermal wave propagation is sensitive to flowing gas parameters, therefore measuring devices need to be calibrated. Kiełbasa presented the analytical solution of thermal wave propagation in a flowing gas, and showed the necessary conditions of absolute measurements the flow velocity [5], a shortly described by Rachalski [6]. To say briefly, the absolute method needs the conditions when the thermal diffusion does not affect the thermal wave velocity. In air, under laboratory conditions the lover limit of flow velocity is about 30cm/s.

2. Theoretical model

The governing equation of thermal wave propagation is advection-convection equation:

$$\frac{\partial T}{\partial t} = \mathbf{div}\left(\kappa \,\mathbf{grad}\, T\right) - V_G \frac{\partial T}{\partial x} + \frac{\mathbf{Q(}t\mathbf{)}}{\rho c} \tag{1}$$

where

$Q(t)$ intensity of wave source

T gas temperature

V_G flow velocity

κ thermal diffusivity

Δx distance between detectors

ω angular frequency of thermal wave

For sinusoidal wave and the probe orientation presented on Fig.1 Kiełbasa [5] came up to the expression for phase shift:

$$\Delta\varphi\left(\Delta x,\omega,\kappa,V_G\right)=\frac{V_G\Delta x}{2\kappa}\sqrt{\frac{1}{2}\left(\sqrt{1+\frac{16\kappa^2\omega^2}{V_G{}^4}}-1\right)} \tag{2}$$

From Eq.3 we can derive the condition of absolute measurement of flow velocity; if the fraction in the inner square root is enough small (but not equals to zero), i.e.:

$$\frac{4\kappa\omega}{V_G^2}\ll 1, \tag{3}$$

after expanding the root into series we obtain approximate relationship:

$$V_T=\frac{\omega\Delta x}{\Delta\varphi}=V_G \tag{4}$$

From Eq.2 and Eq.4 we obtain the relationship between gas flow velocity V_G and thermal wave velocity V_T :

$$V_T=V_G\sqrt{\frac{1}{2}\left(\sqrt{1+\frac{16\kappa^2\omega^2}{V_G{}^4}}+1\right)}. \tag{5}$$

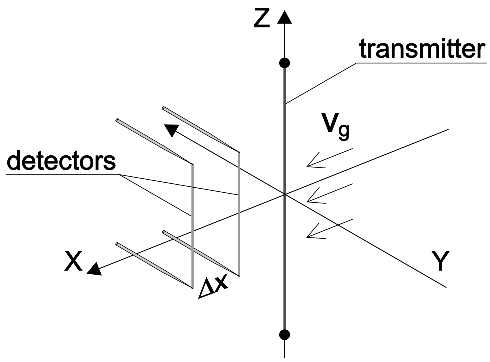

Fig. 1. Probe orientation in flowing gas.

Equation 3 shows dispersion of the thermal wave, which may be significant in low flow velocity range. Since the thermal diffusion in small flow velocities cannot be omitted, the idea is to determine flow velocity V_G by solving the set of equations:

$$\Delta\varphi_i=\frac{V_G\Delta x}{2\kappa}\sqrt{\frac{1}{2}\left(\sqrt{1+\frac{16\kappa^2\omega_i^2}{V_G{}^4}}-1\right)}, \tag{6}$$

where $\Delta\varphi_i$ is measured phase shift of wave of ω_i frequency. Even though Eq.6 contains only the two unknown variables V_G and κ we use, for better accuracy, set of more than two equations. Since of uncertainty of the phase measurement this set of equations is inconsistent, so it must be solved by fitting data points, accordingly to Eq.2 [7]. Above analysis concerns with sinusoidal wave, but may be applied to square waves. Convenient method of the phase shift determination is applying Fourier analysis to recorded detectors' signals.

3. Results

The research was performed in the wind tunnel in velocity within the range of 5 to 30 cm/s. For generating and recording thermal waves, digital anemometer- thermometer CCC2000 was used [8]. The both transmitter and detectors wire were made of tungsten 5μm in diameter. The distance between detectors was 2mm, and between the first detector and transmitter 2mm. Orientation of the sensor in the flow is shown in Fig.1. Figure 2 presents a measured velocity

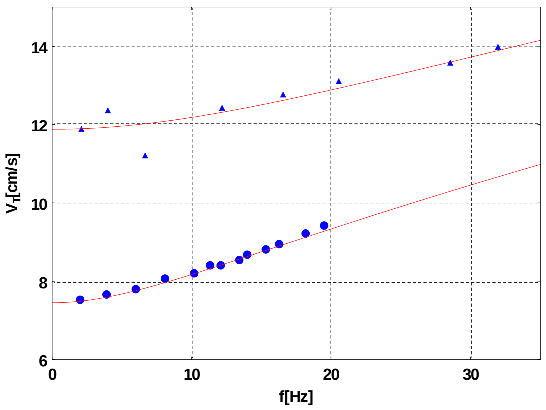

Fig.2. The measured sine thermal wave velocity vs. wave's frequency for flow velocity 7.5 cm/s and 12 cm/s.

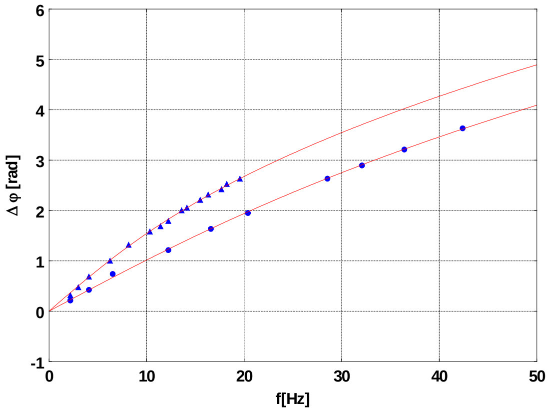

Fig.3. The measured phase shift vs. wave's frequency for flow velocity 7.5 cm/s and 12 cm/s.

of sine thermal wave of various frequencies. For flow velocity of 7.5 cm/s the dispersion is more significant than for flow velocity 12 cm/s, accordingly to discussion presented above. The solid lines represent the numerical fit of Eq.5 to data points. The measured phase shift for sinusoidal wave is shown in Fig.3. The solid lines present a numerical solution of Eq.6 obtained by means of nonlinear regression. Rather than sinusoidal wave, a square wave is applied in thermal wave method, see e.g. [9]. Other idea is to exploit natural or artificial fluctuations of the flowing gas temperature [10]. In Fig.4 presents a comparison of flow velocity measurements by means of spectral analysis of sine and square waves and by means of cross-correlation of random wave. It is shown a good agreement between sinusoidal and square wave, while cross-correlation gives higher values of velocity. The all methods display lower values of velocity than established in the tunnel. In fact, that actually the flow velocity in the area between wave's detectors is being measured. This velocity, is smaller than the inflow velocity, because of the velocity is decreased in the wake of the wire.

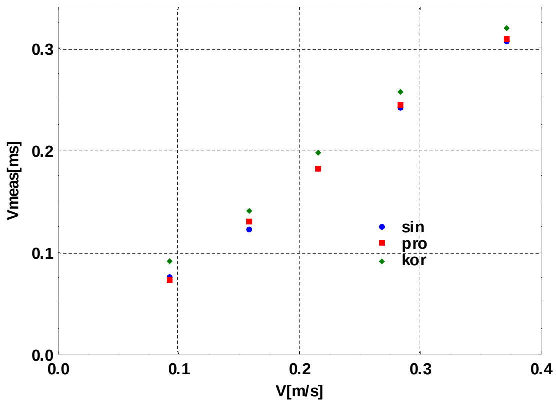

Fig.4. Comparison of measured flow velocity for sinusoidal and square wave as well cross-correlation of pseudorandom signals.

4. Conclusions

To absolute measurement of very low flow velocity, the thermal wave methods needs the spectral analysis of the signal, since the thermal diffusion affects the wave velocity. To make the method practice, necessary is reducing the influence of the velocity wake on measurement results to an acceptable level.

Acknowledgements

This study was performed under the research project: „Investigation of spatial propagation and optimization of methods for generation, detection and analysis of temperature waves in the aspect of absolute measurement of flow velocity and thermal diffusivity of gases" financed by Polish National Science Centre upon a decision number DEC-2012/07/B/ST8/03041. Experimental research was realised in a wind tunnel financed by *Fundusz Nauki i Technologii Polskiej* (Fund of Polish Science and Technology), grant no. 682/FNiTP/34/2011.

References

[1] Kovasznay LSG. Hot wire investigation of the behind cylinders at low Reynolds number. *Proceedings of the Royal Society London A* 198: 174-190, 1949.

[2] Walker RE, Westenberg AA. Absolute low speed anemometer. *Review of Scientific Instruments* 27 (10): 844-848, 1956.

[3] Shoji S, Esashi M. Microflow devices and systems. *Journal of Micromechanics and Microengineering.* 4(4):157, 1994.

[4] Berthet H, Jundt J, Durivault J, Mercier B, Anglescu D. Time-of-flight thermal flowrate sensor for lab-on-chip applications. *Lab on a Chip* 11(2):181, 2011.

[5] J. Kiełbasa. Fale cieplne w metrologii powolnych przepływów (*in polish*), Ed. AGH, Kraków, 1976.

[6] Rachalski A. High-precision anemometer with thermal wave. *Review of Scientific Instruments*, 77 (9): 095107, 2006.

[7] Rachalski A. Absolute measurement of low gas flow by means of the spectral analysis of the thermal wave. *Review of Scientific Instruments,* 84 (2): 025105, 2013.

[8] Ligęza P. Four-point non-bridge constant-temperature anemometer circuit. *Experiments in Fluids* 29(5): 505-507, 2000.

[9] Biernacki Z, Kurkowski M, Zloto T, Ptak P. Analysis of exploitation and metrological properties of a wave thermoanemometer system. *Measurement Science Review,* 1(1): 131-134, 2001.

[10] Ligęza P. Use of Natural Fluctuations of Flow Parameters for Measurement of Velocity Vector. *IEEE Transactions on Instrumentation and Measurement*, 63 (3): 633-640, 2014.

Sensor Based on the Hot-ball Method for Measuring Thermophysical Parameters

[1]J. Hudec, [2]P. Dieška, [3]M. Vitkovič, [1]Ľ, Kubičár

[1]Institute of Physics SAS, Bratislava, Slovakia,
[2]Institute of Nuclear Science and Physical Engineering, FEI STU, Bratislava, Slovakia,
[3]Institute of Anorganic Chemistry SAV, Bratislava, Slovakia
Email: jan.hudec@savba.sk

Abstract. *The hot-ball method is used for measuring thermal conductivity and thermal diffusivity. The aims of this research are reliability of measurement and utilization of the hot-ball method for measuring the thermophysical properties of liquids. Known values for thermophysical properties of distilled water and glycerol are utilized to assess the criteria for method reliability. The structure of the sensor influences the sensor reliability. The viscosity of the liquid is a limiting factor in obtaining reliable data.*

Keywords: Thermophysical Sensor, Hot-Ball Method, Thermal Conductivity, Thermal Diffusivity

1. Introduction

Over the last 20 years, a new class of transient methods for measuring thermophysical properties has become widespread in research laboratories as well as in technological applications. The principal differences between classical and transient methods lie in specimen size. Recently, a method based on a spherically symmetrical thermal field has been published [1]. The method uses two balls, a heater and a thermometer, at a distance of several millimeters from each other. This article deals with the hot-ball sensor in a single-function configuration, i.e. with heat source and thermometer incorporated into a single unit. Our sensor uses the hot-ball method for measuring thermophysical parameters described in [2].

2. Theory and Construction of the Hot-ball Sensor

A diagram of the hot-ball method is shown in Fig. 1a. The method uses a small ball which generates a transient temperature field in its surroundings, while simultaneously measuring the ball temperature. The temperature of the ball can be used to determine the thermophysical parameters of the surrounding material.

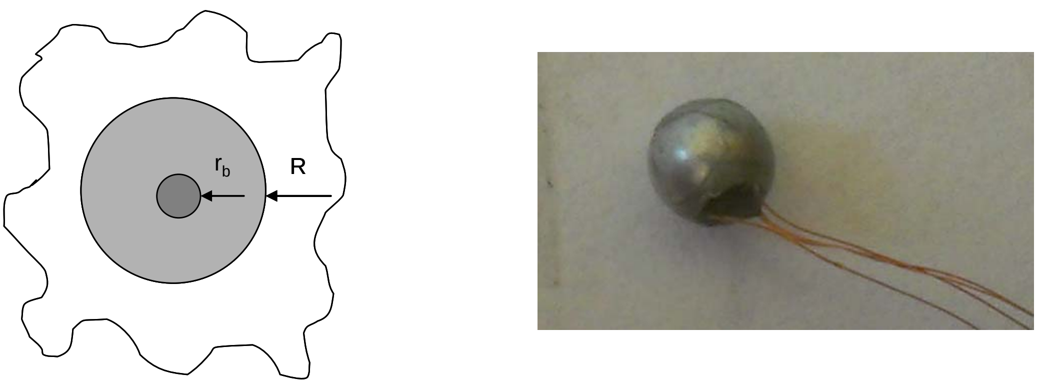

(a) (b)

Fig. 1. (a) Diagram of the hot-ball and (b) photo of a hot-ball sensor. Black region: hot ball, grey region: area penetrated by heat.

The principle of measurement by the hot-ball method is as follows. A heat source, in the form of a small ball, starts to produce heat at a constant rate, whilst simultaneously measuring its own temperature, the evolution of which reflects the temperature response of the surrounding medium. The heat penetrates into a sphere with radius *R* during the temperature stabilization phase.

The working equation for the hot-ball sensor is based on a model which assumes a heat power *q* generated from a ball of radius r_b. If the ball has a heat capacity *C* and a high thermal conductivity ($\lambda_b \rightarrow \infty$), the surface temperature of the ball is characterized by the temperature function

$$T(t, r_b) = T_0 \left\{ 1 + \frac{1}{z_2 - z_1} \left[z_2 w(-iz_1 \sqrt{t}) - z_1 w(-iz_2 \sqrt{t}) \right] \right\} \quad (1)$$

where $w(z) = e^{-z^2} \Theta^*(-iz)$, $\theta^*(u)$ is the complementary error function, $z_{1,2} = A(-1 \pm \sqrt{1-B})$, $T_0 = \frac{q}{4\pi\lambda r_b}$, $A = \frac{2\pi r_b^2 \lambda}{\sqrt{k} C_s}$, $B = \frac{Ck}{\pi\lambda r_b^3}$ and λ and k are the thermal conductivity and thermal diffusivity of the surrounding medium, respectively. Equation (1) is a solution of the partial differential equation for heat conduction under the following boundary and initial conditions:

$$T(r,0) = 0,$$

$$-\lambda \frac{\partial T}{\partial r}\Big|_{r=r_b} \cdot 4\pi r_b^2 + C \frac{\partial T}{\partial t}\Big|_{r=r_b} = q1(t)$$

where $1(t)$ is the step wise unit function.

The hot-ball sensor consists of two electrical components: a resistor and a thermistor. The resistor is used as a heat source for generation of the temperature field. The thermistor is used for measuring the temperature response to this heating. The sensor is made from a copper ball, cut into two halves. The electrical components are positioned on the inside surfaces of the halves. Both of these parts are glued into a ball by epoxy. The diameter of the ball is up to 3 mm. A photo of such a metallic ball sensor is shown in Fig. 1b. A typical measurement is shown in Fig. 2a. The measurement procedure consists of measuring the ball temperature before, during and after the period of heating. Temperature measurement before heating indicates the temperature of the surroundings and provides a baseline; measurement during heating is the basis of determining thermophysical parameters. When the ball temperature reaches a plateau, the heating is stopped and a period of temperature equilibration follows. After the temperature returns to the original baseline, the next measurement may start.

3. Experiment and Discussion

The position of the components in the ball plays a crucial role in the functionality of the sensor. Equation (1) assumes spherical symmetry of the temperature field around the ball. However, the construction of the hot-ball generates irregularities in the sphere due to placement of the active components in the ball. Thus deviations of the isotherms from sphericity can be found around the ball. These irregularities play a significant role in the initial stages of temperature response to heating, when penetration depth is small. The temperature field becomes more perfectly spherical after longer time-periods, i.e. with greater penetration depth. This part of the window of measurement (see Fig. 2a) meets the requirements

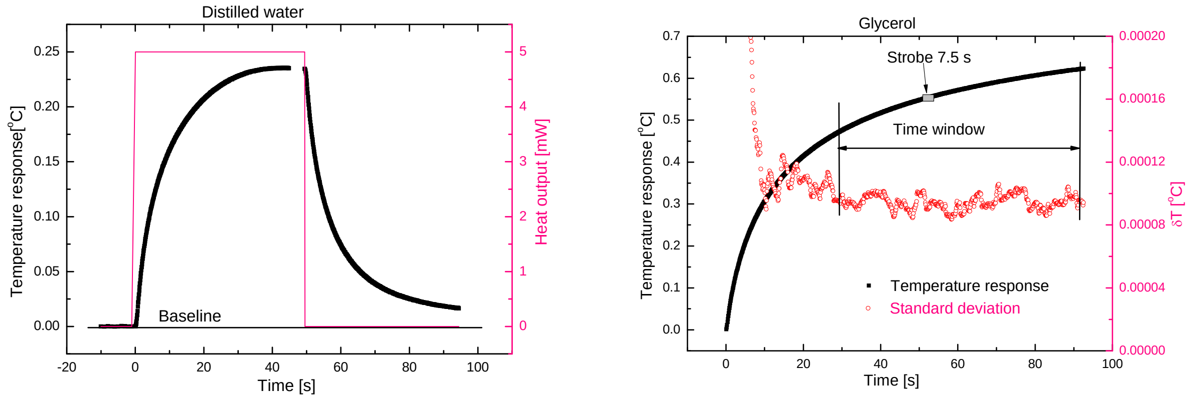

(a) (b)

Fig. 2. a – heat output of the-hot ball (full line) and the corresponding hot-ball temperature (square). Liquid: distilled water. b – temperature response (crosses) and the standard error of the corresponding difference analysis (point). Liquid: Glycerol, $q = 5$ mW.

of our model to a greater extent than the period of initial heating. These requirements are met when the spatial extent of spherical heating exceeds the spatial extent of non-spherical irregularities in the temperature field. However, when measuring properties of liquids over long timescales and with large temperature gradients, convection may occur, causing significant deviation from our model. Due to these factors, the requirements of our model (Fig. 1a), and its boundary and initial conditions, are met only for a part of our measurement period.

A critical factor in the reliability of the hot-ball is how the structure of the hot-ball affects the measured signal. For calibration, the properties of the hot-ball were calculated from measurements in distilled water and glycerol. The hot-ball sensor was affixed into a vessel made of aluminum. The vessel was filled with the liquid to be used. A wireless instrument was used for these experiments. The instrument performs data storage, communication, heating, and temperature measurement before, during and after heating [3]. Measurements were done in a Climate chamber HPP 108. Six different values of heat power were used for experiments, in the range of 2.5 to 16 mW. Three experiments were done for each heat power value. Temperature stabilization between experiments took around 2 hours. All measurements were done at 25°C and 30% environmental humidity. The function in Eq. (1) contains 4 parameters (r_b, C, λ, k). For fitting this function we used the Levenberg-Marquadt procedure. For this experiment we used the known properties of the liquids used (thermal conductivity λ and thermal diffusivity k) as input parameters, and determined the radius r_b and the heat capacity C of the sensor from fitting the data. The resulting values of r_b and C determined from the temperature responses of distilled water and glycerol serve as a measure of the sensor reliability.

To find out which portion of our window of measurement corresponds to our model, we use a special evaluation procedure. Our assumption is that each datapoint measured during heating contains information on the parameters we desire to obtain. Unfortunately, we don't know the procedure for determining the values of these parameters from a single datapoint. Therefore, we work with a strobe, i.e. a short stretch of data centred around the selected datapoint, on which the fitting procedure is performed (Fig. 2b). 75 scan points are included in each strobe. The strobe is shifted along the whole temperature response window. The time interval we are looking for, where our model applies, is that part of our measurement window in which the data show a stable standard deviation. Table 1 gives the input and output data of the parameters used in the evaluation procedure for two experiments.

Table 1. Input and output parameters of the evaluation procedure. The radius of the hot-ball sensor HB 5201 measured by caliper is r_b = 1.58 mm. The data are valid for specified measurements (last row).

Parameter	Water	Glycerol
λ [W m^{-1} K^{-1}]	0.58	0.29
k [mm^2 s^{-1}]	0.14	0.095
r_b [mm]	1.61	1.6
C [mJ K^{-1}]]	31.5	43
Measuring time [s]	37.5	95
Time window [s]	14	62
δT [^{o}C]	0.0001	0.000094
Measurement No.	i2280	i2367

4. Conclusions

Having calibration data on the radius and heat capacity of the sensor, one can begin measurements of liquids. The same evaluation procedure is used, except with the radius and heat capacity of the hot-ball as input parameters, and the thermal conductivity and thermal diffusivity of the tested liquid as the fitted output parameters. The data for radius and heat capacity given in Table 1 are influenced by the choice of surrounding liquid to a small extent. It is clear that liquids having a thermal conductivity above that of distilled water will influence the effective (as concerns our model) radius and heat capacity to a more considerable extent. Thus, for each application, calibration should be performed using appropriate liquids.

Acknowledgements

This research was supported by the project VEGA 2-0190-12.

References

[1] Zhang, H., He, L., Cheng, S., Zhai, Z., Gao, D., A dual-thermistor probe for absolute measurement of thermal diffusivity and thermal conductivity by the heat pulse method Meas. Sci. Technol. 14: 1396-1401, 2003.

[2] Kubičár, Ľ., Vretenár, V., Štofanik, V., Boháč, V. Hot-Ball Method for Measuring Thermal Conductivity. *International Journal of Thermophysics,* 31: 1904-1918, 2010.

[3] Hudec J, Dieška P., Štofanik V., Vretenár V., Kubičár Ľ., Measurement Reliability and Accuracy Analysis of the Hot-ball Sensor, In proceedings of Meeting of the Thermophysical Society, Podkylava, 2014, 47 – 52. www.fch.vutbr.cz/lectures/thermophysics/2014/pdf/Thermophysics_2014_proceedings.pdf

Moisture Sensor for the Monitoring of Temperature-Moisture Regime in Volcanic Tuffs Located in Brhlovce Village

[1]V. Boháč, [1]D. Fidríková, [1]V. Vretenár, [2]T. Durmeková, [2]L. Kralovičová, [2]J.Vlčko

[1]Institute of Physics, Slovak Academy of Sciences, Dúbravská cesta 9, 84511 Bratislava, Slovakia

[2]Department of Engineering Geology, Faculty of Natural Sciences, Comenius University in Bratislava, Mlynská dolina, 842 15 Bratislava, Slovakia

Email: bohac@savba.sk

Abstract. *The field research is based on in-situ monitoring of the temperature-moisture regime of natural rock mass in volcanic tuffs localized in the Tekov Museum of rock dwellings in Brhlovce preserved as historical heritage. The temperature and moisture changes are the parameters that influence deterioration processes of rock massive. The moisture probe uses the increase of thermal conductivity of porous structure when pores are filled by air/vapour, water or ice. The correlation between thermophysical properties and water content in pore exists. For this kind of measurements we calibrate the moisture sensors and determine change of thermal conductivity of porous material for dry and water saturated states in the temperature range that is typical for the locality climate. The moisture monitoring in the field conditions at different depths in the rock massif when they are exposed to climate changes was studied by moisture probes. The experiment was carried out for the needs of correlations between laboratory and field research.*

Keywords: Moisture Probe, Thermal Conductivity, Calibration

1. Introduction

The problem of thermal transport phenomena in the presence of moisture content in porous materials are in high interest of building industry as well as in the area of preservation of historical buildings and monuments. In the nature the water phases are always present in pores in different forms. The massive rock materials in natural conditions are exposed in time to the climate changes like the sun radiation, precipitation and evaporation, freezing and thawing causes deterioration processes of rocks. The resulting thermal conductivity of a porous tuff rock material is a function of the fluctuation of water content in pores (porosity 40-60%). The calibration of the moisture probe from dry to water saturated material sets the working range of measured water content in rock mass.

2. Physical model

In principle, the moisture probe is based on hot ball sensor (HB) in combination with rock cylinder drilled out of tuff massive assembled in a proper way. The measurement principle is based on generation of the heat pulse in the step-wise form and recording the temperature response to this heat pulse. Model for the arrangement on Fig.1 (down) assumes a constant heat flux $\boldsymbol{q}$ from the empty sphere of radius $\boldsymbol{r_b}$ (radius of hot ball probe) into the infinitive medium that starts to be generated for times $t > 0$ (Fig. 1 down). Then the temperature distribution within the medium is characterized by Eq. 1 [1, 2, 3]. The solution of the partial differential equation of the heat conduction for this experimental technique is the temperature function (Eq. 1) that describes the temperature response on Fig. 1.

$$T(t,R) = \frac{qR}{\lambda}\left\{1 + \frac{1}{z_1 - z_2}\left(z_2 w\left(-iz_1\sqrt{t}\right) - z_1 w\left(-iz_2\sqrt{t}\right)\right)\right\} \tag{1}$$

Where $z_{1,2} = \frac{\lambda}{2\sqrt{\kappa}C_s}\left(-1 \pm \sqrt{1 - \frac{4C_s\kappa}{\lambda R}}\right)$, $w(x) = e^{-x^2}\Phi^*(-ix)$, T – temperature, t – time, r – radial space coordinate, ***R*** – radius of the sensor, ***q*** – heat flow density at sensor, ***λ*** – thermal conductivity, ***κ*** – thermal diffusivity, ***Φ**** – complementary error function, ***C$_s$*** – heat capacity of unit area of sensor surface, ***C$_s$ = C/4πR^2*** – heat capacity of unit area of sensor surface, ***C*** – heat capacity of sensor. The thermophysical parameters ***λ, κ*** and ***C*** are calculated from the temperature response (Fig.1.) by fitting procedure using model (Eq. 1).

3. Experiment

The Hot ball probes before inserting to the stone cylinder were primarily calibrated in baths having different thermal conductivity to obtain the basic probe parameters to calculate thermal conductivity and thermal diffusivity from the temperature response. Calibrated sensor inserted in a tuff core creates the moisture sensor (Fig. 1. bottom).

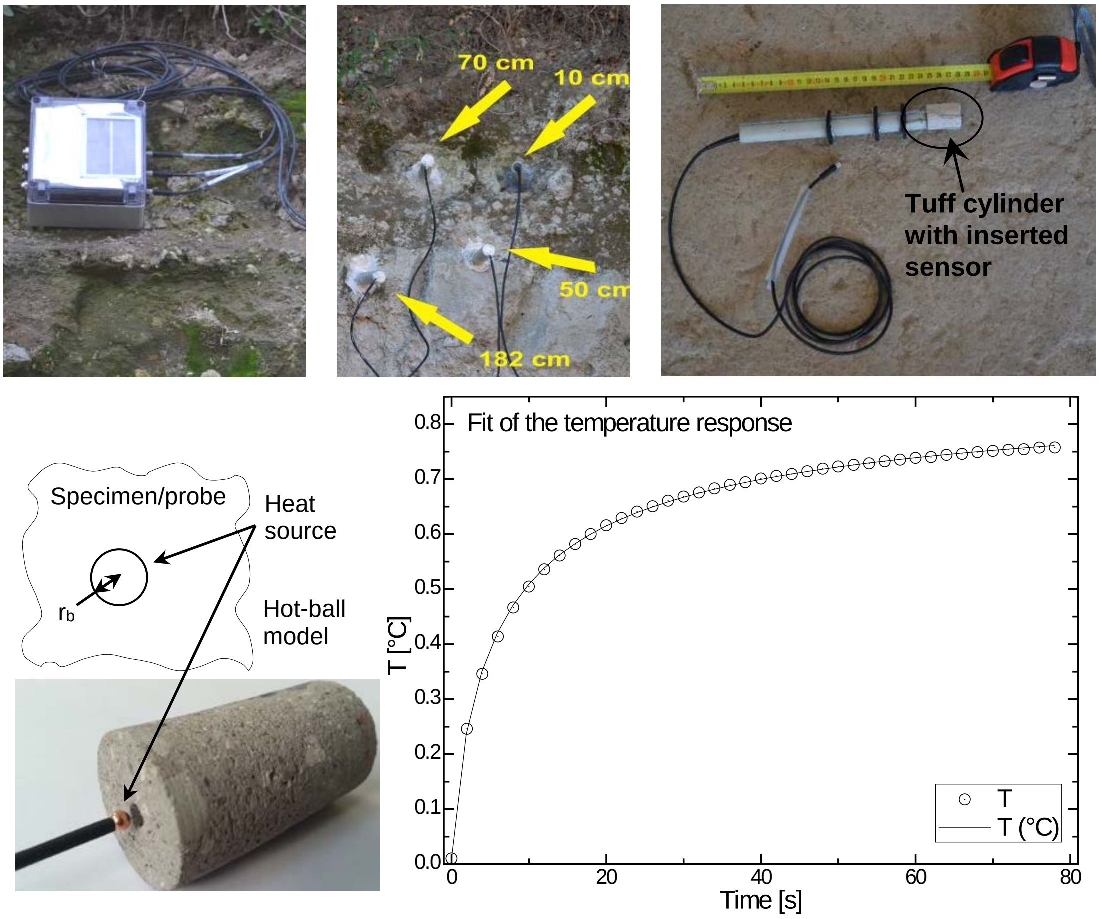

Fig. 1. The electronic instrument RTM powered by solar unit in connection with the moisture probe (left up), the current location of the probes in rock massif (middle up) and the moisture probe ready to be mounted to rock massif with the holder made of plastic tube sealed with rubber rings to prevent air and moisture transport to the 10cm measurement depth (right up). The model of the hot ball sensor with the photo (down left) and the fit of measured temperature response by temperature function (down right).

The next calibration was done for the dry and moisture saturated states. The measured value of heat flux and temperature maximum q/T_m inside the moisture sensor represents thermal conductivity that is changing in dependency of moisture content from 0 up to 100 % (Fig. 2.).

4. Results

The moisture probes were calibrated in dependence of temperature in both – the dry and moisture saturated regime. The calibration data in dependency of the temperature for the moisture sensors made of tuff stone cylinders in dry and moisture saturated states are presented. The thermal conductivity values of moisture probes which correspond to change of moisture content in temperature-moisture dependency calibration procedure were measured in thermostated chamber RTB 1.02. The dry-moisture calibration was performed in laboratory conditions for the range of temperatures from -20 up to 40 °C. After calibration the moisture sensors were inserted in the tuff massif at Brhlovce. Monitoring in tuff massive at depths of 10, 50, 70 and 182 cm was started to run.

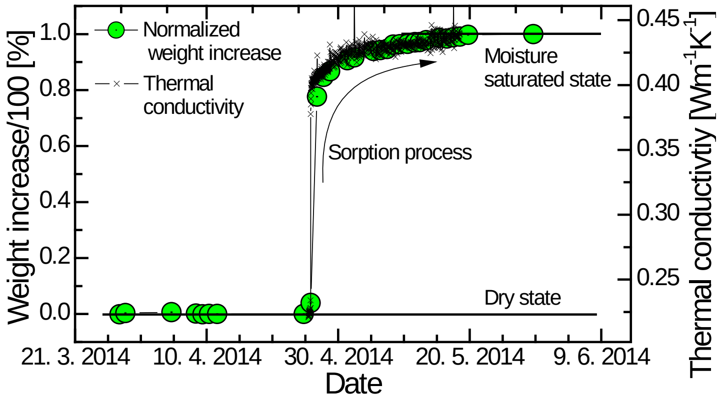

Fig. 2. Sorptivity (moisture content) is related to the pores volume measured by weighting method for the probe made of tuff. The change of thermal conductivity about 50% from dry to moisture saturated state is correlated to normalized weight data during saturation. This difference represents 100% of humidity scale in between dry and fully saturated pores by water [3].

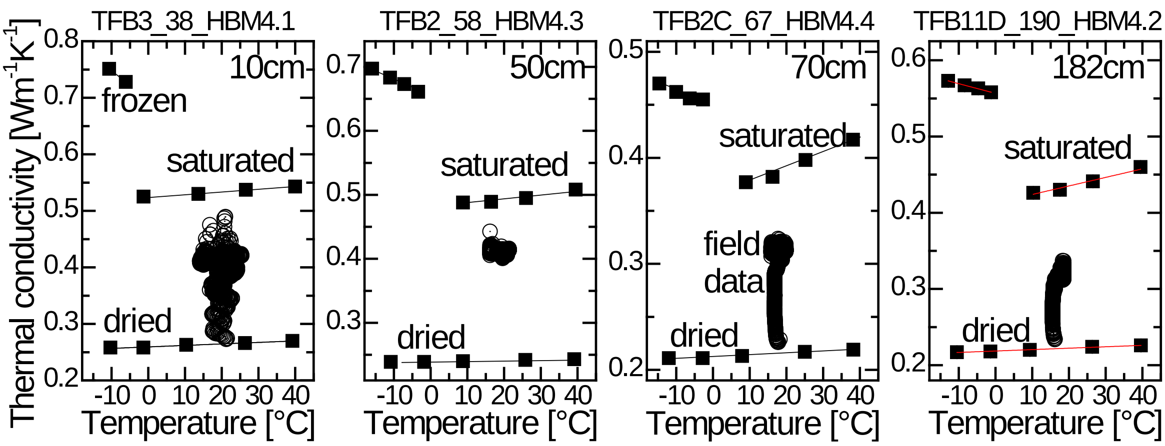

Fig. 3. Calibration of old probe made of tuff stone in dry and moisture saturated state. The calibration lines below zero temperature represent thermal conductivity in frozen state because of jump change after the phase change of water. Data between calibration lines represent field measurements from first month after inserting into the massif.

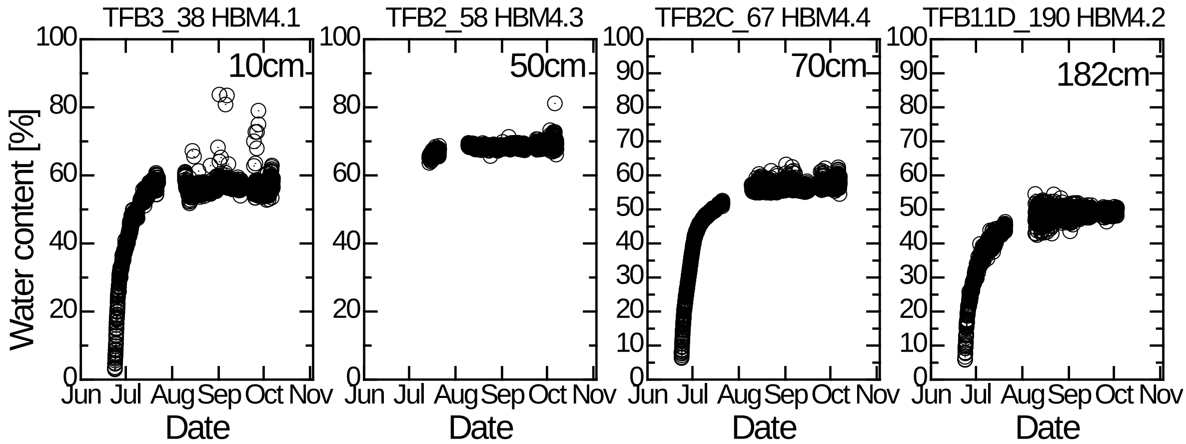

Fig. 4. Field data from Fig. 3. recalculated to a relative water content according the equations of calibration lines drawn for a time period of 3 months after insertion (up). The increase during the first month satisfies to speed of sorption found in laboratory during the calibration on Fig. 3.

5. Conclusions

For the calibrated moisture sensors the variation of λ with variation of moisture content as a parameter, the temperature dependency was found. The moisture change measured as the value in between the maximum and minimum values of λ that define the moisture sensitivity and in the case of this probe it was about 0.5 $Wm^{-1}K^{-1}$ in a given temperature range. For different moisture content a linear dependency is valid, so one can recalculate measured values of λ to the moisture content from this calibration. At the first month of monitoring the rapid increase is evident and gives an image on difference between the dry and stabilized state that corresponds to the moisture content in massif about 50-60%. The data on bottom were recalculated to absolute water content related to a volume of one cubic meter according the equations of calibration lines drawn on Fig. 2 and Fig. 3. Their values in currently saturated state for 50-70% are about 280 to 480kg m^{-3}. This experiment will be helpful in monitoring the moisture in field research, because values of thermal conductivity are defined in extreme dry and wet conditions (Fig.3, 4).

Acknowledgements

This work was supported by Slovak Research and Development Agency under the contract No. APVV-0641-10 „Study of rocks properties and investigation of structural and textural characteristic in correlation with thermo-physical and physico-mechanical properties”.

References

[1] Carslaw, H.S. & Jaeger, J.C. 1986. Conduction of heat in solids, Oxford, Clarendon Press, Second edition, p. 348.

[2] Kubičár, Ľ., Vretenár, V., Štofanik & V. Boháč, V. 2010. Hot-Ball Method for Measuring Thermal Conductivity, International Journal of Thermophysics, 31, 10, p. 1904-1918.

[3] Ekkertová, P., Šimková, I., Brček, M., Durmeková, T. & Boháč, V. Influences of temperature change and moisture content on the thermal conductivity of rocks. Thermophysics 2012 – Conf. Proceedings, 17th International Meeting of Thermophysical Society, 31st Oct. - 2th Nov.2012, Podkylava, Slovak Republic, org. Institute of Physics, Slovak Academy of Science in Bratislava, ISBN: 978-80-214-4599-4, p.33-40.

UHF System for Detection and Spatial Localization of Partial Discharge in High Voltage Power Transformers

[1]M. Cap, [1]P. Fiala, [2]M. Kaska, [3]L. Kocis

[1]Department of Theoretical and Experimental Electrical Engineering, Technicka 12, 612 00 Brno, Czech Republic,
[2]TES s.r.o, Prazska 597, 674 01 Trebic, Czech Republic
[3]EGU Praha Engineering a.s., Podnikatelska 539, 190 11 Praha 9, Czech Republic
e-mail: capm@feec.vutbr.cz

Abstract. *The article presents a new approach to the detection of a very weak electromagnetic (EM) signal, which is generated by partial discharge (PD) in a high-voltage, oil-filled power transformer. The new technique is based on the discrimination of signals with origin in outside of the transformer which are detected by external sensing head. Performed measurement process contains several different measurement modes with corresponding arrangement of sensing heads. The time-shifts of the waveforms related to transient process occurrence in the signals are the main input parameters for localization methods. In order to estimate the position of the signal source in the 3D space a minimum of four antennas has to be used, since the time of the PD is unknown.*

Keywords: Partial Discharge, UHF, Antenna, Detection, Spatial Localization.

1. Introduction

Security of the power transformers is an issue which is closely related to the stability of whole electric power distribution system. High power transformers in nuclear power plant reach power up to hundreds of MVA and any damage or destruction cause big technical problems and financial losses. Various diagnostic methods for transformer condition determination have been developed. Each of these suffers from some disadvantages. The recent technology development and the availability of hi-tech instrumentation have opened new opportunities to employment of advanced diagnostic methods, as the radiofrequency (RF) method is [1]. RF method is based on the sensing, evaluation and source localization of the EM signal in UHF range. Therefore, it is frequently called the UHF method. Our group has developed an UHF method based diagnostic system for detection and localization of partial discharge activity, as described in [2].

2. Subject and Methods

PD signal is detected by the special measuring system. Whole system contains 4 specially designed sensing heads central unit (Fig. 1), and software for PD analysis and

Fig. 1. Left - sensing head, middle - sensing heads mounted on the transformer, right – assembly of the diagnostic system in shielded box.

localization (Fig. 2). Sensing heads are mounted in to the front wall of the transformer. Heads are connected by triaxial cables for simultaneous RF signal transmission and DC powering. Signal preprocessing part of each head includes conical antenna, controllable attenuators, amplifiers, high pass filter and RF limiter. Data are acquired by Agilent data acquisition system which uses a four-channel, 10 bit high speed cPCI digitizer.

Detection methods

Expected duration of signal caused by partial discharge inside of the transformer is under 150ns and is characterized by short rising time. Detection of the partial discharge is based on setting of special antenna setup and trigger conditions. Acquisition system can use four antennas inside of the transformer and one external antenna which can be positioned in dependence on expected location of noise signals. If external antenna is used only three channels are free for acquisition, fourth channel is used as information on signal presence outside of the transformer. Trigger is set on all channels simultaneously to ensure the best trigger condition for signals coming from all parts of transformer. Partial discharge signal level depends on strength of the discharge and its distance to the antenna. This level can vary and to ensure the best trigger conditions different setting of variable attenuators needs to be tested. EM signal of the partial discharge can be distinguish from signal from other types of discharge by its shape and duration time. Ideal signal contain higher frequencies and has a short rising and duration time. Long distance signal propagation attenuate high frequencies and cause extension of those times. Signal changes in dependency on signal origin allow to create specific settings and separate desired signal.

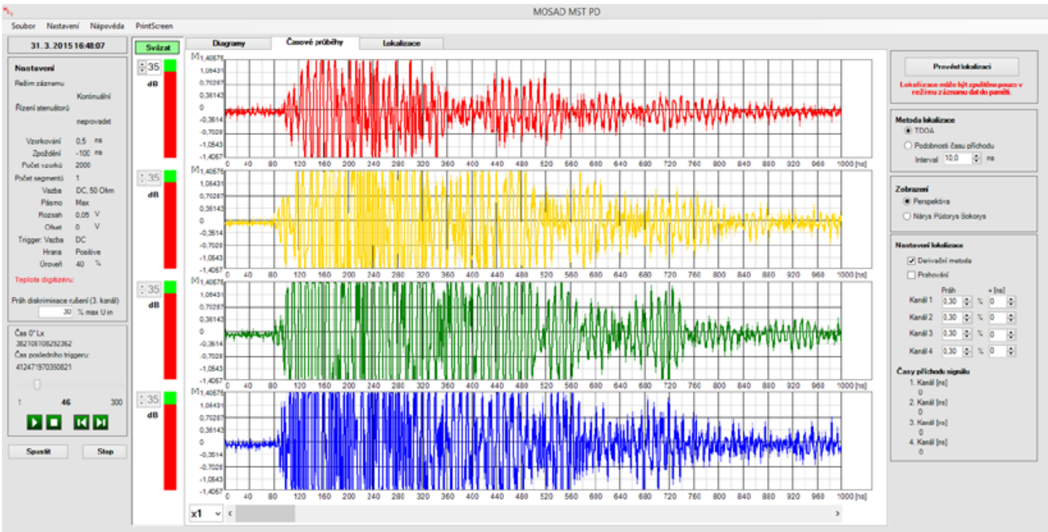

Fig.2. Software for partial discharge analysis and localization

Detecting presence of partial discharge inside of the transformer is several step procedure. First step is analyzing of signals in continual measurement mode where signal can be examined by its shape and position in 20ms of voltage period. If amount of other signals or higher noise level is in comparison to the desired signal high, is necessary to acquire signals into the memory and provide offline analysis. Memory mode is designed to acquire 300 data sets with minimal death time after downloading one data set.

Spatial localization

Accuracy of the spatial localization is determined by accuracy of detection signal arrival time. Localization algorithm is based on Time Difference of Arrival (TDOA) method where position of the signal source is calculated from difference of times of signal arrival in each channel. Time of arrival is determined from energy accumulation curve EAC given by equation [1][2]

$$w_i = \frac{t_s}{Z_0} \sum_{k=0}^{i} u_k^{\,2},\; k = 1 \ldots N \tag{1}$$

Point in data vector could be marked as the time of arrival when EAC or its firs derivation

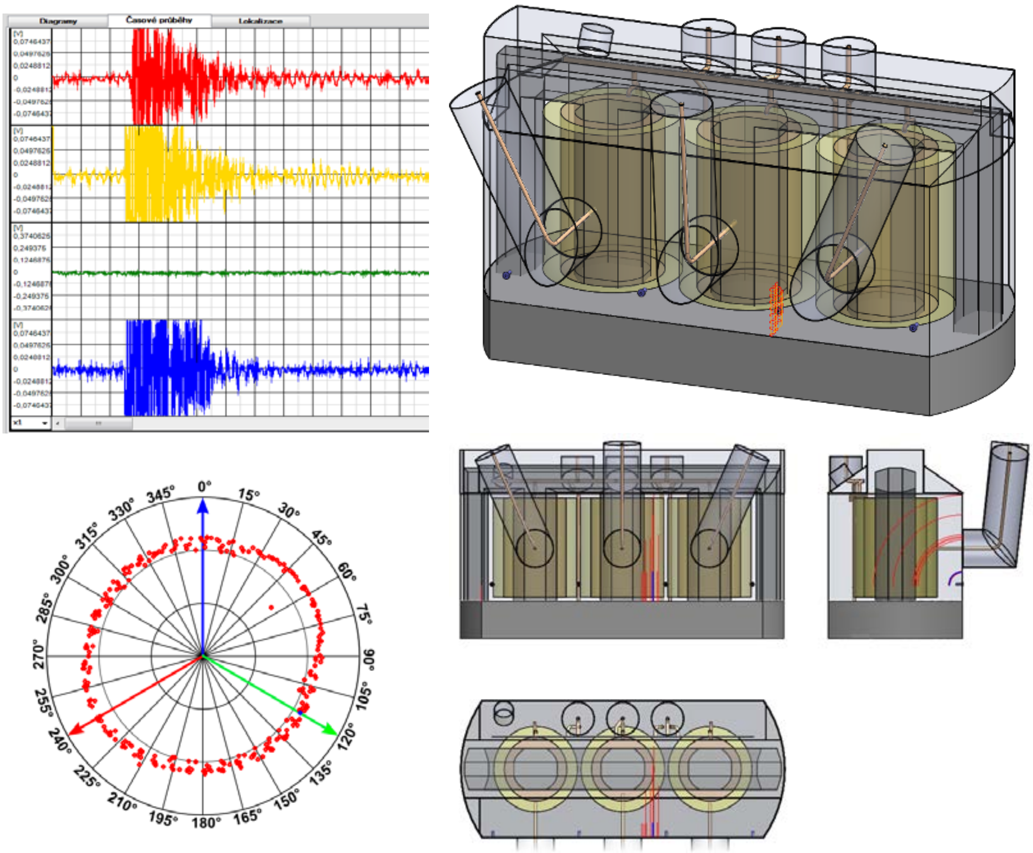

Fig.3. Result of the system calibration. Top left detected signal, down left position of data sets in phase chart, top right – results of localization for matrix method, down right – results of localization for TDOA method.

reach threshold value. Partial discharge can be then localized by two methods. First method use for given antenna arrangement derived equations and calculate position for each data set separately. This is very useful in case where is necessary to localize small amount of data sets manually. Due to high sensitivity of the TDOA method to the precision of the time of the arrival is feasible to use results accumulation. Second method for spatial localization use 4D matrix of signal arriving times. Comparing of the calculated time with the matrix could be area surrounding points which fit to defined interval marked as a potential origin of the partial discharge. In case of periodical presence of the same discharge in 300 data sets is area if its origin contains this area higher values then rest of the space. Localization results are then defined as points where value is higher than 50% of maximal value.

System calibration

Measurement system contains several specially designed devices which need to work properly to give correct measurement output [4]. For this purpose was designed special sensing head containing source of testing discharge [5]. Calibration procedure include definition of specific trigger condition to ensure detection of injected pulse, visual check of the signal shape and its positioning on phase chart and spatial localization of the signal source in third vessel, Fig 3.

Signal discrimination

Settings of the system can be considered as optimal, provided that detected signals has origin only in transformer volume. Even if system uses optimal setting, there is still high number of signal coming from outer space. Determination of which data will be used and what is the noise is based on use of external antenna. Simultaneous detection inside and outside of transformer volume allow us to mark data with signal on external antenna as a noise and delete this data. Assuming the presence of PD only inside of the transformer, then can be data with no signal on external antenna marked as wanted signal an used for analysis and spatial localization. Correct function of this method requires placing antenna in to position where is possible to detect signal from feeding and output bushing simultaneously.

3. Conclusion

Detection system is used for monitoring of presence of partial discharge in power transformers in nuclear power plant Dukovany, Czech Republic. Presence of partial discharge in this transformers is in regard to technological age of transformers not expected. However, number of signals per second detected inside of the transformer is large. Detected signal are caused by other types of discharges coming mostly from feeding and output bushing. Shape of those signals is influenced by propagation process. Long duration discharges are then discriminated by use of external antenna placed close to the feeding and output bushing and by detection of the signal level in range 400-1000ns. In this interval is expected only noise level therefore are all data with higher signal level discriminated. Discrimination efficiency has a strong influence on results of spatial localization and resulting analysis of the transformer.

Acknowledgements

The research described in this paper was financed by the National Sustainability Program under grant No. LO1401 and by Czech Science Foundation under grant No. 13-09086S. For the actual analyses and experiments, infrastructure of the SIX Center was used.

References

[1] Drexler P, Cap M, Fiala P, Steinbauer M, Kaska M, Kocis L, Detection of low-level electromagnetic signal of partial discharge by means of disturbed acquisition discrimination, *Proceedings of Progress in Electromagnetics Research Symposium*, Guanghzou, China, 2014.

[2] Fiala P, Jirku T, Drexler P ,Dohnal P,"Detection of Partial Discharge inside of HV Transformer, Modeling, Sensors and Measurement, in *Proceedings of Progress in Electromagnetics Research Symposium*, Cambridge, USA, , 1013-1016, 2010.

[3] Myška R, Drexler P, Simulation and verification of methods for partial discharge source localization, *Proceedings of Progress in Electromagnetics Research Symposium*, Kuala Lumpur, Malaysia, 2012, 704-108.

[4] Szabo Z, . Fiala, Characterization and Testing Shielding Fabrics, *Proceedings of Progress in Electromagnetics Research Symposium*, Moscow, Russia, 2009, 1273-1276.

[5] Morando A, Borsero M, Sardi A, Vizio G, Critical Aspects in Calibration of ESD Generators, Measurement Science Review, Volume 11, No. 1, 23-28, 2011

Proposal of Power Supply Module for the Electromagnetic Field Probe

J. Slížik, R. Harťanský, V. Smieško

Institute of Electrical Engineering, Faculty of Electrical Engineering and Information Technology, Slovak University of Technology in Bratislava, Slovakia
Email: jozef.slizik@stuba.sk

Abstract. *This article deals with a proposal of power supply for autonomous electromagnetic field probe. The probe consists of three parts: control electronics, electromagnetic fields sensor and power supply. In this article we deal with power supply of the probe analysis and synthesis. We analyze the impact of the power supply part on the measurement error of the electromagnetic field. Result of an analysis will be dependency of the measurement error on the distance of segments which serves as a power supply for probe. Based on this values will be possible defined the overall dimensions of the electromagnetic field probe.*

Keywords: Power Supply, Sensor, Electromagnetic Field Probe, Minimum Distance, Near-Field

1. Introduction

It is necessary propose adequate power supply for device during proposal of electrical equipment. Some equipment has special requirements considering at their construction or function. Our proposed equipment is autonomous electromagnetic (EM) field probe. This probe will measure one or several vector components of the electric field intensity in the near-field region from source of the EM field [1]. The EM field probe consists of electric small sensor(s), control electronics (e.g. operational amplifier, μProcessor, etc.) and power supply. Proposed EM field probe must be autonomous in terms of power supply. The power supply will be designed as a device taking energy from measured EM field. This device will insert in to the near distance from source of EM field. Intensity of electric (magnetic) field reached high value in the near-field region [2]. We know that electric current is generated with EM field in the near area of the antenna from reciprocity theorem [2]. We use elementary electric dipole as an antenna. This component converts electric field intensity to the induced voltage at the end of the dipole. The dipole alone is not good version of power supply. We must to propose electrical component, which provide sufficient power supply for EM field probe. Our device can influence measured EM field in its surroundings. We must verify the effects proposed power supply on the measurement EM field.

2. Conception of power supply

In this part will be proposed power supply for EM field probe. Dipoles convert electric field intensity to the induced voltage at the end of the dipole. The length of the dipole must be significantly less than the wavelength of the EM field. The dipole alone is not enough for power supply of the probe. For the purposes of increasing input voltage are used different types of voltage multiplier [3], [4]. In our proposal we focused on the cascade multiplier (*Cockcroft-Walton* multiplier) as shown in Fig. 1.

A cascade multiplier is an electric circuit with an AC input and DC output of roughly twice the peak input voltage. They are a variety of voltage multiplier circuit and are often, but not always, a single stage of a general form of such circuits. The term is usually applied to circuits consisting of rectifying diodes *D* and capacitors *C* only, other means of doubling voltages are not included. Output of cascade multiplier is theoretically an integer times the

AC peak input, for examples, 2, 3, or 4 times the AC peak input. Thus it is possible to get 200 V DC from a 100 V peak AC.

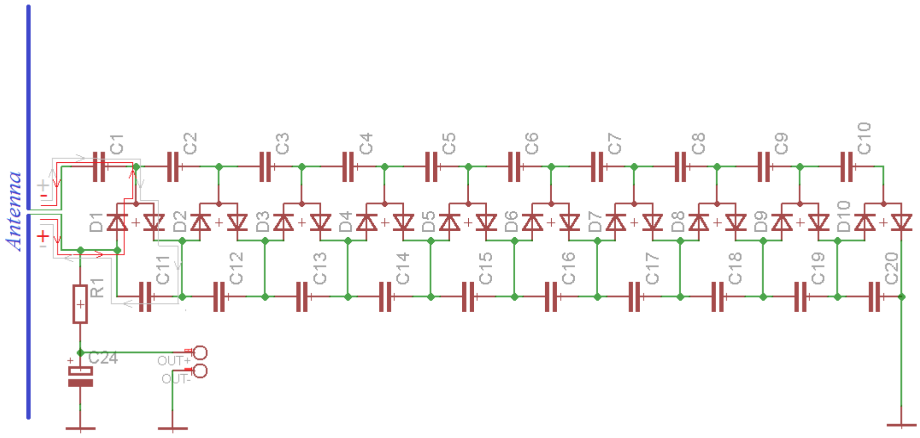

Fig. 1. Cascade multiplier (*Cockcroft-Walton* multiplier)

Principle of the cascade multiplier is simple. At the time when the AC input (antenna) reaches its positive polarity on anode of the first diode in D_1 (D_1 is double diode) is allowing current from the capacitor C_1 back into the input (red line). Capacitor C_1 is charged to the voltage peak of source, $U_{c1} = \sqrt{2}u$. Where u is input AC signal. When the same AC signal reverses polarity, current flows through the second diode in D_1 filling up the capacitor C_{11} with both the positive end from AC source u and the first capacitor U_{c1} (grey line). Second capacitor is charged to the voltage $U_{c11} = \sqrt{2}u + U_{c1} = 2\sqrt{2}u$. With each change in polarity of the input, the capacitors add to the upstream charge and boost the voltage level of the capacitors downstream, towards the output on the right. The output voltage, assuming perfect conditions, is twice the peak input voltage multiplied by the number of stages in the multiplier. Cascade multiplier has 10 stages which are showed in Fig. 1.Each stage containing two capacitors and two diodes. That means on the output will be an integer 10 times the AC peak input, $U_{OUT} = 10\sqrt{2}u$ [4]. As a diode we use Schottky zero bias diode, therefore we neglected voltage losses on the diode.

The DC/DC converter is connected at the output from the cascade multiplier thereby that voltage from power supply reaches the required level. Capacitor C_{24} is to store the voltage from cascade multiplier. Proposed *cascade multiplier* consists of electric short dipole, Cockcroft-Walton multiplier and DC/DC converter.

3. Impact of power supply on the EM field measurement

The existing an interaction between the cascade multiplier and EM field sensor because there are located close to each other. The impact of the cascade multiplier (proposed power supply) is significant only when large current flow from power supply. In our case proposed EM field probe is powered by current 3 mA. Quantifying the change of the electric field intensity caused by the influence of the cascade multiplier in the near EM field is main task of this article part. EM simulation software FEKO was used for calculate it. In the software FEKO was created a first model where the source of the EM field is *electric point source*. The values of the electric field intensity denote as E_1 depended of x coordinate was simulated, Fig. 1a. The value E_1 are not influencing by cascade multiplier. In the next step, insert cascade multiplier into the model. Cascade multiplier is represented by a loaded electric short dipole Fig. 1a. Get the values of the electric field intensity in the vicinity of the cascade multiplier. These values denote as E_{pws1}.

In the FEKO was created a second model where the source of the EM field is *planar wave*. The values of the electric field intensity denote as E_2. Insert cascade multiplier into the model. Cascade multiplier is represented by a loaded electric short dipole, too Fig. 1b. Get the values of the electric field intensity in the vicinity of the cascade multiplier. These values denote as E_{pws2}. Distance between cascade multiplier and source of EM field was $\lambda/10$, in both cases. Both models were supplied with electric field intensity from 0.5 V/m to 100 V/m.

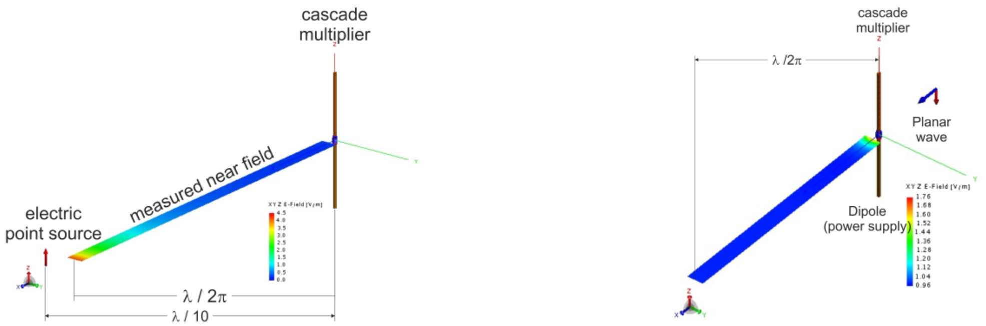

a) Model 1- *electric point* b) Model 2 - *planar wave*

Fig. 2. Measuring impact of cascade multiplier to the measurement

4. Results

The measurement error was calculated for electric field intensity with cascade multiplier. This error we get from equation:

$$\delta_{Ex} = \frac{E_{pwsx} - E_x}{E_x} 100\% \tag{1}$$

Index *x* represents the number of the model. In figure Fig. 3(for *electric point source*) and Fig. 4 (for *planar wave source*) we see dependence of the measurement error δ_{Ex} on the distance from cascade multiplier.

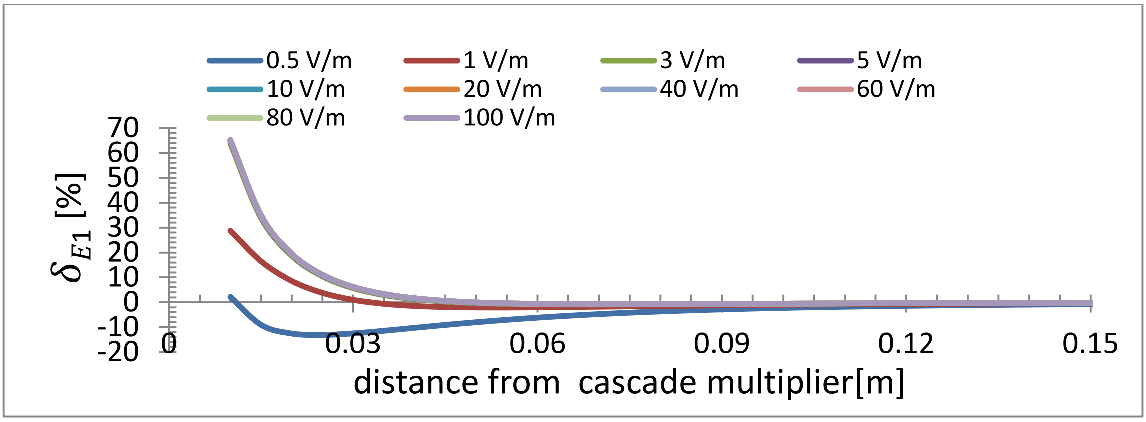

Fig. 3. Dependence of the error δ_{E1} on the distance from cascade multiplier (*electric point source*)

The dipole which represents cascade multiplier flowing current and that generated EM field in the vicinity of the dipole. This EM field influence value of the electric field intensity in the close to the cascade multiplier. In the figure Fig. 3 we can see that to the sustained value of electric field intensity occurs after exceeding distance 10 cm from cascade multiplier. In this case is as a source of EM field used *electric point*. Measurement error δ_{E1} is same for values of electric field intensity greater than 3 V/m. Dependence of the measurement error on the distance from cascade multiplier for *planar wave* is shown in figure Fig. 4. The EM field close to the cascade multiplier reached different value of electric field intensity as when has not been there. In figure Fig. 4 we can see that to the sustained value of electric field intensity occurs after exceeding distance 5 cm from cascade multiplier. Measurement error δ_{E2} is almost same for all values of electric field intensity.

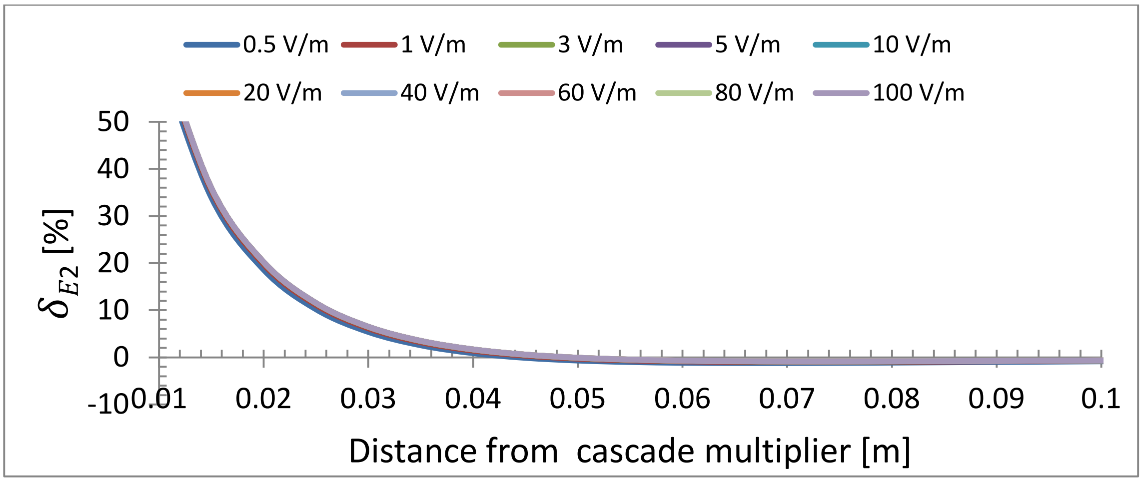

Fig. 4. Dependence of the error δ_{E2} on the distance from cascade multiplier (planar wave)

5. Conclusions

In this article we deals with proposal of power supply for EM field probe. Proposed power supply is powered from measured EM field. Proposed power supply consists from cascade multiplier (*Cockcroft-Walton multiplier*), dipole and DC/DC converter. We were dealing with examination of influence cascade multiplier to the EM field measurement. Conclusion is that minimal distance proposed EM field probe must be 10 cm from the cascade multiplier. Measured EM field is not affected with cascade multiplier in this distance.

Acknowledgements

This work was supported by the projects VEGA 1/0431/15, APVV-0333-11 and ITMS 26240220084.

References

[1] Slížik J., Harťanský, R.: Metrology of Electromagnetic Intensity Measurement in Near Field. In: *Quality Innovation Prosperity*. ISSN 1335-1745. Vol. 17, Iss. 1 (2013), pp. 57-66

[2] Balanis Constantine A. *Antenna theory: analysis and design*. 3rd ed. Hoboken: Wiley-Interscience, 2005, xvii, 1117 s. ISBN 978-0-471-667282-7.

[3] Chung-Ming Young; Ming-Hui Chen; Tsun-An Chang; Chun-Cho Ko; Kuo-Kuang Jen, "Cascade Cockcroft–Walton Voltage Multiplier Applied to Transformerless High Step-Up DC–DC Converter," *Industrial Electronics, IEEE Transactions on* , vol.60, no.2, pp.523-537,

[4] Kobougias, I.C.; Tatakis, E.C., "Optimal Design of a Half-Wave Cockcroft–Walton Voltage Multiplier With Minimum Total Capacitance," *Power Electronics, IEEE Transactions on* , vol.25, no.9, pp.2460-2468

Effect of Conductive Ink on Properties of Tactile Sensors

J. Volf , V. Novak, V. Ryzhenko

Czech University of Life Sciences Prague, Faculty of Engineering, Kamýcká 129, Prague 6, Czech Republic

Email: volf@tf.czu.cz

Abstract. *The present paper deals with tactile sensors with circular electrodes in which conductive ink was used as a converter converting pressure into an electric signal. The dependence was studied on the thickness of the deposited ink layer and the properties were compared. Also the properties of identical tactile sensors in which a conductive elastomer Yokohama rubber CS57-7RSC was used were compared with those with conductive ink.*

Keywords: Conductive Elastomer, Conductive Ink, Tactile Sensors and Transducers

1. Introduction

Up till now the conductive elastomer Yokohama rubber CS57-7RSC was used in the production of tactile sensors [1] - [6], [8]. Properties of different polymers are described in [9] - [10]. Due to some of its negative properties, and due to changes in the design of the Plantograf measuring system, we searched for another type of material for the conversion of the imposed pressure into an electric signal. The decision was to use conductive ink. Four types of conductive inks were obtained for the tests: KH WS SWCNT from the Korean firm KH Chemicals, Luxor from the Taiwanese firm Luxor, NGAP FI Ag-4101 from the Spanish firm NANOGAP and DZT-3K. The last type of ink was the only used in the measurements since owing to its composition it could form a relatively high-quality conductive layer. Carbon particles were used here as a filler. The other inks did not meet the requirements, either they were too thin and did not form a continuous layer or did not adhere to the substrate (first two, both water-based, inks) or were excessively conductive – the resistance was only in units of Ω. The filler in this case was silver (third ink).

2. Subject and Methods

Production of DZT-3K ink specimens

The selected DZT-3K ink was deposited on the surface of a PET foil and applied to the electrodes similarly as the conductive elastomer. The thickness of the selected PET foil was 0.3 mm. The ink was deposited on the foil by a TG 130 spray gun which can spray very low amounts of ink and enables fine control of spraying. A unique 12V Škoda 8P0012615A compressor originally used for inflating tyres was used as a compressor. Three thicknesses were selected of the deposited ink layer: 7 µm, 15 µm and 23 µm. The thicknesses were obtained by 6-fold, 12-fold and 18-fold repeated application. The spray applications were performed through a template made of the same foil with 3mm holes in view of the 2.5mm outer diameter of the circular electrodes. The thickness of the deposited ink layer was measured with a Mitutoyo SR44x1 digital micrometer with a measuring range of 0-25 mm and accuracy of 0.001 mm.

Shape of the measured electrodes

The dimensions of the measured electrodes are in Fig.1. The measurements were performed on a scanning matrix comprising circular electrodes with a 2.5mm diameter. The same sizes of the electrodes as in paper [8] were used to enable comparison of the properties of tactile sensors with a conductive elastomer with those with a conductive ink. Also the designation of the electrodes was the same. The electrodes were placed on a Cuflex printed circuit board. Conductors were soldered to the outlets of lines and columns which enabled easy choice of a particular electrode. The electrodes are denoted accordingly to their marking “PD“: ϕE=2.5 mm, ϕd=0.1 mm, M=0.1 mm.

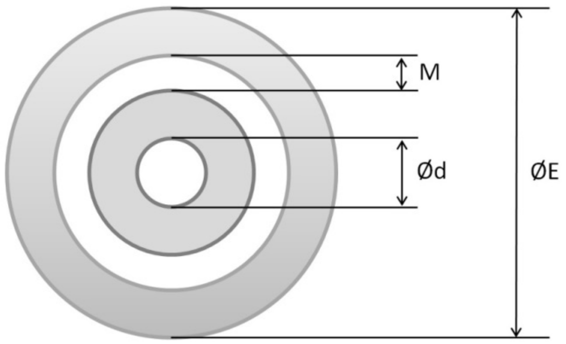

Fig.1. Dimensions of the measured electrodes.

Measurement method

Measurements of the properties of conductive ink were performed at a robotized workplace equipped with a Turbo Scara SR60 robot. Pressure was imposed by means of the vertical motion of the robot´s arm. A Hottinger DF2S-3 tensometer force sensor with a measuring tip with a ϕ3mm circular surface was fixed to the end of the robot´s arm. The foil with the deposited inks was placed on the electrode field. The measuring tip with its circular ϕ3mm surface, which is larger than the diameter of the electrodes, touched down on the surface of one tactile point and pressed on the conductive ink deposited on the foil against the circular electrodes via which the electric resistance of the conductive ink was measured. The pressure imposed on the electrodes was calculated from the known area of the surface of the measuring tip and the exerted force. The output voltage of the type DF2S-3 tensometer force sensor was measured by an Almemo 2890-9 Data Logger [7]. Frequency response of system is possible to measure by [11] eventually.

3. Results

The measured results for LD-type electrodes for all 3 thicknesses of the ink layers - 7 μm, 15 μm and 23 μm – were represented graphically. All measurements were repeated 10 times and the total (combined) measurement uncertainty was calculated and graphically represented by respective intervals for each measured value. In all diagrams both the loading cycle (triangle points) and the unloading cycle (round points) were repeated.

Fig. 2 presents this graphical result for the conductive ink of thickness 7 μm. Hysteresis is apparent in all electrodes, similarly as in the case when a conductive elastic material was used, however, it is much lower [8]. Initial insensitivity is apparent in all electrodes which are obviously caused by the force necessary for the touch-down of the foil with the deposited ink on the electrodes.

Fig. 3 gives the comparison of the dependence of the variation of resistance on the pressure during loading of LD-type electrodes for various thicknesses of the deposited ink layer. From the diagram it is apparent that maximum sensitivity is achieved for a 7μm thickness of the deposited ink.

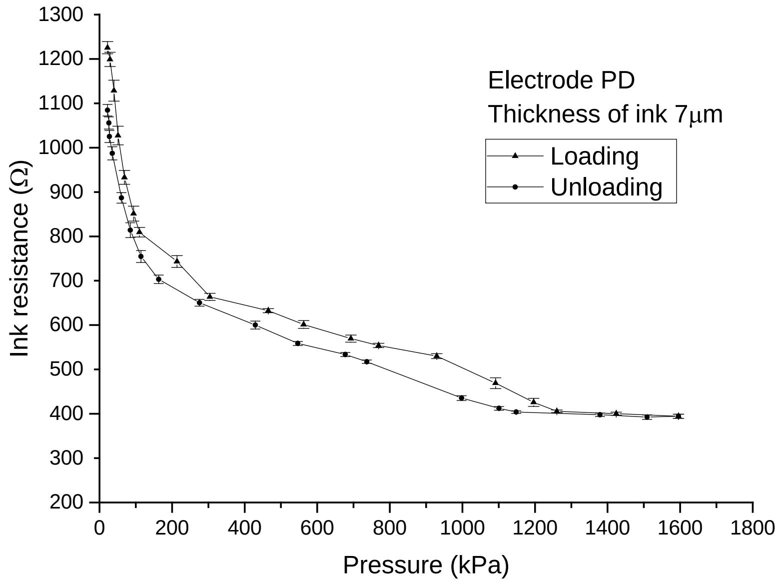

Fig. 2. Dependence of resistance of a 7 μm thick ink layer on the pressure for a PD-type electrode.

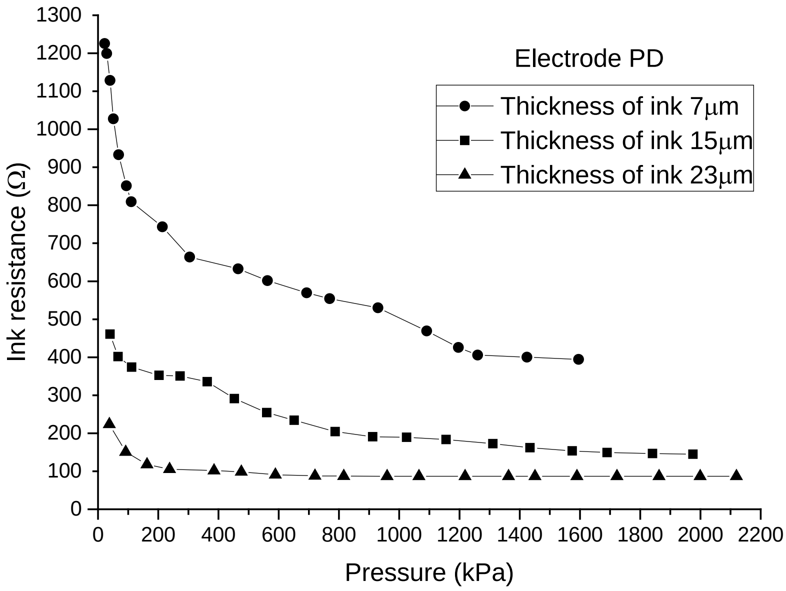

Fig.3. Comparison of PD-type electrodes.

4. Discussion

The aim was to measure the effect of conductive ink on the properties of a tactile transducer. Conductive ink was used as a converter of force to electric resistance. Electrodes are used in the Plantograf V12 apparatus. Here, however, up till now a conductive elastomer was used. We measured PD-type electrodes with conductive ink. Three differently thick ink layers were used for the measurements and their effect determined on the variation of the electric resistance of ink in dependence on the exerted force. Four different types of conductive inks with various properties were tested. Carbon ink DZT-3K appeared to be most appropriate. When applied to the surface of the electrodes it had a very low resistance to mechanical stress and hence an alternative method was selected, i.e. deposition of the ink on a foil substrate which was then pressed against the surface of the electrode.

The dependence of the variation of electric resistance of ink on the magnitude of the load was performed with a Turbo Scara SR60 robot. The measuring electrodes showed best results for a 7μm thick ink layer. Such a combination of electrodes and ink thicknesses gave the best sensitivity, resolution and a partially linear character. Higher thicknesses increased the conductivity of the sensor and consequently decreased its resolution. All measurements showed hysteresis caused predominantly by the inaccuracy of positioning of the robot and relaxation of the ink and foil.

Measurements proved that conductive ink can act as a force transducer converting force to electric resistance. Its application, however, is affected by a number of factors and selection of the most appropriate ink is not easy. A great problem with ink is its adherence and resistance to mechanical stress on the surface of the electrodes. The measurements are expected to continue with other types of conductive inks.

Acknowledgements

The measurements were carried out within the IGA project of the Faculty of Engineering, Czech University of Life Sciences in Prague.

References

[1] Volf J, Trinkl A, Novák M, Bílek J, Prikner P, Neuberger P. Plantograf V12 with Optimal Size Determination Sensor Electrodes and its Using for Pressure Distribution Between Tire and Road. In XX World Congress IMEKO, Busan, 2012, 1-4, ISBN 978-89-950000-5-2 95400.

[2] Volf J, Papežová S, Vlček J, Novák P. Gait Locomotion Analysing System for Relevant Measurement Pressure Cognition. In Proceedings ISHF, Lisbon: Faculdade de Motricidade Humana, 2007, 155-160, ISBN 978-972-735-145-9.

[3] Volf J, Vlček J, Papežová S, Novák P. Orthopaedic Investigation System For Medical Non-Invasive Diagnostics. In IMEKO - XVIII World Congress and IV. Brazilian Congress of Metrology, Rio de Janeiro: IMEKO, 2006.

[4] Volf J, Holy S, Vlcek J. Using of Tactile Transducer for Pressure Distribution Measurement on Sole. *Sensor and Actuators A62*. Physical, ELSEVIER SEQUOIA S.A., 556-561, Lousanne, Switzerland 1997.

[5] Volf J, Trinkl A, Růžička M, Novák M. Optimal Size Determination of Tactile Sensor Plantograf V08 and its Electrodes. In 26th Symposium on Advances in Experimental Mechanics, Leoben, Austria 2009. ISBN: 978-3-902544-025.

[6] Volf J, Trinkl A, Novák M, Bílek J, Prikner P, Neuberger P. Plantograf V12 with Optimal Size Determination Sensor Electrodes and its Using for Pressure Distribution Between Tire and Road”. In XX World Congress IMEKO, Busan, 2012, 1-4, ISBN 978-89-950000-5-2 95400.

[7] Lufinka J. Effect of Conductive Ink on Properties of Tactile Transducers. Diploma thesis, CULS, Prague, 2014 (In Czech).

[8] Trinkl A, Optimization of Design of Flat Tactile Transducers. *Dissertation*, CULS, Prague, 2011 (In Czech).

[9] Souza F.G, Michel R.C, Soares B.G. A methodology for studying the dependence of electrical resistivity with pressure in conducting composites. *POLYMER TESTING,* 24 (8): 998-1004, 2005.

[10] Soares B. G, Amorim G.S, Souza F.G, et al. The in situ polymerization of aniline in nitrile rubber. *SYNTHETIC METALS,* 156 (2-4): 91-98, 2006.

[11] Pavlovkin, J. - Novák, D.: Messung der Frequenzcharakteristiken von Passivfilter mittels des Systems rc2000. *EDUKACJA–TECHNIKA–INFORMATYKA,* 3 (2) 257-264, 2012

Testing of EMC Properties of Electrical Devices Equipped with Wireless Communication

J. Hallon, R. Harťanský, M. Bittera

Slovak University of Technology in Bratislava, Faculty of Electrical Engineering and Information Technology, Institute of Electrical Engineering, Bratislava, Slovak Republic,

Email: jozef.hallon@stuba.sk, rene.hartansky@stuba.sk, mikulas.bittera@stuba.sk

Abstract. *The paper is focused on finding the optimal measurement setup for measuring radiated emissions of devices using wireless transmission paths. The priority is to ensure the full functionality of equipment under test while functionality of measuring system is not affected. A model of the measurement site for analysis of these conflictions was created in numerical simulator and the simulation results were verified by measurements.*

Keywords: EMC, Radiated Emission, Antenna, GSM

1. Introduction

Nowadays, except of common cable transmission paths (LAN, USB, RS485) modern electrical devices have increasingly used wireless transmission paths, as: Wireless LAN (Wi-Fi, WiMAX), PAN (Bluetooth), WAN (2G/3G mobile networks), satellite navigation (GPS) and many others [1]. Electromagnetic compatibility (EMC) properties of equipment under test (EUT) need to be verified in its typical operation condition [2]. Then modification of the measurement procedure is required and an anechoic shielded chamber, as site for radiated emission measurement, hast to be equipped with a new apparatus that enable wireless data transfer from/to the EUT.

This paper focuses on finding the optimal radiated electromagnetic (EM) emissions measurement arrangement which keeps full functionality of the EUT so the measuring system operates without a failure. We created a model to analyze effect of auxiliary devices (used for the wireless transmission) on the measurement process. The model was created in numerical simulator FEKO. Simulated results were verified by measurements.

2. Measurement setup

Shielded chamber prevents the wireless communication in principle. Also due to filtering requirements in wide frequency range the chamber complicates a wire data transfer between devices located inside and outside (because signal filters has to be a part of a measurement chain). The standard measurement methodology requires that the EUT was placed on a measuring table or on the floor of the shielded chamber. Measuring antenna is located in a distance of 3 or 10 m from the EUT [3]. The antenna and the EUT are located in the two foci of imaginary ellipse, creating an obstruction-free area, which defines a minimum area free from scatterers of electromagnetic field (Fig.1). Wireless communication of the EUT requires creating a connection which provides bidirectional data transmission between the EUT and auxiliary equipment situated outside the shielded chamber. In our case we tried to find a solution of a connection between the EUT and mobile phone/data networks. Technical realisation for other wireless networks is similar.

WAN (World Area Network) connection to the EUT needs a communication system (outside shielded chamber) consisting of GSM antenna and repeater that receives and amplifies properly signal of nearby base stations. This signal is applied through coaxial cables and feedthrough filter to the GSM antenna inside the chamber. Location of the GSM antenna inside the chamber and GSM signal level have to choose to enable EUT a reliable communication, while the measuring antenna should receive GSM signal of sufficiently low level (ideally less than relevant limit level, but definitely cannot exceed maximal input power of a measuring preamplifier). High level of signal can cause a disruption of proper function of the measuring preamplifier and then a degradation of the measurement.

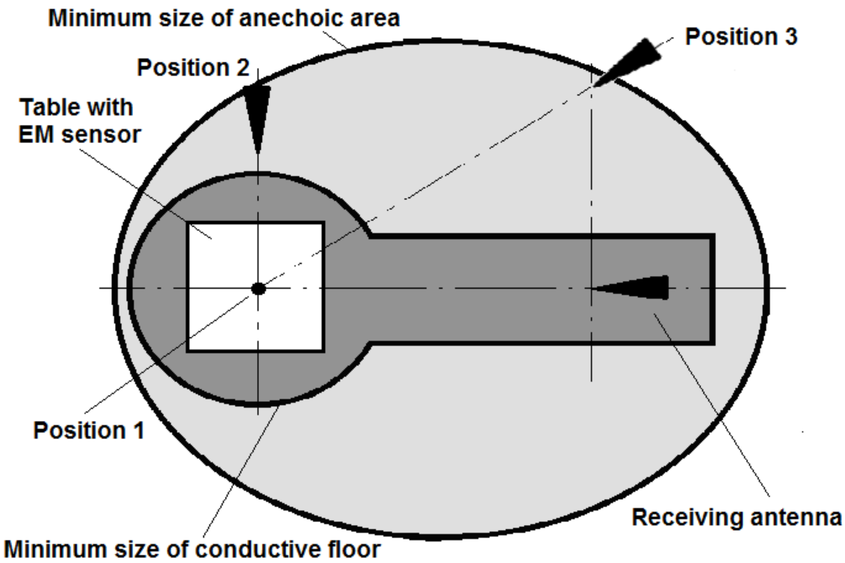

Fig. 1. Setup modifications for radiated emissions measuring

Several GSM antenna locations may be chosen in a shielded chamber (8.5×4.5×4.5 m): These locations have to fulfill following requirements: minimal interference with the obstruction-free area, antenna main lobe cannot direct to the receiving antenna and also a convenient connection of GSM signal to the antenna.

Our experiments were performed with only vertically polarized GSM antenna which was situated in the following three positions (Fig.1): advantage (+) / disadvantage (–)
1 – A rod antenna 10 cm long (located in a cylindrical hollow in a reference ground plane under the measuring table together with power plugs and signal connectors. The antenna is practically connected to one of the RF connector, other side of this connection is outside the chamber (+). Although the antenna is non-directive (–), its location, partially embedded in the floor, helps to reduce effect of the antenna presence on measuring antenna (+).
2 – Directional antennas (YAGI GSM-900, Log-periodic (LP) 300-1000 MHz or HORN 1-18GHz) are perpendicular to the main axis of the chamber, in height of the measuring table, tip of the antenna is situated 1 m from the table. This represents a suitable location because of the antennas directivity (+), the antennas are partly situated in the obstruction-free area (–, however in the larger chamber it is not a problem).
3 – The antennas (YAGI, LP and HORN) are oriented obliquely toward the main axis of the chamber (directed to the table centre) and distance between tips of GSM antenna and the receiving antennas about 150 cm. Such a position is less convenient due to patterns of the antennas (–), however the antennas are outside the obstruction-free area (+).

3. Modeling and measurement

The aim of modeling is to determine level of the GSM signal caused by various position and types of the GSM antennas in the position of receiving antenna if level of the GSM signal in the table centre is 1 V/m. This value were chosen in order to verify the experiment by measuring with omni-directional sensor of EM fields placed on the table, because the value of 1 V/m is a minimal value reliably measured by the sensor. We focused on frequencies of 900, 1800, 1900 and 2100 MHz, which corresponds with GSM 900, GSM 1800, UMTS up-link and down-link frequencies. EM numerical simulator FEKO was chosen to search optimal GSM antenna position. Used model includes a reference ground plane with same dimensions as the chamber has and with the hollow in the table position. Hybrid absorbers of the chamber were replaced by the open space and a wooden table, which has not significant effect on the propagation of EM waves was omitted to simplify the model [4]. For calculation purposes, several numerical methods were necessary to use because the model is very large in terms of the GSM signal wavelength. Properties (near field, radiation pattern, etc.) of the antennas were calculated using method of moments, while propagation of EM waves over the conducting plane was calculated by means of physical optics [5]. Typical distribution EM field generated by the rod antenna at frequency of the GSM-900 is shown in Fig. 2. To speed up a calculation in case of the HORN antenna EM field source the factory radiation pattern was used and then it was verified by measurements.

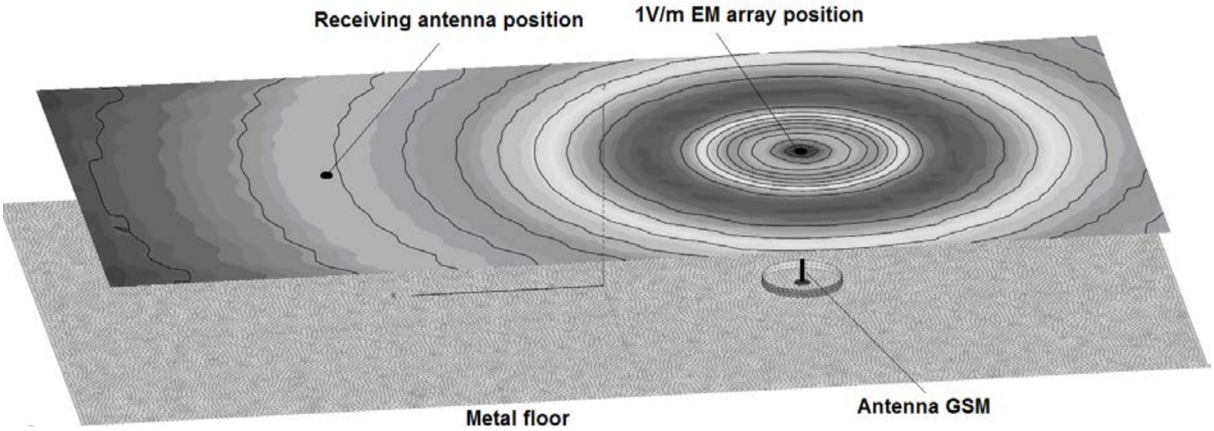

Fig. 2. EM field distribution when rod antenna is used for the GSM-900.

As the lowest signal peak value necessary for reliable function of most devices with GSM or UMTS interface, value of 60 dBμV/m was experimentally determined. Then all simulated as well as measured signal levels at the receiving antenna were recalculated so that these values correspond to real GSM or UMTS operation in the shielded chamber.

4. Results and discussion

All the measured E_{meas} and simulated E_{sim} levels of EM fields at the position of the measuring antenna are summarized in the following table. The values of EM field in a position of the receiving antenna may slightly exceed the limit values prescribed by general EMC standards, however, there is no risk of preamplifier saturation or the measurement distortion at these levels.

Comparison of the EM field values in a position of the receiving antenna shows that position 2 and using HORN or YAGI antenna best suit for GSM field excitation. We observed the GSM levels exceeding the limit values significantly in position 3, so this position is unacceptable. The rod antenna (at position 1) radiation slightly exceeds the limit receiving antenna, but configuration 1 is a very practical solution. However it is necessary to be careful with output level of the GSM repeater, mainly not to exceed the input power of the antenna's preamplifier.

<table>
<tr><th>ROD</th><th colspan="8">position 1</th></tr>
<tr><td>f [MHz]</td><td colspan="2">900</td><td colspan="2">1800</td><td colspan="2">1900</td><td colspan="2">2100</td></tr>
<tr><td>E_{sim} [dBμV/m]</td><td colspan="2">59</td><td colspan="2">58</td><td colspan="2">62</td><td colspan="2">55</td></tr>
<tr><td>E_{meas}[dBμV/m]</td><td colspan="2">60</td><td colspan="2">43</td><td colspan="2">63</td><td colspan="2">50</td></tr>
<tr><th>YAGI</th><th colspan="2">position 2</th><th colspan="2">position 3</th><th>LP</th><th colspan="2">position 2</th><th>position 3</th></tr>
<tr><td>f [MHz]</td><td colspan="2">900</td><td colspan="2">900</td><td>F [MHz]</td><td colspan="2">900</td><td>900</td></tr>
<tr><td>E_{sim} [dBμV/m]</td><td colspan="2">26</td><td colspan="2">45</td><td>E_{sim} [dBμV/m]</td><td colspan="2">26</td><td>45</td></tr>
<tr><td>E_{meas} [dBμV/m]</td><td colspan="2">29</td><td colspan="2">41</td><td>E_{meas} [dBμV/m]</td><td colspan="2">29</td><td>41</td></tr>
<tr><th>HORN</th><th colspan="4">position 2</th><th colspan="4">position 3</th></tr>
<tr><td>f [MHz]</td><td>900</td><td>1800</td><td>1900</td><td>2100</td><td>900</td><td>1800</td><td>1900</td><td>2100</td></tr>
<tr><td>E_{meas} [dBμV/m]</td><td>41</td><td>41</td><td>41</td><td>41</td><td>55</td><td>53</td><td>56</td><td>58</td></tr>
</table>

5. Conclusions

Optimal measurement setup was searched for coexistence of wireless data transmission system and measurement system for radiated emission. Simulated and measured results of the EM field levels are in quite good agreement. The differences may be caused by imperfection of the model, which is always a compromise solution (of model perfection and computing power demand). Presented model may be even in this simplified form used for mapping the distribution of EM fields generated by GSM antennas in shielded enclosures. This fact enables (for various configurations of the EUT and selected GSM antennas) to determine EM field at the receiving antenna and to gain important information for the chamber arrangement. In addition, obtained information can be used to adjust the optimum GSM signal level in the GSM signal path.

Acknowledgements

Work presented in this paper was supported by the Slovak Grant Agency VEGA under grant No. VEGA 1/0431/15.

References

[1] Rappaport TS. Wireless Communications: Principles and Practice. 2nd Ed., Prentice-Hall, Upper Saddle River, NJ, 2002.

[2] IEC 61000-1-2:2001. Electromagnetic compatibility (EMC) - Part 1-2: General - Methodology for the achievement of functional safety of electrical and electronic systems including equipment with regard to electromagnetic phenomena. 2001.

[3] EN 55016-2-3:2010. Specification for radio disturbance and immunity measuring apparatus and methods –Part 2-3: Methods of measurement of disturbances and immunity – Radiated disturbance measurements. 2010.

[4] Maršálka L. Complex electromagnetic sensor structure analysis by numerical modeling. In EQ-2014: In the framework of International Forum "Education Quality - 2014", Izhevsk, Russia, 2014, 260-263.

[5] Bitttera M, Harťanský R. EM Field measurement Aspects for Electromagnetic Compatibility Purposes. In *Measurement Science Review*. Vol. 6, section 3, No. 1, 2006, 14-17.

Comprehensive Numerical Analysis of Designed Force Sensor Based on Changes of Electromagnetic Field Properties

L. Marsalka, R. Hartansky, V. Smiesko

Slovak University of Technology, Faculty of Electrical Engineering and Information Technology, Institute of Electrical Engineering, Bratislava, Slovakia
Email: lukas.marsalka@stuba.sk

Abstract. *This paper deals with force sensor design applicable to measure the forces up to 10 N. Presented sensor is based on the method which is capable to indirectly measure the forces using deformation of load cell. The resonance circuit frequency is primarily affected by deformation or mutual change of load cell specific parts. The resonation circuit itself together with load cell is understood as one single unit. The resonance effect can create the chance of properties in surrounding EM field. This change is easily recognized by change of EM radiator input parameters variation. Our discussed sensor proposal could be used not only in academic sphere but also could have a practical application.*

Keywords: Pressure Sensor, Load Cell, Electromagnetic Field Properties, Resonance Circuit

Introduction

Nowadays there is an exponential growth of the applications, where the force measurement is a goal. The large amounts of application where these measurements are used impose the requirements for sensor characteristics. Beside the basic characteristics like resolution, range and linearity, there could be material and shape realization characteristics also taken into account. For example, in medical area, the MRI device does not allow any ferromagnetic material within its vicinity. Force sensor is one of the most important sensors in robot force control system. These sensors are used to perceive the contact force between the operator and external environment. In this case the shape of force sensor is also very important due to its implementation to the robotic construction [1].

The load cell technology is very popular in matter of force investigating and measuring. As a technology for force sensing, load cell is attractive also because of the fact, that underlying technology are relatively mature and well known. The crucial sensing element is a strain gauge, which is difficult to produce in the case of micro meter scale and is not suitable for unsparing treatment.

The main objective of this paper is to focus on the design of mechanical part – elastic body and electrical part – resonance circuit, which together create a force sensor. The design of elastic body shape was oriented to creation of planar parts, which mutual position is changed by value of sensing force. This effect produces a direct influence to the properties of electrical part of designed sensor. Electrical part of sensor – resonance circuit, makes use of resonance effect which takes the information about measured force. This information is propagating in change of electromagnetic (EM) field which surround designed sensor. This change is easily detected at the input terminal of EM field radiator.

Theoretical background of sensing principle

A physical essence of sensing principle is based on mutual interaction of simple wires structure (Fig. 1). Active wires (marked as 1) generate the EM field and therefore the properties of generated EM field are changed by presence of the next wire (marked as 2).

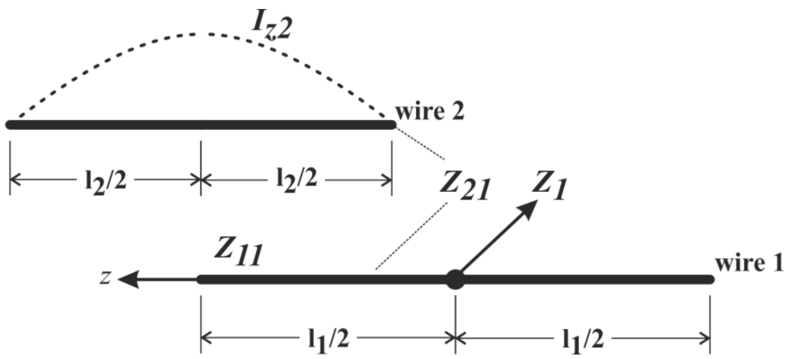

Figure l Mutual coupling of wire structure

The mutual interaction between wire 1 and wire 2 is possible to describe by mathematical formula for mutual impedance:

$$\dot{Z}_{21} = -\frac{2}{\dot{I}_{2k}}\int_{-l_2/2}^{l_2/2} \dot{E}_{z12}(z)\dot{I}_{z2}(z)dz \qquad (1)$$

where:

$\dot{E}_{z21}(z')$ –tangential part of EM field intensity at the point z_2
$\dot{I}_2(z')$ – current distribution across wire 2
$\dot{I}_{2k}$ – the maximal current value on the input terminals of wire 2.

Input parameter – input impedance of wire structure Z_1 is possible to express by simple mathematical formula (2). This formula describes contribution of mentioned mutual effect to the input parameter of wire 1.

$$\dot{Z}_1 = \dot{Z}_{11} + \dot{Z}_{21} \qquad (2)$$

where:

$\dot{Z}_{11}$ – self impedance of wire 1

The solid line graph (Fig.2) indicates the frequency course of wire structure input impedance in dependence on the length of wire 2. This length change can causes the different frequency position of the local minimum. According to [2], this phenomenon is given by resonance of wire 2 let while the value of this resonance is corresponding to the length of wire 2. By using this mutual effect there is possible to directly measure the length or on the other hand to indirectly measure others quantities like force and et cetera.

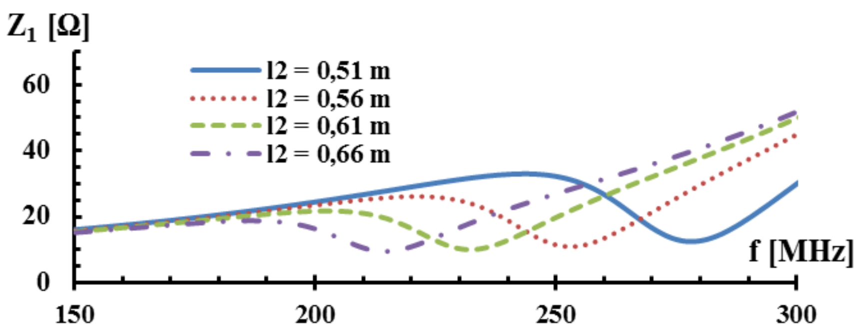

Figure 2 Changes of waving wire structure input impedance as a function length of wire 2

Design of force sensor model for numerical simulation

The final designed shape of proposed elastic body with full load is shown in figure 3. Let us focus to the part of elastic body, where is only negligible deformation influence. This part plays an important role in the application of resonance circuit. Design and numerical simulation of elastic body was executed by simulation software *Multiphysic Comsol* [3].

But the direct implementation of wire structure (Fig.1) is impossible in area of force sensing. Due this fact it is necessary to replace the wires by more convenient elements to force sensing. Our proposed solution is illustrated at the figure 3b).

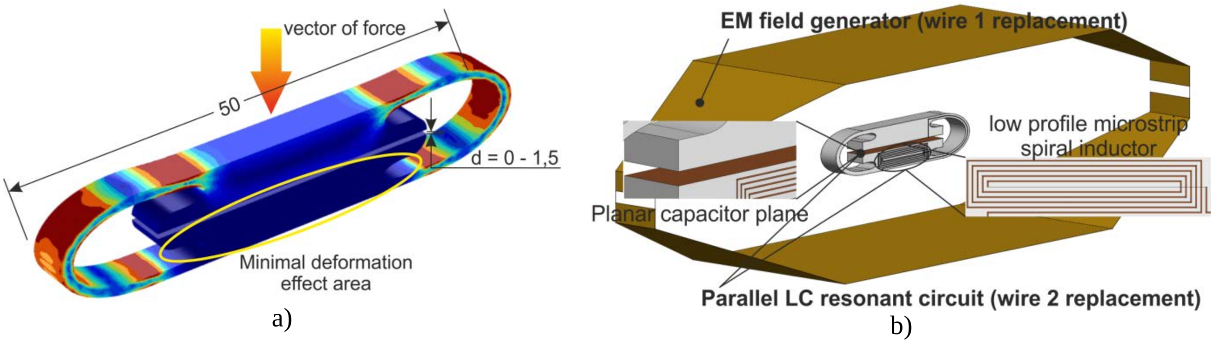

Figure 3. a) Designed mechanical part of pressure sensor (full load $d = 0$ *mm*, dimensions in *mm*), b) implementation of electrical and resonance parts

The wire 1 is replaced by EM radiator with constant input frequency characteristic. The constant course of characteristic is key to be capable to observe the resonance effect more precisely. This kind of EM field radiator is usually knows as *stripline* [4].

The possible replacement of resonance element (wire 2) can be created by parallel resonance LC circuit as we can see at the figure 3b). The main problem still remains to be the technical realization of the inductor. Because of the position of elastic body implementation and measurements of this position there was low profile micro strip spiral inductor chosen. The capacitor or more precisely the capacitor plates are created by silver layer on elastic body planar part.

The sensor resonance frequency is tuned directly to corresponding elastic body deformation. The change of resonance frequency is dependent only to the capacity of the capacitor in this case. Other parameters of resonance circuits are constant during the whole sensing process. The value of capacitor capacity is given only to the mutual distance of capacitor plates d ($0 < d < 1.5$ *mm*). The inverse proportionality is between the capacitor plate distance and sensing value of force.

Results of numerical simulations

A detailed numerical analysis is very important to resonance effect investigation of designed sensor. The numerical *moment method* was used to calculation of EM field changes. Material constants were defined for particular parts of sensor: stripline, inductor – copper, capacitor plates – silver, elastic body – teflon.

The selected frequency courses of stripline input impedance are illustrated at following solid line graph (Fig. 4a). The resonance effect is very clear in the aspect of frequency position of the local minimum in this case too.

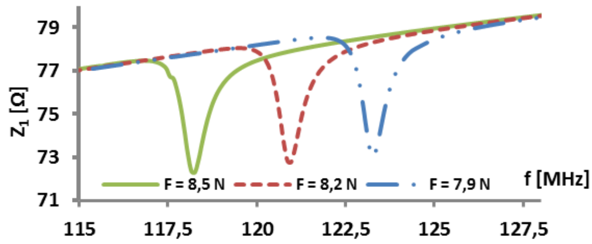

a)

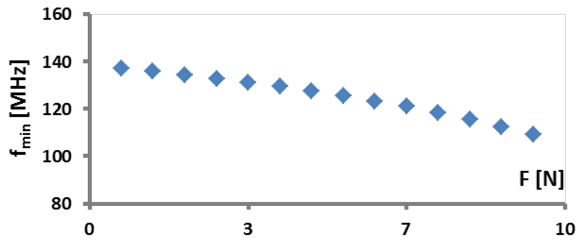

b)

Figure 4. a) resonance effect on the stripline input port, b)transfer curve of sensor obtained by results of numerical simulation

The transfer curve of designed sensor is plotted at the figure 4b. This characteristic was created from results of numerical simulations. The constructed transfer characteristic presents the relationship between sensing value of force and frequency value of resonance effect. This frequency value plays a key role in the next interpretation process.

Conclusions

The presented paper is primarily dealing with design and numerical implementation of force sensor based on the changes of EM field characteristics. These changes are caused and influenced by the shape deformation of our presented load cell structure or more specifically said by the characteristic changes of the most crucial element of sensor - resonance circuit. The detailed numerical analysis confirms the validity and functionality of our presented theory. The described principles of force measurements appear to be very perspective and useful also for other non-electrical quantities like length, vibration, pressure and so on.

Acknowledgements

This work was supported by the Slovak Research and Development Agency under the contract no. APVV-0333-11, by the project VEGA VG 1/0431/15 and by the project ITMS 26240220084.

References

[1] Kumar N, Piccin O, Meylheuc L, Barbe L, Bayle B. Design, development and preliminary assessment of a force sensor for robotized medical applications. *2014 IEEE/ASME International Conference on Advanced Intelligent Mechatronics*. 8-11 July, 2014, s. 1368-1374.

[2] HARTANSKY, R., MARSALKA, L. Wire Structures Mutual Impedance Change in Electromagnetic Field. *Journal of Electrical Engineering Vol. 63, No. 7/s.* s. 152--155. ISSN 1335-3632

[3] HRICKO, J. Sensors and Compliant Robotic Mechanisms for Harsh Working Environments, *Proceedings of the RAAD 2013, 22th International Workshop in Aple-Danube Region*, Portorož, Slovenia, September 11 – 13.

[4] Krammer, A. Bittera, M. Distributed Impedance as Terminating Load at GTEM Cell. In *EMD'2012 : 22nd International Conference "Electromagnetic Disturbances EMD'2012". Vilnius, Lithuania, September 20-21, 2012* : Vilnius Gediminas Technical University, 2012, s.52-55. ISBN 978-609-457-260-9.

Influence of the Environment on the Accuracy of Measurement with Radar Level Gauges

P. Mikuš, R. Harťanský, V. Smieško

Slovak University of Technology in Bratislava, Faculty of Electrical Engineering and Information Technology, Institute of Electrical Engineering, Bratislava, Slovakia

Email: peter.mikus@stuba.sk

Abstract. *This article deals with the problem of the influence of the measuring environment on the accuracy of measurement devices working on the base of the electromagnetic waves. In the measuring environment can occur various steel installations, e.g. constructions which consist of cylindrical steel beams. The radar level gauge is a source of the electromagnetic waves. The input part of the radar level gauge receives reflected waves from the reference interface (reflection board). If the measuring environment contains steel installations, the receiving of the electromagnetic waves can be influenced by high frequency phenomena on the construction. In this article we focus on analytical calculation of the electric field around the steel beam.*

Keywords: Diffraction, Steel Beam, Electromagnetic Field, Radar Level Gauge

1. Introduction

The radar level gauge is a device which measures the distance by using radar technique. It consists of two basic parts: a transmitter and a reciever. The transmitter consists of a signal generator and a parabolical antenna. The receiver is composed of a parabolical antenna, an amplifier, a RF decoder, a circuit with the volltage comparator and a powerline circuit. The worked frequency of the electromagnetic wave is about *10 GHz.* These level gauges are not sensitive to the changes of temperature, pressure, density and the composition of the gas in the measuring environment. The important condition of the measuring process is a correct response of the electromagnetic wave. These devices must be regularly calibrated. The process of calibration is carried out in the accredited laboratory. [1]

The construction of the laboratory

The laboratory for the calibration process of the radar level gauge has given dimensions *16x2,6x1,9 m*. The steel beams which hold the metal guide rail (*2.20 m* high) are fixed under the ceiling of this environment. On this metal guide rail moves the reflection board. By moving of the reflection board simulates measured distance. At one end of the hall is located a massive rack that holds the calibrated level gauge of *1.35 m* above the floor and the etalon of the length - the laser interferometer. In the process of calibration can occur several disturbances. Unless unlimited space is available, there can appear the disturbing effects. The radiation angle of level gauge is *10°* and the steel beams are *0.85 m* distant. From these data we can calculate when steel beams will be irradiated. [1]

$$tg\alpha = \frac{d}{x} \Rightarrow x = \frac{d}{tg\alpha} = \frac{0.85}{tg5} = \frac{0.850}{0.088} = 9.7\,\text{m} \tag{1}$$

d – distance from the ceiling

α – the half of the radiation angle of the level gauge

The construction of this laboratory and the radiation angle of the level gauge are shown in the figure 1a. There are high frequency phenomena (diffraction) on the steel beams at a distance of about *9,7 m* in our conditions. It means that there will occur distortion of measured values if the measuring distance is longer than *9.7 m* . In this article we focus on the solution of the diffractions problem. We would calculate how is influenced the electric field around the steel beam by the diffraction. [1]

2. The diffractions on the steel beam

The steel beam has a cylinder shapes. The circular cylinder, because of its simplicity and its solution is represented in terms of well known and tabulated functions (such as Bessel and Hankel functions). Let us assume that a plane wave is normally incident upon a perfectly conducting circular cylinder of radius *a*, as it is shown in figure 1b.

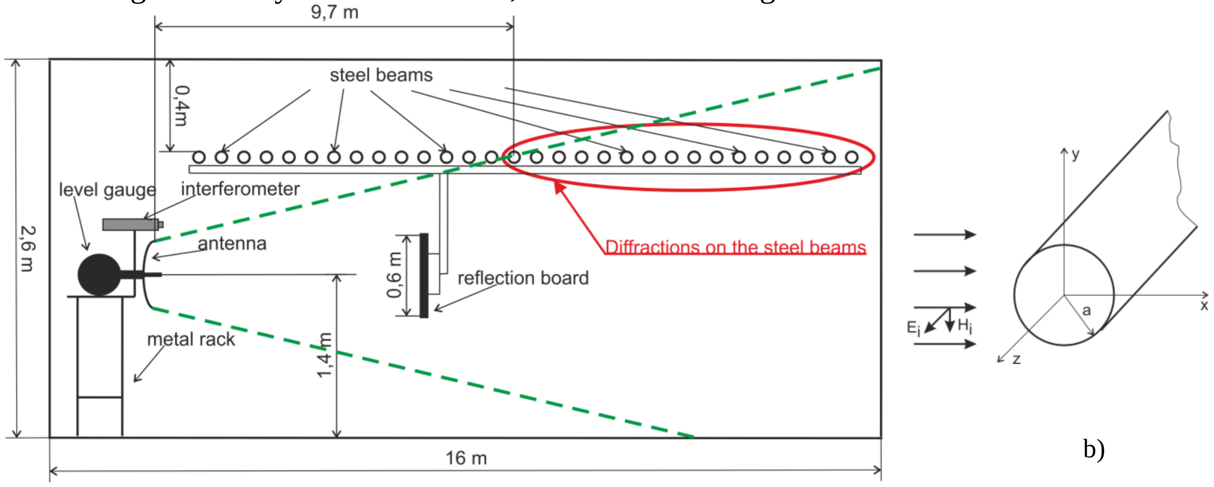

a)

Fig. 1. a) Construction of laboratory with radiation pattern of radar level gauge, b) Plane wave incident on conducting circular cylinder

The incident electric field can be written by [2] as

E_i – incident electric field
J – Bessel function
Φ – angle of observation point
ε_n – Neumann coefficient

$$E_i = \hat{a}_z E_0 (-j)^n \varepsilon_n J_n(k\rho)\cos(n\Phi) \quad (2)$$

The total electric field around the conductive cylinder

E^i – incident electric field
E^t – incident electric field
E^s – incident electric field

$$E^t = E^i + E^s \quad (3)$$

where E^s is the scattered field. Since the scattered fields travel in the outward direction, they must be represented by cylindrical traveling wave functions. Thus we choose to represent E^s by [2]

$H^{(2)}$ – Hankel function of second order
ρ – distance between source of E field and cylinder
k – wave number
a – radius of cylinder

$$E^s = -E_0 \sum_{n=0}^{\infty} (-j)^n \varepsilon_n \frac{J_n(ka)}{H_n^{(2)}(ka)} H_n^{(2)}(k\rho)\cos(n\Phi) \quad (4)$$

3. The diffractions on the steel beam with decreasing of incident field

The solution of diffraction described in chapter 2 is correct, if the incident field is the same in the whole environment. We decided to solve this problem by using the decreasing incident field to ensure better results. Then the incident electric field can be written as

$$E^i = \hat{a}_z E_0 \frac{e^{-jk\rho}}{k\rho} \quad (5)$$

The curve of incident field along the environment is shown in the figure 2a.

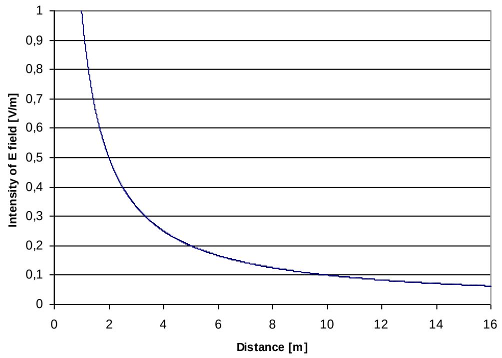

a)

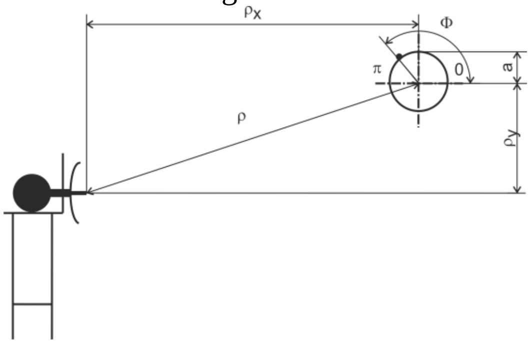

b)

Fig. 2. a) Intensity of electric field along the environment, b) representation of distance the steel beams from level gauge ρ and radius of beam a

If the intensity of the electric field will decrease, it is clear, that the intensity of electric field on the steel beam surface with radius a will be variable too. In the solution is considered only distance ρ, which is described in the chapter 2. Now we calculate the distance for the individual points on the surface of steel beam by using formula (6). The individual dimensions are shown in the figure 2b.

ρ_x – distance between source of E field and cylinder in x axis
ρ_y – distance between source of E field and cylinder in y axis

$$\rho = \sqrt{\rho_x^2 + \rho_y^2} + a\cos\Phi \tag{6}$$

We apply the new proposal of calculating distance ρ to formula (5).

$$E^i = \hat{a}_z E_0 \frac{e^{-jk\rho}}{k\rho} = \hat{a}_z E_0 \frac{e^{-jk(\rho + a\cos\Phi)}}{k(\rho + a\cos\Phi)} \tag{7}$$

By editing the formula (7) step by step and then by using Bessel functions we can write the incident electric field in the form (8). Just this part of our solution is important. This is unique equation, which we made.

$$E^i = \hat{a}_z E_0 \frac{e^{-jk\rho}}{k\rho}\left[J_n(ka) - \frac{a}{\rho}\left[J_{n+1}(ka) - J_{n-1}(ka)\right]\right] \tag{8}$$

We can use formula (6) in the equation (4) similarly as in the previous case. We obtained the final form of equation for calculating scattered field around the steel beams in regard to decreasing incident electric field.

$$E^s = -E_0 \sum_{n=-\infty}^{\infty} j^{-n} \frac{J_n(ka) - j^{-(n-1)}\frac{a}{\rho}\left[J_{n+1}(ka) - J_{n-1}(ka)\right]}{H_n^{(2)}(ka)} H_n^{(2)}(k\rho) e^{jn\Phi} \tag{9}$$

For the comparison we made testing calculations. The results of our calculations we can see in the following chapter.

4. The results

For the comparison we calculated the total electric field around the steel beam with radius *6 cm* observed in distance 30 cm from surface of the beam. The total electric field is sum of incident and scattered electric field. The first results are obtained from formulas (2), (4) and they are shown in the figure 3a. The second results are obtained from formulas (8) and (9). There are shown in the figure 3b.

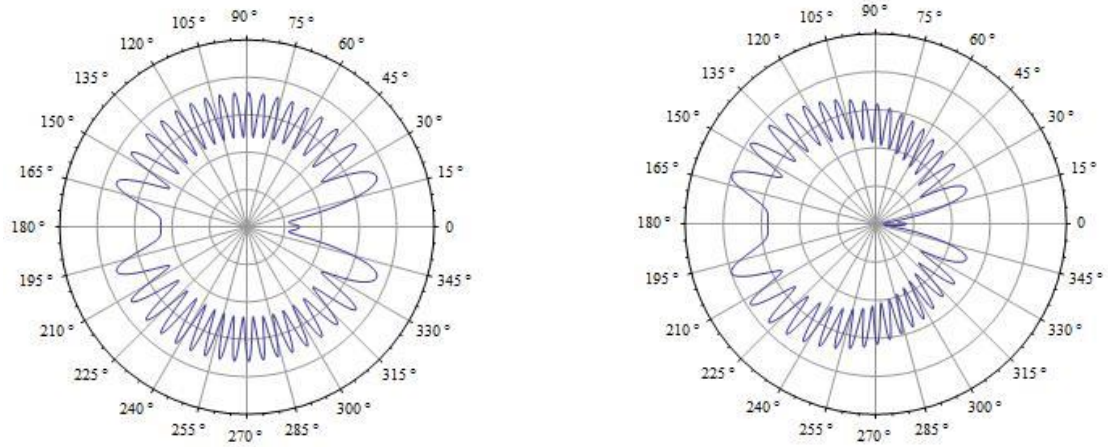

a) b)

Fig. 3. Total electric field around the steel beam a) constant incident electric field, b) decreased incident electric field

As you can see in the pictures, the differences between the first and the second solutions are significant. In the second solution the total electric field is shifted to the left, so the intensity of electric field is higher in front of the beam. In this direction it is also the receiving part of the level gauge. By using both solutions, which are described in the chapter 3, we can obtain more accurate values of the total electric field.

5. Conclusion

In our research we focus on solutions more high frequency phenomena which can occur in the process of calibration of the radar level gauges. The results are applicable in proposal process of accredited laboratory, which carry out calibrations or testing devices on the base of high frequency signals. In this article are presented results obtained by calculating total electric field around the steel beam. We considered constant and decrease incident electric field. The decrease field occurs in the real conditions. The solution, where we considered decrease electric field is very unique and it is our work. We find out the differences between the individual solutions. In the second solution we can obtain more accuracy values.

Acknowledgements

This work was supported by the projects VEGA 1/0431/15, APVV – 0333-11 and ITMS 262402220084.

References

[1] Mikuš, P., Harťanský, R., The Errors in Radar Level Gauge Calibration. In Measurement 2013 : Proceedings of the 9th International Conference on Measurement. Smolenice, Slovakia, May 27-30, 2013. Bratislava:

[2] BALANIS, Constantine A. *Advanced engineering electromagnetics*. 2nd ed. Hoboken: John Wiley, 2012, 602-608. ISBN 978-0-470-58948-9.

Some Features of Dedicated T1-Filters

[1]N.K. Andreev, [2]A. M. Hakimov

[1]Kazan State Power Engineering University, Kazan, Russia
[2]Kazan State University of Architecture and Engineering, Kazan, Russia
Email: ngeikandreev@gmail.com

Abstract. *This report continues developments* of T_1 *-filters aimed for the contrast enhancing in NMR imaging. The characteristic property of the proposed technique is that only 90 and 180 degree pulses are used. The mathematical expressions were presented for transfer functions, time and frequency responses of these filters.*

Keywords: T_1 Filters, NMR, Transfer Functions, Time and Frequency Responses

1. Introduction

Recently T_1 -filters were proposed [1, 2, 3] for the contrast enhancing in NMR-imaging. The structure of the T_1 -filters can be described as

$$90^{\circ} - \tau_1 - 180^{\circ} - \tau_2 - 180^{\circ} - \bullet\bullet\bullet 180^{\circ} - \tau_N - 90^{\circ} \tag{1}$$

The pulse sequences used for the T_1 -filters were named DIFN (differentiation by N exciting radiofrequency pulses) keeping in mind the number of the time intervals between the all pulses and the number of pulses without the last reading 90° pulse. The number of 180° pulses equals to $n = N - 1$. Here n and N are integer numbers.

The aim of the paper is to compare some features of the T_1 -filters with the features of the low-pass Butterworth filters [4].

2. Subject and Methods

One of the features of the polynomials is that the coefficients located symmetrically relative to "the center of gravity" of the polynomials are pairwise equal. These coefficients are calculated by multiplying the factors of the polynomials. The factors are defined by the poles of polynomials. The n poles of the Butterworth filters occur on a circle of radius ω_c (the cut-off frequency) at equally spaced points, and are symmetric around the imaginary axis. The transfer function, $H(s)$, contains only the poles in the negative real half-plane of s.

The frequency response of the Butterworth low-pass filter is maximally flat in the passband and rolls off towards zero in the stopband. The slope of the frequency response $G(\omega) = |H(j\omega)|$ at frequencies higher than the cutoff frequency equals to - $n20$ dB/decade.

Various methods are used to make T_1 -selective pulse sequences in NMR and NMR-imaging. T_1 -filters were proposed for the contrast enhancing. They can be also applied for separation of multicomponent relaxation curves in liquids, heterogeneous and multiphase objects.

The response of the longitudinal magnetization to the pulse sequence (1) is calculated in the following manner. The behavior of the longitudinal magnetization being initially in an equilibrium after excitation by a 90° pulse can be described by

$$M(t) = M_0 - (M_0 - M(0_+))\exp(-\frac{t}{T_1}), \quad (3)$$

where $M(0_-)$ and $M(0_+)$ are the magnetization values prior to and after the exciting pulse.

$$M(0_+) = M(0_-)cos\beta. \quad (4)$$

If $\beta = 90^\circ$, $cos\beta = 0$, and for the saturation-recovery (SR) pulse sequence

$$M(0_+) = 0, M_z(t) = M_0 \left[1 - \exp\left(-\frac{\tau}{T_1}\right)\right] = M_0\,[1 - \mathrm{E}(\tau)]. \quad (5)$$

Here the notation $\mathrm{E}(\tau) = \exp\left(-\frac{\tau}{T_1}\right)$ was introduced.

Then, if $\beta = 180^\circ$, $cos\beta = -1$, and for the inversion-recovery (IR) pulse sequence

$$M_z(t) = M_0 \left[1 - 2\exp\left(-\frac{\tau}{T_1}\right)\right] = M_0\,[1 - 2\mathrm{E}(\tau)]. \quad (6)$$

Calculations can be simplified by introducing the designation $E_i = E(\tau_i)$ and letting $M_0 = 1$.

For $T_1, \tau \gg T_2$ only M_z can be considered.

After the pulse sequence (1) with $i = N$ time intervals, the magnetization equals to

$$M_z(\tau_i) = 1 - 2E_i + 2E_iE_{i-1} - 2E_iE_{i-1}E_{i-2} + \cdots + (-1)^i E_iE_{i-1}E_{i-2} \ldots E_1. \quad (7)$$

The pulse sequences were tested and the time intervals were modified in analog to the electronic and digital filters. After optimization, they became

$90^\circ - \tau_0 - 180^\circ - \tau_0 - 90^\circ$; DIF2

$90^\circ - \tau_0 - 180^\circ - 2\tau_0 - 180^\circ - \tau_0 - 90^\circ$; DIF3

$90^\circ - \tau_0 - 180^\circ - \tau_0(\sqrt{2}+1) - 180^\circ - \tau_0(\sqrt{2}+1) - 180^\circ - \tau_0 - 90^\circ$; DIF4

$90^\circ - \tau_0 - 180^\circ - \tau_0(\sqrt{3}+1) - 180^\circ - \tau_0(\sqrt{3}+2) - 180^\circ - \tau_0(\sqrt{3}+2) -$

$-180^\circ - \tau_0(\sqrt{3}+1) - 180^\circ - \tau_0 - 90^\circ$. DIF6

Here τ_0 is the variable time interval between the first two pulses relative to which the other intervals are calculated. The behavior of the magnetization after these pulse sequences represented in fig. 1. It can be seen from Eq. (7) and Fig.1 that M_z vs t curves are similar to aperiodic unit-step responses which in turn are the linear combinations of the *N* aperiodic unit-step responses. Therefore the aperiodic unit-step response of the T_1-filters can be presented as

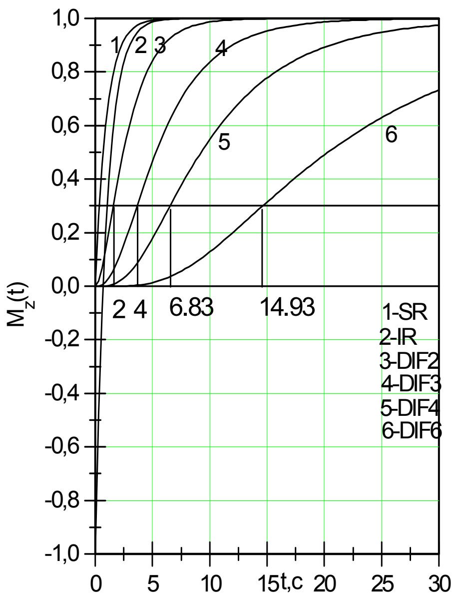

Fig.1. Recovery of normalized longitudinal magnetization after the act of pulse sequences: the horizontal line cuts off 0.3 of the full normalized magnetization: figures near the middle coordinate line are equal to the full duration of an NMR signal before the reading pulse

$$M_z(\sum k_i\tau_0) = 1 - \sum_{i=1}^{N} a_i \exp[-\frac{k_i\tau_0}{T_1}] , \quad (8)$$

where k_i are the coefficients in front of $\frac{\tau_0}{T_1}$ after multiplication of E_i and summation of the time intervals in the exponents, a_i are the coefficients in front of E_i and products of $E_iE_{i-1}E_{i-2} \dots E_1$ in the Eq. (7).

The corresponding to (8) impulse response is

$$\frac{d}{d\tau_0}[M_z(\sum k_n\tau_0)] = \sum_{n=1}^{N} \frac{k_n}{T_1} a_n \exp[-\frac{k_n\tau_0}{T_1}] = \sum_{n=1}^{N} \frac{a_n}{T'_{1n}} \exp[-\frac{\tau_0}{T'_{1n}}],$$

where the designation $T'_{1n} = \frac{T_1}{k_n}$ is introduced.

According the control theory, the transfer functions of the T_1-filters can be presented as

$$W(p) = \sum_{n=1}^{N} \frac{a_n}{T'_{1n}} \frac{1}{(pT'_{1n}+1)}. \quad (9)$$

The correspondent frequency responses can be described as

$$G(\omega) = \sum_{n=1}^{N} \frac{a_n}{T'_{1n}} \frac{1}{\sqrt{(T'_{1n}\omega)^2+1}} . \quad (10)$$

3. Results and Discussion

Hence, the transfer functions of the T_1-filters and the correspondent frequency responses are also the algebraic sums (with alternative signs) of those for the first-order aperiodic units.

The time intervals between the pulses in the T_1-filters located symmetrically relative to "the center of gravity" of the pulse sequences are also are equal, as they are in the Butterworth filters.

In the analogy to the Butterworth filters, the time intervals in the T_1-filters are related with the equally spaced positions of the n points on a circle of unit radius (Fig. 2)

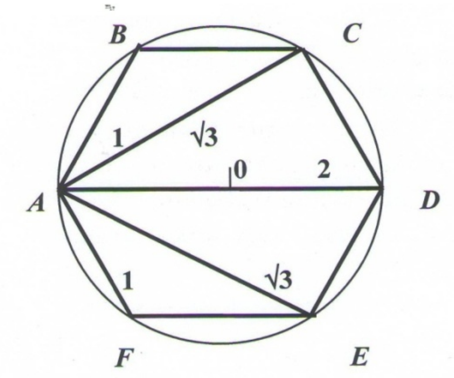

Fig.2. Positions and lengths of the segments of the 6-sided inscribed polygon which constitute (add up to) the time intervals in the *DIF*6 pulse sequence

For the example, let us consider the DIF6 pulse sequence. The time intervals in *DIF*6 pulse sequence equal to the lengths of the segments and consequent pairwise sums of the lengths of the segments of the 6-sided inscribed polygon which originate from one point, *A*: $|AB|$, $|AB|+|AC|$, $|AC|+|AD|$, $|AD|+|AE|$, $|AE|+|AF|$, $|AF|$, in the units of $|AB|$.

4. Summary and Conclusions

It was shown in this report that T_1-filters developed for contrast enhancing in NMR-imaging and differentiating of multiexponential relaxation curves have some relation to the low pass Butterworth filters. The mathematical expressions were presented for transfer functions, time and frequency responses of these filters.

The results reported can be used as a basis to develop more complicated pulse sequences for the synthesis of pass-band, stop-band, high-pass band and other filters in the longitudinal relaxation.

5. References

[1] Hakimov A. M., Idiyatullin D. Sh. On T_1-selective NMR and relaxation time spectroscopy. In extended abstracts of the 27th Congress Ampere, 1994, 1060.

[2] Andreev N. K., Hakimov A. M., Idiyatullin D. Sh. Pulse sequences for T_1 measurement and contrast enhancing in NMR imaging. In proceedings of the International Conference on Measurement, Smolenice, Bratislava, 1997, 167 – 170.

[3] Andreev N. K., Hakimov A. M., Idiyatullin D. Sh. New pulse sequences for T_1- and T_1/ T_2- contrast enhancing in NMR imaging. *Magnetic Resonance Imaging.* 16(8): 981 – 987. 1998.

[4] Åström K.J., MurrayR.M. Feedback Systems: An Introduction for Scientists and Engineers. Princeton University Press. (2008).

Ringing Down Time Measurement of a Receive Coil for NMR Tomography

P. Andris, I. Frollo

Institute of Measurement Science, Slovak Academy of Sciences,
Dúbravská cesta 9, 841 04 Bratislava, Slovak republic
Email: peter.andris@savba.sk

Abstract. *The paper describes studies dealing with problems of the receive coil for NMR scanner connected via a preamplifier with high input impedance. Behaviour of the coil with preamplifier after pulses of RF signal was studied and an equation was derived and verified for investigation of it. The theory is demonstrated on a one-turn surface coil with rather large dimensions. Some parameters of a coil are measureable with difficulties and the derived theory can help to determine them more accurately. The technique of the high–impedance preamplifiers is seldom in experimental systems, though it can simplify their adjustment.*

Keywords: Ringing Down Time, Receive Coil, NMR, Tomography, Low Field

1. Introduction

Receive coils for experimental scanners based on the nuclear magnetic resonance (NMR) are manufactured by users frequently. Mostly the coil is tuned to the working frequency and matched to the impedance of the transmission line and the preamplifier. At lower frequencies also a preamplifier with high input impedance can be used and the coil adjustment can be simplified in the way. Authors [1] introduced interesting solutions of the receiving systems with preamplifier with high input impedance. While the solution of Raad and Darrasse [1] does not need fine tuning the coil, our system is tuned using a variable capacitor. A square-shaped one-turn loop coil was selected for the experiments, arranged as a surface coil. Due to the high-impedance load the transient response of the coil was studied. The equation describing the behaviour of the coil after a signal pulse was derived. The performed experiments proved that it increased number of coil parameters and besides of study of the ring-down problems [2] also the circuital parameters of the coil can be determined more accurately using its help. Authors [3] developed a technique of balancing a receive coil. Authors [4] developed a technique of the magnetic field mapping. Purpose of the article is to help with design of dedicated receive coils for NMR experiments, mainly using the preamplifier with high input impedance. Qualities of the experimental coil system have been verified with an experimental NMR scanner equipped with the low static magnetic field. The coil system is intended for whole-body measurements or for different bigger samples measurements. The solution with the high-impedance preamplifier simplifies tuning and matching the coil and such preamplifier can be used for more purposes.

2. Subject and Methods

A receive coil of an NMR scanner changes pulses of RF magnetic field induced from a sample into an electric signal, usually the voltage. Fig. 1 depicts equivalent circuit diagram of a simple tuned coil, connected to the preamplifier with high input impedance. The voltage V_0 represents the voltage induced from the measured sample, the voltage V_g is the voltage at the input of the preamplifier (with input resistance R_{in}) of the receiver. After switching on the sample voltage V_0 the output voltage V_g can be described by the equations

$$LC\frac{d^2V_g}{dt^2} + \left(R_sC + \frac{L}{R_{in}}\right)\frac{dV_g}{dt} + \left(\frac{R_s}{R_{in}} + 1\right)V_g = 0, \quad (1)$$

$$V_g(0) = \frac{V_0 R_{in}}{R_s + R_{in}},$$

$$\frac{dV_g}{dt}(0) = 0.$$

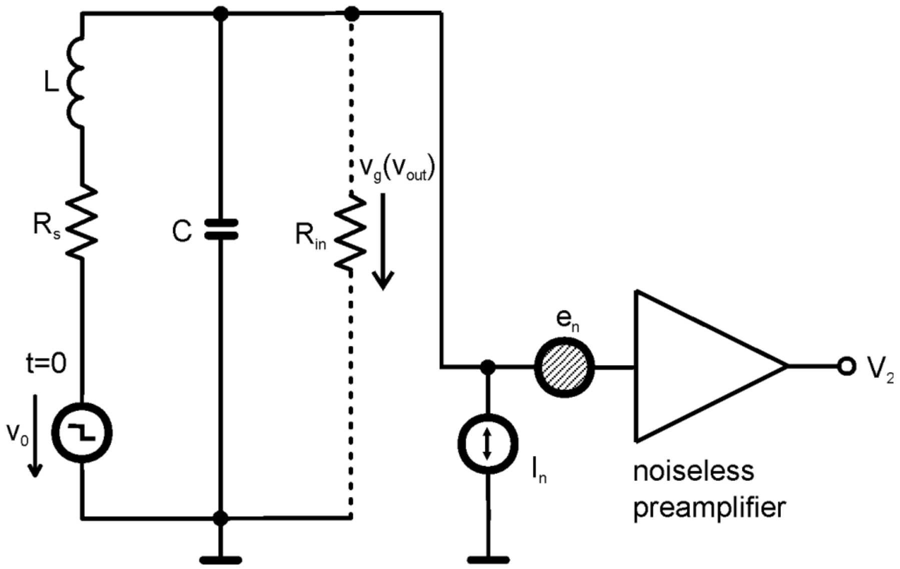

Fig. 1. Equivalent circuit diagram of a single tuned coil connected to a preamplifier with high input impedance. The coil is switched into electrical circuit in the time instant of t=0. A noiseless preamplifier together with voltage and current noise sources simulate noise in the real circuit. In practice the preamplifier always has finite input impedance, represented by R_{in}.

For some calculations it is advantageous to define the following expressions

$$p_1 = \frac{-(CR_sR_{in}+L)+y}{2LCR_{in}}, \quad (2)$$

$$p_2 = \frac{-(CR_sR_{in}+L)-y}{2LCR_{in}}, \quad (3)$$

$$y = \sqrt{(L + CR_sR_{in})^2 - 4LCR_{in}(R_{in} + R_s)}. \quad (4)$$

If y is a real number, the coil circuit is stabile after pulse of the V_0 voltage. If it is an imaginary number the coil starts its work with oscillations. For stabile work the following condition must be fulfilled

$$(L + CR_sR_{in})^2 - 4LCR_{in}(R_{in} + R_s) \geq 0. \quad (5)$$

Considering $LC \cong \frac{1}{\omega^2}$ and $4R_{in}^2 \gg R_sR_{in}$ the Eq. (5) can be modified to

$$\omega L \geq 2R_{in}. \quad (6)$$

It is the condition for the work without oscillations. Nevertheless the quality factor of such coil would be very low ($Q = \frac{\omega L R_{in}}{R_s(R_s+R_{in})+\omega^2L^2}$) and sensitivity of the measurement would be also low. Therefore the conditions must be found under those the oscillations can be acceptable. The solution of Eq. (1) can help it.

The solution of Eq. (1) is given by

$$V_g = \frac{R_{in}V_0\left(-Le^{p_2t}+Le^{p_1t}-CR_{in}R_se^{p_2t}+CR_{in}R_se^{p_1t}+e^{p_2t}y+e^{p_1t}y\right)}{2(R_{in}+R_s)y}. \qquad (7)$$

If the expression (2) or (3) has its imaginary part, it represents the angular frequency of the oscillations, the real part determines exponential damping of the oscillations. In practice a receive coil must fulfill several requirements. Very important requirement is sensitivity of the measuring system. Mostly a coil is designed to maximal possible sensitivity and other parameters are checked or calculated and the qualities of the measuring sequence are accommodated to them. The derived expression can help to do it.

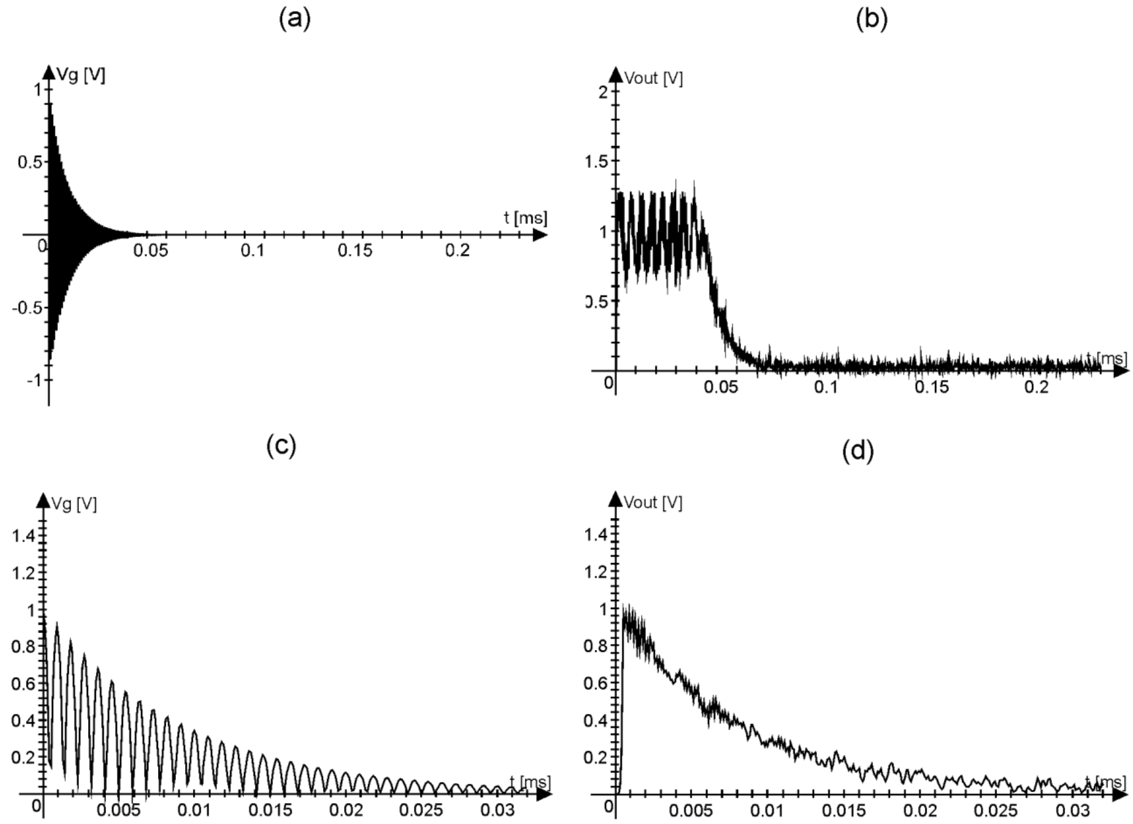

Fig. 2. Transient responds of the coil to switching the signal on: (a) the calculated characteristic, R_{in}=45000 Ω; (b) envelope of the measured and detected signal, R_{in}=45000 Ω. The detail comparison of the measured and the calculated relaxation of the coil: (c) and (d). The calculated values (c) and the measured values (d) are in very good agreement.

3. Results

The verification experiments have been performed on an experimental NMR scanner equipped with home-made resistive magnet of 0.1 T and the Apollo (Tecmag Inc., Houston, TX) console. The coil was made of a copper tube with diameter of 6 mm. Its dimensions are 30 cm × 30 cm. The coil, including non-magnetic ceramic tuning capacitors was encapsulated in a PVC shell. The coil is connected to the preamplifier using a short transmission line which is a part of the tuning capacitance. The electrical parameters of the coil are: L=1.066 µH, C=1200 pF, R_s=0.2079 Ω. The working frequency of the coil is 4.45 MHz. Figure 2(a) depicts transient respond of the coil to switching the signal on, calculated using Eq. (7). The oscillations are at the working frequency of the system and after 0.1 ms they are damped to

0.0027% of the original value. It can be sufficient for most of applications. The transient characteristic of the realized coil was measured using the NMR scanner (the RF hard pulse width of 2 μs, start of the acquisition min. 10 μs after the RF pulse, the sampling interval of 100 ns). The measured course is influenced by radiation damping [2] and only its last part can be compared with the calculated values (figure 2(b)). While the calculated course is a real only signal, the measured signal is a detected signal with its real and imaginary parts making possible to depict its absolute value - an envelope of the signal. The real or imaginary parts are exponentially damped harmonic curves, their frequency after detection determines the frequency deviation between the coil tuning and the working frequency of the scanner.

4. Discussion and Conclusions

The purpose of the studies was to show possible problems occurring in experiment with a preamplifier with high input impedance and to suggest their solutions. The derived theory and the performed experiments proved that such way is possible and the acquired results are promising, mainly using the low-field NMR scanners.

Users needing their own receiving solutions must look for appropriate systems. The article can help in their effort. The derived theory also can help to identify electrical parameters of the individual parts of the system with higher accuracy, mainly difficultly measureable parameters of the coil.

Acknowledgements

The research was sponsored by the Grant Agency of the Slovak Academy of Sciences, grant number VEGA 2/0013/14, by the European Network for Hyperpolarization Physics and Methodology in NMR and MRI number COST TD1103, and by the Slovak Research and Development Agency, project number APVV-0431-12.

References

[1] Raad A, Darrasse L. Optimization of NMR bandwidth by inductive coupling. *Magnetic Resonance Imaging* **10**: 55-65, 1992.

[2] Baudin E, Safiullin K, Morgan SW, Nacher P-J. An active feedback scheme for low field NMR experiments. *Journal of Physics: Conference series* **294**: 012009, 2011.

[3] Décorps M, Blondet P, Reutenauer H, Albrand J P, Remy C. An inductively coupled, series-tuned NMR probe. *Journal of Magnetic Resonance* **65**: 100-109, 1985.

[4] Bartusek K, Dokoupil Z, Gescheidtova E. Mapping of magnetic field around small coil using the magnetic resonance method. *Measurement Science and Technology* **18**: 2223-2230, 2007.

Soft Magnetic Objects in Homogeneous Magnetic Field of an NMR Imager, Mathematical Modelling and Experimental Evaluation

I. Frollo, A. Krafčík, P. Andris, J. Přibil, T. Dermek

Institute of Measurement Science, Slovak Academy of Sciences, Bratislava, Slovakia
Email: frollo@savba.sk

Abstract. *Soft magnetic samples with magnetic particles ingredients were placed into the homogenous magnetic field of an imager based on nuclear magnetic resonance. Theoretical computations based on a magnetostatic models were performed. For experimental verification an MRI 0.2 Tesla ESAOTE Opera imager was used. For modelling and experiments two samples - rectangular and circular were tested. The resultant images correspond to the magnetic field variations in the vicinity of the samples.*

Keywords: Soft Magnetic Objects, Mathematical Modelling, Magnetic Resonance Imaging, Magnetic Liquids, Magnetic Susceptibility

1. Introduction

Theoretically and experimentally was proved that every physical or biological object, which is inserted into magnetic field, deforms this field. Objects attract or detract the magnetic line of force, depending on the object substance: ferromagnetic, paramagnetic or diamagnetic.

The specific quantity is the magnetic susceptibility, which is defined as a change of magnetization in dependence on magnetic field intensity. Values of susceptibility defined as $\chi_i = (dM/dH)_0$ i.e. the slope at the origin, (M - magnetization, H - magnetic field, whereas $M = \chi H$) range from around -10^{-5} in very weak magnetic materials up to values of around $+10^{6}$ in ultra-soft ferromagnets [1].

Imaging methods based on magnetic resonance principles are capable to detect, to measure and to image these deformations [2], [3]. For the purpose of mathematical models based on integral equations, vector potentials are applied. The calculation results are in a form of analytical expressions that for particular evaluation need perfect computational system and considerable computing time [4].

In this paper we try to describe the magnetic field distribution by mathematical modelling with an orientation to the simplest rectangular and circular objects.

2. Subject and Methods

Let us assume that a ferromagnetic or paramagnetic object is placed into the homogeneous magnetic field of an MRI imager. The homogeneous magnetic field near the sample is deformed. For simplicity and easy experimental verification a double rectangular and circular objects were selected and theoretically analyzed.

A. Rectangular Samples

For the purpose of our simple example we suppose that the soft magnetic planar layer is positioned in the x-y plane of the rectangular coordinate system and the thickness of the layer is neglected. According to Fig.1, we suppose the layers are limited by dimensions of 2a and b, with the left-right symmetry. The layers are moved in y direction by distances +c and –c,

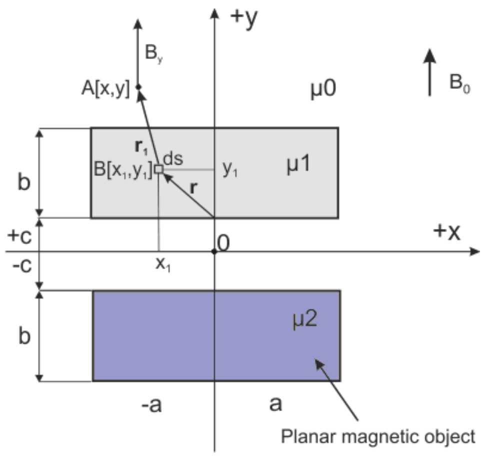

ds[x1,y2] is an elementary surface element. The basic magnetic field B_0 of the MR imager is parallel with the y-axis. The task is to calculate the $B_y(x,y)$ component of the magnetic field in the point A[x,y].

Fig.1. Fundamental configuration of the two magnetic planar rectangular layers. Samples are positioned in x-y plane of the rectangular coordinate system. The thickness of the layers is neglected.

In planar approximation static magnetic objects (linear and isotropic) without any driving current can be described by Laplace equation: $\nabla^2 A(x,y,z) = 0$, (1)

for nonzero z-component of magnetic vector potential $\mathbf{A} = [0,0,A]$, and by boundary conditions at each interface between two media: $\mathbf{n}_{\mathrm{II}} \cdot (\mathbf{B}_{\mathrm{I}} - \mathbf{B}_{\mathrm{II}}) = 0$, $\mathbf{n}_{\mathrm{II}} \times (\mathbf{H}_{\mathrm{I}} - \mathbf{H}_{\mathrm{II}}) = \mathbf{0}$, (2)

(material domains I and II, and $\mathbf{n}_{II}$ is an outward normal from domain II) and outer boundary conditions.

Laplace equation is solvable analytically only for the simplest problems. For rectangular sample, these equations were therefore solved numerically by finite element method (FEM). In this way it was calculated distribution of magnetic flux density field of two parallel bars with rectangular cross-section in x-y plane, with constant permeability μ_k (i.e. for *k*-th bar material domain) in originally homogeneous magnetic field $\mathbf{B}_0 = [0, B_0, 0]$ perpendicular to longitudinal axis of bars, see Fig.2, left.

For experimental evaluation of the mathematical modelling, we have chosen a simple laboratory arrangement by application of the magnetic resonance imaging methods. For sample positioning, a rectangular plastic vessel or holder with tap water was used. Two samples - rectangular vessels filled with doped water (several drops of magnetic liquid based on Dextran) were placed to the centre of the holder. Dimensions of the samples: 50x10 mm, distance between samples: 5 mm. Thickness of the walls of sample vessels: 1 mm. Resultant image is in Fig.2, right.

The contrast of the imaged samples corresponds to the real values of μ1, μ2, and μ0.
Walls of sample vessels with liquid substances are imaged with black colour, no MRI signal.

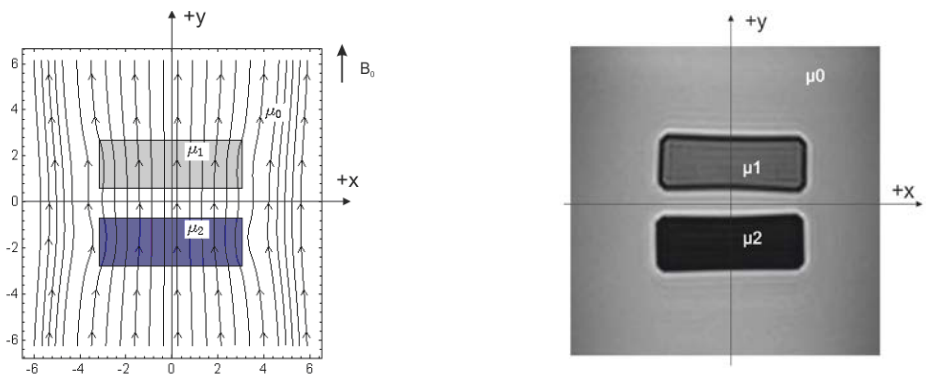

Fig. 2. Left: Calculated magnetic field distribution of the homogeneous magnetic field B_0, lines of force, affected by 2 parallel magnetic bars with relative permeabilities: μ1=2 , μ2=3 and environment μ0. Right: NMR image of two samples (rectangular vessels filled with doped water in the holder with tap water) using GRE imaging sequence, TR = 440 ms, TE = 10 ms. Thickness of the imaged layer: 2 mm.

B. Circular Samples

For circular samples, 3 cylinder vessels placed in a rectangular plastic holder filled with the tap water were used. Cylinder vessels were filled with distilled water doped by several drops of magnetic liquid based on Dextran (polysaccharide).
According to Fig.3, we suppose three circular concentric vessels. Relative permeabilities: μ1, μ2, environment permeability: μ0.

From Fig.3 the position vector can be expressed as: $r = \sqrt{x^2 + y^2}$. (3)

For vector potential we can write [5]: $A_k = (C_k\, r + \frac{D_k}{r})\, \frac{x}{r}$, (4)

where C_k and D_k are constants calculated for every region for relative permeabilities corresponding to the concrete experiment.

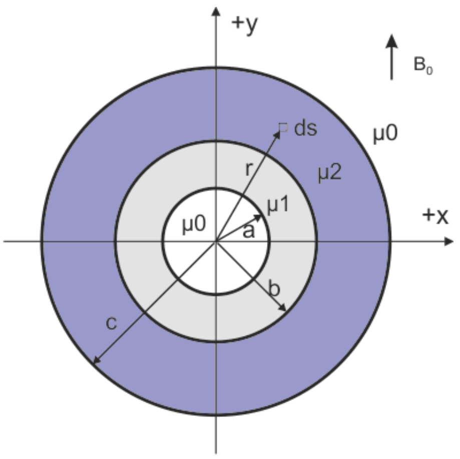

Fig. 3. Basic configuration of the magnetic planar layer circular sample positioned in x-y plane of the rectangular coordinate system.

Resultant field will be: $H_r = \mathrm{Curl}[A_r, \{x, y\}]$. (5)

Using function:
StreamPlot[{H_r}, {x,-0.08, 0.08}, {y,- 0.08, 0.08}]
it is possible to draw the lines of force of the examined objects, relative values, Fig.4, left.

For experimental evaluation of the mathematical modelling a rectangular plastic vessel - holder with tap water inside was chosen. Two samples - circular vessels filled with doped water were placed to the centre of the holder. The central vessel was filled with tap water. Diameters of the vessels: 18, 40, 56 mm, wall thickness: 1 mm. Resultant NMR image is depicted in Fig.4, right.

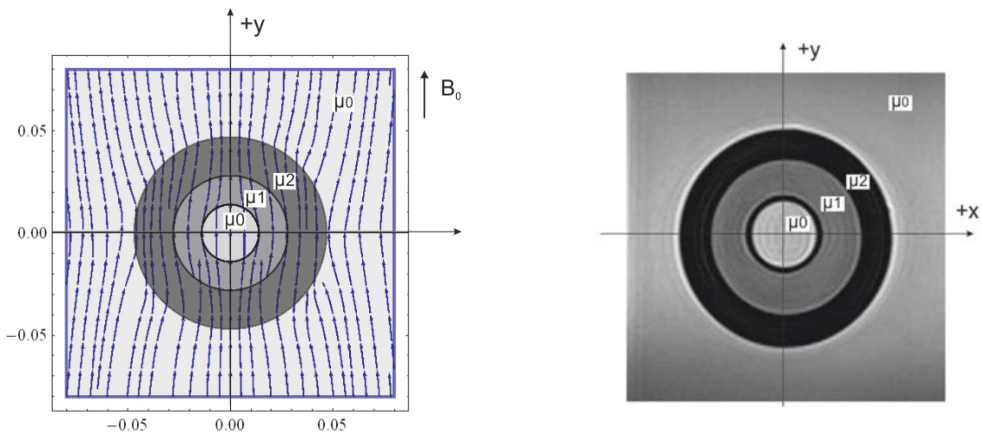

Fig. 4. Left. Mathematical model of the distribution of homogeneous magnetic field H_0, lines of force affected by 2 concentric cylinders with relative permeabilities: μ1=2 and μ2=3, μ0 is an environment permeability.
Right. NMR image of two samples (circular vessels filled with doped water in the rectangular vessels - holder filled with tap water) using GRE imaging sequence: TR = 440 ms, TE = 10 ms. Thickness of the imaged layer: 2 mm.

For experimental verification an MRI 0.2 Tesla ESAOTE Opera imager (Esaote, Genoa, Italy) with vertical orientation of the basic magnetic field was used.

3. Results and Discussion

The goal of this study was to mathematically describe and experimentally depict simple rectangular and circular objects - vessels filled with doped water by very diluted magnetic liquids. Imaging method based on MR principles was used for interpretation of analyzed samples.

Mathematical analysis of rectangular and circular objects, representing a shaped magnetic soft layer, showed theoretical possibilities to calculate magnetic field around any type of sample. Our mathematical model proved that it is possible to map the magnetic field variations - line of force - and to image the specific structures of selected samples placed into a special plastic holders. The calculations were performed with relative values of input quantities, permeabilities and dimensions. The mathematical model was described in the form of general formulas. To present the detailed analytical form of resultant equations would exceed the range of this paper.

For experimental presentation a classical gradient echo measuring sequences were used. The resultant MR images are encircled by narrow stripes that optically extend the width of the sample. This phenomenon is typical for susceptibility imaging, when one needs to measure local magnetic field variations representing sample properties [3].

4. Conclusions

Our experimental results are in good correlation with the mathematical simulations in spite of using relative quantities. This validates the possible suitability of the proposed method for detection of weak magnetic materials using the MRI methods. Presented images of thin objects indicate perspective possibilities of this methodology even in the low-field MRI.

Acknowledgements

This work was supported by the Slovak Scientific Grant Agency VEGA 2/0013/14 and within the project of the Slovak Research and Development Agency Nr. APVV-0431-12.

References

[1] Du Trémolet de Lacheisserie É, Gignoux D, and Schlenker M. Magnetism: Fundamentals, First Springer Science+Business Media, Inc. softcover printing, E-book ISBN 0-387-23062-9, 2005.

[2] Callaghan P. T, Stepisnik J. Spatially-distributed pulsed gradient spin echo NMR using single-wire proximity. *Physical Review Letters*, 75, 4532-4535, 1995.

[3] Haacke E. M, Brown R. W, Thompson M. R, Venkatesan R. Magnetic Resonance Imaging: Physical Principles and Sequence Design, first ed. Wiley-Liss, John Wiley and Sons Ltd, United States, 1999.

[4] Marcon P, Bartusek K, Dokoupil Z, Gescheidtova E. Diffusion MRI: Mitigation of Magnetic Field Inhomogeneities. *Measurement Science Review*, 12, nº. 5, 205-212, 2012.

[5] Henke H. Elektromagnetische Felder, Theorie und Anwendung, ISBN 978-3-540-71004-2 3. Aufl. Springer Berlin Heidelberg New York, 2007.

Study of Effect of Sn doping of $EuBa_2Cu_{3-x}O_{7-\delta}$ Compound on Superconducting Properties by Contactless Methods

[1]M. Majerová, [1]A. Dvurečenskij, [1]A. Cigáň, [2]I. Van Driessche, [1]M. Škrátek, [1]J. Maňka, [2]E. Bruneel, [1]R. Bystrický

[1]Institute of Measurement Science, Slovak Academy of Sciences, Dúbravská cesta 9, 841 04 Bratislava, Slovakia,

[2] Department of Inorganic and Physical Chemistry, Gent University, Krijgslaan 281 (53), 9000 Gent, Belgium

Email: Melinda.Majerova@savba.sk

Abstract. *Effect of Sn addition on structural and superconducting properties in* $EuBa_2Cu_3O_{7-\delta}$ *(Eu-123) compound was studied using XRD and SQUID magnetometric measurements. Transition process from normal to superconducting state was analyzed by the measurement of temperature change of the magnetic moment of the combined ZFC and the remanence technique beside the usual ZFC and FC ones. Samples of the nominal composition* $EuBa_2Cu_{3-x}Sn_xO_{7-\delta}$ *with x ranging from 0.0 to 0.2 were prepared by the solid state reaction technique from* Eu_2O_3, $BaCO_3$, *CuO and* SnO_2 *precursors. The increasing Sn-content deteriorates the superconducting properties of the Sn doped samples.*

Keywords: High-Temperature Superconductors, Eu-123, Transition Characteristics, Sn Doping, Mass Magnetization, T_c^{on}

1. Introduction

In a new class of copper-based high-temperature superconductors (HTS), up to now, there is no generally accepted theory reasonably explaining all experimental results. All HTS are layered systems having the same basic crystallographic structure; they contain parallel two-dimensional layers of CuO_2 planes and a common characteristic dependence on doping. The chemical doping is a useful tool for revealing the HT superconductivity mechanism. With regard to the role of the Cu-O_2 planes, special attention is paid to chemical substitutions into copper positions.

At the study of Sn doping of RE-123 HT superconductors, where RE = Y, and rare earths or mixed rare earths elements, most results were reported for the Sn doping of Y-123 superconductor. In this case, some inconsistent results were also reported, e.g., such as the question of Sn entering the Y-123 phase and the formation of a solid solution or if the tin preferably enters the Cu(2) sites in Cu-O_2 layers or the Cu(1) sites in Cu-O chains [1-6] or the question of an effect of increasing of Sn content on the critical transition temperature. [4,6,7]. Only several results were reported for the Eu-123 system, disregarding the Sn addition in the melt textured Eu-Ba-Cu-O compounds to increase the critical current density and to supply, in the crystal growth process, more oxygen using oxide precursors, [8-10]. In the paper, we studied sintered samples of the nominal composition of $EuBa_2Cu_{3-x}Sn_xO_{7-\delta}$.

2. Subject and Methods

The polycrystalline samples of $EuBa_2Cu_{3-x}Sn_xO_{7-\delta}$, where x = 0.00, 0.01, 0.03, 0.07, 0.10, and 0.20 were prepared by a standard solid-state reaction method from the commercial 99.99 % purity oxide powders of Eu_2O_3, CuO, SnO_2 and $BaCO_3$. The powders were carefully weighed in appropriate weight amounts and homogenized in air in an agate mortar for five minutes and calcined at 930 °C for 40 hours in air. The obtained precursors were again homogenized, pressed into the pellets and sintered in a horizontal tube furnace in flowing oxygen of 20 ml/min at about 1050 °C for 72 h, then cooled to 580 °C and held at this temperature for

24 h and thereafter cooled in the furnace to room temperature. The XRD measurements were performed on powdered samples and the magnetic measurements on cuboid samples ~ (2.2×1.6×8.4) mm cut from pellets. The four-point resistance measurement technique of the *R* vs. *T* dependence is the best-known standard method for determination of various characteristics of superconducting and normal states of superconductors. The other two contactless measuring methods - using a change of the self-inductance of a coil located in vicinity of the measured sample or using a change of the mutual inductance of two coils separated by a sample - were also used.

In the paper, we compared three characteristics of the transition from the normal to the superconducting state obtained by another contactless method. The method is based on the measurement of the temperature dependences of the magnetic moment (magnetization or magnetic susceptibility) of the studied samples. In our case, the temperature dependence of the DC magnetic moment of the superconducting compounds was measured by the Quantum Design SQUID magnetometer MPMS XL-7. The dependences were measured under three different conditions, at the zero field cooling (ZFC), field cooling (FC) and the technique combining the zero field cooling and the measurement of the remanent magnetic moment (ZFC-R). Before the measurement of each of the three characteristics, the shielding of the superconducting magnet has been demagnetized (using Degauss option of the MPMS), superconducting magnet was reset by driving into the normal state and ultra-low field procedure (using Ultra Low Field option) was used to set the zero field value and homogeneity. After stabilizing the temperature, the applied magnetic field of 795 Am^{-1} was set by using the No Overshoot mode.

The measurement of the magnetic moment in each measured point followed after the temperature was stabilized by the system and after the expiration of the waiting time of 90 s. The measured data were obtained using the RSO option. (The amplitude of 4 cm, frequency of 1.5 Hz, 5 cycles of the sample oscillation and two sets of such measurement were averaged to represent one point of the presented data (curve)). The ZFC procedure consists of cooling the sample from the room temperature to ~2 K in the zero applied magnetic field, $H_a = 0$. Thereafter, H_a was set to 795 Am^{-1} and the magnetic moment of the sample was measured at an increasing temperature to 300 K. The FC curve was obtained by the measurement of the magnetic moment at $H_a = 795$ Am^{-1} at a decreasing temperature. In the ZFC-R procedure, the sample was zero-field cooled to 2 K, subsequently, after the application of $H_a = 795$ Am^{-1} for 180 s, the remanent magnetic moment ($H_a = 0$) was measured at an increasing temperature. The temperature resolution was 0.001 K. The DC mass magnetization loops were measured at 77 K and 20 K by the Quantum Design SQUID magnetometer MPMS XL-7 whose differential sensitivity is 10^{-11} Am^2 from 0T to 1T. The phase composition was studied by X-ray diffraction measurements (CuKα radiation).

3. Results and Discussion

From X-ray diffraction data, Fig. 1, it can be concluded that all peaks can be well ascribed to the Eu123 superconducting phase up to $x \leq 0.03$, however, for higher contents of Sn, some new peaks could be identified that could be ascribed to the excess $BaCuO_2$ and CuO and $Eu_2Sn_2O_7Cu$ phase at an increasing of Sn content. The ZFC, FC, and ZFC-R mass magnetization transition curves are in Fig.2. In the case of ZFC-R conditions, the positive values of magnetization in the range of the superconducting state result from the opposite direction of the circulation of the super conducting shielding current as a

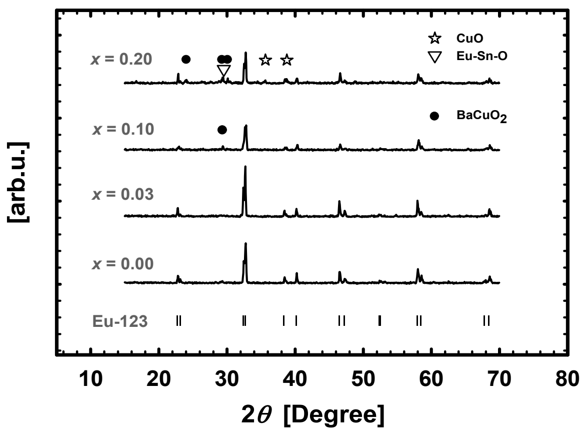

Fig.1. XRD patterns of $EuBa_2Cu_{3-x}Sn_xO_{7-\delta}$ samples showing the nominal x - values.

reaction on the set of $H_a = 0$.

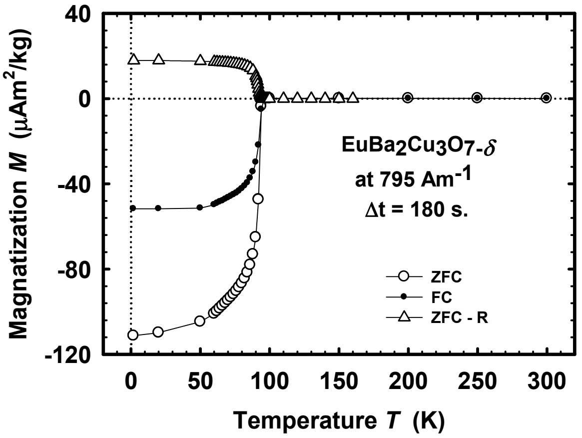

Fig. 2. ZFC, FC, and ZFC-R mass magnetization vs. temperature of the undoped $EuBa_2Cu_3O_{7-\delta}$ sample measured at H_a = 795 Am^{-1}. The H_a was applied for 180 s and then set to zero before the measurement of data in the ZFC-R -procedure.

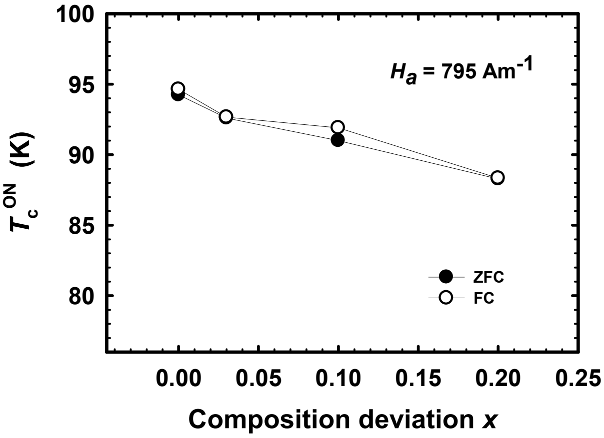

Fig. 3. ZFC and FC T_c^{on} - values of the $EuBa_2Cu_{3-x}Sn_xO_{7-\delta}$ samples vs. the nominal composition deviation of x.

The temperature related to the onset of a diamagnetic change of the transition from the normal to the superconducting state of the ZFC and FC magnetization curves is described as the critical transition temperature, T_c^{on}. The ZFC and FC T_c^{on} - values of some samples are shown in Fig. 3. It can be seen that the T_c^{on} values are still higher than 88 K up to x = 0.20; whereas the ZFC and ZFC-R values are practically the same with respect to the temperature resolution of 0.001K, the FC T_c^{on} - values slightly differentiate; see Fig. 3. In the FC case, the applied magnetic field in the normal state penetrates into the sample volume before the superconducting state (the superconducting shielding current) is present, while in the former cases, the H_a is applied to the sample at a low temperature (in the superconducting state), so the field cannot penetrate into the sample volume, if its value is lower than the mean value of the first penetration magnetic field of the intergrain junctions of the H_{p1}^{IJ} sample. From the magnetization data at 77 K, the estimated value of H_{p1}^{IJ} for the undoped sample is more than one order higher than H_a = 795 Am^{-1}. In the case of the ZFC-R magnetization curve, the T_c^{on} - value was determined as an onset of a paramagnetic trend. In general, the ZFC-R technique can be more useful for verification of the superconducting state and its differentiation from other diamagnetic effects by the contactless methods.

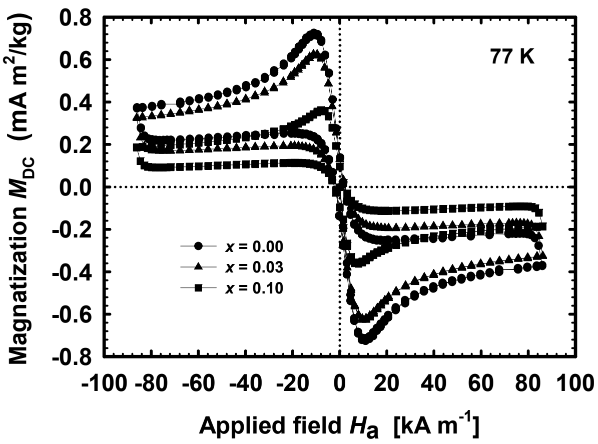

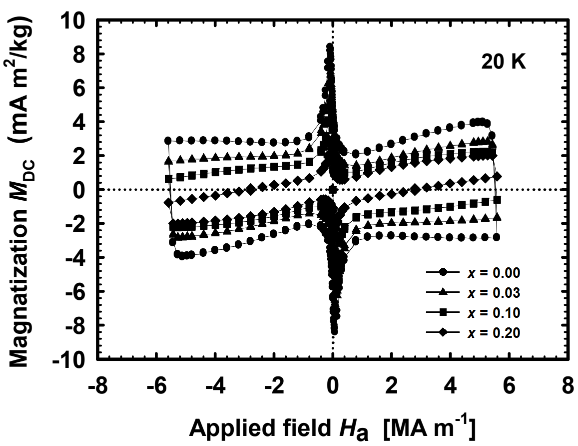

Fig. 4. and 5. M_{DC} vs. H_a dependences of $EuBa_2Cu_{3-x}Sn_xO_{7-\delta}$ samples at 77 K and at lower values of H_a (left) and at 20 K and at higher values of the applied magnetic field H_a (right), respectively.

The DC magnetization hysteresis curves of M_{DC} vs. H_a for $EuBa_2Cu_{3-x}Sn_xO_{7-\delta}$ samples at 77 K and 20 K are shown in Fig. 4 and Fig. 5, respectively.

All the samples show the Z-shape of magnetization curves at the low H_a typical for the superconducting polycrystalline samples. The increasing content of Sn decreases the volume superconducting properties, as the values of M_{DC} and the magnetization hysteresis decrease. At 20 K, the magnetization loops with the Sn content $x \leq 0.03$ indicate the so-called second peak effect, while the M_{DC} vs. H_a curves with a higher Sn content of $x \geq 0.10$ show an evident (para) magnetic "tail" - magnetic contribution indicated by the slope of the curves pointing to the first and third quadrants. The magnetic component can be associated with the origination of excess phases, namely with the $BaCuO_2$ phase [11,12].

4. Conclusions

Effect of the Sn- addition on the structural and superconducting properties in $EuBa_2Cu_{3-x}Sn_xO_{7-\delta}$ compounds with the nominal value of x from zero to 0.20 was studied using the XRD and SQUID magnetometric measurements. The polycrystalline samples were sintered in a horizontal tube furnace in flowing oxygen of 20 ml/min at about 1050°C for 72 h. In the paper, the combined ZFC-R technique was used to study the transition process from the normal to the superconducting state together with the usual ZFC and the FC contactless techniques. The ZFC-R procedure can be more useful for verification of the superconducting state and its differentiation from other diamagnetic effects by the contactless methods. It can be concluded, based on the results and the XRD data, that the superconducting Eu-123 phase is dominant in all our samples and that the solution limit of Sn in Eu-123 is limited to $x = 0.03$, if at all.

Acknowledgements

This research was supported by the Slovak Research and Development Agency by Grant No. APVV-0125-11 and by the Agency of the Ministry of Education of the Slovak Republic for the Structural Funds of the EU, Project Codes 26240220073 and 26240120019.

References

[1] J. Feng, K.K. Yeung, K.W. Wong, Eric C.L. Fu, C. C. Lam, *Supercond. Sci. Technol.,* 13: 215-224, 2000.

[2] H. Zhang, G. M. Wang, Q. R. Zhang, *Physics Letters A*, 138: 517-522, 1989.

[3] Y. Matsumoto, T. Nishida, M. Katada, *Physica B*, 194-196: 2127-2128, 1994.

[4] F. Licci, L. Raffo, T. Besagni, C. Frigeri, C. Paris, *Physica C*, 196: 307-314, 1992.

[5] T.Saito, K. Mizumo,H. Watanabe, K. Koto, *Physica C*, 171: 167-173, 1990.

[6] Y. Maeno, M. Kato, Y. Aoki, T. Nojima, T. Fujita, *Physica B*, 148: 357-359, 1987.

[7] H. Zhang, X. Y. Zhou, Y. Zhao, S. H. Liu, Q. R. Zhang, *Sol. Stat. Comm.*, 72: 75-79, 1989.

[8] P. Boolchand, R. n. Enzweiler, I. Zitkovsky, J. Wells, W. Bresser, Darl McDaniel, R. L. Meng, P. H. Hor, C. W. Chu, C. Y. Huang, *Phys. Rev. B,* 37; 3766-3769, 1988.

[9] E. Kuzmann, Z. Homonnay, A.Vertes, *Phys. Rev. B*, 39: 328-333, 1989.

[10] C. Jiang, Y. Mei, S. M. Green, H. L. Luo, C. Polits, *Z. Phys. B -Cond. Matt.*, 68: 15-18, 1987.

[11] N. Guskos, V. Likodimos, C. A. Londos, V. Psycharis, C. Mitros, A. Koufoudakis, H. Gamari-Seale, W. Windsch, H. Metz, *J. Sol. State. Chem.*, 119: 50-61, 1995.

[12] Yamamoto, T. Mito, S. Wada, R. A. Fisher, N. E. Phillips, Z. P. Wang, D. C. Johnston, *J. Magnetism and Magnetic Materials,* 272-276: 88-89, 2004.

Data Processing Techniques for Fiber Bragg Grating (FBG) Reflectivity Characteristics Measurements

[1]B. Korenko, [1]J. Jasenek, [1]J. Červeňová

[1]Institute of Electrical Engineering, Faculty of Electrical Engineering and Information Technology, Bratislava, Slovakia,
Email: branislav.korenko@stuba.sk

Abstract. *The paper deals with general overview of signal processing techniques for reflectance characteristics of fiber sensors based on FBG technology. Firstly basic principle of FBG measurement is introduced with the stress on characterization and profile of obtained data. Different types of interpolation approximation algorithms are described, tested and compared on real data obtained from spectrum analyzer unit. Developed software for processing is introduced and discussed from the point of usage in different applications with dynamic or static FBG measurements.*

Keywords: Fiber Bragg Grating, Fiber Optic Sensor, Reflectance Characteristic, Interpolation, Interrogation

1. Introduction

In many modern civil engineering projects often more sophisticated materials are used. Especially the term of "energy efficient building" or "green building" are often introduced as a future of modern buildings [1]. With this attitude a lot of problems appear for architects and building constructors according to new materials used and tools for proper structure environment monitoring. Wooden beams are also preferred to replace the steel supports in constructions like houses and small buildings. With wood implementation into buildings monitoring of dilatation, shrinking, temperature, moisture etc. comes in handy. For that purposes optical fiber sensors (OFS) could be used. OFS have many advantages like multiplexing, signal immunity to electro - magnetic interference (EMI), usage of only one signaling data fiber, etc. One type of sensors are fiber Bragg gratings [2].

The structure of uniform FBG consists of dielectric elements with different index of refraction. Grating sensors implemented or bonded on different materials can be used for measuring physical fields like mechanical [3] or thermal stress [4]. The main principle of FBG monitoring is sensing the Bragg grating central wavelength which is given by equation:

$$\lambda_b = 2 n_{eff} \Lambda \tag{1}$$

Where Λ is space period of grating and n_{eff} is effective index of refraction of fiber core. The uniform FBG structure is shown in Fig. 1 a). For measuring reflectivity characteristics broadband optical source like super-luminescent diode (SLD) is need. The light interferes with FBG structure and narrow spectrum light is reflected towards the SLD. The reflective spectrum has Gaussian character. The reflected optical signal is guided through optical circulator to optical spectrum analyser (OSA) and processed. When influence of measured physical field modulates the FBG structure the frequency position of reflectance characteristic changes (Fig. 1 b)).

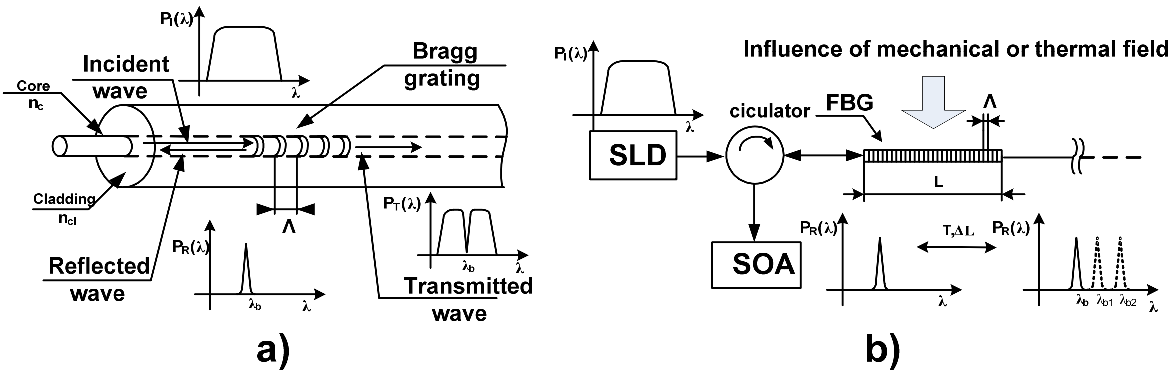

Fig. 1. FBG structure (a), basic measuring apparatus of reflectance characteristics (b).

As it was stated in equation 1the influence on effective refractive index or grating periodicity causes the change in central Bragg wavelength. But the changes in these variables are cross sensitive because any mechanical or thermal influence changes the density of optical material and also the periodicity dimension of the grating [4]. This bounded influence can be described by equation:

$$\Delta\lambda_b = \Delta\lambda_{\Delta\varepsilon} + \Delta\lambda_{\Delta T} \tag{2}$$

It has two contributors to the resulting FBG wavelength shift which could be substituted also with corresponding strain changes $\Delta\varepsilon$ and temperature ΔT [4]. To be more detailed one can write equation 2 in the expanded form:

$$\Delta\lambda_b = 2\left[\Lambda\frac{\partial n_{eff}}{\partial\varepsilon} + n_{eff}\frac{\partial\Lambda}{\partial\varepsilon}\right]\Delta\varepsilon + 2\left[\Lambda\frac{\partial n_{eff}}{\partial T} + n_{eff}\frac{\partial\Lambda}{\partial T}\right]\Delta T \tag{3}$$

The first addend in the equation (3) represents the change due to FBG elongation - strain $\Delta\varepsilon$ and the second one the FBG thermal change ΔT, during thermal stress. The change in refractive index due to strain partial derivative ($\partial n_{eff}/\partial\varepsilon$) represents the photo-elastic and ($\partial n_{eff}/\partial T$) the thermo-optic coefficient. Change in Bragg central wavelength due to the strain application $\Delta\varepsilon$ is described by statement:

$$\Delta\lambda_{\Delta\varepsilon} = \lambda_b(1-\rho)\Delta\varepsilon \tag{4}$$

where ρ is photo-elastic coefficient for fused silica material equal to 0.22 [5]. On the other hand thermal changes ΔT are specified according to:

$$\Delta\lambda_{\Delta T} = \lambda_b(\alpha + \zeta)\Delta T \tag{5}$$

where α is thermal elongation coefficient with typical value 0.55 x 10^{-6} ºC^{-1} [6] and ζ thermo-optic coefficient with approx. value 6.67 x 10^{-6} ºC^{-1} [7].

2. Signal processing techniques

As stated in chapter 1 for accurate physical quantity estimation (strain or temperature) the value $\Delta\lambda_b$ is needed. Due to the fact that reflectance characteristics of FBG structure is not ideal or proportional to Gaussian curve additional signal processing is needed. Simplest way how to estimate the $\Delta\lambda_b$ parameter is to look for local maximum in FBG reflectance characteristics. More accurate method is the calculation of reflectance centroid or Gaussian polynomial fitting. Detailed description could be found in [8]. Graphical demonstration of mentioned methods are shown in Fig.2.

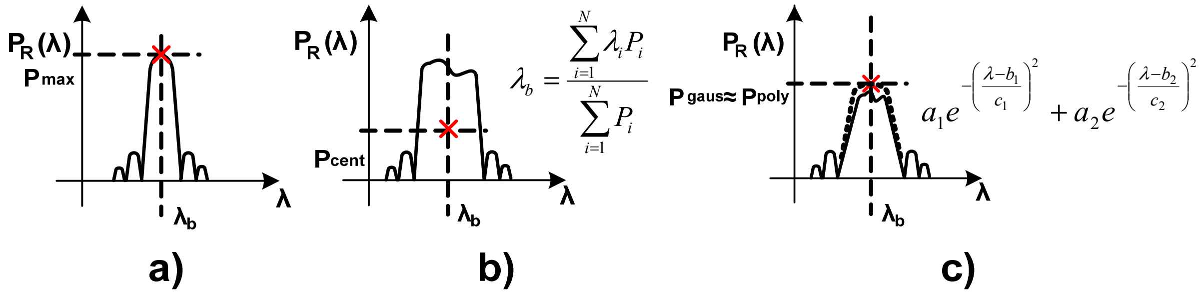

$$\lambda_b = \frac{\sum_{i=1}^{N} \lambda_i P_i}{\sum_{i=1}^{N} P_i} \qquad a_1 e^{-\left(\frac{\lambda - b_1}{c_1}\right)^2} + a_2 e^{-\left(\frac{\lambda - b_2}{c_2}\right)^2}$$

Fig. 2. Signal processing techniques for $\Delta\lambda_b$ estimation: a) maximum detection, b) centroid, c) Gaussian approximation.

To test mentioned methods processing software was created. Test data were obtained from temperature dependence measurement on commercially available uniform high reflectance FBG structure with thermal sensitivity equal to 11 pm/˚C [9]. For heating purposes fiber oven was used. The tested temperatures were t = 25.0, 27.5, 33.1, 41.5, 49.2, 57.9, 72.2, 81.3, 89.8 and 104.1˚C respectively. Temperature was measured with PT100 sensor and given as reference data. For spectral measurement of reflectance FBG characteristic OSA was used with resolution of ± 50pm in 6 nm span bandwidth from 1548 nm to 1554 nm. As broadband light source super-luminescent diode was used. The raw data obtained from OSA is plotted in Fig. 3 a). From graph it is clear that $\Delta\lambda_b$ is increasing with temperature grow. Before signal processing software was used the amplitudes with lower levels than 10 μW were substituted with 0 W (noise cut). After noise cut procedure $\Delta\lambda_b$ was estimated for each temperature with maximum, centroid and Gaussian approximation technique respectively (Fig. 3. b). From obtained $\Delta\lambda_b$ values temperature was calculated and compared with PT100 reference data (Fig. 3. c).

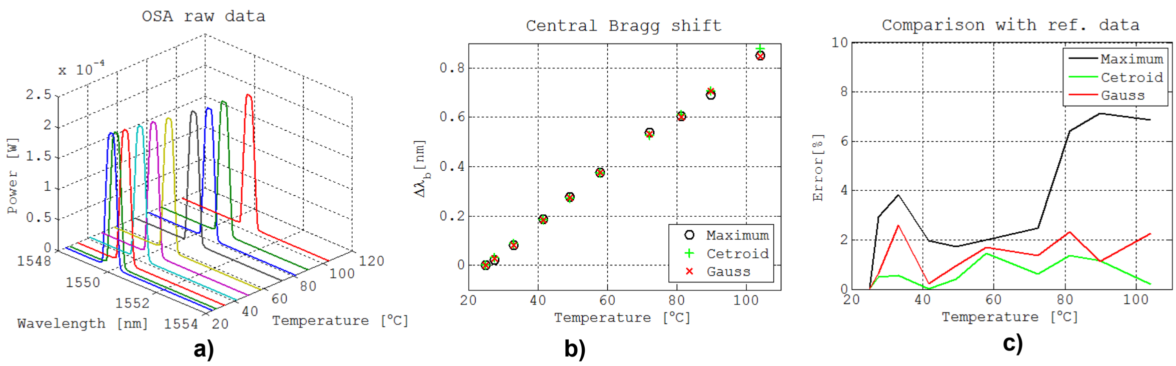

Fig. 3. Measured results: a) raw data, b) $\Delta\lambda_b$ calculation c) data error

The results show that with use of maximum detection algorithm highest error occurred. Especially in the area above 70˚C. Centroid detection had an error below 1.5 % and was also processed with the fastest response in comparison to Gaussian fitting. Therefore one could state that for dynamic and real time measurements centroid method is more suitable than more time consuming polynomial fitting method.

3. Conclusions

In the beginning of the article general overview of uniform FBG structure sensors is brought. The mechanism of sensing and measuring is stated.

In the signal processing techniques chapter three methods for $\Delta\lambda_b$ estimation are introduced and tested. The used experimental data were obtained during heating of the FBG structure. Data comparison shows good correlation between processing techniques in range up to 70˚C. The tested methods especially centroid calculation algorithm is suitable for future planned semi distributed – point sensing application based on FBG.

Usage of FBGs sensors in structure health monitoring application could have a major impact on prevention of overloading conditions and therefore collapsing of the civil engineering buildings. It also could be used as an indicator of inner material properties via monitoring parameters like temperature, moisture and dilatation.

Acknowledgements

This work was supported by the Slovak Research and Development Agency under the contract No. APVV-0062-11.

References

[1] Prindle W., et. al: The Twin Pillars of Sustainable Energy: Synergies between Energy Efficiency and Renewable Energy Technology and Policy, *Aceee.org* , 2008-05-05.

[2] Kersey D., et. al: Fiber Grating Sensors, *Journal of Lightwave Technology*, vol. 15, no. 8., pp. 1442-1463, Aug. 1997.

[3] Lee, B., Jeong, U.: Interrogation Techniques for Fiber Grating Sensors and the Theory of Fiber Gratings, Fiber Optic Sensors, *CRC Press*, 2002, ISBN:082470732X, pp. 295- 381.

[4] Rao Y. J. : In-fibre Bragg grating sensors, *Measuring Science Technology*, vol. 8, pp. 355-375, 1997.

[5] Hill O. K., Meltz G.: Fibre Bragg Grating Technology Fundamentals and Overview, *Journal of Light and Technology*, vol. 15, pp. 1263-76, 1997.

[6] Morey W. W, Meltz G., et al: Fibre optic Bragg grating sensors, *Proc. of SPIE*, 1169, pp. 98-107, 1989.

[7] Kersey A. D., Davis M. A., et al: Fiber Grating Sensors, *Journal of Light Technology*, vol. 15, pp. 1442-1463, 1997.

[8] Negri L., Nied A., et. al: Benchmark for Peak Detection Algorithms in Fiber Bragg Grating Interrogation and a New Neural Network for its Performance Improvement, *Sensors 2011*, vol. 11, pp. 3466-3482, doi: 10.3390/s110403466.

[9] Datasheet paper: *SmartFBG,* Smart Fibers, online: www.smartfibers.com

Experimental Noise Spectroscopy and the Measurement of Periodic Material Structures

P. Drexler, J. Seginak, J.Mikulka, D. Nešpor, M. Friedl, P. Marcoň, P. Fiala

Department of Theoretical and Experimental Electrical Engineering,
Technicka 12, 616 00 Brno, Czech Republic
Email: fialap@feec.vutbr.cz

Abstract. *The authors discuss the application of a broadband noise signal in the research of periodic structures and present the basic testing related to the described problem. Generally, noise spectroscopy tests are carried out to verify the behaviour of the response of periodic structures, and their objective consists in recording the properties of microscopic structures in natural and artificial materials. The aim is to find a metrological method utilizable for the investigation of structures and materials in the frequency range between 100 MHz and 10 GHz; this paper therefore characterizes the design of a suitable measuring technique based on noise spectroscopy and introduces the first tests conducted on a periodic structure. In this context, the applied equipment is also shown to complete the underlying theoretical analysis.*

Keywords: Nanomaterials; Periodic Structures; Noise; Noise Spectroscopy; Microscopic Structures.

1. Introduction

Sir Isaac Newton, the widely recognized founder of spectroscopy [1], discovered monochromatic light (Fig. 1) via an optical prism. The scientist later described his findings in Optics, one of the major works of science of all times; the first spectrometer was nevertheless presented only in 1860 by Kirchhoff and Bunsen. Generally, spectrometry can be defined as a discipline analyzing the properties and generation of the spectra of harmonic signals or electromagnetic waves. The related research methods are based on the interaction between an electromagnetic wave and the measured sample of matter. With respect to electromagnetic spectroscopy, it is vital to refer to the Raman technique, a tool providing information on the structure and spatial arrangement of the quantum mechanical model of a molecule. By extension, spectroscopy in its general sense is also applicable for different materials, such as carbon [2], [3]. The set of central subareas of the discussed field comprises spectroscopy utilizing nuclear magnetic resonance, which is applied to determine the distribution of atoms in the vicinity of nuclei exhibiting non-zero nuclear spin (1H, 13C, 31P, …). In the given context, let us note that nuclear magnetic resonance spectroscopy [4],[5],[6] is a physical-chemical method exploiting the interaction between atomic nuclei of the quantum mechanical model of matter and the external magnetic field. The technique examines the distribution of nuclear spin energies in the magnetic field and investigates the transition between individual spin states caused by radio frequency radiation. Considering noise spectroscopy, we can point out that this method is effectively practiced via both harmonic analysis and statistics. To evaluate the signals in continuous time, it is possible to use suitably the Fourier transform approach [7], which can be further modified for other signal types. The evaluation of discrete signals is then feasible by means of the discrete Fourier transform [8] and the fast Fourier transform algorithms [9]. However, the Fourier transform is not applicable for the investigation of non-stationary signals.

Periodic structures

From the perspective of description, a macroscopic material (MM) can be defined via a quantum mechanical (QM) model. The MM is then examined based on the incidence/radiation of an electromagnetic wave, and from this interaction we then deduce the properties of the sample. The QM model of the sample comprises a high number of repeated structures, and it is thus possible to use the term periodic material structure. Depending on the result of the EMG wave interaction, we can determine the basic and complementary properties of the sample (conductor; semiconductor; or insulator). Such utilization of similar effects is also typical of various subareas of spectroscopy [2]. Research in the given area was already performed by

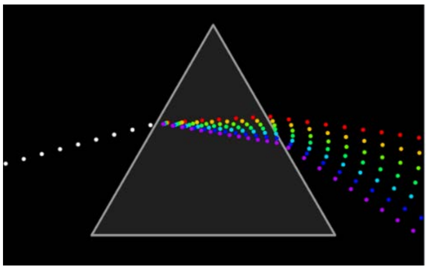

Fig. 1. A prism showing the decomposition of light.

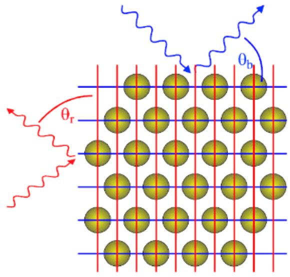

Fig. 2 X-ray reflection from a periodic structure of atoms.

Yablonovitch, but his experiments focused on an EMG wave in the spectrum of light [10]. The first phases of research into the interaction between radiation and a periodic structure can be traced back to the initial years of the 20th century, a period when Bragg discovered by observation that, under certain conditions, atomic structure can behave like a mirror. This holds true, for example, in X-rays if we have the wavelength λ and distance d between two neighbouring atoms at the angle of incidence Θ:

$$\lambda = 2d \cdot sin(\Theta \pm \delta), \qquad (1)$$

where δ is the angle deviation. Reflections of the incident EMG wave will occur, Fig. 2. It is nevertheless obvious that the material and its atoms as such do not exhibit the above-indicated property, and we also need to ensure periodicity of the structure on the scale of wavelengths of the incident EMG wave. In periodic structures, the described effect can be used to determine the properties of the monitored sample of material. If an unknown sample of material (conceived according to the QM model) is irradiated with an EMG wave exhibiting sufficient wavelength, the generated conditions will facilitate reflection of the selected EMG wave from the applied electromagnetic wave spectrum. The wave selection depends on the actual periodicity of the material. The ideal frequency range of the transmitted wave is infinite bandwidth; theoretically, this condition can be satisfied by white noise. When the reflected part of the EMG wave is captured, it is advantageous to employ suitable evaluation tools, for example the Fourier transform, wavelet transform, or other techniques introduced above.

Benefits of Noise Spectroscopy

The contribution of noise spectroscopy consists in the use of an ultra-wideband signal to acquire, within a single instant of time, a response to the entire spectrum of electromagnetic waves. One of the possible ways of suppressing the negative sources of signals consists in the use of wideband signals such as white noise, and this approach can be further reinforced by analyzing the problem of absorption in the examined material. The indicated methods require a source of noise, a receiving and a transmitting antenna, and A/D conversion featuring a large bandwidth; for our purposes, the bandwidth of between 50MHz and 10GHz proved convenient. Until recently, however, it had not been possible to design an A/D converter of the required speed or to materialize devices with the above-mentioned bandwidth. Currently, high-end oscilloscopes are nevertheless available with a sampling frequency of hundreds of Gsa/s.

2. Noise source

At present, the appropriate type of source is supplied by certain manufacturers operating in the given field. Importantly, for the noise spectroscopy application, we require a comparatively large output power of up to 0dB/mW; the assumed bandwidth characteristics then range up to 10GHz. At this point, it is also necessary to mention the fundamental problem of finding active devices able to perform signal amplification at such high frequencies. Our requirements are thus limited by the current status of technology used in the production of commercially available devices; the highest-ranking solution for the bandwidth of up to 10GHz can be found only up to the maximum of 0dB/mW. In the noise spectroscopy experiments, we utilized a generator and an amplifier (NC1128A), Fig. 3. In order to verify the applicability of the noise spectroscopy laboratory arrangement (Figs. 5), we tested a metamaterial (periodic structure) designed for the frequency of 199.9 MHz (Fig. 4).

Fig. 3. The noise generator and power amplifier. The image shows the tested noise generator, whose output power is 0dBm in the frequency range of between 100kHz and 10GHz.

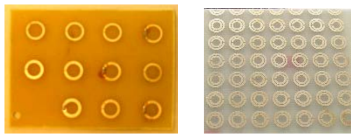

Fig. 4. The first tuned periodic structure tested to verify the noise spectroscopy measurement.

3. Antennas

Wideband antennas have long been used especially for the reception of specific signals. In certain cases, such traditional wideband devices also satisfy the requirements placed on UWB (ultra-wideband) systems. Traditional parameters utilized to describe technical characteristics of antennas may not be suitable for use in UWB systems [11]. The magnitude, impedance, bandwidth, and effectivity are interconnected in such a manner that their mutual proportion is indirect; these characteristics manifest themselves especially in electrically short antennas, the term denoting a layout where the largest dimension of the active part of an antenna is not larger than one tenth of the wavelength of the transmitted/received wave. An antenna electrically short in the entire frequency bandwidth cannot be simultaneously effective and exhibiting the impedance bandwidth (the range of frequencies at which the antenna is impedance matched) necessary for UWB applications. Within our research, some antenna types have been tested, including a Vivaldi antenna, a spiral two-leg antenna, and a hybrid fractal antenna combined with a spiral two-leg antenna (Fig. 5).

4. Method

The initial stage involved repeated transmission and sensing of both the signal provided by the noise generator and the external signals. The repetition was carried out for each sampled frequency, and the incident power spectrum was summed. Thus, we obtained the frequency dependence of the transmitted signal energy distribution. Generally, if the transmitter/receiver set is not located in a room with a defined spectral absorbance, we can expect uniform energy distribution within the whole frequency range. The record is, at its end, transformed to the frequency dependence of the specific power. In the described manner, we acquired the characteristics of the spectrum measurement background. At this point, the examined sample was placed in the support case (Fig.5, 6A, 6B); the sample for such application can be layered or periodic, and it is expected to provide the assumed frequency characteristic. Subsequently, repeated measurement was performed observing the above-outlined procedure. In the case of a markedly frequency-dependent background, the obtained characteristic can be corrected.

Fig. 7 shows the frequency dependencies of the measurement setup and the multi-layer material.

5. Conclusion

The research paper provides an elementary overview and description of the laboratory equipment for the noise spectroscopy measurement and the related experiments. Noise spectroscopy operations within the frequency band of between 10MHz and 10GHz can be performed using currently available technologies. The noise source comprised a generator (NC1108A) and an amplifier (NC1128A).

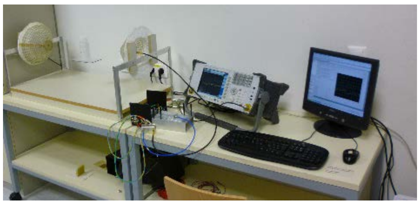

Fig. 5 The arrangement of the noise spectroscopy station (free room).

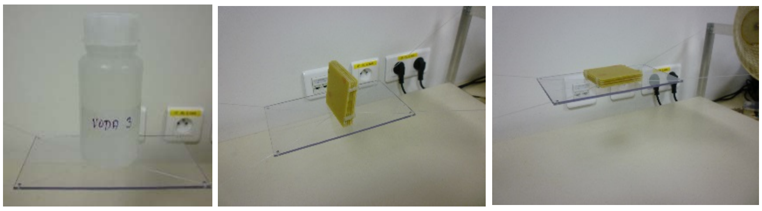

A B

Fig. 6 A liquid (nanomaterials) A, solid B sample arranged in the laboratory for the sensing and evaluation of the spectrum (no shielded chamber; free room).

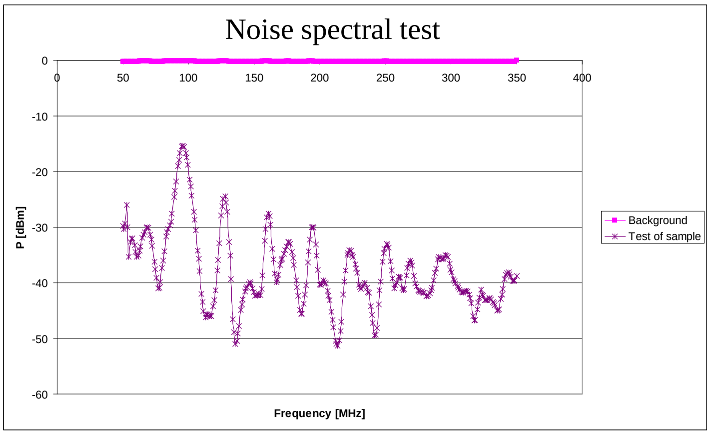

Fig. 7. The waveform and spectrum of the noise generator output for the measured sample; f=50-350MHz.

Acknowledgement

The research described in this paper was financed by the National Sustainability Program under grant No. LO1401 and by Czech Science Foundation under grant No. 13-09086S. For the actual analyses and experiments, infrastructure of the SIX Center was used.

References

[1] http://cs.wikipedia.org/wiki/Spektroskopie
[2] http://cs.wikipedia.org/wiki/Ramanova_spektroskopie
[3] http://spectroscopyonline.findanalytichem.com/spectroscopy/Raman+Spectroscopy
[4] T.P.Pitner, J.D.Glickson, J.Dadok, Nature, London, 250, 582, 1974.
[5] J.Dadok and R.F. Spencer, J.Magn. Reson. 13, 128, 1974
[6] J.Dadok, High-Field NMR Instrumentation, Wiey online, 15.3.2007.
[7] http://www.sci.muni.cz/~sulovsky/Vyuka/Mod_metody/Modmetody5.pdf
[8] Kufner, A.; Kadlec, J. : Fourierovy rady, Academia 1969, Czech Republic
[9] Uhlír, Jan; Sovka, Pavel : Číslicové zpracování signálu, CVUT 1995
[10] Šikula, J., Koktavý, B., Vašina, P., Chobola, Z., Juránková, V. Noise Reliability Indicators. In Procedings of the 4th European Symposium on Reliability of Electron Devices. Bordeaux - France: University of Technology, 1993. s. 341 (s.)
[11] W. Demtröder, Laser Spectroscopy, 3rd Ed. (Springer, 2003).

Magnetic Properties of Yttrium Iron Garnet Polycrystalline Material Prepared by Spray-Drying Synthesis

[1]M. Majerová, [2]A. Prnová, [1]M. Škrátek, [2]R. Klement, [2]M. Michálková, [2]D. Galusek, [3]E. Bruneel, [3]I. Van Driessche

[1]Department of Magnetometry, Institute of Measurement Science, Slovak Academy of Sciences, Dúbravská cesta 9, 841 04 Bratislava, Slovakia
[2]Vitrum Laugaricio – Joint Glass Center of the IIC SAS, TnU AD, FCHTP STU and Rona, a.s., Študentská 2, SK-911 50 Trenčín, Slovakia
[3]Department of Inorganic and Physical Chemistry, Ghent University, Krijgslaan 281 (53), 9000 Ghent, Belgium
Email: melinda.majerova@savba.sk

Abstract. *The yttrium iron garnet polycrystalline powder was prepared by spry-drying synthesis from nitrates solution. The calcined powder was pressed into pellets and sintered at various temperatures for 2 hours. Prepared samples were characterized by XRD analysis and magnetic properties were measured. The magnetic moment of 4.3* μ_B *and saturation magnetization of 24* Am^2kg^{-1} *were observed for sample sintered at 1000 °C.*

Keywords: Yttrium Iron Garnet, Spry-Drying Synthesis, Magnetic Properties

1. Introduction

Yttrium iron garnet ($Y_3Fe_5O_{12}$, YIG) is one of the most important ferromagnetic materials and has been widely applied for tunable microwave devices, circulators, isolators, phase shifters, nonlinear devices, magnetic bubble domain-type digital memories [1], etc. due to its excellent electromagnetic properties, including low dielectric loss, narrow ferromagnetic resonance linewidth in microwave region, adjustable saturation magnetization, good temperature and chemical resistance [2]. In recent years, research attention has been committed to the investigation of YIG and doped YIG nanocrystals since these highly divided materials may be used in Faraday magneto-optical devices for telecommunications [2,3] or for localized hyperthermia by induction heating as biomedical application [4].

Preparation of the YIG materials in polycrystalline or monocrystalline form is associated with technological complications related with high temperatures (≥1600°C) and necessity to apply long annealing times. The successfully preparation of uniform polycrystalline powders with very high homogeneity and particle size distribution by spray drying synthesis and subsequent controlled crystallization is a reasonable economic solution.

In this work, YIG materials were prepared by spry–drying synthesis from nitrates solutions in form of 1μm spheres. Then the prepared powders were calcined and sintered at different temperatures in interval of 800-1000 °C for 2 hours. The sintered samples were characterized by XRD analysis, magnetic properties were measured, quantities of individual crystalline phases were calculated, and the results are reported.

2. Experimental

As starting materials for solution, nitrates $Fe(NO_3)_3 \cdot 9H_2O$ and $Y(NO_3)_3 \cdot 6H_2O$ (Sigma-Aldrich Chemie Gmbh, USA) in a stoichiometric ratio were used. The required amounts of nitrates were weighed and then dissolved in distilled water to a final volume of 250 ml. This way prepared solution was fed into spray-dry apparatus (Büchi Mini-spray dryer B-290). The prepared powder was calcined at 650 °C for 4 h, pressed in the form of pellets with diameter of 8 mm and then sintered at different temperatures (800, 900, 1000 °C) for 2 hours. The X-ray diffraction analyses were performed on a Panalytical Empyrean device (CuKα radiation, 2Θ range 10-80°), to estimate the degree of crystallinity and for qualitative evaluation of individual crystalline phases in samples. The obtained diffraction data have been evaluated by the High Score Plus software (v.3.0.4, PAN Analytical, Netherlands) equipped with the Open Crystallographic Database (OCD, v. 2013). The thermal behaviour of raw material in the temperature range of 35-1200 °C with heating rate of 10 °C/min was studied by DSC analysis (Netzsch STA 449 F1 Jupiter). For this measurement, O_2 atmosphere and platinum crucibles with sample weight of approx. 15 mg were used. After this examination, 5 weight % of Si was added to sintered samples and content of individual crystalline phases was calculated from X-ray diffraction patterns.

DC magnetization measurements were performed on a Quantum Design MPMS XL-7 SQUID magnetometer. Magnetization as a function of temperature was measured in the temperature range of 1,8–400 K. The samples were cooled from the room temperature to the lowest temperature in zero applied field and the magnetization was measured after the application of the field (8000 Am^{-1}), while warming (ZFC, zero-field-cooled measurement). For field-cooled (FC) measurements, the samples were cooled in the presence of field and magnetization was measured as a function of temperature while cooling. Measurement of the magnetization as a function of field was made at two different temperatures (5, 300 K).

3. Results and discussion

The list of prepared samples with calculated content of $Y_3Fe_5O_{12}$ is in Tab.1 (col. 1-3). The prepared precursor powder (YIGP) after 650 °C calcination, was polycrystalline, with content of $Fe_4Y_4O_{12}$ and hematite α-Fe_2O_3 as a major phases. In DTA record of YIGP, the small exothermic effect with maximum at temperature 998 °C was observed, which can be assigned to $Y_3Fe_5O_{12}$ phase formation.

Table 1. Magnetic properties of samples prepared at three different temperatures.

Sample name	Sintering temp. [°C]	XRD YIG quantity[wt %]	Coercitivity H_C [Am^{-1}]	Saturation M_S [Am^2kg^{-1}]	Remanence M_R [Am^2kg^{-1}]
YIG1	800	0	$1{,}87\times10^6$	1,5	5,9
YIG2	900	7	9390	2,7	7,4
YIG3	1000	88	1519	24,0	4,2

From comparison of XRD records of samples was concluded that all prepared samples were polycrystalline with content of $YFeO_3$ (yttrium iron perovskite), $Y_3Fe_5O_{12}$ and α-Fe_2O_3 crystalline phases. Also increasing of portion of $Y_3Fe_5O_{12}$ phase with increasing sintering temperature was observed. The samples sintered at lower temperatures (800, 900 °C) contain mainly α-Fe_2O_3 and $YFeO_3$ and small portion of YIG crystalline phase. The YIG3 sample (Tab.1) contain high portion of YIG phase (88 wt. %), smaller content of $YFeO_3$ (10,8 wt. %) and α-Fe_2O_3 (0,8 wt. %). The presence of the residual phases is the result of incomplete YIG formation according to the reaction scheme:

$Y_2O_3 + Fe_2O_3 \rightarrow 2YFeO_3$ (perovskite) $T = 500 – 900°C$ (1)

$3YFeO_3 + Fe_2O_3 \rightarrow Y_3Fe_5O_{12}$ (garnet) $T = 900 – 1600$ °C. (2)

Hysteresis loops (Fig. 1) recorded at the temperature of 5 K indicate that with increasing of the sintering temperature, the saturation magnetization rises with increasing amount of the $Y_3Fe_5O_{12}$ phase. The profile of the magnetization for the YIG3 sample suggest obtaining of a soft ferromagnetic material, because sample is very sensitive to an external magnetic field, reaches its saturation at relatively small field and the coercivity is small (< 1600 Am^{-1}).

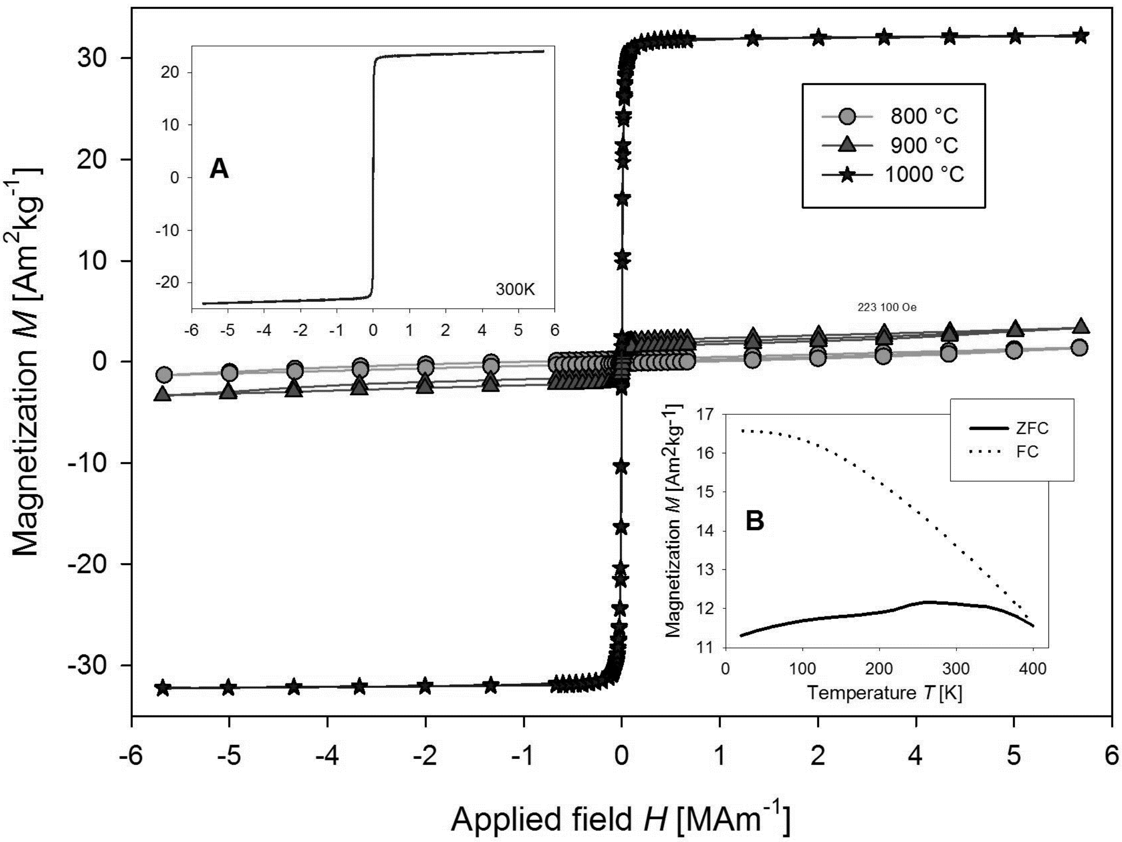

Fig. 1 Hysteresis loops recorded at the temperature of 5K for the samples sintered at three different temperatures. The inset A shows room temperature hysteresis loop for the sample YIG3 annealed at 1000 °C. The inset B shows ZFC and FC magnetization curves measured in a field of 8000 Am^{-1} for the YIG3 sample.

The experimental value of the magnetic moment for this sample is 4,3 μ_B. The inset A of Fig. 1 shows hysteresis loop for the YIG3 sample measured at the room temperature, with the saturation magnetization of 24 Am^2kg^{-1}. These values are lower than expected for bulk YIG (5 μ_B, 26,8 Am^2kg^{-1} [1,2,3]) and it could be attributed to the presence of residual phases. Magnetic properties (for 300 K measurement) of prepared samples are summarized in Tab. 1 (col. 4-6). The inset B of Fig. 1 shows the temperature dependence of the ZFC/FC magnetization measured at applied field of 8000 Am^{-1} for the YIG3 sample in the temperature range of 20–400 K. Although, the Curie temperature T_C for YIG is higher than 400 K [1], the following features can be observed: (1) if we could increase the temperature, both curves will probably collapse above $T_S \geq 400$ K; (2) irreversibility is observed below T_S, with $M_{ZFC} < M_{FC}$; (3) the maximum value of the ZFC magnetization is observed at $T_M < T_S$ (~ 260 K).

4. Conclusions:

Three samples with YIG composition were prepared by spry-drying synthesis and sintered at 800, 900 and 1000 °C for 2 hours. All prepared samples were studied by XRD analysis and magnetic properties were measured**.** The samples sintered at lower temperatures contained mainly perovskite and hematite phases. In contrast, sample sintered at 1000 °C contained 88 % of YIG phase. The magnetic moment of 4,3 μ_B and saturation magnetization of 24 Am^2kg^{-1} was measured for this sample. These results show the possibility of simple preparation of YIG materials with interesting magnetic properties.

Acknowledgements

The financial support of this work to the projects SAS-NSC JRP 2012/14, APVV-0125-11, VEGA 2/0152/13 and VEGA 1/0631/14 is gratefully acknowledged. This publication was created in the frame of the international academic agreement (IIC SAS, IMS SAS, Slovakia and Ghent University, Belgium), with a financial contribution of FWO and KVAB (Belgium) institutions.

References

[1] Nguyet DTT, Duong NP, Satoh T, Anh LN, Hien TD. Temperature-dependent magnetic properties of yttrium iron garnet nanoparticles prepared by citrate sol–gel. *Journal of Alloys and Compounds*, 541: 18-22, 2012.

[2] Zhang W, Guo C, Ji R, Fang C, Zeng Y. Low-temperature synthesis and microstructure-property study of single-phase yttrium iron garnet (YIG) nanocrystals via a rapid chemical coprecipitation. *Materials Chemistry and Physics*, 125(3): 646-651, 2011.

[3] Fu HP, Hong RY, Wu YJ, Di GQ, Xu B, Zheng Y, Wei DG. Preparation and Faraday rotation of Bi-YIG/PMMA nanocomposite. *Journal of Magnetism and Magnetic Materials*, 320(21): 2584-2590, 2008.

[4] Grasset F, Mornet S, Demourgues A, Portier J, Bonnet J, Vekris A, Duguet E. Synthesis, magnetic properties, surface modification and cytotoxicity evaluation of $Y_3Fe_{5-x}Al_xO_{12}$ ($0 \leqslant x \leqslant 2$) garnet submicron particles for biomedical applications. *Journal of Magnetism and Magnetic Materials*, 234(3): 409-418, 2001.

Influence of Pitting Corrosion on Burst Pressure Value

M. Kubiš, D. Šišmišová, J. Pastierová

Faculty of Mechanical Engineering, Institute of Automation, Measurement and Applied Informatics, Mýtna 36, 812 31 Bratislava 1, Slovak Republic
Email: milan.kubis@stuba.sk

Abstract. *The article is focused on the safety assessment of pressure pipelines with corrosion defects and the influence of individual defect distance on burst pressures. The practical part presents the modelling of a pipeline with corrosion defects. Burst pressures were determined for each model with changing corrosion defect parameters and mutual interaction between the actual defects. The paper outlines the results of the numerical simulation by a finite element modeling software. The main aim of the work is to highlight the fact that the currently employed standard procedure used to assess the impact of corrosion defects on pipes is not precise enough and does not fully correspond with the results of the simulations presented here. The simulation results suggest, that the currently used safety factors need to be increased, in order to include the geometric effects of corrosion defects.*

Keywords: Pressure Pipeline, Corrosion Defect, Burst Pressure, Safety

1. Introduction

The main causes of pipeline failure are external disturbances and corrosion [1]. Therefore, novel methods are necessary to evaluate and determine the severity of the fault detected in the pipe. Pipelines will always contain defects at some point during their operational life, thus it will also require a judgment call, whether or not it is necessary to carry out maintenance [2]. Major accidents on pipelines were caused by a combination of several factors, in most cases, however, a corrosion defect was the underlying cause (Hrašovník 2014, Janków Przygodzki 2013, Slanec 2008, Stone Kosihy 2000). This article deals with defects caused by corrosion and assesses its impact on the stress state conditions and the security of the entire operation [3]. In this method, the computation of the burst pressure is based on the tension strength of the material. DNV-RP-F101 also considers a quadrangular defect profile and the depth of the maximum length of the actual defect. Its use is suitable for modern ductile materials. The maximum possible depth of the defect is 0.85 times the residual wall thickness [6].

Simulation of the effect of distance pitting in the direction of the pipe axis

The pipeline section was modeled in the ANSYS finite element modeling software using the Solid 187 element [5].

The models developed here not only vary the length of the corrosion defect but also its depth. Three representative values of depth were selected, namely h_d = 4.6 mm, 6.8 mm and 9 mm. These values correspond to the third, half and two-thirds of the thickness of the undamaged pipeline. First, we investigated the value of the internal pressure at which the notches in the roots reach the peak stress corresponding to the breaking strength of 675.9 MPa material. The results of this simulation are shown in Table 1.

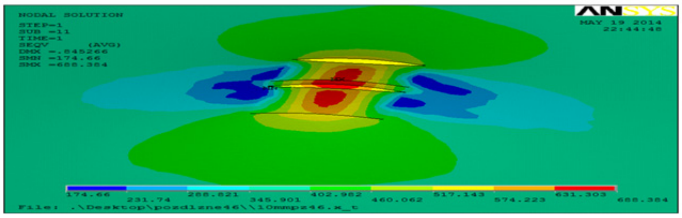

Fig. 2. Simulation of pipe defects with depths of 4.6mm in 10mm distance at which the defects interact

Simulation of the effect of distance pitting around the perimeter of the pipe

The simulation is changed by analyzing the effect of pitting distance running around the perimeter of the pipe, otherwise the simulation conditions are similar to the previous one.

2. Results

Simulation of the effect of distance pitting in the direction of the pipe axis

Table 1. Loading pressure required to achieve the burst pressure for corrosion defects in the axial direction of the pipe

Depth of defects h_{d1} =4.6 mm			Depth of defects h_{d2} =6,8 mm		Depth of defects h_{d3} =9 mm	
Distance of corrosion defects l_d [mm]	Loading pressure p_1 [MPa]	Peak stress σ_{max1} $[Mpa]$	Loading pressure p_2 [MPa]	Peak stress σ_{max2} $[Mpa]$	Loading pressure p_3 [MPa]	Peak stress σ_{max3} $[Mpa]$
110	9.9	678.7	9.1	674.7	7.7	674.9
115	10	680	9.18	674.5	7.9	677.2
120	10	674.1	9.4	675.1	8.15	674.3
125	10	675	9.47	680.2	8	677.5
130	10.1	679.9	9.6	676.2	8.2	675.3
135	10.2	674.5	9.57	679.5	8.25	673.7
140	10.2	676.3	9.6	679	8.4	672.9
150	10.3	678.9	9.64	674.2	8.45	679.1

Table 1 shows that the value of loading pressure required to achieve the expected burst pressure decreases with respect to the increasing depth of corrosion damage. The change in the loading pressure required to achieve the burst pressure for one deep defect but with variable distance of the corrosion defects is not as significant.

Simulation of the effect of pitting distance around the perimeter of the pipe

Table 2. Loading pressure required to achieve the burst pressure for corrosion defects distributed over the circumference of the pipe

Depth of defects h_{d1} =4,6mm			Depth of defects h_{d2} =6,8mm		Depth of defects h_{d3} =9mm	
Distance of corrosion defects l_d [mm]	Loading pressure p_1 [MPa]	Peak stress σ_{max1} $[Mpa]$	Loading pressure p_2 [MPa]	Peak stress σ_{max2} $[Mpa]$	Loading pressure p_3 [MPa]	Peak stress σ_{max3} $[Mpa]$
110	11.2	673.2	10.2	677.1	674.9	9.6
115	11.2	680.1	10.2	674.8	677.2	9.6
120	11.2	677.4	10.2	678.1	674.3	9.55
125	11.2	674.9	10.2	679.9	677.5	9.5
130	11.2	677.3	10.2	678.4	675.3	9.6
135	11.2	675.8	10.2	674.5	673.7	9.6
140	11.2	678.6	10.2	677.0	672.9	9.55
150	11.2	676.9	10.15	677.2	679.1	9.55

As we can see from Table 2, the pressure required to achieve burst pressure that would correspond to the actual material strength does not vary substantially with the depth and distance of the corrosion defects. One possible reason is the geometry of the corrosion defects themselves. Since by varying the position of the defects in the axial direction of the pipe were defects together with sharp edges. There was thus a situation that even with the smallest distance is corrosion defects of varying depth and distance does not affect. This finding is a nice proof that the interactions between defects are highly dependent on the geometry.

3. Discussion

For a pipe with the dimensions of 1200 x 13.6 mm, for which the nominal stress (unaffected by corrosive defects) is known, the peak stress affected by the corrosive defects can be estimated by the presented analysis. If the internal pressure of the pipeline is 8 MPa, and we suppose that a nominal stress of 323.9 MPa and defects with identical geometry are present (e.g. depth of 6.8 mm), and if the distance of these defects is 120 mm then we may estimate a peak stress caused by the corrosion defects as 542 MPa. If one is aware of this information, then may calculate the actual safety factor as the ratio of the maximum stress in the roots of the notches and the actual allowable stress [7]:

$$k_{actual} = \frac{\sigma_{dov}^{actual}}{\sigma_{max}} = \frac{675.9 \text{ MPa}}{542 \text{ MPa}} = 1.23 \,.$$

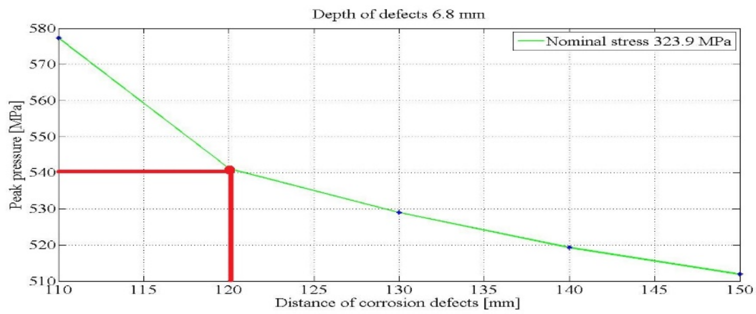

Graph 1. A graph of the peak stress within the defect at a line pressure 8Mpa

4. Conclusions

We may conclude from the presented analysis of burst pressure for pipes with different depths of corrosion defects and various mutual spacing that the real destructive forces can be significantly higher than the pressure calculated in accordance with the procedures outlined by DNV-RP-F101. The established procedures unite corrosion defects on the surface and thus their actual impact underrated. By continuing in this sense, it would be possible to perform more calculations (in this work, there were about 200) with the aim of creating a comprehensible set of guidelines that would allow for the known load distribution of defects and their depth (found e.g. internal inspections) to establish genuine security against destruction and then decide on the maintenance schedule.

Acknowledgement

The authors wish to thank the Faculty of Mechanical Engineering of the Slovak Technical University in Bratislava, grant agency VEGA project no. 1/0604/15 and no. 1/0748/15 for their support in writing this article.

Appendix

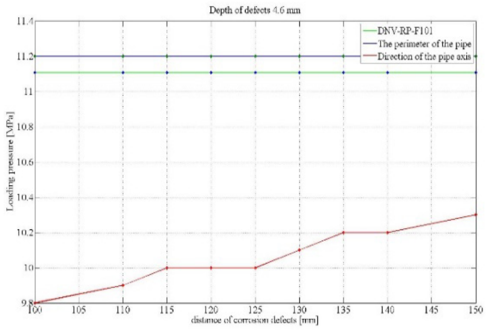

Graph 2. Comparison of the load pressure required to achieve the destruction of the pipe for 4.6 mm deep defects

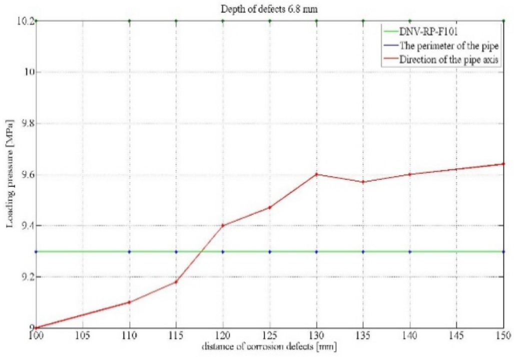

Graph 3. Comparison of the load pressure required to achieve the destruction of the pipe for 6.8 mm deep defects

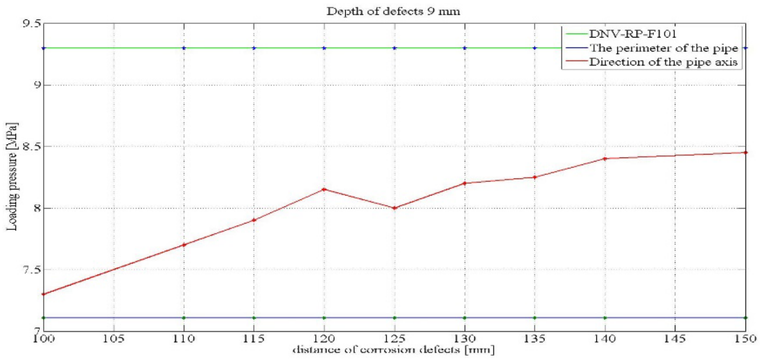

Graph 4. Comparison of the load pressure required to achieve the destruction of the pipe for defects 9 mm depth

References

[1] Cosham, Hopkins, The Pipeline Defect Assessment Manual, Verlag Berlin, 2003

[2] Jon Juel Thompsen, Vibrations and Stability, Springer Verlag Berlin, 2003

[3] Hardrath, F.-H.,Ohman L., A study of Elastic and Plastic Stress Concentration Factors Due to Notches and Fillet in Flat Plates, NACA TN 1117, 1951

[4] Robert D. Cook, Finite Element Modeling for Stress Analysis, John Wilez & Sons Inc., 1995

[5] ANSYS Incorporated, ANSYS Theory reference, ANSYS Inc. 2003

[6] O.H. Bjørnøy (Det Norske Veritas) | B. Fu (BG Technology) | G. Sigurdsson (Det Norske Veritas) | E.H. Cramer (Det Norske Veritas) | D. Ritchie (Shell Global Solutions), Introduction And Background to DNV RP-F101 "Corroded Pipelines", The Ninth International Offshore and Polar Engineering Conference, 30 May-4 June, Brest, France, 1999

[7] Kubiš M, Vplyv jamkovej korózie na hodnotu deštrukčného tlaku potrubia. Diplomová práca. Bratislava: SjF STU, 2014.

Method of Indirect Measurement of Motor Output Torque

P. Klouček, Z. Braier
VÚTS, a.s., Liberec, Czech Republic
Email: pavel.kloucek@vuts.cz

Abstract. *A method of indirect measurement of a motor output torque by using actual values of the angular velocity and the input power quantities was tested. The motor output torque is an important parameter for designer for example during overhaul of older machines or for design of a new generation. It is not possible to place a torque sensor into a machine quite often, so this method can evaluate output torque indirectly in synchronous measurement with other important quantities. The testing stand with Siemens Sinamics/Simotion system and AC servomotor 1FT6 was used for verification of this method.*

Keywords: Output Torque, Indirect Torque Measurement, Dynamic Measurement.

1. Introduction

The method of indirect torque measurement was used in Measurement department, VÚTS, several times for machines with standard asynchronous motor. The motor output torque is an important parameter for designer for example during overhaul of older machines or for design of a new generation. It is not possible to place a torque sensor into a machine quite often, so this method can evaluate output torque indirectly in synchronous measurement with other important quantities.

The method application on servomotor was verified at the mechatronic stand with Sinamics/Simotion system and the three phase AC synchronous servo motor type 1FT6084-8AC71-3AA0 (all the servomotor parameters are in datasheet [1]). The control of servo motor was realized by modular system of converter Sinamics S120, control unit Sinamics CU320 with plug-in terminal board TB30 and controller Simotion. The torque sensor was connected between the output shaft of the motor and the input of the planetary gearbox using shaft couplings and diameter reductions. The torsion bar with the flywheel was connected to the planetary gearbox output. Figure 1 shows the schematic drawing of the stand with measured and calculated quantities. A multifunctional modular all-in-one portable analyzer Dewetron DEWE-2602 was used for synchronous data recording of all measured quantities.

All the measurements, evaluations and results are summarized in [2]. This paper is focused to the verification of the method.

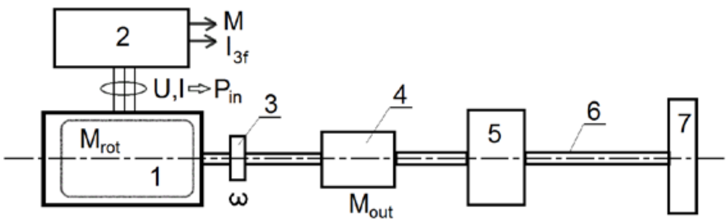

Fig. 1. Schematic view of the used stand and measured quantities: 1 - servomotor, 2 – Sinamics/Simotion system, 3 – encoder Renishaw Signum, 4 - torque sensor ESA DR-2477, 5 – gearbox Spinea, 6 – torsion bar, 7 – flywheel, M – total torque from Sinamics/Simotion, I_{3f} – total current from Sinamics/Simotion, U,I – voltages and currents for three phases, P_{in} – calculated input power, M_{rot} – torque for acceleration of motor rotor, ω – angular velocity, M_{out} – torque on motor shaft

2. Measurement conditions

The three phase AC synchronous servo motor type 1FT6084-8AC71-3AA0 was connected to the gearbox through the torque sensor ESA DR-2477 with measuring range 100 Nm. The planetary gearbox Spinea TS170-33 has a reduction ratio 33:1 and it is made as preloaded (backlash free). The flywheel with weight 13.825 kg and moment of inertia J = 0.0797 kgm^2 was connected to the output of the gearbox via the torsion bar. Natural oscillation frequency of this set is approximately 16 Hz.

The servo motor operated with three different position functions: polynomial, harmonic and parabolic. The stand output runs in function of a four step gearbox with holding time and position feedback. The output movement was made by rotation of the flywheel in angle 90° for each step. The three position functions use almost the same position curve and motion time, but they have quite different angular velocity and acceleration curves. The measurement and evaluation was made for standard control and also for control with special inverse filter applied [3]. The inverse filter was primarily designed for decreasing of the residual oscillations.

The signals measured by external sensors were voltage and current of phase U, V, W, the servo motor shaft torque and angular velocity and angle of the servo motor shaft. The motor torque signal was measured as the analog voltage output from the Sinamics unit and from the TB30 board. A sampling frequency of the measurement was set to 200 kHz with respect to basic switching voltage frequency of the converter 4 kHz.

3. Results

The two different analog outputs of motor torque from the Sinamics/Simotion system were measured. Basic shape of both signals is similar, but signal from the terminal board TB30 is limited by the time period used for the data bus. Minimal time for change of output values is 1.5 ms, so fast changes are misshapen by steps. For next evaluation the signal from the Sinamics unit was used. The torque of motor in the Sinamics unit is obtained from the total current quantity by multiplication by a "torque constant". The torque constant for the used motor is 2.26 Nm/A. It can be easily verified, because current analog output signal from the TB30 board was measured, too. The current signal sent to output gives only absolute value and it doesn't respect orientation, but for the torque calculation the orientation is reflected (see Fig. 2).

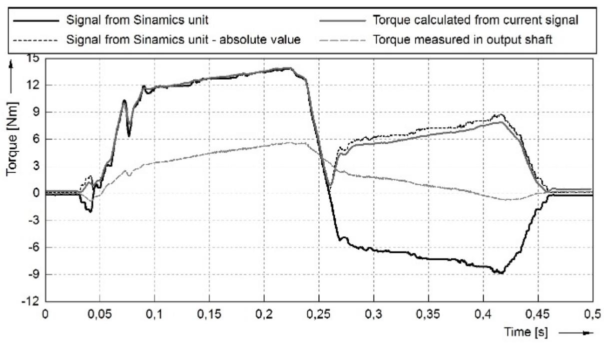

Fig. 2. The torque signals for one step of the output shaft with parabolic position function used.

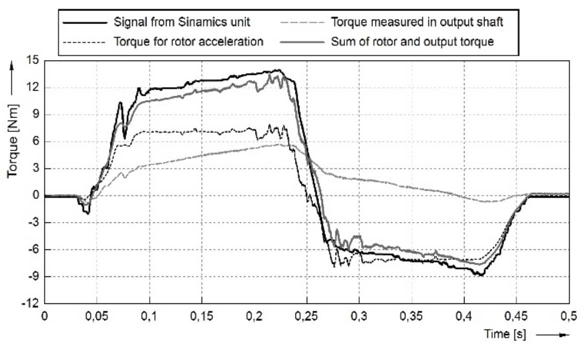

Fig. 3. The torque of shaft and rotor compared with the total torque signal for one step of the output shaft with parabolic position function used.

Figure 2 also shows that the torque measured in the servomotor shaft gives quite different results in comparison with signal from the Sinamics. It is because these measured signals represent different quantities. The signal from the Sinamics unit is the total torque of the servomotor and it consists of an output torque necessary for driving of connected load (measured by the sensor in output shaft) and of a torque necessary for the motor rotor acceleration. We can calculate the torque for the rotor acceleration as

$$M_{rot} = J_{rot}\,\varepsilon \tag{1}$$

where

M_{rot}	torque for the rotor acceleration
J_{rot}	the rotor moment of inertia
ε	angular acceleration of the rotor

The moment of inertia for rotor of the used motor is J_{rot} = 48*10^{-4} kgm^2 [1]. The angular velocity from external encoder placed on the motor output shaft was evaluated through measuring card DMU-PCI developed in VÚTS, a.s. This card is the fifth generation of the DMU device for dynamic measurement of angular velocity and position with patented principle [4]. The DMU device gives much precise results than convention methods of angular velocity measurement. The angular acceleration was directly calculated from the angular velocity signal using differentiation, only the low pass filter for reduction of frequencies higher than 3 kHz was applied. When we calculate sum of the measured torque M_{out} from the external torque sensor and the calculated torque for rotor acceleration M_{rot}, the result is quite similar to the output torque signal M from the Sinamics unit (see Fig. 3) but with lower amplitude. The main reason is the principle of the total torque calculation from the input current used in the Sinamics. Some part of the current is transformed to heat, there are some torque losses for example in bearings etc. and also the motor efficiency is not included.

The opposite calculation can be applied for verification. The input power of a motor P_{in} can be calculated from the measured voltages and currents of all three phases. The output power *Pout* can be calculated from the total torque M and the measured angular velocity ω as

$$P_{out} = M\,\omega. \tag{2}$$

The output power was calculated from the Sinamics torque signal and also from the torque obtained as sum of the output torque and the rotor torque M_{rot}. Figure 4 shows that output power calculated from the Sinamics torque has higher values than the input power in some parts. This would mean efficiency higher than one. This error is caused by the influences described above. The output power calculated from the measured torque is more accurate and the ratio between this output torque curve and the input power curve gives an approximate efficiency of the measured motor (see Fig. 4). Strong peaks in the efficiency curve at time approximately 0.27 s and 0.45 s are caused by the denominator values close to zero.

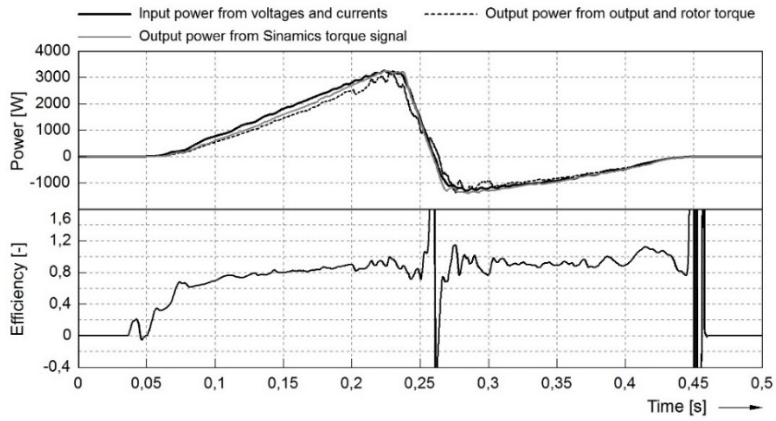

Fig. 4. The input and output power curves for one output cycle of the stand with usage of parabolic position function. Efficiency of the motor was calculated as ratio between output power and input power calculated from voltages and currents.

4. Conclusions

The method of indirect measurement of the motor output torque was tested on stand with the synchronous servomotor Siemens and Sinamics/Simotion system. The motor output torque is an important parameter for designer for example during overhaul of older machines or for design of a new generation. This method is useful for applications where output torque of a motor can't be measured directly by a torque sensor, but synchronous measurement of torque together with other quantities is necessary. Typical application is measurement of a rotating machine with highly variable angular velocity, where is angular sampling instead of time sampling of signals used. The method was applied several times in the past in Measurement department, VÚTS, for measurement of an asynchronous motor with a frequency converter. The torque calculation for an asynchronous motor is easier because of known and nearly constant efficiency of motor.

The results from the test showed that the output torque can be calculated from the measured voltages and currents and the angular velocity/acceleration of the motor. For calculation, the motor rotor moment of inertia must be known. If the motor runs in some continuous mode or in standard range of angular velocity, we can calculate the efficiency close to 1. Much more problematic are modes where the motor stops and runs up again, because the efficiency for low velocities changes a lot and it strongly influences the results (the difference between the input and output power is high). In opposite way, if the real output torque is measured, the real efficiency curve of the tested motor can be evaluated.

The output signals from the frequency converter can be used only for a very rough estimation of the output torque. Both the angular velocity and the torque can be exported, but synchronisation with other quantities is problematic. Conversion to analog output values in control system are limited by resolution of the output A/D converters, by time period of the conversion and different time delays. The torque signal presented by the control system represents the total torque of the motor, which includes also the torque necessary for the rotor acceleration. This torque signal is calculated from the measured total current and doesn't respect motor efficiency and other factors, so the value is quite incorrect. For highly dynamic tasks the rotor torque part can be bigger than the output torque.

Acknowledgements

This work was supported by the Czech Ministry of Education, Youth and Sports, project LO1213.

References

[1] Simodrive 611/Masterdrive MC 1FT6 Synchronous Motors – Configuration Manual. Siemens AG 2004-2005

[2] Klouček P, Bušek M, Antoš J, Braier Z. System of mechanisms with servomotors classification including evaluation of mechanical, electrical and control quantities. report MER-23/2014, VÚTS, a.s., 2014 (in Czech)

[3] Lindr D. Drive control for highly dynamic applications. Ph.D. work, FM TUL, 2011 (in Czech)

[4] Šidlof P, Škop P, Svoboda M. Dynamic measuring method of linear, rotary and pendulum motions by employing a measuring system containing at least one incremental motion pickup and precise generator as well as measuring system for making the same. Patent No. CZ296922 (B6), Int. art.: G01P21/00; G01P21/02; G01P3/42; G01P3/489, Office for Inventions and Discovery, 09.06.2006

The Use of Multifrequency Binary Sequences MBS Signal in the Anemometer with Thermal Wave

M. Bujalski, A. Rachalski, P. Ligęza, E. Poleszczyk

Strata Mechanics Research Institute of the Polish Academy of Sciences, Krakow, Poland

Email: bujalski@img-pan.krakow.pl

Abstract. *Measurement of the very low air flow velocity by means of the spectral analysis of the thermal wave was described. The method is based on the relationship between the phase shifts of the thermal wave's harmonic components in the function of frequency. Experimental research conducted in a wind tunnel was presented and discussed. In this paper applying of multi frequency MBS signal as a source of thermal wave was investigated.*

Keywords: Air Flow Velocity Measurements, Thermal Wave, MBS Signal

1. Introduction

Thermal wave propagation in a flowing gas can be used to measure flow velocity. The method is based on the dispersion of wave, which means that waves of different frequency travel at different phase velocities. Intermittently heated thin wire is used to generate a hot spot in the flowing medium that is convected past temperature sensors placed downstream. Several types of anemometers with thermal wave have been reported in the literature. A broad description was provided by Lomas [1]. Rachalski [2] developed a method that is based on applying a series of sinusoidal waves with different frequencies and measuring phase shifts of the relevant harmonics. A square wave also can be applied [3]. In this paper, we propose the use of Multifrequency Binary Sequences signal MBS [4] as a source of thermal wave.

2. Subject and Methods

Spatial configuration of the proposed system that consists of a three thin, parallel and coplanar hot-wire transducers supplied from the electronic circuit was presented on the Fig. 1. One of them is the thermal wave transmitter. The two remaining wires, placed downstream are wave receivers. The idea is to measure the time of wave passage within the flow at known distance. Simple relation between the phase shift and velocity of the wave is given by Eq. 1.

$$\Delta\varphi = \frac{\omega \Delta x}{V_T} \qquad (1)$$

where

Δx	the distance between the two receivers
ω	angular frequency of the thermal wave
V_T	velocity of the thermal wave

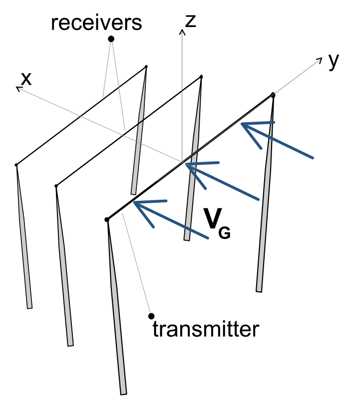

Fig. 1. Spatial configuration of the transmitter and receivers in the air flow.

Kielbasa [5] provided analytical solution for the phase shift *Δφ* of the sinusoidal wave in the flowing medium at known distance (Eq. 2). It can be noticed from Eq. 1 and Eq. 2, that velocity of the flowing gas is lower than velocity of the thermal wave. For low velocities below 30 cm/s, thermal diffusion of air affects the temperature wave propagation.

$$\Delta\varphi\left(\Delta x,\omega,\kappa,V_G\right)=\frac{V_G\Delta x}{2\kappa}\sqrt{\frac{1}{2}\left(\sqrt{1+\frac{16\kappa^2\omega^2}{{V_G}^4}}-1\right)} \tag{2}$$

where

κ	thermal diffusivity of air
V_G	gas flow velocity

Velocity of the flowing gas V_G can be obtained by solving the set of equations (Eq. 3), by means of nonlinear estimation. Applying a series of waves at different frequencies f_i allow to determine the phase shift φ_i for each frequency [6]. However, the sinusoidal wave has one dominant harmonic on the power spectrum. Here, we propose application of the multi frequency Stratchclyde MBS signal on the transmitter. First eight harmonic of that signal contain 76.6% of the power spectrum [7].

$$\Delta\varphi_i=\frac{V_G\Delta x}{2\kappa}\sqrt{\frac{1}{2}\left(\sqrt{1+\frac{16\kappa^2{\omega_i}^2}{{V_G}^4}}-1\right)} \tag{3}$$

3. Results

The experimental research was conducted in a wind tunnel. The probe in the configuration presented in Fig. 1. was inserted in a test section. The distance between the transmitter and the first receiver was set to 3.0 mm, while the distance between two receivers 2.0 mm. The diameter of the transmitter was 8 μm, while the receivers 5 μm. The transmitter operated in the constant temperature anemometer (CTA) system, which forces the temperature of the source to be a time dependent function for a given frequency and amplitude. The system was controlled by non-bridge constant-temperature anemometer circuit [8]. The temperature was varied by modulating the overheating ratio of the transmitter wire ±25% from 1.5. The voltage signals from the wires were acquired by an analog to digital converter. In order to compute the phase shift, signals on the receivers were analyzed via Fourier transform.

Two periods of the MBS waveform on the transmitter and receivers was presented on the Fig. 2. The voltage spikes, related to the change in the overheating ratio, can be found. Thus, short electrical transients in voltage do not affect the signal obtained on the receivers. It can be noticed, that temperature signal diffuses, as the thermal wave is transported simultaneously through convection and thermal diffusion. This effect increases with a decrease in gas velocity. On the Fig. 3 amplitude spectrum of received signal was shown. It can be observed that applying of multi frequency signal allows determining phase shift for several harmonics simultaneously.

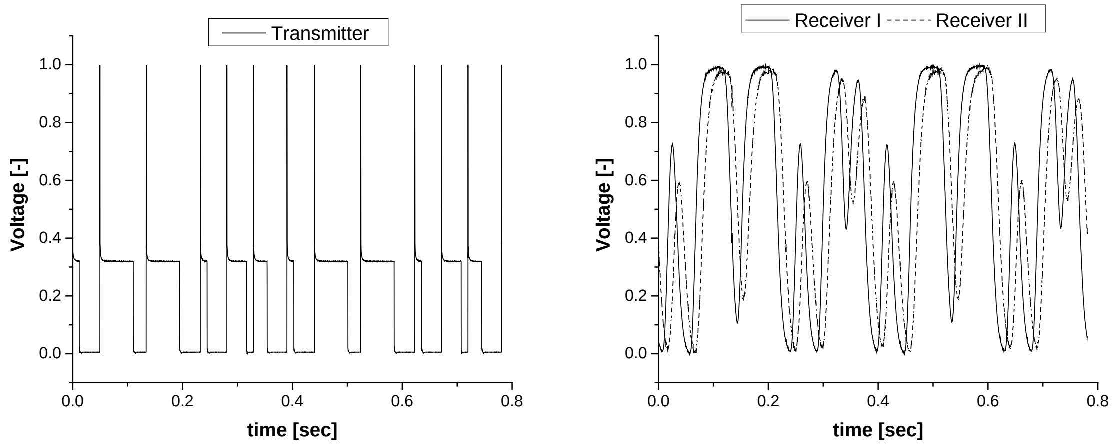

Fig. 2. Two periods of the normalized voltage waveform on the transmitter (left) and receivers of the thermal wave (right) for V_G = 18.48 cm/s (right).

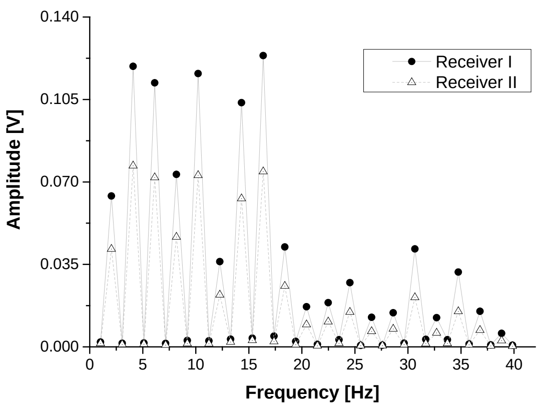

Fig. 3. Amplitude spectrum of temperature signal on the receivers for V_G = 18.48 cm/s.

Measured phase shifts as a function of frequency for four flow velocities was presented on the Fig. 4. The results were compared with the phase shifts obtained from sinusoidal wave. A good agreement between two different waveforms can be found. The result of the air flow velocity estimation and corresponding error of fitting was presented in Tab. 1.

Table 1. Measured velocity of the air flow using the sinusoidal and MBS wave.

Velocity from the sinusoidal signal [cm/s]	Standard Error [cm/s]	Velocity from the MBS signal [cm/s]	Standard Error [cm/s]
7.44	0.05	7.68	0.09
18.21	0.26	18.48	0.17
24.06	0.25	24.00	0.14
30.55	0.23	30.02	0.14

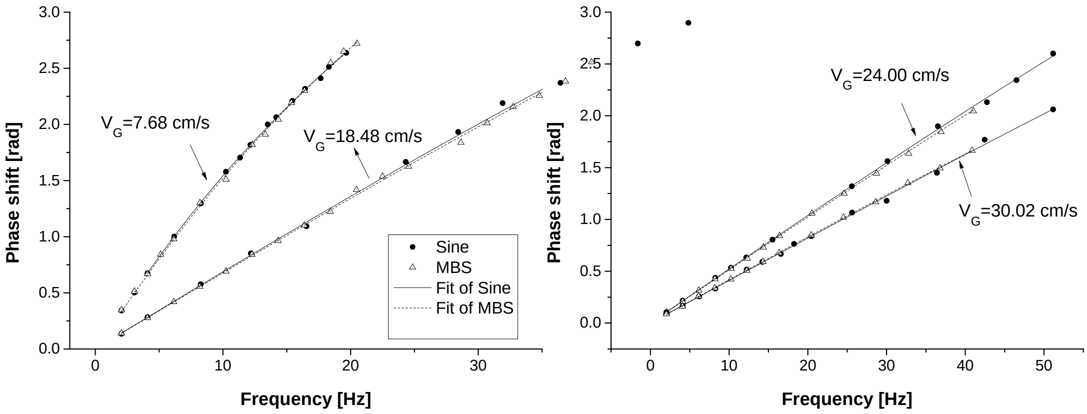

Fig. 4. The measured phase shift as a function of the frequency for the sine and MBS wave.

4. Discussion

Thermal wave propagation in a flowing gas can be used to measure velocity in the very low range. Presented method is restricted to laminar flow conditions. In this paper, the MBS signal on the transmitter of the wave was applied. The experimental results were compared with sinusoidally heated wire. The main advantage of using the MBS signal is that one can obtain phase shift for several harmonics simultaneously, which reduces the measurement time.

Acknowledgements

This study was performed under the research project: „Investigation of spatial propagation and optimization of methods for generation, detection and analysis of temperature waves in the aspect of absolute measurement of flow velocity and thermal diffusivity of gases” financed by Polish National Science Centre upon a decision number DEC-2012/07/B/ST8/03041.

References

[1] Lomas C.G. Fundamentals of Hot Wire Anemometry, Cambridge University Press, 2011.

[2] Rachalski A. High-precision anemometer with thermal wave. Review of Scientific Instruments, 77 (9): 095107, 2006.

[3] Biernacki Z, Kurkowski M, Zloto T, Ptak P. Analysis of exploitation and metrological properties of a wave thermoanemometer system. *Measurement Science Review*, 1(1), 2001 131-134

[4] Henderson I, McGhee J Compact symmetrical binary codes for system identification Mathematical and Computer Modelling, 14 213-218, 1990.

[5] Kielbasa J. Measurements of Steady Flow Velocity Using the Thermal Waves, Archives of Mining Sciences, 50, 2005, 191-208

[6] Rachalski A. Absolute Measurements of Very Low Gas Flow Velocity by Means of Spectral Analysis of Thermal Wave. Review of Scientific Instruments, 77, 2006, 095107.

[7] Jackowska-Strumillo L, Sankowski D, McGhee J, Henderson I.A. Modelling and MBS experimentation for temperature sensors, Measurement, 20, no 1/1997, 49-60.

[8] Ligeza P. Four-point non-bridge constant-temperature anemometer circuit, Experiments in Fluids, 29, no 5/2000, 505-507

Evaluation of Error of Method of Thermocouple with Controlled Profile of Temperature Filed

[1]Su Jun, [2]O. Kochan, [2]R. Kochan

[1]School of Computer Science, Hubei University of Technology, Hubei, China,
[2]Department of Information-Measuring Engineering, Lviv National Polytechnic University, Lviv, Ukraine,
Emails: sjhosix@gmail.com, orestvk@gmail.com, kochan.roman@gmail.com.

Abstract. *It was proposed to reduce the impact of error due to thermoelectric inhomogeneity of thermocouple electrodes using stabilization of the temperature field along the main thermocouple (that measures the temperature of an object) [1, 2].However, the error of method occurs. It is related to errors of the main thermocouple and a thermocouple from the subsystem of control of the temperature along the main thermocouple electrodes. This paper proposes a method for theoretical evaluation of error of method.*

Keywords: Thermocouple, Error Due to Inhomogeneity of Thermocouple, Thermocouple with Controlled Profile of Temperature Field, Measurement Error, Error of Method.

1. Introduction

During operation of thermocouples (TC) over time degradation processes take place in the electrodes under the influence of the operating temperature. The rate of the degradation processes depends on the temperature at which certain sections of TC electrodes operated. That is, thermoelectric inhomogeneity of TC electrodes increases over operating time. Thus, degradation processes lead to two types of interrelated temperature measurement errors [3]:
1. Error which depends on the change of conversion characteristic (CC) of TC in time (drift);
2. Error which depends on the change of the output thermo-emf when the profile of the temperature field along TC electrodes changes.

Attempts have been made to correct the errors of the first type by periodic verification of TC and their drift prediction [4, 5]. However, thermoelectric inhomogeneity doesn't allow getting high accuracy of temperature measurement in this way [6]. This led to the development of verification methods [5] or calibration [7] in situ as well as their combination. However, these methods work properly only at steady temperature field along TC thermoelectrodes. Therefore the study of error due to inhomogeneity of thermoelectrodes has been made [6].

2. Thermocouple with Controlled Profile of Temperature Field

To eliminate the changes of the thermo-emf of inhomogeneous TCs due to the change of temperature field profile along their electrodes, a new TC based sensor, thermocouple with controlled profile of temperature field (TCPTF), was proposed [1]. TCPTF contains several temperature control subsystems that are located along the main TC (MTC) to stabilize the temperature field. So inhomogeneity of MTC cannot manifest itself. Errors of temperature measurement of systems using TCPTF are discussed in detail in [2]. The purpose of this paper is to develop a method for evaluating the upper limit of error of method of TCPTF.

Just the first section of heater H1 of TCPTF and its main thermocouple are shown in Fig. 1. The source of error of method is the heat flux q from heater H1 to the measuring junction of MTC. To reduce the influence of the heat flux q, that is for MTC being able to measure the temperature of environment T_S, firstly, its measuring junction should be put to a relatively large distance L1 from the nearest heater H1 (the ratio of L1 to the thermowell diameter of MTC is greater than 10); and secondly, the temperature which heater H1 should support (its controlling subsystem setpoint) is set equal to the temperature of measuring junction of MTC.

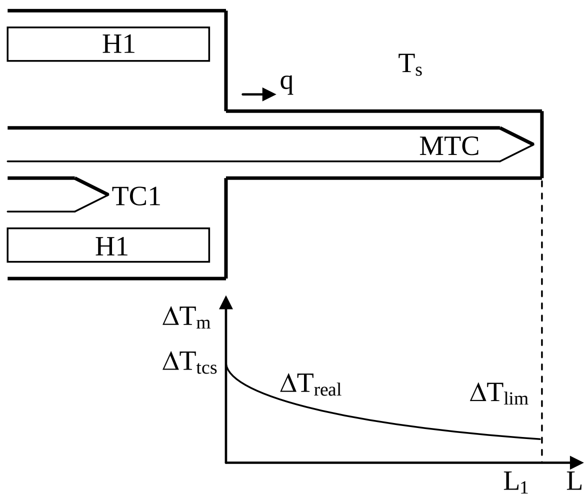

Fig. 1. Appearing of error of method of TCPTF and the plot of temperature changes along the MTC thermowell.

Therefore, ideally, the heat flux q, due to lack of temperature difference along the interval L1, is equal to zero and error of method is absent. But due to the dispersions in CC of thermocouples MTC and TC1 [8], temperature difference ΔT_{tcs} along the distance interval L1 is not equal to zero (in Fig. 1 the case with maximum error of method is shown). Therefore heat flux q and error of method occur. If MTC and TC1 are of the same type and their maximum permissible error (tolerance [8]) is ΔT_{tc} °C, then the temperature difference ΔT_{tcs}, which causes error of method along the distance L1 is $\Delta T_{tcs} = \sqrt{2} \times \Delta T_{tc}$ °C. Due to the heat exchange with the environment of the temperature T_s from the thermowell surface of MTC, which is shown in Fig. 1 to the right of heater H1, the temperature difference between the environment and the electrodes of the MTC along L changes according to the curve ΔT_{real}. Then the value ΔT_{lim} which corresponds to the value of coordinate L1 is equal to the maximum value of error of method of the proposed TCPTF that distorts reading of MTC.

3. Analytical Determination of Error of Method

It is a very complex task to find ΔT_{lim} on the basis of static distribution of temperature. However, there is no need to calculate the whole curve ΔT_{real} (see Fig. 1) for determination of the limit of error of method ΔT_{lim}, as it is enough to find the change of temperature at the coordinate L1, which corresponds to the value of error of method ΔT_{lim}. Therefore, the method for evaluating ΔT_{lim} on the basis of its dynamic change of temperature difference ΔT_{tcs} has been developed.

We assume that at a certain moment the temperature difference between heater H1 and the measuring junction of the MTC is equal to zero. Subsequently, heater H1 abruptly increases this difference to the value of ΔT_{tcs} (see Fig. 1). In this case, there comes a transition process that can be described using Newton's law of cooling [9]. Theoretically, this transition process continues indefinitely, but the limit of it, as time approaches infinity, can be evaluated. This limit will correspond to the error of method ΔT_{lim} caused by temperature difference ΔT_{tcs} between heater H1 and the measuring junction of the MTC.

To find error of method ΔT_{lim}, we write the heat balance equation for the thermowell of the MTC. The amount of heat flux q emitted by heater H1 during time dt is absorbed for changing the metal thermowell temperature on quantity dT as well as heat dissipation in environment with temperature T_S. According to Newton's law [9], we write the differential equation for the steady state mode by determining the temperature of heating thermowell T as a function of time t:

$$qdt = cV\rho dT + \alpha S(T - T_S)dt \, , \tag{1}$$

where q - heat flux caused by temperature difference between heater H1 and the measuring junction of the MTC; c- specific heat capacity of thermowell material of the MTC; V- volume of the thermowell of the MTC; S - the area of external surface, which is in thermal contact with the environment, that is the area of thermowell of the MTC; α - heat transfer coefficient of steel to air; ρ - density of thermowell material of the MTC.

It should be noted that the Eq. 1 is written in case heater H1 is not on the side of the thermowell (as seen in Fig. 1), but it is located in its center. However, such an incorrect physical meaning of the Eq. 1 does not lead to a significant distortion of the result, if the heat flux q generated by H1 under the influence of ΔT_{tcs}, corresponds to the real one. Then the evaluation of error of method will be slightly overstated, with what we can reconcile. And, by the same token, the heat flux q can be calculated by the formula [9, 10]:

$$q = \frac{\lambda \Delta T_{tcs} S_N}{L} , \qquad (2)$$

where λ - thermal conductivity of the thermowell material of the MTC; ΔT_{tcs} - the temperature difference between heater H1 and the measuring junction of the MTC; S_N - the area of the surface through which heat flux is transmitted (cross-section area of the thermowell); L - distance from heater H1 to the measuring junction of the MTC.

Solving the Eq. 1 with respect to time t, we obtain the temperature dependence of the measuring junction of the MTC on time.

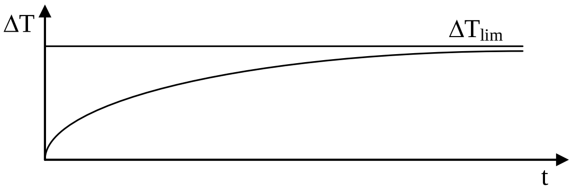

Fig. 2 The change of error of method ΔT_{lim} in time under the temperature jump of heater H1.

$$T = T_S + \frac{q}{\alpha S}\left(1 - e^{-\frac{\alpha S}{cV\rho}t}\right) . \qquad (3)$$

In Eq. 3, the term $\frac{q}{\alpha S}\left(1 - e^{-\frac{\alpha S}{cV\rho}t}\right)$ actually corresponds to the error of method ΔT_{lim}, and describes the change of error of method in time (see Fig. 2). If time t approaches infinity, then the term $e^{-\frac{\alpha S}{cV\rho}t}$ tends to zero. Thus, the upper limit of error of method ΔT_{lim} asymptotically approaches its limit

$$\Delta T_{lim} = \lim_{t \to \infty} \frac{q}{\alpha S}\left(1 - e^{-\frac{\alpha S}{cV\rho}t}\right) = \frac{q}{\alpha S} . \qquad (4)$$

4. Evaluation of Dependence of Error of Method on Measured Temperature

As can be seen from (1) ... (4), error of method ΔT_{lim} is a function of several variables. We evaluate its value for a specific pattern of TCPTF based on type K TC and has a body made of stainless steel [7]. For such a sensor

$S_N = 6{,}3 \times 10^{-5}\, m^2$; $L = 0{,}15\, m$; $S = 5{,}5 \times 10^{-3}\, m^2$; $\alpha = 44 \frac{W}{m^2 \times K}$; $\lambda = 14{,}2 \frac{W}{m \times K}$ [10].

The permissible deviation of CC of TC from the nominal one depends on the measured temperature T_s. According to [8], the maximum permissible deviation of actual CC from the nominal one ΔT_{tc} for the type K TC is ±2,5ºC for temperature interval 40 - 333ºC and $\Delta T_{tc} = \pm 0{,}0075|T|$ for temperature interval 333 - 1200ºC. The values ΔT are put into (2).

Calculation results of evaluation of the upper limit of error of method ΔTlim are shown on the graph in Fig. 3. As can be seen from the graph, ΔT_{lim} is a function of the maximum error of TC ΔT_{tc}. The upper limit of ΔT_{lim} increases linearly at temperatures over 333ºC.

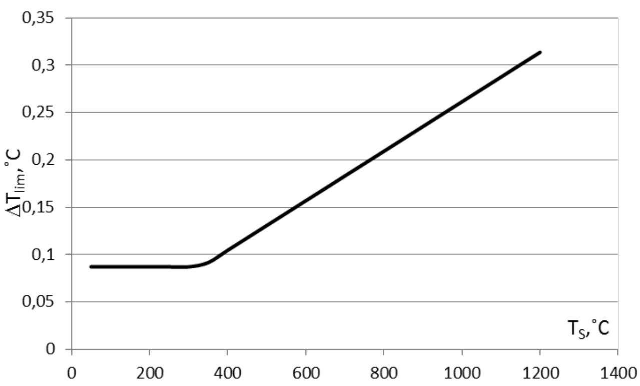

Fig. 3 Dependence of error of method ΔTlim on measured temperature Ts.

At lower temperatures, the upper limit of error of method ΔT_{lim} remains constant, as for type K TC in this range the maximum permissible deviation of CC from the nominal one ΔT_{tc} does not change.

5. Conclusions

The proposed method for evaluation of error of method of TCPTF [2] is quite correct in terms of physics and quite simple. It provides a numerical evaluation of its upper limit. According to Fig. 3, the upper limit of the error of method of the proposed TCPTF is ten times smaller than the maximum deviation of CC of TC from the nominal one [8].

Acknowledgment

This work was supported by Natural Science Foundation of Hubei Province of China (2014CFB605), Foundation of Wuhan Science and technology Bureau (2015030809020370).

References

[1] Kochan O., Kochan R. Thermoelectric transducer. Ukraine Patent № 97464. G01K 7/02.

[2] Kochan O., Kochan R., Bojko O., Chyrka M. Temperature measurement system based on thermocouple with controlled temperature field. Proceedings of the 4-th IEEE international workshop on Intelligent Data Acquisition and Advancing Computing Systems (IDAACS’2007), 2007, 47-51.

[3] Su Jun, Kochan O. The mechanism of the occurrence of acquired thermoelectric inhomogeneity of thermocouples and its effect on the result of temperature measurement. *Measurement Techniques*, 57 (10): 1160–1166, 2014.

[4] Su Jun, Kochan O. Investigations of thermocouple drift irregularity impact on error of their inhomogeneity correction. *Measurement science review*, 14 (1): 29-34, 2014.

[5] Kortvelyessy L. Thermoelement Praxis. Vulkan-Verlag, Essen, 1981. (in German)

[6] Holmsten M.,·Ivarsson J., Falk R., Lidbeck M., Josefson L.-E. Inhomogeneity measurements of long thermocouples using a short movable heating zone. *International Journal of Thermophysics*, 29 (3): 915-925, 2008.

[7] Hundves A., Buschfort H. Self calibrating temperature sensing probe and probe – indicator combination-United State Patent 3.499.340. 73-1, G01 -15/00.

[8] International Standard IEC 584-2. Part 2: Tolerances.

[9] Lienhard J. IV, Lienhard J. V. A Heat Transfer Textbook, Phlogiston Press, Cambridge, 2008.

[10] Kuchling H. Taschenbuch der Physik, VEB Fachbuchferlag, Leipzig, 1980.

Gravimetric Preparation of Primary Gas Mixtures with Liquid Component in Air Matrix

[1,2]Z. Ďurišová, [2]S. Ďuriš, [2]R. Palenčár

[1]Slovak Institute of Metrology, Bratislava, Slovakia,
[2]Slovak University of Technology in Bratislava, Faculty of Mechanical Engineering Bratislava, Slovakia
Email: durisova@smu.gov.sk

Abstract. *This contribution is describing the preparation procedure of primary gas mixtures of ethanol in synthetic air at Slovak Institute of Metrology (SMU). This gas mixture is under the development and in case of good values of repeatability, reproducibility, linearity and stability it should be the part of National standard of mole fraction in gaseous phase (NE 023/99) in SMU.*

Keywords: Gravimetric Preparation of Gas Mixtures, Liquid Ethanol, Air Matrix, ND-IR Analyser

1. Introduction

Primary standard gas mixtures (PSMs) are the basis for the disseminating traceability for the analysis of gases. They are prepared by gravimetric method using the weighing of stable gases and volatile liquids into cylinders. Binary gas mixtures prepared at Slovak Institute of Metrology (SMU) are validated on non-dispersive infrared analyser (ND-IR). Determination of the certified values is given by the comparison of measured values with the values of PSMs, which are the part of National Standard. The National standard of mole fraction in gaseous phase has 6 PSMs of ethanol in synthetic air under development. In case of good values of repeatability, reproducibility, linearity and stability it should be the part of National Standard. This contribution is describing the preparation procedure of primary gas mixtures of ethanol in synthetic air at SMU. [1]

2. Subject and Methods

Gravimetric preparation of gas mixtures

The primary gas mixtures are prepared by gravimetric method according to methods that have been widely agreed upon [2].

The gravimetric preparation consists of:

- **a)** **pre-treatment** (calculations, preparation of suitable cylinder),
- **b)** **filling of parent gases and liquids into the cylinder,**
- **c)** **weighing of separate components**

Before starting these circumstances should be taken into account:

- the pressure of parent gases in the cylinders and the pressure of their condensation
- maximum of the filling pressure
- concentration of the parent gases
- methods of filling (directly or by sequential diluting)
- parameters of weighing (uncertainties).

The possibility of the preparation of gas mixture depends on the following conditions: condensation of the components, reaction between the components, interaction between the gases and the inner surface of the cylinder and the parameters of the balances.

The condensation of components can be prevented by lower pressure of filling than is the critical pressure of liquefaction of any from the component at the filling temperature. It is also needed to ensure the suitable temperature during the manipulation and storage of filled cylinders. Before the preparation of gas mixtures it is necessary to investigate, if the components react with each other to prevent possible explosion. The inner surface of the cylinders, valves and pipes should have suitable parameters to prevent the interaction with used gases. [3]

a) Pre-treatment

To obtain as complete composition of the parent gases (purity tables) we measure the purity of the parent gases in our laboratories. Before the starting of the gas mixture preparation it is needed to analyse the pure gases, e.g. the components that will be use in prepared mixture. Amount fraction of the pure gas is calculated according Eq. 1:

$$x_{pure} = 1 - \sum_{i=1}^{n} x_i \tag{1}$$

where

x_{pure} amount fraction of the pure gas
x_i amount fraction of impurities.

Description of the state of a homogeneous gas mixture and its composition are disclosed in ISO 14912 „Gas analysis – Conversion of gas mixture composition data“. [4] Pre-treatment of the cylinder involves removing the previous gas mixture and then vacuum during 22 hours.

b) Filling of parent gases and liquids into the cylinder

Filling of cylinders by gases is carried out by filling station. Filling can be done on the basis of a different pressure of parent gases, so that the parent gases must have a higher pressure than the gas mixture filled in a cylinder. Generally is preferred order of addition of the component from lowest to highest. The ambient conditions are limited by demands of used devices as turbo molecular pump, diaphragm pump, pressure sensors and vacuum sensors.

Before every filling it is needed to check the filling station, e.g. for leaks on the pipes and the whole way of filling. In case of no leak the vacuum reaches 9×10^{-5} mbar.

c) Weighing of separate components

Relative uncertainties of certified values of amount fractions are on level of 0.1 % , that is why relative uncertainties of the parent gas mass should be under 0.03 %. As the standard uncertainty from weighing is 6 mg, the weighed mass should be 20 g and more.

For weighing separate components we use comparator balances. It should be turn on 4 hours before weighing. We use reference cylinder with approximately same mass as the weighed cylinder. If the difference is smaller than 50 g, we can add to the weighed cylinder maximum 850 g of gas. In case of liquid component we use a syringe for filling it. The mass of the liquid is determined by weighing the full and then the empty syringe on analytical balances. The mass of the added component is calculated from the difference of cylinder masses before and after filling.

After adding of all components we calculate the amount fraction of the component in gas mixture using Eq. 2 shown below and published values of mol masses [5]:

$$x_i = \frac{\sum_{A=1}^{P}\left(\frac{x_{i,A}\cdot m_A}{\sum_{i=1}^{n} x_{i,A}\cdot M_i}\right)}{\sum_{A=1}^{P}\left(\frac{m_A}{\sum_{i=1}^{n} x_{i,A}\cdot M_i}\right)} \tag{2}$$

where

x_i amount fraction of the component
$x_{i,A}$ amount fraction of the component in parent gas
m_A mass of the added component
M_i mol mass of the added component

The standard uncertainty of amount fraction is given by:

$$u(x_k) = \sqrt{u_1^2(x_k) + u_{ver}^2(x_k)} \tag{3}$$

where

$u(x_k)$ standard uncertainty of amount fraction
$u_1(x_k)$ standard uncertainty from gravimetric preparation
$u_{ver}(x_k)$ standard uncertainty from verification

The expanded uncertainty of certified value of amount fraction for component *k* for 2 years is:

$$U(x_k) = 2\,u(x_k) \tag{4}$$

Preparation of primary gas mixture of ethanol in synthetic air

Preparation of primary gas mixture of ethanol in synthetic air is carried out by gravimetric method as it is described above. In case of ethanol should be considered its concentration of explosiveness which is 3.3 % - 19.0 % in atmospheric pressure and also the temperature of filling 70 °C. Taking into account all of the above limitations, we have developed preparation scheme showed at Tab.1.

Tab. 1. *Preparation scheme of ethanol in synthetic air*

Preparation scheme of ethanol in air						
x; mol/mol	**0.0008**	**0.00065**	**0.00049**	**0.00026**	**0.00015**	**0.00007**
P; bar	**35**	**45**	**55**	**80**	**80**	**80**
*m*Et,add; g	0.26	0.28	0.25	0.07	0.11	0.05
*V*Et,add 22°C; µL	**330.1**	**355.4**	**317.4**	**253.9**	**139.6**	**63.5**
m(N2), g	157.4852	202.5115	247.554	360.162	360.2018	360.2308
m(O2),g	48.24447	62.03791	75.83626	110.33	110.3448	110.3536
concentration of explosion	**0.000943**	**0.000733**	**0.0006**	**0.000413**	**0.000413**	**0.000413**

We have prepared primary gas mixtures in accordance with this scheme. In this procedure we used both methods of filling – direct method and sequential diluting of the concentrated mixture. At first step we have prepared 3 mixtures for testing the preparation method, the detection limit of the measuring device and for checking the linearity of the calibration curve.

Tab. 2. *Primary gas mixtures for testing*

No. of cylinder	Cert. compon.	Matrix	*x*cert. mol/mol	*u*(xcert). k=1
0078F_3	ethanol	air	0.0000707	0.0000003
9383E_5	ethanol	air	0.00026406	0.00000099
9334E_6	ethanol	air	0.0009643	0.0000025

3. Results

As the results of tested criteria were satisfactory, in the next step we have prepared 6 primary gas mixtures in whole concentration range. These 6 PSMs were checked for its linearity, repeatability, short time stability and reproducibility. Validation of the certified values was carried out on non- dispersive infrared analyser and the difference between the measured value and the value from gravimetric preparation was under 1%.

Tab. 3**.** *Primary gas mixtures of ethanol in air*

No. of cylinder	Cert. compon.	Matrix	*x*cert. mol/mol	*u*(xcert). k=1
0078F_4	ethanol	air	0.00007191	0.00000059
0695E_11	ethanol	air	0.00015121	0.00000057
9383E_6	ethanol	air	0.0002669	0.000002
0007F_13	ethanol	air	0.0004739	0.0000013
0072F_6	ethanol	air	0.0006684	0.0000017
9334E_7	ethanol	air	0.0008024	0.0000047

It is needed to carry out the long time stability testing of these primary gas mixtures during 2 years and in case of good values of repeatability, reproducibility, linearity and stability it should be the part of National standard of mole fraction in gaseous phase (NE 023/99) in SMU.

4. Conclusions

In this contribution we report the methods and results of gravimetric preparation of binary gas mixtures of ethanol in synthetic air. The results show that the used method of preparation was suitable for this type of gas mixtures.

Acknowledgements

Authors would also like to thank the Slovak University of Technology in Bratislava, Slovak Institute of Metrology in Bratislava, the grant agency VEGA project numbers 1/0604/15 and 1/0748/15.

References

[1] Ďurišová, Z.: Využitie matematických modelov pri validácii RM s matricou vzduch v aplikácii na rozšírenie NE zloženia zmesí plynov: Písomná práca k dizertačnej skúške. Bratislava : SjF STU, SMU, jún 2014.
[2] ISO 6142: Gas analysis – Preparation of calibration gas mixtures – Gravimetric method, SÚTN, 2001
[3] Musil S. a kol. Etalón vybraných zmesí plynov, Súhrnná správa, SMU, 1998.
[4] ISO 14912: Gas analysis – Conversion of gas mixture composition data, SÚTN, 2001
[5] IUPAC, Commission on atomic weights and isotopic abundances: Atomic weights of the elements, 1993.

Software for Sonic Well-Logging Control Apparatus with Single-Sided Access

N.K. Andreev, A.S. Malatsion
Kazan State Power Engineering University, Kazan, Russia
Email: ngeikandreev@gmail.com

Abstract. *This report continues developments* of *a sonic testing technique aimed for the detection of defects of long pipes and bond of various materials to the surfaces of pipes in water and oil wells. The characteristic property of the proposed technique is that the longitudinal waves at 1 – 20 kHz are used for inspection and only single-sided access is needed for transducers located at a head of a pipe. The system was designed to be self-contained and easy to activate. Some characteristic features of a software made in the National Instruments LabVIEW environment and details of the construction of the sonic testing apparatus are considered.*

Keywords: Software, LabVIEW, Well-Logging, Defects of Cementation

1. Introduction

Recently results of developments of a sonic testing technique aimed for the detection of defects of long pipes and bond of various materials to the surfaces of pipes of oil and water wells were discussed [1, 2, 3, 4, 5]. The characteristic property of the proposed well-logging technique is that longitudinal waves at 1 – 20 kHz are used for inspection and only single-sided access is needed for transducers located at a head of a pipe. The method reduces to pulse exciting of longitudinal elastic waves in a body of a pipe coated by a cement slice and receiving of echo signals from defects of the pipe and bonding of a cement slice to the surfaces of pipes. The time of flight of a wave from the defect to the transmitter (receiver) can be converted through the velocity of propagation of sonic waves in a steel pipe to the value of the correspondent source-defect distance.

Sonic waves moving in a pipe are attenuated. Often amplitudes of detected signals are very small and comparable with the amplitudes of various types of noise. The detection, filtration and selection of the useful fraction of the signal are a complex problem.

Therefore the object of the paper is to report the results of the development of the software for the control and synchronization of the apparatus under consideration, signal detection, registration, data processing and displaying. Some characteristic features of a software made in the National Instruments LabVIEW environment and details of the construction of the sonic testing (ST) apparatus are also considered.

2. Subject and Methods

The software is one of the main parts of the single-sided well-logging system reported here.

The described inspection system (Fig.1) consists of several functional units, such as the pulser/receiver (home-made), transmitter and receiver transducers (home-made), display devices, analog-to-digital (ADC) and digital-to analog (DAC) converters produced by the Nationals Instruments, computer ASUS”EeePC1000H” and power supplier. The software is developed in the National Instruments LabVIEW environment.

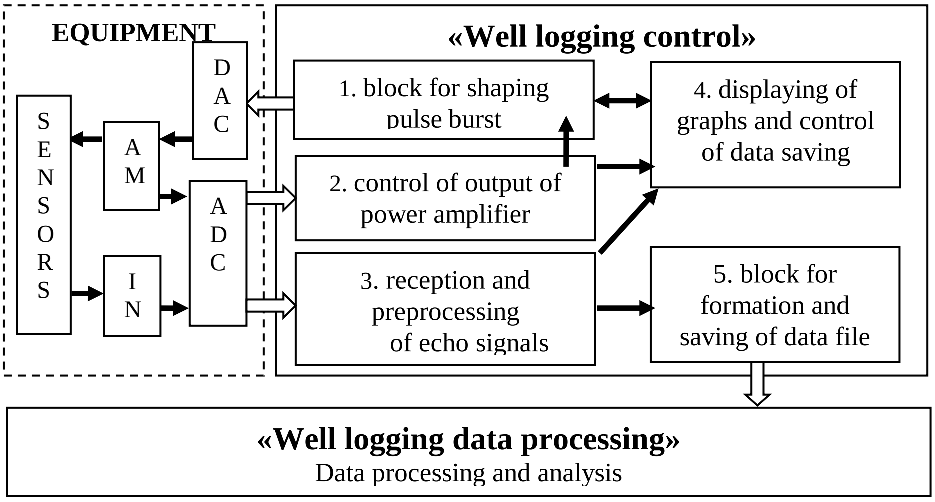

Fig. 1 Scheme of the well-logging measurement and control system:
AM – power amplifier, IN – interface, DAC – digital-to-analog converter, ADC – analog-to-digital converter

The sound energy is introduced into the pipe body through its head. When there is a crack or partial bond with cementation in the wave path, part of the energy will be reflected back from the flaw surface. Reflected signals are detected by a receiver transducer fastened also to the head of the pipe (well) near the transmitter transducer. If there is necessity in multifrequency measurements additional transducers can be fastened to the same head.

The generation of a carrier code is fulfilled by the computer. Then a DAC unit converts a carrier code to an analog form which is amplified in turn by the power amplifier. An ADC unit connected by an interface to a receiver transducer serves for conversion of received echo signals to a digital form and control of the output level of the power amplifier (AM).

The pulser used is an electronic device that can produce electrical pulses up to 3 kV of amplitude. Driven by the pulser, the transmitter transducer connected to a power amplifier through the electric transformer generates sonic energy at desired frequencies in the range of 1...20 kHz. The length of the exciting pulse can be changed from two to ten cycles of a carrier.

Let us consider methods and algorithms of data processing in acoustic cementometry (AC).
There are two main blocks in the software: “Well logging control” [6] and “Well logging data processing” [7]. The “Well logging control” block consists of five programs which serve for: 1) shaping pulse burst; 2) control of output of power amplifier; 3) data acquisition and preprocessing of echo signals; 4) displaying of graphs and control of data saving and 5) formation and saving of data files. The “Well logging data processing” program attends to complete data processing.

The data of echo signals reflected from the defects and end of a pipe are saved in a computer memory in the text format “.*lmv*”. The graphing of diagrams such as “signal amplitude vs depth” can be fulfilled by using the table processors Microsoft Excel or Origin. The following data processing must be fulfilled in a correct order and by using additional programs.
Input of data from file is an operation that performs the insertion of the file containing data concerning the amplitudes and number of samples to the program of data processing. This insertion is organized as a semiautomatic procedure by a virtual button by which a user points the way to the file through the program envelope.
Signal detection is an operation of the signal module calculation that saves values of the signal amplitude and its frequency.

Signal filtration consists of two stages. The software incorporates blocks for spectral wavelet analysis. The signal contains noises at frequencies out and near of the spectrum of the response of a cemented steel pipe to the acoustic pulse excitation. At the first stage the part of a signal with a spectrum that differs from the spectrum of a well pipe response is removed. This procedure is used before the signal detection. The second procedure of the low frequency filtration allows select the information about the amplitude.
The essential part of the software is the exponential approximation and following normalization of an echo signal by point-by-point dividing of the signal to an exponential approximation function of its envelope.
The next step is the setting of the control level that determines what signal amplitude will be taken into account. The control level must be equal or greater than the noise level.
The essential part of the software is the procedure for localizing of defects (Fig.3). Calculation of the correlation functions for two signals measured at different frequencies or after a given time expiration is a basic operation of this procedure. The procedure includes also calculation of the value of the ratio of sites occupied by defects to the length of the whole pipe (in meters /meters). Using this procedure a user can detect such deviations in the structure of a well that indicate to serious cracks requiring to stop the process of production and start-up the process of repair.

3. Results

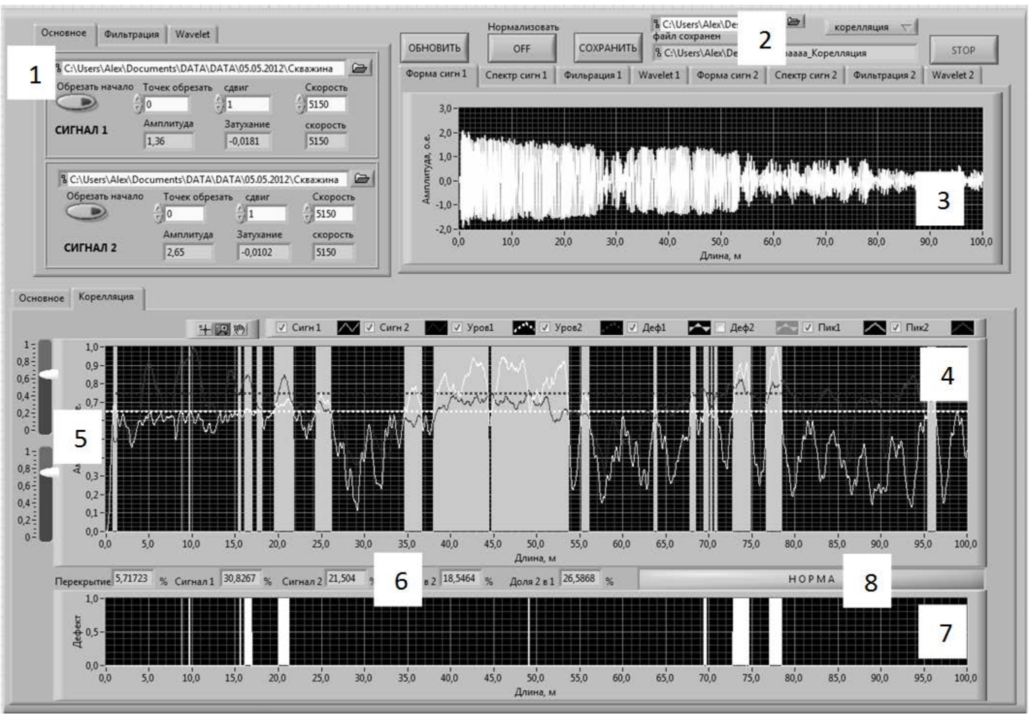

Fig.2. VI front panel of the program «Well logging data processing»

The image of the VI front panel of the program «Well logging data processing» is presented in Fig. 2. The front panel includes instruments for setting of parameters of testing (1), signal cut-off, filtration and wavelet analysis (2), image of signals (3), setting of a control level (5) and comparing of signals (4). The bright regions in the panels (4) and (7) indicate the places where the signal correlation is maximal. The experiment presented was fulfilled using the home-made laboratory equipment for testing of the developed single-sided well logging control system.

4. Discussion and Conclusions

Thus sophisticated routines are available for displaying results, and for preparing the data for spectral, statistical or correlation analysis in the software reported. The software is an integrated software package which contains all the necessary tools for the representation and evaluation of coordinates and dimensions of the defects, and evaluation of the degree of degradation of the structure quality of the tested well.

References

[1] Blizeyev A.B., Kozlov A.V., Smerkovich E.C. Acoustical diagnostics of the quality of the cement ring out of the well pipe. Russian patent 2055176, cl. IPC E 21 B 47/00. Claim 5029717 from 27.02.92, published 27.02.96. Bull. No 6.

[2] Andreev N.K., Malatsion A.S. Nondestructive acoustic monitoring and diagnostics of technical state of water and oil wells. *Russian News of Higher Educational Institutes. Energetic Problems.* No. 1-2: 107-115. 2014.

[3] Andreev N.K., Sadykov M.F., Malatsion A.S., Chernysheva M.G. Device for acoustic quality control cementing : Pat . Rus. Federation: MPK7 E21B47/00, applicant and patentee " KSPEU ." - № 133193 appl . 07.05.2013; publ . 10.10.2013, Bull.No. 28.

[4] Andreev N.K., Malatsion A.S., Chernyshova M.G. Sonic Testing of Long Pipes by Using Longitudinal Waves. In proceedings of the 9th International Conference on Measurement, 2013, 267-270.

[5] Andreev N.K., Malatsion A.S., Chernyshova M.G. Noninvasive Sonic Testing of Water Wells. In proceedings of the 1st International Global Virtual Conference GV-CONF 2013, 2013, 525-528.

[6] A.S. Malatsion, N.K. Andreev, M.F. Sadykov/ Certificate of state registration of the computer program No 2014613168 : WELL LOGGING CONTROL / application No. 2013661587 , DC . 12/12/2013 ; publ.20.04.2014, bull. No.4.

[7] A.S. Malatsion, N.K. Andreev. Certificate of state registration of the computer program No 2014611721: WELL LOGGING DATA PROCESSING / application No. 2013661584, DC . 12/12/2013; publ.20.03.2014, bull. No.3.

Sensor Node for the Remote River Water Quality Monitoring

P. Galajda, M. Drutarovsky, J. Saliga, M. Ziga, L. Macekova, S. Marchevsky, D. Kocur,

Department of Electronics and Multimedia Communications, FEI TU of Kosice
Park Komenskeho 13, Kosice, Slovakia
Email: {pavol.galajda, milos.drutarovsky, jan.saliga, dusan.kocur}@tuke.sk

Abstract. *The paper describes digital sensors and front-end electronics of a wireless sensor network node developed for water quality monitoring. The nodes are realized as buoys fixed in a river stream, carrying the water quality sensors, power supply and communication system for wireless data transfer. The buoy monitors four basic water quality parameters (pH, conductivity, dissolved oxygen, temperature) and transmits acquired data via gateway to the network control server for further advanced processing, visualization and archiving.*

Keywords: Water Quality, ph, Conductivity, Dissolved Oxygen, Modbus 485, Monitoring Buoy

1. Introduction to water quality monitoring

The river Water Quality Monitoring (WQM) belongs to the most required and important measurements in environmental monitoring. The basic requirements for modern river WQM systems can be summarized as follows: 1) sustained and autonomous observations, 2) remote control and data acquisition, 3) limited power sources, 4) reliable functionality at difficult environment conditions, 5) robust and reliable construction of sensing system, 6) advanced data processing with the alarm generation, 7) easy reconfiguration. WQM in Europe is intended to monitor water pollution. With a view of unifying Europe, national regulations have to be harmonized with water policy in compliance with the Water Framework Directive (WFD) [1]. Due to WFD an integrated approach on basin of rivers with respect to water quality management and monitoring is pursued in the individual European countries [2] and will be mandatory in the future. One crucial issue within WQM as required by the WFD is to have sufficient and comparable information on water quality. Thus remote sensing technology for water quality monitoring is a valuable tool how to obtain continuous information on the processes taking place in the surface waters. For example, new technology and instrumentation automatic stations are effectively used in quite a number of networks not only in Europe [3], [4], [5] but also worldwide [6]. Currently, in Slovakia there are no studies about WQM using remote sensing in compliance with that of the WFD. However, the Wireless Sensor Network for wAter QaUAlity Monitoring project (WSN-AQUA) for an early warning system of surface water pollution was initiated in 2013 within the Hungary- Slovakia Cross- border Co-operation Programme established between the BME- Infokom Company (BME) and the Technical University of Kosice (TUKE). The goal of this project is to develop automated station that will monitor several water parameters on a selected river. In this paper we present digital sensors and front-end electronics of the developed sensor node (buoy) for remote WQM.

2. Architecture of developed sensor node

The developed sensor node diagram (buoy station) for WQM as well as the remote gateway used for wireless data collection by the sensor network is shown in Fig.1. We use compact

Ponsel digital sensors [7] for monitoring pH, conductivity (EC), dissolved oxygen (DO) and temperature as well as embedded microcontroller (MCU) for sensors configuration, data packing and RF channel transmission. We connected these robust waterproof (with IP68) digital sensors to the MCU electronics by using standard Modbus RS485 bus. This approach allows us to extend easily the functionality of the node by adding new digital sensors in the future. We used following Ponsel digital sensor's features: 1) low power consumption with auto-shutdown capability, 2) internal sensor temperature compensation, 3) conformity with international water quality monitoring standards [8], [9] and [10], 4) operation configurable by external MCU master, 5) storage of calibration constants in the sensor embedded flash memory. Our implemented control software fully supports low power node operation. We cross-developed control software in C by using PC platform with Modbus RS485 adapter. Our software was than ported to the custom MCU hardware in cooperation with BME partner. In order to increase reliability of node operation our control software writes to sensor configuration FLASH memories only during cold system start and during normal sensors operation we use only sensor RAM only. Our control software configures modes of sensors operation, periodically acquires measured compensated data from digital Ponsel sensors, parses acquired data and forms data packet for transmission acquired data through RF channel in 433 MHz frequency band. Encrypted RF channel communication was implemented by our BME partner. Proposed protocol uses standard 128-bit AES symmetric encryption algorithm and protects network communication against typical attacks including repetition one.

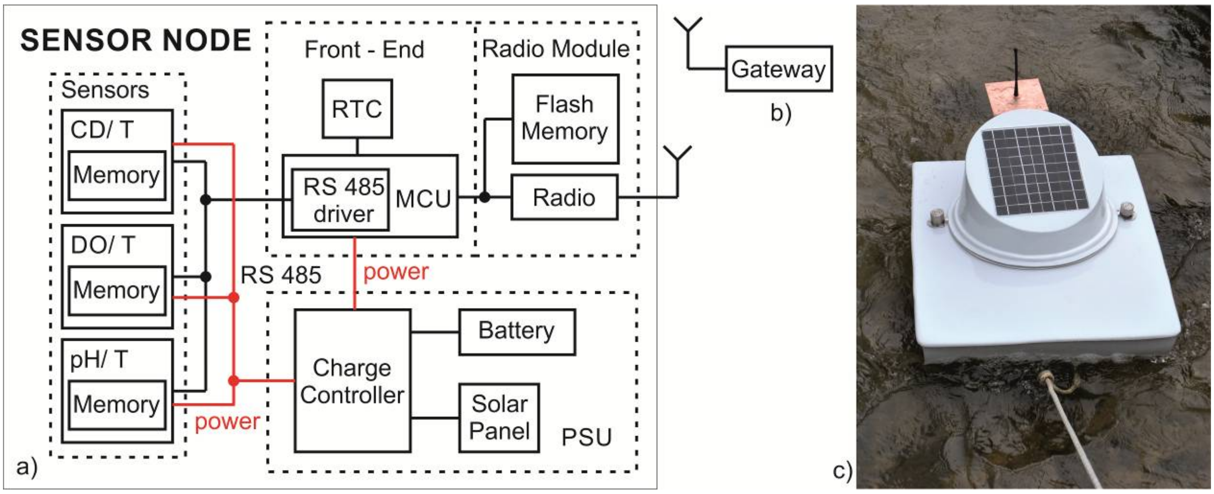

Fig. 1 Water quality monitoring sensor node: a) block scheme of the node including digital sensors, embedded electronics and power supply unit (PSU) b) remote gateway, c) photo of complete monitoring station showing buoy platform, solar panel of PSU and RF antenna for 433 MHz frequency band

3. Digital sensors and settings of alarm threshold indicators for WQM

Since measured values of pH, EC and DO are strongly temperature dependent, we selected Ponsel sensors (probes) that are internally temperature compensated (Table 1 for specific features or [7]). Ponsel sensors recalculate measured data to the reference temperature defined in WQM standards (typically 25°C). We have to calibrate used sensors before the use in the measurement campaign, and then they can work autonomously during relatively longer time period (several weeks or months) without recalibration. These sensors are able to store the calibration constants. The compensated DO measurement requires also air pressure value to provide correct results. We measure the air pressure (and compute compensated results) in the remote gateway. Remote air pressure simplifies whole monitoring buoy construction significantly.

Table 1. Digital physico- chemical Ponsel sensor specifications.

Sensor	Values	Ranges, Units	Power consumption
PHEHT (gel base)	pH/ REDOX/ Temperature	0-14 [-] / -1000 to +1000mV/ 0 to 50°C	Standby: 25µA, Average RS485: 39 mA, Current pulse: 500 mA
C4E (4 electrodes)	Conductivity Salinity	0µS/cm-200.0mS/cm 5-60g/kg	Standby: 25 µA, Average RS485:6.3 mA, Current pulse : 500 mA
OPTOD (luminescent optical)	Dissolved oxygen	0.00 to 20.00 mg/L 0.00 to 20.00 ppm 0-200%	Standby 25 µA, Average RS485: 4.4 mA, Current pulse : 100 mA

We evaluate physico-chemical indicators for WQM by 90th percentile of measured values [2]. The government and WQM legislatives specify limits of all these indicators for the ‘high’ (the best), ‘good’ and ‘moderate’ (or I., II., and III.) status classes of ecological and chemical states of the surface water quality (see e.g. Table 2 specified for Ipel River). Our system automatically activates alarm for responsible persons and institutions if at least one of monitored indicators achieves the predefined limits between good and moderate states. We provide also protocol reporting measured results in accordance with ISO standards [8], [9], [10]. Generated protocols include main monitored values, but also actual temperature, pressure and additional relevant information about WQM measurement conditions.

Table 2. Limit values, determining the good status of the Ipel River part in the Slovak territory close to Hungary border (K2S type) [2].

Parameter	Limits of the good status	Parameter	Limits of the good status
Temperature [°C]	< 24	pH [-]	(6; 7> or <8.5;9)
Conductivity [mS/m]	< 70	Dissolved oxygen [mg/l]	>6.5

4. Conclusions and pilot measurement campaign

We introduced main facts about developed sensor node for the remote river water quality monitoring, designed in the frame of HUSK WSN-AQUA project. We integrate the presented sensor nodes in pilot implementation of our complex river WQM system developed as a main outcome of our project [12]. We will install the whole WQM system in the river Ipel near Slovak-Hungarian border during the period May– June 2015. Our complete WQM system will transfer data from 10 sensor nodes described in this paper by using the gateway and Internet connection to the data server placed in Budapest, Hungary. The data server collects data from our sensor nodes, checks data integrity, errors and temporally stores the data before the transfer to the second server placed in Kosice, Slovakia [12]. The data server in Budapest also allows advanced user interactions with the sensor nodes such as firmware upgrade, calibration, etc. The server also can send alarms on system failure or breaking set-up limits of monitored parameters of river water quality. Our server in Kosice collects data sent by data server in Budapest, stores data in the central cloud-based database, and performs calculations related to advanced data analysis. We can present acquired data and monitor them by using implemented web interface. Our web presentation interface has two levels: the basic one for general public access and the advanced one, which is accessible only to private users and protected by password. The private user can also set-up limits for monitored parameters, generate protocols from acquired and monitored data as well as to be informed about exceeding predefined limits of monitored parameters by email.

Acknowledgement

This work is the result of the Wireless Sensor Network for wAter QaUAlity Monitoring (WSN-AQUA) project of Hungary-Slovakia Cross-border Co-operation Programme, project No. HUSK/1101/1.2.1/0091.

References

[1] Directive 2000/60/EC of the European Parliament and of the Council of 23 October 2000 establishing a framework for Community action in the field of water policy” Official Journal of the European Communities, vol. 22, 2000.

[2] Directive No. 269 of Slovak republic government with requirements for good state of water bodies. 2010.

[3] Q. Chen, Y. Zhang, and M. Hallikainen, “Water quality monitoring using remote sensing in support of the EU Water Framework Directive (WFD): a case study in the Gulf of Finland,” Environmental Monitoring and Assessment, vol. 124, no. 1-3, pp. 157–166, 2007.

[4] S. Mijovic and B. Palmar, “Water quality monitoring automation of rivers in Serbia,” Facta universitatis, Series: Working and Living Environmental Protection, vol. 9, no. 1, pp. 1–10, 2012.

[5] S. Winkler, N. Kreuzinger, A. Pressl, N. Fleischmann, G. Gruber, and M. Ecker, “Innovative technology for integrated water quality measurement,” in Proceedings International Conference on Automation in Water Quality Monitoring (AutMoNet2002), 2002, pp. 21–22.

[6] R. D. Woodsmith, P. K. Wilkins, and A. Bookter, Water Quality Trends in the Entiat River Watershed: 2007–2010, 2013

[7] Digital sensors (SDI-12 or Modbus RS485 protocol (pH-Redox-Conductivity-Turbidity-Dissolved Oxygen)) http://www.ponsel-web.com/cbx/s747_cat15034.htm, Online: 2015/03/09.

[8] International Standard ISO 7888-1985: Water quality–Determination of electrical conductivity, first edition 1985-05-15.

[9] International Standard ISO 17289-2014: Water Quality–Determination of dissolved oxygen– Optical sensor method, first edition 2014-07-01.

[10] International Standard ISO 10523- 2008: Water quality–Determination of pH, second edition 2008-12-15.

[11] ASTM International, D0888-12e1: Standard Test Methods for Dissolved Oxygen in Water, July 2013.

[12] WSN-AQUA Wireless Sensor Network for wAter QaUAlity Monitoring http://husk.fei.tuke.sk, Online: 2015/03/26.

Method and Device for Yarn Packages Classification

N. Pomp, K. Adámek, P. Škop

VÚTS, a. s., Svárovská 619, Liberec, 460 01, Czech Republic
Email: norbert.pomp@vuts.cz

Abstract. *For the purpose of yarn dyeing the yarn packages is characterised by the properties which influence the dyeing process indirectly only. Newly developed method and device is aimed to classify the packages by means of air flow resistance, the property similar to dyeing process driving one. The first tests display the close relationship between the air flow resistance and the yarn package density and prove the sensitivity of new developed method is better than the density measuring.*

Keywords: Yarn Package Hardness, Yarn Package Density, Air Flow Resistance, Yarn Dyeing

1. Introduction

The yarn is usually dyed in the form of packages wound on dying spring submerged to dyebath in pressurised tank. The dyebath is pushed through the package in and out saturating the yarn. This process is not elementary and it depends strongly on the package properties which in present are mostly valuated by the mean of package density or hardness. Thus these properties influence the dyeing process indirectly. Because it is necessary to set the dyeing process in a correct way to ensure the augmentative quality, there are set higher requirements on recognition the package properties. Therefore the new, fast and compact method for recognition parameters of the yarn package has been designed.

2. Newly developed method

The target set to new method is to find the simply and quick measurable property which can characterize the yarn package for purpose of dyeing in more direct way. The air flow resistance seems to be suitable for it well. Air flow resistance is given:

$$r = \Delta p / Q \tag{2}$$

where

Δp loss of pressure on the porous layer

Q volumetric flow rate

Numerical simulation

First the numerical simulation of the air flow through the yarn package, which was represented by a porous layer, was done. There the air flow velocity was expected low and the porous layer

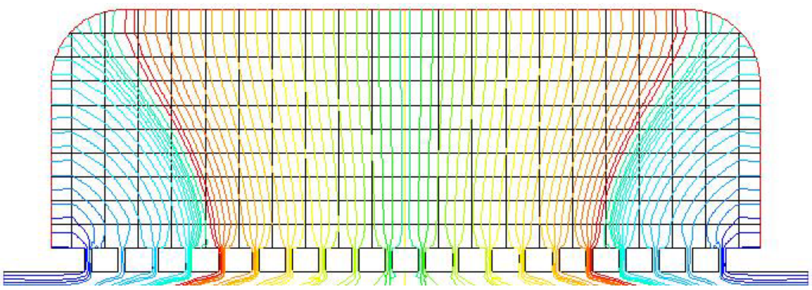

Fig. 1. Shape of the streamlines as a result of numerical model simulation – half of the package cross-section

homogenous. The shape of the streamlines is presented in Fig. 1 where the half of the package cross-section is shown (axis is horizontal). It is clearly seen the air tends to flow in the direction of the thinnest layer, the streamlines are near parallel in the middle part.

3. Testing device

The prototype of yarn package classification device suitable for pilot use in dye-works laboratories was designed and built. It is based on the measurement of air flow resistance. According the numerical model results the measuring zone is localized to the package middle part only.

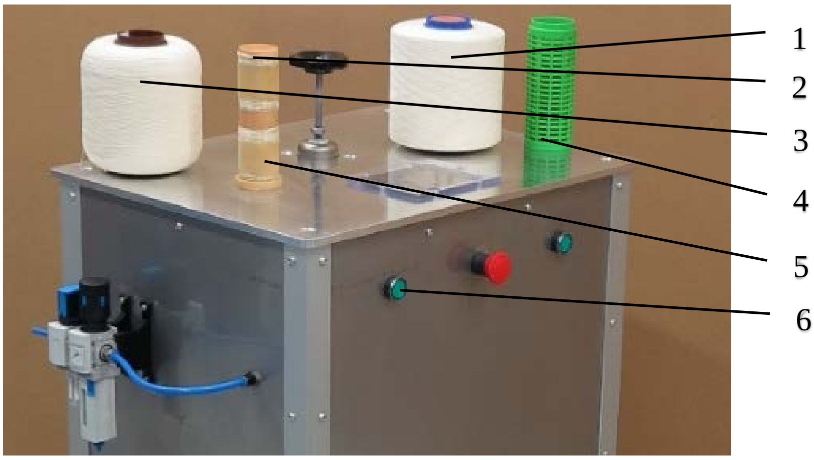

Fig. 2. Prototype of new package testing device based on the measurement of flow resistance. Two kinds of tested packages and plastic spring tube are also shown

The prototype of that device is shown in Fig. 2. The tested package is slipped freely over the measuring thorn, item 2. The measuring thorn shoulder defines position of the yarn package. When pushing the start button, item 6, the measuring line valve is open. Compressed air in measuring line will start to flow through the tested yarn package, item 3. Sealing bags item 5 are inflated to seal the measuring thorn and the inner surface of the spring tube, whereby the measuring zone is delimited between the top and bottom bag. Duration of measuring cycle is driven by time delay relay. Two kinds of yarn package, item 1 and 3, and used spring tube, item 4, can be seen on the top of the prototype.

Fig. 3 presents the pneumatic schema arrangement. On entrance to system there is pressured air reduced to 0.2 MPa by the pressure control valve (item 1). The next is the diaphragm pressure reducer (item 2) deflating the air to requisite pressure, usually 5 kPa. Item 3 is the differential pressure sensor indicating the pressure of air incoming to the measuring line. Solenoid valve, item 4, opens the measuring line. The flow sensor, item 5, measures the volume flow rate of compressed air running through the package. Pressure sensor, item 6, measures the air pressure just in front of the yarn package. Since this sensor measures the pressure difference between the air pressure just in front of the package and the atmospheric pressure, it is in principle the flow loss on the yarn package.

The pressured air is incoming into the central zone of perforated spring tube only, the rest of the tube hole is sealed by inflatable bags. It avoids air leakage through the package front ends. Data acquisition from flow sensor 5 and pressure sensor 6 is provided by analyser Waweon of our own design connected to the master PC. Data evaluation is done by this PC.

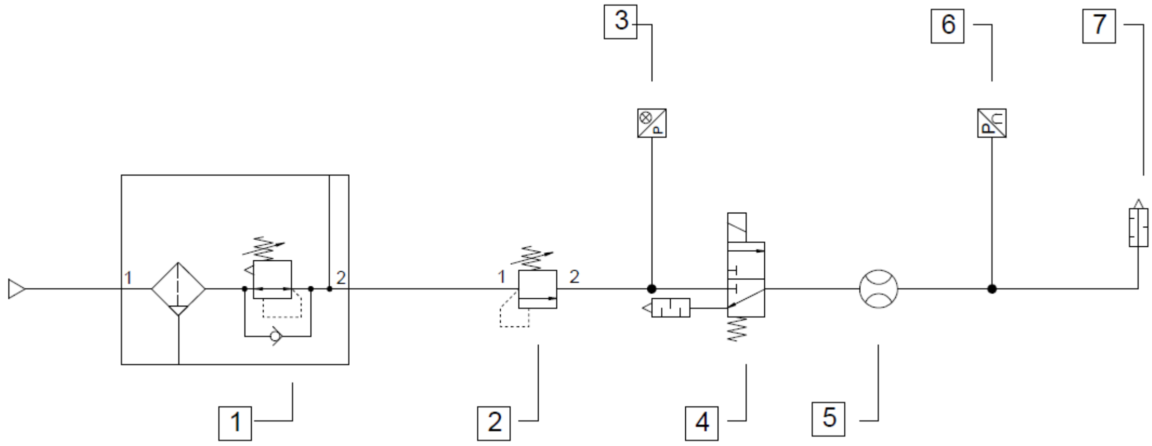

Fig. 3. Pneumatic schema of measuring device: 1 – Filter-pressure regulator unit, 2- Pressure reducing valve, 3 – Input pressure sensor, 4 – Solenoid valve, 5 – Flow rate sensor, 6 – Outgoing pressure sensor, 7 – Measured yarn packing

4. Experiments and Results

The method and the designed sorting device were verified by testing of two sets of yarn packages. It was cotton yarn of linear mass density 16×2 tex. Samples on the blue tubes were wounded with wide range of package density (0.2528–0.4501 g/cm^3). The density range of packages wounded on the brown tubes is relative narrow and it corresponds to typical packages prepared for dyeing (0.2875–0.2980 g/cm^3).

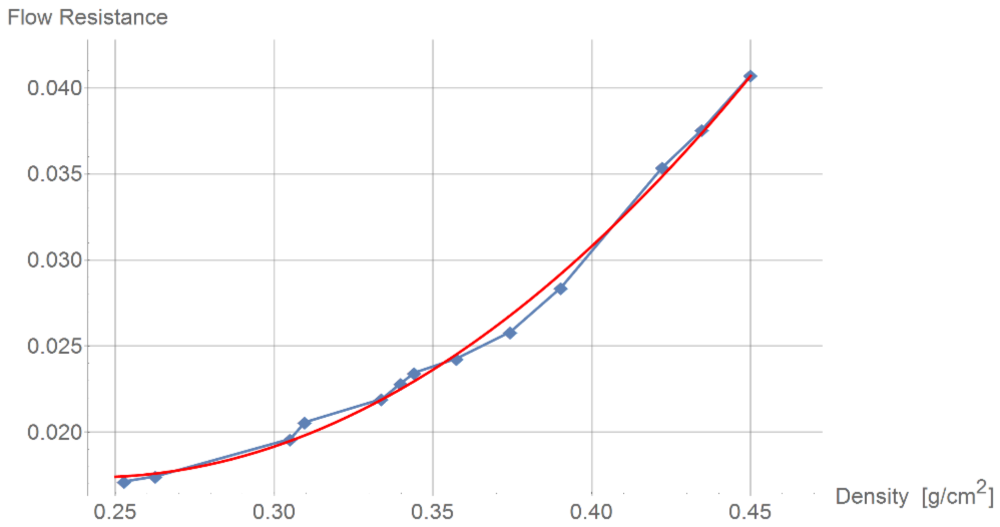

Fig. 4. Flow Resistance of blue packages with wide range of density. Line with points depicted is measured and the smooth line is quadratic fit of measured data

As you can see in Fig. 2 the shape of packages on blue and brown tubes is not the same. The brown packages' edges are rounded. Because the volume measurement neglected the shape details the density of blue and brown packages cannot be compared. Thus it is not needed as the method should typically sort the packages of the same type.

In Fig. 4 there is the dependency of the flow resistance on the package density, line with points depicted. Measured data were interpolated by polynomial function of degree 2, smooth line. The very close dependency was found.

The repeated measurement of flow resistance on the brown package is captured in Fig. 5. The mean value of this is highlighted by black punctuated line. Every curve in Fig. 5 represents the values measured on one set of samples immediately one sample after the other. The packages relaxed for one hour before next measurement set except of the lines 6, 7 and 8 which were obtained without delay. It is clear the shape of every curve does not change. The lines slightly move up and down, there are almost no intersections of these. It can be concluded that the diameter *D* deviation of 1 mm, and it can occurre if the dimensions are measured manually leads to density deviation of 0,005 g/cm^3. That deviation can rapidly change the shape of presented curves.

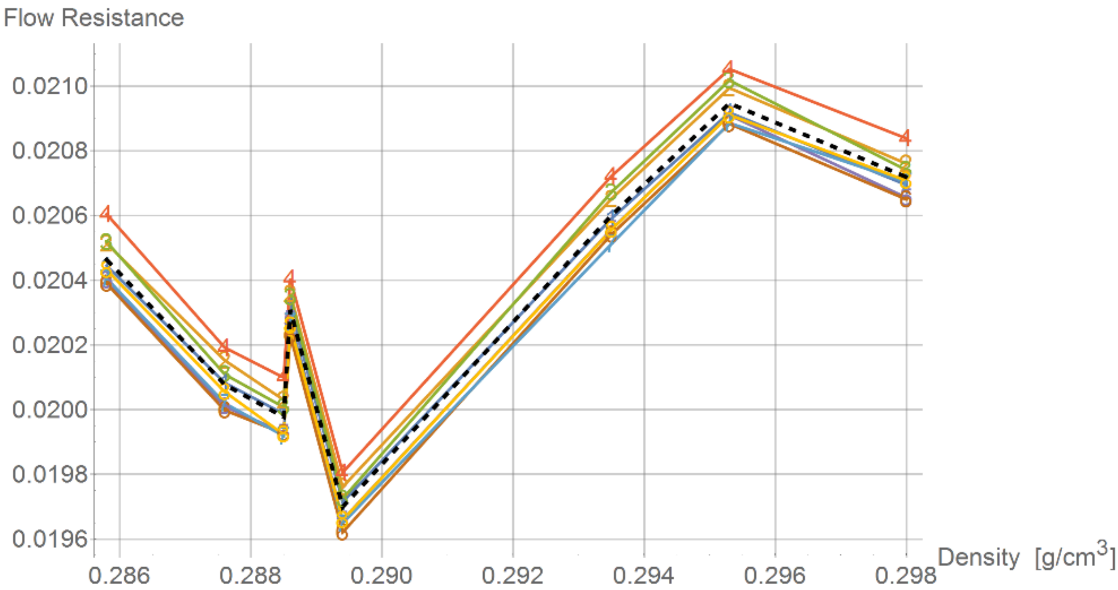

Fig. 5. Method stability measured on samples with narrow range of package density, black dashed line is the mean value of measured data

5. Conclusion

The method and device for measuring the air flow resistance, which represents the yarn packages quality from the dyeing point of view in much exact way than present used ones, was introduced. The first tests results, which compared the measured air flow resistance and the package density, proof the device sensitive is at least as good as the density measurement. The actual long term field test in dye-works has to confirm the conclusions of laboratory tests and find the direct dependences between the air flow resistance determined by introduced device and dying quality or needed setting of dying process.

Acknowledgement

This work was supported by the Czech Ministry of Education, project LO1213.

References

[1] Sinaiski E. G. Hydromechanics. John Wiley & Sons, 2011.

[2] Adámek K. Fabric air permeability numerical modeling. Strutex 2006, 16-17.

[3] Bušek M., Čejka V., Klouček P., Šidlof P., Škop P. Method of measuring the hardness and/or density of yarn packages and a device for carrying out the method. International patent no. EP1653212 (A2), 2006.

[4] Křemenáková D., Rubnerová J., Aneja A. P. Influence of fibers geometry on the polyester yarns packing density and porosity. The Fiber Society, Fall 2001 Annual Technical Conference, 47-48.

[5] Shamey R., Zhao X. Properties of Yarn. Modelling, Simulation and Control of the Dyeing Process. Elsevier, 2014.

Applications of MeV Ion Beams, Nuclear Techniques and Computer Simulation to Surface Analysis of Materials

[1,2]J. Pacheco de Carvalho, [2]C. Pacheco, [1,2]A. Reis

[1]Departamento de Física, [2]U. de Detecção Remota,
Universidade da Beira Interior, Rua Marquês d'Ávila e Bolama,
6201-001 Covilhã, Portugal
Email: pacheco@ubi.pt

Abstract. *This work involves surface analysis by nuclear techniques, which are essentially non-destructive, and computer simulation. The energy analysis method for nuclear reaction analysis is used. Energy spectra are computer simulated and compared to experimental data, giving target composition and concentration profile information. The simulations use, mainly, target parameterization and available nuclear data. The method is successfully applied to determination of a diffusion concentration profile of* ^{18}O *in a thick oxide target. A uniform concentration profile of* ^{12}C *is obtained for a very thin film. Uniform concentration profiles of* ^{16}O *are also obtained from (d,p) and (d,α) reactions along large depths. Elastic scattering is used for depth profiling of Al and Ag and Au thin films.*

Keywords: Surface Analysis, Nuclear Reaction Analysis, Carbon, Oxygen, Elastic Scattering, Computer Simulation

1. Introduction

A broad range of surface analysis techniques has been developed, involving e.g. ion, electron and photon beams interacting with a solid target. The techniques are, generally, complementary and provide target information for depths near the surface. Both nuclear and non-nuclear techniques have been available. Nuclear techniques, which are essentially non-destructive, provide for analysis over a few microns close to the surface giving absolute values of concentrations of isotopes and elements. Their main applications have been in areas such as scientific, technologic, industry, arts and medicine, using MeV ion beams [1-7]. Nuclear reactions permit tracing of isotopes with high sensitivities. We use ion-ion reactions and the energy analysis method where, at a conveniently chosen energy of the incident ion beam, an energy spectrum is recorded of ions from the reaction, coming from several depths in the target. Θ_L is the laboratory detection angle and Θ_R is the target rotation angle. Such spectra are computationally predicted, giving target composition and concentration profile information [4-8]. Elastic scattering is a particular and important case. A computer program has been developed in this context, mainly for flat targets [4-7]. The non-flat target situation arises as an extension [9]. Imaging techniques are important for checking target surface topography. Applications of the method are made to depth profiling of light nuclei e.g. ^{18}O and ^{12}C, for a thick target and a very thin film, using $^{18}O(p,\alpha_0)^{15}N$ and $^{12}C(d,p_0)^{13}C$ reactions, respectively. ^{16}O nuclei are profiled by (d,p) and (d,α) reactions for a thick target. The usefulness of elastic scattering is also shown. Scanning electron microscopy is used as an imaging technique to check target surface topography.

The rest of the paper is structured as follows: Section 2 is about the experimental details i.e. the measurement setup and procedure. Results and discussion are given in Section 3. Conclusions are drawn in Section 4.

2. Subject and Method

The experimental arrangement has been mentioned [5]. For an incident beam of accelerated ions, and an ion-ion nuclear reaction experiment, ion detection from the sample at laboratory angles Θ_L of 135º and 165º used silicon surface barrier detectors, chosen as suitable for the reaction and energy ranges involved. Spectral data were acquired as counts per channel versus channel number, usually for ion beam perpendicular incidence (rotation angle Θ_R=0º), through charge preamplifiers, amplifiers and analogue to digital converters providing for pulse pile-up rejection, data interfaces and an on-line computer equipped with data acquisition software. Following energy calibration of the spectra, spectral yields as counts per unit energy versus energy were obtained. The following samples were used as targets for acquisition of charged particle spectra: (1) an austenitic steel (20/25/Nb steel) sample, labelled S1, which was obtained by high temperature sequential oxidation first in $C^{16}O_2$ gas and then in $C^{18}O_2$ gas for 40 hours; an ^{18}O diffusion erfc concentration profile [4] was expected; scanning electron microscopy has shown a reasonably flat oxide; (2) a thick flat sample of quartz (SiO_2), labelled S2; it had a very thin surface film of carbon with thickness X_1=0.062 μm [7]; (3) a flat sample, labelled S3, obtained by sequential vacuum deposition of Ag and Au onto an Al thick flat substrate (Al/Ag/Au); film thicknesses of X_1=0.0648 μm and X_2=0.1333 μm were initially expected for Au and Ag, respectively.

3. Results and Discussion

Computer simulated spectra mainly take into account: target parameters, such as composition and concentration profiles; energy spread of the incident ion beam; geometric factors and target rotation; stopping power; differential cross section; energy straggling; detector resolution [5]. An option permits calculation of effects from: small forward angle multiple scattering; incident beam size and angular divergence; detector angular aperture. Gaussian straggling is considered, based on Bohr theory [10]. Lindhard-Scharff theory [11] is the main option. In building a basic spectrum, with ingoing ions penetrating the target and outcoming ions travelling towards the detector, we calculate mainly: ingoing and outcoming energy distributions, dependence of the yield on detection system resolution and final yield versus energy [6]. By varying target parameters, for visually fitting simulated spectra to experimental data, target composition and concentration profiles are obtained. In simulating spectra for nuclear reactions we used published stopping power [12-15] and differential cross-section data [5, 16-17]. Similarly for elastic scattering, where Rutherford differential cross-sections applied.

The oxidized steel sample containing ^{18}O, S1, was analysed through a proton beam at a bombarding energy E_p=1.78 MeV, an energy slightly above the resonance energy at 1.766 MeV of the $^{18}O(p,\alpha_0)^{15}N$ reaction, and 165º. A good computer fit to data was obtained, as shown in Fig. 1. An ^{18}O distribution due to diffusion was found, described by a complementary error function [4] with a diffusion coefficient D=2.7 x 10^{-14} cm^2 s^{-1}. This value was also confirmed from analysis of the spectrum obtained at 165º in another detector, symmetrically located with respect to the incident beam. This diffusion coefficient is higher than the value determined from the resonance method of analysis using the 1.766 MeV resonance [18], as the method of the present work permits higher depth resolution.

The quartz sample, S2, was analysed with a deuteron beam at E_d=0.993 MeV and 135º. The bombarding energy was chosen to obtain insignificant yields of deuteron induced reactions in ^{28}Si. For the (d,p_0) reaction in ^{12}C, published differential cross-section data were used [5]. A good computed fit to data was obtained. A very thin surface film of ^{12}C was found with uniform concentration and thickness X_1=0.061 μm. A uniform step concentration profile distribution of ^{16}O was found in the quartz substrate. The corresponding thickness parameters X_2 used in the predictions were, by descending order, 5.49 μm for (d,p_0), 5.20 μm for (d,p_1) and 3.39 μm for (d,α_0). Details of the fit are shown in Fig. 2, for the spectral shape of the ^{16}O (d, p_1) $^{17}O^*$ reaction peak.

The sample Al/Ag/Au, S3, was analysed with a $(^4He)^+$ ion beam at E_α=1.5 MeV, and 165°. This initial fit suggested that a small percentage of Ag might be incorporated in the Au film. A further analysis at a higher bombarding energy, E_α=2.9 MeV, permitted to conclude that the sample is better described by a structure Al/Ag/(Au,Ag) where the surface film consists of a mixture of Au and Ag as a result of the sequential vacuum evaporation. An improved computer fit to the new data was obtained as shown in Fig. 3. Step concentration profiles were used for Au and Ag in the surface layer with X_1=0.060 μm and for Ag in the middle layer with X_2=0.126 μm. These thickness values are close to the nominal values initially estimated. A relative atomic density C_{Ag}/C_{Au} of 5.6% in the mixture was used. Details of the new fit are shown in Fig. 4 for the Au and Ag shapes.

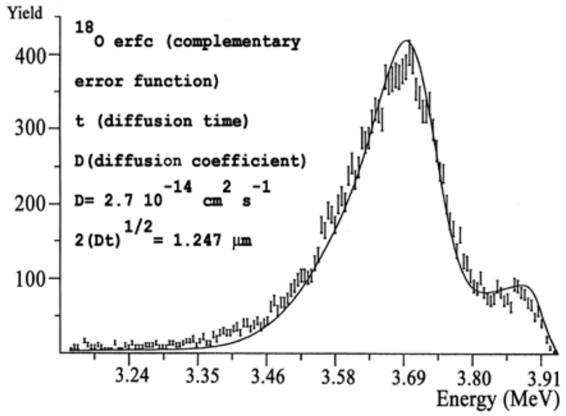

Fig. 1. Computed fit to the $^{18}O(p,\alpha_0)^{15}N$ reaction data from the oxidized steel target, S1, for E_p=1.78 MeV, Θ_L=165°.

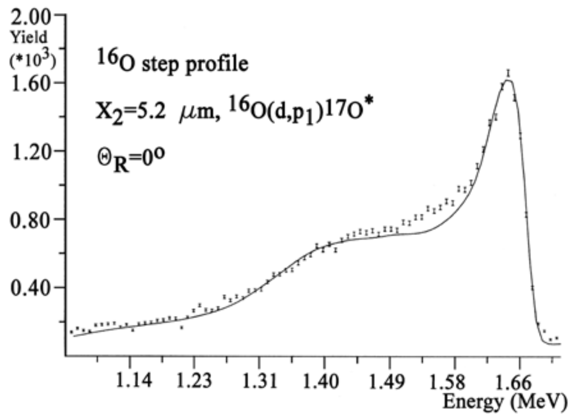

Fig. 2. Computed fit to data of the ^{16}O (d, p1) $^{17}O^*$ reaction peak from the quartz target, S2, for E_d=0.993 MeV, Θ_L=135°.

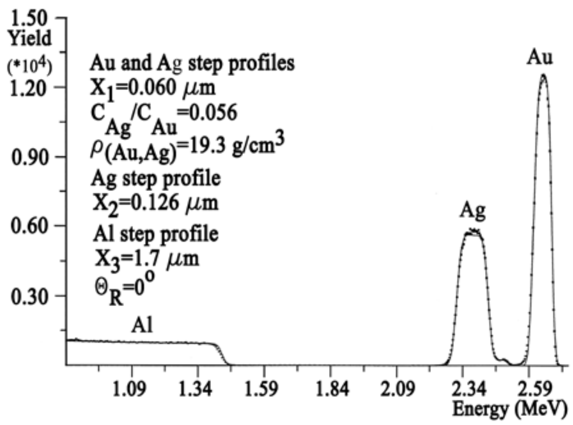

Fig. 3. Computed fit to the elastic scattering data from the Al/Ag/Au sample, S3, for E_α=2.9 MeV, Θ_L=165°.

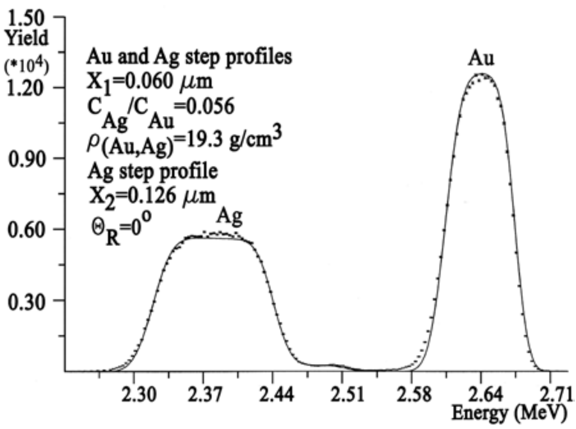

Fig. 4. Computed fit to the elastic scattering shapes from Ag and Au in the Al/Ag/Au sample, S3, for E_α=2.9 MeV, Θ_L=165°.

4. Conclusions

The present work has given positive results in surface analysis by nuclear reactions, for depth profiling of ^{12}C, ^{16}O and ^{18}O nuclei, and elastic scattering. The predictions obtained by computer simulation have given good descriptions of experimental spectra for relevant profiling of: ^{12}C for a very thin film; ^{16}O along large depths in a thick target; ^{18}O in a thick oxidized steel target; thin films of Ag and Au deposited onto a thick Al substrate. Nuclear techniques have shown to be highly powerful and important analytical tools in this context. SEM was useful for checking surface topography. The results presented would be very difficult to obtain by non-nuclear techniques.

Acknowledgements

Supports from University of Beira Interior and FCT (Fundação para a Ciência e a Tecnologia)/ PEst-OE/FIS/UI0524/2014(ProjectoEstratégico-UI524-2014) are acknowledged.

References

[1] Tesmer JR, Nastasi M. (Eds.) Handbook of Modern Ion Beam Materials Analysis, Materials Research Society, Pittsburgh, PA, 1995.

[2] Amsel G, Battistig G., Nucl. Instr. and Meth. B 240 (2005) 1.

[3] Calvert JM, Derry DJ, Lees DG. J. Phys. D: Appl. Phys. 7 (1974) 940.

[4] Pacheco de Carvalho JAR. Ph. D. Thesis, University of Manchester, England, 1984.

[5] Pacheco de Carvalho JAR, Reis AD. Nucl. Instr. and Meth. B 266, 10 (2008) 2263.

[6] Pacheco de Carvalho JAR, Reis AD. Bol. Soc. Esp. Ceram. V. 47, 4 (2008) 252.

[7] Pacheco de Carvalho JAR, Ribeiro Pacheco CFFP, Reis AD. Nucl. Instr. and Meth. B 269, 24 (2011) 3054.

[8] Barradas NP, Arstila K, Battistig G, Bianconi M, Dytlewski N, Jeynes C, Kótai E, Lulli G, Mayer M, Rauhala E, Szilágyi E, Thompson M. Nucl. Instr. and Meth. B 262 (2007) 282.

[9] Pacheco de Carvalho JAR, Pacheco CFFPR, Reis AD. Bol. Soc. Esp. Ceram. V. 49, 1 (2010) 23.

[10] N. Bohr, Mat. Fys. Medd. Dan. Vid. Selsk. 18 (8) (1948) 1.

[11] J. Lindhard, M. Scharff, Mat. Fys. Medd. Dan. Vid. Selsk. 27 (15) (1953) 1.

[12] D. C. Santry , R. D. Werner, Nucl. Instr. and Meth. 188 (1981) 211.

[13] C. Williamson, J. P. Boujot, J. Picard, C. E. A. Rep. Nº 3042, Centre d’Études Nucleaires de Saclay, 1966.

[14] H. H. Andersen, J. F. Ziegler, in: J. F. Ziegler (Ed.), The stopping and ranges of ions in matter: Hydrogen stopping powers and ranges in all elements, vol.3, Pergamon Press Inc., Oxford. 1977.

[15] J. F Ziegler, in: J. F. Ziegler (Ed.), The stopping and ranges of ions in matter: Helium stopping powers and ranges in all elements, Vol.4, Pergamon Press Inc., Oxford, 1977.

[16] G. Debras, Thesis, Facultés Universitaires de Namur, Belgium, 1977.

[17] G. Amsel, Thesis, University of Paris, Faculty of Science, Orsay, 1963.

[18] Reich DF. Ph. D. Thesis, University of Manchester, England, 1982.

AUTHORS INDEX